Version 10.0
August 2008

Wide Field and Planetary Camera 2 Instrument Handbook

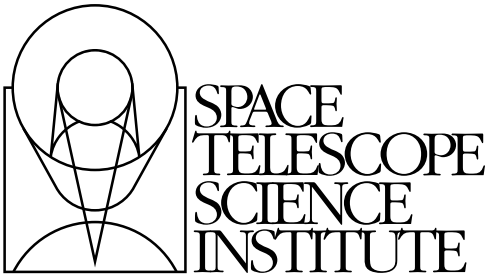

Space Telescope Science Institute
3700 San Martin Drive
Baltimore, Maryland 21218
help@stsci.edu

Operated by the Association of Universities for Research in Astronomy, Inc., for the National Aeronautics and Space Administration

User Support

For prompt answers to any question, please contact the STScI Help Desk.

- **E-mail:** help@stsci.edu
- **Phone:** (410) 338-1082
  (800) 544-8125 (U.S. only, toll free)

World Wide Web

Information, software tools, and other resources are available on the WFPC2 World Wide Web page:

- URL: http://www.stsci.edu/hst/wfpc2

Revision History

Instrument	Version	Date	Editor
WFPC2	10.0	August 2008	Matt McMaster, John Biretta
WFPC2	9.2	October 2006	John A. Biretta
WFPC2	9.1	October 2005	Inge Heyer, John A. Biretta
WFPC2	9.0	October 2004	Inge Heyer, John A. Biretta
WFPC2	8.0	October 2003	Anton Koekemoer, Inge Heyer
WFPC2	7.0	October 2002	John A. Biretta, Lori M. Lubin
WFPC2	6.1	July 2001	John A. Biretta, Inge Heyer
WFPC2	6.0	June 2001	John A. Biretta, Inge Heyer
WFPC2	5.0	June 2000	John A. Biretta, Inge Heyer
WFPC2	Update	June 1999	Stefano Casertano
WFPC2	Update	June 1998	Andrew Fruchter, Inge Heyer
WFPC2	4.0	June 1996	John A. Biretta
WFPC2	1.0; 2.0; 3.0	March 1993; May 1994; June 1995	Christopher J. Burrows
WF/PC-1	3.0	April 1992	John W. MacKenty
WF/PC-1	1.0; 2.0; 2.1	October 1985; May 1989; May 1990	Richard Griffiths

Send comments or corrections to:
Space Telescope Science Institute
3700 San Martin Drive
Baltimore, Maryland 21218
E-mail:help@stsci.edu

Table of Contents

Acknowledgments

Handbook Authors and Contributors

Sylvia Baggett, Luigi Bedin, John Biretta, Gabriel Brammer, Chris Burrows, Stefano Casertano, Marco Chiaberge, Mark Clampin, Van Dixon, Harry Ferguson, Andrew Fruchter, Ron Gilliland, Dave Golimowski, Shireen Gonzaga, Richard Griffiths, Inge Heyer, Jon Holtzman, Steve Hulbert, Anton Koekemoer, Vera Kozhurina-Platais, John Krist, Lori Lubin, Jennifer Mack, John MacKenty, Matt McMaster, Max Mutchler, Keith Noll, Christopher O'Dea, James Rhoads, Adam Riess, Susan Rose, Al Schultz, Marco Sirianni, Mark Stevens, Massimo Stiavelli, Anatoly Suchkov, Jean Surdej, Michael Wiggs, Brad Whitmore.

Attribution

In publications please refer to this document as:

"McMaster, Biretta, et al. 2008, WFPC2 Instrument Handbook, Version 10.0 (Baltimore: STScI)."

CHAPTER 1:

Introduction

In this chapter . . .

1.1 Instrument Overview

Wide Field and Planetary Camera 2 (WFPC2) was placed aboard the Hubble Space Telescope in December, 1993 during the first servicing mission (SM1). It is due to be replaced by Wide Field Camera 3 (WFC3) during SM4, currently scheduled for Fall, 2008.

The instrument is a two-dimensional imaging photometer, located at the center of the Hubble Space Telescope (HST) focal plane and covers the spectral range between approximately 1150Å to 10500Å. It simultaneously images a 150″ x 150″ "L"-shaped region with a spatial sampling of 0.1″ per pixel, and a smaller 34″ x 34″ square field with 0.046″ per pixel. The total system quantum efficiency (WFPC2+HST) ranges from 4% to 14% at visual wavelengths, and drops to ~0.1% in the far UV. Detection of faint targets is limited by either the sky background (for broad band filters) or by noise in the read-out electronics (for narrow band and UV filters) with an RMS equivalent to 5 detected photons. Bright targets can cause saturation (>53000 detected photons per pixel), but there are no related safety issues. The sections below give a more detailed overview.

1.1.1 Field-of-View

The WFPC2 field-of-view is divided into four cameras by a four-faceted pyramid mirror near the HST focal plane. Each of the four cameras contains an 800x800 pixel Loral CCD detector. Three cameras operate at an image scale of 0.1″ per pixel (F/12.9) and comprise the Wide Field Camera (WFC) with an "L" shaped field-of-view. The fourth camera operates at 0.046″ per pixel (F/28.3) and is referred to as the Planetary Camera (PC). There are thus four sets of relay optics and CCD sensors in WFPC2. The four cameras are called PC1, WF2, WF3, and WF4, and their fields-of-view are illustrated in Figure 1.1 (also see Section 7.8). Each image is a mosaic of three F/12.9 images and one F/28.3 image.

Figure 1.1: WFPC2 Field-of-View Projected on the Sky. The readout direction is marked with arrows near the start of the first row in each CCD. The X-Y coordinate directions are for POS-TARG commands. The position angle of V3 varies with pointing direction and observation epoch, and is given in the calibrated science header by keyword PA_V3.

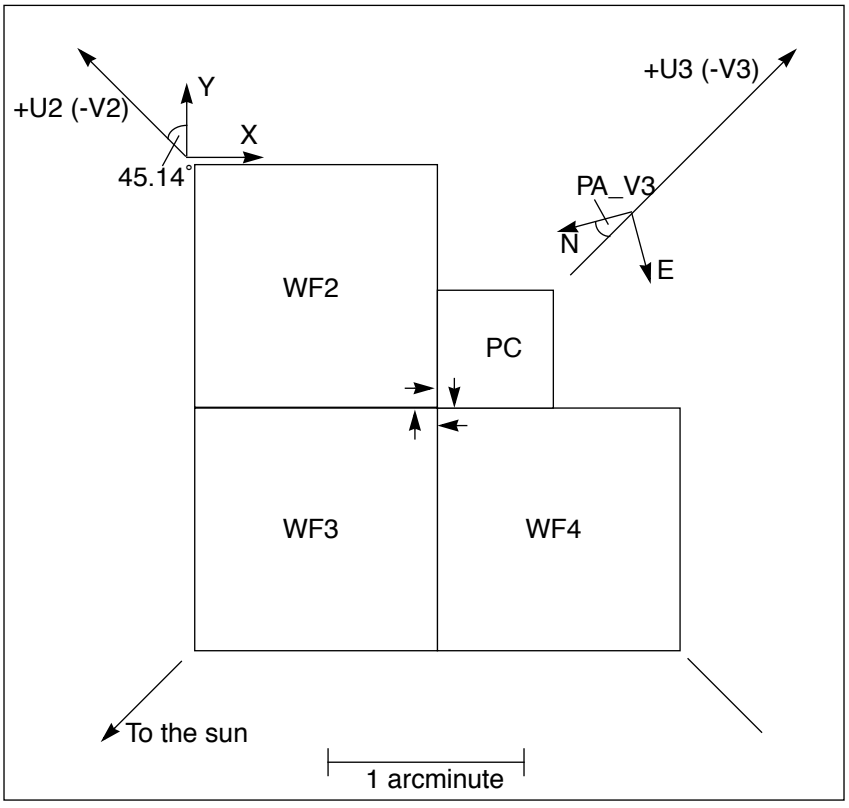

1.1.2 Spectral Filters

The WFPC2 contains 48 filters mounted in 12 wheels of the Selectable Optical Filter Assembly (SOFA). These include a set of broad band filters approximating Johnson-Cousins UBVRI, as well as a set of wide U, B, V, and R filters, and a set of medium bandwidth Strömgren *u, v*, *b*, and *y* filters.

Narrow band filters include those for emission lines of Ne V (3426Å), CN (~3900Å), [OIII] (4363Å and 5007Å), He II (4686Å), Hβ (4861Å), He I (5876Å), [OI] (6300Å), Hα (6563Å), [NII] (6583Å), [SII] (6716Å and 6731Å), and [SIII] (9531Å). The narrow band filters are designed to have the same dimensionless bandpass profile. Central wavelengths and profiles are uniformly accurate over the filter apertures, and laboratory calibrations include profiles, blocking, and temperature shift coefficients.

There are also two narrow band "quad" filters, each containing four separate filters which image a limited field-of-view. The UV quad contains filters for observing redshifted [OII] emission and are centered at 3767Å, 3831Å, 3915Å, and 3993Å (see Section 3.4). The Methane quad (Section 3.6) contains filters at 5433Å, 6193Å, 7274Å, and 8929Å. Finally, there is a set of narrow band "linear ramp filters" (LRFs) which are continuously tunable from 3710Å to 9762Å; these provide a limited field-of-view with a diameter of ~10″. More information on the LRFs can be found in Section 3.3.

At ultraviolet wavelengths, there is a solar-blind Wood's UV filter (1200-1900Å); please see Section 3.7 for more information on the Woods filter. The UV capability is also enhanced by control of UV absorbing molecular contamination, the capability to remove UV absorbing accumulations on cold CCD windows without disrupting the CCD quantum efficiencies and flat field calibrations, and an internal source of UV reference flat field images.

Finally, there is a set of four polarizers set at four different angles, which can be used in conjunction with other filters for polarimetric measurements. However, due to the relatively high instrumental polarization of WFPC2, they are best used on strongly polarized sources (>3% polarized). Sources with weaker polarization will require very careful calibration of the instrumental polarization. For more information on the polarizers, please see Section 3.5.

1.1.3 Quantum Efficiency and Exposure Limits

The quantum efficiency (QE) of WFPC2+HST peaks at 14% in the red, and remains above 4% over the visible spectrum. The UV response extends to Lyman α wavelengths (QE~0.1%). Spherical aberration correction is achieved via internal optics.

Exposures of bright targets are limited by saturation effects, which appear above ~53000 detected photons per pixel (for setting ATD-GAIN=15), and by the shortest exposure time which is 0.11 seconds. There are no instrument safety issues associated with bright targets. Detection of faint targets is limited by the sky background for broad band filters at visual wavelengths. For narrow band and ultraviolet filters, detections are limited by noise in the read-out amplifier ("read noise"), which contributes an RMS noise equivalent to ~5 detected photons per pixel for an ATD-GAIN of 7.

1.1.4 CCD Detector Technology

The WFPC2 CCDs are thick, front-side illuminated devices made by Loral Aerospace. They support multi-pinned phase (MPP) operation which eliminates quantum efficiency hysteresis. They have a Lumogen phosphor coating to give UV sensitivity; the on-orbit performance of the detectors is discussed in Chapter 4. Technical details may be summarized as follows:

- **Read noise:** WFPC2 CCDs have ~5e^- RMS read noise (for ATD-GAIN=7) which provides good faint object and UV imaging capabilities.
- **Dark noise:** Inverted phase operation yields low dark noise for WFPC2 CCDs. They are being operated at -88˚C and the median dark current is about 0.0045 e^- $pixel^{-1}$ s^{-1}.
- **Flat field:** WFPC2 CCDs have a uniform pixel-to-pixel response (<2% pixel-to-pixel non-uniformity) which facilitates accurate photometric calibration.
- **Gain switch:** Two CCD gains are available with WFPC2, a 7 e^- DN^{-1} channel which saturates at about 27000 e^- (4096 DN with a bias of about 300 DN) and a 14 e^- DN^{-1} channel which saturates at about 53000 e^-. The Loral devices have a full well capacity of ~90,000 e^- and are linear up to 4096 DN in both channels.
- **DQE:** The peak CCD DQE in the optical is 40% at 7000Å. In the UV (1100-4000Å) the DQE is determined by the phosphorescent Lumogen coating, and is 10 - 15%.

- **Image Purge:** The residual image resulting from a 100x (or more) full-well over-exposure is well below the read noise within 30 minutes. No CCD image purge is needed after observations of very bright objects. The Loral devices bleed almost exclusively along the columns.
- **Quantization:** The systematic Analog-to-Digital converter errors have been largely eliminated, contributing to a lower effective read noise.
- **QEH:** Quantum Efficiency Hysteresis (QEH) is not a significant problem in the Loral CCDs because they are front side illuminated and use MPP operation. The absence of any significant QEH means that the devices do not need to be UV-flooded and the chips can be warmed monthly for decontamination purposes without needing to maintain a UV-flood.
- **Detector MTF:** The Loral devices do suffer from low level detector MTF (Modulation Transfer Function) perhaps caused by scattering in the front side electrode structure. The effect is to blur images and decrease the limiting magnitude by about 0.5 magnitudes.

1.1.5 UV Imaging

WFPC2 had a design goal of 1% photometric stability at 1470Å over a month. This requires a contamination collection rate of less than 47 ng cm^{-2} $month^{-1}$ on the cold CCD window. Hence, the following features were designed into WFPC2 in an effort to reduce contaminants:

1. Venting and baffling, particularly of the electronics, were redesigned to isolate the optical cavity.
2. There was an extensive component selection and bake-out program, and specialized cleaning procedures.
3. Molecular absorbers (Zeolite) were incorporated.

The CCDs were initially operated at -77˚C after launch, which was a compromise between being as warm as possible for contamination reasons, while being sufficiently cold for an adequate dark rate. However, at this temperature significant photometric errors were introduced by low-level traps in the CCDs. This problem with the charge transfer efficiency of the CCDs has been reduced since 23 April 1994 by operating the CCDs at -88˚C, but this leads to significantly higher contamination rates than hoped for. On-orbit measurements indicate that there is a decrease in throughput at a repeatable rate of ~30% per month at 1700Å (see Section 6.11). Monthly decontamination procedures are able to remove the contaminants completely and recover this loss. As of Cycle 12, the interval between decontaminations has been increased from 30 days to approximately 49 days.

1.1.6 Aberration Correction and Optical Alignment

WFPC2 contains internal corrections for the spherical aberration of the HST primary mirror. These corrections are made by highly aspheric surfaces figured onto the Cassegrain relay secondary mirror inside each of the four cameras. Complete correction of the aberration depends on a precise alignment between the OTA pupil and these relay mirrors.

Mechanisms inside WFPC2 allow optical alignment on-orbit. The 47˚ pick-off mirror has two-axis tilt capabilities provided by stepper motors and flexure linkages to compensate for uncertainties in our knowledge of HST's latch positions (i.e., instrument tilt with respect to the HST optical axis). These latch uncertainties would be insignificant in an unaberrated telescope, but must be compensated for in a corrective optical system. In addition, three of the four fold mirrors, internal to the WFPC2 optical bench, have limited two-axis tilt motions provided by electrostrictive ceramic actuators and invar flexure mountings. Fold mirrors for the PC1, WF3, and WF4 cameras are articulated, while the WF2 fold mirror has a fixed invar mounting. A combination of the pick-off mirror and actuated fold mirror (AFMs) has allowed us to correct for pupil image misalignments in all four cameras. Since the initial alignment, stability has been such that mirror adjustments have not been necessary. (The mechanisms were not available for GO commanding.)

1.2 Comparison of WFPC2, ACS, NICMOS, and STIS

In this section we briefly compare the performance of contemporary HST instruments with imaging capability in the UV to near-IR spectral range. These instruments include WFPC2, STIS, NICMOS, and ACS. Important imaging parameters for all instruments are summarized in Table 1.1.

The instrument parameters given here only represent a snapshot in time when multiple instruments were operational, and may not accurately reflect the history of each instrument. Please see the individual instrument Handbooks for the detailed parameters and history of each instrument.

Table 1.1: Comparison of WFPC2, ACS, NICMOS, and STIS Instrumental Imaging Parameters[a].

Parameter	WFPC2	ACS	NICMOS	STIS
Wavelength range	1150Å - 11,000Å	WFC: 3700 Å - 11000 Å HRC: 2000 Å - 11000 Å SBC: 1150 Å - 1700 Å	8000Å - 25,000Å	FUV-MAMA: 1150Å - 1700Å NUV-MAMA: 1700Å - 3100Å CCD: 2000Å - 11,000Å
Detector	Si CCDs	CCDs (WFC, HRC) MAMA (SBC)	HgCdTe arrays	CCD, MAMAs
Image Format	4 x 800 x 800	WFC: 2 butted 2048x4096 HRC: 1024x1024 SBC: 1024x1024	3 x 256 x 256	1024 x 1024
Field-of-view and pixel size	150" x 150" @ 0.1" /pix 34"x 34" @ 0.046"/pix [(b)]	WFC: 202"x202" @0.05" /pix HRC: 29"x26" @0.028"x0.025" /pix SBC: 35"x31" @0.033"x0.030" /pix	NIC1: 11"x 11" @ 0.043" /pix NIC2: 19" x 19" @ 0.075″ /pix NIC3: 51″ x 51″ @ 0.2″ /pix	MAMAs: 25" x 25" @ 0.024"/pix CCD: 51" x 51" @ 0.05″ /pix [(c)]
Read noise	5 e^-	WFC: 5 e^- HRC: 4.7 e^- SBC: 0 e^-	30 e^-	MAMAs: 0 e^- CCD: 5.4e^-
Dark current	0.002[WF2] - 0.006[PC] e^- /s/pix	WFC: 0.002 e^-/s/pix HRC: 0.0025 e^-/s/pix SBC: $1.2x10^{-5}$ e^-/s/pix	<0.1 e^- /s/pix	NUV-MAMA: 0.0001 e^- /s/pix FUV-MAMA: $7x10^{-6}$ e^- /s/pix CCD: 0.004 e^- /s/pix
Saturation	53,000 e^-	WFC: 80,000 e^- HRC: 140,000 e^- SBC: 100 counts/s/pix	200,000 e^-	MAMAs: 100 counts/s/pix CCD: 140,000 e^-

a. These parameters refer to specific times when multiple instruments were operational and may not accurately reflect the total history of each instrument. For detailed information on a specific instrument, please consult the Handbook for that instrument.
b. “L”-shaped field-of-view using 3 CCDs with 0.1" pixels, and one CCD with 0.046" pixels.
c. Field-of-view is up to 51" x 51" if no filter is used, and down to 12" x 12" for some neutral density filters.

1.2.1 Comparison of WFPC2 and ACS

Advantages of each instrument may be summarized as follows. WFPC2 advantages are:

- Wider field of view in the UV - effective area of 134"x134" vs. 35"x31".
- Wider field of view in many narrow band filters - effective area of 134"x134" vs. up to 40"x70" (ACS LRFs).

ACS advantages are:

- Wider field of view in broad band optical filters - effective area of 202"x202" vs. 134"x134".
- Factor of ~2 better sampling of the PSF.

- Higher detective efficiency (factor of 2-10 depending on wavelength). Table 1.2 compares the detective efficiency for WFPC2 and ACS filters with similar band passes.
- True solar blind imaging in the UV due to the MAMA detector.
- Coronagraphic capability.

Table 1.2: Comparison of WFPC2 and ACS Filters.

WFPC2			ACS				ACS / WFPC2 Wide-Field Imaging Effic'y[a]
Filter	FOV (arcsec)[b]	Approx Peak Effic'y[c]	Filter	Camera	FOV (arcsec)[d]	Approx Peak Effic'y[c]	
Broad Band							
F160W	90" x 90"	0.07%	F150LP	SBC	31" x 35"	3%	5.74
F170W	134" x 134"	0.17%	F165LP	SBC	31" x 35"	0.9%	0.32
F185W	134" x 134"	0.19%	-	-	-	-	-
F218W	134" x 134"	0.28%	F220W	HRC	26" x 29"	5%	0.75
F255W	134" x 134"	0.45%	F250W	HRC	26" x 29"	6.1%	0.56
F300W	134" x 134"	1.9%	-	-	-	-	-
F336W	134" x 134"	3.5%	F330W	HRC	26" x 29"	10.5%	0.13
F380W	134" x 134"	3.7%	-	-	-	-	-
F439W	134" x 134"	3.9%	F435W	WFC HRC	202" x 202" 26" x 29"	33% 22%	19.2 0.24
F450W	134" x 134"	8.5%	F475W	WFC HRC	202" x 202" 26" x 29"	36% 24%	9.62 0.12
F555W	134" x 134"	11%	F555W	WFC HRC	202" x 202" 26" x 29"	37% 23%	7.64 0.09
F569W	134" x 134"	11%	-	-	-	-	-
F606W	134" x 134"	14%	F606W	WFC HRC	202" x 202" 26" x 29"	44% 27%	7.14 0.08
F622W	134" x 134"	14%	F625W	WFC HRC	202" x 202" 26" x 29"	43% 26%	6.98 0.08
F675W	134" x 134"	14%	-	-	-	-	-
F702W	134" x 134"	14%	-	-	-	-	-
F785LP	134" x 134"	5%	-	-	-	-	-
F791W	134" x 134"	9%	F775W	WFC HRC	202" x 202" 26" x 29"	42% 22%	10.6 0.10

Table 1.2: Comparison of WFPC2 and ACS Filters.

WFPC2			ACS				ACS / WFPC2 Wide-Field Imaging Effic'y[a]
Filter	FOV (arcsec)[b]	Approx Peak Effic'y[c]	Filter	Camera	FOV (arcsec)[d]	Approx Peak Effic'y[c]	
F814W	134" x 134"	10%	F814W	WFC HRC	202" x 202" 26" x 29"	42% 22%	9.54 0.09
F850LP	134" x 134"	3.9%	F850LP	WFC HRC	202" x 202" 26" x 29"	25% 13%	14.6 0.14
	Medium Band						
F122M	134" x 134"	0.11%	F122M	SBC	31" x 35"	0.9%	0.49
F410M	134" x 134"	4%	-	-	-	-	-
F467M	134" x 134"	5.5%	B. Ramp (FR459M)	WFC HRC	65" x 100" 26" x 29"	29%	0.44
F547M	134" x 134"	11%	F550M	WFC HRC	202" x 202" 26" x 29"	40% 25%	8.26 0.10
F1042M	134" x 134"	0.5%	B. Ramp (FR914M)	WFC HRC	65" x 100" 26" x 29"	4%	1.0
	Narrow Band						
F343N	134" x 134"	0.39%	F344N	HRC	26" x 29"	10%	1.08
F375N	134" x 134"	0.9%	OII Ramp (FR388N)	WFC HRC	65" x 100" 26" x 29"	4%	0.22
FQUVN 3767Å	60" x 60"	1.3%	OII Ramp (FR388N)	WFC HRC	65" x 100" 26" x 29"	6%	1.2
FQUVN 3831Å	67" x 67"	1.5%	OII Ramp (FR388N)	WFC HRC	65" x 100" 26" x 29"	8%	1.0
FQUVN 3915Å	67" x 67"	1.9%	OII Ramp (FR388N)	WFC HRC	65" x 100" 26" x 29"	10%	0.9
FQUVN 3993Å	67" x 67"	2.3%	OII Ramp (FR388N)	WFC HRC	65" x 100" 26" x 29"	10%	0.8
F390N	134" x 134"	1.9%	OII Ramp (FR388N)	WFC HRC	65" x 100" 26" x 29"	10%	0.23
F437N	134" x 134"	3%	OII Ramp (FR423N)	WFC	45" x 85"	10%	0.16
F469N	134" x 134"	3.7%	OII Ramp (FR462N)	WFC	60" x 85"	13%	0.17
F487N	134" x 134"	4.8%	OIII Ramp (FR505N)	WFC HRC	65" x 100" 26" x 29"	18%	0.20
F502N	134" x 134"	5.8%	F502N	WFC HRC	202" x 202" 26" x 29"	28% 19%	11.0 0.14

Table 1.2: Comparison of WFPC2 and ACS Filters.

WFPC2			ACS				ACS / WFPC2 Wide-Field Imaging Effic'y[a]
Filter	FOV (arcsec)[b]	Approx Peak Effic'y[c]	Filter	Camera	FOV (arcsec)[d]	Approx Peak Effic'y[c]	
FQCH4 5435Å	30" x 30"	9.5%	OIII Ramp (FR551N)	WFC	45" x 85"	28%	2.7
F588N	134" x 134"	13%	OIII Ramp (FR551N)	WFC	45" x 85"	34%	0.12
FQCH4 6199Å	30" x 30"	12%	OIII Ramp (FR601N)	WFC	60" x 85"	29%	2.3
F631N	134" x 134"	13%	OIII Ramp (FR601N)	WFC	60" x 85"	31%	0.11
F656N	134" x 134"	11%	Hα Ramp (FR656N)	WFC HRC	65" x 100" 26" x 29"		
F658N	134" x 134"	11%	F658N	WFC HRC	202" x 202" 26" x 29"	44% 26%	9.09 0.10
F673N	134" x 134"	12%	Hα Ramp (FR656N)	WFC HRC	65" x 100" 26" x 29"	28%	0.11
FQCH4 7278Å	30" x 30"	10%	Hα Ramp (FR716N)	WFC	45" x 85"	31%	3
FQCH4 8930Å	30" x 30"	2.9%	F892N	WFC HRC	202" x 202" 26" x 29"	12%	3.47
F953N	134" x 134"	2.2%	IR Ramp (FR931N)	WFC	60" x 85"	12%	0.31

a. Relative efficiency for ACS vs. WFPC2 for wide-field imaging. Defined as [(ACS FOV area)x(ACS efficiency)] / [(WFPC2 FOV area) x (WFPC2 efficiency)]. For WFPC2 we have reduced FOV for the missing "L" shaped region around PC1.

b. The full WFPC2 FOV is a 150" x 150" L-shaped region, with area equivalent to a 134" x 134" square, which we use for comparisons to ACS.

c. Efficiency near filter pivot wavelength; includes HST+instrument+filters.

d. For ACS the full WFC FOV is 202"x202", the full HRC FOV is 26"x29", and the full SBC FOV is 31" x 35". When using the narrow band ramp filters the larger WFC FOV gets reduced, depending on the FOV location. There are three possible locations: inner region (45"x85"), middle region (65"x100"), and outer region (60"x85").

1.2.2 Comparison of WFPC2 and NICMOS

Both WFPC2 and NICMOS are capable of imaging at wavelengths between ~8000Å and ~11,000Å. Table 1.3 compares the detective efficiency of WFPC2 and NICMOS in the wavelength region where both instruments overlap in capabilities. Count rates for a V=20 star of spectral class A0 are given for all filters at common wavelengths; the signal-to-noise (S/N) is also given for a 1 hour exposure of this same star. For bright continuum sources, WFPC2 and NICMOS have similar efficiency over the spectral range from 8800Å to 10,500Å, and the choice of instrument may depend on other factors such as field size and details of the passband shape.

Both instruments have polarimetry capability, but the WFPC2 polarizers are not viable above 8000Å.

Table 1.3: Comparison of WFPC2 and NICMOS Count Rates for a V=20 A0 Star.

Instrument	Filter	Mean Wavelength (Å)	Effective Width (Å)	Count Rate ($e^- s^{-1}$)	SNR in 1 hour[a]
WFPC2	F785LP	9366	2095	14	215
	F791W	8006	1304	30	314
	F814W	8269	1758	33	333
	F850LP	9703	1670	7.1	150
	FQCH4N (Quad D)	8929	64	0.47	34, 29[b]
	F953N	9546	52	0.21	19, 15[b]
	F1042M	10,443	611	0.20	18, 15[b]
	LRF[c]	8000 9000 9762	105 113 126	1.5 0.64 0.23	66 40 20
NICMOS[d]	F090M[e]	8970	1885	17.4	89
	F095N[d]	9536	88	0.883	9.2
	F097N[d]	9715	94	1.19	12
	F108N[d]	10,816	94	1.17	9.9
	F110W (Camera 1)	11,022	5920	73	170
	F110W (Camera 2)	11,035	5915	83.7	290
	F110W (Camera 3)	11,035	5915	75.9	390

a. WFPC2 SNR assuming two 1800s exposures for cosmic ray removal. NICMOS SNR for central pixel of PSF.
b. Values given for WFC (0.10″ pixels) and PC (0.046″ pixels).
c. LRF filter is continuously tunable from 3710Å to 9762Å. LRF field-of-view is 10″x10″.
d. These NICMOS filters are available only on Camera 1 which has 11″x11″ field-of-view.
e. The NICMOS ETC performs S/N calculations for the brightest pixel with the detector temperature at 77.1°K.

1.2.3 Comparison of WFPC2 and STIS

Both WFPC2 and STIS are capable of imaging over the same wavelength range, between ~1150Å and ~11000Å.

Advantages of each instrument may be summarized as follows.

WFPC2 advantages are:

- Wider field-of-view, effective area of 134″ x 134″ vs. 50″ x 50″ or less.
- Greater selection of filters, including polarizers.
- Bright Targets: WFPC2 has no bright target safety issues, and can give useful data on faint targets near very bright objects. STIS MAMAs can be damaged by bright objects.

STIS advantages are:

- Much higher UV throughput.
- True solar blind imaging in UV due to MAMA detectors. WFPC2 CCDs are very sensitive to filter red-leak.
- PSF sampling: STIS offers 0.024″ pixels vs. 0.046″ on WFPC2.
- High time resolution is possible (τ ~125μs) with the MAMA detectors. Also the STIS CCD may be cycled on ~20s time scale using a sub-array.

In general, WFPC2 has a much greater selection of filters and wider field-of-view than STIS, but STIS has greater detective efficiency in the UV and for its long-pass and unfiltered modes. Table 1.4 compares the detective efficiency for WFPC2 and STIS filters with similar bandpasses. For UV imaging STIS is greatly superior due to higher throughput and insensitivity to filter red-leak.

For both [OII] 3727Å and [OIII] 5007Å imaging STIS has much higher QE, though the larger WFPC2 field-of-view may be an important factor. The WFPC2 [OIII] filter is wider than its STIS counter-part, which may also be useful for redshifted lines. For broad-band imaging the unfiltered and 5500Å long-pass modes of STIS again have higher efficiency than WFPC2, though with reduced field-of-view.

Table 1.4: Comparison of WFPC2 and STIS Detector Efficiencies.

Instrument	Filter	Mean Wavelength (Å)	Bandpass FWHM (Å)[a]	Peak QE[b]
WFPC2	F122M	1420	100	0.11%
STIS	F25LYA	1216	85	0.32%
WFPC2	F160BW	1492	500	0.07%
STIS	25MAMA (FUV)	1370	320	4.5%
WFPC2	F255W	2586	393	0.5%
STIS	25MAMA (NUV)	2220	1200	3.1%
WFPC2	F375N	3738	42	0.9%
STIS	F28X50OII	3740	80	3.7%
WFPC2	F502N	5013	37	5.8%
STIS	F28X50OIII	5007	5	11%
WFPC2	F606W	5935	2200	14%
STIS	F28X50LP	~7300[c]	2720	12%
STIS	50CCD	~5800	4410	15%

a. Note that definition of FWHM is different from "effective width" elsewhere herein.
b. Includes instrument and OTA.
c. 5500Å long pass filter.

1.3 History of WFPC2

The original Wide Field and Planetary Camera (WF/PC-1) served as the prototype for WFPC2. In many respects the two instruments were very similar. Both were designed to operate from 1150Å to 11000Å, both use 800x800 CCD detectors, and both provide spatial samplings of ~0.045″ and ~0.1″ per pixel. The development and construction of WF/PC-1 was led by Prof. J. A. Westphal, Principal Investigator (PI), of the California Institute of Technology. The instrument was built at the Jet Propulsion Laboratory (JPL) and was launched aboard HST in April 1990. It obtained scientific data until it was replaced by WFPC2 during the first servicing mission in December 1993.

Because of its important role in the overall HST mission, NASA decided to build a second Wide Field and Planetary Camera (WFPC2) as a backup clone of WF/PC-1 even before HST was launched. WFPC2 was already in the early stages of construction at JPL when HST was launched. After the discovery of spherical aberration in the HST primary mirror, it was quickly

realized that a modification of the WFPC2 internal optics could correct the aberration and restore most of the originally expected imaging performance. As a result, development of WFPC2 was accelerated. Dr. J. T. Trauger of JPL was the project PI for WFPC2 and led the Investigation Definition Team (IDT[1]).

The WFPC2 completed system level thermal vacuum (SLTV) testing at JPL in April and May 1993. Between June and November there were payload compatibility checks at Goddard Space Flight Center (GSFC), and payload integration at Kennedy Space Center (KSC). WF/PC-1 was replaced by WFPC2 during the first servicing mission in December 1993. WFPC2 was shown to meet most of its engineering and scientific performance requirements by testing conducted during the three month Servicing Mission Observatory Verification (SMOV) period following the servicing mission. The General Observer community has had access to WFPC2 since the start of Cycle 4 in January 1994.

WFPC2 accurately corrected the HST spherical aberration, was a scientifically capable camera configured for reliable operation in space without maintenance, and was an instrument which could be calibrated and maintained without excessive operational overhead. It incorporated evolutionary improvements in photometric imaging capabilities. The CCD sensors, signal chain electronics, filter set, UV performance, internal calibrations, and operational efficiency were all improved through new technologies and lessons learned from WF/PC-1 operations and the HST experience since launch.

WFPC2 SMOV requirements were developed by the IDT, GSFC, and the STScI to include: verification of the baseline instrument performance; an optical adjustment by focusing and aligning to minimize coma; the estimation of residual wave front errors from the analysis of star images; a photometric calibration with a core set of filters (including both visible and UV wavelengths); and the evaluation of photometric accuracy and stability over the full field with the core filter set. The results of these studies are documented in Holtzman, et al., 1995a and 1995b, and are summarized in this Handbook.

Despite these successes, the first years of scientific operation of WFPC2 revealed a number of relatively minor instrumental defects that were not expected from the pre-launch testing. These included a low-level charge transfer inefficiency, a higher than expected level of scattered light around bright objects, and variable and lower than expected ultraviolet (UV) efficiency. In addition, we have come to understand the instrument more fully -- particularly in terms of its overall photometric performance, geometric distortion, scale and alignments, hot pixels, and CCD traps. All of this new information is described here.

---

1. The members of the IDT were: John T. Trauger, Christopher J. Burrows, John Clarke, David Crisp, John Gallagher, Richard E. Griffiths, J. Jeff Hester, John Hoessel, Jon Holtzman, Jeremy Mould, and James A. Westphal.

1.4 The Previous vs. Current Generation: WF/PC-1 vs. WFPC2

For historical reasons, it is useful to offer comparisons between WFPC2, and its predecessor WF/PC-1, which was returned to Earth in December 1993.

- **Field format:** WF/PC-1 contained 8 cameras and CCDs, each CCD having 800 x 800 pixels. Four were used in the Planetary Camera mode (0.043″ pixels), and four were used in the Wide Field Camera mode (0.10″ pixels). The two pixel formats were selected by rotating the pyramid mirror by 45°. WFPC2 budget and schedule constraints forced a reduction from 8 to 4 camera channels in August 1991. WFPC2 contains only 4 CCDs; the pyramid mirror is fixed and the 4 cameras are physically located in the bays occupied by the WF/PC-1 WFC.
- **Aberration correction:** WF/PC-1 contained no correction for spherical aberration of the OTA primary mirror. Only about 15% of light from a stellar target fell into the core of the PSF (diameter ~0.1″). WFPC2 incorporates corrective figures on the Cassegrain secondary mirrors inside the relay cameras, and as a result places ~60% of the light from a star inside a diameter of 0.1″. Precise alignment of the OTA pupil on these mirrors is required to attain full correction of the spherical aberration. Hence the pick-off mirror (POM) is steerable in WFPC2, and three of the fold mirrors contain tip-tilt actuators.
- **CCD Technology:** Many properties of WF/PC-1 and WFPC2 CCDs are compared in Table 4.1. Many differences derive from the fact that the WF/PC-1 CCDs were thinned, backside illuminated devices whereas the WFPC2 CCDs are thick, front side illuminated devices. In the WF/PC-1 CCDs the active silicon layer was a free-standing membrane somewhat less than 10μm thick, with photons impinging directly on the silicon layer, without attenuation in the polysilicon gate structure built on the other ('front') side of the device.
- **Quantum Efficiency Hysteresis (QEH):** The WF/PC-1 CCD's required a UV flood procedure and continuous cold temperatures to avoid QEH and hence non-linearity. A UV flood was performed early in the WF/PC-1 mission, but could not be repeated due to problems with the HST magnetometers. This in turn limited the temperature range allowable during decontaminations, since high temperatures would remove the UV flood, which in turn severely limited UV science capabilities. Some QE instability was also seen, particularly in

the B band, due to changes in the UV flood. WFPC2 CCDs support multi-pinned phase (MPP) operation which eliminates quantum efficiency hysteresis.

- **Charge Transfer Efficiency:** WF/PC-1 devices suffered from significant charge transfer efficiency (CTE) errors at image intensities below ~200 electrons per pixel. This was overcome by preflashing virtually all science images. WFPC2 devices have much less CTE error, and hence no preflash is used. However, low-level charge traps are present in the WFPC2 devices, and are increasing slowly with time. See the discussions in Section 4.12 for details of WFPC2 CTE behavior.
- **Detector MTF:** The WFPC2 Loral devices do suffer from poorer CCD detector MTF than the WF/PC-1 CCDs, perhaps caused by scattering in the front side electrode structure. The effect is to blur images and decrease the limiting magnitude by about 0.5 magnitudes.
- **Flat field quality:** WF/PC-1 CCDs were chemically thinned devices and therefore varied in thickness across the field-of-view causing large features in the flat fields. WFPC2 CCDs are un-thinned and the intrinsic response is uniform to ~3% across the field.
- **DQE:** The WFPC2 CCDs have intrinsically lower QE than WF/PC-1 CCDs above 4800Å, which is due to attenuation by front side electrode structures.
- **Gain switch:** WF/PC-1 had only a single analog-to-digital converter gain setting of 8 e^- DN^{-1} which saturated at about 30,000e^-. Two gains are available with WFPC2: a 7 e^- DN^{-1} channel which gives reasonable sampling of the 5e^- read noise, and which saturates at about 27,000e^-, and a 14 e^- DN^{-1} channel which saturates at about 53,000e^- and extends the useful dynamic range.
- **Quantization:** The systematic analog-to-digital converter errors that were present in the low order bits on WF/PC-1 have been largely eliminated, contributing to a lower effective read noise in WFPC2.
- **Calibration Channel:** WF/PC-1 contained a solar UV flood channel which was physically in the location of the present WFPC2 calibration channel. This transmitted solar UV light into the camera to provide a UV flood capability.
- **Entry Port:** The WF/PC-1 camera was sealed by an afocal MgF_2 window immediately behind the shutter. The WFPC2 entry port is open.

- **Chronographic Capability:** WF/PC-1 contained a low reflectance spot on the pyramid (known as the Baum spot) which could be used to occult bright objects. This has been eliminated from WFPC2, since the spherical aberration severely reduces its utility.
- **Contamination Control:** Since launch, WF/PC-1 suffered from the accumulation of molecular contaminants on the cold (-87˚C) CCD windows. This molecular accumulation resulted in the loss of FUV (1150-2000Å) throughput and attenuation at wavelengths as long as 5000Å. Another feature of the contamination was the "measles" — multiple isolated patches of low volatility contamination on the CCD window. Measles were present even after decontamination cycles, when most of the accumulated molecular contaminants were boiled off by warming the CCDs. In addition to preventing UV imaging, these molecular contamination layers scattered light and seriously impacted the calibration of the instrument. WFPC2 has far less contamination than WF/PC-1 owing to pre-launch cleaning and bake-out procedures, careful design of venting paths to protect the optical bench area, and inclusion of Zeolite molecular absorbers in the design. There is now a decrease in throughput of about 30% per month at 1700Å, but decontamination procedures completely remove this material. This throughput drop is also highly predictable and can be calibrated out during photometric analyses.

1.5 Organization of this Handbook

A description of the instrument is contained in Chapter 2. The filter set is described in Chapter 3. CCD performance is discussed in Chapter 4. A description of the Point Spread Function is given in Chapter 5. The details necessary to estimate exposure times are described in Chapter 6. A summary of observation strategies is given in Chapter 7. Data products, standard calibration methods, and calibration plans are summarized in Chapter 8. A complete list of references is given in "References".

This document summarizes the performance of the WFPC2 as known in March 2008 after more than 14 years of on-orbit operation. For further information or questions not addressed in this manuscript, please contact the STScI Help Desk(help@stsci.edu) or to consult the WFPC2 WWW pages (http://www.stsci.edu/hst/wfpc2).

1.6 The Help Desk at STScI

STScI maintains a Help Desk whose staff quickly provide answers to any HST-related topic, including questions about WFPC2. The Help Desk staff has access to all of the resources available at the Institute. They maintain a database of frequently asked questions and answers, so that many questions can be answered immediately. The Help Desk staff can also provide copies of STScI documentation, in either hardcopy or electronic form, including Instrument Science Reports and Instrument Handbooks.

Questions sent to the Help Desk are usually answered within two business days. Usually, the Help Desk staff will reply with the answer to a question, but occasionally they will need more time to investigate the answer. In these cases, they will reply with an estimate of the time needed to reply with the full answer.

We ask that you please send *all* initial inquiries to the Help Desk. If your question requires a WFPC2 Instrument Scientist to answer it, the Help Desk staff will put a WFPC2 Instrument Scientist in contact with you. By sending your request to the Help Desk, you are guaranteed that someone will provide a timely response.

To contact the Help Desk at STScI:

- **Send e-mail:** help@stsci.edu
- **Phone:** 1-410-338-1082

The Space Telescope European Coordinating Facility (ST-ECF) also maintains a Help Desk. European users should generally contact the ST-ECF for help; all other users should contact STScI.

To contact the ST-ECF Help Desk in Europe:

- **Send e-mail:** stdesk@eso.org.

1.7 Further Information

The material contained in this Handbook is derived from ground tests and design information obtained by the IDT and the engineering team at JPL, and from on-orbit measurements. Other sources of information are listed below. For a complete reference list please see “References”.

- The WFPC2 web pages:

  `http://www.stsci.edu/hst/wfpc2`

- *HST Data Handbook*, (Version 4.0, January 2002 - update planned for late 2008 or early 2009

  http://www.stsci.edu/instruments/wfpc2/Wfpc2_dhb/WFPC2_longdhbcover.html.[2]

- *Calibrating Hubble Space Telescope: Post Servicing Mission* (1995),

  http://www.stsci.edu/hst/wfpc2/documents/proceedings/post_serv.html[2]

- *The 1997 HST Calibration Workshop* (1997), available online:

  http://www.stsci.edu/stsci/meetings/cal97/proceedings.html[2]

- *The 2002 HST Calibration Workshop* (2002), available online:

  http://www.stsci.edu/hst/HST_overview/documents/calworkshop/workshop2002[2]

- *The 2005 HST Calibration Workshop* (2005), available online:

  http://www.stsci.edu/hst/HST_overview/documents/calworkshop/workshop2005/[2]

- *Proceedings of the CTE Workshop* (2000):

  http://www.stsci.edu/hst/acs/performance/cte_workgroup/cte_papers.html

- *STSDAS Users Guide*, (April 1994, version 1.3)[2].
- *The Reduction of WF/PC Camera Images,* Lauer, T., P.A.S.P. 101, 445 (1989).
- *The Imaging Performance of the Hubble Space Telescope,* Burrows, C. J., et. al., Ap. J. Lett., 369, L21 (1991).
- Interface Control Document (ICD) 19, “PODPS to STSDAS”
- Interface Control Document (ICD) 47, “PODPS to CDBS”
- *The Wide Field/Planetary Camera in The Space Telescope Observatory,* J. Westphal and the WF/PC-1 IDT, IAU 18th General Assembly, Patras, NASA CP-2244 (1982).
- *The WFPC2 Science Calibration Report,* Pre-launch Version 1.2, J. Trauger, editor, (1993). [IDT calibration report]
- *White Paper for WFPC2 Far-Ultraviolet Science,* J. T. Clarke and the WFPC2 IDT (1992).
- *The Performance and Calibration of WFPC2 on the Hubble Space Telescope,* Holtzman, J., et al., P.A.S.P., 107, 156 (1995).

2. These documents may be requested from the help desk at: help@stsci.edu

- *The Photometric Performance and Calibration of WFPC2,* Holtzman, J., et al., P.A.S.P., 107, 1065 (1995).
- *Charge-Transfer Efficiency of WFPC2,* B. Whitmore, I. Heyer, S. Casertano, PASP, 111, 1559 (1999).
- The Institute's WFPC2 Space Telescope Analysis Newsletter (STAN), which is distributed via e-mail, and provides notification of any changes in the instrument or its calibration. To subscribe, send e-mail to help@stsci.edu. Previous issues are at:

  `http://www.stsci.edu/hst/wfpc2/documents/newsletters`

CHAPTER 2:

Instrument Description

In this chapter . . .

2.1 Science Objectives

The scientific objective of the WFPC2 is to provide photometrically and geometrically accurate images of astronomical objects over a relatively wide field-of-view (FOV), with high angular resolution across a broad range of wavelengths.

WFPC2 was designed with a goal of 1% rms photometric accuracy, which means that the relative response in all 800x800 pixels per CCD must be known to better than 1% through each filter, and that standard calibrations be done at this level. The absolute calibration in the primary broadband photometric filters is accurate at around the 2% level, and there are on-going efforts to further improve the accuracy. Success in this area is dependent on the stability of all elements in the optical train, particularly the CCDs and filters.

The narrow point spread function is essential to all science programs being conducted with the WFPC2, because it allows one to both go deeper than ground based imagery, and to resolve smaller scale structure with higher reliability and dynamic range. Further, many of the scientific goals which originally justified the HST require that these high quality images be obtained across a wide field-of-view. The Cepheid distance scale program, for example, cannot be accomplished without a relatively wide field-of-view.

A unique capability of the WFPC2 is that it provides a sustained, high resolution, wide field imaging capability in the vacuum ultraviolet. Considerable effort has been expended to assure that this capability is maintained. Broad passband far-UV filters, including a Sodium Wood's filter, are included. The Wood's filter has superb red blocking characteristics. Photometry at wavelengths short of 3000Å is improved through the control of internal molecular contamination sources and the ability to put the CCDs through warm-up decontamination cycles without loss of prior calibrations.

2.2 WFPC2 Configuration, Field-of-View, and Resolution

The field-of-view and angular resolution of the wide field and planetary camera is split up as follows (see Chapter 4 for more details on CCDs):

Table 2.1: Summary of Camera Format.

Camera	Pixel and CCD Format	Field-of-View	Pixel Scale	F/ratio
Wide Field	800 × 800 × 3 CCDs	2.5′ × 2.5′ (L-shaped)	~100 milli-arcseconds	12.9
Planetary	800 × 800 × 1 CCD	35″ × 35″	~46 milli-arcseconds	28.3

Figure 2.1: Wide Field Planetary Camera 2 Concept Illustration. The calibration channel, and pick-off mirror mechanisms are not shown.

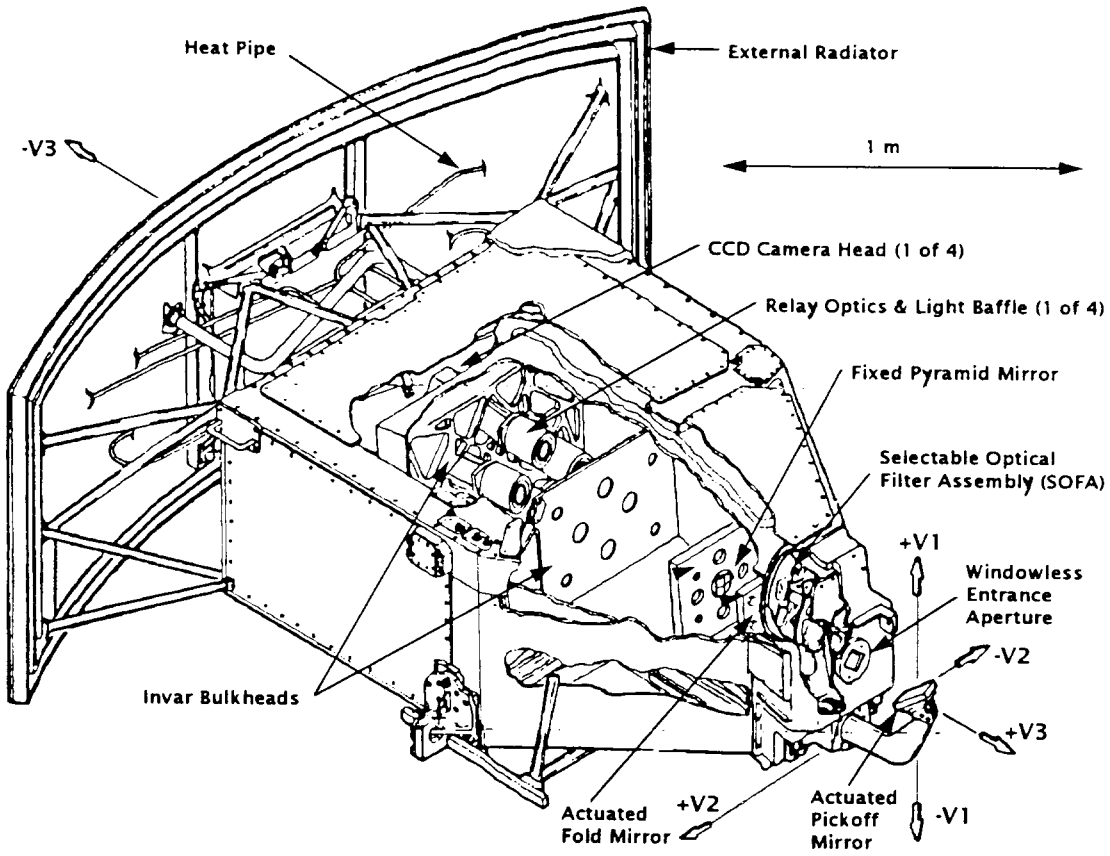

2.3 Overall Instrument Description

The Wide-Field and Planetary Camera 2, illustrated in Figure 2.1, occupies the only radial bay allocated to a scientific instrument. Its field-of-view is centered on the optical axis of the telescope and it therefore receives the highest quality images. The three Wide-Field Cameras (WFC) at F/12.9 provide an "L" shaped field-of-view of 2.5x2.5 arcminutes with each 15 μm detector pixel subtending 0.10″ on the sky. In the Planetary Camera (PC) at F/28.3, the field-of-view is 35″ x 35″, and each pixel subtends 0.046″. The three WFCs undersample the point spread function of the Optical Telescope Assembly (OTA) by a factor of 4 at 5800Å in order to provide an adequate field-of-view for studying galaxies, clusters of galaxies, etc. The PC resolution is over two times higher. Its field-of-view is adequate to provide full-disk images of all the planets except Jupiter

(which is 47″ in maximum diameter) and Venus (which is not normally observable with HST). The PC has numerous extra-solar applications, including studies of galactic and extra-galactic objects in which both high angular resolution and excellent sensitivity are needed. In addition to functioning as the prime instrument, the WFPC2 can be used for parallel observations.

Figure 2.2 shows the optical arrangement (not to scale) of the WFPC2. The central portion of the OTA F/24 beam is intercepted by a steerable pick-off mirror attached to the WFPC2, and is diverted through an open entry port into the instrument. The beam then passes through a shutter and filters. A total of 48 spectral elements and polarizers are contained in an assembly of 12 filter wheels. Then the light falls onto a shallow-angle, four-faceted pyramid located at the aberrated OTA focus, each face of the pyramid being a concave spherical surface. The pyramid divides the OTA image of the sky into four parts. After leaving the pyramid, each quarter of the full field-of-view is relayed by an optical flat to a Cassegrain relay that forms a second field image on a charge-coupled device (CCD) of 800x800 pixels. Each detector is housed in a cell that is sealed by a MgF_2 window. This window is figured to serve as a field flattener.

The aberrated HST wave front is corrected by introducing an equal but opposite error in each of the four Cassegrain relays. An image of the HST primary mirror is formed on the secondary mirrors in the Cassegrain relays. (The fold mirror in the PC channel has a small curvature to ensure this.) The spherical aberration from the telescope's primary mirror is corrected on these secondary mirrors, which are extremely aspheric.

Figure 2.2: WFPC2 Optical Configuration.

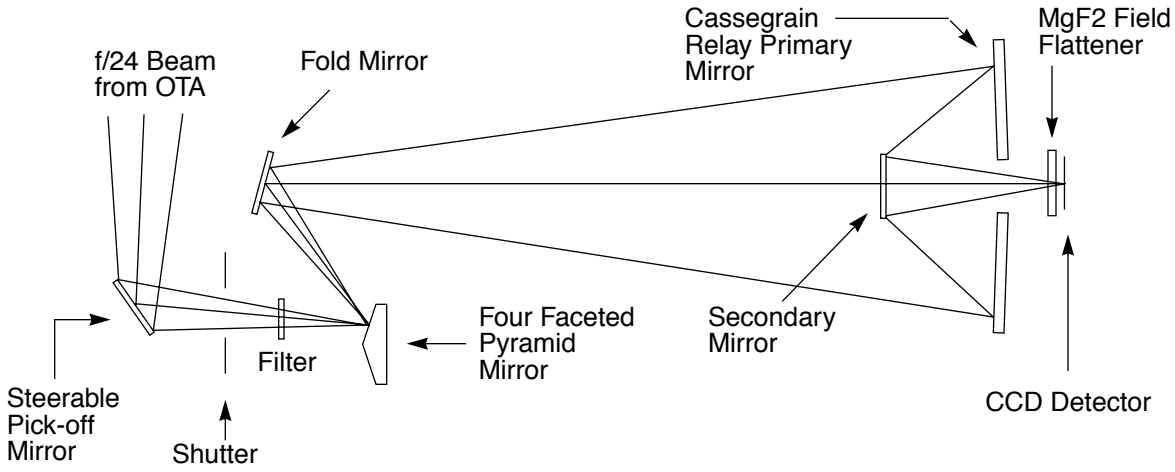

The single most critical and challenging technical aspect of applying a correction is assuring exact alignment of the WFPC2 pupils with the pupil of the HST. If the image of the HST primary does not align exactly with the repeater secondary, the aberrations no longer cancel, leading to a wavefront error and comatic images. An error of only 2% of the pupil diameter would produce a wavefront error of 1/6 wave, leading to degraded spatial resolution and a loss of about 1 magnitude in sensitivity to faint point sources. This error corresponds to mechanical tolerances of only a few microns in the tip/tilt motion of the pick-off mirror, the pyramid, and the fold mirrors.

Mechanisms inside WFPC2 allow optical alignment on-orbit; these are necessary to insure correction of the OTA spherical aberration. The beam alignment is set with a combination of the steerable pick-off mirror and actuated fold mirrors in cameras PC1, WF3 and WF4. The 47° degree pick-off mirror has two-axis tilt capabilities provided by stepper motors and flexure linkages, to compensate for uncertainties in our knowledge of HST's latch positions (i.e., instrument tilt with respect to the HST optical axis). These latch uncertainties would be insignificant in an unaberrated telescope, but must be compensated for in a corrective optical system. In addition, three of the four fold mirrors, internal to the WFPC2 optical bench, have limited two-axis tilt motions provided by electrostrictive ceramic actuators and invar flexure mountings. Fold mirrors for the PC1, WF3, and WF4 cameras are articulated, while the WF2 fold mirror has a fixed invar mounting. A combination of the pick-off mirror and fold mirror actuators has allowed us to correct for pupil image misalignments in all four cameras. Since the initial alignment, stability has been such that mirror adjustments have not been necessary. The mechanisms are not available for GO commanding.

The WFPC2 pyramid cannot be focused or rotated. WFPC2 is focused by moving the OTA secondary mirror, and then other science instruments are adjusted to achieve a common focus for all the HST instruments.

The four CCDs provide a 1600 x 1600 pixel field-format; three of the 800 x 800 CCDs have 0.1″ pixels (WFC), and one has 0.046″ pixels (PC). The CCDs are physically oriented and clocked so that the pixel read-out direction is rotated approximately 90° in succession (see Figure 1.1). The (1,1) pixel of each CCD array is thereby located near the apex of the pyramid. As a registration aid in assembling the four frames into a single picture, a light can be turned on at the pyramid to form a series of eleven fixed artificial "stars" (known as Kelsall spots or K-spots) along the boundaries of each of the quadrants. This calibration is normally done in a separate exposure. The K-spot images are aberrated and similar in appearance to the uncorrected HST PSF. The relative alignment of the four channels has been more accurately determined from star fields, and is stable over long periods, but the K-Spot images are useful for verifying the stability.

Figure 2.3: Cooled Sensor Assembly.

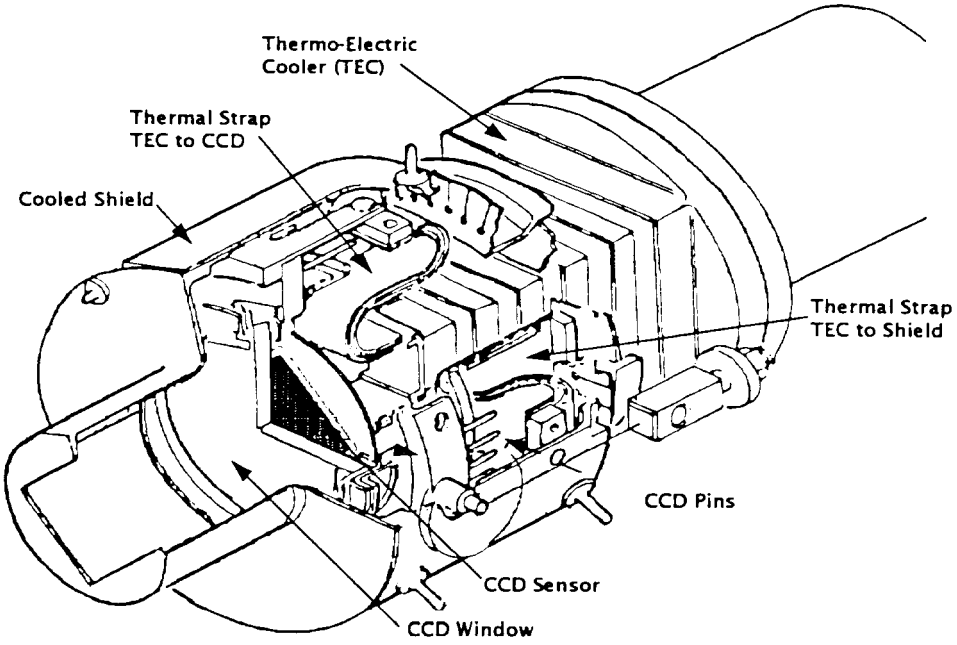

Each CCD is a thick front side-illuminated silicon sensor, fabricated by Loral Aerospace. Each CCD is mounted on a header, is hermetically packaged in a ceramic-tube body that is filled with 1.1 atmosphere of Argon (to prevent degradation of the UV sensitive phosphor), and then is sealed with a MgF_2 field flattener. This complete cell is connected with compliant silver straps to the cold junction of a thermo-electric cooler (TEC). The hot junction of the TEC is connected to the radial bay external radiator by an ammonia heat pipe. This sensor-head assembly is shown in Figure 2.3. During operation, each TEC cools its sensor package to suppress dark current in the CCD.

2.4 Quantum Efficiency

The WFPC2 provides useful sensitivity from 1150Å to 11000Å in each detector. The overall spectral response of the system is shown in Figure 2.4 (not including filter transmissions). The curves represent the probability that a photon that enters the 2.4m diameter HST aperture at a field position near the center of one of the detectors will pass all the aperture obscurations, reflect from all the mirrors, and eventually be detected as an electron in the CCD. The throughput of the system combined with each filter is tabulated in Table 6.1 and also shown in Appendix A.1.

Figure 2.4: WFPC2 + OTA System Throughput. This is the current SYNPHOT model (June 2001) as determined by on-orbit measurements.

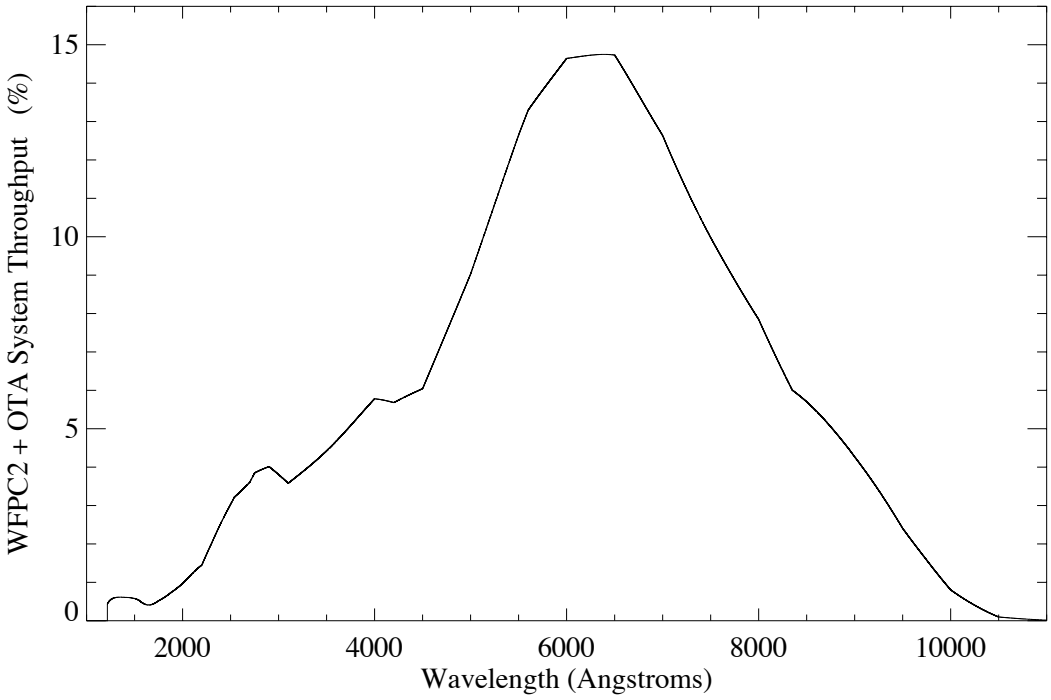

The visible and red sensitivity of the WFPC2 is a property of the silicon from which the CCDs are fabricated. To achieve good ultraviolet response, each CCD is coated with a thin film of Lumogen, a phosphor. Lumogen converts photons with wavelengths less than 4800Å into visible photons with wavelengths between 5100Å and 5800Å, which the CCD detects with good sensitivity. Beyond 4800Å, the Lumogen becomes transparent and acts to some degree as an anti-reflection coating. Thus, the full wavelength response is determined by the MgF_2 field flattener cutoff on the short-wavelength end and the silicon band-gap in the infrared at 1.1 eV (~11000Å).

With the WFPC2 CCD sensors, images may be obtained in any spectral region defined by the chosen filter with high photometric quality, wide dynamic range, and excellent spatial resolution. The bright end of the dynamic range is limited by the 0.11 seconds minimum exposure time, and by the saturation level of the analog-to-digital converter (ADC) at the chosen gain, which is roughly 53000 (gain=14, though called ATD-GAIN=15 when specifying the Phase II) or 27000e^- (gain=7) per pixel. The maximum signal-to-noise ratio corresponding to a fully exposed pixel will be about 230. The faint end of the dynamic range is limited by photon noise, instrument read noise and, for the wide-band visible and infra-red filters, the sky background.

Table 2.2 gives characteristic values of the expected dynamic range in visual magnitudes for point sources. The minimum brightness is given for an integrated S/N ratio of 3, and the maximum corresponds to CCD ADC saturation (selected as 53000e^-). The quoted values assume an effective

bandwidth of 1000Å at about 5600Å (filter F569W). The planets and many other resolved sources are observable in this filter with short exposures even if their integrated brightness exceeds the 8.4 magnitude limit.

Table 2.2: WFPC2 Dynamic Range in a Single Exposure.

Configuration	Exposure (seconds)	Min. V Magnitude	Max. V Magnitude
Wide Field	0.11	8.82	17.83
Wide Field	3000.	19.91	28.19
Planetary	0.11	8.40	17.47
Planetary	3000.	19.49	28.25

2.5 Shutter

The shutter is a two-blade mechanism used to control the duration of the exposure. A listing of the possible exposure times is contained in Table 2.3. These are the only exposure times which can be commanded. Current policy is to round down non-valid exposure times to the next valid value. However, an exposure time shorter than the minimum allowed (0.11 seconds) is, instead, rounded up to this minimum value.

Some exposures should be split into two (CR-SPLIT) in order to allow cosmic ray events to be removed in post-processing. By default, exposures of more than 10 minutes are CR-SPLIT. If an exposure is CR-SPLIT, the exposure time is divided into two fractions and then rounded down. Normally the fractional split is 50%/50% but, unless constrained by the user with CR-TOLERANCE, the ratio may be up to 70%/30%, as allowed by the default CR-TOLERANCE=0.2. Note that some exposure times in the table do not correspond to commandable values when halved. In preparing a proposal containing an exposure that is to be CR-SPLIT, the simplest procedure to use in order to be sure of a given total exposure time, is to enter double a legal value, and impose CR-TOLERANCE=0.

For the shortest exposure times, it is possible to reconstruct the actual time of flight of the shutter blades. Encoder disks, attached to the shutter blade arms, are timed by means of a photo-transistor. The maximum error is 5 milliseconds. The necessary information is contained in the WFPC2 engineering data stream, however, this information is not in the processed science header.

Diffraction effects from the edges of the shutter blades affect the point spread function for very short exposures. It is advisable to use exposure times greater than 0.2 seconds when obtaining point spread functions in

support of long exposure observations (see the WF/PC-1 IDT OV/SV Report, Chapter 9, for further discussion in the spherically aberrated case).

The control of the initial opening of the WFPC2 shutter during an observation is held by the internal WFPC2 microprocessor in all cases. However, control over closing of the shutter is held by the microprocessor only for exposures less than 180 seconds in duration. For longer exposures, control passes to the Application Processor (AP-17) in the NSSC-1 spacecraft computer. The consequence of this arrangement is that loss of guide star lock will result in the WFPC2 shutter being closed only for those observations with planned durations of 180 seconds or longer. The AP-17 always controls the shutter closing if the serial clocks are enabled during the exposure (CLOCKS=YES), which then has a minimum planned duration of 1 second, and exposures are rounded to the nearest second. If guide star lock is reacquired prior to the end of the planned observation time, the shutter will reopen to obtain a portion of the planned integration. As discussed in the next section, CLOCKS=YES should generally not be used with exposures shorter than 30 sec., if 1% or better photometric accuracy is needed.

Table 2.3: Quantized Exposure Times (Seconds). Exposure times that should not be used for CLOCKS=YES are shaded and flagged with table footnote (a). Exposure times where the PSF is affected by the shutter blade flight time are underlined and flagged with table footnote (b). Exposures normally without loss of lock checking are in italics. Times that are CR-Split by default are in boldface; exposures longer than 5400 seconds must be CR-split. Exposures that take more than one orbit, even when CR-split, are not normally accessible to GOs and are crossed out and flagged with table footnote (c).

0.11 [a,b]	*0.4* [a]	*2.0*	*10.*	*40.*	200.	**900.**	**1900.**	**2900.**	**3900.**	**4900.**	**6200.**	~~**15000.**~~[c]
0.12 [a,b]	*0.5* [a]	*2.3* [a]	*12.*	*50.*	230.	**1000.**	**2000.**	**3000.**	**4000.**	**5000.**	**6400.**	~~**20000.**~~[c]
0.14 [a,b]	*0.6* [a]	*2.6* [a]	*14.*	*60.*	260.	**1100.**	**2100.**	**3100.**	**4100.**	**5100.**	**6600.**	~~**25000.**~~[c]
0.16 [a,b]	*0.7* [a]	*3.0*	*16.*	*70.*	300.	**1200.**	**2200.**	**3200.**	**4200.**	**5200.**	**6800.**	~~**30000.**~~[c]
0.18 [a,b]	*0.8* [a]	*3.5* [a]	*18.*	*80.*	350.	**1300.**	**2300.**	**3300.**	**4300.**	**5300.**	**7000.**	~~**40000.**~~[c]
0.20 [a,b]	*1.0*	*4.0*	*20.*	*100.*	400.	**1400.**	**2400.**	**3400.**	**4400.**	**5400.**	**7500.**	~~**50000.**~~[c]
0.23 [a]	*1.2* [a]	*5.0*	*23.*	*120.*	500.	**1500.**	**2500.**	**3500.**	**4500.**	**5500.**	**8000.**	~~**75000.**~~[c]
0.26 [a]	*1.4* [a]	*6.0*	*26.*	*140.*	600.	**1600.**	**2600.**	**3600.**	**4600.**	**5600.**	**8500.**	~~**100000.**~~[c]
0.30 [a]	*1.6* [a]	*7.0*	*30.*	*160.*	**700.**	**1700.**	**2700.**	**3700.**	**4700.**	**5800.**	**9000.**	
0.35 [a]	*1.8* [a]	*8.0*	*35.*	180.	**800.**	**1800.**	**2800.**	**3800.**	**4800.**	**6000.**	**10000.**	

a. Exposure times that should not be used for CLOCKS=YES

b. Exposure times where the PSF is significantly affected by the shutter blade flight time

c. Exposure times that take more than one orbit, even when CR-split; these are not normally accessible to GOs

In August 2000, WFPC2 began experiencing occasional anomalies in the operation of the shutter mechanism. The problem was traced to an encoder wheel and photo transistor assembly that serves to sense the position of the "A" shutter blade. This sensor is polled by the WFPC2 computer prior to each exposure. Later, in October 2000, we began seeing a more serious problem where multiple mis-readings would lead to the "A" shutter blade attempting to close even though the "B" blade was already closed, hence causing a collision of the two shutter blades. Since there was some potential for this to damage the mechanism, we ceased WFPC2 observations for several days until corrective action could be taken. On November 8, 2000, we modified the WFPC2 microprocessor software to activate the position sensor 10 milliseconds earlier, thus giving it more time to respond prior to being read by the microprocessor. An extensive series of tests were run on the shutter after the installation of the software patch, and no unexpected side effects or abnormalities in its operation were seen. No further incidences of the anomaly have been seen as of this writing (June 2004).

The anomaly affected only about 0.3% of the images from August to October 2000. In most cases the shutter failed to open, producing a blank image. A few images were also seen with trailed targets, due to the shutter being open prior to the nominal exposure start, or due to the shutter remaining open past the nominal exposure end.

As of this writing the exact cause of the anomaly is still not entirely clear. Much evidence points to radiation damage to the photo transistor, causing its response time to slow, while other evidence points to mechanical wear in the encoder wheel linkage, leading to misalignment of the wheel relative to the photo transistor. In most scenarios the software patch should permanently fix the problem, but there is always some small chance it will reappear.

2.6 Serial Clocks

The serial transfer registers of the CCDs can be kept running during an exposure (CLOCKS=YES), or run only during the readout (CLOCKS=NO, the default).

The serial clocks are sometimes used on very bright targets where extensive blooming up and down the CCD columns is expected. CLOCKS=YES causes charge which blooms to the ends of the CCD to be read out and disposed of, thus preventing it from flowing back into the image. They will be useful when any single CCD column contains in excess of $\sim 10^8$ electrons. Note that the serial clocks do not actually suppress the blooming process, instead they merely remove any charge that blooms to the top or bottom of the CCD.

Although only 6% of all WFPC2 observations have been obtained with CLOCKS=YES, this mode has now been calibrated using observations of the standard star GRW+70D5824 (HIC 66578; V=12.77; B-V=-0.09) [proposal ID: 9252]. The comparison between count rates of the standard star for different filters obtained with CLOCKS=YES and CLOCKS=NO indicates that the normal WFPC2 photometric calibration with CLOCKS=NO is sufficient for data obtained with CLOCKS=YES and CLOCKS=NO. The count rates are generally within 2% (0.02 mag) peak to peak of each other with the associated errors being quite small.

Analysis of darks indicate that the count levels for the CLOCKS=YES darks are similar to those for the CLOCKS=NO darks. However, when the 1 minute difference in exposure time between the CLOCKS=YES and CLOCKS=NO dark is taken into account (see below), the CLOCKS=YES dark current is found to be a few percent higher than the CLOCKS=NO dark current. Since the pipeline dark reference files for CLOCKS=YES mode have always been generated from CLOCKS=NO darks (minimizing the number of calibration observations), the difference in dark current may slightly affect the calibration of some CLOCKS=YES observations. In general, it now appears that there are no major artifacts, induced noise, or cross talk when obtaining data with CLOCKS=YES (Schultz, Baggett & Biretta 2002).

For most circumstances, we recommend CLOCKS=NO. The reasons for this recommendation are:

1. As stated above, CLOCKS=YES is not widely used. Although the consistency of this mode has been examined for a bright star, we cannot guarantee that there are no minor artifacts for very faint targets.
2. The shutter open time when CLOCKS=YES can have significant errors. In this mode, there are delays of up to 0.25 seconds in opening the shutter (which are not present when CLOCKS=NO). This means that for exposures of less than ~30 seconds, there may be photometric errors greater that 1%, unless special precautions are taken in the data reduction. Furthermore, if a non-integral exposure time is specified in the proposal, it will be rounded to the nearest second. See below for details.

On the other hand:

1. We do advise CLOCKS=YES if you expect star images to be so saturated that a significant amount of charge will bleed off the chip during the exposure. This would mean that you expect much more than 10^8 electrons from at least one star in the exposure (more than 1000 pixels would be saturated). Without CLOCKS=YES the bleed-off charge may corrupt other parts of the image.

2. One advantage of CLOCKS=YES is that the overhead time is 1 minute less for exposures longer than 180 seconds. This can be significant if you have a large number of exposure times in the 3 to 10 minute range.
3. Unlike the original WF/PC-1, we do not see a significant variation of WFPC2 dark level with CLOCKS=YES.

In summary:

0-0.8 sec	CLOCKS=NO is required.
1 - 30 sec	Use CLOCKS=NO (or attempt photometric corrections during the analysis of the data).
20 - 180 sec	Use CLOCKS=NO unless more than 10^8 detected electrons from a single star are expected.
180+ sec	Use CLOCKS=NO unless more than 10^8 detected electrons are expected, or if you need to save 1 minute of overhead.

While exposure times are corrupted for CLOCKS=YES, and are not accurately reported in the image headers, correct values can be computed. Details are as follows:

1. Non-integer exposure times <3 minutes are rounded to the nearest integer (e.g., 1.2 sec and 1.4 sec will actually be 1.0 sec long, 3.5 sec exposures take 4.0 sec). This round off is due to the way the spacecraft computer monitors the take-data flag (AP-17 uses its own integer-based timecode). This rounding is reflected properly in the header keywords (keywords UEXPODUR, EXPSTART, EXPEND, EXPTIME, and EXPFLAG in the `.c0h` file headers, or UEXPODUR and CMD_EXP in the `.shh` headers).
2. All CLOCKS=YES exposures are also shortened by either 0.125 or 0.250 seconds. This decrease in exposure time is ***not*** reflected in the file headers; the amount depends upon which shutter blade was in place at the start of the exposure. The decrease in exposure time is due to the manner in which the application processor (AP-17) in the spacecraft computer operates the shutter blades. When CLOCKS=NO (default), the WFPC2 microprocessor opens the shutter, the AP-17 closes the shutter, and the exposure time is as requested. However, with CLOCKS=YES, the AP-17 opens the shutter, first blade A, then blade B. If blade A is closed at the start of the exposure, the actual exposure begins 0.125 seconds after the AP-17 issues the blade command. If blade B is closed at the exposure start, the exposure starts 0.250 seconds later (after the AP-17 sends the open-A command followed by open-B). The shutter in place at exposure start is given in the SHUTTER keyword in the `.c0h` file.

2.7 Overhead Times

Efficient use of the WFPC2 requires an understanding of the overhead times of the instrument. In this section, the various causes of overhead are presented in a manner that should allow the user to make a fairly accurate prediction of the cost in time of a given sequence of exposures. This information is provided for completeness and background. Guidelines given in the Phase I and Phase II Proposal Instructions should be followed to develop Phase I and II proposals, respectively. (See also Section 6.6.)

1. Telescope alignments. A telescope alignment is, in practice, a set of images uninterrupted by target position change or the end of orbit. The start of an alignment requires 1 minute overhead in order to synchronize timing with a major frame (all commands to the instrument take place on major frames which last 1 minute). The end of alignment uses one minute for tape recorder overhead. If images are requested in real-time, another 2 minutes must be added to the alignment end. There are additional overheads at the start of each target visibility period associated with guide star acquisition (currently 6 minutes), or reacquisition (currently 5 minutes).

2. Filter changes. A filter change requires at least 1 minute, the use of 2 filters requires 2 minutes of overhead. Furthermore, since the filter history is lost across telescope alignments, at least one minute is spent on selecting the filter at an alignment start, regardless of the filter in place before the alignment.

3. CCD clearing. Clearing the CCD is done before every exposure and requires 16 seconds. This time is part of the first major frame of the exposure. Therefore, time taken for a given exposure (excluding all other overheads) is the exposure time plus 16 seconds rounded up to the next integral minute. For example, all legal exposure times up to 40 seconds inclusive cost one minute.

4. CCD readout. The readout time for an exposure is one minute. An additional minute is required for exposures 180 sec. or longer, taken with CLOCKS=NO. This extra minute can be saved by using CLOCKS=YES, but this is not generally recommended (see Section 2.6). If the exposure is CR-SPLIT, the readout overheads (calculated with the split exposure times) are of course doubled. There is normally no overhead time advantage in reading out a subset of the CCDs. The exception is if the WFPC2 readout occurs in parallel with the operation of a second instrument, when at least 2 minutes is required to read all 4 CCDs.

5. Dithering. Dithering is the use of small spatial displacements to allow better removal of chip defects and/or the reconstruction of sub-pixel

resolution. During Phase II the user will be given access to "canned" dithering routines which will allow him/her to avoid many of the tricky details involved in planning spatial scans. The spatial offsets will require additional overheads, which must be included. POS-TARG special requirements can also be used to generate offsets.

6. During early proposal Cycles "spatial scans" were used to effect series of offsets, but they are no longer available, and have been replaced with the "dither" commands. The overhead of a spatial scan was similar to that of a sequence of images taken in one alignment; however, at least one minute of overhead was required for each change in pointing. Furthermore, an extra minute of overhead was incurred at the end of the scan, and typically about 1 minute of overhead was used at the beginning of the scan positioning the first image.

In summary, it is not possible to schedule exposures in different filters less than 3 minutes apart: commands to the WFPC2 are processed at spacecraft "major frame" intervals of one minute. A typical sequence of events is:

- Return filter wheel to "clear" position, select new filter (1 min).
- Expose image (minimum 1 min).
- Readout CCDs (1 or 2 min depending on exposure time and CLOCKS). Hence a simple exposure requires a minimum of 3 minutes.

Table 2.4: Instrument Overheads. The first and last exposures of an alignment contain extra overheads.

Overhead Type	Time (min.)	Overhead
First exposure	1	Major frame uncertainty, clock synchronization
First exposure	1	To put in initial filter
Per image:	1	Per filter change
Per image:	int(t)+1	t=(shutter-open time in seconds +16 seconds)/60
Per image:	1	If CLOCKS=NO (default) and exposure ≥180 sec
Per image:	1	Readout
Per image:	1	If image done in parallel with another instrument
Last exposure	1	Data recorder overhead
Last exposure	2	If data requested down in real-time
Last exposure	1	If a scan was done

2.8 CCD Orientation and Readout

The relation between the rows and columns for the four CCDs is shown in Figure 1.1, where the short arrows on each CCD are placed near pixel (1,1) and point in the -Y (readout) direction. Each CCD's axes are defined by a 90˚ rotation from the adjacent CCD. If a 4-CCD image is taken and then each subimage is displayed with rows in the "X" direction and columns in the "Y" direction, each successive display would appear rotated by 90˚ from its predecessor.

Table 2.5: Inner Field Edges. The CCD X,Y (Column, Row) numbers given vary at the 1-2 pixel level because of bending and tilting of the field edge in detector coordinates due to the camera geometric distortions.

Camera	Start Vignetted Field (Zero Illumination)	50% Illumination	Start Unvignetted Field (100% Illumination)
PC1	X>0 and Y>8	X>44 and Y>52	X>88 and Y>96
WF2	X>26 and Y>6	X>46 and Y>26	X>66 and Y>46
WF3	X>10 and Y>27	X>30 and Y>47	X>50 and Y>67
WF4	X>23 and Y>24	X>43 and Y>44	X>63 and Y>64

Figure 1.1 also illustrates the projected orientation of the WFPC2 CCDs onto the sky. The beam is split between the four cameras by a pyramid-shaped mirror in the aberrated HST focal plane. In an effort to insure images from the four CCDs can be reassembled into a single image without gaps, there is a small overlap region on the sky between each CCD and its neighbors (see also Figure 3.12). On the CCDs this region appears as a blank "shadow" region along the X~0 and Y~0 edges of each CCD; the exact limits of this region are given in Table 2.5 for each CCD. Because the OTA beam is aberrated at the pyramid mirror, the edges of the shadow region are not sharp, but instead there is a gradual transition from zero to full illumination on each CCD. The width of this vignetted region is essentially that of the aberrated OTA beam (~5″). Table 2.5 gives approximate limits of this vignetted region on each CCD. Note that astronomical sources in the vignetted region are imaged onto two or more CCDs.

The WFPC2 has two readout formats: full single pixel resolution (FULL Mode), and 2x2 pixel summation (AREA Mode which is obtained by specifying the optional parameter SUM=2x2 as described in the Proposal Instructions). Each line of science data is started with two words of engineering data, followed by 800 (FULL) or 400 (AREA) 16-bit positive numbers as read from the CCDs (with 12 significant bits). In FULL Mode the CCD pixels are followed by 11 "bias" words ("over-clocked" pixels), yielding a total of 813 words per line for 800 lines. In AREA Mode, there

are 14 bias words giving a total of 416 words per line for 400 lines. Either pixel format may be used to read out the WFC or PC. These outputs are reformatted into the science image and extracted engineering (over-clocked) data files during processing in the HST ground system prior to delivery to the observer. *Note that calibration support for AREA Mode data has been curtailed since Cycle 10, since this mode is very seldom used.*

The advantage of the AREA Mode (2x2) on-chip pixel summation is that readout noise is maintained at 5 e^- RMS for the summed (i.e., larger) pixels. This pixel summation is useful for some photometric observations of extended sources particularly in the UV. Note, however, that cosmic ray removal is more difficult in AREA Mode.

The readout direction along the columns of each CCD is indicated by the small arrows near the center of each camera field in Figure 1.1 (see also Figure 3.12). Columns and rows are parallel and orthogonal to the arrow, respectively. Each CCD is read out from the corner nearest the center of the diagram, with column (pixel) and row (line) numbers increasing from the diagram center. In a saturated exposure, blooming will occur almost exclusively along the columns because of the MPP operating mode of the CCDs. Diffraction spikes caused by the Optical Telescope Assembly and by the internal Cassegrain optics of the WFPC2 are at 45° to the edges of the CCDs. Unless specified otherwise in the Phase II proposal, the default pointing position when all 4 CCDs are used is on WF3, approximately 10″ along each axis from the origin (WFALL aperture, see Table 3.14).

Observations which require only the field-of-view of a single CCD are best made with the target placed near the center of a single CCD rather than near the center of the 4 CCD mosaic. This results in a marginally better point spread function, and avoids photometric, astrometric, and cosmetic problems in the vicinity of the target caused by the overlap of the cameras. Even so, for such observations the default operational mode is to read out all four CCDs. This policy has resulted in serendipitous discoveries, and sometimes the recovery of useful observations despite pointing or coordinate errors.

On the other hand, any combination of 1, 2 or 3 CCDs may be read out in numerical order (as specified in the Proposal Instructions). This partial readout capability is not generally available to GOs, although it can be used if data volume constraints mandate it, after discussion with the WFPC2 instrument scientists. It does not result in a decrease in the readout overhead time but does conserve space on the HST on-board science data recorders. This was especially useful with the initial science *tape* recorder, which had a capacity slightly over 7 full (4-CCD) WFPC2 observations or 18 single CCD WFPC2 observations on a single tape recorder side (of two sides). Readout of only a subset of the WFPC2 CCDs, or use of AREA mode, was advantageous when many frames needed to be obtained in rapid succession. However, the new Solid State Recorders installed during the

1997 and 1999 servicing missions are capable of holding well over one hundred 4-CCD WFPC2 images. This capability was phased in during Cycle 7, and has lead to relaxation of the above data rate restrictions.

Multiple exposures may be obtained with or without interleaved spacecraft repointings and filter changes without reading the CCDs (READ=NO). These would then be followed by a readout (READ=YES). Note that WFPC2 must be read out at least once per orbit.

2.9 Calibration Channel

An internal flat field system provides reference flat field images over the spectral range of WFPC2. These are provided by a "calibration channel" optical system mounted outside the main shroud of WFPC2. The system consists of a series of lamps and diffusers, and a flip mirror which directs the beam into the WFPC2 entrance aperture. The lamp set contains Tungsten incandescent lamps with spectrum shaping glass filters and a Deuterium UV lamp. The flat field illumination pattern is fairly uniform for wavelengths beyond about 1600Å. Short of 1600Å the flat field is distorted due to refractive MgF_2 optics. In practice, the flat fields used routinely to calibrate WFPC2 data have been generated by combining flats taken with an external stimulus in thermal vacuum testing with Earth "streak" (unpointed) flats to give the low frequency terms in the OTA illumination pattern. The calibration channel is used primarily to check for internal instrumental stability.

CHAPTER 3:

Optical Filters

In this chapter . . .

3.1 Introduction

This chapter describes the overall design of the WPFC2 filter set. Further information on individual filter bandpasses and their characteristic wavelengths may be found in Table 6.1 and Appendix A of this Handbook.

A set of 48 filters are included in WFPC2 with the following features:

1. It approximately replicates the WF/PC-1 "UBVRI" photometry series.
2. The broad-band filter series extends into the far UV.
3. There is a Strömgren series.
4. A Wood's filter is available for far-UV imaging without a red leak.
5. There is a 1% bandpass linear ramp filter series covering 3700-9800Å.
6. The narrow-band series is uniformly specified and well calibrated.

The filters are mounted in the Selectable Optical Filter Assembly (SOFA) between the shutter and the reflecting pyramid. The SOFA contains 12 filter wheels, each of which has 4 filters and a clear "home" position. A listing of all simple optical elements in the SOFA mechanism, and the location of each element (by wheel number 1-12, and position 1-4) is given in Table 3.1. Wheel number 1 is located closest to the shutter. The categories are simple filters (F), long-pass (LP), wide (W), medium (M), and narrow (N). Most of these filters are either flat single substrates or sandwiches.

The filter complement includes two solar blind Wood's filters, F160AW, and F160BW. F160BW is used in all science observations because the other filter has some large pinholes that lead to significant red leak.

In addition to the above complement of broad and narrow-band filters, WFPC2 features a set of three specialized quadrant (quad or Q) filters in which each quadrant corresponds to a facet of the pyramid, and therefore to a distinct camera relay. There is one quad containing four narrow-band, redshifted [OII] filters with central wavelengths from 3763Å to 3986Å, one quad with four polarizing elements (POL) with polarization angles, 0°, 45°, 90°, and 135°, and one quad with four methane (CH4) band filters with central wavelengths from 5433Å to 8929Å. The polarizer quad filter can be crossed with any other filter over the wavelength range from 2800Å to 8000Å, with the exception of the Methane Quad and Redshifted [OII] Quad which share the same wheel. The SOFA also contains four linearly variable narrow-band ramp (FR) filters (in the twelfth wheel - closest to the focus). The quad and ramp filters are listed in Table 3.2.

In Table 3.1 and Table 3.2, each of the type "A" filters is equivalent to inserting 5 mm of quartz in terms of optical path length, with compensation for wavelength such that focus is maintained on the CCDs. A configuration with no filters in the beam results in out-of-focus images and generally will not be used. With the exception of the quad polarizer and blocking (Type "B") filters, all filters are designed to be used alone. Type "B" filters introduce no focus shift, so they can be used in combination with any type "A" filter. All combinations where the number of type "A" filters is not unity will result in out-of-focus images. The image blur resulting from two or zero type "A" filters at visible wavelengths is equivalent to 2.3 mm defocus in the F/24 beam, which corresponds to 1/5 wave RMS of defocus at 6328Å, and a geometrical image blur of 0.34″. While this is a large defocus, the images are still of very high quality compared to seeing limited images. Some such combinations may be scientifically attractive. For example, the Wood's filter may be crossed with another UV filter to provide a solar blind passband (although the efficiency will be low).

Table 3.1: WFPC2 Simple Filter Set. The effective wavelength, width, and transmission quoted are defined precisely in Chapter 6, but here are quoted without the system (OTA+WFPC2) response.

Name	Type	Wheel	Slot	Notes	In WF/PC-1?	$\bar{\lambda}$(Å)	$\Delta\bar{\lambda}$(Å)	Peak T (%)	Peak λ (Å)
F122M	A	1	4	H Ly α - Red Leak	Y	1259	224.4	19.3	1240
F130LP	B	2	1	CaF2 Blocker (zero focus)	N	2681	5568.3	94.5	8852
F160AW	A	1	3	Woods A - read leak from pinholes	N	1471	457.2	10.1	1403
F160BW	A	1	2	Woods B	N	1446	457.1	12.1	1400
F165LP	B	2	2	Suprasil Blocker (zero focus)	N	3301	5533.2	95.4	5796
F170W	A	8	1	-	N	1666	434.6	30.7	1655
F185W	A	8	2	-	N	1899	297.4	25.9	1849
F218W	A	8	3	Interstellar feature	N	2117	367.9	21.1	2092
F255W	A	8	4	-	N	2545	408.2	14.8	2489
F300W	A	9	4	Wide U	N	2892	727.6	50.8	2760
F336W	A	3	1	WFPC2 U, Strömgren *u*	Y	3317	370.5	82.6	3447
F343N	A	5	1	Ne V	N	3427	23.5	9.3	3432
F375N	A	5	2	[OII] 3727 RS	Y	3732	24.4	19.5	3736
F380W	A	9	1	-	N	3912	694.8	65.0	3980
F390N	A	5	3	CN	N	3888	45.0	36.5	3886
F410M	A	3	2	Strömgren *v*	N	4086	147.0	70.4	4097
F437N	A	5	4	[OIII]	Y	4369	25.2	52.0	4368
F439W	A	4	4	WFPC2 B	Y	4283	464.4	68.2	4176
F450W	A	10	4	Wide B	N	4410	925.1	91.4	5060
F467M	A	3	3	Strömgren *b*	N	4663	166.4	75.3	4728
F469N	A	6	1	He II	Y	4694	25.0	52.4	4697
F487N	A	6	2	H β	Y	4865	25.9	58.6	4862
F502N	A	6	3	[OIII]	Y	5012	26.9	63.7	5008
F547M	A	3	4	Strömgren y (but wider)	Y	5446	486.6	91.3	5360
F555W	A	9	2	WFPC2 V	Y	5202	1222.6	94.6	5148
F569W	A	4	2	F555W generally preferred[a]	Y	5524	965.7	94.2	5310
F588N	A	6	4	He I & Na I (NaD)	Y	5893	49.0	91.4	5894
F606W	A	10	2	Wide V	Y	5767	1579.0	96.7	6186
F622W	A	9	3	-	Y	6131	935.4	95.6	6034
F631N	A	7	1	[OI]	Y	6306	30.9	85.7	6301
F656N	A	7	2	Hα	Y	6564	21.5	77.8	6562
F658N	A	7	3	[NII]	Y	6591	28.5	79.7	6591
F673N	A	7	4	[SII]	Y	6732	47.2	87.0	6732
F675W	A	4	3	WFPC2 R	Y	6714	889.5	97.3	6780
F702W	A	10	3	Wide R	Y	6940	1480.6	97.1	6538
F785LP	A	2	3	F814W generally preferred[a]	Y	9283	2096.1	91.7	9959
F791W	A	4	1	F814W generally preferred[a]	Y	7969	1304.6	95.9	8082
F814W	A	10	1	WFPC2 I	Y	8203	1758.0	94.8	8387
F850LP	A	2	4	-	Y	9650	1672.4	89.2	10028
F953N	A	1	1	[SIII]	N	9546	52.5	95.6	9528
F1042M	A	11	2	-	Y	10437	611.0	81.6	10139

a. Filters F555W and F814W are generally preferred, as they are part of the "standard" WFPC2 filter set, and will tend to have slightly better photometric calibration. See Section 3.2

The mean wavelength, $\bar{\lambda}$, is similar to that defined in Schneider, Gunn and Hoessel (ApJ 264, 337). The width is the FWHM of a Gaussian filter with the same second moment, and is reasonably close to the FWHM. The values tabulated here do not include the CCD DQE or the transmission of the OTA or WFPC2 optics (as given in Figure 2.4). In Chapter 6, the corresponding quantities are given including the effect of the other optical elements and the CCD DQE.

Table 3.2: WFPC2 Quad and Ramp Filters. Segments of the UV and CH4 quads are labeled here by their usual physical designations (A, B, C, and D); see following sections for filter and aperture names which are to be used in writing a Phase II proposal. The quad polarizer is represented for both parallel and perpendicular polarization to its polarization direction, which is different in each quadrant.

Physical Name	Type	Wheel	Slot	Notes	In WF/PC-1?	$\bar{\lambda}$(Å)	$\Delta\bar{\lambda}$(Å)	Peak T (%)	Peak λ (Å)
FQUVN-A	A	11	3	Redshifted [OII] 375	N	3763	73.3	25.9	3769
FQUVN-B	A	11	3	Redshifted [OII] 383	N	3829	57.3	29.5	3828
FQUVN-C	A	11	3	Redshifted [OII] 391	N	3912	59.5	34.3	3909
FQUVN-D	A	11	3	Redshifted [OII] 399	N	3992	63.7	41.0	3989
FQCH4N-A	A	11	4	CH4 543	N	5435	34.4	77.0	5442
FQCH4N-B	A	11	4	CH4 619	N	6199	33.8	82.7	6202
FQCH4N-C	A	11	4	CH4 727	N	7279	38.1	90.9	7278
FQCH4N-D	A	11	4	CH4 892	N	8930	54.8	64.8	8930
POLQ_par	B	11	1	Pol angle 0°,45°,90°,135°	N	4404	5796.8	90.7	11000
POLQ_per	B	11	1	Pol angle 0°,45°,90°,135°	N	6682	6654.2	89.7	11000
FR418N	A	12	1	3700-4720	N	W	W/75	~20-50	W
FR533N	A	12	2	4720-6022	N	W	W/75	~40-50	W
FR680N	A	12	3	6022-7683	N	W	W/75	~60-80	W
FR868N	A	12	4	7683-9802	N	W	W/75	~70-85	W

Figure 3.1 summarizes the normalized transmission curves for the simple filters and narrow-band quad filters. It does not include curves for the polarizing quad, or the linear ramp filters which are documented in Section 3.5 and Section 3.3, respectively. Figure 3.1 divides the filters into the following groups:

1. Long pass filters designed to be used in combination with another filter.
2. Wide bandpass filters with FWHM ~25% of the central wavelength.
3. Approximations to the UBVRI sequence, generally with wider bandpasses, designed for use on faint sources.

4. A photometric set of approximations to UBVRI passbands (see Harris, et al. 1991, AJ 101, 677). Note, however, that the WFPC2 UBVRI series is not the Johnson-Cousins photometric series, neither is it identical with the WF/PC-1 series.
5. Medium bandpass filters with FWHM ~10% of the central wavelength, including an approximation to the Strömgren photometric series.
6. Narrow bandpass filters for isolating individual spectral lines or bands.
7. Redshifted [OII] and CH4 narrow bandpass quad filters.

Note that the UV filters have some degree of "red leak," which is quantified in Section 6.9 where the system response is included. We also note that the F1042M filter suffers an anomalous PSF as described in Section 5.8.

In addition, the flat fields of images taken in most WFPC2 filters reveal an apparently randomly occurring rotational offset of about 0.42 degrees in some images. This quantity closely corresponds to one filter wheel step (0.5 degrees). The pivot point of the rotation implicates the filter wheel as the source of the inconsistency. We expect no impact on observations as any photometric effect is typically only 1%. At this time, the cause of this anomaly, whether it is mechanical or due to a software error, is unknown (Gonzaga, Baggett and Biretta 2001, 2002; Gonzaga and Biretta 2002).

Figure 3.2 shows the normalized passbands including the system response. Individual filter transmission curves are shown in Appendix A.

A passband calibration is maintained in the calibration database system (CDBS). It has been updated following on orbit calibrations. The ground based calibration of the narrow-band filters' central wavelengths has not been corrected for temperature effects and is therefore accurate to about 2Å. Because of this, it is not advisable to place narrow emission lines at the half power points of such filters and expect to predict the throughput to high accuracy. The standalone software package XCAL, or SYNPHOT running under IRAF, can be used to access these calibrations which are available on the Institute's WWW page.

Figure 3.1: Summary of Normalized Filter Curves.

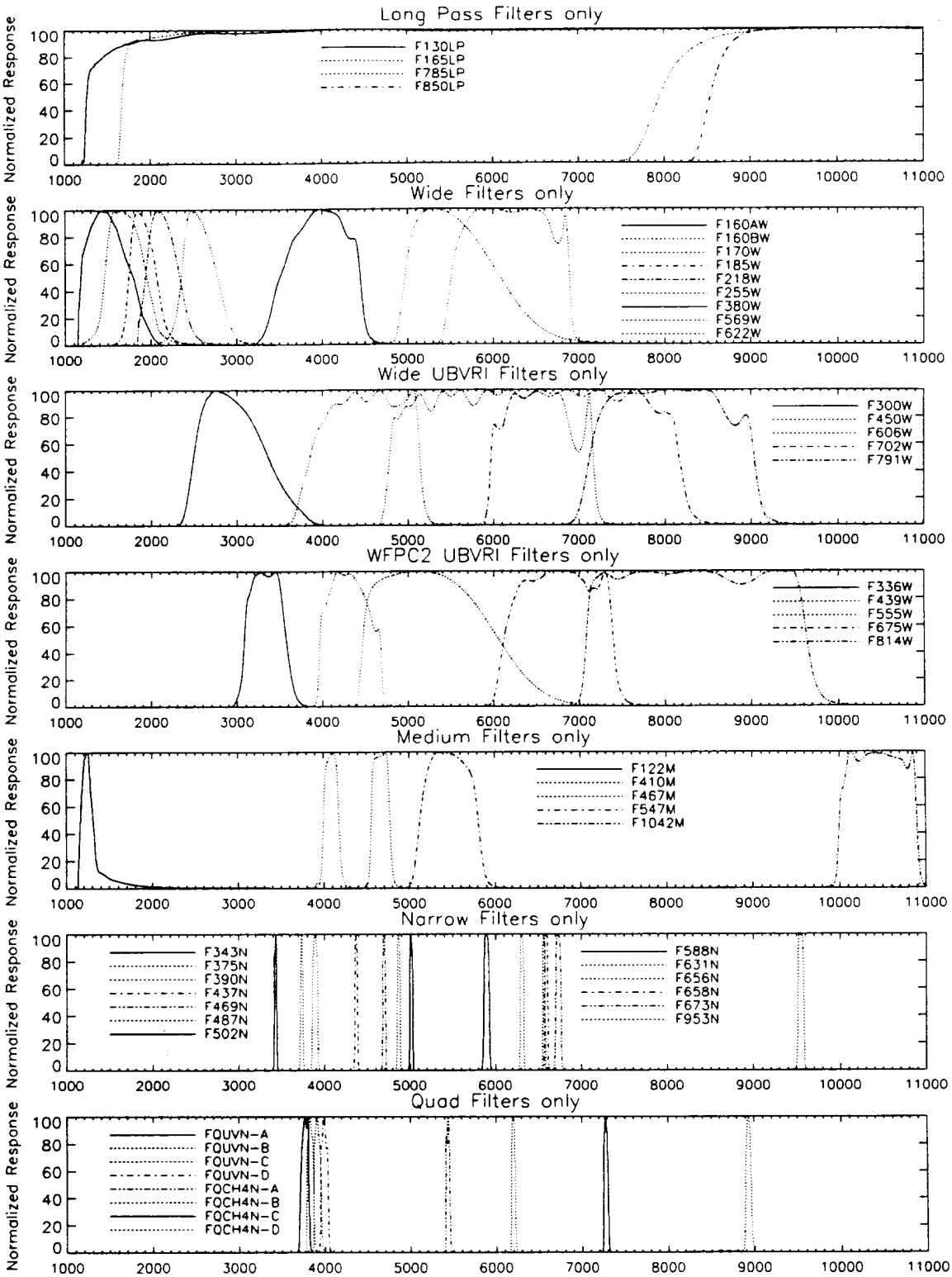

Figure 3.2: Normalized Passbands including System Response.

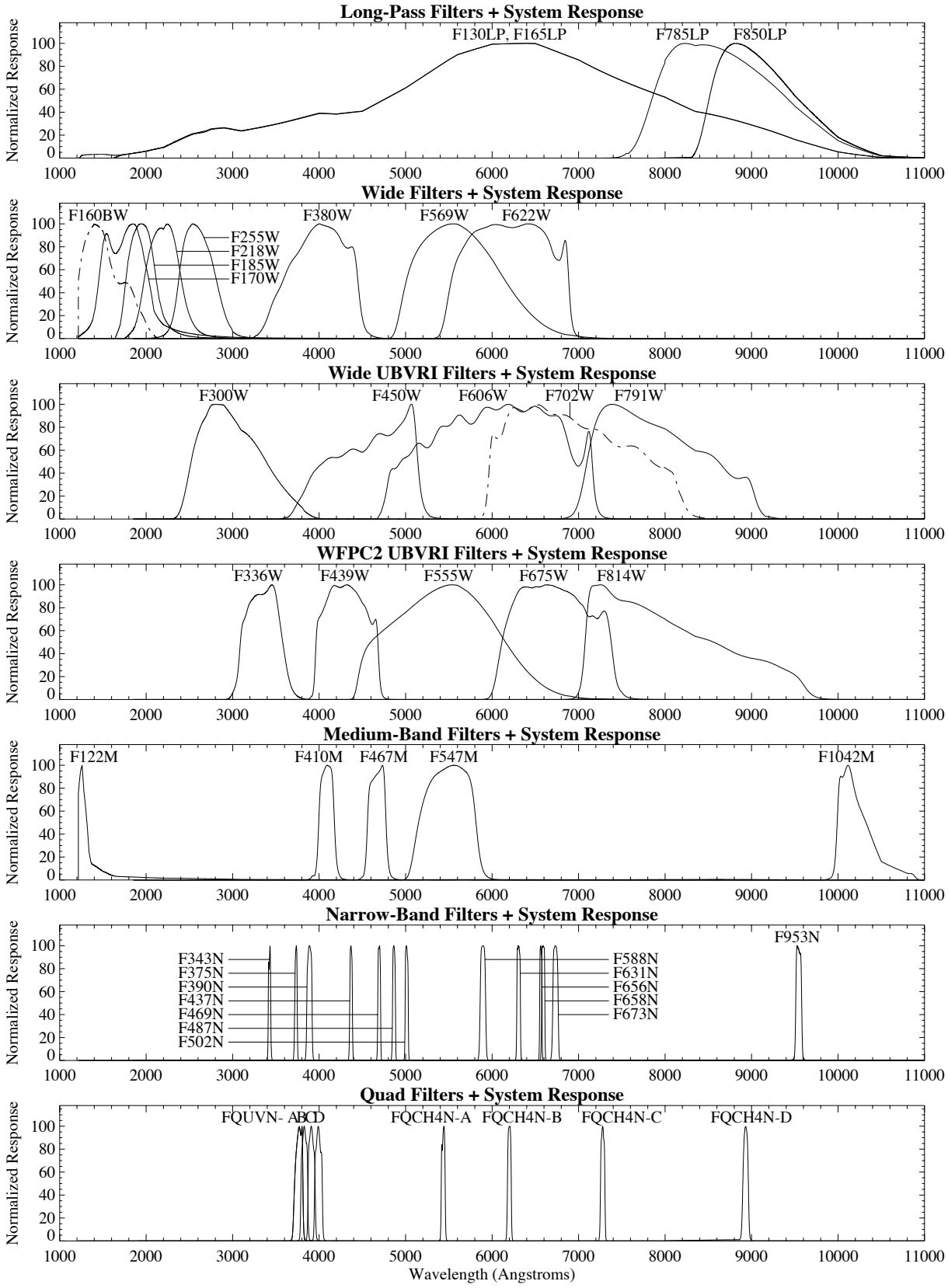

3.2 Choice of Broad Band Filters

A number of different choices are possible on WFPC2 in order to approximate the Johnson-Cousins system often used in ground based observing. These choices differ in throughput, wavelength fidelity, color transformability, and cosmetics. The HST science program as a whole benefits if a standard set can be agreed upon by the community for broad band photometry. This will allow theoretical isochrones and other models to be published in the standard system, and allow ready comparison of the results from different observers. Furthermore, although all filters will be calibrated photometrically and with flat fields, a core set must be chosen for monitoring the instrument both photometrically and in imaging performance. There was a substantial consensus between the accepted Cycle 4 GO programs and the WF/PC-1 and WFPC2 science teams that F336W, F439W, F555W, F675W, and F814W should be the preferred set to approximate the Johnson Cousins U, B, V, R, I passbands. These filters form the basis for the WFPC2 broad band photometric system. As will be seen from the figures in Section 8.9, the preferred set is accurately transformable with the exception of the U bandpass.

On the other hand, there are situations where concerns such as maximum throughput must override the above arguments. For example, filters F300W, F450W, F606W, and F814W were chosen for the Hubble Deep Field (HDF), due to their wider bandpasses.

3.3 Linear Ramp Filters

The linear ramp filters are designed for narrow-band absorption and emission line imaging of moderately extended objects. Each filter is divided into four parallel strips where the central wavelength across each strip varies by approximately 6%. Each CCD pixel is mapped to a unique central wavelength with a FWHM bandwidth of approximately 1.3% of the central wavelength. The maximum size of an object which can be imaged at a given wavelength is approximately 13″ and is determined by the width of the strips and the image size at the filter. The cumulative wavelength range of the four linear ramp filters is 3710Å to 9762Å. Originally intended for a four WFC configuration, the linear ramp filters require partial rotation of the SOFA wheels to +15˚, -18˚ and -33˚ from their nominal positions, to recover wavelength regions which would otherwise fall on the un-imaged region adjacent to the PC CCD. There will be vignetting at some wavelengths for these partial rotations.

3.3.1 Spectral Response

A JPL Memorandum (DFM #2031, 1992) gives the results of a prediction scheme to locate and quantify the passbands of the four WFPC2 ramp filters, FR418N, FR533N, FR680N and FR866N. The results are summarized here.

Laboratory (room temperature) measurements of the passbands of the four ramp filters were made at five equally spaced intervals on each of the four ramp stripes on each filter for a total of 80 passband measurements. The laboratory measurements were made with a narrow beam and were then integrated over an annular area of the filter to simulate the beam profile. The radius of the beam is 3.7 mm, or 13″. The integration was carried out by assuming the nominal linear shift in wavelength with position, and that no significant changes in the passband shape occur across the beam. The integration makes the shape of the passband quite symmetrical.

The resulting spectral response can be fitted to within a few percent with a Munson function:

$$T = T_0 / \{1 + (1-a)x^2 + a(1-b)x^4 + ab(1-c)x^6 + abcx^8\}$$

where a, b and c are shape parameters, and $0 \le (a,b,c) \le 1$; T_0 is the peak transmission of the passband, $T=T_0$ at $x=0$; x is related to wavelength λ by $x=(\lambda-\lambda_0)/H$, $T=T_0/2$ at $x=1$ (so H is the half width at half maximum).

The parameters, (λ_0, T_0, H, a, b, c) were then fitted to polynomial functions of position Y (which starts at 0 inches at the lower wavelength edge of each strip) to predict the filter response for areas of the filters between the tested points. Good quadratic fits are available for all the parameters except for T_0 which requires a cubic. The results are given in Table 3.3 on page 48 through Table 3.6 on page 51, which give the polynomial fit coefficients for the ramp filter parameters. The table entries, except for the first line, are used as parameter=$A_0+A_1Y+A_2Y^2+A_3Y^3$. The short wavelength side of the filter is opposite for alternate ramps. The first line in each table gives the Y position as a function of λ. If the polynomial fit predicts a, b, or $c < 0$ or > 1 then the quantities are set to 0 or 1, respectively.

Use of these fits should be restricted to objects near the center of the ramp, otherwise the beam will combine light from adjacent ramps. The fit should also not be used within 13″ of the end of the ramp. There is enough wavelength overlap between ramps that the extreme ends need not be used, except at the very lowest and highest wavelengths. Figure 3.3 on page 52 shows the fit parameter T_0 as a function of λ_0 for all 16 ramp filter strips. Figure 3.4 on page 52 shows $2H/\lambda_0$.

Table 3.3: Ramp Filter FR418N Parameters.

Quantity	A0	A1	A2	A3
Ramp 1 Position	-26.1083	0.00713888	0.0000	
Wavelength	3657.7	138.7	0.6178	
Peak transmission	-0.01667	0.2188	0.04138	-0.03489
Half width at half max	21.95	-0.8347	2.143	
a	0.2120	0.002857	0.002596	
b	1.181	-0.8138	0.3535	
c	0.3301	-0.3715	0.3825	
Ramp 2 Position	-24.2554	0.00625704	0.0000	
Wavelength	3876.9	158.6	0.5472	
Peak transmission	0.1660	0.2288	-0.1080	0.004005
Half width at half max	21.50	3.315	-0.7079	
a	0.1592	-0.003687	-0.0008497	
b	0.7938	0.2355	-0.09124	
c	0.9306	0.01366	0.007458	
Ramp 3 Position	-24.7145	0.00598254	0.0000	
Wavelength	4130.5	168.8	-0.7389	
Peak transmission	0.1352	0.6200	-0.5226	0.1529
Half width at half max	22.09	1.306	-0.1181	
a	0.2300	0.05586	-0.03044	
b	1.096	-0.3185	0.1396	
c	1.276	-1.279	0.5721	
Ramp 4 Position	-23.4440	0.00536340	0.0000	
Wavelength	4371.3	185.8	0.2913	
Peak transmission	0.3189	0.1287	-0.01160	-0.001712
Half width at half max	25.62	1.015	0.1161	
a	0.3123	-0.2055	0.09535	
b	0.9222	0.1167	-0.04673	
c	1.033	-0.1356	0.05660	

Table 3.4: Ramp Filter FR533N Parameters.

Quantity	A0	A1	A2	A3
Ramp 1 Position	-26.7670	0.00572115	0.0000	
Wavelength	4677.7	177.3	-1.125	
Peak transmission	0.5450	-0.3612	0.3623	-0.1281
Half width at half max	25.67	0.3168	0.8873	
a	-0.009839	0.4644	-0.2039	
b	0.31511	0.9473	-0.4516	
c	-0.3379	2.788	-1.346	
Ramp 2 Position	-24.6600	0.00498393	0.0000	
Wavelength	4948.4	199.2	0.6484	
Peak transmission	0.4546	0.4188	-0.5456	0.1548
Half width at half max	32.10	-1.204	3.171	
a	0.1678	-0.02726	0.09521	
b	0.9345	0.1935	-0.1224	
c	0.9571	0.02919	-0.009393	
Ramp 3 Position	-24.5038	0.00465985	0.0000	
Wavelength	5257.3	217.9	-1.481	
Peak transmission	0.4944	-0.1714	0.1890	-0.0631
Half width at half max	34.03	5.078	-1.347	
a	0.3851	-0.06264	0.003163	
b	0.5605	0.6642	-0.2751	
c	0.9665	0.05543	-0.03654	
Ramp 4 Position	-25.5182	0.00455886	0.0000	
Wavelength	5596.9	220.9	-0.6938	
Peak transmission	0.5058	-0.2715	0.3203	-0.1230
Half width at half max	35.06	-2.856	2.382	
a	0.06553	0.2253	-0.08275	
b	1.043	-0.1190	0.02889	
c	1.162	-0.4910	0.2059	

Table 3.5: Ramp Filter FR680N Parameters.

Quantity	A0	A1	A2	A3
Ramp 1 Position	-21.8962	0.00370137	0.0000	
Wavelength	5916.0	269.4	0.3460	
Peak transmission	0.1198	1.005	-0.4015	-0.00162
Half width at half max	41.50	-5.873	4.038	
a	0.1743	-0.05050	0.06481	
b	0.8320	0.3326	-0.1858	
c	0.9682	-0.09110	0.05122	
Ramp 2 Position	-22.6919	0.00360750	0.0000	
Wavelength	6290.8	275.6	0.7184	
Peak transmission	0.7918	-0.02034	0.1086	-0.05945
Half width at half max	39.48	2.120	0.3703	
a	0.05596	0.3034	-0.1333	
b	1.017	-0.27026	0.04560	
c	0.7244	0.8326	-0.5107	
Ramp 3 Position	-22.0719	0.00330755	0.0000	
Wavelength	6673.5	301.6	0.3321	
Peak transmission	0.9494	-1.008	1.161	-0.3777
Half width at half max	42.81	0.8193	0.4269	
a	0.1038	0.09020	-0.02747	
b	0.8415	0.3045	-0.1930	
c	1.017	-0.1732	0.07463	
Ramp 4 Position	-24.7447	0.00346462	0.0000	
Wavelength	7141.9	289.3	-0.2999	
Peak transmission	0.4823	0.4479	-0.07484	-0.05868
Half width at half max	44.72	0.8952	-0.0756	
a	0.1612	-0.01167	0.01355	
b	0.2708	1.077	-0.4757	
c	0.9941	-0.02694	0.01685	

Table 3.6: Ramp Filter FR868N Parameters.

Quantity	A0	A1	A2	A3
Ramp 1 Position	-23.2685	0.00308029	0.0000	
Wavelength	7555.5	320.4	1.906	
Peak transmission	0.7524	-0.3328	0.4543	-0.1343
Half width at half max	49.32	1.742	0.4914	
a	0.2958	-0.3877	0.2465	
b	1.321	-0.9156	0.3666	
c	0.3762	1.668	-0.9499	
Ramp 2 Position	-22.9766	0.00286673	0.0000	
Wavelength	8014.3	350.5	-0.7500	
Peak transmission	0.8204	-0.3368	0.3815	-0.1057
Half width at half max	54.17	1.579	0.2196	
a	0.05832	0.7525	-0.3625	
b	0.4582	0.8433	-0.4350	
c	0.6422	0.3247	-0.1593	
Ramp 3 Position	-22.6085	0.00265657	0.0000	
Wavelength	8510.7	375.6	0.3706	
Peak transmission	0.5817	-0.1920	0.4517	-0.1627
Half width at half max	55.19	-0.7459	1.433	
a	0.5422	-0.2444	0.03545	
b	1.420	-1.176	0.4814	
c	0.4257	-0.2522	0.1777	
Ramp 4 Position	-23.2142	0.00256976	0.0000	
Wavelength	9034.3	387.2	0.8722	
Peak transmission	0.6241	0.2403	-0.1230	0.02829
Half width at half max	59.69	2.167	-0.1996	
a	0.2376	-0.01879	-0.00864	
b	0.9670	0.02456	-0.00477	
c	0.7829	0.03750	0.02393	

Figure 3.3: Ramp Filter Peak Transmission. The four line types correspond to the four different filters (each containing four ramps).

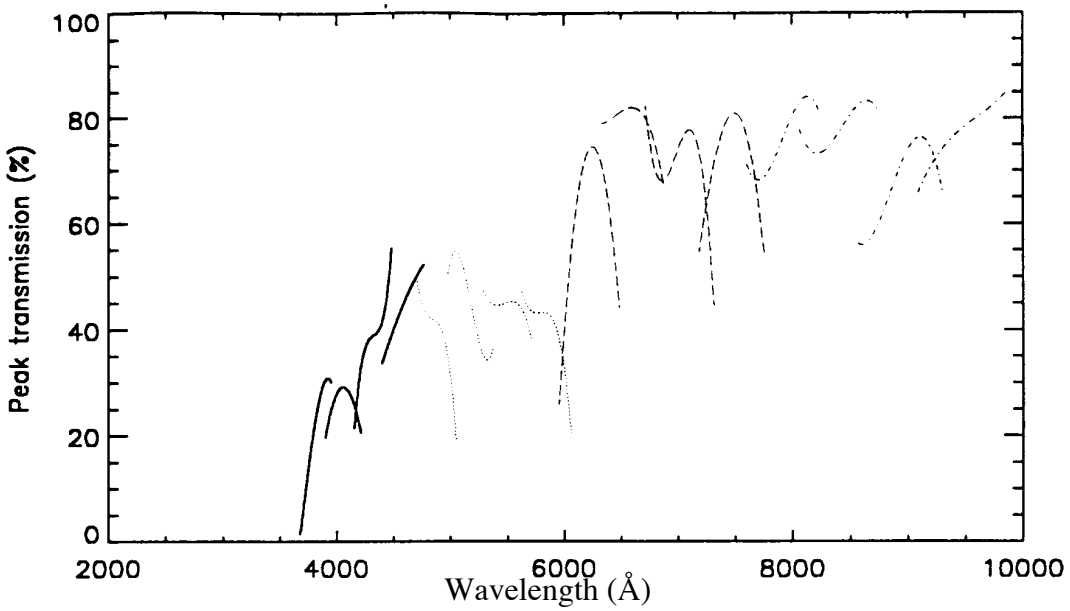

Figure 3.4: Ramp Filter Dimensionless Widths.

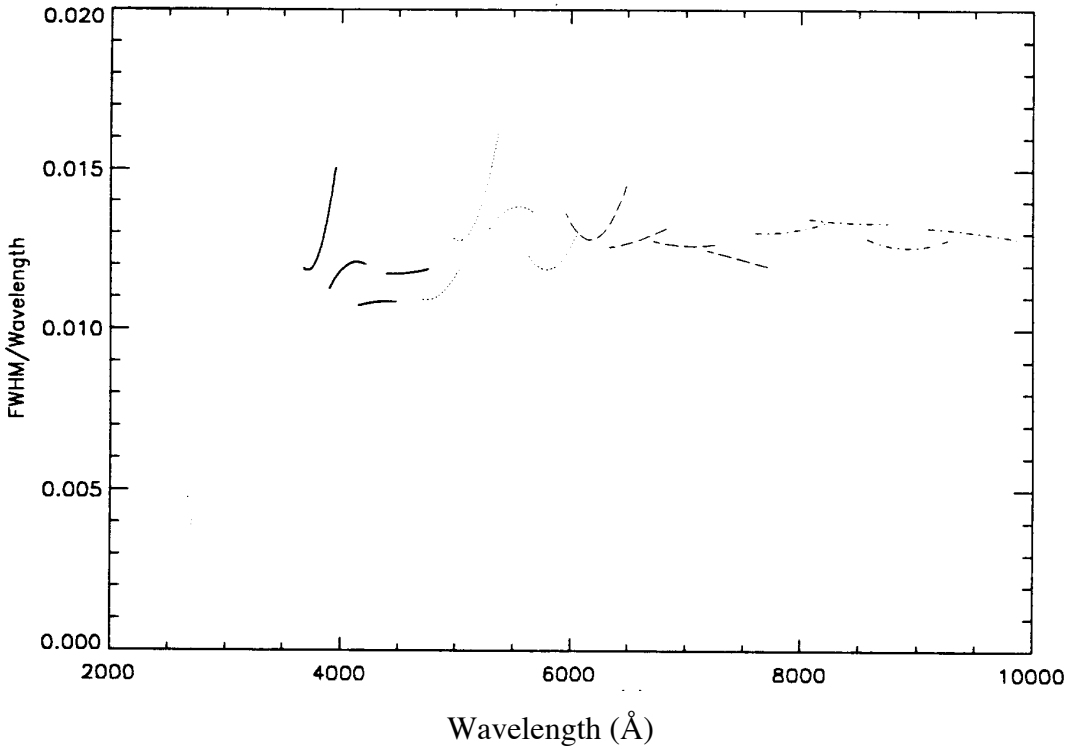

3.3.2 Target Locations

In Figure 3.5 and Figure 3.6 we show the correspondence between central wavelength and location in the focal plane for the nominal and rotated filter positions. The selection of filter and aperture for the linear ramp filters is transparent to the user who is required only to specify the linear ramp filter name LRF and a central wavelength. Each central wavelength is assigned to a unique filter and CCD location in the Phase II proposal.

Following on-orbit testing of WFPC2, a revised table of linear ramp filter wavelengths was compiled and is shown in Table 3.7 (Biretta, et al. 1995, ISR WFPC2 95-05). For each wavelength listed, there is a minimum 10″ diameter unvignetted field-of-view. Some wavelengths can be obtained with several different settings of the ramps, however, for simplicity, the redundant wavelengths have been removed from the table. Note that this table supports observation with the PC and a new +15° rotation of the filter wheel. Table 3.8 lists wavelengths which are available, but with some compromise in data quality, so as to avoid gaps in wavelength coverage. Most of these wavelengths are observed slightly off the central wavelength of the passband. This implies a slightly reduced throughput (see estimates of the light reduction in the table), and some additional difficulties in flattening the data to remove variations in the passband across the target. A few other wavelengths are observed slightly off the unvignetted center line of the ramps, and these are indicated by note “FOV” in Table 3.8. Again, this vignetting will present some additional complications when calibrating the data. Further details regarding the ramp filter wavelengths and apertures will be made available in a separate instrument science report.

We note that an interactive tool is available on the WFPC2 WWW pages which will compute target locations for LRF observations. The user inputs either the central wavelength or the target location in the field-of-view, and the other quantity is returned.

Figure 3.5: FR418N and FR533N Wavelength Mapping.

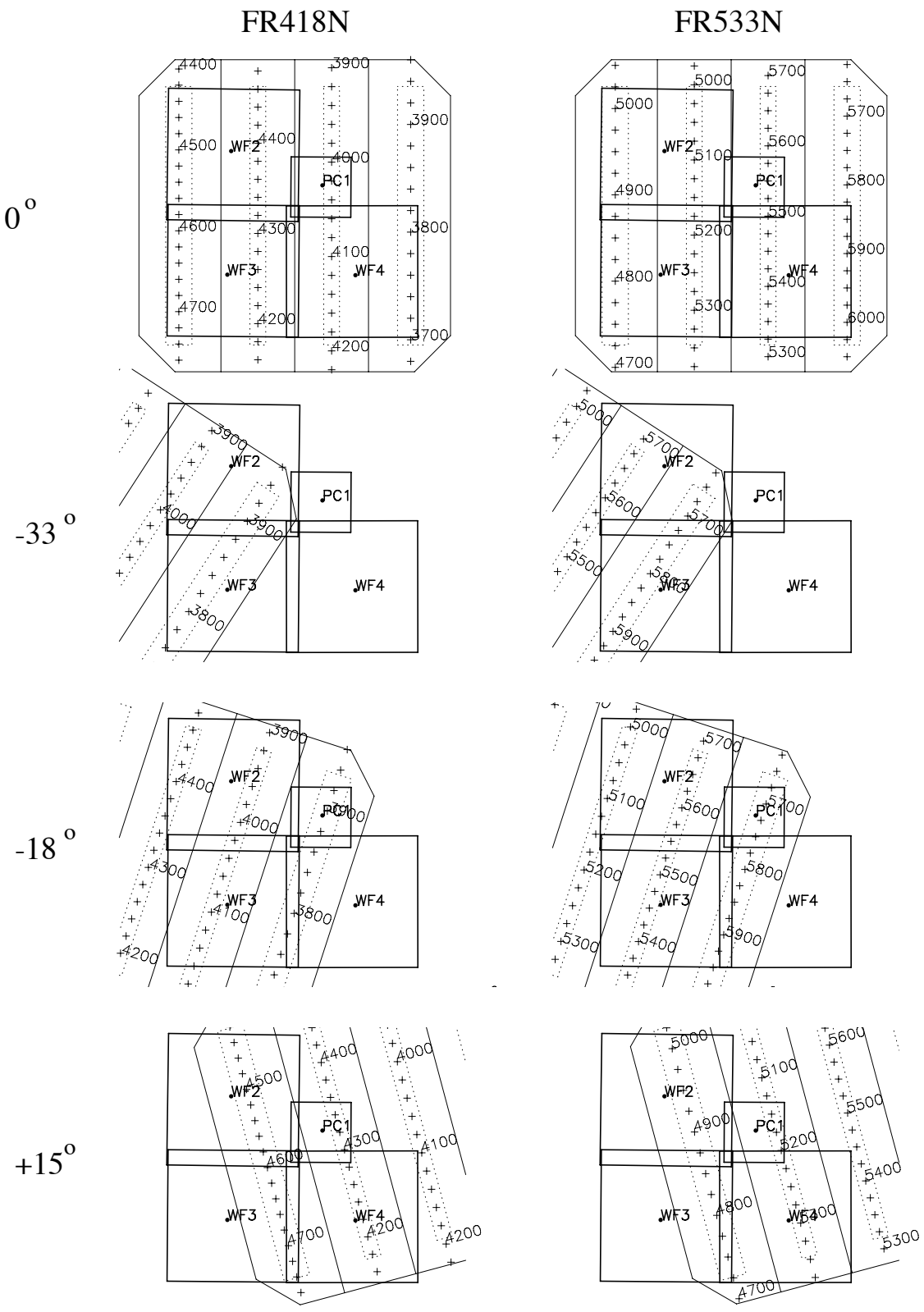

Figure 3.6: FR680N and FR868N Wavelength Mapping.

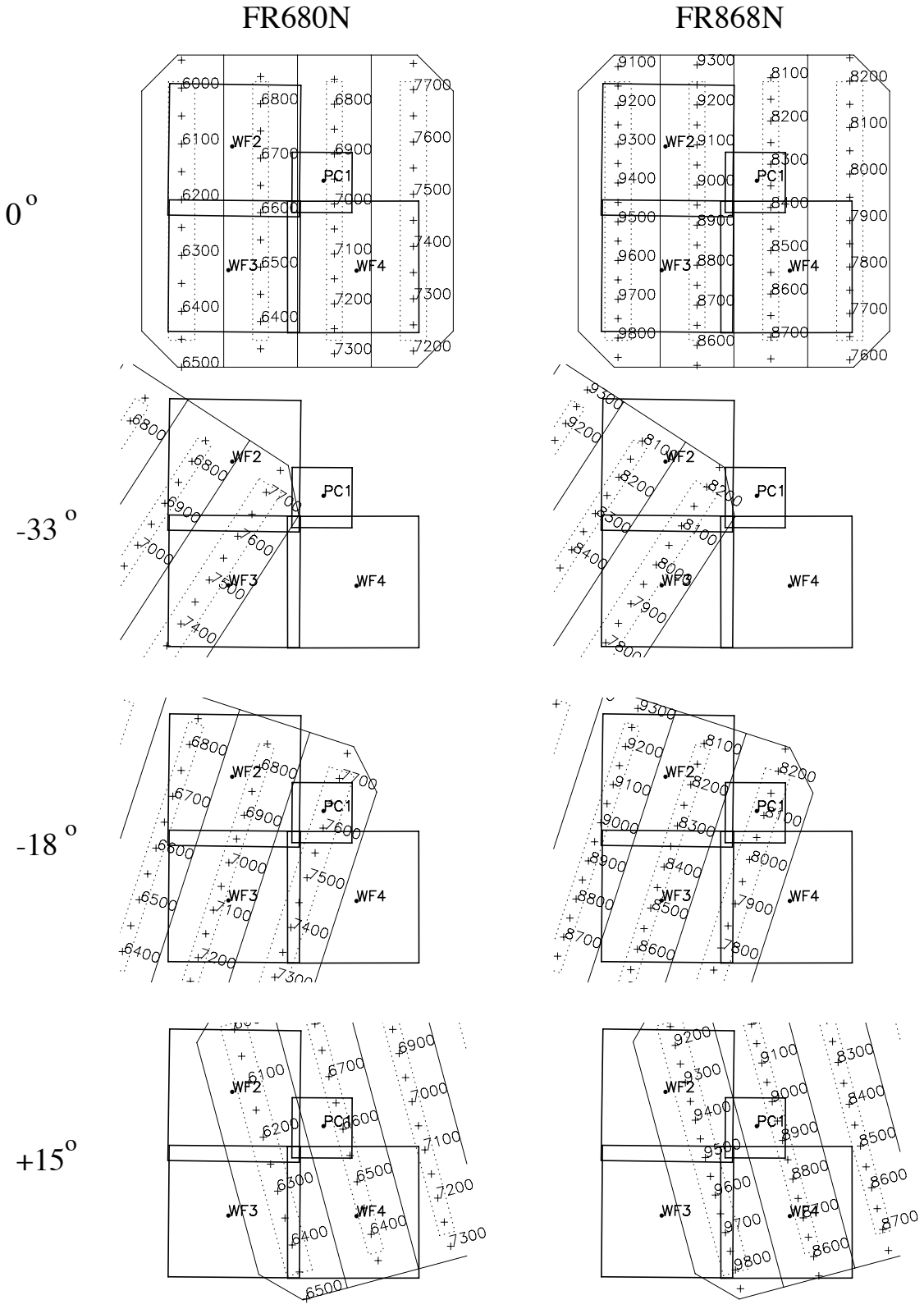

3.3.3 LRF Photometric Calibration

As of this writing, the preferred method of flat fielding LRF data is to use a narrow band flat observed nearby in wavelength. This will remove pixel-to-pixel effects, as well as effects of distortion and vignetting in the cameras, while avoiding the complications of pinholes on the LRFs and spurious variations due to the spectrum of the flat field light source.

Conversion of counts to source flux is best achieved by using the SYNPHOT synthetic photometry package. An LRF filter setting is simply specified by including "LRF#*xxxx*" in the OBSMODE, where *xxxx* is the central wavelength specified on the Phase II proposal (see Biretta, Baggett, and Noll 1996, ISR WFPC2 96-06).

Comparisons between the SYNPHOT predictions and on-orbit observations of standard stars show a small, systematic offset between the two (in the sense that fewer counts are observed than expected), plus scatter about this trend. A linear fit to the photometric offset gives:

$$M_{obs} - M_{calc} = (0.09 \pm 0.01) + (3.11e^{-5} \pm 0.67e^{-5}) * (\lambda - 6500)$$

with an RMS scatter about the trend of 0.12 mag. It may be possible to further reduce the calibration errors for certain wavelength ranges that were well sampled by the calibration programs. Additional on-orbit observations with the LRFs have been undertaken as part of the WFPC2 Calibration Closeout program in Cycle 16 (proposal 11038). An effort will be made to improve the photometric accuracy of the LRFs and appropriately revise the SYNPHOT tables.

For the FR533N filters, please note that a randomly occurring filter anomaly could affect photometric accuracy for extended targets, please see Section 7.10 for details.

Table 3.7: Aperture Locations and Wavelengths for Ramp Filters.

Start (Å)	End (Å)	Filter	CCD / Aperture	x1 (pix)	y1 (pix)	x2 (pix)	y2 (pix)
3710	3800	FR418N	WF4-FIX	750	736.8	161 .5	737.7
3800	3878	FR418N33	WF3-FIX	669.5	559.2	395.1	128.9
3881	3907	FR418N18	PC1-FIX	402.3	225	515.4	579.5
3907	3929	FR418N33	WF2-FIX	128.4	286.7	250.1	209.9
3929	4008	FR418N18	WF2-FIX	562.7	233	130.1	367.1
4008	4038	FR418N	PC1-FIX	541.3	632.7	543.3	256.5
4038	4100	FR418N18	WF3-FIX	425.3	130.8	532 4	469.9
4100	4177	FR418N	WF4-FIX	309	276.2	750.3	275.5
4186	4210	FR418P15	WF4-FIX	596.5	515.9	469.4	482.1
4210	4308	FR418N	WF3-FIX	248.2	665.9	252.7	128.5
4308	4337	FR418P15	PC1-FIX	690.2	264.6	598.4	599.9
4337	4446	FR418N	WF2-FIX	127.9	247.6	725.4	255.7

Table 3.7: Aperture Locations and Wavelengths for Ramp Filters.

Start (Å)	End (Å)	Filter	CCD / Aperture	x1 (pix)	y1 (pix)	x2 (pix)	y2 (pix)
4446	4550	FR418N	WF2-FIX	691.7	716.2	180.6	709.2
4550	4571	FR418P15	WF2-FIX	230	253.8	130.7	225.8
4593	4720	FR418N	WF3-FIX	713.7	125.6	708.5	749.9
4746	4863	FR533N	WF3-FIX	689.3	748.9	694.4	135.5
4884	4900	FR533P15	WF2-FIX	128.3	205.1	209	227.9
4900	5013	FR533N	WF2-FIX	153.6	689.6	745.9	697.7
5013	5020	FR533N18	WF2-FIX	693.4	642.4	662.9	651.8
5020	5153	FR533N	WF2-FIX	737.3	236.6	130	228.4
5153	5176	FR533P15	PC1-FIX	637.9	614.9	698.6	393.3
5188	5310	FR533N	WF3-FIX	233.5	127.4	228.8	684.7
5310	5335	FR533P15	WF4-FIX	482.8	505.5	593.1	534.9
5339	5450	FR533N	WF4-FIX	750.9	294.7	277.2	295.5
5450	5528	FR533N18	WF3-FIX	504.4	445.3	404.1	127.6
5528	5566	FR533N	PC1-FIX	585.3	277.5	583.4	632.3
5566	5671	FR533N18	WF2-FIX	124.1	348.8	552.3	216.1
5671	5700	FR533N33	WF2-FIX	224.8	203.2	122.3	267.7
5700	5741	FR533N18	PC1-FIX	558.8	577	444.9	220.1
5743	5910	FR533N33	WF3-FIX	370.8	126.5	745.9	714.9
5910	6007	FR533N	WF4-FIX	333.8	747.6	738.8	746.9
6007	6192	FR680N	WF2-FIX	750.3	706.9	122.9	698.4
6192	6208	FR680P15	WF2-FIX	177.1	228.4	124.9	213.6
6238	6409	FR680N	WF3-FIX	703.6	128.1	698.8	708.2
6409	6584	FR680N	WF3-FIX	237.8	705.6	242.6	127
6590	6631	FR680P15	PC1-FIX	699.1	315.3	620.9	601.2
6631	6800	FR680N	WF2-FIX	125.9	237.5	684.5	245.1
6800	6921	FR680N18	WF2-FIX	480.1	248	129.9	356.6
6921	6976	FR680N	PC1-FIX	563.3	639.2	565.3	274.6
6976	7061	FR680N18	WF3-FIX	413.2	126	490.8	371.7
7061	7241	FR680N	WF4-FIX	203	286.4	748.3	285.6
7251	7420	FR680N	WF4-FIX	749.6	743.5	213.3	744.3
7420	7600	FR680N33	WF3-FIX	688.9	608.4	381.6	126.4
7605	7658	FR680N18	PC1-FIX	427	230	538.9	580.6
7658	7690	FR680N33	WF2-FIX	126.2	276.1	212.1	222
7690	7830	FR868N	WF4-FIX	711.5	751.3	316.5	751.9
7830	8072	FR868N33	WF3-FIX	728.2	705.8	360.9	129.7
8077	8140	FR868N18	PC1-FIX	471.5	231	589.7	601.5
8140	8300	FR868N18	WF2-FIX	527.6	213.2	126.2	337.6
8300	8362	FR868N	PC1-FIX	605.4	644.1	607.3	287.9
8362	8460	FR868N18	WF3-FIX	393.1	126.1	470.6	371.7

Table 3.7: Aperture Locations and Wavelengths for Ramp Filters.

Start (Å)	End (Å)	Filter	CCD / Aperture	x1 (pix)	y1 (pix)	x2 (pix)	y2 (pix)
8460	8661	FR868N	WF4-FIX	196.9	305.7	724.7	304.9
8661	8910	FR868N	WF3-FIX	218.3	731.6	223.4	125.3
8945	8980	FR868P15	PC1-FIX	701.1	467.5	651.9	647.3
8980	9200	FR868N	WF2-FIX	142.7	218.5	678.2	225.8
9200	9415	FR868N	WF2-FIX	668.4	686.5	162.2	679.6
9415	9456	FR868P15	WF2-FIX	219.9	220.5	127	194.2
9501	9762	FR868N	WF3-FIX	684.3	135.4	679.2	750.2

Table 3.8: Vignetted Wavelengths for Ramp Filters. The right column gives the maximum throughput reduction (in %) for these settings where the target must be placed away from the optimal location on the filter glass. “FOV” denotes settings where transmission is optimal, but the usable field-of-view is reduced below 10″ to the indicated diameter (in arcseconds).

Start (Å)	End (Å)	Filter	CCD / Aperture	x1 (pix)	y1 (pix)	x2 (pix)	y2 (pix)	Max % Light Loss
3878	3881	FR418N18	PC1-FIX	402.3	225.0	402.3	225.0	2
4177	4182	FR418N	WF4-FIX	750.3	275.5	750.3	275.5	3
4182	4186	FR418P15	WF4-FIX	596.5	515.9	596.5	515.9	2
4571	4582	FR418P15	WF2-FIX	130.7	225.8	130.7	225.8	13
4582	4593	FR418N	WF3-FIX	713.7	125.6	713.7	125.6	13
4720	4733	FR418N	WF3-FIX	708.5	749.9	708.5	749.9	14
4733	4746	FR533N	WF3-FIX	689.3	748.9	689.3	748.9	14
4863	4873	FR533N	WF3-FIX	694.4	135.5	694.4	135.5	8
4873	4884	FR533P15	WF2-FIX	128.3	205.1	128.3	205.1	8
5176	5183	FR533P15	PC1-FIX	698.6	393.3	698.6	325.9	FOV~9”
5183	5188	FR533N	WF3-FIX	233.5	127.4	233.5	127.4	2
5335	5337	FR533P15	WF4-FIX	593.1	534.9	593.1	534.9	1
5337	5339	FR533N	WF4-FIX	750.9	294.7	750.9	294.7	1
5741	5743	FR533N33	WF3-FIX	370.8	126.5	370.8	126.5	1
6208	6221	FR680P15	WF2-FIX	124.9	213.6	124.9	213.6	8
6221	6238	FR680N	WF3-FIX	703.6	128.1	703.6	128.1	11
6584	6587	FR680N	WF3-FIX	242.6	127.0	242.6	127.0	1
6587	6590	FR680P15	PC1-FIX	699.1	294.3	699.1	315.3	FOV~9”
7241	7246	FR680N	WF4-FIX	748.3	285.6	748.3	285.6	2
7246	7251	FR680N	WF4-FIX	749.6	743.5	749.6	743.5	2
7600	7602	FR680N33	WF3-FIX	381.6	126.4	381.6	126.4	1
7602	7605	FR680N18	PC1-FIX	427.0	230.0	427.0	230.0	1
8072	8074	FR868N33	WF3-FIX	360.9	129.7	360.9	129.7	1
8074	8077	FR868N18	PC1-FIX	471.5	231.0	471.5	231.0	1
8910	8920	FR868N	WF3-FIX	223.4	125.3	223.4	125.3	2
8920	8945	FR868P15	PC1-FIX	701.1	339.1	701.1	467.5	FOV~7”
9456	9478	FR868P15	WF2-FIX	127.0	194.2	127.0	194.2	13
9478	9501	FR868N	WF3-FIX	684.3	135.4	684.3	135.4	13

3.4 Redshifted [OII] Quad Filters

The redshifted [OII] quad filter was designed to map onto a four-faceted WFC configuration. A partial SOFA wheel rotation of -33˚ is required to move filter quadrant 1 (3763Å) into WF2 and WF3, with some vignetting of both camera fields. The projections of the redshifted [OII] filter settings FQUVN and FQUVN33 onto the field-of-view are essentially identical to those of the POLQ and POLQN33 filters, respectively (Figure 3.7). The vignetted regions are similar, and the location of aperture FQUVN33 is identical to that of POLQN33.

The nominal and rotated filter wheel positions for the redshifted [OII] quad filter are each associated with different filter names. This allows pipeline calibration and database retrievals to proceed smoothly. The filter names are summarized in Table 3.9.

The required central wavelength is selected by filter name and aperture location. Filter element FQUVN (Filter Quad Ultra Violet Narrow) has three possible apertures, each of which is nominally centered in one of the three WF channels and associated with a unique central wavelength. The filter element FQUVN33 corresponds to a single central wavelength. In addition to the filter name and aperture, a central wavelength is also requested in the proposal instructions in order to provide a consistency check. Aperture names are discussed further in Section 3.9.

Table 3.9: Redshifted [OII] Quad Filter Elements.

Filter Name	Aperture Name	FOV Location	Quad	Mean Wavelength (Å)	Effective Width (Å)	Comments
FQUVN	WF2	WF2	D	3992	64	Nominal filter wheel position
FQUVN	WF3	WF3	C	3912	60	Nominal filter wheel position
FQUVN	WF4	WF4	B	3829	57	Nominal filter wheel position
FQUVN33	FQUVN33	WF2	A	3763	73	Filter rotated -33˚

3.5 Polarizer Quad Filter

The polarizer quads were also designed to map onto a four-faceted WFC configuration and, consequently, also require a partial filter rotation of -33˚ to move the filter quadrant 1 (nominal polarization angle 135˚) into WFCs 2 and 3, with some vignetting of both camera fields. Several additional partial rotations have been added to allow observations with different polarization angles on the same CCD.

The polarizer quad may be used in several ways: by observing the target with each camera, by observing the target with the same camera using different partial rotations of the polarizer quad, or by observing the target with the same camera using different roll angles of the spacecraft. The first method has the drawback that calibration is complicated by uncertainties in the relative photometric calibration between cameras, while the second method uses the same camera but has non-optimal polarization angles and limited fields of view. The third method may present scheduling difficulties due to constraints on the spacecraft roll angle, and the need to rotate undersampled images. (See Biretta and Sparks 1995, "WFPC2 Polarization Observations: Strategies, Apertures, and Calibration Plans," WFPC2 ISR 95-01.)

The required polarization angle is selected by filter name and aperture location as shown in Table 3.10. The transmission of the quad polarizer is shown in Figure 3.8. The polarizer is afocal and must therefore usually be used with another filter which will largely define the shape of the passband.

The polarizer is designed for problems where large polarizations are observed, and will need very careful calibration for problems requiring precision of order 3% or better.

Table 3.10: Polarizer Quad Filter. Polarization angle 0˚ lies along +X direction in Figure 3.12.

Filter Name	Aperture Name	FOV Location	Polarization Angle	Comments
POLQ	PC1	PC1	135˚	Nominal filter wheel position
POLQ	WF2	WF2	0˚	Nominal filter wheel position
POLQ	WF3	WF3	45˚	Nominal filter wheel position
POLQ	WF4	WF4	90˚	Nominal filter wheel position
POLQN33	POLQN33	WF2	102˚	Filter wheel rotated -33˚
POLQP15	POLQP15P	PC	15˚	Filter wheel rotated +15˚
POLQP15	POLQP15W	WF2	15˚	Filter wheel rotated +15˚
POLQN18	POLQN18	WF2	117˚	Filter wheel rotated -18˚

3.5.1 Polarization Calibration

Substantial improvements in the polarization calibration of WFPC2 were made after Cycle 6. These results are fully described in Biretta and McMaster (1997), and are based on a physical model of the polarization effects in WFPC2, described via Mueller matrices, which includes corrections for the instrumental polarization (diattenuation and phase retardance) of the pick-off mirror, as well as the high cross-polarization

transmission of the polarizer filter. New polarization flat fields were also made available. Comparison of the model against on-orbit observations of polarization calibrators shows that it predicts relative counts in the different polarizer/aperture settings to 1.5% RMS accuracy.

To assist in the analysis of polarization observations, we provide two Web-based utilities, available at

http://www.stsci.edu/hst/wfpc2/software/wfpc2_pol_top.html

by which users can simulate and calibrate their data. These tools have been upgraded to include effects related to the MgF_2 coating on the pick-off mirror, as well as the more accurate matrices for the cross-polarization leakage in the polarizer filter. Differences between the previous and current versions of the tools are typically around 1% in fractional polarization.

Figure 3.7: Polarizer Quads. The schematics show the filter projected onto the field-of-view for all rotated positions. Apertures are marked. Dashed lines indicate the central region of each quad which is free of vignetting and cross-talk. Grey-scale images are VISFLATs of the polarizer with F555W.

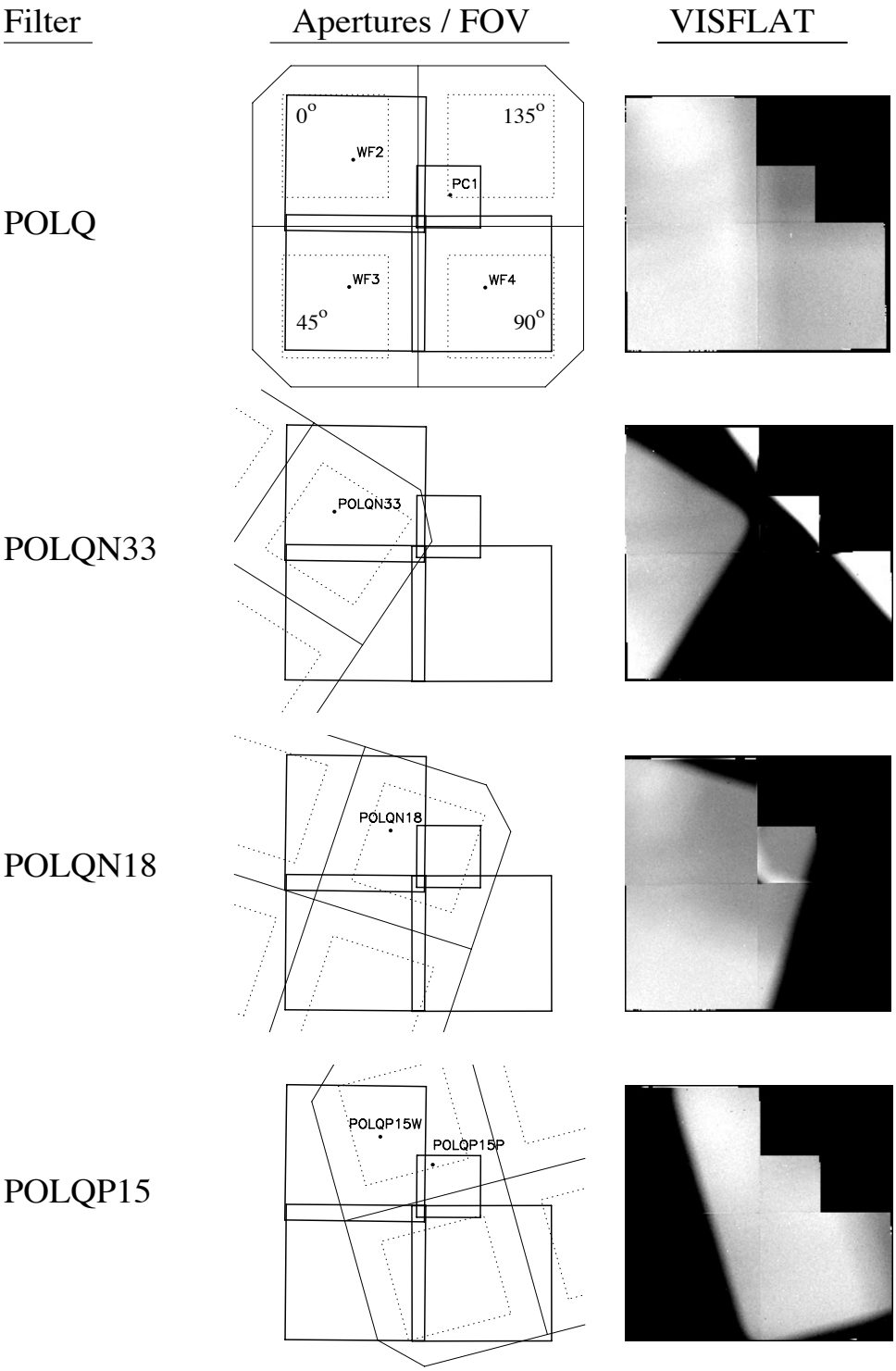

Figure 3.8: Polarizer Transmission for light polarized perpendicular (dotted curve) and parallel (solid curve) to the filter polarization direction.

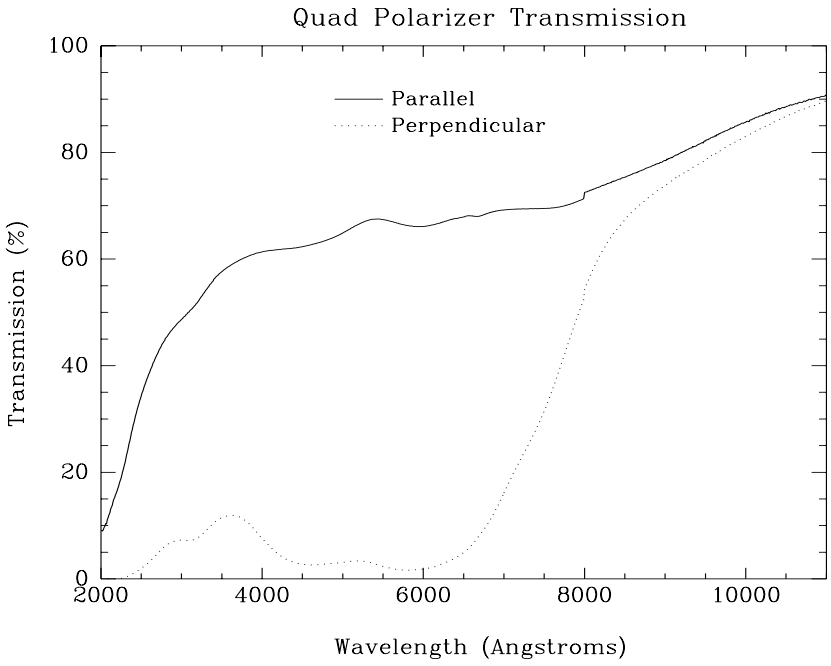

3.6 Methane Quad Filter

The methane band quad filter, known as the jewel-quad, was designed for a four-faceted WF/PC configuration to permit imaging with both four WFC CCDs and four PC CCDs. The camera was constructed, however, with only one PC CCD and three WF CCDs. WFC imaging is recovered for the first quadrant element of the filter (6193Å) by a partial SOFA wheel rotation of -33° which moves quadrant 1 into WF2 and WF3 with some vignetting of both camera fields. PC imaging with all four elements of the methane band jewel-quad cannot be recovered, but partial SOFA wheel rotations of -15° and +15° are implemented to recover two of the four methane band filters (8929Å and 6193Å). The +15° rotation of the filter wheel, however, results in some vignetting of PC1's field-of-view. The filter projections associated with the methane band jewel-quad are shown in Figure 3.9. Each of the four filter wheel positions are associated with unique filter names, as summarized in Table 3.11.

The required central wavelength is selected by filter name and aperture location. Filter element FQCH4N (Filter Quad Methane Narrow) has three possible apertures, each of which is located in one of the three WF channels and associated with a unique central wavelength, while FQCH4N33 is associated with one possible central wavelength. FQCH4N15 and FQCH4P15 are both associated with one central

wavelength for PC1 observations. In addition to the filter name and aperture, a central wavelength is also requested in the proposal instructions in order to provide a consistency check.

Table 3.11: Methane Band Quad Filter. The filter and aperture names should be specified on the Phase II proposal as shown here.

Filter Name	Aperture Name	FOV Location	Quad	Mean Wavelength (Å)	Effective Width (Å)	Comments
FQCH4N	FQCH4W2	WF2	A	5435	34	Nominal filter position
FQCH4N	FQCH4W3	WF3	D	8930	55	Nominal filter position
FQCH4N	FQCH4W4	WF4	C	7279	38	Nominal filter position
FQCH4N33	FQCH4N33	WF2/WF3	B	6199	34	Filter rotated -33°
FQCH4N15	FQCH4N15	PC1	B	6199	34	Filter rotated -15°
FQCH4P15	FQCH4P15	PC1	D	8930	55	Filter rotated +15°

Figure 3.9: Methane Quad Filter. The mapping to the focal plane for nominal and rotated (-33°, -15°, and +15°) SOFA positions is shown. Dashed lines indicate the limits of the unvignetted field-of-view on each quad.

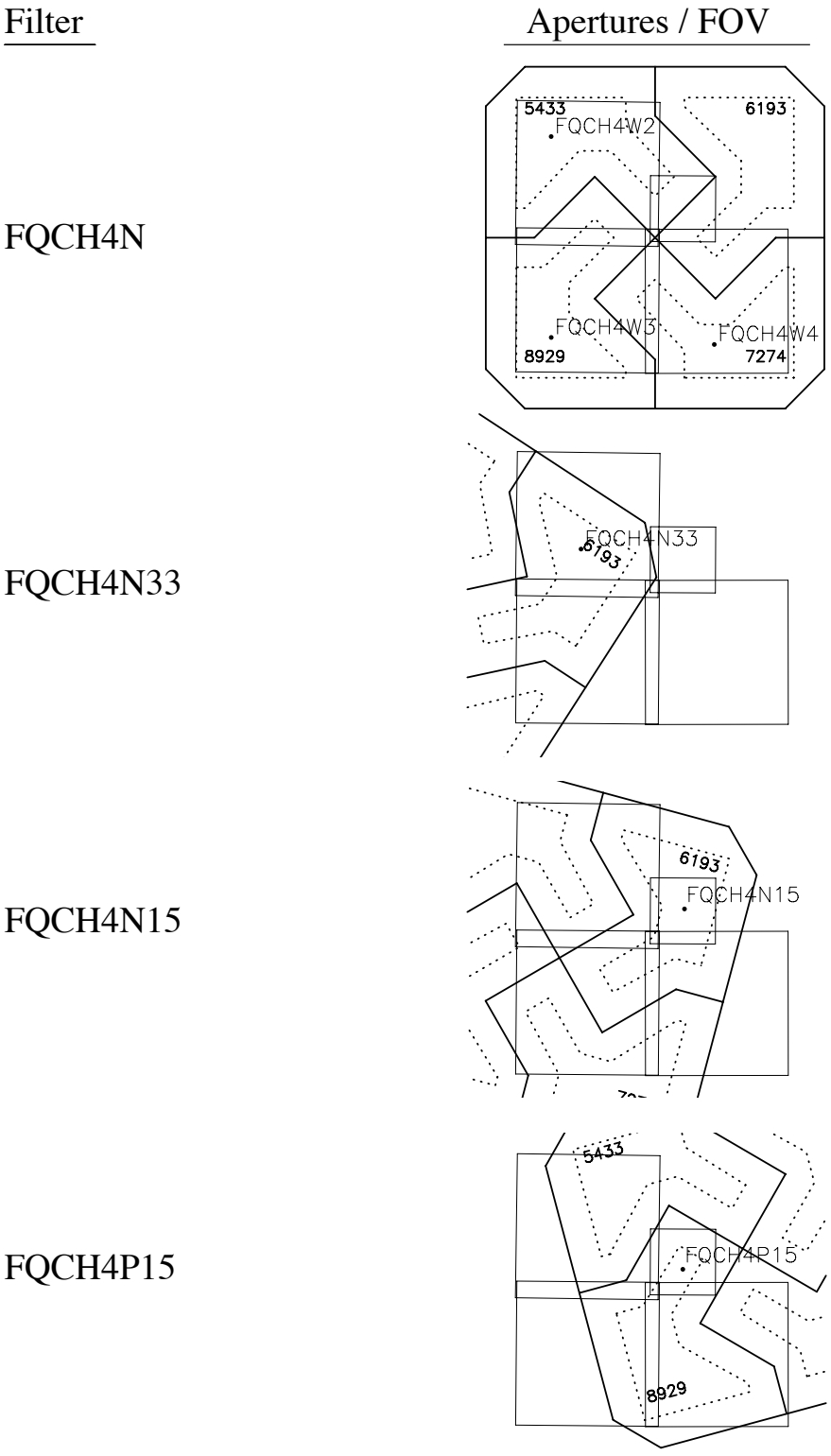

3.7 Wood's Filters

WFPC2 features two solar-blind Wood's filters, for FUV (<2000Å) imaging. It was shown by Wood in the 1930s (Physical Optics, 1934, R. W. Wood) that thin layers of alkali metals transmit FUV wavelengths while providing very efficient long wavelength blocking due to the plasma frequency of the free electrons. Wood's filters have been built for WFPC2 at JPL using thin (5000Å) layers of sodium sandwiched between two MgF_2 substrates. These Wood's filters have a broad bandpass from 1200Å to 2100Å with visible-light transmission lower than 10^{-8}. The best conventional UV filters exhibit visible-light transmission of 10^{-3} to 10^{-4}. Many astronomical objects emit 10^4 to 10^7 visible photons for every FUV photon. In such cases, a Wood's filter (or "solar blind" detector as on STIS) is essential for FUV imaging so that the visible light leak does not dominate the observation. The main problem experienced with Wood's filters is long term instability. Sodium is a very reactive metal, and attempts to passivate the sodium layer have met with limited success. It is possible that, as the Wood's filters age, pinholes will form which transmit visible light. This transmitted light will appear as an increase in the background level at the focal plane. So far no indications of any degradation on-orbit have been observed.

Figure 3.10: Wood's Filters. Greyscale flat field images show the field-of-view available with the two Wood's filter options F160BW and F160BN15.

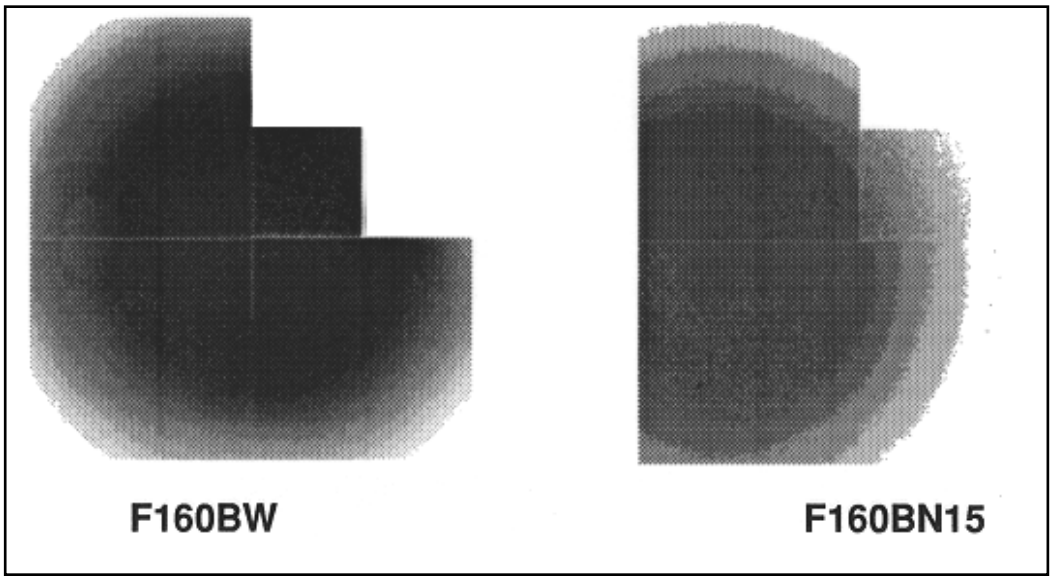

The Wood's filters can be used as a broadband filter, or in combination with the CaF_2 long-pass filter to suppress geocoronal emission, or, crossed with one of the other UV filters, such as the suprasil blocker F165LP, to

define a solar-blind UV photometric system. As discussed at the beginning of this chapter, the image will be out of focus in the last case. WFPC2's Wood's filters are circular with a clear aperture of 41 mm. Two similar Wood's filters (F160AW and F160BW) were mounted in SOFA wheel 1 to provide some redundancy. In Thermal Vacuum testing F160AW showed evidence for pinholes, which cause excessive red leak in some parts of its field. Therefore the preferred filter for far UV imaging with minimal red leak in WFPC2 is F160BW.

In the nominal filter wheel position PC1 has a clear field-of-view, but there is significant vignetting in all three WFCs. A partial filter wheel rotation of -15˚ produces a larger field-of-view in WF3, although some vignetting remains. The options are illustrated in Figure 3.10. The imaging performance of the Wood's filters is continually monitored for signs of aging such as visible light leaks. Additional partial rotations could be implemented in the future, to position an unaffected region of the filter into a WF or PC1, if necessary. The unvignetted filter projections associated with the two planned filter positions are shown schematically in Figure 3.10. Each filter position is associated with a unique name as summarized in Table 3.12.

The filter name must be selected on the basis of whether a PC or WF3 observation is required.

Table 3.12: Wood's Filters. The filter and aperture names should be specified on the Phase II proposal as shown below.

Filter Name	Aperture Name	FOV Location	Mean Wavelength (Å)	Effective Width (Å)	Comments
F160BW	PC1	PC1	1446	457	Nominal filter position
F160BN15	F160BN15	WF3	1446	457	Filter rotated -15˚

3.8 Red Leaks in UV Filters

The "red leaks" in the UV filters are shown in Figure 3.11 for F122M, F160BW (the new Wood's filter), F170W, F185W, F218W F255W, F300W, and F336W. The presence of significant red leaks in the UV filters, together with the much greater sensitivity and wavelength coverage in the red part of the spectrum, makes calibration of UV observations difficult. Table 3.13 shows red leak estimates as a percentage of the total detected flux from de-reddened stellar sources, ordered by spectral type. In each column, the red leak is defined as the percentage of the detected flux longward of the cutoff wavelength in the third row. In the presence of interstellar reddening, the red leaks will be larger.

Figure 3.11: UV Filter Red Leaks. Includes the on-orbit measurements of system response.

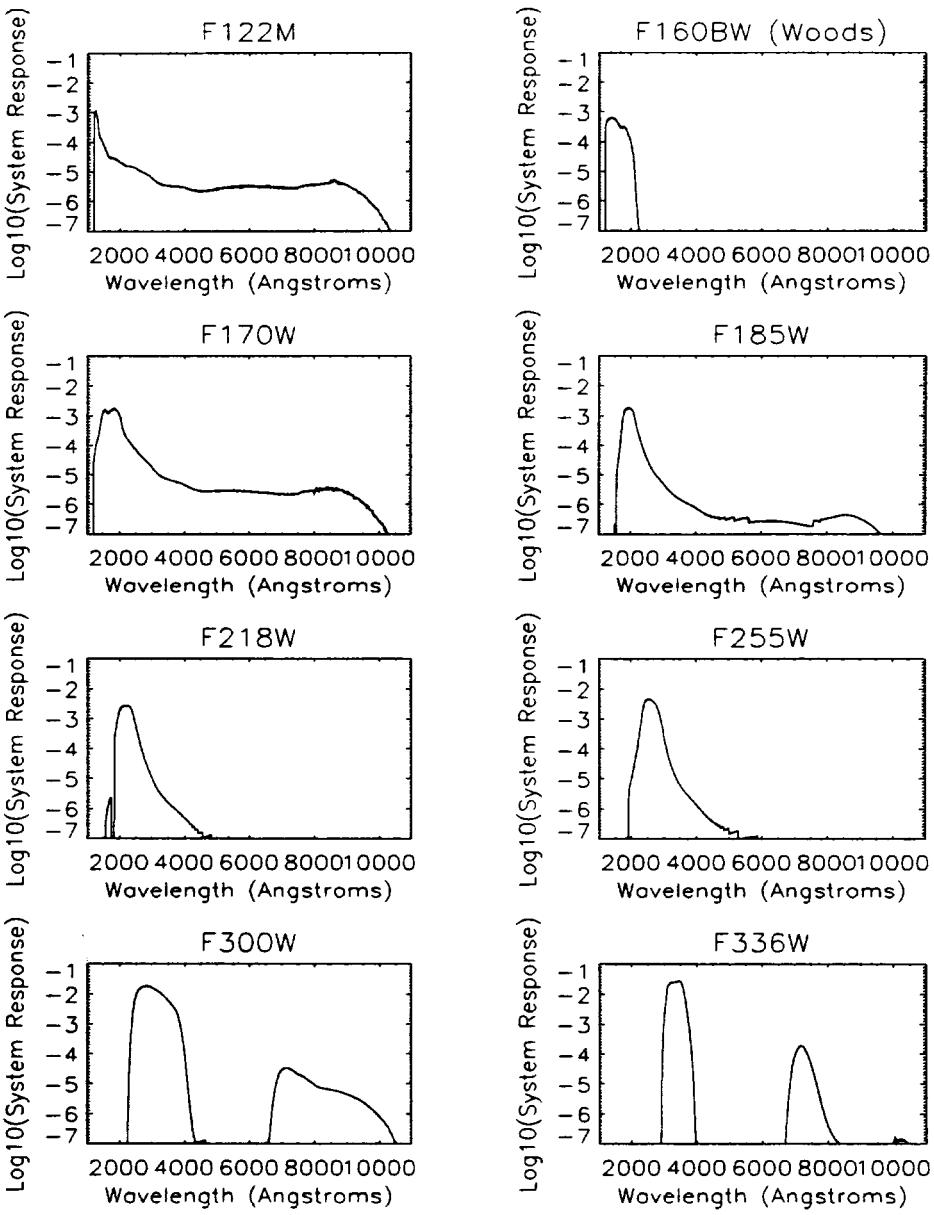

Table 3.13: Red Leak in UV Filters. A synthetic photometry calculation with de-reddened BPGS stellar spectra and system response from on-orbit data.

Filter		F122M	F160BW	F170W	F185W	F218W	F255W	F300W	F336W	F122M	F160BW	F170W	F185W	F218W	F255WI	F300W	F336W
Central λ (nm)		122	160	170	185	218	255	300	336	122	160	170	185	218	255	300	336
Cutoff λ (nm)		140	240	260	260	280	310	400	400	380	380	380	380	380	380	380	380
9 SGR	O5	16.9		0.7	0.4	0.2	0.3		0.1	0.3		0.1				0.5	0.1
9 SGE	O8F	16.9		0.7	0.4	0.2	0.3		0.1	0.3		0.1				0.5	0.1
HR 8D23	O6	21.8		1.0	0.5	0.3	0.4		0.1	0.6		0.1				0.6	0.1
-1935	B1V	20.1		0.8	0.4	0.3	0.4		0.1	0.6		0.1				0.6	0.2
60 CYG	B1V	20.1		0.8	0.4	0.3	0.4		0.1	0.6		0.1				0.6	0.2
102 HER	B2V	22.5		1.2	0.6	0.4	0.4	0.1	0.1	1.1		0.2	0.1			0.8	0.2
ETA HYA	B3V	22.7		1.2	0.6	0.4	0.5	0.1	0.1	1.3		0.3	0.1			0.9	0.2
IOTA HER	B3V	22.7		1.2	0.6	0.4	0.5	0.1	0.2	1.3		0.3	0.1			0.9	0.2
HR 7899	B4V	22.7		1.2	0.6	0.4	0.5	0.1	0.2	1.4		0.3	0.1			0.9	0.2
38 OPH	A1V	30.0		1.6	0.7	0.5	0.5	0.1	0.2	2.9		0.5	0.1			1.1	0.3
HR 7174	B6V	30.7		1.8	0.8	0.5	0.5	0.1	0.3	3.8		0.7	0.2		0.1	1.3	0.4
9 VUL	B7V	30.8		1.8	0.8	0.5	0.5	0.1	0.3	3.9		0.7	0.2		0.1	1.4	0.4
HD 189689	B9V	41.1		2.4	0.9	0.5	0.6	0.2	0.3	7.4		1.0	0.2		0.1	1.6	0.4
THETA VIR	A0V	59.6		4.0	1.2	0.6	0.8	0.3	0.6	20.3		2.2	0.4	0.1	0.1	2.5	0.7
NU CAP	B9V	58.6		3.7	1.2	0.6	0.8	0.3	0.5	18.3		2.0	0.4	0.1	0.1	2.2	0.6
HR 6169	A2V	59.5		4.0	1.2	0.6	0.8	0.3	0.6	20.1		2.2	0.4	0.1	0.1	2.3	0.7
HD 140849A	A1V	73.7		3.8	1.1	0.6	0.7	0.3	0.5	23.7		2.0	0.4	0.1	0.1	2.0	0.6
69 HER	A2V	59.5		3.9	1.2	0.6	0.8	0.3	0.6	20.0		2.2	0.4	0.1	0.1	2.2	0.7
HD 140849B	A3V	89.0		6.5	1.5	0.8	1.0	0.4	0.6	44.0		3.9	0.6	0.1	0.2	2.4	0.7
58 AQL	A0V	75.5		4.3	1.3	0.6	0.8	0.3	0.7	28.6		2.5	0.5	0.1	0.1	2.7	0.8
78 HER	B9V	75.0		4.2	1.2	0.6	0.7	0.3	0.7	27.5		2.4	0.5	0.1	0.1	2.4	0.8
HR 6570	A7V	89.7		7.0	1.6	0.8	1.0	0.4	0.7	47.6		4.4	0.7	0.1	0.2	2.6	0.9
HD 187754	A2V	97.9		11.0	2.1	0.9	1.2	0.5	0.9	64.4		7.4	1.0	0.2	0.2	3.2	1.1
THETA 1 SER	A5V	97.7		9.8	1.9	0.9	1.1	0.4	0.8	60.3		6.2	0.8	0.1	0.2	2.6	0.9
PRAESEPE 276		99.7		12.1	2.2	1.0	1.2	0.5	0.9	67.5		8.1	1.1	0.2	0.2	2.9	1.0
PRAESEPE 114		99.7		11.6	2.2	1.0	1.2	0.5	0.9	66.0		7.6	1.0	0.2	0.2	2.7	1.0

Table 3.13: Red Leak in UV Filters. A synthetic photometry calculation with de-reddened BPGS stellar spectra and system response from on-orbit data.

Filter		F122M	F160BW	F170W	F185W	F218W	F255W	F300W	F336W	F122M	F160BW	F170W	F185W	F218W	F255WI	F300W	F336W
Central λ (nm)		122	160	170	185	218	255	300	336	122	160	170	185	218	255	300	336
Cutoff λ (nm)		140	240	260	260	280	310	400	400	380	380	380	380	380	380	380	380
PRAESEPE 154		100.0		17.0	3.0	1.1	1.3	0.5	0.9	71.9		11.4	1.4	0.2	0.2	2.8	1.0
HD 140192	A5V	100.0		17.4	3.0	1.1	1.3	0.6	0.9	72.7		11.7	1.5	0.2	0.2	2.9	1.1
PRAESEPE 226		100.0		17.2	3.0	1.1	1.3	0.6	1.0	72.7		11.6	1.4	0.2	0.2	2.7	1.1
PRAESEPE 37		100.0		38.8	7.7	2.0	1.7	0.6	1.0	80.8		27.0	3.9	0.3	0.3	2.8	1.1
HD 191177	F4V	100.0		64.9	17.6	3.0	2.3	0.8	1.1	86.1		48.4	10.1	0.6	0.5	3.6	1.3
PRAESEPE 332		100.0		62.4	16.3	2.9	2.2	0.7	1.0	84.6		44.9	8.8	0.5	0.4	2.9	1.1
BD+293891	F6V	100.0		67.4	19.4	3.7	2.5	0.8	1.1	86.4		49.8	11.0	0.7	0.4	3.1	1.2
PRAESEPE 222		100.0		50.7	11.4	2.8	2.2	0.8	1.1	84.7		36.8	6.2	0.5	0.4	2.8	1.2
HD 35246	F8V	100.0		52.1	11.8	2.9	2.2	0.8	1.3	85.8		38.6	6.6	0.5	0.4	2.8	1.4
BD+263780	G0V	100.0		52.4	11.9	2.9	2.2	0.9	1.3	86.0		38.9	6.7	0.5	0.4	2.8	1.4
HD 148816	F9V	100.0		51.1	11.5	2.8	2.2	0.8	1.2	85.0		37.2	6.3	0.5	0.3	2.8	1.3
HD 155675	F8V	100.0		69.0	20.5	4.7	3.4	1.0	1.3	88.7		53.3	12.4	0.9	0.6	3.3	1.4
PRAESEPE 418		100.0		70.2	21.1	4.8	3.5	1.0	1.4	89.4		55.0	13.2	1.0	0.6	3.2	1.5
HYAD 1		100.0		71.4	21.9	4.8	3.5	1.1	1.5	90.0		56.8	14.1	1.0	0.6	3.4	1.6
HD 122693	F8V	100.0		71.6	22.1	4.9	3.5	1.1	1.6	90.1		57.1	14.2	1.1	0.6	3.5	1.7
HD 154417	F8V	100.0		70.6	21.4	4.8	3.5	1.1	1.4	89.5		55.5	13.4	1.0	0.6	3.2	1.5
HYAD 2		100.0		89.2	46.7	7.9	3.4	1.2	1.6	91.2		71.6	30.3	1.7	0.6	3.3	1.7
HD 227547	G5V	100.0		89.5	47.2	8.0	3.4	1.2	1.7	91.4		72.0	30.7	1.7	0.6	3.3	1.8
HD 154760	G2V	100.0		89.3	46.8	7.9	3.4	1.2	1.6	91.3		71.6	30.3	1.7	0.6	3.3	1.7
HD 140605	G2V	100.0		89.9	48.2	8.1	3.5	1.3	1.8	91.8		73.2	32.0	1.8	0.7	3.4	1.9
HYAD 15		100.0		90.1	48.5	8.0	3.5	1.3	1.8	92.1		73.7	32.5	1.8	0.7	3.4	1.9
HD 139777A	K0V	100.0		89.8	47.7	8.0	3.4	1.3	1.8	91.7		72.8	31.5	1.7	0.6	3.5	1.9
HD 136274	G8V	100.0		91.4	51.6	8.3	3.5	1.7	2.3	93.4		77.1	36.6	2.0	0.7	3.6	2.4
HYAD 26		100.0		91.6	52.3	8.3	3.6	1.7	2.3	93.5		77.6	37.3	2.1	0.7	3.6	2.4
HD 150205	G5V	100.0		91.7	52.3	8.4	3.6	1.7	2.4	93.5		77.6	37.4	2.1	0.8	3.8	2.4
HYAD 21		100.0		92.8	55.7	8.6	3.7	2.1	2.8	94.6		80.7	41.8	2.4	0.8	3.9	2.9

Table 3.13: Red Leak in UV Filters. A synthetic photometry calculation with de-reddened BPGS stellar spectra and system response from on-orbit data.

Filter		**F122M**	**F160BW**	**F170W**	**F185W**	**F218W**	**F255W**	**F300W**	**F336W**	**F122M**	**F160BW**	**F170W**	**F185W**	**F218W**	**F255Wl**	**F300W**	**F336W**
Central λ (nm)		**122**	**160**	**170**	**185**	**218**	**255**	**300**	**336**	**122**	**160**	**170**	**185**	**218**	**255**	**300**	**336**
Cutoff λ (nm)		**140**	**240**	**260**	**260**	**280**	**310**	**400**	**400**	**380**	**380**	**380**	**380**	**380**	**380**	**380**	**380**
+02 3001	G8V	100.0		93.0	56.1	8.6	3.6	2.2	3.1	94.8		81.1	42.3	2.4	0.8	4.3	3.2
HD 190571	G8V	100.0	0.3	99.5	95.2	40.0	11.3	3.4	3.6	96.7	0.1	91.4	80.4	16.0	3.0	6.1	3.7
HYAD 183		100.0	0.3	99.6	96.0	41.6	11.7	4.3	4.6	97.5	0.1	93.1	83.8	18.3	3.4	6.7	4.7
HD 140470	K3V	100.0	0.3	99.6	96.2	42.2	11.9	4.5	4.8	97.5	0.1	93.3	84.4	19.0	3.5	7.0	4.9
HD 154712	K4V	100.0	0.2	99.7	95.7	45.7	15.8	6.6	6.7	98.3	0.1	95.3	87.4	24.6	5.4	9.4	6.8
HYAD 185		100.0	0.2	99.7	96.7	50.0	15.7	8.0	7.9	98.6	0.1	96.0	89.5	28.6	5.5	10.6	8.0
+382457	K8V	100.0	0.2	99.7	96.6	48.6	16.5	8.8	9.1	98.7	0.1	96.4	90.1	28.7	6.3	11.5	9.1
HYAD 173		100.0	0.1	99.5	93.8	32.0	8.5	11.8	12.8	99.0		96.9	88.7	19.8	3.8	14.3	12.9
GL 40	M0V	100.0	0.1	99.6	94.9	34.5	8.8	14.5	15.4	99.2		97.5	90.7	22.8	4.2	17.4	15.5
HYAD 189		100.0	0.1	99.6	95.3	35.8	9.1	15.7	16.8	99.3		97.7	91.5	24.3	4.4	18.4	16.9
HD 151288	K7V	100.0	0.1	99.7	95.6	37.0	9.4	16.5	17.4	99.3		97.8	91.9	25.5	4.7	19.3	17.4
HD 157881	K7V	100.0	0.1	99.7	95.6	36.6	9.2	16.7	17.6	99.3		97.8	91.9	25.2	4.5	19.4	17.7
HD 1326d3	M0V	100.0	0.1	99.7	95.8	37.5	9.4	17.7	18.9	99.4		97.9	92.3	26.2	4.7	20.5	18.9
GL 15A	M0V	100.0	0.1	99.8	97.7	48.6	11.5	27.3	26.7	99.6	0.1	98.8	95.6	38.8	6.7	30.4	26.8
GL 49	M2V	100.0	0.1	99.8	97.3	45.8	10.7	25.5	25.0	99.6	0.1	98.7	95.1	35.9	6.0	28.7	25.1
GL 1D9	M4V	100.0	0.1	99.9	98.2	54.5	12.5	34.1	32.2	99.7	0.1	99.1	96.7	46.1	7.9	37.2	32.3
GL 15B	M6V	100.0	0.2	99.9	99.2	69.7	17.7	51.1	46.0	99.9	0.1	99.6	98.4	64.0	13.3	53.5	46.1
GL 83.1	M8V	100.0	0.1	99.7	95.9	38.2	8.9	17.4	15.5	99.4		97.9	92.4	26.8	3.9	20.1	15.5
GL 65	M5V	100.0	0.1	99.8	97.0	43.3	9.2	22.4	17.8	99.6		98.5	94.4	33.0	4.3	25.2	17.9

Note that the SYNPHOT synthetic photometry package can be used to estimate the counts contributed by red leaks for various particular situations, and for filters other than those plotted below.

There is significant time-variation of the UV throughput due to build-up of molecular contaminants on the CCD windows, and monthly decontamination procedures used to remove this contamination are discussed in Section 6.11.

As part of the WFPC2 Calibration Closeout program performed in Cycle 16, we have made new observations to directly measure red leaks (programs CAL/WF2 11036 and 11327). We obtained images of 15 Mon, a bright (mV = 4.6) Type O star with eight UV filters (F122M, F160BW, F170W, F185W, F218W, F255W, F300W, and F336W). We used red crossing filters (F450W, F606W, and F814W) to isolate and measure the red leaks at different wavelengths for each of the UV filters. The star was imaged at five different positions on the four WFPC2 chips which will allow us to check for filter dishomogeneities. The observations were obtained between September 2007 and January 2008 and at the time of this writing (March 2008) we are in the process of reducing all of the datasets. An Instrument Science Report containing all of the results will be released later in the year. Preliminary results show that the observed redleaks do not significantly exceed the level expected from current SYNPHOT simulations.

3.9 Apertures

The WFPC2 camera configuration and filter set require a substantial number of apertures for full utilization of its capabilities. All possible aperture and filter combinations are given in Table 3.14.

Each camera has an associated 'optimum' aperture close to the geometric center of its field-of-view (FOV). These positions have been adjusted to reflect CCD performance following SMOV and to allow for pyramid vignetting. The aperture designations are WF2, WF3, WF4, and PC1 for the individual cameras and WFALL for the three-WFC combination. WFALL is located close to the pyramid apex in WF3 (see Figure 3.12). Observers are expected to place small or unresolved targets on these apertures. Note that normally all four CCDs are read out even if a specific CCD is selected with an aperture. This is discussed in Section 2.8. The positions of these apertures may be updated if bad pixels, etc., appear on the CCDs.

In cases where the observer did not want to use the 'optimum' centers, a complimentary set of apertures were implemented specifically for this purpose. These locations remain fixed and correspond roughly to the geometric center of each camera's field-of-view. They are designated WF2-FIX, WF3-FIX, WF4-FIX, PC1-FIX, and WFALL-FIX. Observers were expected to place extended targets on these apertures.

Table 3.14: Aperture Definitions. The pixel coordinate system uses pixel numbers (row, column) for the CCD in use. See Figure 3.12 or Figure 1.1 for the definition of the V2-V3 coordinate system.

Aperture Name	Filter Name	CCD	Location	CCD Pixel		Coordinates[a]	
				X	Y	V2	V3
PC1		PC	Optimum center PC	420	424.5	2.160	-30.490
WF2		WF2	Optimum center WF2	423.5	414	-51.530	-5.920
WF3		WF3	Optimum center WF3	436[b]	424.5[b]	-0.150	48.470
WF4		WF4	Optimum center WF4	423	421	54.830	-6.320
WFALL		WF3	Optimum near apex	133[c]	149[c]	2.020	7.920
PC1-FIX		PC	Fixed center PC	420	424.5	1.810	-30.900
WF2-FIX		WF2	Fixed center WF2	423.5	414	-51.530	-5.920
WF3-FIX		WF3	Fixed center WF3	416.5	424.5	1.230	47.100
WF4-FIX		WF4	Fixed center WF4	423	421	54.830	-6.320
WFALL-FIX		WF3	Fixed near apex	133[c]	149[c]	2.020	7.920
FQUVN33	FQUVN33	WF2	Optimum for FOV	292	520	-49.924	10.802
POLQN33	POLQN33	WF2	Optimum for FOV	292	520	-49.924	10.802
POLQN18	POLQN18	WF2	Optimum for FOV	380[d]	200[d]	-33.280	-17.717
POLQP15P	POLQP15	PC	Optimum for FOV	200	680	-13.057	-31.643
POLQP15W	POLQP15	WF2	Optimum for FOV	500	260	-45.892	-22.069
FQCH4NW2	FQCH4N	WF2	Optimum for FOV	602	608	-77.669	-5.102
FQCH4NW3	FQCH4N	WF3	Optimum for FOV	602	608	0.928	72.995
FQCH4NW4	FQCH4N	WF4	Optimum for FOV	640	386	67.687	11.323
FQCH4N33	FQCH4N33	WF2	Optimum for FOV	264	436	-41.997	6.950
FQCH4N15	FQCH4N15	PC	Optimum for FOV	420	424.5	2.164	-30.494
FQCH4P15	FQCH4P15	PC	Optimum for FOV	400	312	5.129	-26.221
F160BN15	F160BN15	WF3	Optimum for FOV	436	424.5	-0.153	48.470

a. V2-V3 coordinates in effect 1996 day 127 (May 6) to 1997 day 335 (December 1). CCD pixel positions unchanged.
b. CCD pixel position in effect after 1994 day 101 (April 11).
c. WFALL and WFALL-FIX “meta-chip” coordinates are (903,904).
d. CCD pixel position in effect after 1995 day 86 (March 27).

Figure 3.12: Precise CCD Alignments and Primary Aperture Locations. “FIX” apertures are in the same locations, unless otherwise indicated. Dashed lines show vignetted region along CCD boundaries. Short lines and “X”s in outer corners indicate directions of CCD bloom and OTA diffraction spikes, respectively. Origin of the (V2, V3) system is at the origin of the plot axes, with V2, V3, and U3 exactly along diagonal lines as marked. (V2,V3) system is post-1996 day 127. CCDs have pixel (1,1) located where the four CCDs overlap.

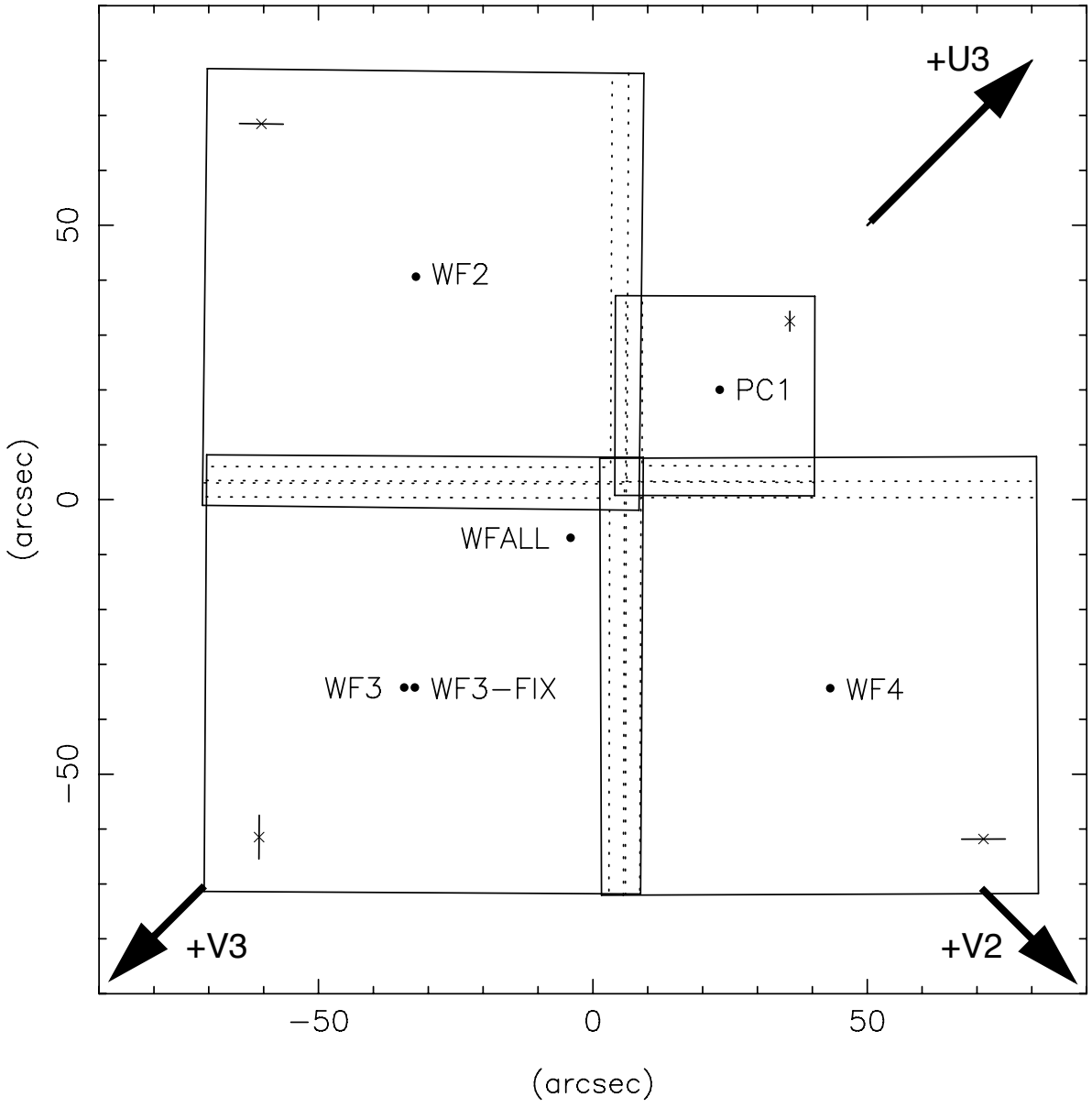

As of July 2004 the 'optimum' apertures have remained identical to their 'FIX' counterparts, with the only exception being WF3 which has moved slightly from WF3-FIX.

An additional set of aperture names have been defined for use with the WFPC2 filters which require partial rotations. The characteristics and uses

of these filters are discussed earlier in this chapter. In the nominal filter position, the three WFC segments of the [OII], Methane and Polarizer quad filters can be selected with an aperture for each camera corresponding to the optimum or geometric camera centers. The partially rotated quad filters, which generally fall into more than one camera, have been assigned apertures in the camera which provides the largest clear aperture. The pixel coordinates of these apertures will be reviewed on a regular basis to reflect changes in CCD and filter cosmetics. There are no analogous fixed apertures for the partially rotated filter configurations. The aperture name is generally the same as the (rotated) filter name. For the Wood's filters, the nominal filter position is used for the PC1 FOV only, while the rotated filter position is used for WFC observations. The linear ramp filters are unique because the ultimate location of the target will be determined from the central wavelength specified, and therefore only the generic aperture name LRF is required.

Occasionally the V2-V3 coordinates of the WFPC2 apertures are updated to correct slow drifts of the HST focal plane relative to the spacecraft (V1, V2, V3) system. Table 3.15 shows this history. The V2-V3 coordinates prior to 1996 day 127 for any aperture can be derived by setting ($V2_2$,$V3_2$) to the values in Table 3.14, and then computing the earlier coordinates. The V2-V3 coordinates after 1997 day 335 can also be computed in a similar maneuver.

Table 3.15: Updates to (V2,V3) Positions of WFPC2 Apertures.

Date in Effect	V2	V3	Rotation
1994 day 101 - 1996 day 105	$V2_0$	$V3_0$	PA_0
1996 day 105 - 1996 day 127	$V2_1 = V2_0 - 0.12''$	$V3_1 = V3_0 + 0.11''$	$PA_1 = PA_0 + 0.14°$
1996 day 127 - 1997 day 335	$V2_2 = V2_0 + 0.46''$	$V3_2 = V3_0 + 0.39''$	$PA_2 = PA_0 + 0.14°$
> 1997 day 335	$V2_3 = V2_0 + 0.67''$	$V3_3 = V3_0 + 0.61''$	$PA_3 = PA_0 + 0.14°$

CHAPTER 4:

CCD Performance

In this chapter . . .

4.1 Introduction

The CCD sensors for all four cameras of WFPC2 are the same type and were constructed by Loral in 1991; they were packaged for flight at JPL. The CCDs are thick, front-side illuminated devices with a format of 800x800 pixels and a pixel size of 15x15μm. They are operated in multi-pinned phase (MPP), which allows CCD exposures with the total inversion of all phases. The Si-SiO_2 interface, at the surface of the CCD, is pinned at the substrate potential, directing signal charge away from the Si-SiO_2 interface states towards the buried n-channel. Figure 4.1 shows a schematic which illustrates the principle of MPP (modified from Janesick, et al. 1989). The front-side Si-SiO_2 interface significantly affects the performance of CCDs, so MPP operation yields many practical benefits including reduced dark noise, better charge transfer efficiency (CTE), rapid

removal of residual images, excellent pixel-to-pixel uniformity, and improved radiation hardness. MPP technology has been demonstrated and characterized in both Loral (Janesick, et al., 1989) and Tektronix devices (Woodgate, et al., 1989).

Figure 4.1: MPP Operating Principle. A schematic showing the ideal potential profile through a frontside illuminated CCD whose front surface is inverted with multi-pinned phase (MPP); the profile is the same for a backside illuminated CCD. The CCD consists of a polysilicon gate, which forms part of the electrode structure, a surface layer of oxidized silicon (SiO_2) and the epitaxial layer which comprises p-doped silicon with an n-doped buried channel for charge transfer. MPP pins the surface potential by populating the Si-SiO_2 interface with holes. The holes passivate the Si-SiO_2 interface states and create an electric field which directs signal charge away from the interface towards the buried n-channel.

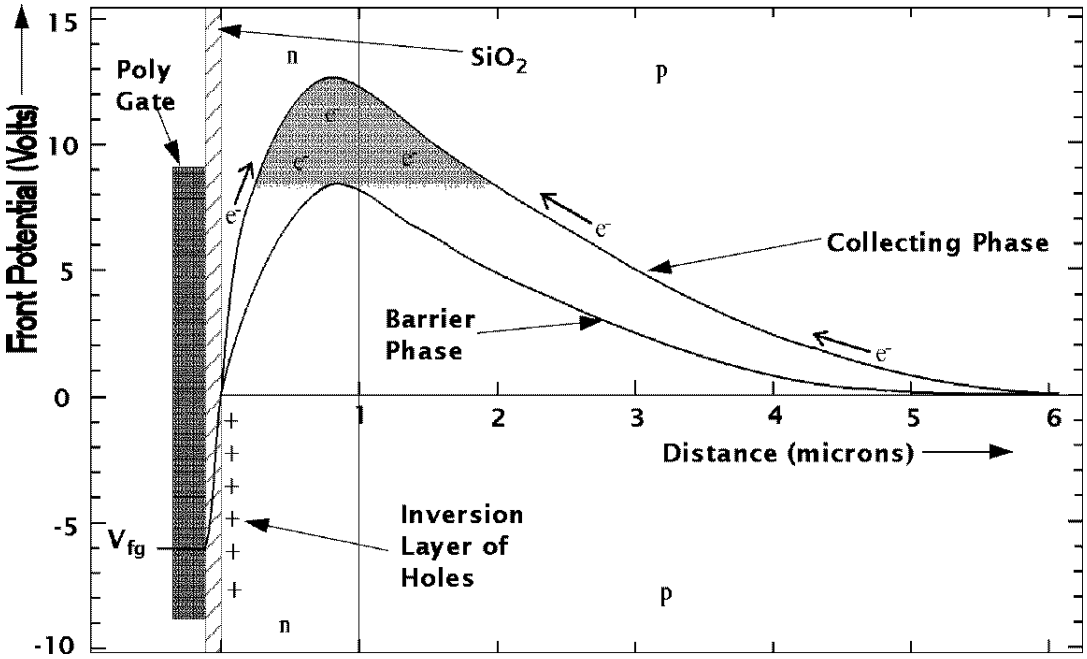

The Loral CCDs are illuminated from the 'front' surface, i.e., the light passes through the polysilicon gate structure overlying the 10μm thick active silicon layer. Because the WFPC2 devices are front-side illuminated and supported by a bulk silicon substrate, the CCD surface is flat, which has reduced the uncertainties in the astrometric calibration to about the 1/10 pixel level.

In this section, the performance of the WFPC2 CCDs is reviewed and compared to the earlier WF/PC-1 devices. A summary of device characteristics is given in Table 4.1.

Table 4.1: Comparison of WFPC2 and WF/PC-1 CCDs.

Parameter	WFPC2	WF/PC-1[a]
Manufacturer	Loral	TI
Architecture	Thick	Thinned
Illumination	front-side	back-side
Format	800×800	800×800
Pixel size	15^2 μm	15^2 μm
UV Phosphor	Lumogen	Coronene
Dark rate (e^- pixel^{-1} s^{-1})	~0.0045 (-88°C)	0.03 (-87°C)
Read noise	5e^- RMS	13e^- RMS
Full well depth	~90,000 e^-	40,000 e^-
Gain (e^- DN^{-1})	7 or 14	8
ADC range	12 bits (4096 DN)	12 bits (4096 DN)
Digital Saturation	~27,000e^- (Gain=7) ~53,000e^- (Gain=14)	~30,000e^-
QE 6000Å	35%	50%
QE 2500Å	15%	12%
WFC resolution	0.0996″ pixel^{-1}	0.10″ pixel^{-1}
PC resolution	0.0455″ pixel^{-1}	0.043″ pixel^{-1}

a. WF/PC-1 data are available through the STScI data archive.

4.2 Quantum Efficiency

The Loral CCDs are thick, front-side illuminated devices. This lowers their intrinsic QE, due to the absorption of incident light by the polysilicon electrode structure on the front-side surface of the CCD.

The front surfaces of the CCDs are overcoated with a Lumogen phosphor, which serves as the primary detection medium for photons shortward of about 4800Å, down-converting these to 5100Å - 5800Å. Its long wavelength cutoff (4800Å) is also well matched to a CCD's intrinsic sensitivity. The QE of the four flight WFPC2 CCDs is shown in Figure 4.2, which demonstrates the uniform UV response of 10-15% and a peak optical QE of 40%.

This phosphor coating also produces an enhancement of DQE at visual wavelengths, since it acts as an anti-reflection coating.

Figure 4.2: Pre-flight DQE Measurements on WFPC2 CCDs.

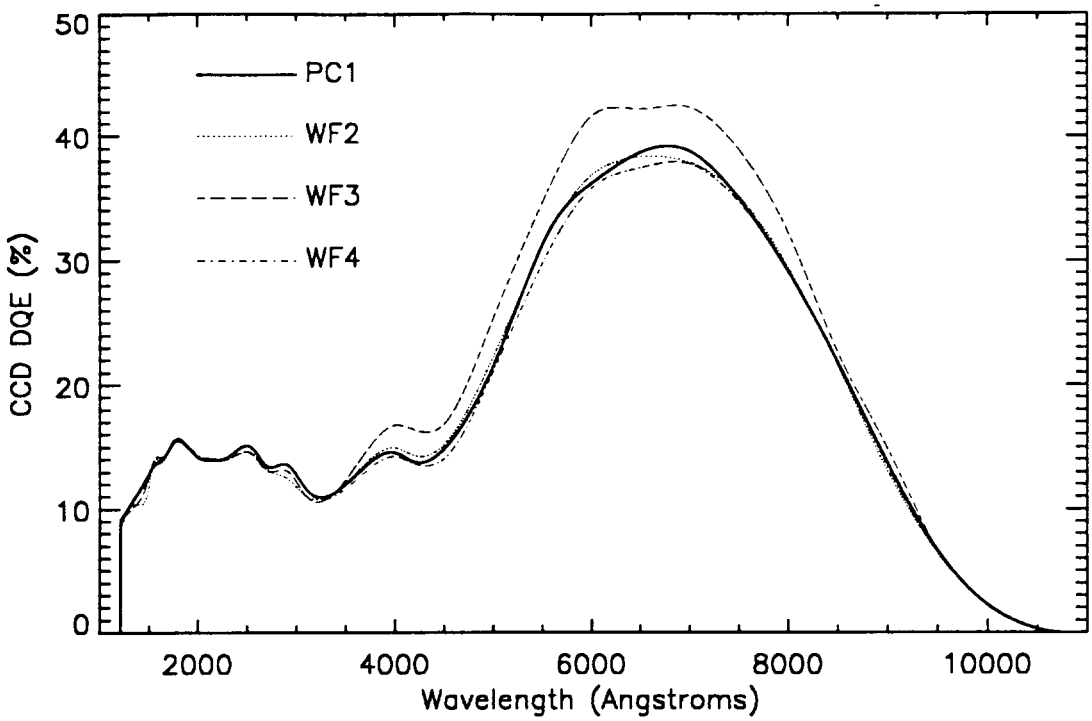

The previous camera, WF/PC-1, suffered a problem known as quantum efficiency hysteresis (QEH). This was due to back-side charge accumulation (see Griffiths, et al. 1989 and Janesick and Elliot 1991), and led to a need for UV-flooding of the CCDs. QEH is not present in the WFPC2 Loral CCDs, because they are front-side illuminated and incorporate MPP operation. This was verified in component tests at JPL.

4.3 Dynamic Range

Linear full well capacity for these devices, clocked appropriately for the MPP mode, is approximately 90,000e^- $pixel^{-1}$. Flight qualified ADCs with higher dynamic range (>12 bits) were not available, so WFPC2 operates the two available ADCs at different gain factors, to take partial advantage of both the low read noise and large available full well depth.

One channel has a gain of 14e^- DN^{-1}, which significantly undersamples the CCD read noise, and gives a digital saturation of about 53,000e^-. The other channel has a gain of 7e^- DN^{-1} which is comparable to the CCD read noise (5e^- $pixel^{-1}$ RMS), and saturates at about 27,000e^-. The choice of gain factor is determined by the scientific objective. The 7e^- DN^{-1} channel is best suited for faint object and UV imaging, where the lower CCD read noise will be most effective. For example, it should be used for UV

imaging of planets or narrowband imaging of high redshift galaxies. The 14 e^- DN^{-1} channel has slightly higher effective read noise due to the quantization granularity, but can be used for programs where a signal level in excess of 27,000e^- is required. Even when imaging faint sources, it may be desirable to retain the high signal-to-noise information on brighter field stars as a PSF reference.

Use of the 14 e^- DN^{-1} channel also allows reasonable recovery of counts for isolated, saturated point sources by summing over the saturated pixels (assuming that the charge bleeding does not extend to the edges of the CCD). See Gilliland (1994).

4.4 Read Noise and Gain Settings

The CCDs and their associated signal chains have readout noise levels (in the absence of signal shot noise or interference) of approximately 5e^-. The analog-to-digital converter is highly accurate, and makes virtually no contribution to the read noise, other than the normal information loss caused by digitization of the signal.

The conversion factors from detected electrons (QE x number of incident photons) to data numbers (DN) are tabulated in Table 4.2, as are read noise and linearity ("gamma" is the power law index relating detected DN to input flux). Note that all calculations of sensitivity in this manual assume gains of 7 and 14 for two gain channels, choices very close to the measured gains. The photometric calibration is based on an assumed exact gain of 14 in all CCDs. The measurements given here were derived from thermal vacuum testing. On-orbit measurements have confirmed that the gain ratios are correct to within a possible systematic error of 1%—which will feed directly into a photometric calibration error for gain 7 data, as most of the photometric calibration was done with gain 14 data. Note that the gain ratios are known much more accurately than the individual gains; they are derived from flat field ratios instead. Also, note that the Phase II proposal instructions refer to the ~14 e^- DN^{-1} setting as ATD-GAIN=15.

Table 4.2: Signal Chain Gains.

Parameter	Gain	PC1	WF2	WF3	WF4
Noise (e^-)	"7"	5.24 ± 0.30	5.51 ± 0.37	5.22 ± 0.28	5.19 ± 0.36
	"15"	7.02 ± 0.41	7.84 ± 0.46	6.99 ± 0.38	8.32 ± 0.46
Gain (e^- DN^{-1})	"7"	7.12 ± 0.41	7.12 ± 0.41	6.90 ± 0.32	7.10 ± 0.39
	"15"	13.99 ± 0.63	14.50 ± 0.77	13.95 ± 0.63	13.95 ± 0.70
Gamma	"7"	1.0015 ± 0.0006	1.0015 ± 0.0006	1.0020 ± 0.0006	1.0038 ± 0.0007
	"15"	1.0004 ± 0.0001	1.0023 ± 0.0004	1.0032 ± 0.0006	1.0018 ± 0.0012
14/7	ratio	1.987 ± 0.02	2.003 ± 0.02	2.006 ± 0.02	1.955 ± 0.02

4.5 Bright Object Artifacts

4.5.1 Blooming

Blooming up and down a CCD column occurs when more than about 90,000e^- (the full well capacity, or saturation level) are collected in any pixel. When the pixel is full, the charge will flow into the next pixels along the column, and so on. The orientation of the bloomed column(s) on the sky depends on the readout direction of the particular CCD (see Figure 1.1 or Figure 3.12) and the roll angle of the spacecraft. This effect is visible in Figure 4.3 which shows a logarithmic stretch of the image resulting from a 100s exposure on a star of V magnitude 2.6 through filter F502N in the PC.

Extreme overexposure of the Loral CCDs is not believed to cause any permanent effects, and therefore the WFPC2 did not have a bright object limit.

The WFPC2 CCDs could be operated in a non-standard mode during the integration phase of an exposure, in order to limit the blooming to only those columns containing the bright sources. This is accomplished by operating the serial transfer register clocks during the integration (using the optional parameter CLOCKS as specified in the Proposal Instructions). See section 2.6 for details.

4.5.2 Horizontal Smearing

During readout of a badly overexposed image, there is spurious charge detected by the readout electronics. The apparent brightness of the stellar halo is higher to the right of the saturated columns. This is particularly obvious at the bottom of the image in Figure 4.3 which is a region in the shadow of the pyramid edge.

The horizontal “smearing” seen in highly saturated images can be modeled as an exponential function which decays over a few rows. After about ten saturated pixels, the smearing effect itself will temporarily saturate (subsequent saturated pixels have no effect). The effect is twice as bad with gain 7 e^- DN^{-1} than with gain 14 e^- DN^{-1}. This model only works on very highly saturated stellar images.

In Figure 4.3, the image to the right side of the saturated columns is brighter than the left side; and the brightness increases as the number of saturated columns increases. This effect appears to be a signal which starts at a saturated pixel and decays over the next few rows, wrapping around as it does so. The signal is additive with each successive saturated pixel. Jumps are obvious when the number of saturated columns changes. The problem is a known characteristic of the amplifier electronics, and an effort was made to minimize it during design. The increase in signal in rows with

saturated pixels is also seen in the over-scan region (the over-scans are provided in "`.x0d`" files from the pipeline).

An approach to calibrating out the horizontal smearing is described here. An exponential function fits the effect reasonably well. An appropriate algorithm creates an array to contain the signal model. It searches through the uncalibrated image (with the over-scan region included) in the sequence in which the pixels are read out. When it encounters a saturated pixel, it adds an exponential function to the model array, beginning at that pixel. The function has the form $s(x)=Ae^{-x/h}$, where x is the offset from the saturated pixel and only positive x values are included. The half-width, h, and amplitude, A, appear to vary from frame to frame and must be determined on the image itself. As more saturated columns are encountered in a row, the signal intensity builds up in the model image. The image can then be "improved" by subtracting the model from the raw image.

The amplitude and half-width parameters can be obtained by trial and error. The typical parameters vary slightly for each chip. The amplitude per saturated pixel is typically 1.75 DN (gain 7) or 0.2 DN (gain 14). On the other hand the half-width at a gain of 14 is larger (h=1800) than at 7 (h=350). So the total integrated effect is about twice as bad at gain 7. A straightforward application of the above algorithm cleaned up most of the signal in rows which had a few saturated columns, but over-subtracted in rows with a large number. The algorithm can be modified to saturate by making the parameter A, which gives the peak contribution from a single saturated pixel, depend on the current level of the effect: $A=A_0*(1-C/C_{max})$. This implies that the correction is never larger than C_{max} no matter how many saturated pixels are encountered. C_{max} is approximately 14 DN for a gain of 7 and 10 DN for a gain of 14.

The algorithm gives improvement only on highly saturated stellar images (where the star is saturated to 3 or 4 columns at the edges of the chip). On less saturated data, it over-subtracts significantly. This indicates that the problem is nonlinear, and therefore a general algorithm applicable to all data will be difficult to develop.

4.5.3 Diffraction Effects and Ghost Images

Several other artifacts that are common in saturated stellar images are also obvious in Figure 4.3. The spider diffraction spikes caused by both the OTA spiders and internal WFPC2 spiders are at 45° to the CCD columns in all cameras.

The halo around the stellar image is well above the diffraction limit in intensity. Also there are ghost images which result from internal reflections in the filters and in the field-flatteners. These topics are discussed fully in the next Chapter.

Figure 4.3: Saturated Stellar Image Showing Horizontal Smearing.

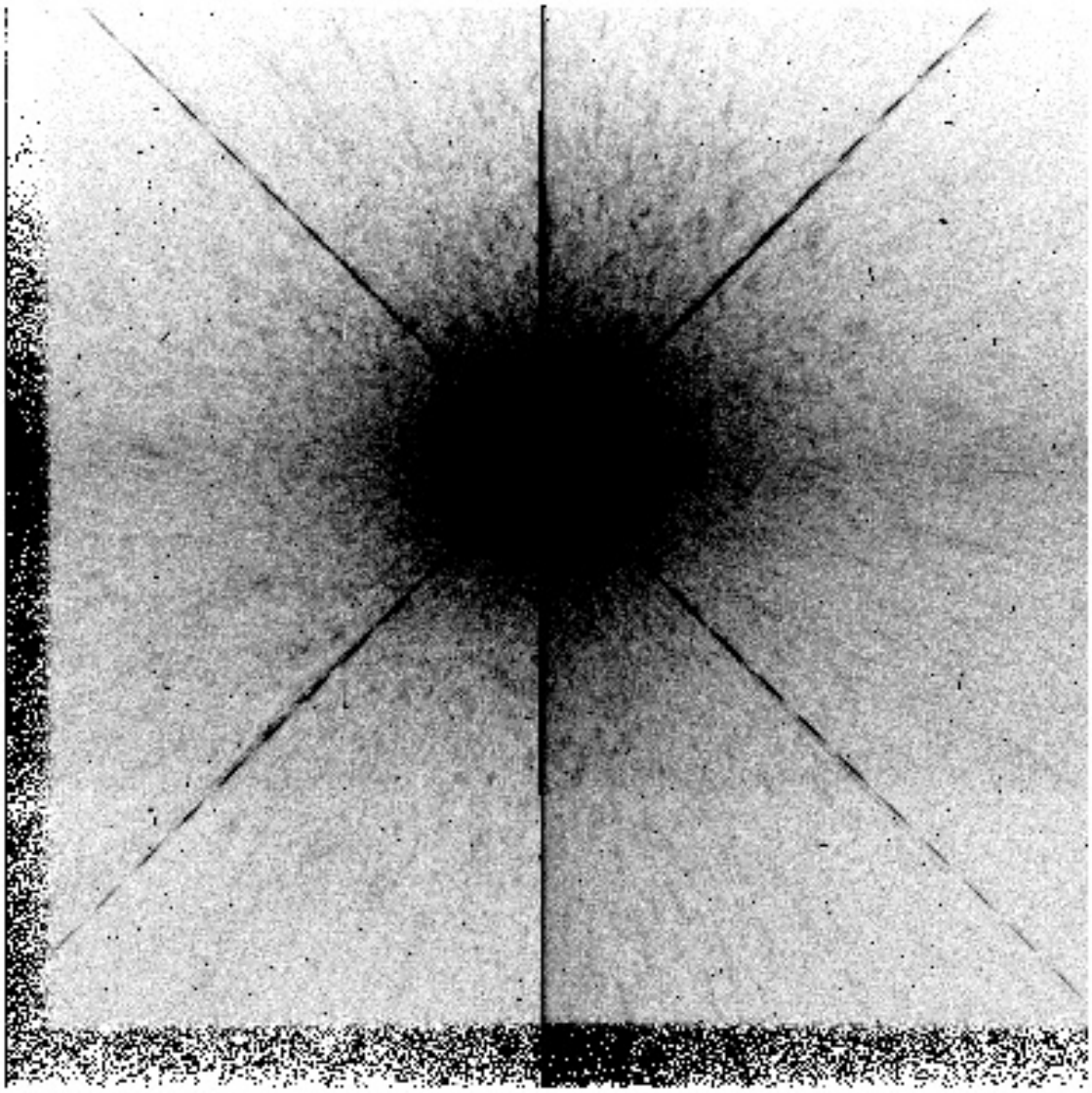

4.6 Residual Image

Residual images are seen in front-side-illuminated CCDs, and are associated with the front-side Si-SiO_2 surface interface. When the full well is exceeded, electrons can become trapped at the Si-SiO_2 interface. This trapped charge is slowly released giving rise to residual images. Inverted phase operation (MPP) allows holes to recombine with the trapped electrons at the front-side interface, and so residual images dissipate in a matter of minutes.

A second potential source of residual images, which occurs only in front-side-illuminated CCDs, is known as residual bulk image (RBI). Long

wavelength photons can penetrate deeply enough to produce charge in the substrate. Most of this charge recombines rapidly (due to short carrier lifetimes), but some may diffuse into the epitaxial layer, where it can become trapped in epitaxial interface states. Residual images can occur as this charge is slowly released during an exposure. RBI is temperature sensitive since the bulk trapping time constants decrease with increasing temperature. The WFPC2 CCDs do exhibit RBI, but at -70˚C trapped charge rapidly escapes so that residual images disappear within 1000s (currently the CCDs are operated at -88˚C). Driven by the WFPC2 electronics, the CCDs recover quickly from large over-exposures (100 times full well or more), showing no measurable residual images a half hour after the overexposure.

For images exposed below the saturation level there is a very weak residual image due to charge trapping and charge transfer efficiency (CTE) problem. Measurements on 1800s dark frames interleaved with 2800s exposures of a star field yield a residual flux of 0.3% ± 0.1% of the original star flux, for stars with fluxes from 65 to 17,000 total counts. For typical star fields observed by WFPC2, these residual images are likely to be a problem only for stars that were saturated in a previous image, or for programs where long exposures in low throughput filters are taken immediately after highly exposed images. Hence, repeated exposures at the same CCD position should not lead to any appreciable systematic offset in photometry. CTE is further discussed in Section 4.12.

4.7 Flat Field Response

The flat field response is uniform within a few percent, with the exception of a manufacturing pattern defect which generates a 3% reduction in QE once every 34 rows. This pattern defect is caused by a manufacturing error in producing the CCDs; there was a 0.5μm overlap between adjacent 1024x0.5μm raster scans during the construction of the masks used to fabricate the chips. It is identical in all CCDs. The net effect is that every 34^{th} row on the CCD is approximately 3% too narrow. Photometry of point sources imaged onto these defects will be affected, since the error conserves counts, while flat fields (which are designed to produce a uniform image from a uniformly illuminated target) will effectively multiply the counts in these rows by 1.03. In applications requiring precision photometry across a wide field, it may be useful to correct the images for this flat field effect before performing photometry. There is also an astrometric offset of approximately 3% of the pixel height (0.003″ in the WFCs) every 34 rows. Anderson and King (1999) present a nice discussion of these effects.

WFPC2 flat fields also include instrumental effects such as vignetting and shadowing by dust particles, and illumination variations related to optical geometric distortion. For further discussion see Section 5.11.

Figure 4.4: WFPC2 CCD Flat Field.

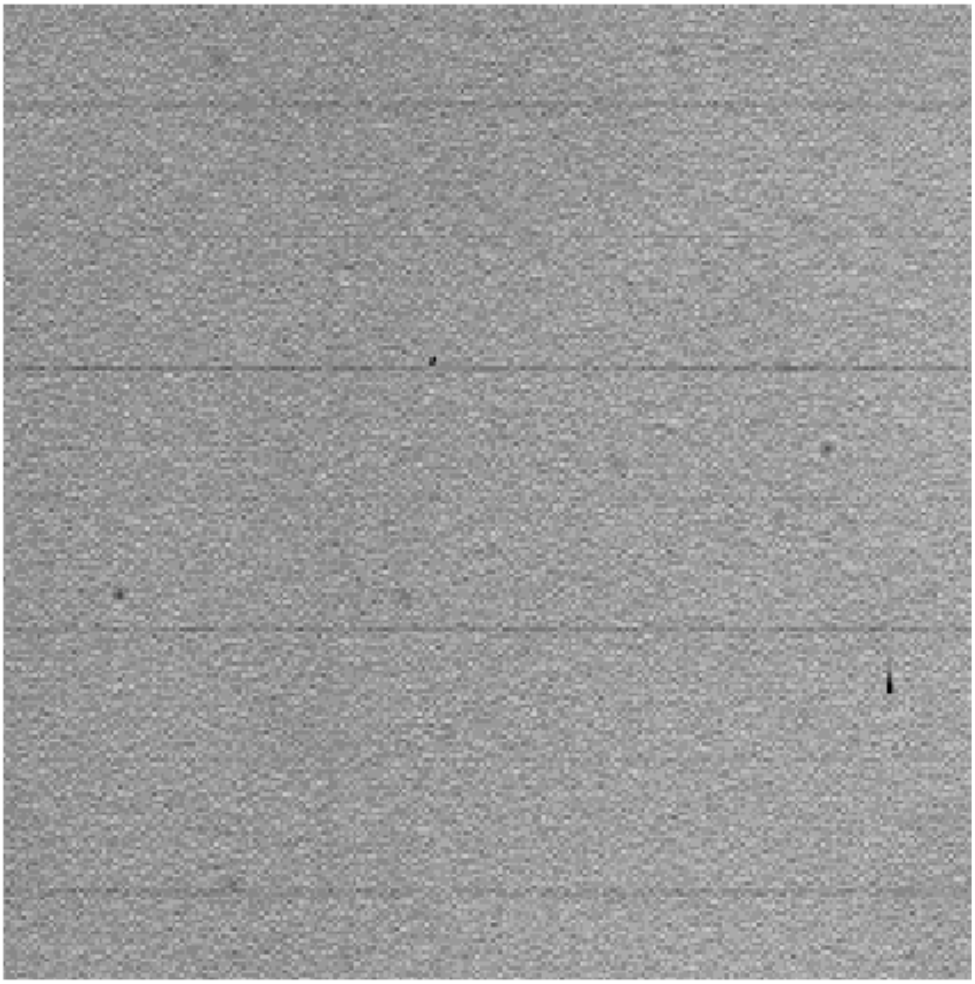

The WFPC2 CCDs have an intrinsically uniform flat field response since they are not thinned, so there are no large-scale chip non-uniformities resulting from the thinning process. MPP operation also improves pixel-to-pixel uniformity because charge transfer is driven deep into the buried n-channel, away from the influence of Si-SiO_2 interface states. The WFPC2 CCD flat fields show an overall pixel-to-pixel response having <2% non-uniformity. Figure 4.4 shows a portion of a WFPC2 CCD flat field obtained during quantum efficiency measurements at JPL. The image illustrates the excellent pixel-to-pixel uniformity of the Loral devices. The 34th row defect is clearly visible, and its amplitude of 3% serves to calibrate the gray scale.

4.8 Dark Backgrounds

Low dark noise is one of the benefits of MPP, since inverted phase operation suppresses the dominant source of CCD dark noise production (Si-SiO_2 surface states. For MPP operated CCDs, the main source of dark noise is the thermal generation of electron-hole pairs in the silicon bulk, which is determined by the quality of the silicon used in the chip fabrication and the operating temperature. After more than 14 years on orbit, the dark rate of the WFPC2 CCDs remained below 0.01 e^- $pixel^{-1}$ s^{-1} at the normal operating temperature of -88˚C.

The temperature set-points for the WFPC2 TECs are: -88, -83, -77, -70, -50, -40, -30 and -20 ˚C. The corresponding approximate median dark rates are given in Table 4.3. (For instrument health and safety reasons, GOs could not command temperature changes).

Table 4.3: Dark Count Rates (e^- s^{-1} $pixel^{-1}$)[a]

CCD Temperature (˚C)	PC1	WF2	WF3	WF4
-20	53.0	45.0	55.0	48.0
-30	14.0	9.7	11.0	11.0
-40	3.0	2.3	2.8	2.2
-50	0.86	0.68	0.80	0.65
-70	0.043	0.032	0.041	0.032
-77	0.014	0.011	0.014	0.011
-83	0.0060	0.0041	0.0051	0.0045
-88	0.0034	0.0027	0.0025	0.0028

a. Pre-flight values from Trauger et. al. 1993

4.8.1 Sources of Dark Current

The on-orbit dark current appears to have two components: one from the normal generation of spurious charge within each pixel, which is strongly dependent on the operating temperature, and a second component whose strength correlates with the cosmic ray flux. Both components are affected by the radiative environment of HST. The on-orbit performance of CCDs is degraded by radiation damage. Consequently, the dark current of all CCDs on HST has shown an increase which correlates with the amount of on-orbit damage imparted by incoming protons (see Section 4.11).

The strength of the second component drops toward the edges of each CCD, and is both chip- and time-dependent. The edge drop off can be seen

in Figure 4.5 and Figure 4.6, where the average line of each chip (after cosmic ray and hot pixel rejection) is plotted in e^- sec^{-1} as a function of the column number. The drop near the edge is consistent with a "dark glow" due to luminescence from the CCD windows, shadowed by a field stop mask just in front of the CCD.

Figure 4.5: Average Dark Rates vs. CCD Row (plot generated using darks from 1998).

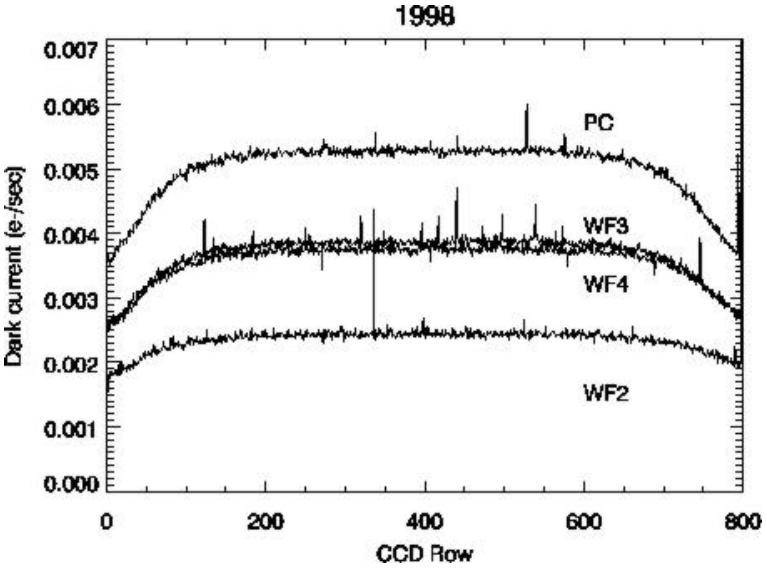

Figure 4.6: Average Dark Rates vs. CCD Row for 2007 (note differences from 1998).

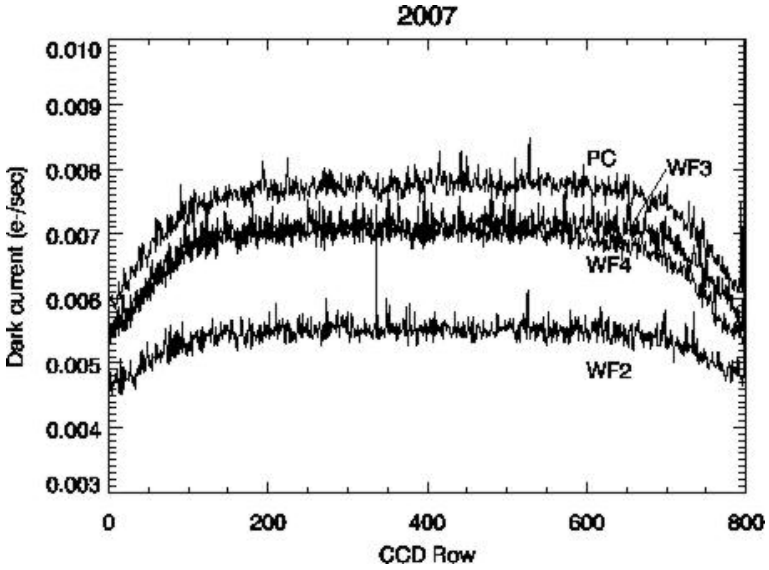

A further indication of the possible origin of this second component is the correlation between its amplitude and the cosmic ray activity in the same exposure, as shown in Figure 4.7. For example, the cosmic ray flux in

the PC varies from $7x10^5$ to $13x10^5$ DN for a 1000 second exposure, while the total dark signal in the PC varies concurrently between 0.0007 and 0.0010 DN s^{-1}. Similar, though slightly smaller effects are seen in the WFC CCDs. These clues point to cosmic-ray induced scintillation of the MgF_2 field-flattening windows as a likely source of the second dark current component. However, other explanations cannot be completely ruled out at this point.

Figure 4.7: Dark Signal vs. Cosmic Ray Flux. Slopes and intercepts ("int") are given on plots. Units are DN; 1 DN ~ 7 e^-.

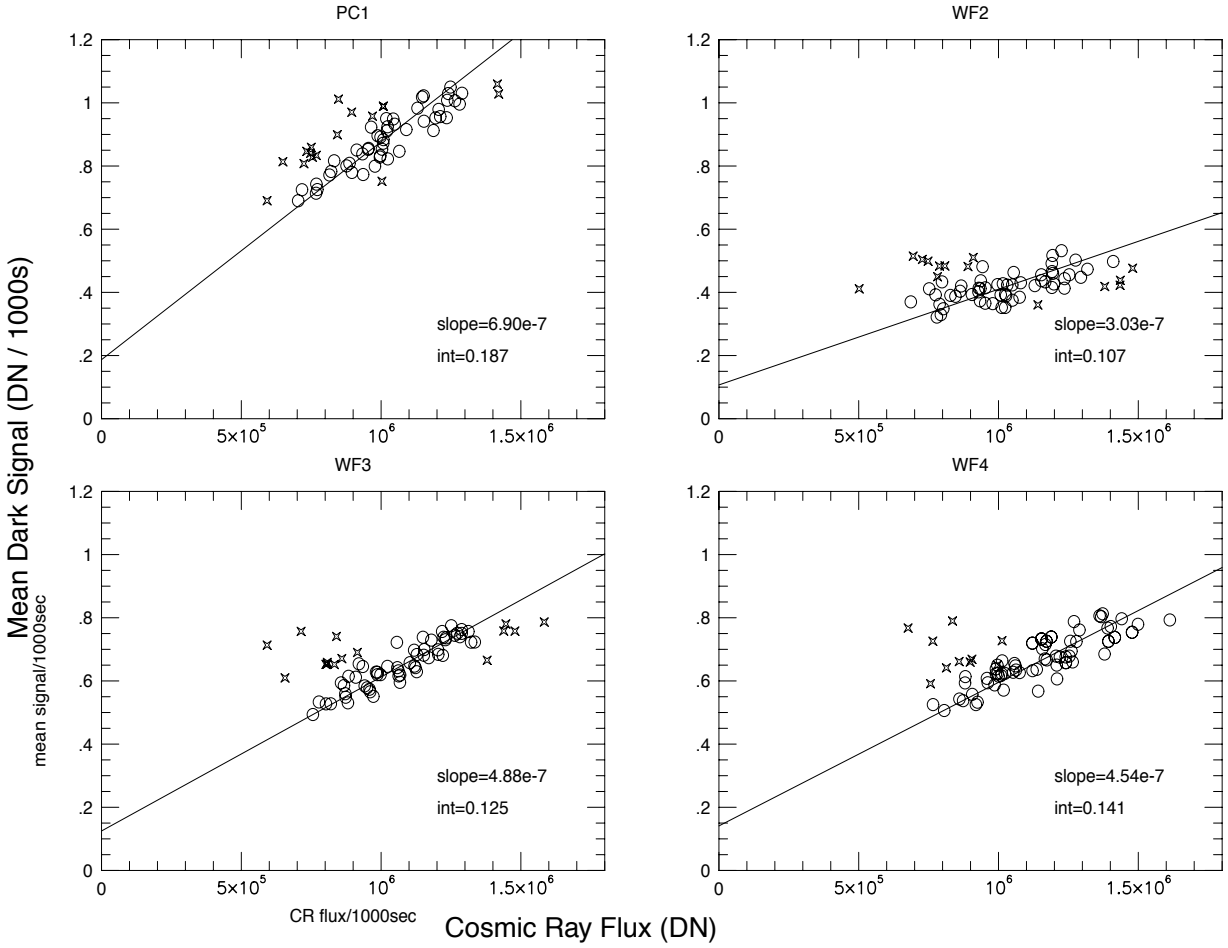

4.8.2 Dark Current Evolution

The dark current in WFPC2 has had an interesting evolution over the lifetime of the instrument. Figure 4.8 shows the median dark current for the central 400 x 400 pixels of each CCD at gain 7, each taken just after WFPC2's monthly decontamination. Each data point represents the median of five raw 1800s dark frames (after rejection of cosmic rays and bias

subtraction, normalized to units of DN/1000sec). As such, this plot reflects the uniform, low-level dark current near the center of each detector. During the first six years the dark current increased approximately linearly with time; the dark current increased by a factor of about 2 in the WFC CCDs and by a factor of ~1.3 in the PC. But after 1998 (MJD > 51200) the dark current leveled-off until mid 2003 then began to increase linearly with time again, though at a slightly lower rate.

Figure 4.8: Dark Evolution from 1994 to 2007. Note that for the WF4 panel shows a few points, around 2005, that were affected by the WF4 anomaly but were not corrected; the measurement of the dark current from those frames is therefore inaccurate.

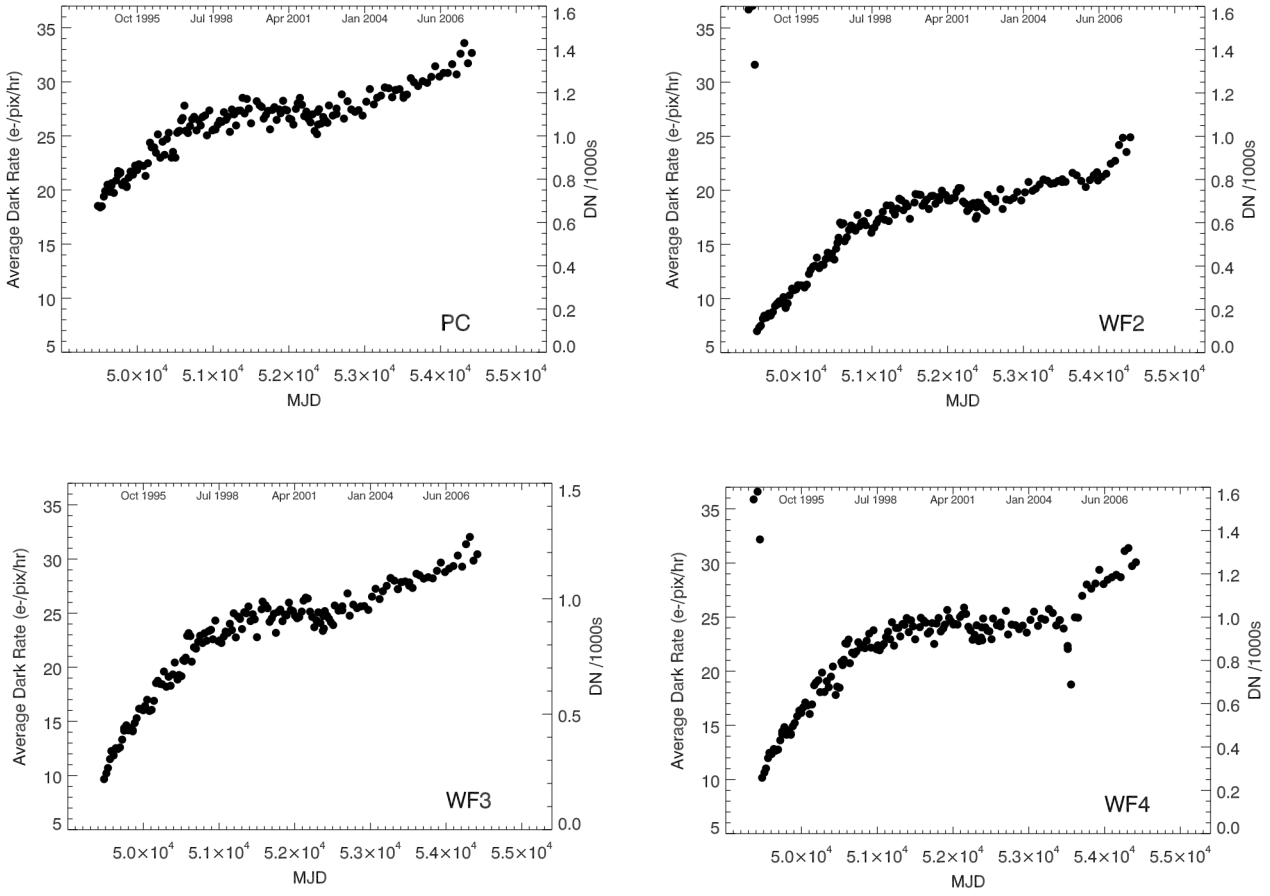

As mentioned before, there are two primary sources of dark current -- a dominant component which is strongly correlated with the cosmic ray flux in the image (probably due to scintillation in the MgF_2 CCD windows; see Figure 4.7), and a smaller thermal dark current in the CCD itself.

Note that the dark current increase prior to 1998 was smaller in the optically vignetted regions near the CCD edges. Also, the ratio between the dark current at the CCD edge and the CCD center has remained nearly constant throughout the mission (ISR WFPC2 01-05), even though the dark

current itself doubled in WF2, WF3, and WF4. Hence, it is likely that most of the long-term increase is related to the scintillation component of the dark current, which in turn is correlated with the cosmic ray flux.

Long-term changes in the cosmic ray flux are perhaps most easily attributed to the solar cycle. The Earth's geomagnetic field, the solar wind, and the solar magnetic field deflect galactic cosmic rays (GCR). During the solar maximum, the magnetic field of the sun increases and solar flares are more common, producing magnetic clouds and therefore GCR are more readily deflected than during a solar minimum. Therefore, when the sun is active, fewer galactic cosmic rays reach Earth's atmosphere. The leveling-off of the dark current ~1998 is coincident with the approaching solar maximum which has the effect of reducing the cosmic ray flux at HST's low Earth orbit. Figure 4.9 shows the correlation between the smoothed sunspot number and the trend in dark current for all four CCDs. At 2001, the dark current in each chip has been normalized to unity. The figure shows that the variation of the dark current is remarkably similar in all four chips, and that the periods of growth occur both before and after the solar maximum.

Figure 4.9: Solar Cycle and Dark Current Correlation. Solar cycle data (solid line) are the smoothed monthly sunspot data and obtained from: http://www.ngdc.noaa.gov/stp/SOLAR/ftpsunspotnumber.html#american

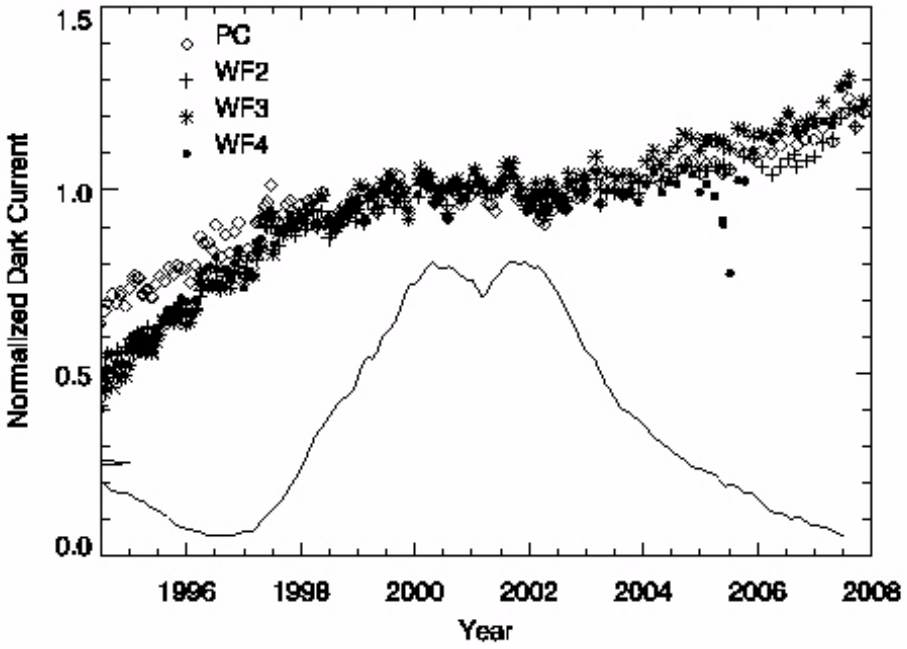

Ground based and on orbit cosmic ray detectors show that the number of GCR decreased from 1997 to 2000, remained low between 2001 and mid-2003, and then started increasing again after 2004 (e.g. http://ulysses.sr.unh.edu/NeutronMonitor/neutron_mon.html), a trend in very good agreement with the dark current of the WFPC2 CCDs. It should be noted that the number of cosmic rays detected by the WFPC2 CCDs has remained fairly constant with time (see Section 4.9). It is likely that the population of cosmic rays that ionize a CCD is different than the one responsible for the luminescence of the CCD window. It is possible that other effects might also play some role. For example, portions of the HST orbit near the South Atlantic Anomaly experience higher cosmic ray rates, and it is possible that changes in the HST scheduling system could produce long-term changes in cosmic ray flux and hence dark current. It is also conceivable that long-term changes in the instrument itself might indirectly influence the sensitivity to scintillation effects (e.g. long-term radiation damage might modify the luminescence of camera components).

The thermal dark current of the CCD may also undergo long-term change (i.e. from radiation damage, etc.), and contribute some minor variation. A small increase in the CCD cold junction temperature was seen early in the mission; however, the temperature change can account for only a very small portion of the increase in dark current.

Since the dark current is generally a minor contributor to the total noise in WFPC2 images, its long-term variation is unlikely to impact the quality of WFPC2 observations, except perhaps in special cases (faint sources observed through narrow-band or UV filters, especially in AREA mode).

We note that the variation in dark signal reported here affects all pixels, and thus is distinct from hot pixels which vary in a more cyclic fashion. The hot pixels are highly localized, and are almost certainly due to radiation-damaged sites on the CCD detectors. Their number and intensity increase continuously, but are significantly reduced during decontamination procedures where the CCDs are warmed to +22˚C to clear the CCD windows of contaminants. These “decontaminations” were conducted monthly until June 2003, after which their frequency was reduced to 49-day intervals. Apparently the decontaminations anneal defects in the CCDs which produce hot pixels (see Section 4.11).

4.8.3 Darktime

As of this writing, the “*DARKTIME*” keyword in the WFPC2 image headers does not reflect correctly the actual time during which the CCD collects dark current. Instead, *DARKTIME* is merely set equal to *EXPTIME* (the exposure time) in the data headers, and this value is used for calibration. The error is small, and usually unimportant, but could be

significant for programs aimed at measuring the absolute level of the sky background. The actual darktime in seconds is given by

$$DARKTIME = 60 \times int\left(\frac{t + 16.4}{60}\right) + 43.6 + 13.6 \times (n - 1) + 60 \times (restart) \qquad (4.1)$$

where t is the requested exposure time in seconds, and n is the number of the CCD (PC1=1, WF2=2, etc.), and *int()* indicates the next lower integer. A duration of 16.4s is required to clear the CCDs before the exposure begins, and 13.6s is needed to read each CCD after the exposure. External exposures of 180s or longer made with the serial clocks off (CLOCKS=NO; the default setting) suffer an additional 60s of darktime (*restart*=1). This delay is associated with restarting the serial clocks for readout in exposures where the spacecraft AP-17 processor provides shutter control with loss-of-lock checking. Exposures made with the serial clocks on (CLOCKS=YES) avoid this extra 60s (*restart*=0).

We note that bias frames contain approximately $43.6 + 13.6 \times (n - 1)$ seconds of dark current. No attempt is made to subtract this from the bias images when creating calibration files for use in the calibration pipeline. This effect is unimportant for most observations, but could be significant if one averaged many undithered deep exposures of the same field, or if one is interested in measuring the absolute level of the sky background. If the dark current were constant in time, this could be corrected by merely changing the value of *DARKTIME* used during calibration. However, the hotpixels vary on monthly timescales, so this simple correction is only partially successful.

The timing of dark calibration frames is slightly different from that of external science exposures. Dark calibration frames always have *restart*=0 in Equation 4.1.

The dark calibration reference file in the pipeline is revised weekly to track variations in the hot pixels. The current method of generating these files is to combine the bright hot pixels from typically five on-orbit dark frames taken over the space of about one week, with the low-level dark current from the average of 120 on-orbit dark frames spanning a much longer time period. This method gives an optimal combination of low noise and accurate tracking of hot pixels. Care is also taken that the same super-bias reference files is used for both science data and generation of the dark reference file, as this tends to reduce the noise in long exposures. (Early dark reference files used a much simpler method, and were typically combinations of about ten dark frames taken over two weeks.)

4.9 Cosmic Rays

HST is subjected to cosmic rays and protons from the Earth's radiation belts. The cosmic ray signature in the Loral CCDs is essentially the same as was seen in the WF/PC-1 devices. Electron-hole pairs generated in the thicker substrate by cosmic rays (and infrared photons) are usually removed by recombination in the low resistivity substrate material, because electrons do not diffuse efficiently up to the collecting phase.

Cosmic ray events usually deposit significant quantities of charge in more than one pixel. This is due partly to the finite thickness of the CCD detectors, and partly to the less than perfect collection efficiency of each pixel. Figure 4.10 shows a histogram of the number of affected pixels for each cosmic ray event. For the purposes of the figure, a cosmic ray is defined as having a peak pixel value more than 10 DN above the background; and an affected pixel is an attached pixel with a value more than 2 DN above the background. Cosmic ray events do have a clear lower cutoff at around 500 electrons of the total signal.

Cosmic ray events impact scientific imaging with WFPC2 differently from WF/PC-1, the previous generation camera. Firstly, the WFPC2 CCDs have an epitaxial thickness of about 10μm compared to 8μm for the thinned WF/PC-1 device, and a recombination length of 8-10μm in the substrate. These facts lead to a higher total number of electrons being deposited per event. WFPC2 CCDs also have lower read noise, and so the number of cosmic ray events apparently differs from that of the WF/PC-1 CCDs, since low amplitude events are detected. In practice, this means that the number of pixels apparently contaminated by cosmic rays in an image is higher in WFPC2, although the underlying event rate is similar to that experienced in WF/PC-1.

Figure 4.10: Histogram of Cosmic Ray Event Sizes. A cosmic ray event is defined by having a peak pixel of at least 10 DN (at gain 7).

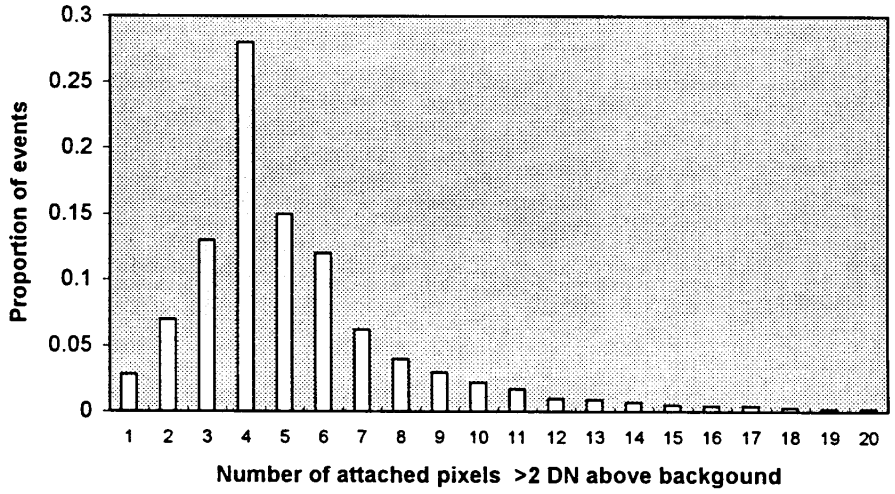

Secondly, stellar images are undersampled and much more difficult to separate from cosmic rays, as is shown in Figure 4.11. Faint stellar images and low energy cosmic rays are often indistinguishable. Long science observations are therefore usually broken into at least two exposures (CR-SPLIT) to ensure that events can be identified.

The average properties of on-orbit cosmic ray events have been determined from examination of several dark exposures, each 2000s long. After bias and dark subtraction, "cosmic rays" were identified in each input frame by first looking for pixels more than 5σ above the background, and then including in each event all adjacent pixels more than 2σ above the background. Very occasionally, two or more physically separate events will be merged into one as a result of this procedure; visual inspection confirms that in the vast majority of cases, this procedure correctly identifies each event and the area affected by it. The typical value of σ was 5 to 6 electrons, including both read and dark noise. The region near the borders of each CCD was excluded in order to avoid edge effects, but all results given here are rescaled to the full area of the CCD.

Figure 4.11: Comparison of Star Images and Cosmic Ray Events. An 80x80 pixel subimage of a 400 second F336W WF2 exposure in ω Cen.

One difficulty in this measurement is caused by hot pixels, for some of which the dark current has significant fluctuations from frame to frame; these can be mistakenly identified as cosmic rays when the dark current is at a maximum. Single-pixel events constitute 10% of the total number of events identified by our procedure, but at least half of them recur in the same position in several frames, thus identifying them as damaged (hot) pixels, rather than true cosmic rays. Also, unlike the majority of cosmic ray events, single-pixel events tend to have a very small total signal; the majority have a total signal of less than 200 electrons, as expected from hot pixels, while the signal distribution of multiple-pixel events peaks around

1000 electrons. For this reason, single-pixel events have been classified as “bad pixels" rather than “cosmic rays". While we cannot exclude that some true single-pixel events do occur, they are very rare, probably less than 2% of the total.

Cosmic ray events are frequent, occurring at an average rate of 1.8 events chip^{-1} s^{-1}. The distribution of the total signal is shown in Figure 4.12; it has a well-defined maximum at about 1000 electrons, and a cut-off at about 500 electrons. The latter is well above the detection threshold used for the above measurements (25 electrons in the central pixel of the cosmic ray), and is therefore undoubtedly real.

Figure 4.12: Histogram of Cosmic Ray Event Energies.

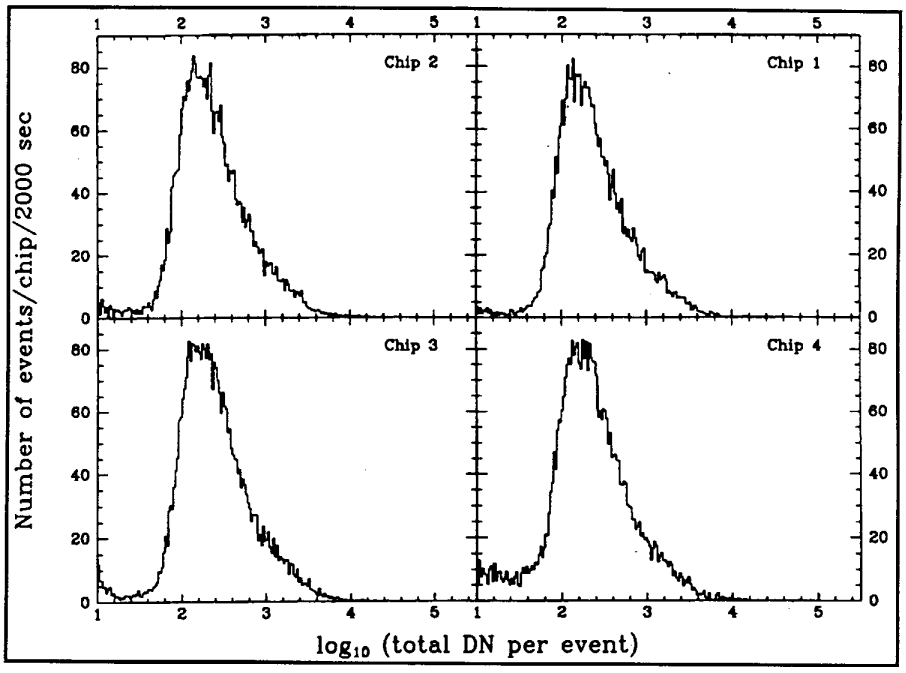

The histogram in Figure 4.12 shows the distribution of the total energy of all cosmic ray events. One encouraging feature is the very small number of events below about 30 DN. This low energy drop is well above the energy level of excluded single-pixel events.

A good approximation to the cumulative distribution of events as a function of the total signal is given by a Weibull function with exponent 0.25. This function has the form:

$$N > S = N_0[-\lambda(-S^{1/4} - S_0^{1/4})]$$

where N is the total number of events which generate a total signal larger than S. The best fit to the observed events gives N_0=1.4 events chip^{-1} s^{-1}, S_0=700 electrons, and λ= 0.57. The fit fails below S_0, and should not be extrapolated to low-signal events. The rate of events with the total signal

below 700 electrons is 0.4 events chip^{-1} s^{-1} (i.e. total events per CCD per second is N_0+0.4≈1.8).

The number of pixels affected by cosmic ray events in a given exposure is a slightly more sensitive function of the threshold used. While there is a clear drop at low signal for both total and peak signal, neighboring pixels can be affected at low levels. Each event (defined as before) affects an average of 6.7 pixels, for about 12 affected pixels chip^{-1} s^{-1}. For a 2000s exposure, this results in about 24,000 affected pixels, or 3.8% of all pixels. As cosmic rays are expected to be randomly placed, a pair of such exposures would have about 900 pixels affected in both exposures; cosmic ray correction is impossible for such pixels. For a pair of 1000s exposures, about 220 pixels will be affected in both frames.

Cosmic ray activity varies as a function of time, geomagnetic latitude of the spacecraft, and other factors. The average numbers given here are subject to change in individual exposures. After studying about one month's worth of dark exposures, we estimate a total range of about a factor of two in cosmic ray rates.

4.10 SAA and Scheduling System Issues

Changes in the WFPC2 observation scheduling system were introduced early in 1999 primarily in order to increase the scheduling efficiency of HST observations starting with Cycle 8.

First, the South Atlantic Anomaly (SAA) contours used to limit WFPC2 observations were modified slightly. The SAA is a region where irregularities in the Earth’s magnetic field cause very high cosmic ray rates. WFPC2 imaging is generally not scheduled near the SAA, so as to avoid excessive cosmic ray hits which degrade images by obliterating data in numerous pixels. These adverse effects are usually minimized by operating each instrument only when HST is outside a designated “SAA avoidance contour.” (WFPC2 observations of time-critical phenomena can be taken inside the SAA avoidance contour, if necessary.) Biretta and Baggett (1998) analyzed available WFPC2 data, together with data from Air Force satellites flying in similar orbits, and redefined the WFPC2 SAA avoidance contour. This resulted in a 3% increase in designated SAA-free orbits, which allows better scheduling efficiency, and negatively impacts less than 0.1% of WFPC2 science observations. The current (post-1999) contour is given by the M26 area in Figure 4.13.

Figure 4.13: SAA Avoidance Contours.

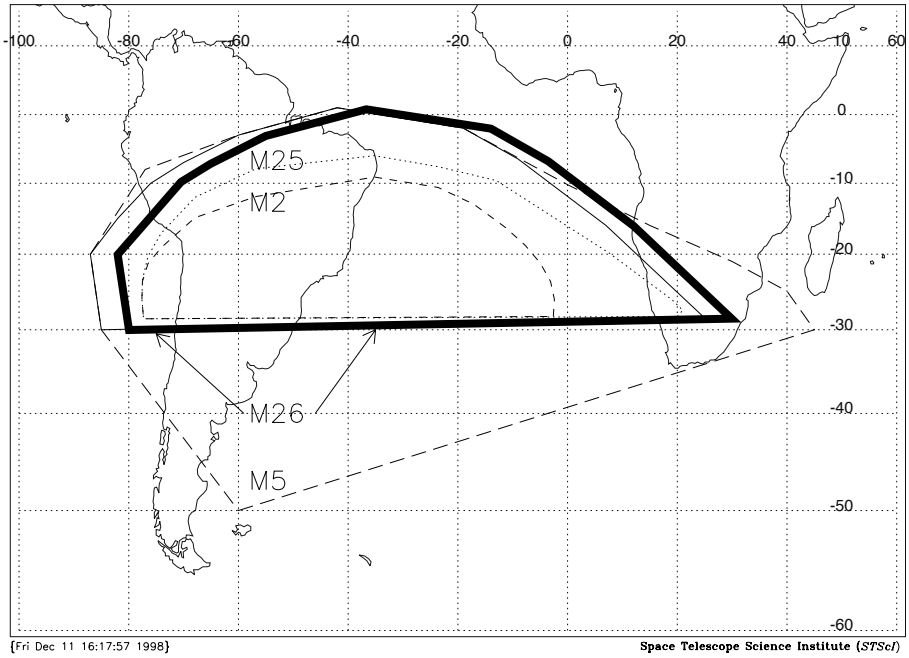

Second, WFPC2 visits are limited to a maximum length of 5 orbits. Very long visits (up to an earlier maximum of 8 orbits) have very limited opportunities for scheduling, reduce the efficiency of telescope use, and can cause long delays in execution, with long GO wait times. Shorter visits improve the scheduling opportunities for large proposals. One possible drawback is the lower pointing repeatability across visits; this is significant only for programs with special dithering requirements.

A third change since Cycle 8 is that an extra minute of overhead was added to each orbit, which allows splitting an orbit in the Phase II proposal into two separate spacecraft alignments. This one-minute “efficiency adjustment” allows much more efficient scheduling of HST orbits impacted by the SAA.

4.11 Radiation Damage and Hot Pixels

In low Earth orbit (LEO) the CCDs are subject to radiation damage from the Earth's radiation belts. The WFPC2 CCDs are shielded from energetic electrons and about half the incident energetic protons. Long term radiation damage to the CCDs from high energy protons leads to an increase in the non-uniformity of the dark current image (mainly from the creation of hot pixels), baseline shifts in the CCD amplifiers, and long term degradation of Charge Transfer Efficiency (CTE). There has not been a significant degradation in the amplifier baselines. CTE is discussed in the Section 4.12. On the other hand, one of the major radiation damage mechanisms is the creation of new Si-SiO_2 interface states, which cause increased dark current rates in affected pixels. In the MPP CCD these states immediately recombine with holes, reducing the gradual increase in dark noise by factors of about 25, compared to normal three-phase CCDs (Woodgate, et al. 1989, Janesick, et al. 1989b).

Figure 4.14 is a histogram of the dark current distribution (in $e^- s^{-1}$) for hot pixels. It contains three curves: solid for the histogram of all hot pixels just before a decontamination (April 7, 1995); dashed only for the pixels that were hot just before the decontamination and were not hot at the beginning of the cycle (March 10); and long-dashed for pixels that were hot at the start of the cycle and were fixed by a decontamination. Thus, the dashed line represents the “new” hot pixels, and the long dashed line represents the fixed hot pixels. The fact that these two curves are very similar shows that the number of hot pixels is roughly in equilibrium. The majority of new hot pixels have low dark current. The hot pixels that constitute the accumulated legacy of previous periods, and thus survived one or more decontaminations, include higher-current pixels. The population of hot pixels increases at a rate of approximately 33 pixels CCD^{-1} day^{-1} above a threshold of 0.02 e^- $pixel^{-1}$ s^{-1}, while the camera remains at the normal operating temperature.

About 80% of the new hot pixels return to a normal state at decontamination events when the CCDs are warmed to a temperature of +22˚C for 6-12 hours. There is no evidence that the fraction of hot pixels that returns to normal is related to the length of the decontamination. Of those pixels that are not fixed, about half will be fixed after two or three additional decontaminations. After that, the rate of correction decreases. Figure 4.15 shows the secular increase in the number of hot pixels in each of the four WFPC2 CCDs.

Figure 4.14: Hot Pixel Histogram.

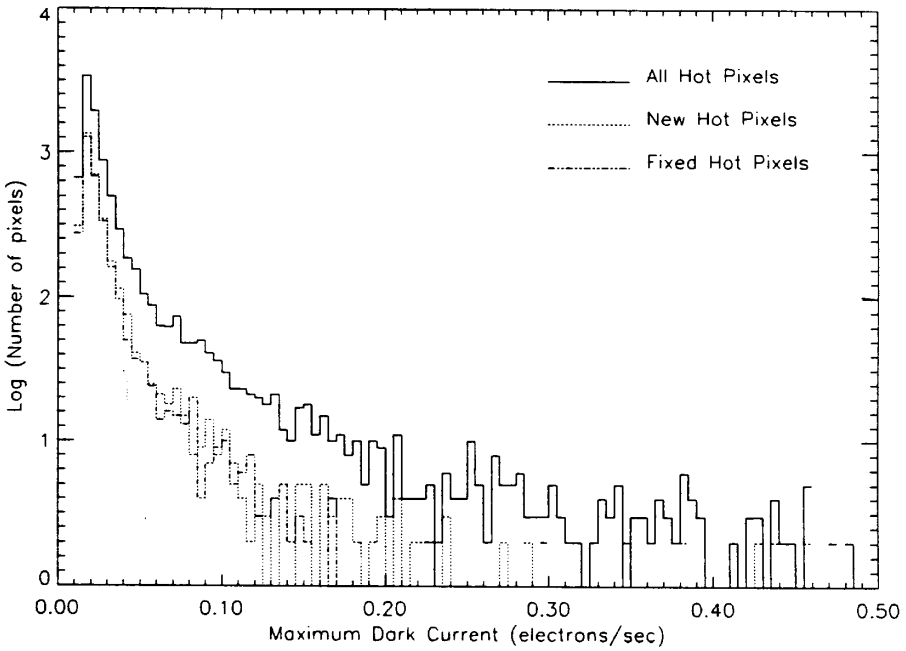

Figure 4.15: Number of Hot Pixels as a Function of Date for all CCDs

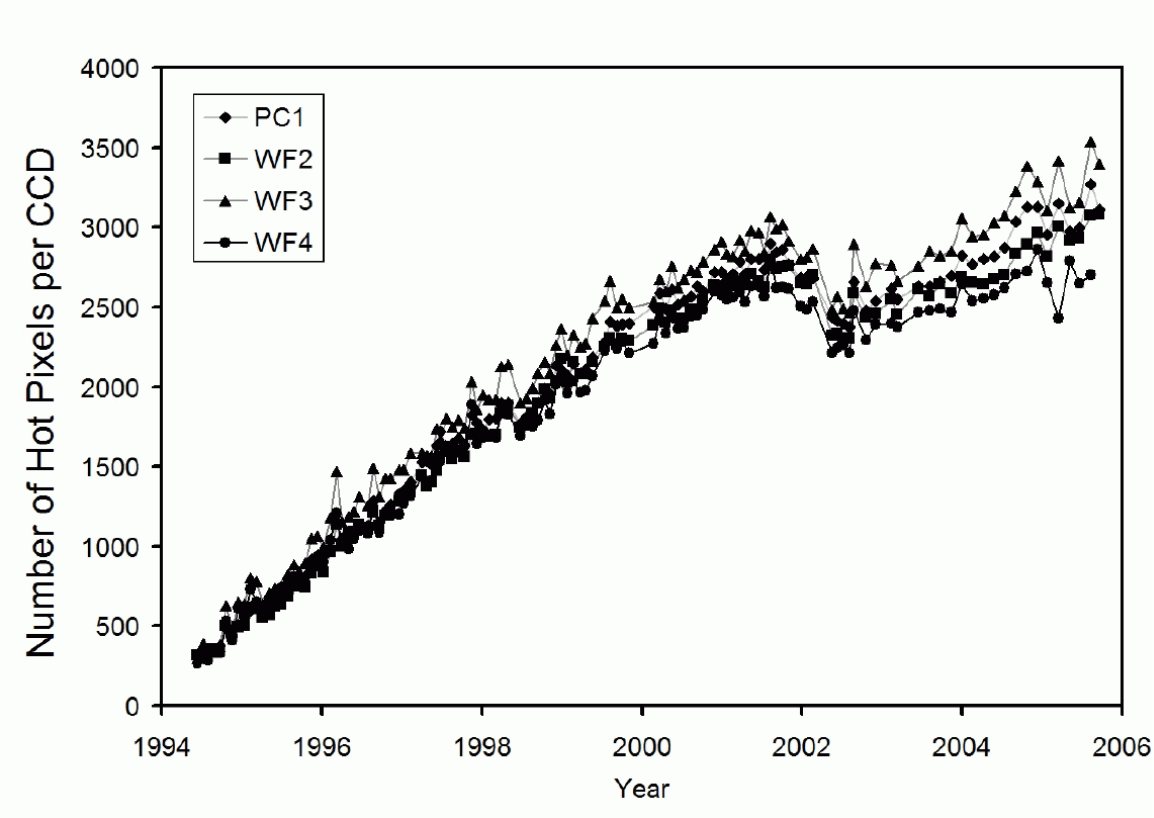

In order to deal with the hot pixels, we provide lists of them, separated by decontamination procedure epochs, via the WFPC2 web pages. The lists can be found at:

http://www.stsci.edu/hst/wfpc2/analysis/warmpix.html

These lists are best used to flag hot pixels as bad. While we do provide an estimate of dark current for each hot pixel as a function of time, there are indications that the noise in hot pixels is much higher than the normal shot noise, and thus dark current subtraction is unlikely to give good results.

4.12 Photometric Anomalies: CTE and "Long vs. Short"

Two anomalies affecting WFPC2 photometry have been extensively investigated. The first anomaly is due to the imperfect charge transfer efficiency (CTE) of WFPC2's CCDs. Imaged sources located far from the readout amplifier appear fainter than those close to the readout amplifier because a small fraction of the charge packet is lost with every transfer of the packet across the rows and columns of the CCD toward the amplifier. The CTE anomaly is increasing with time, especially for faint sources, because of on-orbit radiation damage. In this section, we provide a correction formula that reduces the impact of this anomaly to about 1-3% in typical cases.

The second anomaly, called "long vs. short", is based on the perception that sources appear fainter in short exposures than they do in longer exposures. This nonlinear effect appears independent of the source's location on the CCD. The effect is very small (a few percent) or nonexistent for WFC fields with less than ~1000 stars. For WFC fields with ~10,000 stars, however, nonlinearities of tens of percent have been noted for large exposure differences (e.g., 10 vs. 1000 sec). The reality of the "long vs. short" anomaly has been much debated, and it appears to be an artifact of overestimated background measurements in the short exposures caused by scattered light from bright stars. Because the magnitude of the "long vs. short" anomaly is dependent on the method of the photometric analysis, no universal correction formula has been derived. The CTE and "long vs. short" anomalies are more fully described below.

4.12.1 CTE Trends and Causes

Shortly after the installation of WFPC2, it was recognized that the CCDs had a small but significant problem with CTE that caused the loss of some signal as the charge packet was transferred down the columns of the CCD during readout. Thus, imaged objects located at high row numbers (i.e., far from the CCD serial register) appeared fainter than they would have if they had been imaged at low row numbers. At the original CCD temperature of -76° C, as much as 10-15% of the signal within a 0".5 radius aperture around a bright star was lost from images located at the highest rows. To improve the CTE and mitigate the loss of signal, the temperature of the CCDs was lowered to -88° C on 23 April 1994. This temperature change reduced the maximum lost signal to ~4% for conditions of moderate-to-high aperture signals (1500-20000 e^-) and low sky background (< 20-30 e^-). For higher background levels (~30-250 e^-), the maximum fraction of lost charge was ~2% (Holtzman et al. 1995a,b).

Over the years, the CTE of the WFPC2 CCDs has steadily deteriorated, such that now ~40% of the signal from a point source with an intrinsic aperture signal of 100-1000 e^- is lost from 800 vertical charge transfers over a low sky background (Figure 4.16). On the other hand, only ~15% of the charge from sources of 1000-30000 e^- is lost over 800 transfers in the presence of a moderately high sky (~85 e^-) background (Figure 4.17).

The CTE of CCDs is influenced by several factors, including charge drift from thermal diffusion, electrostatic repulsion, and charge trapping from imperfectly manufactured or damaged pixels (Janesick 2001). Charge trapping is believed to be the principal cause of WFPC2's deteriorating CTE because of its prolonged exposure to energetic protons and electrons in the Van Allen radiation belts and the South Atlantic Anomaly that can damage a CCD's bulk-silicon lattice (Jones 2000). During CCD readout, these traps capture electrons from the charge packets as they are clocked across the CCD toward the readout amplifier. The trapped electrons are eventually released, but only after the affected charge packet has been clocked away from the trap. The reemergent electrons thus produce "tails" on the images that point in directions opposite those of the vertical and horizontal transfers of the charge packet (Section 4.12.3). Images with high background signal suffer relatively little charge loss because the background signal fills the traps and prevents them from robbing the charge packets during readout. The behavior of large signals vs. small signals is complex, but in essence, the larger charge packets fill more volume of the bulk silicon and experience additional traps; as a consequence, while they lose more electrons than a small signal, they lose a smaller proportion of the signal. Hence, a small signal might lose 50% of its charge for some background level, while a signal 100 times brighter might lose only 15% of its charge.

Figure 4.16: Magnitude Differences with Low Background. Difference in magnitudes measured from two images of a star as a function of the change in CCD row position between the two images. The data come from WFPC2 images of Omega Cen taken at two different roll orientations in April and August 2007. Each panel shows the magnitude differences of stars whose aperture signals lie in the given ranges under conditions of very low sky background (< 2 e^-/pixel). The dotted lines are weighted linear fits to the data in each panel. The positive slopes of the fits indicate that stars appear brighter at rows nearer to the CCD readout amplifier than at rows farther from the amplifier because of imperfect CTE. The effect is more pronounced for fainter stars because the amount of trapped charge is a larger fraction of their total aperture signals.

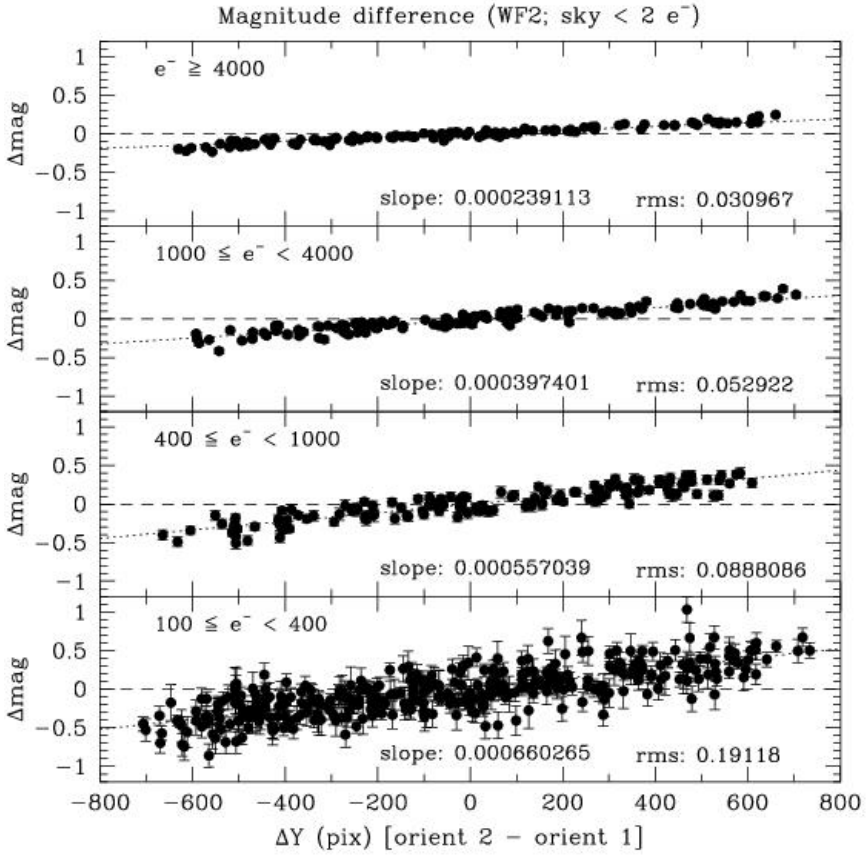

Figure 4.17: Magnitude Differences with Moderately High Background. Same as Figure 4.16, except for conditions of moderately high sky background (~85 e^-). The magnitude differences are diminished because the sky signal fills most of the charge traps and thus reduces the lost aperture signal. This mitigation of the CTE effect comes at the expense of reduced image S/N ratios.

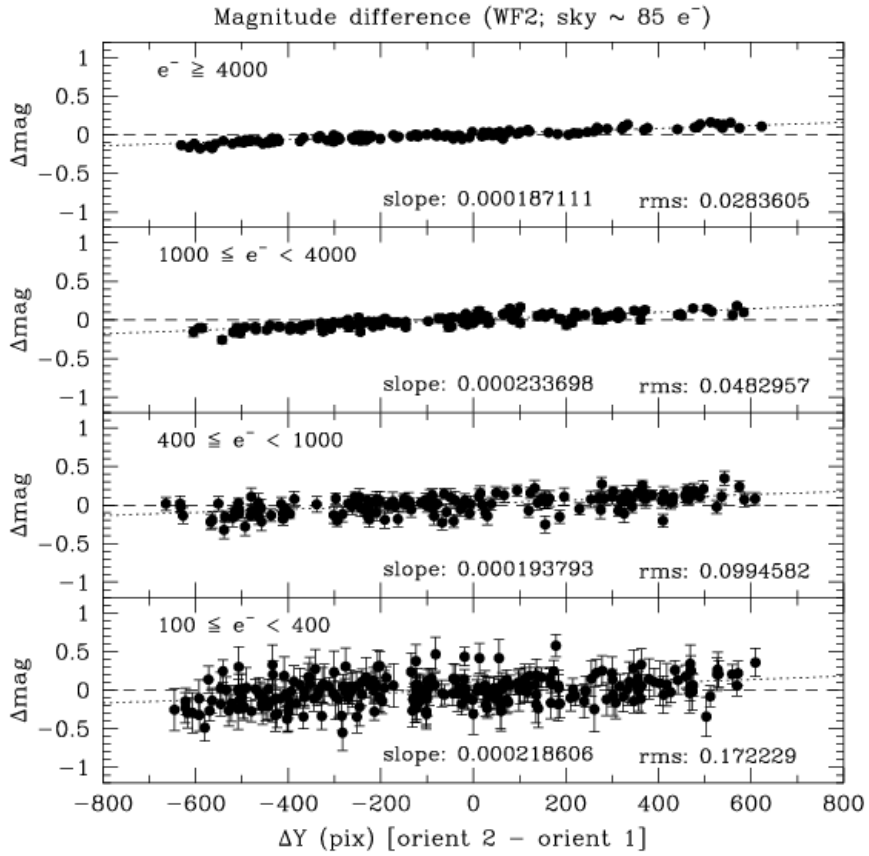

4.12.2 Photometric Effects of the CTE Anomaly

Many studies of the photometric effects of WFPC2's CTE problem have been undertaken, although no results have been made publicly available since December 2004. Most of these studies are based on multi-epoch images of the globular clusters NGC 2419 and Omega Cen, the latter of which was imaged in a CTE monitoring program by STScI. This monitoring program has been revised many times over the years, but it has consistently featured contemporaneous broadband imaging of a standard calibration field ~13'.6 from the center of Omega Cen (Harris et al. 1993) with the WF2 and WF4 cameras. Because the orientations of the two cameras on the sky differ by 180°, images of the same calibration field are read out in opposite directions by simply slewing the telescope from the WF2 aperture to the WF4 aperture. Thus stars imaged at high row and column positions by one camera are imaged at low row and column

positions by the other. Relative measurements of the photometric losses from imperfect CTE across the CCDs can then be made, assuming a negligible difference between the CTE of WF2 and WF4. This assumption is supported by early analyses of the photometric performances of the WFCs (Whitmore and Heyer 1997).

The earliest assessment of WFPC2 CTE was provided by Holtzman et al. (1995a,b), who offered a simple linear correction for CTE losses by assuming a 4% loss of signal for all point sources clocked across 800 rows of the CCD under conditions of low sky background (< 30 e^-). Holtzman et al. assumed a maximum 2% loss for higher sky backgrounds (30-250 e^-). Because these corrections have no temporal dependence, they are only applicable for WFPC2 images obtained soon after the adjustment of WFPC2's temperature to -88° C in April 1994. Subsequent studies of Omega Cen and NGC 2419 by Whitmore & Heyer (1997), Whitmore (1998), and Stetson (1998) identified the dependencies of CTE losses on source brightness, sky background, observing epoch, and both the row and column positions of the source. Whitmore, Heyer, & Casertano (1999) confirmed the background and time dependencies (Figure 4.18), and provided a formula for correcting point-source photometry as a function of source brightness, sky background, and epoch of observation. Saha, Labhardt, & Prosser (2000), however, found no detectable charge losses in the horizontal (serial) transfers and no dependence of the vertical charge losses on source brightness. Dolphin (2000) sought to reconcile these discrepancies by reanalyzing the Omega Cen and NGC 2419 data with the HSTPhot package. He confirmed the dependencies on source brightness, sky background, and observational epoch, and presented a correction formula for point sources that yielded good results regardless of the brand of photometry package used. Dolphin has since provided two updates to his formula (Dolphin 2002, 2004), which remains the best available CTE-correction formula for WFPC2.

Figure 4.18: Y-CTE Loss as a Function of Epoch and Background Light. Each panel corresponds to a different range of aperture signals (1 DN = 14 e^-). Different symbols correspond to different background levels; the larger symbols indicate images with higher backgrounds. The lines represent the best-fit multilinear regression for Y-CTE as functions of time, log (aperture signal), and log (background). See Whitmore et al. (1999).

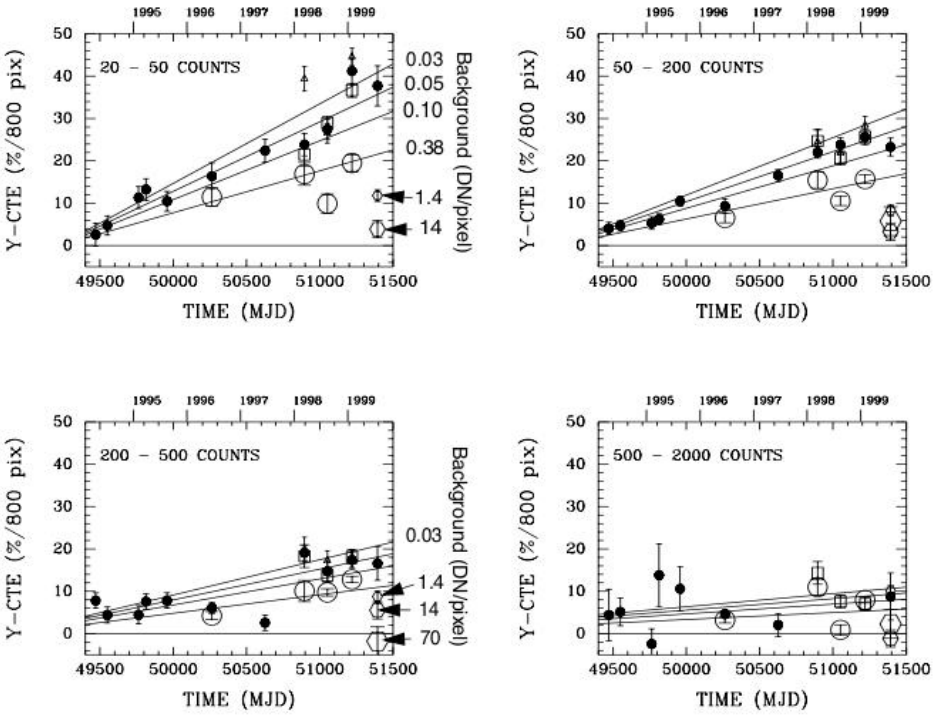

The latest version of Dolphin's WFPC2 CTE-correction formula for point sources, dated 20 December 2004, is given below. It is based upon revised HSTPhot analyses of images of Omega Cen obtained through January 2004. The formula is available along with supporting information at http://purcell.as.arizona.edu/wfpc2_calib/. WFPC2 users are strongly encouraged to check this Web site for revisions of the formula that may appear after the release of this version of the WFPC2 Instrument Handbook.

Dolphin's formula is more complex than other CTE-correction formulae because it accounts for changing source brightness as the charge packet is read out (i.e., the signal loss per pixel changes during readout). First, calculate the values of the following parameters:

$$lct0 = \ln(CTS) - 7$$

$$bg = \sqrt{(BKG^2 + 1)} - 10$$

$$lbg = \ln(\sqrt{(BKG^2 + 1)}) - 1$$

$$yr = \frac{(MJD - 50193)}{365.25}$$

where CTS is the point-source signal in electrons measured within the default HSTPhot apertures of radius 3 pixels for the PC and 2 pixels for the WF cameras, BKG is the true background signal in electrons around the source (i.e., excluding any star light in the sky annulus), and MJD is the Mean Julian Date of the observation. Second, correct for CTE losses during the horizontal (i.e., X direction) transfers of the charge packet:

$$XCTE(mags) = Ae^{(B \times bg)} \times \frac{X}{800}$$

where X is the abscissa of the source coordinate on the CCD, A=0.0021 +/- 0.0004, and B=-0.234 +/- 0.023.

Third, recalculate lct:

$$lct = lct0 + 0.921 \times XCTE$$

Finally, correct for CTE losses during the vertical (i.e. Y direction) transfers of the charge packet:

$$c1 = C \times (De^{(E \times lbg)} + Fe^{(G \times bg)}) \times (1 + H \times yr + I \times yr^2) \times \frac{Y}{800}$$

$$c2 = Je^{(K \times lct)}$$

$$YCTE(mags) = \ln(e^{(c1)} \times (1 + c2) - c2)/L$$

where Y is the ordinate of the source coordinates, C=0.0114 +/- 0.0008, D=0.670 +/- 0.028, E=-0.246 +/- 0.017, F=0.330 +/- 0.028, G=-0.0359 +/- 0.0056, H=0.335 +/- 0.006, I=-0.0074 +/- 0.0009, J=3.55 +/- 0.30, K=-0.474 +/- 0.015, and L=0.436 +/- 0.013.

Note that the choice of photometry parameters can affect the CTE correction. For apertures smaller than the default apertures given above, XCTE becomes independent of the background and increases to approximately 0.022*X/800.

Figures 4.19 and 4.20 show the effect of Dolphin's 2004 CTE-correction formula on the recent (2007) data shown in Figures 4.16 and 4.17. For very low sky background, the formula works well for aperture signals larger than a few hundred e^-, but appears to overcorrect significantly for aperture signals less than a few hundred e^-. A similar trend is seen for high sky background, except that the formula undercorrects the CTE losses for signals greater than ~1000 e^-.

Figure 4.19: CTE Corrected Magnitude Differences with Low Background. Same as Figure 4.16 after applying the CTE correction formula of Dolphin (2004).

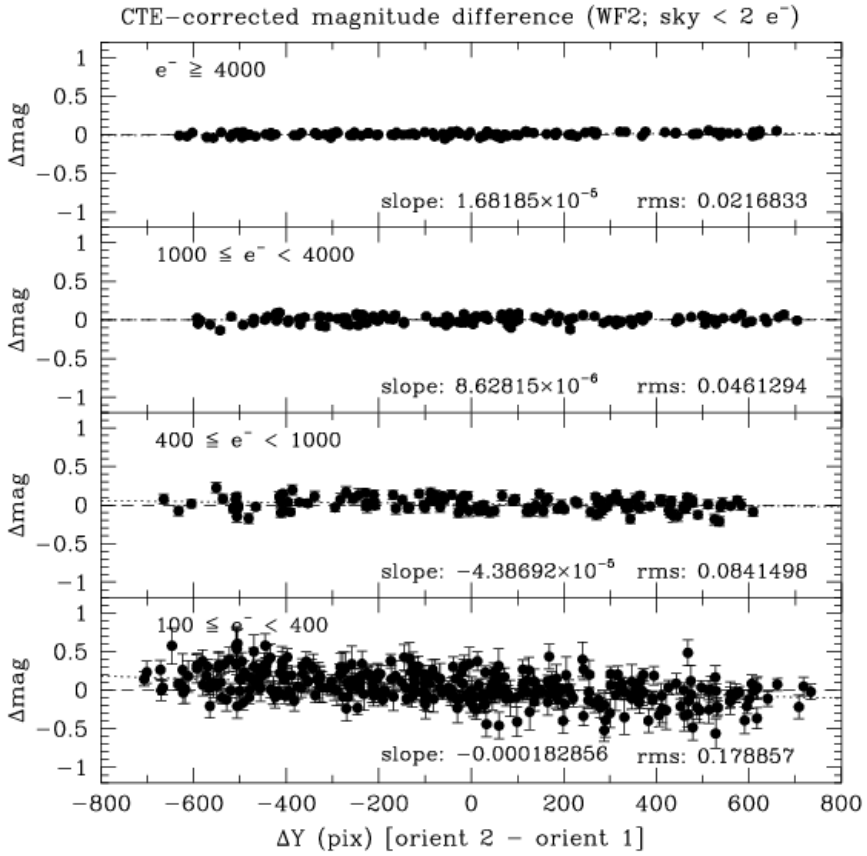

Figure 4.20: CTE Corrected Magnitude Differences with Moderately High Background. Same as Figure 4.17 after applying the CTE correction formula from Dolphin (2004).

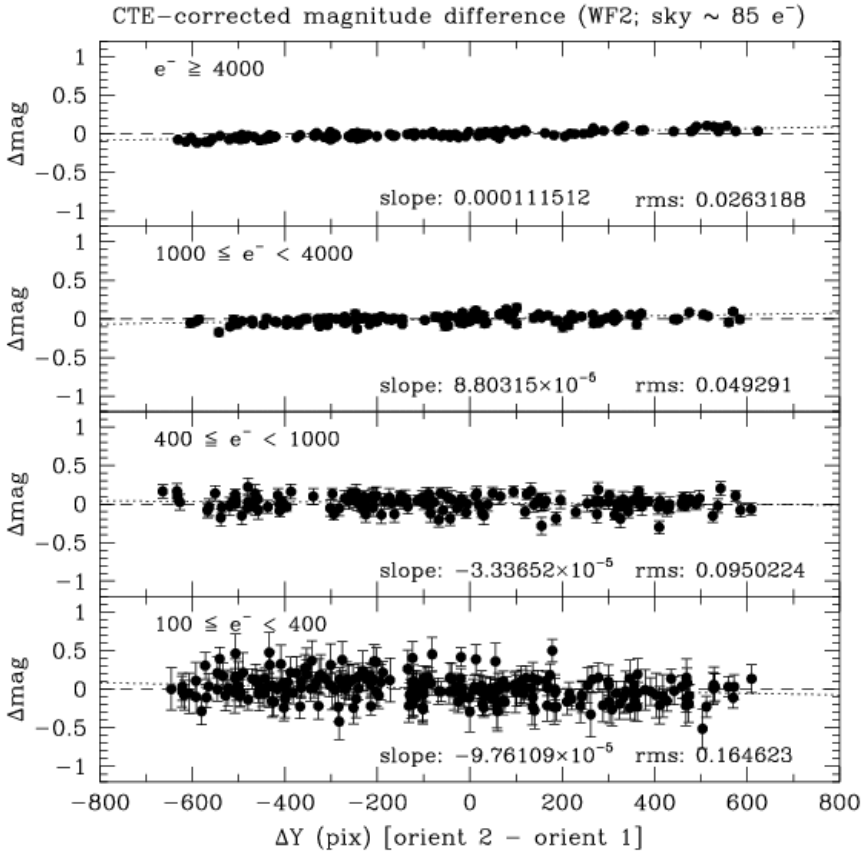

The CTE-correction formula of Whitmore, Heyer, & Casertano (1999) was derived from images of Omega Cen using DAOPhot and an aperture radius of 2 pixels. It is functionally simpler than the formula of Dolphin (2004), but it is equally effective for WFPC2 data obtained before and soon after 1999. The reader is referred to Whitmore, Heyer, & Casertano (1999) for details.

4.12.3 Physical Effects of the CTE Anomaly

Late in 1999, efforts were made to understand the detailed effects of CTE on a single pixel during CCD readout (Biretta & Kozhurina-Platais 2005). Figure 4.21 shows the average of 700 hot pixels taken from WFPC2 dark frames in 1999, and it represents the average response to a single bright pixel at the center of a CCD. Charge is deferred into obvious "tails" extending in both the X and Y directions of the CCD. Three components of

deferred charge can be discerned and characterized according to the release time of the trapped charge from a hot pixel:

1. A short Y component that decays rapidly over a few pixels (i.e., 10s of milliseconds);
2. A short X component that decays rapidly over a few pixels (i.e., 10s of microseconds);
3. A long Y component that decays slowly over dozens of pixels (i.e., 100s of milliseconds).

Figure 4.21: Average of 700 Hot Pixels Illustrating the CTE Effect. Dolphin's formula is more complex than other CTE-correction formulae because it accounts for changing source brightness as charge packet is read out (i.e., the signal loss per pixel changes during readout).

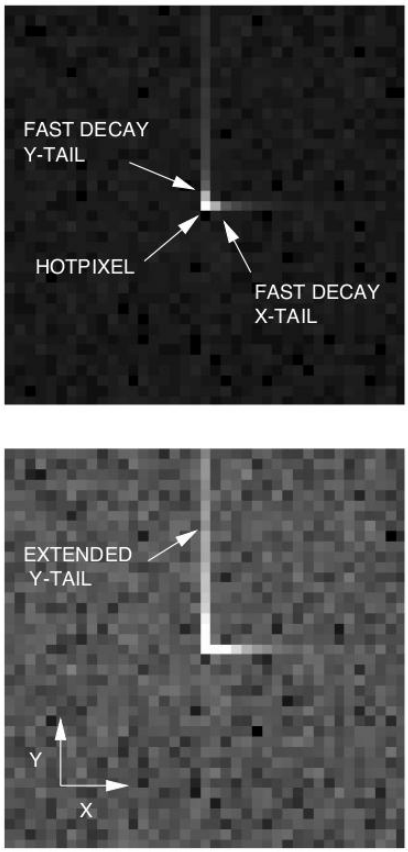

These components effectively rob charge from the typically small apertures used in WFPC2 stellar photometry. A fourth component is responsible for long-lived residual images and will be discussed later.

The average Y profiles of hot pixels observed in 1994, 1997, and 2001 are shown in Figure 4.22. CTE degradation is evident over this time. While the tail was very weak in 1994, it became quite significant by 1997, and by 2001 its integrated charge was twice its 1997 value (Figure 4.23). This rate of increasing deferred charge from hot pixels agrees well with the rate of

increasing CTE losses measured from stellar photometry. Figure 4.24 shows the integrated charge within the Y tail as a function of the intensity of hot pixels measured from four monthly darks in 2001. The data approximately follow the relation:

$$I_Y = (8.0 \pm 0.3) \times \log(I) - (8.1 \pm 0.5)$$

where I is the intensity of the hot pixel in DN at a gain of 7 e-/DN. This relation can be used with Figure 4.23 and model PSFs to estimate the lost or deferred charge from stellar images obtained at different epochs under similar background conditions.

Figure 4.22: Average Y Profiles of Hot Pixels. Average WFPC2 hot pixel tails for years 1994 (lower line), 1997 (middle line), and 2001 (upper line). Hot pixels with signals of 100-4000 DN were selected throughout all four WFPC2 CCDs. The 1994 and 2001 profiles are produced from ~200 and ~2400 hot pixels, respectively, and effectively reflect the hot pixel tail near the center of a CCD.

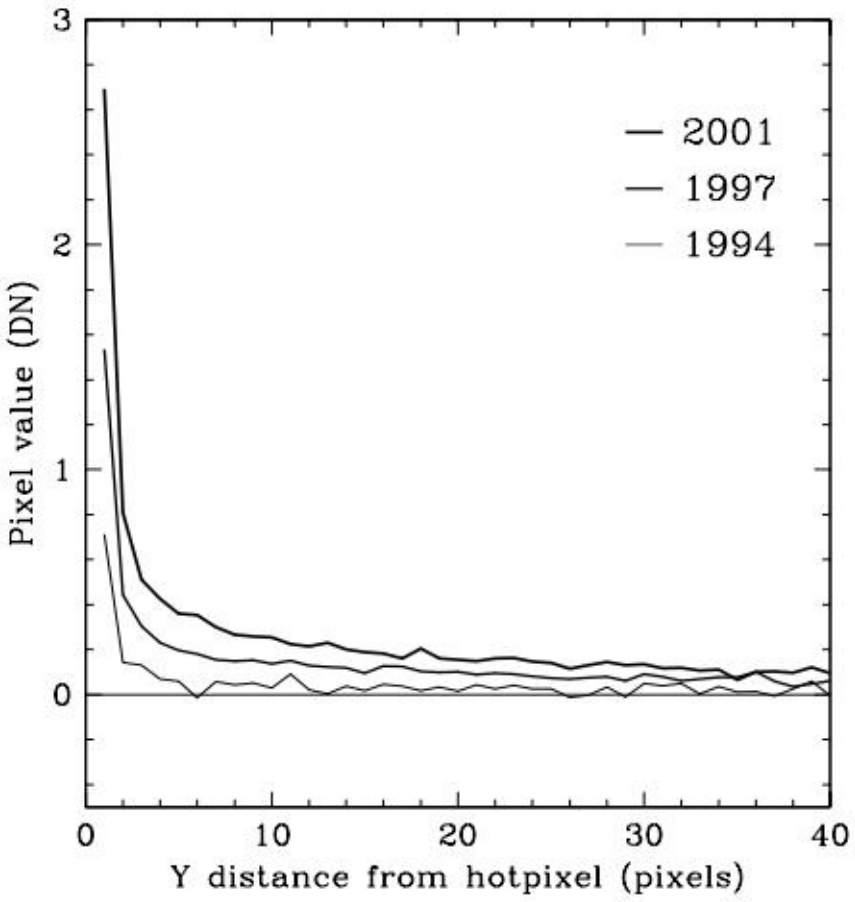

Figure 4.23: Integrated Brightness of Hot Pixel Charge Tails Versus Epoch. The amount of deferred charge in the tails doubles in approximately 4.4 years.

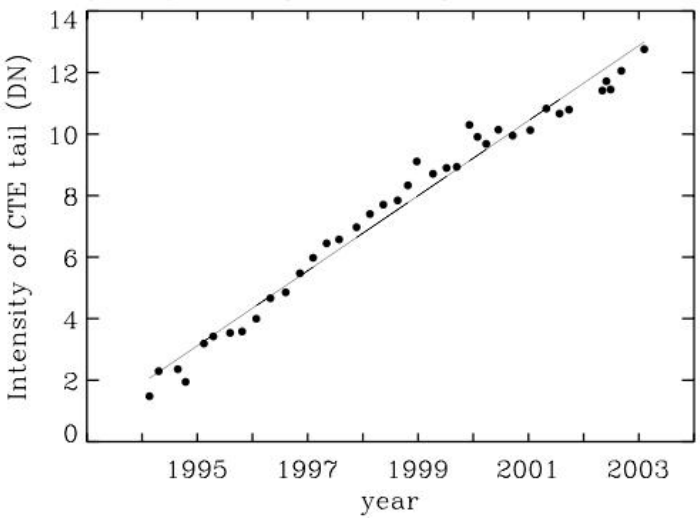

Figure 4.24: Integrated Brightness of the Vertical Hot Pixel Tail as a Function of Hot Pixel Brightness. The four symbols represent data from different monthly dark frames taken in 2001. The hot pixel tails are integrated between 1 and 40 pixels above the hot pixel.

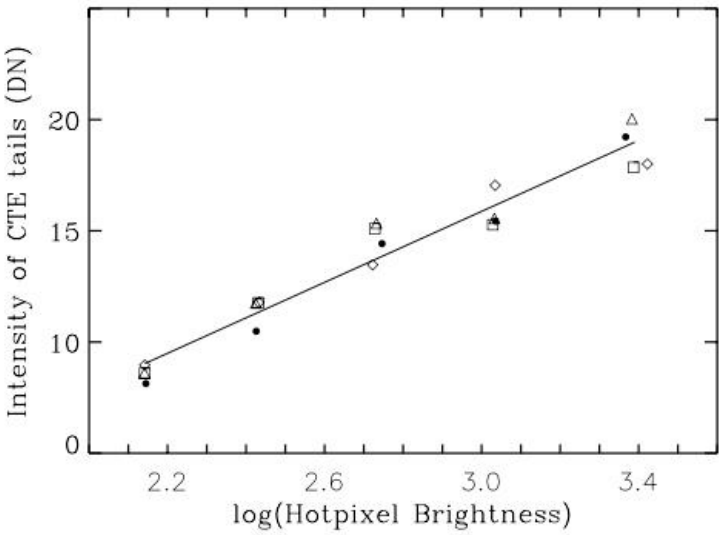

Images of cosmic rays (CRs) are similarly affected by poor CTE. Although CRs themselves have complex shapes, their deferred-charge tails still display a statistical asymmetry that can be used as a quantitative measure of CTE (Riess, Biretta, and Casertano 1999). Figure 4.25 shows no tail at low Y positions, but exponentially decaying tails with an e-folding length of 2 pixels (or an e-folding time of 10s of milliseconds) are evident at high Y positions. Figure 4.26 displays the integrated signal in the vertical and horizontal tails of CRs located at row (Y) 800 as a function

of time. The data were obtained from thousands of dark frames, and they clearly show CTE degradation from 1994 to 2000. The curvature in both the horizontal (X) and vertical (Y) data suggests that the degradation may be nonlinear and accelerating with time. The difference between the amplitudes of the X and Y effects (roughly 3:1 in 2000) agrees well with the relative strengths of the X and Y CTE losses measured from stellar photometry (Whitmore, Heyer, & Casertano 1999). Thus, monitoring CTE from CRs in dark frames provides another useful tool for CTE studies, and does not require pointed HST observation time.

Figure 4.25: Deferred Charge Tails from Cosmic Rays at Low and High Row (Y) Positions in a Single WFPC2 Dark Frame. Each point represents one cosmic ray (CR) and shows the differences between pixels that are equal distances from a CR pixel. The curves track the median of the data. Almost no deferred charge is seen at low row (1 < Y < 100) values, but CR tails are evident at high row (700 < Y < 800) values.

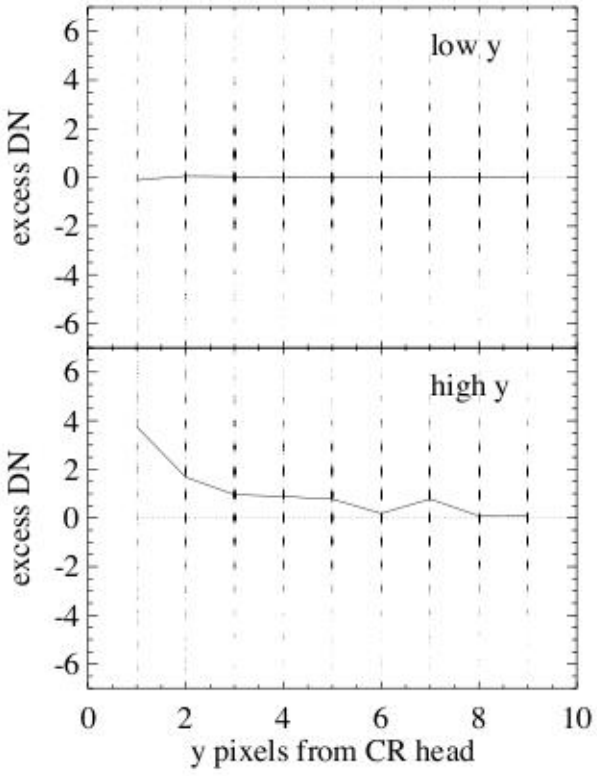

Figure 4.26: Integrated Signal in Deferred Charge Tails from Cosmic Rays. Separate distributions are shown for the horizontal (X-CTE) and vertical (Y-CTE) tails.

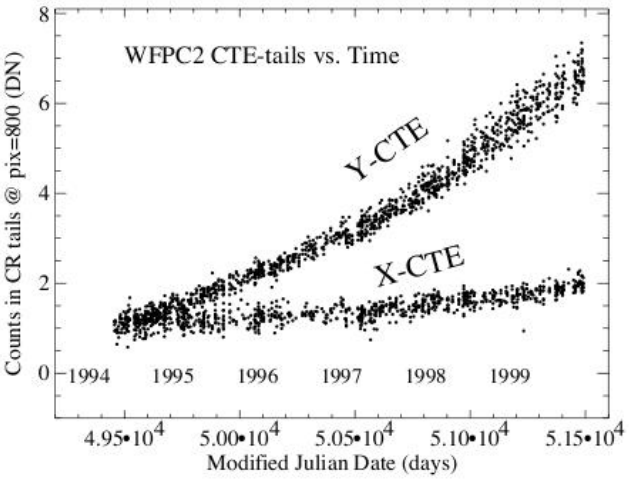

As mentioned previously, a fourth component of deferred charge from poor CTE manifests itself in faint residual images that persist for 10 to 20 minutes after highly exposing a source (Biretta & Mutchler 1997; Baggett, Biretta, & Hsu 2000). These residual images usually appear at the location of the source and along the pixel columns below the source (Figure 4.27). The trail below the source is caused by the slow release of charge which was trapped during the readout of the highly exposed image. The effect is most pronounced when long exposures in low-throughput narrow-band or UV filters immediately follow a highly exposed image in a broadband filter. These long-lived residual images may be caused by surface traps in the CCD, whereas the other CTE components are probably caused by traps in the bulk silicon.

The effects of CTE on the photometry and morphology of extended sources are much more difficult to quantify than the effects on point sources. Riess (2000) subtracted pairs of images of individual galaxies observed near and far from the WF2 and WF4 readout amplifiers. The average profile of the subtraction residuals is distinctly asymmetric and indicates that charge is primarily deferred from the amplifier-side of the galaxy image. The side of the galaxy further from the amplifier suffers little charge loss because the traps encountered during readout have already been filled with charge from the side nearer the amplifier. Moreover, some of the trapped charge from the near side is quickly released and reappears on the far side of the galaxy image. Unfortunately, no recipe for CTE correction exists yet for extended sources. Nevertheless, users are advised that the total CTE loss expected for an extended source probably applies only to the side of the source near the amplifier. During 2007-2008, new data are being taken to study the effects of CTE on extended sources (program 11032); users are encouraged to check the WFPC2 Web site for the results.

Figure 4.27: Long-lived Residual Charge Trails. Trails persist after readout of a well exposed star field. (a) PC1 image of a star field taken through a broadband filter. (b) 1500 second dark exposure taken immediately after the image shown in (a). The readout direction is toward the bottom of the image. Cosmic rays have been removed from the images.

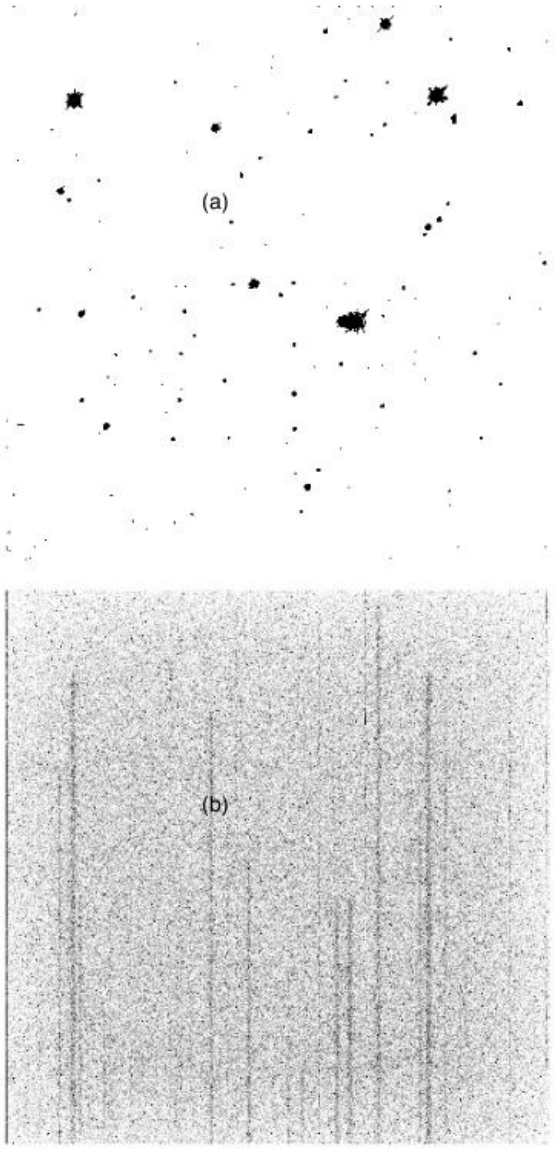

4.12.4 Mitigating CTE During Observations

Several observational strategies exist for mitigating CTE losses. Most involve raising the background signal enough to fill the charge traps in the silicon, but not so much that the signal-to-noise (S/N) ratio of the photometric measurement is significantly degraded. Figures 4.28 and 4.29 illustrate the trade off between reduced charge loss and reduced S/N for

varying levels of source and background signals. CTE tends to be most sevre.in narrow-band or UV filters, where the background is low. For example, a 600 second exposure in the F656N narrow-band filter has a background level of ~3 e^-/pixel, meaning that a 1000e^- star will suffer a CTE charge loss of ~20% and result in a S/N of ~19. Alternatively, the background could be pre-flashed to ~100 e^-/pixel, thereby reducing the CTE loss to approximately 8%; along with increasing the background noise, this would decrease the S/N to ~15. However, for the example above, many broad-band filters (F606W, etc.) will already have enough background light to keep CTE losses at modest levels.

Figure 4.28: Simulated Effects of Increasing Background Signal. CTE charge loss for stars with brightnesses of 100, 1000, and 10000 e^- located at the center of a WF camera. The curves reflect the expected state of WFPC2 CTE in mid-Cycle 16 (~ January 2008). The expected background for 600 second exposures through a broadband (F606W) and narrowband (F656N) filter are marked by the vertical lines.

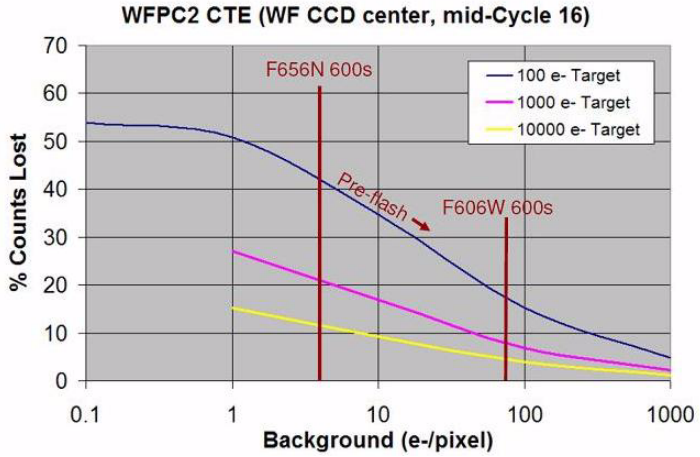

Figure 4.29: Simulated Effect of Background Signal on S/N. Same as Figure 4.28 except for illustrating the effects on S/N. Background signals < 100 e^-/pixel do not significantly affect the S/N ratio.

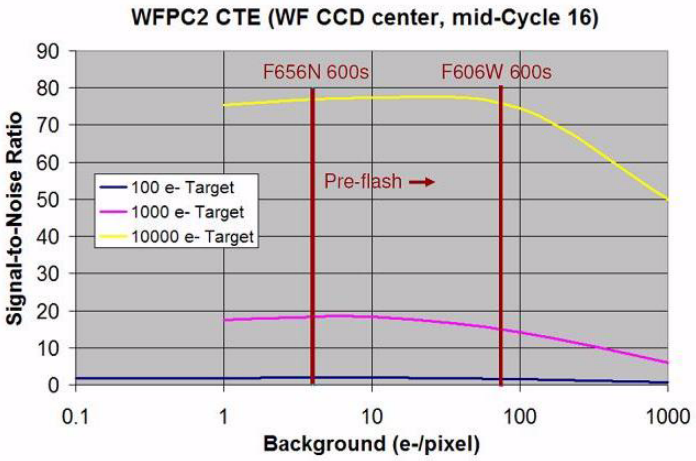

Some suggested methods of mitigating CTE losses are:

- Position the target close to a readout amplifier. --- If a target has an angular size less than a few arcseconds, CTE losses can be reduced by a factor of ~3 by placing the target near a readout amplifier (i.e., at small X and Y pixel coordinates). For the WFCs, this can be done by specifying the WFALL aperture [WF3 pixel (133, 149)], which is located ~10 arcseconds from the apex of the pyramid that divides the WFPC2 field of view. For the PC, users should specify POS TARG -7,-8 in the Phase 2 proposal to offset the target from the nominal PC1 aperture. Users need to be careful not to move the target too close to any readout amplifier or risk having the target move into the vignetted region along the common edges of the four cameras' fields of view. Targets need to be positioned within the regions of 100% illumination indicated in the right-most column of Table 2.5.
- Using longer exposures and fewer dither positions. --- Positioning targets that are large, dispersed, or have highly uncertain coordinates toward the readout amplifier may not be practical. Longer individual exposures of such targets will increase source and background signal, both of which reduce CTE losses. Observers should consider the benefit of longer exposures, especially if they are considering shortening exposures to allow for more dither positions.
- Use a WFC instead of the PC. --- The WFC pixels subtend ~5 times more area than the PC pixels, so the sky background levels in the WFCs will be ~5 times higher than those in the PC for the same exposure times. Higher backgrounds reduce CTE losses, so use of WFCs are recommended when lower image resolution is not a concern.
- Preflashing (or postflashing) the CCD using internal lamps. --- Internally flashing the CCDs raises the background signal and mitigates CTE losses, but there are some negative side effects. Preflashing significantly increases the overhead per science exposure because time is needed to change filters, turn the internal lamps on and off, and take the preflash exposure itself. A single preflash will generally require 3 minutes of overhead. During this time, cosmic rays continue to be absorbed, which further reduces image quality. As Figure 4.29 shows, preflashing does not increase the S/N ratio of the image. Consequently, post-observation CTE correction using the formula given in Section 4.12.2 is recommended over pre-flashing in most cases. Some programs requiring high absolute photometric accuracy above all else may benefit from preflashing. Observers who are inclined to try preflashing are advised to contact the Help Desk (help@stsci.edu) for additional details.

4.12.5 Final Characterization of the CTE Anomaly

Three CTE characterization programs have been implemented during the final year of WFPC2 operations:

- Program 11025 is the final installment of the long-term CTE monitoring program begun in Cycle 7 and described in Section 4.12.2. This program obtains relatively short exposures of Omega Cen with WF2 and WF4 during two epochs with a roll offset of ~180 degrees. This program enables the computation of relative CTE losses between images of the same star located near and far from the readout amplifiers in WF2 and WF4. Because most of the exposure times are 100 seconds or less, this program measures the CTE loss under conditions of low to moderate sky backgrounds.
- Program 11031 aims to assess the accuracy of the latest CTE-correction formulae as a function of sky background. Images of Omega Cen are obtained with all four WFPC2 cameras after preflashing the CCDS with internal lamps, yielding average background signals of 0, 20, 80, and 160 e^-. These preflash levels span the range of expected sky background for the longest broadband exposures possible within a standard HST orbit.
- Program 11032 examines the effect of lost and deferred charge on extended sources. Images of the galaxy cluster Abell 1689 are obtained in all four WFPC2 cameras, and third-epoch images of the Hubble Deep Field North are obtained at the usual WFALL-FIX aperture. These images will be compared with others of the same field taken throughout the lifetime of WFPC2 to assess the impact of CTE on galaxy photometry, morphology, and classification derived from commonly used analysis techniques.

As of this writing (March 2008), analysis of the images from these programs is underway. Initially, the results will be published as Instrument Science Reports, and then in this handbook and/or the WFPC2 Data Handbook. Users are advised to check the STScI Web pages for updates about the characterization and correction of the WFPC2 CTE anomaly.

4.12.6 The Long vs. Short Anomaly

The "long vs. short" anomaly is an apparent nonlinearity of source signal as a function of exposure time. Sources in crowded fields appear brighter in a long exposure than in a short exposure. This nonlinearity was first noted by Peter Stetson in 1994 from WFPC2 images of globular clusters, and then examined in more detail by Kelson et al. (1996), Saha et al. (1996), and Casertano & Mutchler (1998). Hill et al. (1998) noted that the anomaly was consistent with an overestimation of the sky background in the short exposures by 2 e^-. Re-analyzing the globular cluster data with

the HSTPhot package, Dolphin (2000) found no evidence for a "long vs. short" anomaly, and surmised that it was an artifact of improper background subtraction by other commonly used stellar photometry packages.

Whitmore & Heyer (2002) re-examined the "long vs. short" anomaly using the same images of the globular cluster NGC 2419 analyzed previously by Casertano & Mutchler (1998). In their study, Whitmore & Heyer analyzed both the WF2 field containing the center of the cluster (which was previously studied by Casertano & Mutchler) and the WF4 field containing a much less dense region of the cluster. In the less crowded WF4 field (~1000 stars), the "long vs. short" effect was small (a few percent) to nonexistent for aperture counts of 20-400 DN (150-3000 e^-) in the short exposure. In the densely packed WF2 field (~10,000 stars), the effect was also generally smaller than the tens of percent reported by Casertano & Mutchler. Although the "long vs short" discrepancies can be large for very faint stars in very crowded fields, it appears that the correction formula of Casertano & Mutchler, which was derived for such worst cases, significantly overestimates the effect for more typical cases.

Figure 4.30 (adapted from Whitmore & Heyer 2002) illustrates the prevailing wisdom that the "long vs short" anomaly is the result of inaccurately measured sky background. The top panel shows the long/short ratios of the aperture counts of individual stars in the crowded WF2 field of NGC 2419 measured in 1000 second and 10 second exposures, assuming constant sky values of 30 DN for the long exposure and 0.30 DN for the short exposure. The dashed line is a linear fit to the data whose slope is consistent with normal CTE losses. The value at the bottom row (Y = 0) is within ~2 sigma of the theoretical value of 100. Thus, there appears to be no "long vs short" problem for the stars themselves. On the other hand, the ratios of the measured sky values surrounding these stars (bottom panel of Figure 4.30) generally fall well below the theoretical value of 100. The sky values in the 10 second exposure are ~35% larger than the values predicted from the sky measurements from the 1000 second exposure.

Figure 4.30: Ratios of Star and Sky Counts. Ratios were measured in 1000 second and 10 second exposures of the crowded NGC 2419 field as a function of Y (row) position. The top panel shows the long/short ratios for the star apertures, assuming constant sky values of 0.3 DN for the 10 second exposure and 30 DN for the 1000 second exposure. The dashed line shows the linear fit to the data; its positive slope reflects normal CTE losses. The Y=0 value is 102.6 +/- 1.2, which is within ~2 sigma of the theoretical values of 100. The bottom panel shows the 1000s/10s ratios of the local sky values for the stars plotted above. The mean sky ratio is 75.9 +/- 0.6 (median = 74.1), which is well below the predicted value of 100. This result implies that the "long vs. short" effect is caused by inaccurate sky measurements rather than some esoteric instrumental anomaly.

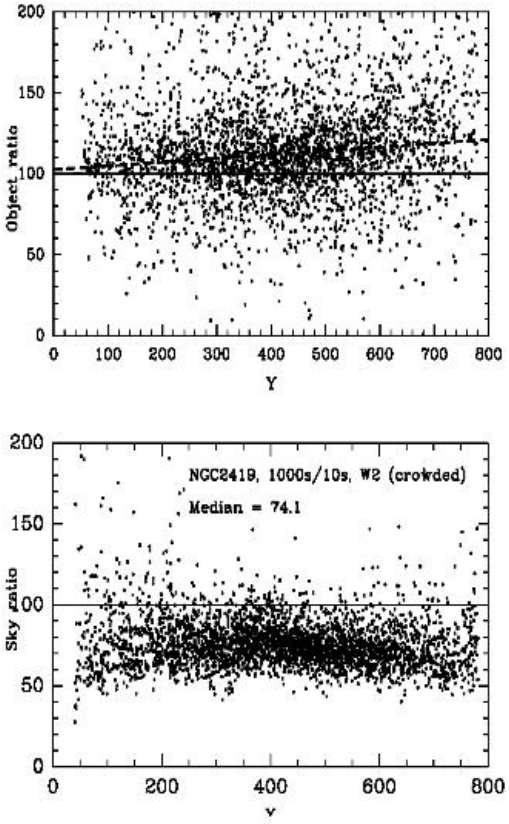

Because inaccurate sky measurement is the likely cause of the "long vs. short" anomaly, the magnitude of the effect is highly dependent on both the degree of image crowding and the photometric methods used by the observer. Consequently, we do not provide a formula for correcting this effect. We refer the user to Whitmore & Heyer (2002) for more information about the anomaly and possible ways of dealing with adversely affected datasets.

4.13 WF4 CCD Anomaly

Over the last few years, a serious anomaly has developed in the electronics of the WF4 CCD, resulting in sporadic images with a low bias level and low photometric counts. In most cases, the bias level itself is corrected in the calibration pipeline, but the photometry remains low. In more severe cases, the bias level is zero (i.e., below the A-to-D converter zero level) and the resulting image appears blank (although bright objects and cosmic rays are sometimes visible). This problem has not manifested itself in the three other CCDs, only in WF4.

Examination of archival data revealed that the problem began shortly after Servicing Mission 3B in March 2002, when occasional images began to exhibit bias levels one or two DN below the nominal WF4 value of 311 DN. The frequency and severity of the problem gradually increased with time. By 2003 the lower envelope of WF4 bias levels was clearly drifting downwards, and by 2004 there were many images with bias below 300 DN. By early 2005 a few blank images with zero bias level began to appear. By late 2005, nearly all images had significantly low bias levels, and 10 to 20 percent had zero bias. Bias levels for a gain of 7 are shown in Figure 4.31. Bias levels at gain 15 show similar behavior.

Figure 4.31: CCD Bias Level vs. Time for Gain 7. CCD bias levels for WFPC2 images (all with gain 7) as a function of time for the period 01/2003 through 4/2007. After each temperature reduction, (01/2006, 02/2006, and 03/2007), the WF4 bias level rises sharply, then declines slowly. Bias levels for the other three CCDs (PC1, WF2, and WF3) are very stable. Each point represents one image.

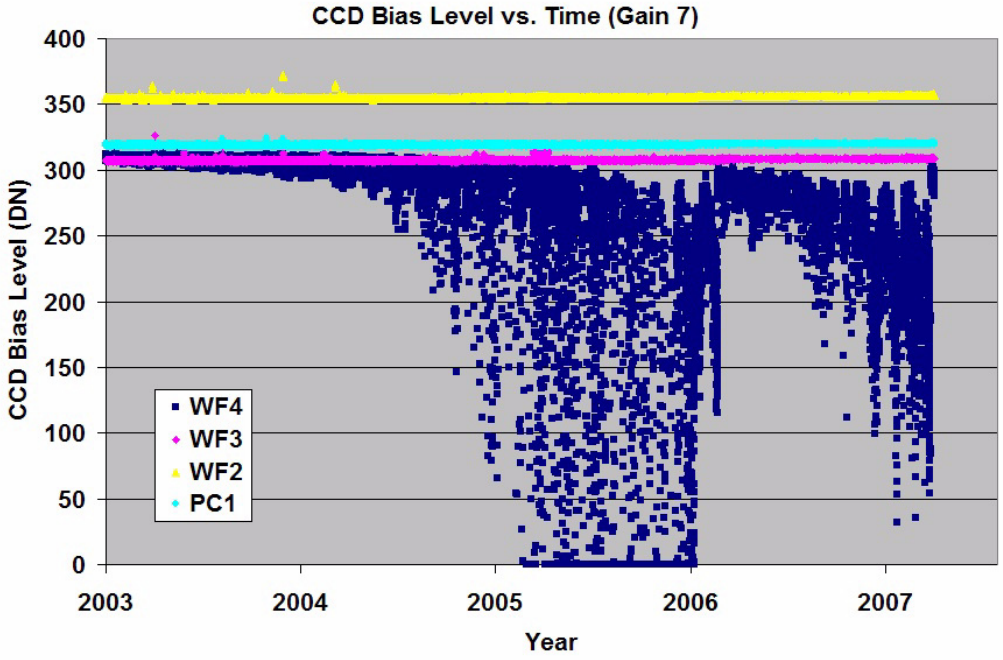

The problem appears to be correlated with the temperature of the warm electronics board inside the WF4 CCD camera head. Specifically, images with low or zero bias are associated with peaks in the temperature, which occur as heaters within WFPC2 cycle on and off. Apparently, some failing component in the CCD signal chain developed a hyper-sensitivity to temperature and has affected the gain of the WF4 CCD amplifier. While there is no direct control of the temperature of this circuit board, we do have some ability to adjust the overall operating temperature of WFPC2; this is not to be confused with the temperature of the CCDs, which has been -88^{o} C since April 1994. In January 2006, an experiment was performed in which the WFPC2 temperature was lowered, and the WF4 anomaly was greatly reduced. Based on this success, a second downward temperature adjustment was made in February 2006. Additional adjustments have been made at roughly six-month intervals. The WF4 bias level remains slightly low, but the photometry is correctable and no further blank images have been seen.

The temperature adjustment was achieved by modifying the replacement heater set points. These heaters are located throughout WFPC2 and have a single control. The heaters are turned on when the WFCP2 temperature drops to a lower limit and are turned off when the temperature reaches an upper limit. These limits are set in the WFPC2 flight software. A time line of the replacement heater set points is given in Table 4.4. The effects of the 2006/01, 2006/02, and 2007/03 temperature adjustments can be seen in Figure 4.31: after each adjustment, the bias level rose sharply, then began a slow decline.

Table 4.4: WFPC2 Replacement Heater Set Points

Date	Lower	Upper
1993 - 2006	10.9	14.9
01/09/2006	10.9	12.2
02/20/2006	10.0	11.3
03/27/2007	8.8	10.0
08/14/2007	7.8	9.0
02/26/2008	7.2	8.4

The temperature reductions appear to have had no adverse impact on WFPC2 performance. The PSF size is actually smaller than before the first adjustment. Motion of the CCDs in the focal plane has been seen, but it is small (about 0.01" per temperature reduction) and similar in size to long-term drifts in the CCD positions.

The photometric impact of the anomaly is illustrated in Figure 4.32, which plots the ratio of observed to reference DN values for a range of bias

levels. We see that the photometric error depends on both the pixel DN value and the overall bias level of the image. To the extent that the curves in Figure 4.32 are well-defined and repeatable over time, the photometry is correctable. A module to perform this correction has been added to CALWP2.

Figure 4.32: Relative Photometry as a Function of Pixel DN. Relative photometry as a function of pixel DN value, plotted for a variety of image bias levels (all with gain 7). Photometric losses are greater for low bias levels and for low DN values. Each set of points, labeled with the observed bias, represents a single image. The figure was generated by comparing internal flats affected by the anomaly to internal flats with normal bias levels.

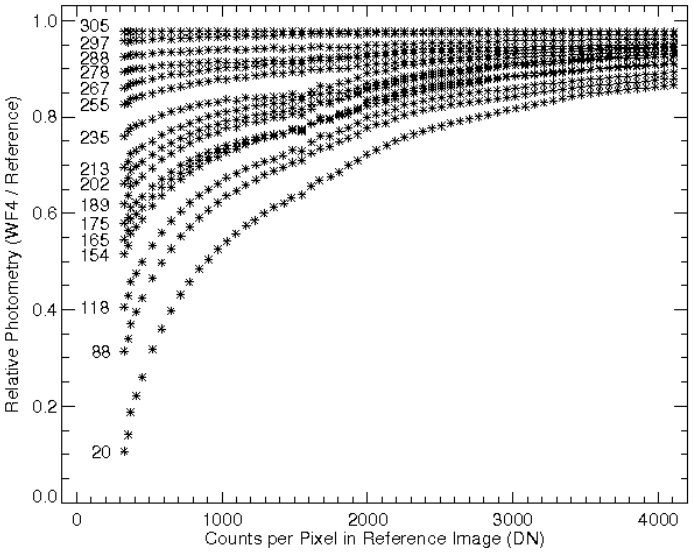

Besides the photometric effects, WF4 images with low bias levels suffer increased background noise in the form of faint horizontal streaks and stripes. These can have an amplitude up to ~1 DN RMS at low bias levels (bias <200 DN) and are generally weaker at higher bias levels. An IRAF/STSDAS task (**DESTREAK**) to identify and remove these streaks is currently under development.

CHAPTER 5:

Point Spread Function

In this chapter . . .

5.1 Effects of OTA Spherical Aberration

The OTA spherical aberration produces a Point Spread Function (PSF—the apparent surface brightness profile of a point source), as presented to the instruments, with broad wings. Briefly, the fraction of the light within the central 0.1″ was reduced by a factor of about 5. The resulting PSF had "wings" which extended to large radii (several arcseconds), greatly reducing the contrast of the images and degrading the measurements of sources near bright objects or in crowded fields. Burrows, et al. (1991, Ap. J. Lett. 369, L21) provide a more complete description of the aberrated HST PSF. Figure 5.1 shows the PSF in three cases.

Figure 5.1: PSF Surface Brightness. The percentage of the total flux at 4000Å falling on a PC pixel as a function of the distance from the peak of a star image.

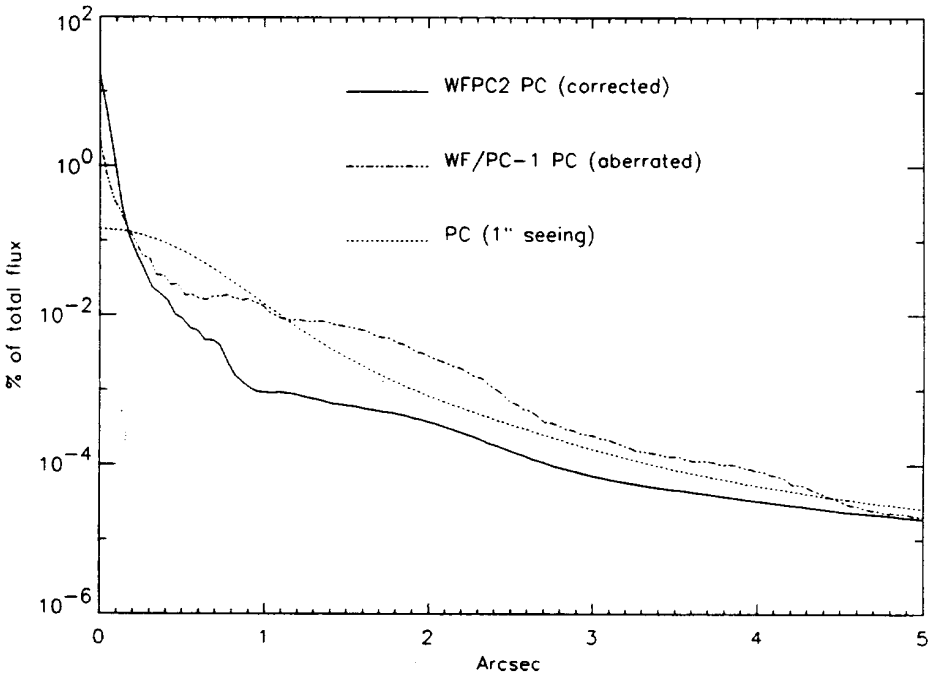

It shows the aberrated HST PSF, the WFPC2 PSF, and for comparison the PSF that would be obtained from a long integration if HST were installed at a ground based observatory with one arcsecond seeing. All of the PSFs were computed at 4000Å. The FWHM of the image both before and after the installation of WFPC2 is approximately proportional to wavelength, at least before detector resolution and MTF effects are considered. (The WF/PC-1 core was approximately 50% broader than the core that is obtained with WFPC2). Figure 5.2 shows the encircled energy (EE), the proportion of the total energy from a point source within a given radius of the image center, for the same three cases.

Figure 5.2: Encircled Energy. The percentage of the total flux at 4000Å within a given radius of the image peak.

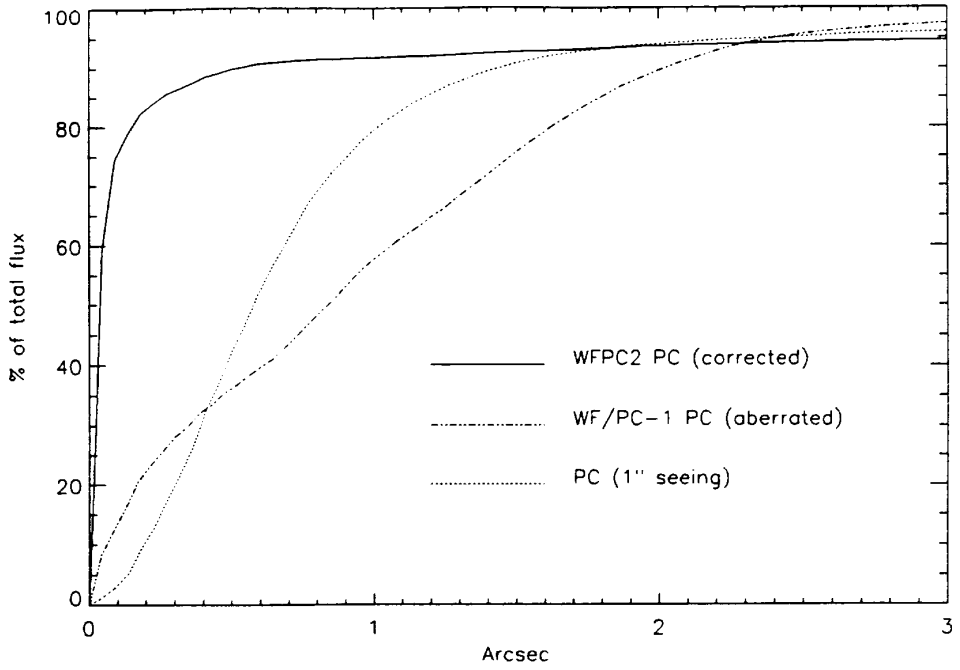

The WFPC2 curve shown is the average of measurements taken with F336W and F439W. It can be seen that the core of the image in WFPC2 contains most of the light. At this wavelength, 65% of the light is contained within a circle of radius 0.1″. However, this proportion is considerably less than the optics deliver. The reason for this is discussed in Section 5.4. Encircled energy curves for other filters are shown in Figure 5.3 and Figure 5.4; note that these curves are normalized to unity at 1.0″ radius.

Figure 5.3: Encircled Energy for CCD PC1. The fraction of energy encircled is plotted vs. aperture radius for several filters. Curves are normalized to unity at a radius of 1.0″. From Holtzman, et al. 1995a.

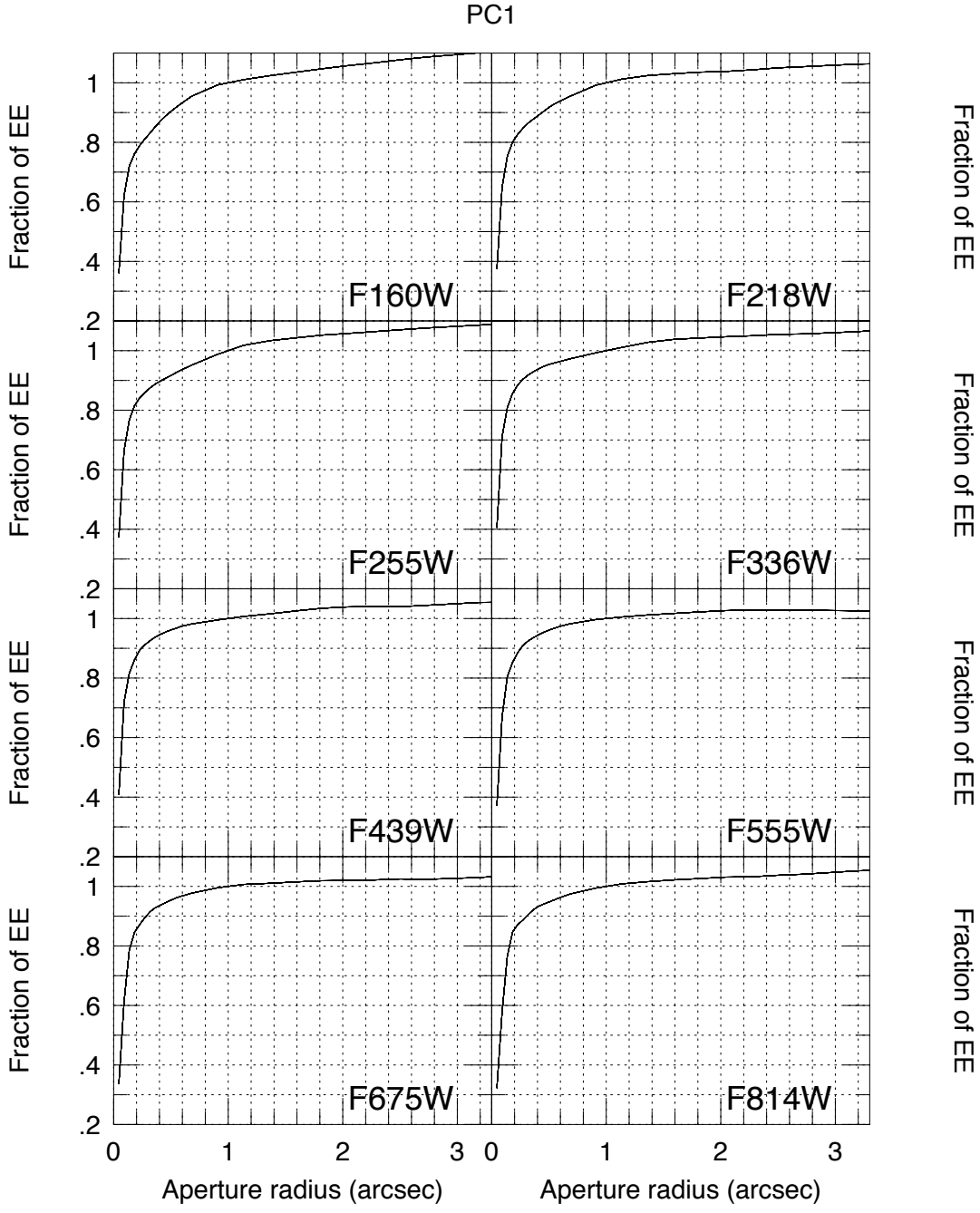

Figure 5.4: Encircled Energy for CCD WF3. The fraction of energy encircled is plotted vs. aperture radius for several filters. Curves are normalized to unity at a radius of 1.0″. From Holtzman, et al. 1995a.

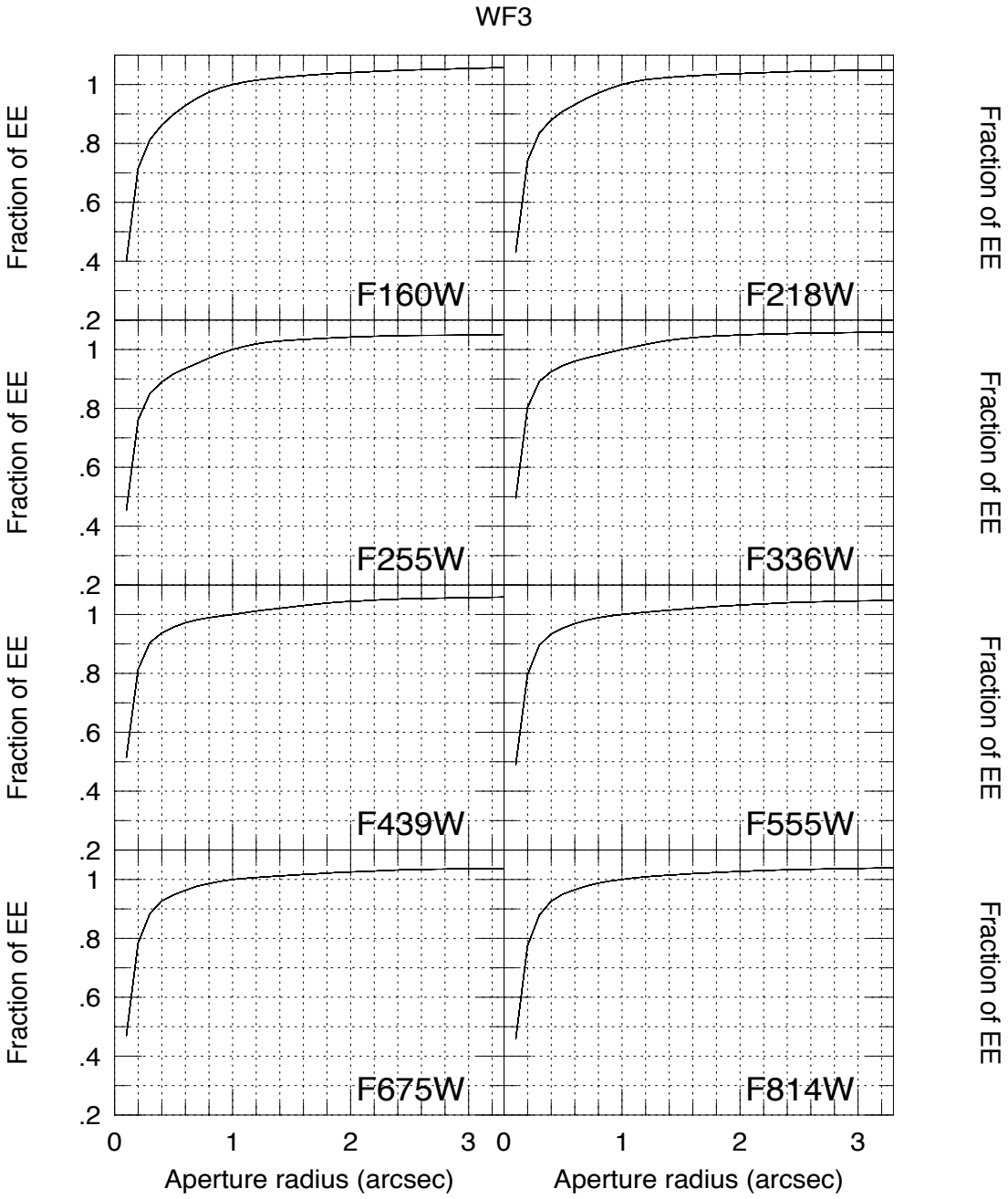

5.2 Aberration Correction

WFPC2 has corrective figures on the relay secondary mirrors where the primary mirror is imaged; this optical correction recovers near-diffraction limited images over the entire CCD fields-of-view. Proper correction requires tight optical alignment tolerances, which are facilitated on-orbit by actuated optics. The corrective optics enable essentially all of the scientific objectives of the original WF/PC-1 to be met.

Table 5.1: Wavefront Error Budget.

Camera	WFC (F/12.9)	PC(F/28.3)
Design error	λ/143	λ/50
Fabrication and alignment error	λ/14.7	λ/14.7
Alignment stability error	λ/25	λ/25
Total wavefront error	λ/12.6	λ/12.3

Through a number of independent analyses, based on investigations of star images obtained on-orbit, and the examination of fixtures used during the figuring of the primary mirror, the aberrations of the HST optics were accurately characterized. The primary mirror was figured to an incorrect conic constant: –1.0139±0.005 rather than the –1.0023 design requirement, resulting in a large amount of spherical aberration. The optical design of WFPC2 creates an image of the OTA primary mirror near the surface of the relay Cassegrain secondary mirror in each of its channels. This design minimizes vignetting in the relay optics, but more importantly, facilitates correction of spherical aberration in the OTA primary by application of the same error (but with opposite sign) to the relay secondary. The optical figure of the WFPC2 secondary mirrors contains a compensating “error” in the conic constant. By adopting a prescription within the error bars for the HST primary mirror, corrective secondary mirrors were made with sufficient accuracy that the residual spherical aberration in the WFPC2 wavefront is small compared to other terms in the WFPC2 optical wavefront budget.

On the other hand, new and stringent alignment requirements were created by the steep optical figure on the corrective relay secondary mirrors. The primary mirror image must be accurately centered on the corrective mirror, and must have the correct magnification. Centering is the most demanding requirement. A failure to center accurately would create a new aberration in the form of coma. A misalignment of 7% of the pupil diameter introduces as much RMS wavefront error as was present in the form of spherical aberration prior to the introduction of corrective optics. The new requirements for alignment accuracy and stability led to the

introduction of a tip-tilt mechanism on the pick-off mirror, to compensate for camera alignment uncertainties with respect to the OTA, and actuated fold mirrors which can compensate for internal misalignments. There was an additional term in the CEIS specification of the overall instrument wavefront error budget for alignment stability. It is λ/25 RMS at 6328Å, as shown in Table 5.1.

"Design error" refers to the aberrations inherent in the design itself, which would be seen if the optics conformed perfectly to their specifications. All of the optics were fabricated and integrated into the WFPC2 optical bench. It was established on the basis of component tests, end-to-end optical interferometry, and through focus phase retrieval, that the WFPC2 optical system performed within the stated tolerances for "fabrication and alignment" in the laboratory environment. What remained was to demonstrate the stability of the optical alignment after launch vibration and in response to the thermal environment on-orbit. The "stability" line anticipated these uncertainties, and was verified during early science operations.

5.3 Wavefront Quality

The conclusion of the extensive optical testing in Thermal Vacuum was that the cameras are well corrected to within the specifications. The dominant problem was a small difference in focus between the four cameras (Krist and Burrows 1995). The actuated fold mirrors and pick-off mirror mechanism performed flawlessly in correcting residual coma aberrations in the image, and enabled the on-orbit alignment procedures. Using out-of-focus images, a very accurate alignment of the cameras was accomplished. A side product was that the aberrations in each camera were measured (Krist and Burrows, Applied Optics, 1995). The results are given in Table 5.2. These values were used in generating the simulated PSFs given in Section 5.5. The WF3 wavefront error is higher than that of the other chips because it is the most out-of-focus relative to the PC (which is assumed to be in focus). It is the equivalent of about 10 microns of breathing out-of-focus.

Table 5.2: Aberrations in Each Camera. The numbers quoted are RMS wavefront errors in microns over the HST aperture (Zernike coefficients).

	Aberration	PC1	WF2	WF3	WF4
Z4	Defocus	0.0000	0.0410	0.0640	0.0480
Z5	0° Astig	0.0229	0.0109	0.0126	0.0163
Z6	45° Astig	0.0105	0.0041	0.0113	0.0190
Z7	V2 Coma	0.0000	0.0012	-0.0037	-0.0090
Z8	V3 Coma	-0.0082	0.0061	-0.0100	0.0019
Z9	X Clover	0.0063	0.0121	0.0010	0.0096
Z10	Y Clover	0.0023	0.0091	0.0130	0.0042
Z11	Spherical	-0.0131	-0.0215	-0.0265	-0.0247
Z22	5th Spherical	0.0034	0.0034	0.0036	0.0029
	Zonal Errors	0.0180	0.0180	0.0180	0.0180
	Total (RSS)	0.0353	0.0537	0.0755	0.0637
	Budget	0.0813	0.0794	0.0794	0.0794

5.4 CCD Pixel Response Function

From Thermal Vacuum testing, there was evidence that the images are not as sharp as expected, despite the good wavefront quality. The decrease in sharpness corresponds to a loss in limiting magnitude of about 0.5 magnitudes in the WF cameras, and less in the PC.

Further testing, by covering a flight spare CCD with a 2μm pinhole grid in an opaque metallic mask and illuminating it with a flat field source, showed that even when a pinhole was centered over a pixel only about 70% of the light was detected in that pixel.

For practical purposes, the effect can be modeled as equivalent to about 40 mas RMS gaussian jitter in the WFC, and 18 mas in the PC (as compared with the typical real pointing jitter of ~3 mas delivered by the excellent HST pointing control system). Alternatively, at least in the V band, it can be modeled by convolving a simulated image by the following kernel, which gives the pixel response function averaged within pixels:

$$K = \begin{bmatrix} 0.0125 & 0.050 & 0.0125 \\ 0.0500 & 0.750 & 0.0500 \\ 0.0125 & 0.050 & 0.0125 \end{bmatrix}$$

One clue is the wavelength dependence of the observed sharpness: the results from the 2μm pinhole grid test get worse at longer wavelengths. This may reflect the greater penetration into the silicon of low energy photons, which facilitates the diffusion of photoelectrons across the pixel boundaries defined by the frontside gate structure.

There is also evidence for sub-pixel QE variations at the 10% level. There is an implied dependence on pixel phase for stellar photometry. This has been seen at about the 1-3% level in on-orbit data. The work of Jorden, Deltorn, and Oates (Greenwich Observatory Newsletter 9/93) has yielded quite similar results, and suggests that sub-pixel response must be taken into account when seeking to understand the behavior of all CCD detectors forming undersampled images.

5.5 Model PSFs

Considerable effort has gone into the modeling of the HST point spread function (PSF), both in order to measure the optical aberrations in support of the WFPC2, COSTAR, and advanced scientific instruments, and to provide PSFs for image deconvolution in the aberrated telescope. Such PSFs are noise free and do not require valuable HST observing time. Software to generate model PSFs for any filter and at any location within the field-of-view is available from the STScI (TIM package, Hasan and Burrows 1993; TinyTIM package, Krist 1995). The results are illustrated in Table 5.3 and Table 5.4 for the PC1 and WF2 cameras, respectively. A representative PSF is on the left in each panel. It meets the wavefront error budget, with the measured mix of focus, coma, astigmatism, and spherical aberration. It has been degraded by the pixel response function as discussed in Section 5.4. On the right is the diffraction limited case for comparison. In each case the percentage of the total flux in a central 5x5 pixel region of a point source is displayed. The peak of the star image can be at an arbitrary point relative to the boundaries of the CCD pixels. Two cases are shown: one where the star is approximately centered on a pixel, and one where it is approximately centered at a pixel corner. As a consequence of the under-sampling in the WFPC2, the limiting magnitude attainable in the background limit varies by about 0.5 magnitude, depending on the position of the source within the CCD pixel. This point is discussed in more detail in Chapter 6.

Neither observed nor modeled PSFs will provide a perfect match to the PSF in actual science observations, due to modeling uncertainties, the "jitter" in the HST pointing, and orbit to orbit variations in telescope focus ("breathing"—which seems to be generally limited to about 1/20 wave peak-to-peak). Jitter is not predictable but can be recovered to a reasonable extent for observations obtained in Fine Lock. In long exposures, up to

about 10 mas of apparent pointing drift may occur as a result of the breathing effects in the FGS, although smaller variations of ~3 mas are typical.

5.6 PSF Variations with Field Position

The WFPC2 PSFs vary with field position due to field-dependent aberrations, obscuration shifting, and scattering. This complicates photometry, PSF subtraction, and deconvolution (Krist, 1995).

The coma and astigmatism aberrations vary significantly within a camera across the field-of-view. These variations are simply part of the optical design. At the extreme corners of the WFC CCDs, away from the OTA axis, there is about 1/5 wave of astigmatism (referenced at 633 nm), which decreases to nearly zero at the CCD centers. Astigmatism at this level causes the PSF core to become elliptical and slightly less sharp; note the flattening of the PSF at pixel positions (54,777) and (605,148) in Figure 5.5. Coma also varies, but to a much lesser extent. Coma and astigmatism variations are considerably smaller in PC1 (though we note the astigmatism at the center of PC1 is fairly significant - see Table 5.2).

Table 5.3: PC Point Spread Functions. Shown as percentages (out of 100 percent) of the total flux in a 5 by 5 pixel region. On the left in each case is a model PSF with the observed wavefront errors and pixel response function. On the right is the diffraction limited case for comparison.

WFPC2 Model PSF					Diffraction Limited PSF				
2000 Å: Peak near corner of PC pixel									
0.9	2.3	2.3	0.9	0.3	0.2	0.6	0.5	0.3	0.1
2.5	10.3	12.7	2.5	0.5	0.6	17.6	20.9	0.5	0.1
1.9	11.2	13.3	2.6	0.5	0.5	20.9	26.0	0.6	0.2
0.9	2.1	2.7	1.4	0.3	0.3	0.5	0.6	0.3	0.1
0.3	0.5	0.5	0.4	0.2	0.1	0.1	0.2	0.1	0.2
Peak near center of pixel									
0.3	0.7	1.3	0.8	0.5	0.1	0.3	0.4	0.2	0.2
0.7	2.6	6.4	3.2	0.8	0.3	0.6	4.9	0.6	0.3
1.2	6.3	25.0	6.9	1.4	0.4	4.9	62.9	6.3	0.4
0.6	2.2	5.9	3.6	0.9	0.3	0.5	6.3	0.7	0.4
0.4	0.8	1.4	1.1	0.4	0.2	0.3	0.4	0.4	0.2
4000 Å: Peak near corner of PC pixel									
0.9	2.5	3.5	1.2	0.2	0.3	2.5	2.5	0.3	0.1
3.6	10.8	12.0	3.1	0.4	2.5	14.3	15.8	2.7	0.2
2.7	11.5	12.9	3.5	0.4	2.5	15.8	17.6	3.0	0.2
0.8	3.0	3.4	1.3	0.3	0.3	2.7	3.0	0.4	0.1
0.2	0.4	0.4	0.3	0.2	0.1	0.2	0.2	0.1	0.1
Peak near center of pixel									
0.3	0.6	0.8	0.9	0.3	0.1	0.2	0.3	0.2	0.1
0.9	4.0	6.6	4.9	0.8	0.2	3.8	4.4	3.8	0.2
0.9	6.9	26.1	7.0	0.8	0.3	4.5	49.4	5.1	0.4
0.5	3.4	6.8	4.9	0.9	0.2	3.8	5.0	4.3	0.2
0.2	0.6	0.8	0.9	0.4	0.1	0.2	0.4	0.2	0.1
6000 Å: Peak near corner of PC pixel									
2.0	2.6	3.4	2.4	0.5	2.1	2.3	2.0	2.1	0.2
3.4	9.8	10.4	2.9	0.6	2.2	11.4	12.8	2.1	0.6
2.8	10.6	11.2	3.2	0.6	2.0	12.9	14.1	2.1	0.6
1.6	2.8	3.1	2.4	0.5	2.0	2.0	2.1	2.3	0.2
0.4	0.6	0.7	0.5	0.2	0.2	0.5	0.6	0.2	0.1
Peak near center of pixel									
0.5	1.2	1.7	1.7	0.6	0.2	1.5	1.8	1.4	0.3
1.7	3.1	5.9	3.6	1.6	1.5	2.4	4.3	2.2	1.6
2.0	6.0	20.7	6.6	1.8	1.8	4.4	31.6	5.3	2.0
1.2	2.9	6.2	3.7	1.7	1.4	2.1	5.4	2.3	1.7
0.4	1.3	2.0	1.7	0.6	0.2	1.5	1.9	1.7	0.3
8000 Å: Peak near corner of PC pixel									
1.6	1.9	2.2	1.9	1.1	1.8	0.9	0.9	1.5	1.1
2.1	9.3	9.7	2.1	1.1	0.9	11.7	12.6	1.0	1.4
2.0	9.8	10.1	2.4	1.1	0.9	12.6	13.3	1.0	1.5
1.4	2.1	2.1	1.8	1.1	1.5	1.0	1.0	1.6	1.2
0.8	1.2	1.3	1.1	0.4	1.1	1.4	1.5	1.2	0.2
Peak near center of pixel									
1.2	1.4	1.5	1.8	1.4	1.3	1.8	1.1	1.6	1.4
1.8	2.5	6.0	2.8	1.6	1.8	1.5	6.2	1.7	1.6
1.6	6.0	15.4	6.6	1.5	1.1	6.2	22.5	7.1	1.0
1.3	2.7	6.3	3.0	1.7	1.6	1.7	7.1	1.9	1.7
1.0	1.4	1.5	1.7	1.4	1.4	1.6	1.0	1.7	1.5

Table 5.4: WFC Point Spread Functions. Shown as percentages (out of 100 percent) of the total flux in a 5 by 5 pixel region. On the left in each case is a model PSF with the observed wavefront errors and pixel response function. On the right is the diffraction limited case for comparison.

WFPC2 Model PSF					Diffraction Limited PSF				
2000 Å: Peak near corner of WF pixel									
0.5	1.8	2.1	0.8	0.3	0.4	0.4	0.4	0.3	0.1
1.5	9.9	13.6	3.1	0.5	0.4	15.4	21.5	0.4	0.1
1.5	9.8	24.0	4.7	0.5	0.4	21.5	33.4	0.4	0.1
0.5	2.1	3.6	1.3	0.3	0.3	0.4	0.4	0.4	0.1
0.2	0.4	0.4	0.2	0.2	0.1	0.1	0.1	0.1	0.1
Peak near center of pixel									
0.2	0.4	0.5	0.5	0.3	0.2	0.2	0.2	0.1	0.2
0.3	1.7	5.3	3.0	0.8	0.1	0.8	1.3	0.6	0.1
0.5	5.4	28.5	14.0	2.2	0.2	1.3	86.2	1.4	0.2
0.3	2.2	9.1	4.5	1.0	0.1	0.6	1.4	0.9	0.2
0.3	0.6	1.2	0.8	0.3	0.2	0.1	0.2	0.2	0.2
4000 Å: Peak near corner of WF pixel									
0.8	2.6	2.5	0.8	0.2	0.4	0.5	0.5	0.2	0.1
2.6	16.1	16.4	3.0	0.4	0.5	17.7	21.2	0.6	0.1
2.0	12.9	17.3	3.0	0.4	0.5	21.2	26.7	0.6	0.1
0.6	2.0	2.6	0.9	0.2	0.2	0.6	0.6	0.4	0.2
0.2	0.4	0.3	0.2	0.1	0.1	0.1	0.1	0.2	0.2
Peak near center of pixel									
0.3	0.6	0.7	0.5	0.3	0.3	0.2	0.3	0.2	0.2
0.6	3.1	7.2	3.4	0.7	0.2	0.7	3.7	0.7	0.2
0.9	8.5	33.3	10.2	1.2	0.3	3.7	68.8	5.3	0.4
0.4	2.5	8.8	3.0	0.6	0.2	0.7	5.3	0.8	0.2
0.2	0.5	0.9	0.5	0.3	0.2	0.2	0.4	0.2	0.3
6000 Å: Peak near corner of WF pixel									
0.7	2.6	2.6	0.9	0.3	0.2	0.5	0.4	0.2	0.2
3.0	14.9	15.6	3.3	0.5	0.5	18.3	20.7	0.5	0.3
2.2	13.7	16.3	3.2	0.4	0.4	20.7	24.2	0.6	0.2
0.6	2.3	2.9	0.7	0.2	0.2	0.5	0.6	0.2	0.2
0.2	0.3	0.3	0.2	0.2	0.2	0.3	0.2	0.2	0.2
Peak near center of pixel									
0.3	0.7	0.9	0.6	0.2	0.2	0.3	0.2	0.3	0.2
0.7	4.1	7.8	4.1	0.8	0.3	1.8	6.1	1.9	0.3
1.0	8.6	30.4	9.4	1.3	0.2	6.1	54.9	6.2	0.3
0.5	2.8	8.2	3.5	0.6	0.3	1.9	6.2	2.5	0.3
0.2	0.5	1.0	0.6	0.3	0.2	0.3	0.3	0.3	0.2
8000 Å: Peak near corner of WF pixel									
1.0	3.0	2.9	1.1	0.3	0.1	2.0	2.0	0.2	0.2
3.6	13.1	13.6	4.0	0.5	2.0	15.8	17.3	2.2	0.1
2.6	12.6	14.2	3.5	0.5	2.0	17.3	19.3	2.5	0.1
0.8	3.2	3.6	1.0	0.3	0.2	2.2	2.5	0.2	0.2
0.2	0.4	0.5	0.2	0.1	0.2	0.1	0.1	0.2	0.1
Peak near center of pixel									
0.2	0.8	0.8	0.7	0.3	0.1	0.2	0.3	0.2	0.1
0.9	4.6	6.9	4.4	1.0	0.2	3.5	4.6	3.4	0.2
0.9	7.5	30.8	8.1	1.2	0.3	4.6	52.0	5.0	0.3
0.5	3.1	7.3	3.7	0.7	0.1	3.4	5.1	3.9	0.2
0.2	0.5	1.0	0.7	0.2	0.1	0.2	0.3	0.2	0.1

Figure 5.5: PSF Variations with Field Position - Aberrations. Nine observed PSFs (filter F814W) are shown from a widely spaced grid on WF3. CCD pixel positions are labeled. Note the flattening of the PSF in the (54,777) and (605,148) positions.

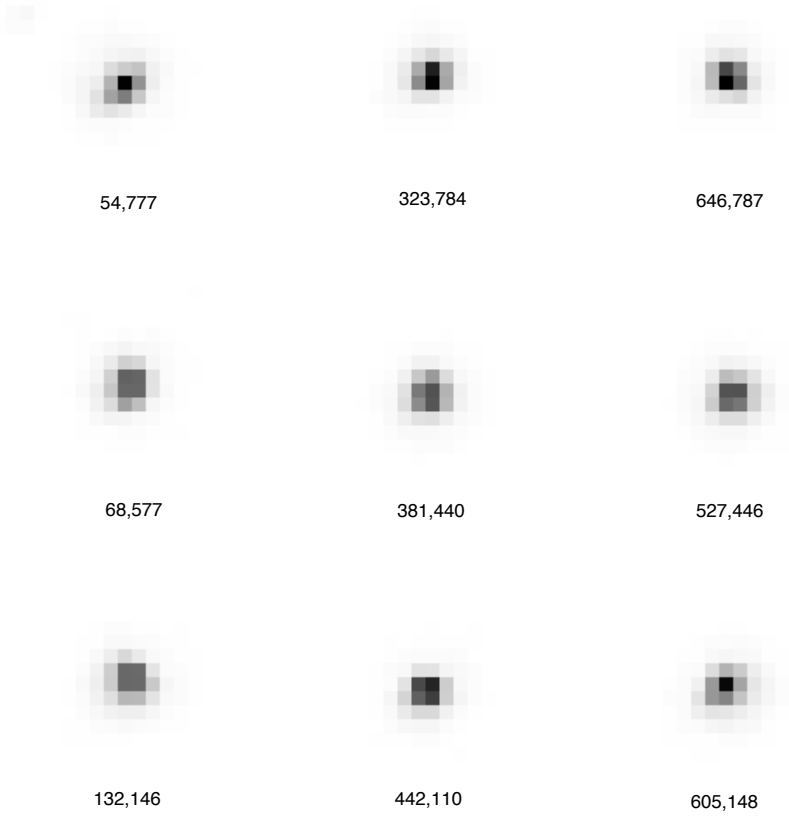

The obscuration patterns due to the camera optics (relay secondary mirror and spiders) appear to shift with respect to the OTA obscurations, depending on field position. The interacting diffraction patterns of the WFPC2 and OTA spiders cause ripples in the spider diffraction spikes, which vary with field position as the two spiders shift relative to each other. In Figure 5.6 the OTA spider is hidden behind the WFPC2 spider at the field center and hence the diffraction spikes there have a simple, smooth appearance (c.f. position 446,425). At the CCD corners, however, one or more vanes of the OTA spider move out from behind the WFPC2 spider, and the double set of obscurations causes a "beating" pattern in the diffraction spikes.

The spiders also interact with light diffracted from zonal errors in the OTA mirrors, causing streaks in the scattering halo which vary in position and intensity.

Figure 5.6: PSF Variations with Field Position - Obscuration Shifts. Five saturated PSFs observed in F814W are shown from a widely spaced grid on WF4. Note the changes in the spider diffraction spikes. CCD pixel positions are labeled. The vertical feature is caused by saturation and blooming (see Section 4.5.1).

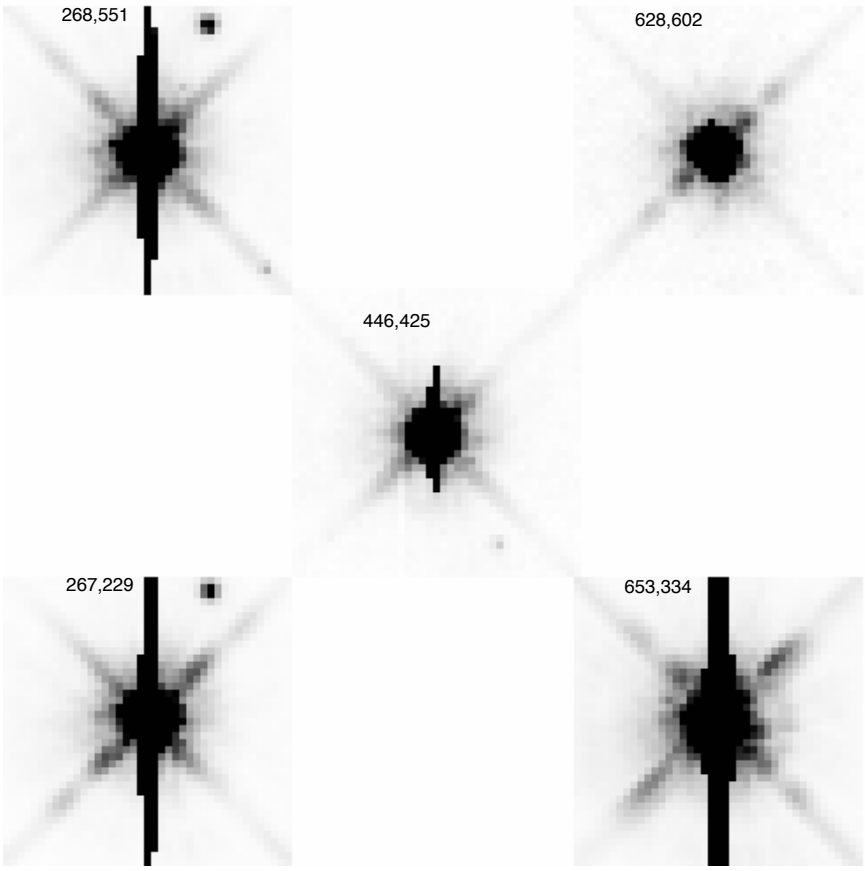

5.6.1 Aperture Corrections vs. Field Position

The amount of energy encircled by an aperture used for stellar photometry will depend on the aperture size, and on any variations in the PSF with field position, time, etc. In general, larger apertures will provide more stable results in the presence of PSF variations. However, large apertures will also exacerbate many problems: contamination from residual cosmic rays, scattered light from nearby stars, and the lower signal-to-noise (S/N) that typically results.

Gonzaga et al. (1999) have measured aperture corrections and characterized their change as a function of field position and filter. The differences in photometric magnitude between apertures with various radii (i.e. aperture corrections), and their mean and standard deviations for the F555W filter, are presented in Table 5.5. For example, the first row of the table indicates that stars measured with a 1 pixel radius aperture will be about 0.887 magnitude fainter than if a 5 pixel radius aperture were used

(averaged over entire PC CCD), and this difference will vary by about 0.054 magnitudes RMS across the CCD.

Variations in the PSF with field position will, of course, cause a position dependence in the aperture corrections. Figure 5.7 illustrates how the aperture correction varies with distance from the CCD center, R, for different pairs of aperture sizes. The scatter in the plots is due to contamination from residual cosmic rays and nearby faint stars within the larger aperture. While the data are somewhat incomplete, a clear trend is present: the aperture correction generally increases linearly as a function of distance from the CCD center. For example, the aperture correction between 1 to 5 pixel radius is about 0.82 magnitudes at the PC center, and increases to about 0.94 magnitude at the far corners of the CCD. (The average correction is about 0.89 magnitude, as given in the first line of Table 5.5.) The other WFPC2 CCD chips show results similar to the PC chip.

Table 5.5: Magnitude differences produced by different aperture sizes. Results given for PC, WF2, WF3, and WF4 in F555W.

Chip	Filter	Aperture Radii (pixels)	Number of Stars	Mean Magnitude Difference[a]	RMS of Magnitude Difference[b]
PC	F555W	1 vs. 5	116	0.887	0.054
PC	F555W	2 vs. 5	115	0.275	0.028
PC	F555W	2 vs. 10	115	0.401	0.075
PC	F555W	5 vs. 10	115	0.106	0.055
WF2	F555W	1 vs. 5	558	0.608	0.130
WF2	F555W	2 vs. 5	558	0.160	0.085
WF2	F555W	2 vs. 10	544	0.310	0.257
WF2	F555W	5 vs. 10	548	0.133	0.204
WF3	F555W	1 vs. 5	660	0.680	0.133
WF3	F555W	2 vs. 5	656	0.188	0.076
WF3	F555W	2 vs. 10	649	0.376	0.308
WF3	F555W	5 vs. 10	647	0.154	0.233
WF4	F555W	1 vs. 5	828	0.672	0.129
WF4	F555W	2 vs. 5	831	0.198	0.115
WF4	F555W	2 vs. 10	815	0.386	0.350
WF4	F555W	5 vs. 10	814	0.160	0.252

a. Magnitude difference averaged around CCD.
b. RMS magnitude difference around CCD.

In practice, the aperture correction also depends on defocus. The interplay between aperture correction and defocus may be complex, since the optimal focus changes with field position. A full correction has not been established, but the TinyTIM PSF model (see Section 5.7) can be used to estimate the extent of the variation in the aperture correction. In general, we recommend that a minimum aperture radius of 2 pixels be used whenever possible, in order to reduce the impact of variations of the aperture correction with focus and field position. If the field is too crowded and a smaller aperture is needed, we recommend that users verify the validity of the corrections on a few well-exposed stars.

The following section includes a discussion of aperture corrections as a function of OTA focus.

Figure 5.7: Aperture correction (delta) between two given apertures within the PC chip versus radial distance of the target from the center of the chip. Open symbols indicate spurious data.

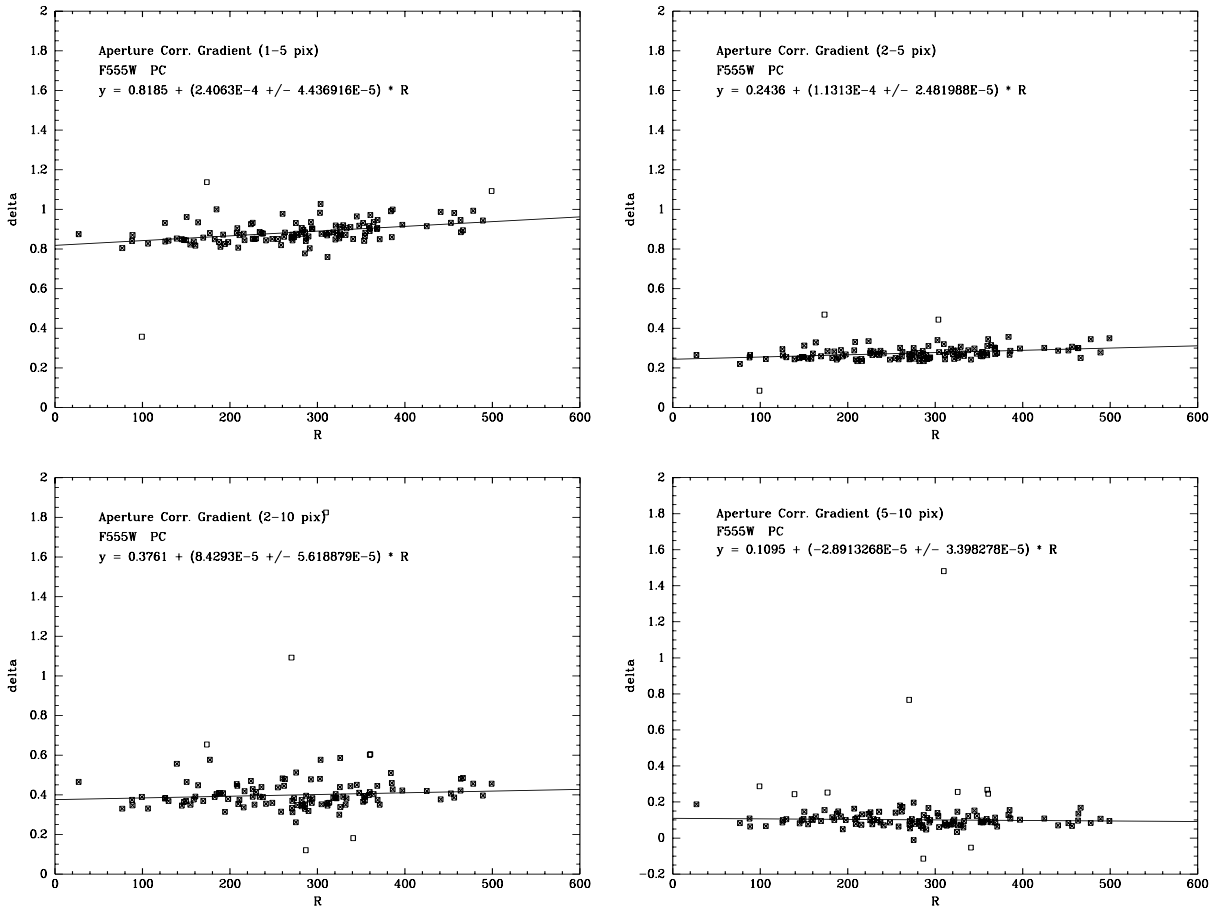

5.7 PSF Variations with Time / OTA Focus

The shape and width of observed PSFs varies slightly over time, due to the change in focus of the telescope. The focus variation consists of two terms: a secular change due to the ongoing shrinkage of the Metering Truss Assembly at an estimated rate of 0.25 μm per month in 1995 (Note: the shrinkage essentially stopped around 2000), and short-term variations, typically on an orbital time-scale (the so-called "breathing" of the telescope, see Figure 5.9). The breathing is probably due to changes in the thermal environment as the telescope moves through its orbit, and has a typical peak-to-peak amplitude of 4 μm; larger variations are occasionally seen.

These small focus shifts will impact photometry performed with small (few pixel radius) apertures. Typical ±2 μm focus shifts will result in photometric variations in the PC1 of 6.8%, 4.5%, 2.0%, and 0.2% for aperture radii of 1, 2, 3, and 5 pixels, respectively, in F555W. This is based on the focus monitoring data taken over the period from January 1994 to February 2003 (see Figure 5.9). Hence, "breathing" is often one of the major sources of errors for small-aperture photometry. However, relative photometry (i.e. the difference in magnitudes of stars in the same image) is less affected by this variation, since all the stars in an image tend to be impacted by the defocusing in a similar way.

Figure 5.8: HST Focus Trend over Mission Life.

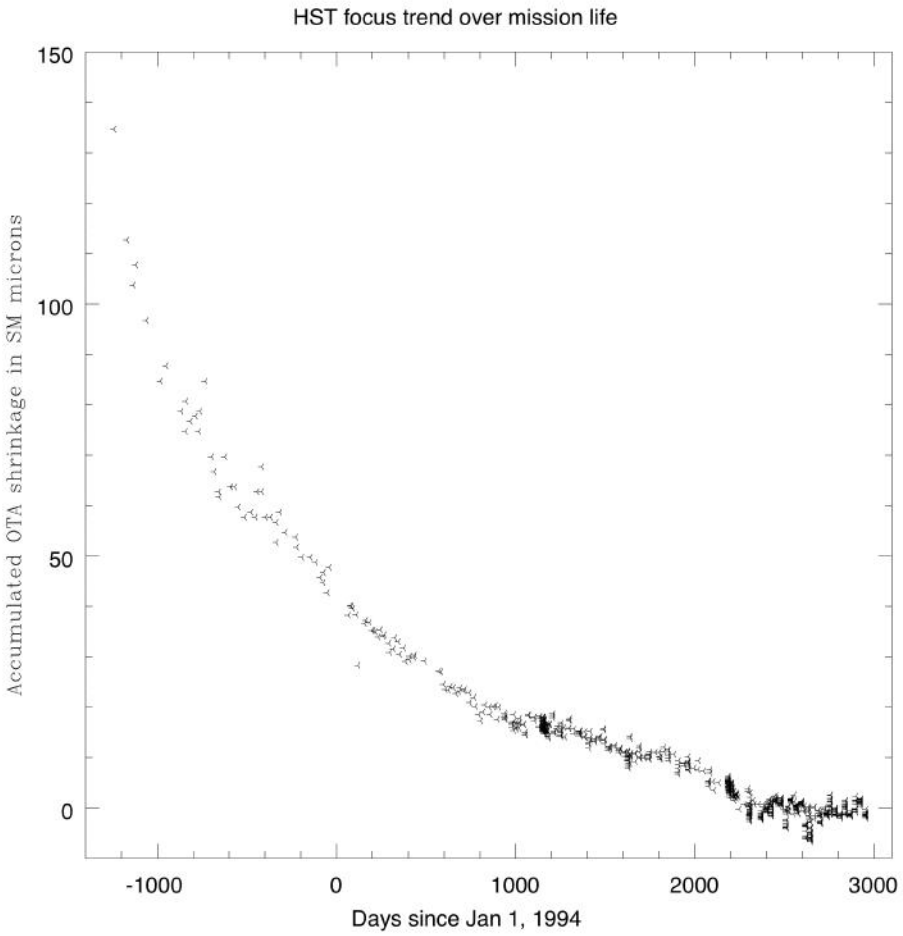

Up-to-date focus information is maintained on the observatory Web page at: http://www.stsci.edu/hst/observatory/focus

Figure 5.9: Measured OTA Focus Position (microns) as Function of Days since January 1, 1994. The focus position is defined as the difference between the optimal PC focus and the measured focus, in microns at the secondary mirror. Times and size of OTA focus adjustments are indicated along the bottom of the plot.

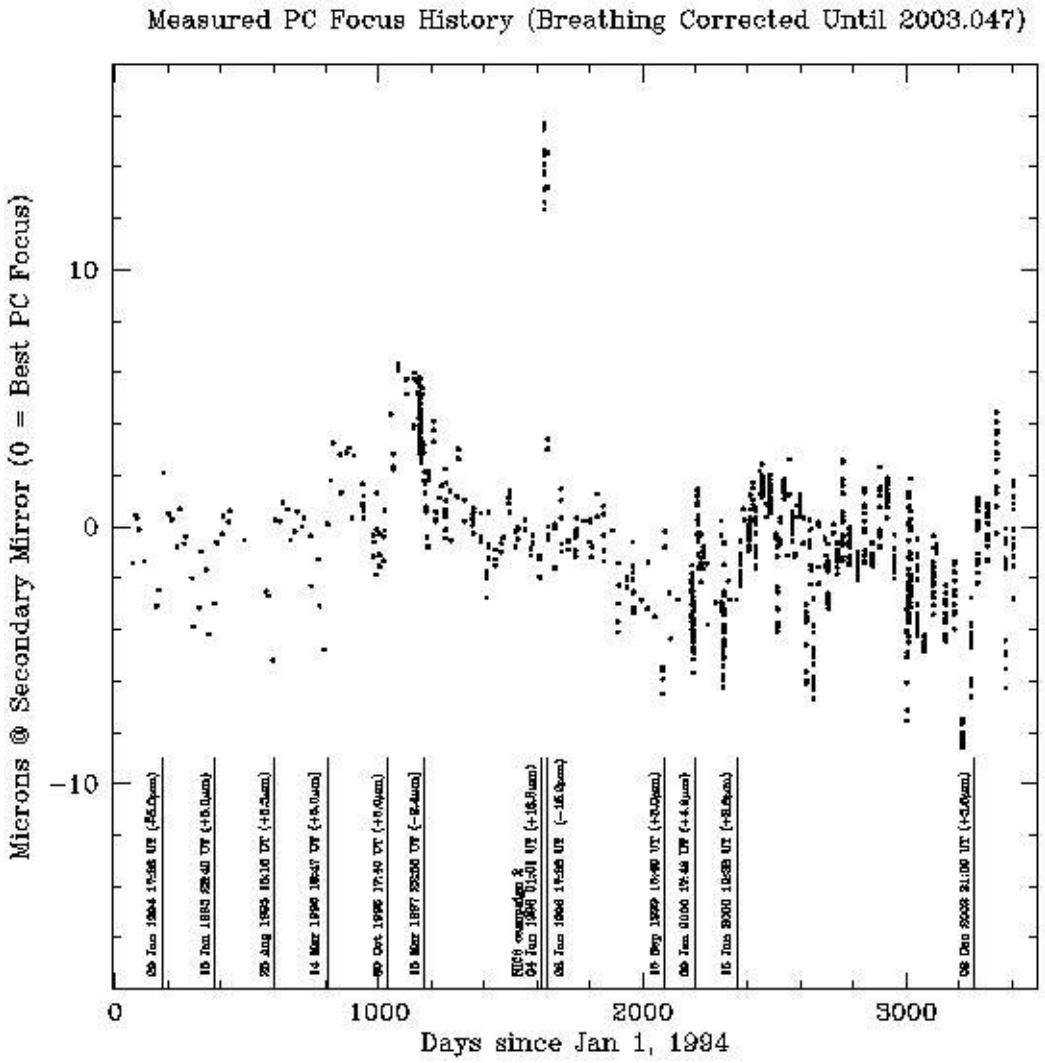

Figure 5.10: Measured Aperture Correction, V(r) - V(r=10 pix), in Magnitudes as Function of Shift from Optimal Focus. Data are given for aperture radii r=1, 2, 3, and 5 pixels for F555W filter on CCD PC1.

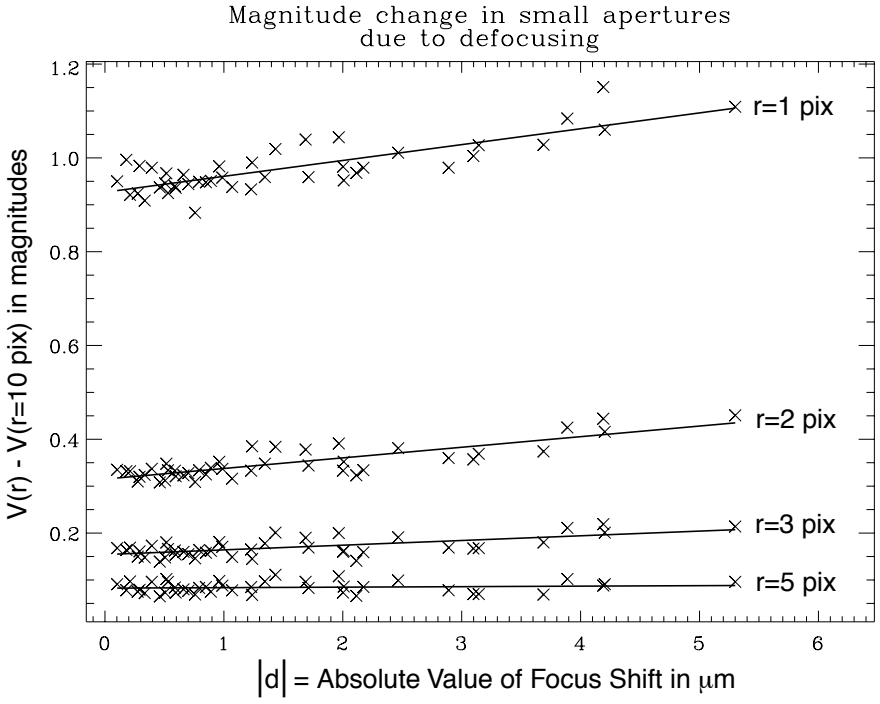

Systematic errors due to the secular focus drift can be corrected using aperture corrections as a function of focus change (see Figure 5.10). The aperture correction adjusted for focus change is hence:

```
ap_corr = ap_corr_nominal + a(r) x d
```

where ap_corr_nominal is the nominal aperture correction (mag) as derived from Table 2a in Holtzman et al. (1995a), a(r) is the flux variation per 1 μm of focus drift (mag per micron) using an aperture with radius r (pixels), and d (μm) is the focus shift from the nominal position. The monitoring data mentioned above yield for PC1 and F555W, the following values for a(r):

$$a(1\ \text{pix}) = 0.0338 \pm 0.0038$$
$$a(2\ \text{pix}) = 0.0226 \pm 0.0024$$
$$a(3\ \text{pix}) = 0.0100 \pm 0.0018$$
$$a(5\ \text{pix}) = 0.00105 \pm 0.0015$$

Suchkov and Casertano (1997) provide further information on aperture corrections. They find that the aperture correction varies with focus by up to 10% for a 1-pixel radius in the PC, and is generally well-fitted by a quadratic function of focus position (see Figure 5.11). A 10% change is measured only for 5 μm defocus, which is about the largest that is expected during normal telescope operations.

It is important to note that WF cameras can also have significant variations in their aperture corrections as the focus varies. While one would naively expect the larger pixels on the WFC to produce weaker variations in the aperture corrections, in practice, the focus offsets between cameras, and the fact that the overall OTA focus is usually optimized for PC1, can lead to significant corrections in the WFC.

Suchkov and Casertano provide formulae that estimate the change in the aperture correction due to defocus for a variety of circumstances.

Figure 5.11: Magnitude change for a 1 pixel radius aperture as function of focus position. Derived from quadratic fits to observed data. Note offset between optimal focus for PC1 (solid line) and WF3 (dashed lines). From Suchkov and Casertano (1997).

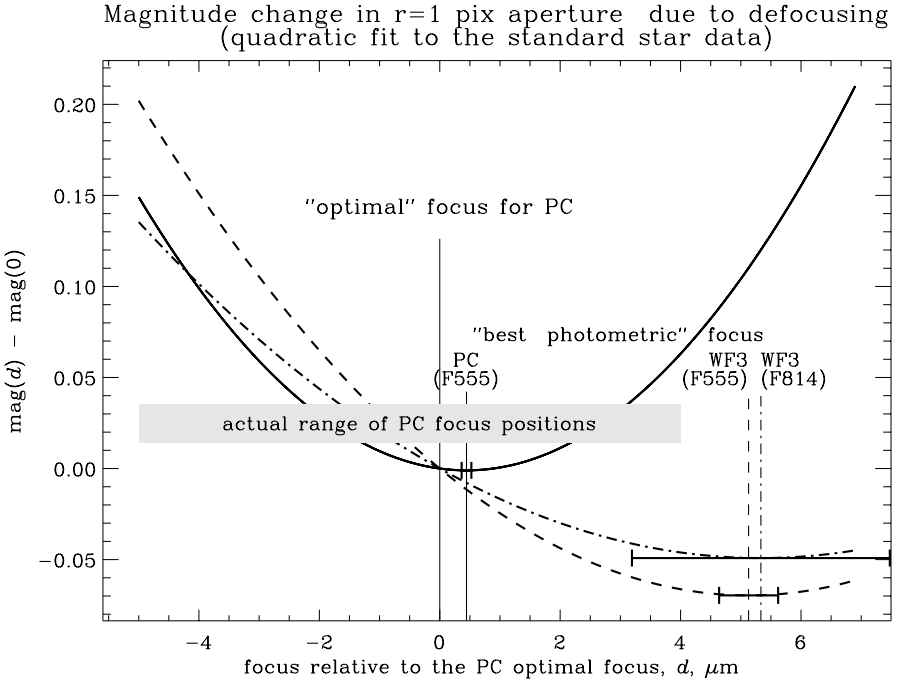

Large focus changes, with amplitudes up to 10μm, are seen occasionally (See Hasan and Bely 1993, Restoration of HST Images and Spectra II, p. 157). On May 1, 1994, and February 27, 1995, a short-lived defocusing of the telescope of up to 10μm was seen, probably due to extreme thermal conditions after the telescope was at an almost exact anti-sun pointing for an extended time. Such a defocusing causes an increase of the PSF width by about 5-10% and a significant change in its shape. This is especially evident in the PC both because of its higher resolution and its astigmatism, which makes the out-of-focus image appear elongated. The change in the PSF appears to be modeled adequately by the TinyTIM software. (See Hasan and Bely 1993, Restoration of HST Images and Spectra II, p. 157. Also see the sample PSF subtraction in Figure 7.2).

For more information, see the HST focus Web site at:

http://www.stsci.edu/hst/observatory/focus

5.8 PSF Anomaly in F1042M Filter

We note that the F1042M filter has an anomalous PSF containing additional light in a broad halo component. This is due to the CCD detector becoming transparent at these wavelengths, so that light is reflected and scattered by the back of the CCD producing a defocused halo. Figure 5.12 compares the F1042M PSF with the more normal PSF seen slightly blueward in F953N. This scattering will impact photometry in the F1042M filter relative to other filters, since a greater fraction of the counts will lie outside the 1 arcsecond diameter aperture used herein for photometry on standard stars.

Figure 5.12: Comparison of azimuthal averages for observed F1042M and F953N PSFs. Courtesy of John Krist.

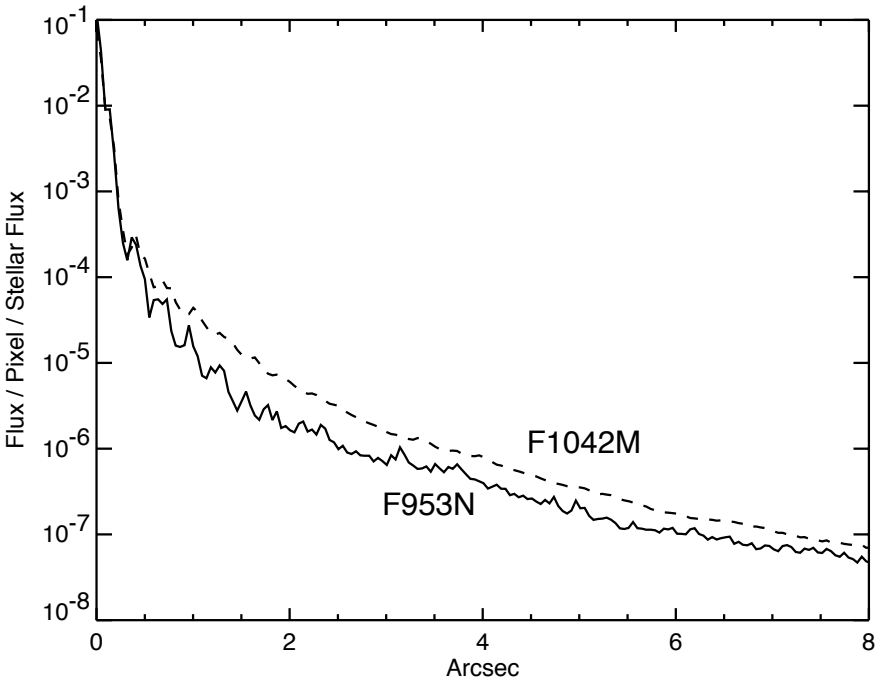

5.9 Large Angle Scattering

Analysis of the WFPC2 saturated star images indicate that the large angle scattering (>3″ from a star) is significantly higher than expected.

Three data sets were used to determine the WFPC2 scattering. The first set was from the SMOV Ghost Check Proposal 5615, in which 100-second images of δ Cas (V=2.7) were obtained at the center of each chip in F502N. The second set was a series of 6-second exposures of Vega (V=0.0) centered on WF2 through F410M (WFPC2 GTO Proposal 5205). The third set was ε Eridani (V=3.73) centered on the PC and taken through F631N (500s each) and F953N (2200s each). These were from GTO Proposal 5611.

WFPC2 scattering was determined by computing the azimuthal average and azimuthal median profiles. The regions near the diffraction spikes and saturated columns were not used. The profiles were determined using images corrected for horizontal smearing.

The measurements indicate that the average scatter in WFPC2 is an order of magnitude greater than in WF/PC-1. The increase is due to scattering in WFPC2, not due to the OTA. In the WFPC2 images, the pyramid edge shadow is not visible in the scattered light; the light is spread out to the chip edges, indicating that most of the scattering occurs after the pyramid. However, the light level in adjacent channels is back down at the WF/PC-1 levels as shown in Figure 5.13.

The scattering does not show any strong dependence on wavelength between 410 nm and 953 nm, within the uncertainties of the measurements.

The scattered light is not uniform. There are high frequency spatial structures in the form of streaks radiating outwards from the star. These features are probably both wavelength and position dependent, and so cannot be readily subtracted.

The source of the WFPC2 scattering may be the CCDs. The WF/PC-l CCDs were back illuminated and had shiny surfaces. The electrode structure was not visible over most of the wavelength range. The WFPC2 CCDs, however, are front illuminated, so the electrode structure is visible and may be scattering the light. There was a large ghost in WF/PC-l due to a reflection between the CCD and filter, but no such feature has been seen in WFPC2. The flux from this missing ghost may instead constitute part of the scatter. For more information on scattering within WFPC2 images, please see the related material in Section 7.3.

Figure 5.13: Large Angle Scattering. The proportion of the total flux in F555W falling per square arcsecond as a function of the distance from the peak of a saturated stellar image. These curves are for a target in the PC. Note the large drop in the scattered light level when looking in an adjacent camera.

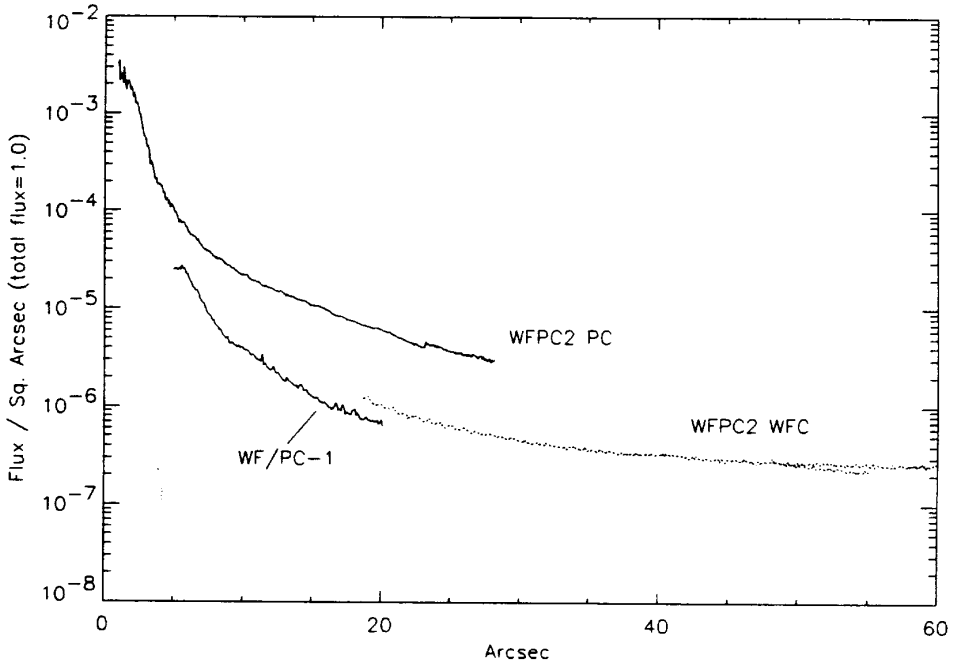

5.10 Ghost Images

Common ghost images result from internal reflections in the filters and in the field-flatteners. Two filter ghosts, caused by double (and quadruple) reflection inside the filter, are visible below and to the right of the star in Figure 5.14. The position and brightness of these ghosts varies from filter to filter, typically being most obvious in interference filters. The comatic shape of the ghost is caused by the camera optics being effectively misaligned for the light path followed by the ghost. The relative position of these ghosts does not vary much over the field.

An additional ghost is caused by an internal reflection inside the MgF_2 field flattener lens immediately in front of each CCD (see Figure 5.15). The field flattener ghost is doughnut shaped (image of OTA pupil) in the WFC, but is smaller and more disk-like on the PC. This ghost contains ~0.15% of the total energy of the star. It is positioned on a line through the CCD center and the bright star; the distance from the ghost to the CCD center is 1.25 to 1.4 times the distance from the bright star to the CCD center. This geometry results from curvature of the field flattener lens.

The large ghost image expected to be caused by reflection off the CCD back to the filter and then back to the CCD is not seen. It was deliberately eliminated in the PC by slightly tilting the CCD.

Figure 5.14: Saturated Stellar Image Showing Filter Ghosts. Intensity scale is logarithmic.

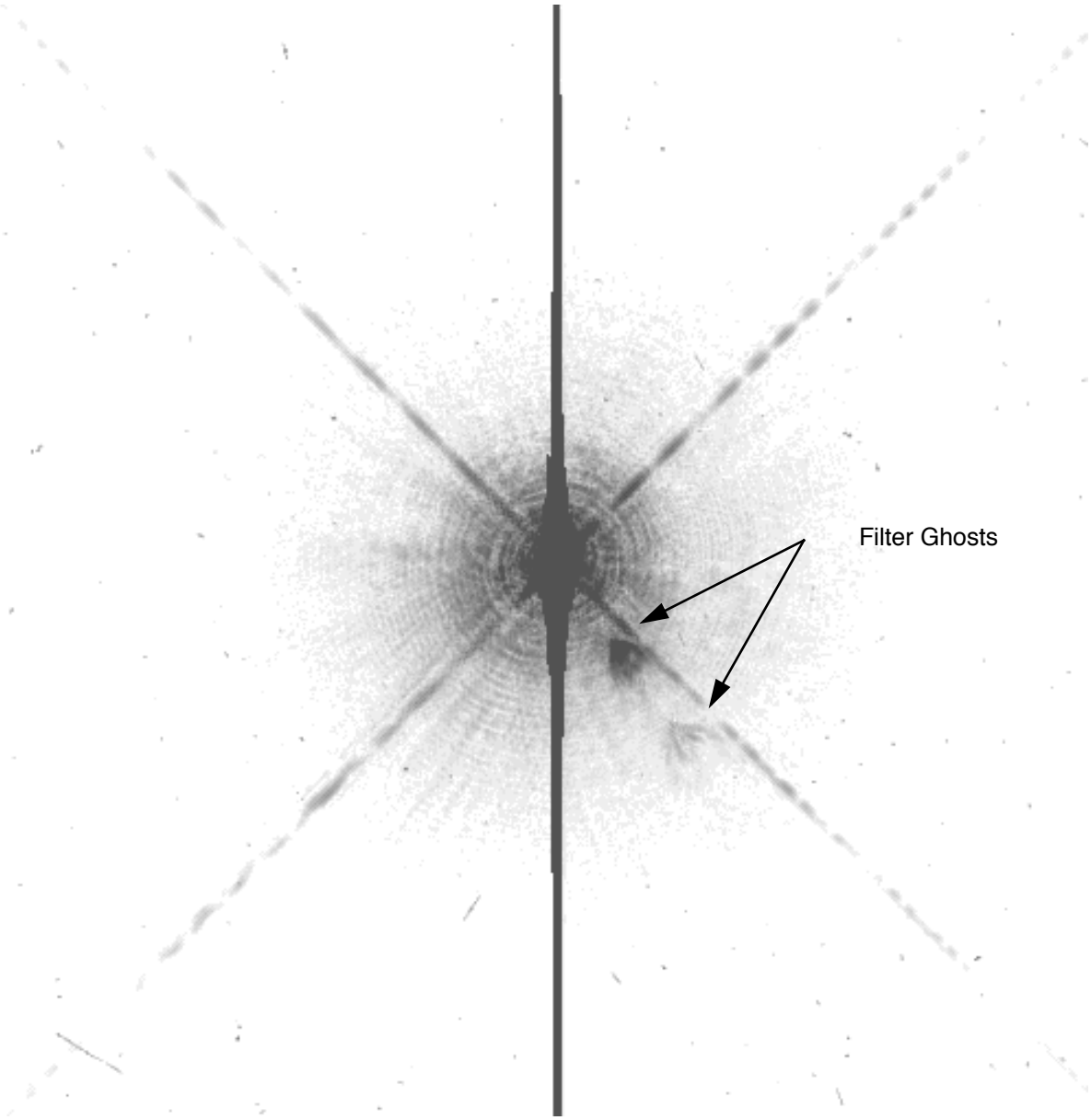

Figure 5.15: Saturated Stellar Image Showing Field Flattener Ghost on WF2.

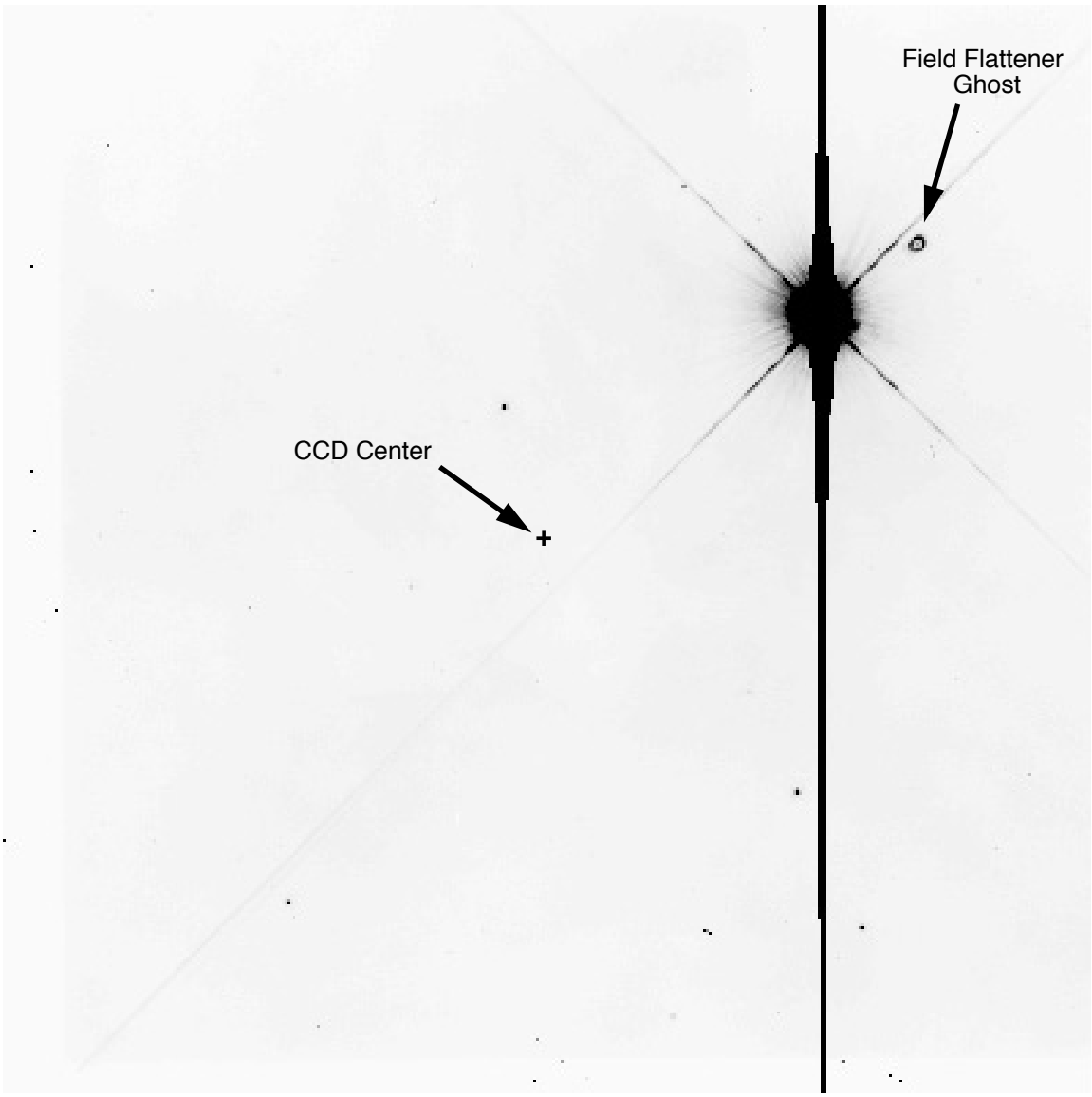

5.11 Optical Distortion

The geometric distortion of WFPC2 is complex since each individual CCD chip is integrated with its own optical chain (including corrective optics), and therefore each chip will have its own different geometric distortion. Apart from this, there is also a global distortion arising from the HST Optical Telescope Assembly (Casertano and Wiggs 2001).

Early attempts to solve the WFPC2 geometric distortion were made by Gilmozzi et al. (1995), Holtzman et al. (1995), and Casertano et al. (2001),

using third order polynomials for all chips in the PC system, i.e. the coordinates X,Y were transformed into one meta-chip coordinate system and fitted to find the offsets, rotation and scale for each of the four chips. These early meta-chip solutions failed to constrain the skew-related linear terms, which actually are responsible for ~0.25 pix residual distortion. These solutions did not have on-orbit data sets which were rotated with respect to each other.

In 2003, Anderson and King derived a substantially improved geometric distortion solution for WFPC2 in the F555W filter. First, the measured positions X_{obs},Y_{obs} were normalized over the range of (50:800) pixels excluding the pyramid edges (Baggett, S., et al. 2002) and adopting the center of the solution at (425,425) with a scale factor of 375, i.e:

$$X = (X_{obs} - 425)/375$$

$$Y = (Y_{obs} - 425)/375$$

The final solution was presented as a third-order polynomial:

$$X_g = a_1 + a_2X + a_3Y + a_4X^2 + a_5XY + a_6Y^2 + a_7X^3 + a_8X^2Y + a_9xXY^2 + a_{10}Y^3$$

$$Y_g = b_1 + b_2X + b_3Y + b_4X^2 + b_5XY + b_6Y^2 + b_7X^3 + b_8X^2Y + b_9XY^2 + b_{10}Y^3$$

where Xg and Yg are the corrected coordinates.

The coefficients of the polynomials for F555W filter are given in Table 5.6 (Anderson and King 2003).

Figure 5.16 shows the vector diagram of the geometric distortion in filter F555W.

Table 5.6: Polynomial Coefficients of the Geometric Distortion for F555W.

	APC	AWF2	AWF3	AWF4	BPC	BWF2	BWF3	BWF4
1	0.000	0.000	0.000	0.000	0.000	0.000	0.000	0.000
2	0.000	0.000	0.000	0.000	0.418	0.051	-0.028	0.070
3	0.000	0.000	0.000	0.000	-0.016	-0.015	-0.036	0.059
4	-0.525	-0.624	-0.349	-0.489	-0.280	-0.038	-0.027	-0.050
5	-0.268	-0.411	-0.353	-0.391	-0.292	-0.568	-0.423	-0.485
6	-0.249	-0.092	0.009	-0.066	-0.470	-0.444	-0.373	-0.406
7	-1.902	-1.762	-1.791	-1.821	-0.011	0.003	0.004	-0.015
8	0.024	0.016	0.006	0.022	-1.907	-1.832	-1.848	-1.890
9	-1.890	-1.825	-1.841	-1.875	0.022	0.011	0.006	0.022
10	-0.004	0.010	0.021	-0.006	-1.923	-1.730	-1.788	-1.821

Figure 5.16: The geometric distortion map for F555W filter using the Anderson and King solution (2003). The size of the longest arrows are 6.29 pixel for the PC (in PC pixels) and ~6 pixel for WF cameras (in WF pixels). The panels correspond to PC - upper right; WF2 - upper left; WF3 - lower left and WF4 - lower right. The size of the residuals are scaled by a factor of 10 relative to the pixel coordinates.

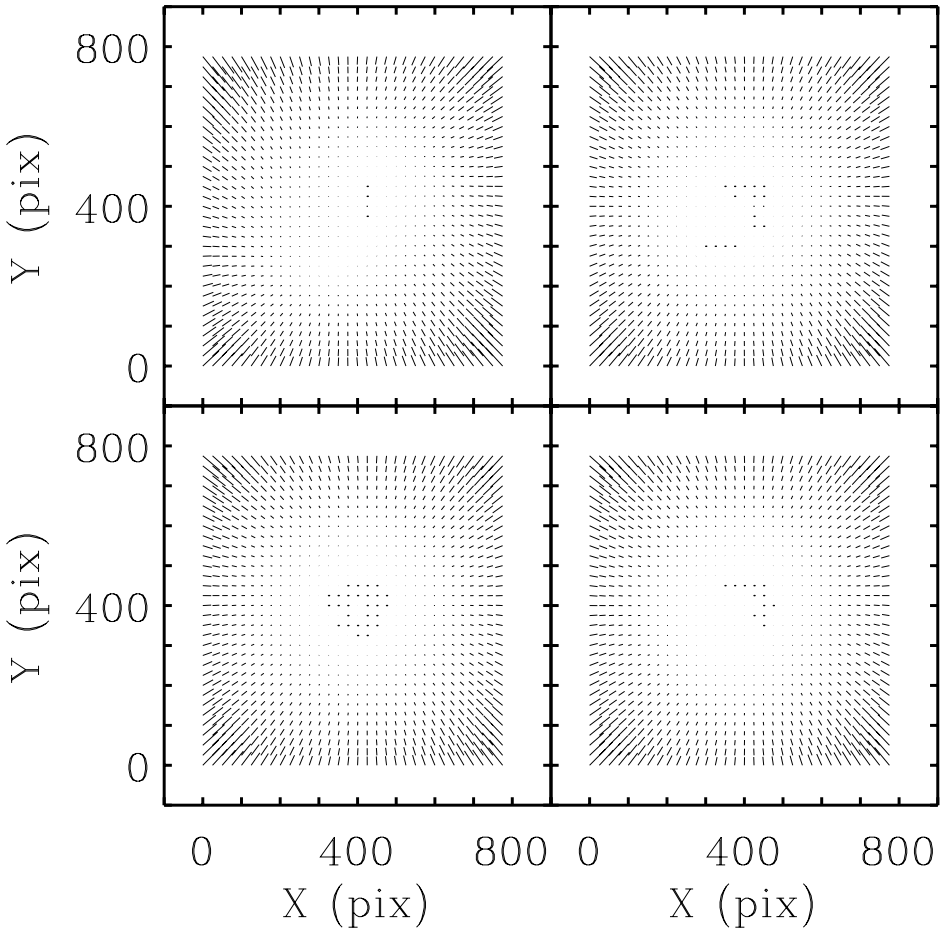

Trauger et al. (1995) showed that the geometric distortion for WFPC2 also depends on wavelength. This is due to the refractive MgF_2 field-flattener lens in front of each CCD. They computed the wavelength-dependent geometric distortion by analyzing the results of ray tracing, where the coefficients were represented as a quadratic interpolation function of the refractive index of the field-flattener lenses. Kozhurina-Platais et al. (2003), using the Anderson and King methodology (2003), derived the geometric distortion solutions for two other filters: F814W and F300W. Figure 5.17 presents the difference in distortion between F555W and F300W, which clearly indicates a large amount of distortion in F300W, especially at the corners of the chips. An average increase of distortion in the F300W filters is ~3%, or 0.18 pixels in PC and 0.25 pixels in WF cameras. In contrast, there is only a small ~1% difference in distortion between F555W and F814W. Figure 5.18 presents the difference between the filters F555W and F814W. The coefficients of the polynomials for filters F300W and F814W are given in Tables 5.7 and 5.8.

Figure 5.17: Difference in the distortion correction between F555W and F300W (F555W-F300W). The size of the longest arrows are 0.18 pixel for PC (in PC pixel) and 0.25 pixel for WF cameras (in WF pixels). The panels are the same as in Figure 5.16, except the size of the residuals are scaled by a factor of 300.

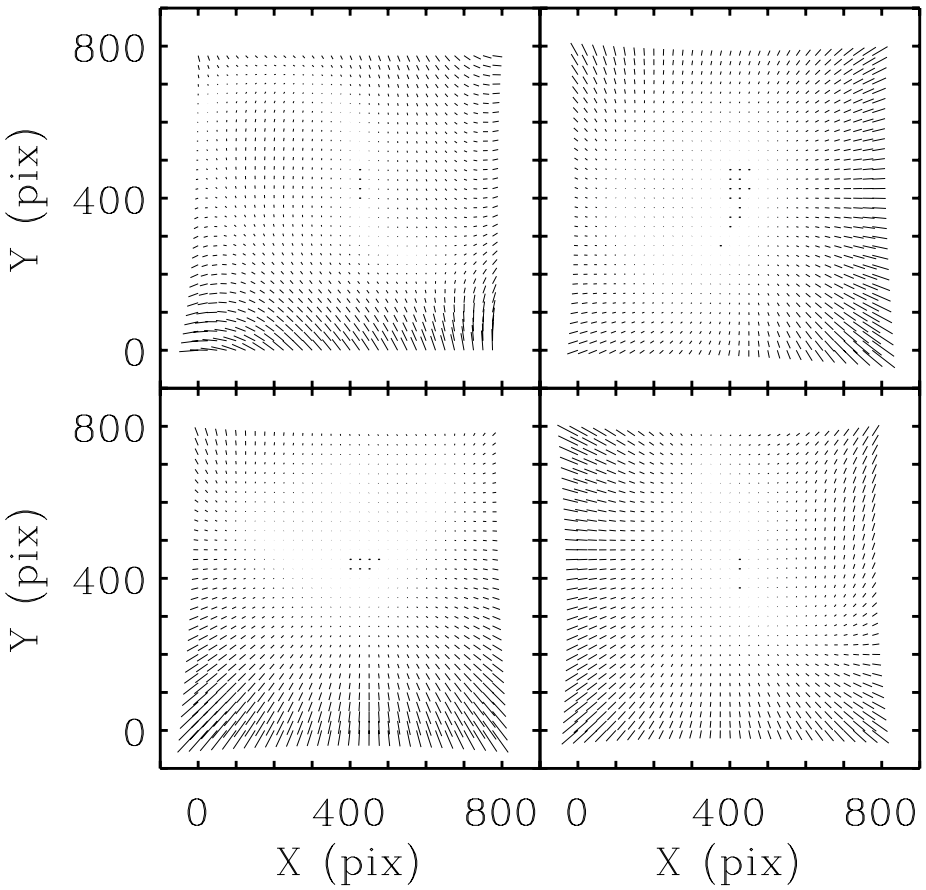

Figure 5.18: Difference in the distortion correction between F555W and F814W. The small amount of these differences along with fairly random pattern changing from chip to chip indicate that the differences are very small, if present at all. The size of the longest arrow is 0.04 PC pixels for the PC, and ~0.05 pixels for the WF cameras. The panels are the same as in Figure 5.17, except the size of the residuals are scaled by a factor of 300.

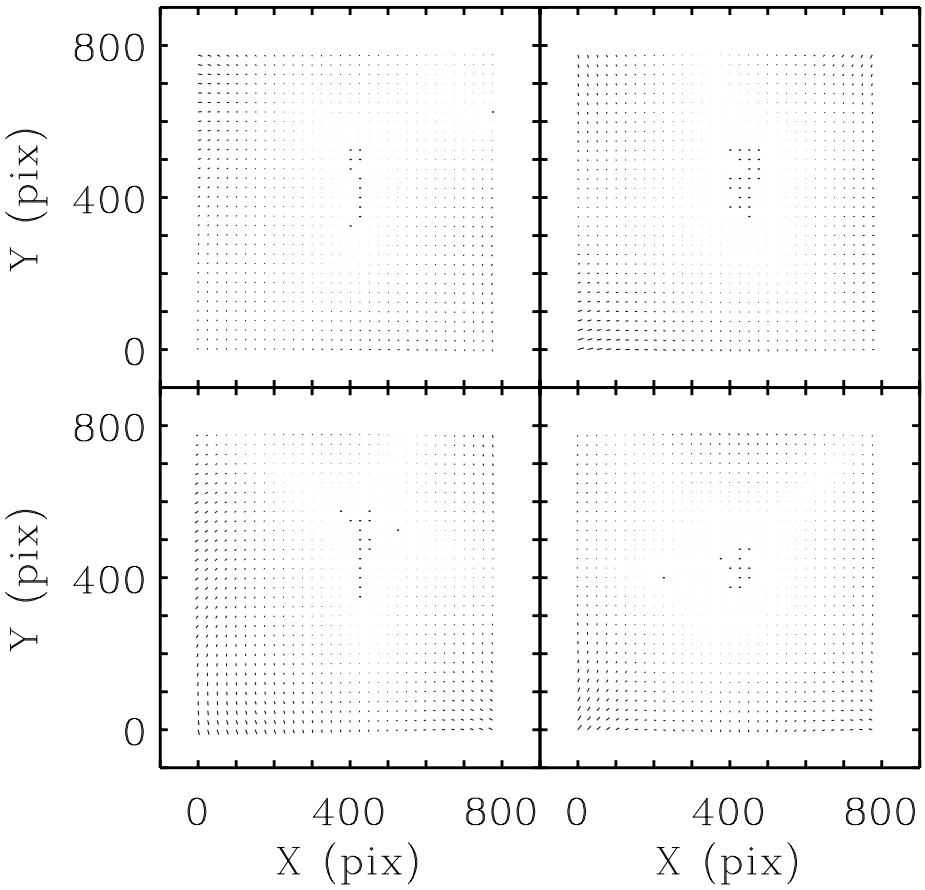

Application of the distortion coefficients are straight forward. To correct for geometric distortion, the measured raw coordinates should be normalized as in the first set of equations on page 151. Then the second set of equations in Section 5.11 should be used, employing the coefficients from Table 5.6, Table 5.7, or Table 5.8, depending on the filter used. Finally, the corrected coordinates Xg, Yg should then be shifted back to the natural system of the detector, with proper orientation and scale, specifically:

$$X = (X_g - 425)$$

$$Y = (Y_g - 425)$$

The constant terms a1 and b1 are offsets (or zero-points) between any two frames and can be ignored for most purposes. The linear coefficients a2 and b3 represent the plate scale and can be found in Anderson and King

(2003) and Kozhurina-Platais et al. (2003). The FORTRAN code developed by Anderson which correct the measured coordinates X and Y can be down-loaded from

http://www.stsci.edu/hst/wfpc2/analysis/andersonking_distortion_routine.html

The same program could be used to correct for distortion in filters F300W and F814W, using the coefficients from Table 5.7 or Table 5.8, respectively.

Table 5.7: Polynomial Coefficients of the Geometric Distortion for F300W.

	APC	AWF2	AWF3	AWF4	BPC	BWF2	BWF3	BWF4
1	0.374±0.047	0.149±0.010	-0.142±0.014	-0.072±0.012	0.267±0.021	-0.164±0.014	-0.113±0.011	0.174±0.014
2	0.999±0.091	0.999±0.009	0.999±0.009	0.999±0.015	0.480±0.069	0.042±0.010	-0.028±0.008	0.048±0.006
3	0.055±0.032	0.001±0.009	0.006±0.008	-0.027±0.009	0.999±0.101	0.999±0.010	0.999±0.013	0.999±0.012
4	-0.547±0.035	-0.687±0.009	-0.363±0.005	-0.469±0.007	-0.298±0.113	-0.043±0.006	-0.019±0.005	-0.078±0.005
5	-0.255±0.035	-0.394±0.008	-0.299±0.007	-0.386±0.010	-0.265±0.051	-0.592±0.011	-0.419±0.005	-0.489±0.006
6	-0.235±0.078	-0.098±0.007	0.015±0.008	-0.079±0.005	-0.479±0.052	-0.453±0.018	-0.335±0.006	-0.386±0.008
7	-1.937±0.139	-1.837±0.019	-1.838±0.011	-1.874±0.022	-0.079±0.126	0.006±0.015	0.007±0.008	-0.028±0.008
8	0.003±0.067	0.034±0.016	0.003±0.013	0.054±0.012	-1.913±0.113	-1.877±0.024	-1.891±0.014	-1.950±0.014
9	-1.909±0.056	-1.869±0.010	-1.875±0.015	-1.936±0.009	-0.021±0.083	0.040±0.016	0.016±0.008	0.049±0.018
10	-0.039±0.064	0.001±0.007	0.021±0.012	-0.011±0.017	-1.863±0.148	-1.773±0.018	-1.846±0.016	-1.852±0.014

Table 5.8: Polynomial Coefficients of the Geometric Distortion for F814W.

	APC	AWF2	AWF3	AWF4	BPC	BWF2	BWF3	BWF4
1	-0.029±0.009	0.075±0.009	0.081±0.003	0.046±0.006	0.048±0.007	0.075±0.004	0.055±0.008	-0.015±0.006
2	1.000±0.017	1.000±0.007	1.000±0.004	1.000±0.004	0.428±0.016	0.049±0.004	-0.037±0.004	0.066±0.004
3	0.002±0.014	-0.009±0.004	-0.011±0.002	-0.010±0.003	1.000±0.018	1.000±0.003	1.000±0.007	1.000±0.004
4	-0.526±0.009	-0.636±0.005	-0.344±0.002	-0.494±0.003	-0.281±0.005	-0.032±0.003	-0.018±0.002	-0.055±0.002
5	-0.264±0.008	-0.407±0.003	-0.365±0.004	-0.404±0.003	-0.305±0.008	-0.566±0.003	-0.401±0.003	-0.485±0.002
6	-0.253±0.009	-0.092±0.003	0.009±0.002	-0.059±0.002	-0.465±0.007	-0.439±0.004	-0.371±0.002	-0.408±0.003
7	-1.891±0.019	-1.769±0.005	-1.805±0.006	-1.832±0.004	-0.011±0.015	0.003±0.006	0.003±0.006	-0.013±0.003
8	0.005±0.013	0.027±0.004	0.005±0.005	0.017±0.005	-1.912±0.017	-1.809±0.005	-1.834±0.005	-1.858±0.004
9	-1.895±0.013	-1.806±0.004	-1.822±0.005	-1.853±0.005	0.014±0.017	0.017±0.005	0.009±0.003	0.029±0.006
10	0.004±0.016	0.016±0.004	0.018±0.004	0.000±0.003	-1.917±0.018	-1.735±0.007	-1.799±0.005	-1.837±0.006

5.11.1 Pixel Area Correction

Geometric distortion not only affects astrometry but photometry as well, since it induces an apparent variation in surface brightness across the field of view. The effective pixel area can be derived from the geometric distortion coefficients, and is presented in Figure 5.19. The pixel area map correction is necessary since the flat fields are uniformly illuminated, and do not explicitly conserve the total integrated counts for a discrete target, whereas the geometric distortion conserves the total counts and redistributes the counts on the CCD chip. Thus, for precise point-source photometry, the flat fielded images require a correction for the pixel area: they should be multiplied by the pixel area map so as to restore the proper total counts of the target. The pixel area map is available as a fits file in the HST archive (f1k1552bu_r9f.fits). (Some additional discussion of the pixel area correction can be found in the ACS Instrument Handbook for Cycle 14.)

Figure 5.19: A map of the effective pixel areas of the WFPC2 chips. The areas are normalized to unity at the center of each chip. The contours are approximately at quarter percent levels. The panel corresponds to PC -upper right; WF2 - upper left; WF3 - lower left and WF4 - lower right.

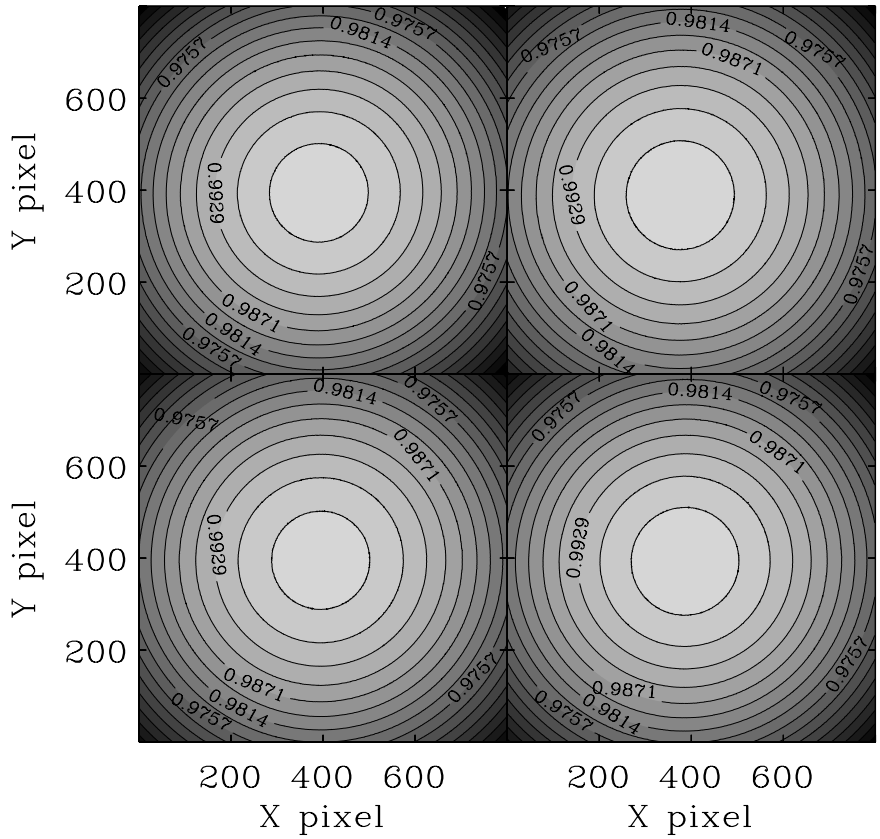

5.11.2 34th-Row Defect

Every 34th row on the CCD is approximately 3% too narrow due to a manufacturing error in producing the CCDs. This defect impacts both precision astrometry and photometry. A discussion of the astrometric effects may be found in Anderson and King 1999. Details of the manufacturing defect and photometric impacts are discussed further in Section 4.7.

5.11.3 Geometric Distortion Closeout Calibrations

As WFPC2 approaches the end of its operation, a complete study of the short-, medium-, and long- term geometric distortion solution is being studied as a function of several quantities (temperature, velocity, etc.). In so doing, the superior astrometric capabilities of the ACS/WFC will be utilized. Indeed, the ACS/WFC observations provide an ideal astrometric reference frame to conduct a number of investigations.

Four WFPC2 calibration fields were selected for this purpose: two in NGC 5139 and two in NGC 104. A few thousand WFPC2 images, in several filters, were taken in total. There are also several ACS/WFC observations available for three of these fields.

The main purpose of these efforts is to extend and update the work done by Anderson and King (2003, PASP, 115, 113 - hereafter AK03) which made use of data up to 2002, and to investigate unexplained systematic errors found there.

The full results will be presented in a WFPC2 Instrument Science Report. Here, the following preliminary results are presented.

Chip Motions

The most important information needed to bring all of the WFPC2 chips into a common reference frame is the measurement of the relative motions of the chips. These motions can be up to 5 pixels and need to be properly calibrated in order to build images in a meta-chip system as is being planned with pydrizzle. The work done by Anderson and King only covers the epoch up to the beginning of the ACS era, but since a chip can move up to 0.4 pixel per year, it becomes fundamental to monitor these relative motions of the chips.

The chip motions will be extended up to early 2008. An additional entry for 2004 has been added to Table 3 from AK03 and is shown in Table 5.9.

Table 5.9: Interchip Transformation Parameters

Parameter	PC1	WF2	WF3	WF4
α_k	0.45729	1.00020	1.00000	1.00048
θ_k(deg)	180.178	269.682	0.000	90.551
X_0(1994-)	-140.5	+430.2	+425.0	-346.7
X_0(1994+)	-140.2	+430.1	+425.0	-347.2
X_0(1998)	-139.4	+430.0	+425.0	-346.1
X_0(2002)	-138.8	+430.3	+425.0	-345.5
X_0(2004)[a]	-138.6	+430.4	+425.0	-345.3
X_0(2007)	-138.6	+430.3	+425.0	-345.9
X_0(2008)	-138.5	+430.3	+425.0	-345.9
Y_0(1994-)	-123.3	-328.4	+425.0	+423.9
Y_0(1994+)	-123.3	-328.8	+425.0	+423.7
Y_0(1998)	-121.5	-327.9	+425.0	+424.2
Y_0(2002)	-120.8	-327.2	+425.0	+424.4
Y_0(2004)[a]	-120.5	-327.1	+425.0	+424.5
Y_0(2007)	-120.8	-327.4	+425.0	+424.3
Y_0(2008)	-120.9	-327.5	+425.0	+424.2

a. The preliminary precision is +/- 0.2 pixel

New observations were collected in February and March of 2008 and are in the process of being reduced and analyzed in order to complete the update of the table.

Plate Scale

Adopting an average plate scale of 49.7248 +/- 0.0006 mas/pixel for ACS/WFC (see ACS ISR 07-07), it was possible to independently link the scale of the WFPC2 chips, for eight filters, to this value. The results are given in Table 5.10.

Table 5.10: WFPC2 Plate Scales as a Function of the ACS/WFC Plate Scale

Filter	PC1[a]	WF2[a]	WF3[a]	WF4[a]
F218W	45.4274	99.3761	99.3602	99.4059
F300W	45.5134	99.5531	99.5372	99.5791
F336W	45.5326	99.6010	99.5810	99.6269
F439W	45.5468	99.6110	99.5930	99.6409
F450W	45.5518	99.6269	99.6064	99.6509
F555W	45.5547	99.6389	99.6190	99.6669
F606W	45.5543	99.6150	99.6090	99.6469
F675W	45.5681	99.6749	99.6489	99.7008
F814W	45.5743	99.6789	99.6529	99.7048

a. Units are mas/pixel (+/- 0.005 mas for the PC and +/- 0.010 mas for the WF chips)

CHAPTER 6:

System Throughput and SNR / Exposure Time Estimation

In this chapter . . .

6.1 System Throughput

A decision on a suitable exposure time will require the combination of

- The overall spectral response of the system (Figure 2.4).
- The spectral transmission of the filters (Chapter 3 and Appendix A.1).
- The spectral energy distribution and spatial profile of the target.

- The pixel response function and pixel size of the instrument (Section 5.4 and Section 2.3, respectively).
- Criteria for specifying desirable charge levels.

When the transmissions of filters $T(\lambda)$ are combined with the overall system response $Q(\lambda)$, we obtain detector quantum efficiency (DQE) plots (electrons-per-photon as a function of λ) for each filter. These DQE plots link the output of the CCD to the photon flux at the input to an unobscured 2.4 m telescope.

These calibrations exist in the STScI Calibration Data Base, and are accessible with the STSDAS SYNPHOT package or with the XCAL software. The XCAL and SYNPHOT Users Guides should be consulted for further details.

The throughput calibration presented here is accurate to at least 10%—which is sufficient for planning observations, but not for the analysis of many programs. Investigators wishing to do photometry on WFPC2 images should refer to the *HST Data Handbook* for an explanation of the conventions used in determining WFPC2 zeropoints and should use the zeropoints given in Table 5.1 of the WFPC2 Data Handbook (Version 4.0, January 2002). For the most accurate and up-to-date calibrations, users should examine the on-line version of the *Data Handbook* to verify that no numbers of interest have changed since the last paper publication. A recent study has examined the issue of WFPC2 zeropoints (Heyer, et al. 2004, WFPC2 ISR 04-01) and recommends using the zeropoints of Dolphin, found at:

http://purcell.as.arizona.edu/wfpc2_calib/2004_12_20.html/

In Table 6.1 the dimensionless efficiency and the mean wavelength for each filter are tabulated together with the effective width, the equivalent Gaussian dimensionless width, the maximum transmission, the derivative of the mean wavelength with respect to spectral index, the pivot wavelength, average wavelength, and wavelength of maximum transmission. The parameters are defined as follows. The dimensionless efficiency is

$$\int Q(\lambda)T(\lambda)d\lambda/\lambda$$

The mean wavelength is defined in Schneider, Gunn, and Hoessel (1993, ApJ 264, 337).

$$\bar{\lambda} = \exp\left[\frac{\int Q(\lambda)T(\lambda)\log_e(\lambda)d\lambda/\lambda}{\int Q(\lambda)T(\lambda)d\lambda/\lambda}\right]$$

This rather unconventional definition has the property that the correspondingly defined mean frequency is just $c/\bar{\lambda}$. It is in some sense

halfway between the conventional frequency mean and the wavelength mean.

The pivot wavelength is defined as

$$\lambda_p = \left[\frac{\int Q(\lambda) T(\lambda) \lambda d\lambda}{\int Q(\lambda) T(\lambda) d\lambda / \lambda} \right]^{1/2}$$

The average wavelength $\langle \lambda \rangle$ is that defined in the simplest sense

$$\langle \lambda \rangle = \frac{\int Q(\lambda) T(\lambda) \lambda d\lambda}{\int Q(\lambda) T(\lambda) d\lambda}$$

The effective dimensionless Gaussian width is defined implicitly by

$$\sigma^2 = \left[\frac{\int Q(\lambda) T(\lambda) \left[\log_e \left(\frac{\lambda}{\bar{\lambda}} \right) \right]^2 \frac{d\lambda}{\lambda}}{\int Q(\lambda) T(\lambda) \frac{d\lambda}{\lambda}} \right]$$

The effective width of the bandpass is

$$\delta\bar{\lambda} = 2[2\log_e 2]^{1/2} \sigma\bar{\lambda}$$

We note that all of the above integrals have been evaluated over the range $\lambda = \bar{\lambda}(1 - 5\sigma)$ to $\bar{\lambda}(1 + 5\sigma)$ so as to avoid unrealistic contributions from imperfect blocking far from the bandpass. Where necessary, the integration range was further constrained to the range 1000Å to 11000Å.

Parameters QT_{max} and λ_{max} are the respective parameters at the peak throughput.

The parameter $d\bar{\lambda}/d\alpha$ is defined in Section 6.3.2.

The final two columns in Table 6.1 are defined as follows. In the next-to-last column $m_{e/sec}$ is the zero-point magnitude for 1 e^- s^{-1} (with AB_v=0). The final column gives t_{wfsky}, which is the exposure time (in seconds) needed to make the sky noise equal to 5 e^- RMS (i.e. ~read noise) in the WFC for a sky level of V=23.3 mag arcsec^{-2}.

Table 6.1: System Efficiencies and Zeropoints. See Section 6.1 for definitions. [a]

Filter	$\int QT\, d\lambda/\lambda$	$\bar{\lambda}$	$\delta\bar{\lambda}$	σ	QT_{max}	$d\bar{\lambda}/d\alpha$	λ_p	$\langle\lambda\rangle$	λ_{max}	$m_{e/sec}$	t_{wfsky}
F122M	0.00010	1305.6	239.1	0.0778	0.00107	7.90	1321.6	1326.2	1260	18.48	1.1E+07
F130LP	0.10175	4285.9	4755.4	0.4712	0.13936	951.53	5814.6	6137.5	6398	26.01	1.9E+02
F160BW	0.00024	1473.0	449.1	0.1295	0.00074	24.69	1521.9	1534.9	1400	19.46	9.2E+05
F165LP	0.10091	4494.4	4528.9	0.4279	0.14066	823.00	5852.9	6155.6	6400	26.00	1.9E+02
F170W	0.00057	1707.7	545.1	0.1355	0.00169	31.37	1769.7	1786.3	1857	20.38	2.3E+06
F185W	0.00038	1941.6	334.3	0.0731	0.00196	10.38	1962.3	1967.7	1940	19.93	7.3E+06
F218W	0.00059	2177.4	395.0	0.0770	0.00286	12.92	2203.1	2209.6	2242	20.42	5.4E+06
F255W	0.00080	2577.7	395.1	0.0651	0.00462	10.92	2599.4	2604.9	2536	20.76	2.6E+06
F300W	0.00571	2919.8	740.2	0.1077	0.01974	33.84	2986.8	3004.3	2804	22.89	6.7E+04
F336W	0.00497	3329.3	374.3	0.0477	0.03558	7.59	3344.4	3348.2	3454	22.74	3.6E+04
F343N	0.00003	3426.9	23.5	0.0029	0.00397	0.03	3426.9	3427.0	3432	17.27	4.7E+06
F375N	0.00008	3732.2	24.4	0.0028	0.00983	0.03	3732.3	3732.3	3736	18.24	1.1E+06
F380W	0.00779	3940.5	681.8	0.0735	0.03752	21.27	3982.7	3993.1	3999	23.22	7.1E+03
F390N	0.00031	3888.0	45.0	0.0049	0.01999	0.09	3888.2	3888.2	3889	19.72	2.1E+05
F410M	0.00183	4085.7	146.8	0.0153	0.04027	0.95	4087.6	4088.1	4097	21.65	2.7E+04
F437N	0.00022	4369.1	25.2	0.0025	0.03065	0.03	4369.2	4369.2	4368	19.37	1.7E+05
F439W	0.00576	4292.6	473.2	0.0468	0.03903	9.41	4311.3	4316.0	4318	22.90	7.1E+03
F450W	0.01678	4483.6	950.8	0.0901	0.08671	36.36	4555.4	4573.0	5069	24.06	2.0E+03
F467M	0.00250	4667.7	166.5	0.0151	0.05582	1.07	4669.8	4670.4	4731	21.99	1.2E+04
F469N	0.00027	4694.4	25.0	0.0023	0.03784	0.02	4694.4	4694.4	4698	19.56	1.1E+05
F487N	0.00034	4865.1	25.9	0.0023	0.04811	0.02	4865.2	4865.2	4864	19.81	8.1E+04
F502N	0.00041	5012.4	26.9	0.0023	0.05800	0.03	5012.4	5012.4	5009	20.04	5.9E+04
F547M	0.01342	5467.8	483.2	0.0375	0.11515	7.70	5483.3	5487.1	5558	23.81	1.6E+03
F555W	0.03012	5336.8	1228.4	0.0977	0.11194	50.99	5439.0	5464.6	5550	24.69	7.3E+02
F569W	0.02343	5582.3	965.7	0.0735	0.11518	30.13	5642.0	5657.4	5549	24.42	8.9E+02
F588N	0.00145	5893.2	49.0	0.0035	0.13078	0.07	5893.5	5893.5	5896	21.40	1.3E+04
F606W	0.04513	5860.1	1502.4	0.1089	0.14220	69.46	5996.8	6030.8	6185	25.13	4.2E+02
F622W	0.02882	6137.4	917.1	0.0635	0.14096	24.71	6186.2	6198.6	6405	24.64	6.3E+02
F631N	0.00084	6306.4	30.9	0.0021	0.12632	0.03	6306.4	6306.4	6301	20.81	2.1E+04
F656N	0.00049	6563.8	21.5	0.0014	0.11273	0.01	6563.8	6563.8	6562	20.21	3.5E+04

Table 6.1: System Efficiencies and Zeropoints. See Section 6.1 for definitions. [a]

Filter	$\int QT\, d\lambda/\lambda$	$\bar{\lambda}$	$\delta\bar{\lambda}$	σ	QT_{max}	$d\bar{\lambda}/d\alpha$	λ_p	$\langle\lambda\rangle$	λ_{max}	$m_{e/sec}$	t_{wfsky}
F658N	0.00068	6590.8	28.5	0.0018	0.11443	0.02	6590.8	6590.8	6591	20.58	2.5E+04
F673N	0.00113	6732.2	47.2	0.0030	0.11978	0.06	6732.3	6732.3	6730	21.12	1.4E+04
F675W	0.02344	6677.4	866.8	0.0551	0.13604	20.29	6717.4	6727.6	6624	24.42	7.0E+02
F702W	0.03429	6818.0	1384.7	0.0862	0.14185	50.71	6918.5	6944.3	6513	24.83	4.6E+02
F785LP	0.00900	8627.9	1381.2	0.0680	0.04831	39.88	8707.0	8727.5	8226	23.38	1.3E+03
F791W	0.01694	7811.2	1230.7	0.0669	0.09530	34.97	7880.6	7898.4	7397	24.07	7.6E+02
F814W	0.01949	7904.8	1539.4	0.0827	0.10343	54.06	8012.2	8040.3	7255	24.22	6.5E+02
F850LP	0.00473	9086.1	1037.5	0.0485	0.03939	21.37	9128.8	9139.8	8810	22.68	2.4E+03
F953N	0.00016	9544.7	52.5	0.0023	0.02213	0.05	9544.9	9545.0	9525	19.00	6.9E+04
F1042M	0.00017	10220.5	448.9	0.0187	0.00481	3.56	10227.6	10229.4	10110	19.10	6.0E+04
FQUVN-A	0.00033	3764.4	73.2	0.0083	0.01326	0.26	3764.5	3764.6	3801	19.78	2.5E+05
FQUVN-B	0.00030	3829.3	57.3	0.0064	0.01557	0.15	3829.5	3829.6	3828	19.68	2.4E+05
FQUVN-C	0.00037	3912.6	59.5	0.0065	0.01900	0.16	3912.9	3913.0	3909	19.92	1.7E+05
FQUVN-D	0.00047	3991.8	63.6	0.0068	0.02329	0.18	3992.2	3992.3	3989	20.17	1.2E+05
FQCH4N-A	0.00076	5435.3	34.4	0.0027	0.09537	0.04	5435.4	5435.4	5442	20.70	2.9E+04
FQCH4N15-B	0.00088	6199.2	33.8	0.0023	0.12242	0.03	6199.4	6199.4	6202	20.85	2.0E+04
FQCH4N33-B	0.00087	6199.3	33.8	0.0023	0.12165	0.03	6199.4	6199.4	6202	20.85	2.0E+04
FQCH4N-C	0.00070	7278.5	38.1	0.0022	0.10275	0.04	7278.5	7278.5	7278	20.60	2.1E+04
FQCH4N-D	0.00021	8930.2	54.9	0.0026	0.02917	0.06	8930.2	8930.2	8930	19.31	5.0E+04
POLQ_par	0.06695	4978.4	4226.0	0.3605	0.09998	646.91	6099.9	6355.5	6493	25.56	–
POLQ_per	0.01494	6257.6	5233.7	0.3552	0.04268	789.39	7613.6	7843.4	8001	23.93	–

a. All values have been computed using the WF3 chip, except for the Quad filters.

6.2 On-Line Exposure Time Calculator

We note that most of the calculations below are incorporated in the on-line WFPC2 Exposure Time Calculator (ETC) program, which is available on the WFPC2 web pages at:

http://www.stsci.edu/hst/wfpc2/software/wfpc2-etc.html.

To use this program, the user fills out an HTML form giving the target information (magnitude, color, and reddening), camera configuration (PC or WFC, desired gain setting, and filter), and either the exposure time or the desired signal-to-noise ratio. There are separate HTML forms for point sources, extended sources, point sources with a diffuse stellar background, and extended sources on a diffuse stellar background. After filling out the form the user then clicks on "calculate" and the program returns the resulting signal-to-noise ratio if the exposure time was specified, or vice versa. Examples of completed HTML forms and results are shown in Section 6.7. Note that clicking on any colored text on the form while viewing the web page will give a description of that item.

The ETC program handles sources with stellar spectra, power law sources, and emission line sources; point sources and extended sources; and sources superposed on a diffuse stellar background. The latest version (V4.0) includes calculations of exposure times and/or signal-to-noise ratios for point sources (plus background) using either the traditional "optimal PSF weighting" method or simple aperture photometry in a fixed aperture radius specified by the user. The latter option is more appropriate when comparing with the ACS ETC, which assumes the use of aperture photometry as a default.

In addition, the ETC allows for a flexible specification of the sky background. There are now three options. The first option uses a rough estimate of "average" or "high" or "low" sky background conditions. The second option estimates the sky background based on the position of the target and (optionally) an estimate for the heliocentric longitude of the target (sun angle). The last option allows the user to explicitly provide a value for the sky background, in magnitudes per square arcsecond. Finally, the program also returns advice on CR-SPLITing, use of CLOCKS=YES, and warnings about saturation, if appropriate. Results are typically accurate to a few percent.

While observers should familiarize themselves with the material below, most will find the ETC program faster and easier to use for actual calculations. The ETC program will also be updated to reflect any changes in instrument performance, so observers can be assured of up-to-the-minute information.

6.3 Target Count Rates

We now consider estimation of count rates for objects with stellar, power law, and emission line spectra.

6.3.1 Count Rates for Stellar Sources

To estimate the number of electrons collected from a point source of apparent visual magnitude V, one can use the equation:

$$N = 2.5 \times 10^{11} \cdot t \cdot [\int Q(\lambda) T(\lambda) d\lambda / \lambda] \times 10^{-0.4(V + AB_\nu)} \quad (6.1)$$

where t is the exposure time in seconds, the QT integral is given in Table 6.1, and AB_ν is given in Table 6.2 as a function of spectral type and wavelength for some example spectral energy distributions. The quantity AB_ν is a color-dependent correction from V magnitude to AB magnitude at frequency ν. The AB magnitude system is defined as (Oke and Gunn 1983)

$$AB = V + AB_\nu = -2.5 \cdot \log F_\nu - 48.60$$

where F_ν is the flux in erg cm^{-2} s^{-1} Hz^{-1}.

Table 6.2: AB_ν as a Function of Wavelength. AB_ν is defined as a color-dependent correction from V magnitude to AB magnitude at frequency ν. Wavelength (Å) runs along the top; spectral classes run down the left most column. The second column contains B-V. For more information, see Section 6.3.

	B-V	1500	2000	2500	3000	3500	4000	4500	5000	6000	7000	8000	9000	10000
sky	1.10	2.45	5.46	5.46	3.12	2.00	1.03	0.55	0.18	-0.11	-0.33	-0.55	-0.65	-0.75
B0	-0.31	-1.60	-1.50	-1.20	-0.78	-0.62	-0.46	-0.36	-0.22	0.16	0.46	0.76	0.96	1.17
A0	0.00	2.22	1.35	1.11	1.21	1.00	-0.23	-0.16	-0.09	0.11	0.22	0.33	0.36	0.4
F0	0.27	7.22	4.10	3.11	1.99	1.38	0.29	0.06	0.03	0.03	0.05	0.08	0.09	0.1
G0	0.58	8.9	6.35	4.61	2.46	1.63	0.67	0.26	0.08	-0.04	-0.12	-0.21	-0.23	-0.25
K0III	1.07	13	10.3	8.11	5.46	2.13	1.16	0.46	0.2	-0.24	-0.42	-0.61	-0.66	-0.72
M0III	1.60	15	12.3	9.36	6.21	4.63	2.26	0.96	0.51	-0.46	-0.76	-1.06	-1.12	-1.19
gE	1.00	6.82	6.41	5.43	3.63	2.49	1.40	0.55	0.21	-0.19	-0.52	-0.81	-1.07	-1.29
Sa	0.80	5.40	4.80	4.10	3.00	2.01	1.12	0.44	0.19	-0.17	-0.44	-0.7	-0.95	-1.16
Sbc	0.60	4.03	3.18	2.86	2.46	1.54	0.84	0.34	0.17	-0.14	-0.37	-0.6	-0.84	-1.04
Scd	0.45	2.67	2.29	2.15	1.76	1.35	0.65	0.28	0.13	-0.11	-0.26	-0.39	-0.47	-0.58
Ir I	0.30	1.77	1.40	1.36	1.24	0.94	0.43	0.34	0.17	0.13	-0.04	-0.21	-0.33	-0.45

Equation 6.1 may be trivially rewritten to give the count rate R_{object} in units of $e^- s^{-1}$ $pixel^{-1}$ for a target with a stellar spectrum as:

$$R_{object} = 2.5 \times 10^{11} \cdot [\int Q(\lambda)T(\lambda)d\lambda/\lambda] \cdot 10^{-0.4(V + AB_\nu)} \qquad (6.2)$$

6.3.2 Count Rates for Power Law Sources

If one knows the spectral index α (which is zero for a source with a flat continuum), $V+AB_\nu$ can also be calculated as the monochromatic Oke system magnitude at the corrected mean wavelength of the filter:

$$V + AB_\nu = -2.5\log_{10}(S_\nu[\bar{\lambda} + \alpha(d\bar{\lambda}/d\alpha)]) - 48.6$$

where S_ν is the flux in ergs cm^{-2} s^{-1} Hz^{-1} as in Oke and Gunn, Ap. J., 266, 713 (1983) at the effective mean wavelength of the filter $\bar{\lambda} + \alpha(d\bar{\lambda}/d\alpha)$. It can be shown that

$$\frac{d\bar{\lambda}}{d\alpha} = \bar{\lambda}\sigma^2$$

if the integrands are weighted by a source with spectral index α in the definition of λ. Also see Koornneef, J., et al. "Synthetic Photometry and the Calibration of the Hubble Space Telescope" in Highlights of Astronomy (7, 833, J.-P. Swings Ed (1983). Combining the above equations gives

$$R_{object} = 6.9 \times 10^{30} \cdot [\int Q(\lambda)T(\lambda)d\lambda/\lambda] \cdot S_\nu\left(\bar{\lambda} + \alpha\frac{d\bar{\lambda}}{d\alpha}\right) \qquad (6.3)$$

6.3.3 Count Rates for Emission Line Sources

The count rate in units of $e^- s^{-1}$ for a monochromatic emission line is given by

$$R_{object} = 2.3 \times 10^{12} \cdot (QT) \cdot F \cdot \lambda \qquad (6.4)$$

where F is the emission line flux in units of ergs cm^{-2} s^{-1}, and λ is the wavelength of the line in Angstroms. The quantity QT is the (system + filter) quantum efficiency at the wavelength of the line, which can be determined from inspection of the figures in Appendix A.1. For lines near the maxima of the filter transmission curves, it should be sufficient to use QT_{max} from Table 6.1. Note that the integrated filter efficiency is not relevant for the signal calculation.

In cases where the width of the line approaches that of the filter, it will be necessary to convolve the line shape and filter bandpass using either the SYNPHOT or XCAL programs.

For example, H_α emission at 6563Å, with total source flux $F=10^{-16}$ erg s^{-1} cm^{-2}, observed through the F656N filter (total system throughput T=0.11 from the plots in Appendix A.1.10), will produce a target count rate $R_{object}=0.17$ e^- s^{-1} integrated over the entire source.

6.4 Sky Background

The sky background can contribute significant Poisson noise in broad and medium band filters, and must be taken into account during noise calculations. The actual sky brightness depends on the heliocentric ecliptic coordinates (latitude and longitude) in a manner summarized in Table 6.3. The appropriate AB_V can be taken from Table 6.2. To convert mag $arcsec^{-2}$ to mag $pixel^{-1}$ one needs to add 5 magnitudes (WFC) or 6.7 magnitudes (PC1). These values are actually lower limits on the effective sky-brightness that will be seen, because light from the bright Earth limb can scatter into the aperture.

If your observations are sky background limited, and signal-to-noise is a driver, consider the use of the special requirement LOW-SKY as described in the *Call for Proposals* or the *Phase II Proposal Instructions*. LOW-SKY has two effects:

- It causes the observation to be scheduled at the time of year when the zodiacal background light is no more than 30% greater than the minimum possible background value for the target, and
- It requires that the observation be made when the bright Earth limb is more than 40° from the OTA axis, which greatly reduces scattered light.

For many targets LOW-SKY will have minimal impact on the observing efficiency. Note, however, that targets in the Continuous Viewing Zone (CVZ) cannot be observed if LOW-SKY is specified. See Section 7.1 for more information.

Table 6.3: Sky Brightness (V mag arcsec^{-2}) as a Function of Heliocentric Ecliptic Latitude and Longitude. “SA” denotes that the target is unobservable due to solar avoidance.

Heliocentric Ecliptic Longitude	Ecliptic Latitude						
	0°	15°	30°	45°	60°	75°	90°
180°	22.1	22.4	22.7	23.0	23.2	23.4	23.3
165°	22.3	22.5	22.8	23.0	23.2	23.4	23.3
150°	22.4	22.6	22.9	23.1	23.3	23.4	23.3
135°	22.4	22.6	22.9	23.2	23.3	23.4	23.3
120°	22.4	22.6	22.9	23.2	23.3	23.3	23.3
105°	22.2	22.5	22.9	23.1	23.3	23.3	23.3
90°	22.0	22.3	22.7	23.0	23.2	23.3	23.3
75°	21.7	22.2	22.6	22.9	23.1	23.2	23.3
60°	21.3	21.9	22.4	22.7	23.0	23.2	23.3
45°	SA	SA	22.1	22.5	22.9	23.1	23.3
30°	SA	SA	SA	22.3	22.7	23.1	23.3
15°	SA	SA	SA	SA	22.6	23.0	23.3
0°	SA	SA	SA	SA	22.6	23.0	23.3

Another option for reducing the sky brightness, is the special requirement SHADOW, which forces the observation to be made when HST is in the Earth’s shadow. This usually has a large negative impact on the observing efficiency, and is recommended only when attempting to avoid geocoronal lines when observing far-UV emission lines (e.g. Ly α and OI 1304Å). Moreover, it does not attempt to minimize zodiacal emission, which dominates at visible wavelengths.

Table 6.4 shows approximate sky count rates for the WFC and PC1 for filters with significant sky count rates. An average sky brightness of V=22.9 mag arcsec^{-2} is assumed. Filters not listed in the table have sky count rates below that of the dark current, so the sky contribution will generally be unimportant. Values for other filters or sky brightnesses can be computed from Table 6.1, Table 6.2, Table 6.3, and Equation 6.2.

Table 6.4: Sky Count Rate per Pixel (P_{sky}). An average sky brightness of V = 22.9 mag arcsec^{-2} is assumed. Filters not listed have sky rate significantly below the dark current.

Filter	Sky Count Rate (P_{sky}) ($e^- s^{-1}$ pixel^{-1})	
	WFC	PC1
F336W	0.0009	0.0002
F380W	0.005	0.001
F439W	0.005	0.0011
F450W	0.018	0.004
F467M	0.003	0.0006
F547M	0.021	0.0045
F555W	0.052	0.010
F588N	0.002	0.0006
F569W	0.040	0.0081
F606W	0.090	0.020
F622W	0.060	0.012
F673N	0.002	0.0006
F675W	0.056	0.012
F702W	0.082	0.0016
F785LP	0.024	0.0050
F791W	0.048	0.010
F814W	0.054	0.011
F850LP	0.012	0.0024

6.5 Signal-to-Noise Ratio Estimation

The signal-to-noise ratio (SNR) for a point source depends on both the Poisson noise of the object, and on noises associated with the background. Sources of background noise include “read noise” of the CCDs, and Poisson noise in the dark current, sky background, and any smooth galaxy light superposed on the target.

The SNR obtained for photometry of a point source will depend on the analysis technique used. The optimum SNR will be obtained when the pixels of the point source PSF are weighted in proportion to their expected intensity by PSF fitting. Aperture photometry will tend to give lower SNR, especially for sources where the background is important, but nonetheless is widely used. We now consider both methods.

6.5.1 Point Sources -- PSF Fitting

In the bright target limit, Poisson noise sets the SNR and

$$SNR = (S)^{1/2} = (R_{object} \cdot t)^{1/2}$$

where S is the number of detected photons, and R_{object} is given by the above Equations 6.2 through 6.4, and t is the exposure time.

In the background limited case (e.g. read noise, dark current, or sky noise limited) the SNR is a function not only of the expected number of detected photons S from the source but also of the average effective background count rate B in each pixel, the point spread function $(PSF)_{i,j}$, and the weights used to average the signal in the pixels affected by the source. It is easy to show that the signal-to-noise ratio for optimal weights (which are proportional to the point spread function) is given by:

$$SNR = \frac{S}{\sqrt{B}} \cdot \left(\sum (PSF)_{i,j}^{2}\right)^{1/2} = \frac{S}{\sqrt{B}} \cdot (sharpness)^{1/2} \qquad (6.5)$$

where *sharpness* is effectively the reciprocal of the number of pixels contributing background noise. The summation is tabulated for a few representative cases in Table 6.5. To estimate the signal-to-noise, multiply the signal-to-noise obtained, assuming all the flux is in one pixel, by the square root of the value in the table.

Table 6.5: Sharpness as a Function of Wavelength, Camera, and Location of the Star Center with Respect to the Pixel Grid. The "Obs." columns represent the values for the real OTA, WFPC2 optics, and CCD MTF function. The "Diff." column represents values for the theoretical diffraction limit with perfect optics and detectors. Target location refers to both the camera used (PC or WFC), and the location of the star center on the pixel grid.

Target Location	2000 Å		4000 Å		6000 Å		8000 Å	
	Obs.	Diff.	Obs.	Diff.	Obs.	Diff.	Obs.	Diff.
PC Pixel Center	0.084	0.409	0.095	0.259	0.066	0.115	0.046	0.073
PC Pixel Corner	0.063	0. 186	0.065	0.107	0.054	0.072	0.045	0.068
WFC Pixel Center	0.120	0.745	0.145	0.482	0.128	0.318	0.124	0.285
WFC Pixel Corner	0.102	0.228	0.105	0.193	0.098	0.178	0.081	0.126

We note that PSF fitting is equivalent to convolving the image with the PSF, and then measuring the peak counts for stellar objects. Also, the location of the star on the pixel grid will be impossible to know in advance of the observation (i.e. pixel center vs. pixel corner in Table 6.5). In

general, the lower "pixel corner" values should be used, so as to insure adequate SNR.

The average effective background counts per exposure and per pixel can be expanded to include various sources:

$$B = readnoise^2 + P_{dark} \cdot (t + 46) + P_{sky} \cdot t + P_{background} \cdot t$$

where terms include the read out noise of the CCD (*readnoise*), the dark current (P_{dark}), sky background count rate (P_{sky}), and the count rate of any diffuse background light from astrophysical sources ($P_{background}$). Herein we will use "*P"* to represent count rates **per pixel**, and "*R"* to represent the **total** counts for an object. The exposure time is represented by *t*.

For example, Table 2.2 lists the faintest V magnitude star, V=28.19, measurable with a signal-to-noise ratio of 3 in a 3000s integration in F569W in the Wide Field Cameras. The calculation to check this goes as follows. The efficiency of the filter is 0.02343 from Table 6.1. The sky background in each pixel is 23.3+5=28.3, assuming an ecliptic latitude of 90˚ from Table 6.3, and the pixel area correction for the WFC given in that section. The total sky background collected per pixel in 3000 seconds is given by Equation 6.1 as 84.1 electrons. Note that the AB_V color correction required for the sky in the wavelength range of the filter is 0.0 from Table 6.2. From Table 4.2, the read noise for WF3 is 5.2 electrons and the median dark current at -88 ˚C is 0.0045. Therefore the total dark current (on which there will be shot noise) is only 13.5 electrons. The equivalent background per pixel is then given as B=84.1+5.2^2+13.5=124.5. The total number of detected electrons from a star with V=28.19 is S=93 electrons, again using Equation 6.1. (We note that AB_V is approximately zero at this wavelength, so the spectral class is unimportant.) From Table 5.4 (peak near pixel center), the expected peak count is 28 detected electrons, which is much less than B, requiring the use of Equation 6.5 for the background limited case. The sharpness for the WF camera in the best case, when the star is centered on a pixel, is given in Table 6.5 as 0.128. Then Equation 6.5 above gives the signal-to-noise as 3.0:

$$SNR = \left(\frac{93}{\sqrt{124.5}} \cdot \sqrt{0.128} \right) = 3.0$$

If, instead, the peak count rate comes out much greater than the background, the observation is photon noise limited, and the signal-to-noise should be computed as the square root of the signal S in electrons.

In principle, one should also include contributions in the signal-to-noise for flat fielding uncertainties, noise in the bias and dark calibration files, and quantization noise. Flat fielding errors will be of order 1%, and will limit SNR in the large-signal limit. Noise in the bias and dark calibration files will be unimportant in most pixels, although these could become

important if many (>10) non-dithered frames of the same field are combined.

Quantization noise can be estimated as $gain/\sqrt{12}$ (i.e., $\sqrt{4.1}$ in the 7 e^- DN^{-1} channel, and $\sqrt{16.3}$ in the 14 e^- DN^{-1} channel). In nearly all situations it can be ignored. In the weak signal case, the quantization noise is effectively included in the read noise values given throughout this Handbook; in the strong signal case it is very small compared to the Poisson noise and can be ignored.

A generalized equation for estimating point source signal-to-noise ratio per exposure is given below (Equation 6.6). It is exact in both the bright and faint object limits, and is a reasonable approximation to the intermediate case. $P_{background}$ represents any generalized source of diffuse background light (e.g. galaxy on which target is superposed). Table 6.6 gives rough values for some of the parameters, along with references for more accurate values.

$$SNR = \frac{R_{object} \cdot t}{\sqrt{R_{object} \cdot t + \frac{readnoise^2 + P_{dark} \cdot (t + 46) + P_{sky} \cdot t + P_{background} \cdot t}{sharpness}}} \quad (6.6)$$

Note that in this formulation, $sharpness^{-1}$ is the equivalent number of pixels the weighted signal is integrated over. In the event that multiple exposures are taken (e.g. to remove cosmic rays), the signal-to-noise ratio for the final averaged image is approximately given by:

$$SNR_{total} = SNR \cdot \sqrt{N}$$

where N is the number of images averaged.

Table 6.6: Parameters for Point Source SNR Estimation - PSF Fitting

Parameter	Description	Units	Approx. Value	Better Value
R_{object}	object count rate	$e^- s^{-1}$		Equation 6.1, 6.2, or 6.3
P_{dark}	dark count rate	$e^- s^{-1}$ pixel^{-1}	0.004	Table 4.2, Eqn. 4.1 (page 92)
P_{sky}	sky count rate	$e^- s^{-1}$ pixel^{-1}	Table 6.4	Table 6.1, Table 6.2, Table 6.3, Eqn 6.1
$P_{background}$	count rate from background light (if any)	$e^- s^{-1}$ pixel^{-1}		Table 6.1, Table 6.2, Eqn 6.1
read noise		e^-	ATD-GAIN=7 use 5.3[a] ATD-GAIN=15 use 7.5	Table 4.2
sharpness			WFC use 0.11 PC1 use 0.06	Table 6.5
t	exposure time	s		

a. ATD-GAIN defaults to 7 unless otherwise specified on Phase II proposal.

6.5.2 Point Sources -- Aperture Photometry

When aperture photometry is used, one must consider the fraction of the object counts encircled by the aperture, as well the background noise in the aperture. In the bright target limit the SNR is given by

$$SNR = (S \cdot f(r))^{1/2} = (R_{object} \cdot f(r) \cdot t)^{1/2}$$

where S is the number of detected photons, $f(r)$ is the fraction of the total counts encircled by the aperture with radius r, and R_{object} is target count rate. Representative values of $f(r)$ are given in Table 6.7; values for other aperture sizes and filters can be estimated from Figure 5.3, or Figure 5.4.

In the faint target limit the noise contributed by background counts determines the SNR

$$SNR = \frac{S \cdot f(r)}{\sqrt{B \cdot \pi r^2}}$$

where B represents the effective background counts per pixel, and r is the aperture radius in pixels.

In the generalized case the SNR per exposure for aperture photometry is given approximately by:

$$SNR = \frac{f(r) \cdot R_{object} \cdot t}{\sqrt{(f(r) \cdot R_{object} \cdot t) + \left[readnoise^2 + P_{dark} \cdot (t + 46) + P_{sky} \cdot t + P_{background} \cdot t\right] \cdot \pi r^2}} \quad (6.7)$$

where the parameters are summarized in Table 6.8.

Table 6.7: Encircled Energy for Representative Filters. Encircled energy values are normalized to unity at large radius.

CCD	Aperture Radius (r)	Encircled Energy f(r)		
		F218W	F555W	F814W
PC1	0.1″	0.60	0.67	0.53
	0.2″	0.73	0.85	0.78
	0.5″	0.84	0.96	0.87
	1.0″	0.92	1.00	0.92
WF3	0.1″	0.40	0.46	0.44
	0.2″	0.69	0.76	0.74
	0.5″	0.85	0.90	0.91
	1.0″	0.94	0.94	0.96

Table 6.8: Parameters for Point Source SNR Estimation - Aperture Photometry.

Parameter	Description	Units	Approx. Value	Better Value
R_{object}	object count rate	$e^- s^{-1}$		Equation 6.1, 6.2, or 6.3
P_{dark}	dark count rate	$e^- s^{-1}$ pixel^{-1}	0.004	Table 4.2; Eqn 4.1 on page 90
P_{sky}	sky count rate	$e^- s^{-1}$ pixel^{-1}	Table 6.4	Table 6.1, Table 6.2, Table 6.3; Eqn 6.1
$P_{background}$	count rate from background light (if any)	$e^- s^{-1}$ pixel^{-1}		Table 6.1, Table 6.2; Eqn 6.1
readnoise		e^-	ATD-GAIN=7 use 5.3[a] ATD-GAIN=15 use 7.5	Table 4.2
f(r)	encircled energy		Table 6.7	Figure 5.3 or Figure 5.4
r	aperture radius	pixels		
t	exposure time	s		

a. ATD-GAIN defaults to 7 unless otherwise specified on Phase II proposal.

6.5.3 Extended Sources

The calculations for extended sources are nearly identical to those for point sources. The easiest procedure is to compute the SNR per detector pixel, and then adjust this value if the total SNR is required for an area encompassing many pixels.

In general, one will have the target magnitude or flux per square arcsecond. To compute the flux per pixel for the PC one merely multiplies the flux per square arcsecond by 0.00207, or instead, adds the value 6.7 to the magnitude per square arcsecond to get the necessary magnitude per PC pixel. For the WFC, one either multiplies the flux per square arcsecond by 0.00993, or adds 5.0 to the magnitude per square arcsecond. Equations 6.2, 6.3, and 6.4 can be rewritten including these factors as below.

PC Camera

For the PC camera, sources with stellar spectra, and V surface brightness per square arcsecond σ_V we have a count rate in $e^- s^{-1}$ pixel^{-1} of

$$P_{object} = 2.5 \times 10^{11} \cdot [\int Q(\lambda)T(\lambda)d\lambda/\lambda] \cdot 10^{-0.4(\sigma_V + AB_v + 6.7)} \quad (6.8)$$

For power law sources where B_ν is the target flux in units of ergs cm^{-2} s^{-1} Hz^{-1} arcsec^{-2} we have

$$P_{object} = 1.4 \times 10^{28} \cdot [\int Q(\lambda)T(\lambda)d\lambda/\lambda] \cdot B_\nu\left(\bar{\lambda} + \alpha\frac{d\bar{\lambda}}{d\alpha}\right) \qquad (6.9)$$

And finally for emission line sources where I_ν is the flux in ergs cm^{-2} s^{-1} arcsec^{-2} we have

$$P_{object} = 4.8 \times 10^{9} \cdot (QT) \cdot I_\nu \cdot \lambda \qquad (6.10)$$

where the emission line wavelength λ is in Angstroms.

WFC Cameras

For the WFC cameras and stellar sources with V surface brightness per square arcsecond σ_V we have a count rate in e$^-$ s^{-1} pixel^{-1} of

$$P_{object} = 2.5 \times 10^{11} \cdot [\int Q(\lambda)T(\lambda)d\lambda/\lambda] \cdot 10^{-0.4(\sigma_V + AB_\nu + 5)} \qquad (6.11)$$

For power law sources where B_ν is the target flux in units of ergs cm^{-2} s^{-1} Hz^{-1} arcsec^{-2} we have

$$P_{object} = 6.9 \times 10^{28} \cdot [\int Q(\lambda)T(\lambda)d\lambda/\lambda] \cdot B_\nu\left(\bar{\lambda} + \alpha\frac{d\bar{\lambda}}{d\alpha}\right) \qquad (6.12)$$

And finally for emission line sources where I_ν is the flux in ergs cm^{-2} s^{-1} arcsec^{-2} we have

$$P_{object} = 2.3 \times 10^{10} \cdot (QT) \cdot I_\nu \cdot \lambda \qquad (6.13)$$

where the emission line wavelength λ is in Angstroms.

SNR

The generalized SNR per pixel per exposure for an extended source is then obtained simply by setting the sharpness to unity in Equation 6.5:

$$SNR = \frac{P_{object} \cdot t}{\sqrt{P_{object} \cdot t + (readnoise^2 + P_{dark} \cdot (t + 46) + P_{sky} \cdot t + P_{background} \cdot t)}} \qquad (6.14)$$

Table 6.9: Parameters for Extended Source SNR Estimation.

Parameter	Description	Units	Approx. Value	Better Value
P_{object}	object count rate	$e^- s^{-1}$ pixel^{-1}		Equations 6.9 to 6.12
P_{dark}	dark count rate	$e^- s^{-1}$ pixel^{-1}	0.004	Table 4.2; Eqn 4.1 (page 92)
P_{sky}	sky count rate	$e^- s^{-1}$ pixel^{-1}	Table 6.4	Table 6.1, Table 6.2, Table 6.3; Eqn 6.7 (PC) or 6.10 (WFC)
$P_{background}$	count rate from background light (if any)	$e^- s^{-1}$ pixel^{-1}		Table 6.1, Table 6.2; Eqn 6.7 (PC) or 6.10 (WFC)
readnoise		e^-	ATD-GAIN=7 use 5.3[a] ATD-GAIN=15 use 7.5	Table 4.2
t	exposure time	s		

a. Default value is ATD-GAIN=7.

Since many observations of extended sources are for galaxies in broad-band filters, a few rules of thumb can be useful. Saturation is seldom a concern, except in very bright spots such as the inner core of ellipticals and of some bulges. Count rates for spiral galaxies range typically from 2 to 0.01 e^- pixel^{-1} s^{-1} (and lower) for filters such as F555W, F606W, F702W, and F814W; the lower end of the range corresponds roughly to the de Vaucouleurs D_{25}. Count rates are significantly lower in blue and UV filters. Spiral structure can typically be traced reasonably well with total exposures of 3000 seconds or longer in the above filters.

For galaxies of very small angular size at redshifts of cosmological interest, the image may cover a small number of pixels; thus the detection of such objects follows rules similar to those of point sources. However, the fraction of light falling in the central pixel is smaller for most galaxies than it is for true point sources. The approximate magnitude difference between the light falling in the central pixel and the entire galaxy is plotted in Figure 6.1 for a typical giant elliptical galaxy, as a function of redshift. For other types of galaxies, a morphological term can be added to the values (for example, 0.6 magnitudes for lenticulars, 0.7 for S, 0.8 for Sab, 0.9 for Sbc, 1.2 for Scd, and 1.8 for Irr). These values must be increased by an additional 1.7 magnitudes for the PC.

Figure 6.1: Giant Elliptical Galaxy.

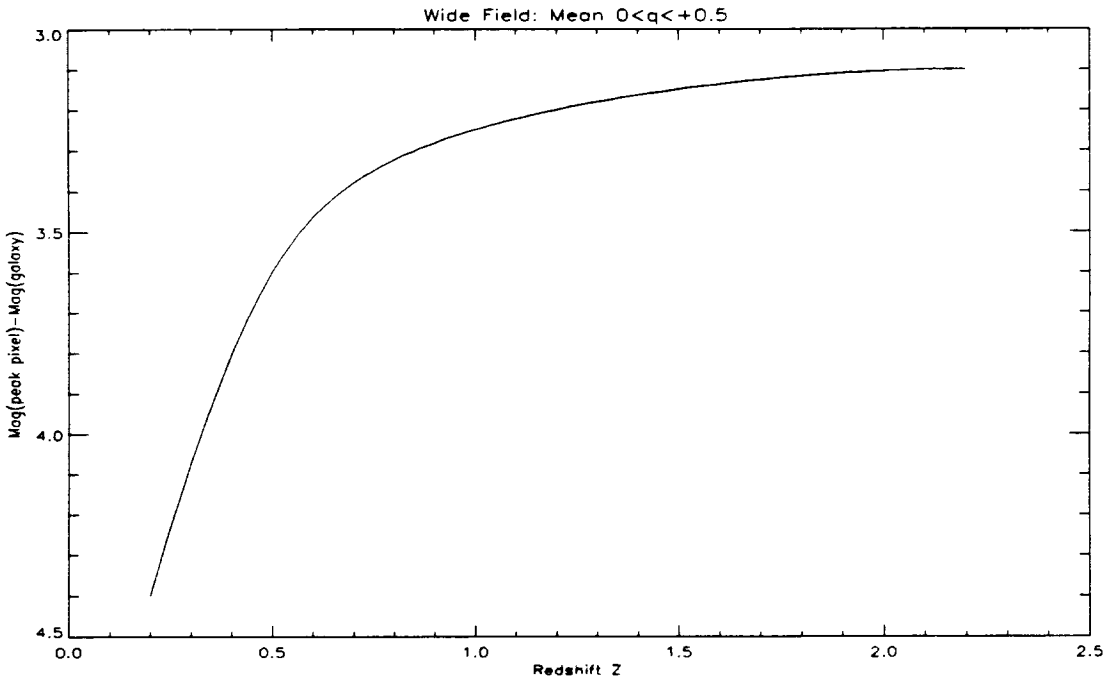

6.6 Exposure Time Estimation

In many instances one desires a certain SNR, and wishes to solve for the corresponding exposure time. Given the SNR, Equations 6.6, 6.7, or 6.14 can be solved for the exposure time, *t*. Since there are time-dependent and time-independent noise sources, quadratic equations are obtained. For example, we may solve Equation 6.6 for the point source exposure time:

$$t = \frac{1}{2Y} \cdot (b + \sqrt{b^2 + 4aY})$$

where the term *A* contains the time-independent noise sources

$$a = \frac{readnoise^2 + 46P_{dark}}{sharpness}$$

and *B* contains the time-dependent noise sources

$$b = \frac{P_{dark} + P_{sky} + P_{background}}{sharpness} + R_{object}$$

and

$$Y = \left(\frac{R_{object}}{SNR}\right)^2$$

Equations for aperture photometry (6.7) and extended sources (6.12) can be solved with similar results. Parameters are as described in Table 6.6, Table 6.8, and Table 6.9. We again note that the on-line WFPC2 Exposure Time Calculator program provides an easy method for these calculations.

6.7 Sample SNR Calculations

Below we give further examples of SNR calculations. Appendix B also contains SNR plots for a wide range of representative cases.

6.7.1 Point Sources

Simple Star, Manual Calculation, PSF Fitting

We begin with the simple example of a V=20 star of spectral class G0. We want to observe with the PC using filter F555W. The star is somewhere near the ecliptic pole. We want to know the SNR for a 1200s CR-SPLIT exposure. Default ATD-GAIN=7 is used. We plan to use PSF fitting to analyze the data.

First we estimate the count rate for our target. Consulting Equation 6.2, Table 6.1, and Table 6.2 we have:

$$R_{object} = 2.5 \times 10^{11} \cdot \left[\int Q(\lambda)T(\lambda)d\lambda/\lambda\right] \cdot 10^{-0.4(V + AB_v)}$$

$$= 2.5 \times 10^{11} \cdot [0.030] \cdot 10^{-0.4(20 + 0.02)} = 74$$

in units of $e^- s^{-1}$. Next we fill out Equation 6.6. To keep things simple we just use values from Table 6.6, and get the sky count rate from Table 6.4.

There is no background light (i.e. no superposed galaxy), so $P_{background}$=0. The exposure time t=600 for each exposure of the CR-SPLIT:

$$SNR = \frac{R_{object} \cdot t}{\sqrt{R_{object} \cdot t + \frac{readnoise^2 + P_{dark} \cdot (t + 46) + P_{sky} \cdot t + P_{background} \cdot t}{sharpness}}}$$

$$= \frac{74 \cdot 600}{\sqrt{74 \cdot 600 + \frac{(5.3)^2 + 0.004 \cdot (600 + 46) + (0.01 \cdot 600) + (0 \cdot 600)}{0.06}}}$$

$$= \frac{44400}{\sqrt{44400 + 611}} = 209$$

The SNR for the total 1200s exposure, i.e. both halves of the CR-SPLIT, would simply be:

$$SNR_{total} = SNR \cdot \sqrt{N} = 209 \cdot \sqrt{2} = 296$$

At these high SNR levels, it is likely that flat fielding would limit the photometric accuracy, rather than the noise. If we have a look at the terms in the SNR equation, we can see that the Poisson noise dominates; the term containing the sharpness and background noise sources is unimportant.

Just for fun, let us see what happens if we keep everything the same, but give the target V=25. Now we have R_{object}=0.74 $e^- s^{-1}$, and:

$$SNR = \frac{0.74 \cdot 600}{\sqrt{0.74 \cdot 600 + \frac{(5.3)^2 + 0.004 \cdot (600 + 46) + (0.01 \cdot 600) + (0 \cdot 600)}{0.06}}}$$

$$= \frac{444}{\sqrt{444 + 611}} = 13.7$$

We see that now the term with the background noise (in particular, the read noise) limits the SNR. For the full 1200s exposure the SNR_{total}=19.3.

Simple Star, Manual Calculation, Aperture Photometry

What if we now want to observe this same V=25 star, but we plan to reduce the data by measuring counts in a 0.5″ radius aperture? We now use

Equation 6.7 instead, consult Table 6.7 for the encircled energy *f(r),* and note that 0.5″ corresponds to *r*=11.6 PC pixels:

$$SNR = \frac{f(r) \cdot R_{object} \cdot t}{\sqrt{(f(r) \cdot R_{object} \cdot t) + [readnoise^2 + P_{dark} \cdot (t + 46) + P_{sky} \cdot t + P_{background} \cdot t] \cdot \pi r^2}}$$

$$= \frac{0.96 \cdot 0.74 \cdot 600}{\sqrt{(0.96 \cdot 0.74 \cdot 600) + ((5.3)^2 + 0.004(600 + 46) + 0.01 \cdot 600 + 0 \cdot 600) \cdot \pi(11.6)^2}}$$

$$= \frac{426}{\sqrt{426 + 15500}}$$

$$= 3.4$$

Apparently using aperture photometry with a 0.5″ radius aperture reduces the SNR by a factor ~4 as compared to PSF fitting, for this background limited case.

Simple Star, SNR Plots, PSF Fitting

We now repeat the first calculation above for the V=20 star using the SNR plots in Appendix B. We look up the G0 spectral class and F555W filter (5500Å) in Table B.1, and obtain AB_V=0.02. For the V=20 star, we thus have V+AB_V=20.02. We look at Figure B.10 and find this value on the horizontal axis. We locate exposure time 600s (one-half of the total 1200s CR-SPLIT exposure), and find SNR~200. For the total 1200s exposure the SNR would be $200\sqrt{2} = 280$.

Simple Star, On-Line Calculator, PSF Fitting

The above calculation for a V=20 G0 star may also be performed using the WFPC2 Exposure Time Calculator program, which is available on the WFPC2 web pages at:

http://www.stsci.edu/hst/wfpc2/software/wfpc2-etc.html

Figure 6.2: Sample Fill-out Form for WFPC2 On-Line Exposure Time Calculator.

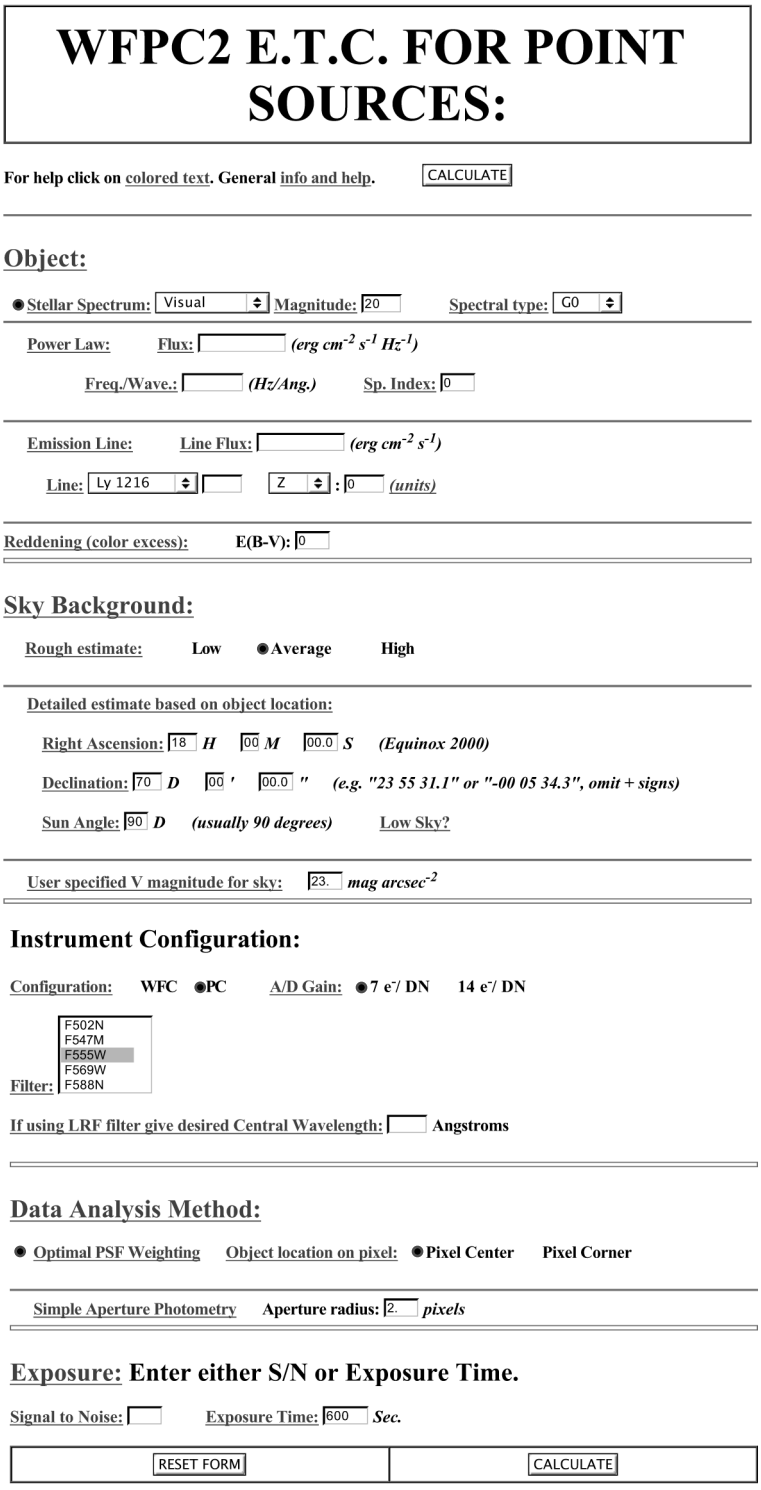

WFPC2 E.T.C. FOR POINT SOURCES:

For help click on colored text. General info and help. CALCULATE

Object:

● Stellar Spectrum: Visual Magnitude: 20 Spectral type: G0

Power Law: Flux: *(erg cm^{-2} s^{-1} Hz^{-1})*

Freq./Wave.: *(Hz/Ang.)* Sp. Index: 0

Emission Line: Line Flux: *(erg cm^{-2} s^{-1})*

Line: Ly 1216 Z : 0 *(units)*

Reddening (color excess): E(B-V): 0

Sky Background:

Rough estimate: Low ●Average High

Detailed estimate based on object location:

Right Ascension: 18 *H* 00 *M* 00.0 *S* *(Equinox 2000)*

Declination: 70 *D* 00 ' 00.0 " *(e.g. "23 55 31.1" or "-00 05 34.3", omit + signs)*

Sun Angle: 90 *D* *(usually 90 degrees)* Low Sky?

User specified V magnitude for sky: 23. *mag arcsec^{-2}*

Instrument Configuration:

Configuration: WFC ●PC A/D Gain: ●7 e$^-$/ DN 14 e$^-$/ DN

Filter: F502N F547M F555W F569W F588N

If using LRF filter give desired Central Wavelength: Angstroms

Data Analysis Method:

● Optimal PSF Weighting Object location on pixel: ●Pixel Center Pixel Corner

Simple Aperture Photometry Aperture radius: 2. *pixels*

Exposure: Enter either S/N or Exposure Time.

Signal to Noise: Exposure Time: 600 *Sec.*

RESET FORM CALCULATE

To use this program, access the above address. For the first example above, choose the “Point Source” form and complete it as shown in Figure 6.2 for the 600s sub-exposure. Then click the “calculate” button and after a

few seconds the result is displayed (Figure 6.3). The answer, SNR=208, is comparable to that obtained by the manual calculation above for the 600s sub-exposure (SNR=209). Alternatively, one can input the total exposure time (1200s), and then use the result farther down the output page for "No. Sub-Exposures = 2" (see Figure 6.4), thereby obtaining SNR=291 for the total 1200s CR-SPLIT exposure.

Figure 6.3: Sample Results from WFPC2 On-Line Exposure Time Calculator.

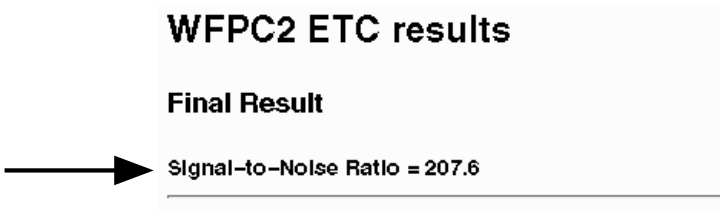

Figure 6.4: Sample Results on CR-SPLITing from WFPC2 On-Line Exposure Time Calculator Results Page.

No. Sub-Exposures	Total SNR	Pixels Lost
(No Split)	294.2	3.981250%
2	290.7	0.039626%
3	291.1	0.000234%
4	291.0	0.000001%
6	290.3	0.000000%
8	289.4	0.000000%
12	287.4	0.000000%
16	285.3	0.000000%
32	277.1	0.000000%

Star Superposed on Galaxy, Manual Calculation

We now consider a B=25 point source of spectral class B0, which is superposed on an elliptical galaxy with σ_V=22 mag arcsecond^{-2}. We want to compute the SNR obtained from a one-orbit (40 min.) non-CR-SPLIT observation in filter F300W on the WFC. PSF fitting will be used for the photometry.

We begin by computing the total count rate for the target. Using Table 6.2 we see that this target will have V=25.31. From Table 6.1 we obtain the filter efficiency and mean wavelength. Interpolating by mean wavelength in

Table 6.2 we obtain AB_V=-0.83 for the B0 star. Using Equation 6.2 we have:

$$R_{object} = 2.5 \times 10^{11} \cdot \left[\int Q(\lambda)T(\lambda)d\lambda/\lambda\right] \cdot 10^{-0.4(V + AB_V)}$$
$$= 2.5 \times 10^{11} \cdot [0.00571] \cdot 10^{-0.4(25.31 - 0.83)}$$
$$= 0.23$$

in units of e^- s^{-1}. Next we consider the background light from the superposed galaxy. We set σ_V=22 mag arcsecond^{-2} in Equation 6.11, and AB_V=3.63 for a gE galaxy at λ=3000Å (filter F300W) from Table 6.2. Hence the count rate per pixel due to the background light is:

$$P_{background} = 2.5 \times 10^{11} \cdot \left[\int Q(\lambda)T(\lambda)d\lambda/\lambda\right] \cdot 10^{-0.4(\sigma_V + AB_V + 5)}$$
$$= 2.5 \times 10^{11} \cdot [0.00571] \cdot 10^{-0.4(22 + 3.63 + 5)}$$
$$= 0.00080$$

For the sky background, we note that Table 6.4 has no entry for F300W, so that the sky must be unimportant. If we wanted to calculate it anyway, as a check, we would use Table 6.3 for the sky brightness, Table 6.2 for the sky's AB_V, and again Equation 6.11. We will assume the target is near the ecliptic pole.

$$P_{sky} = 2.5 \times 10^{11} \cdot \left[\int Q(\lambda)T(\lambda)d\lambda/\lambda\right] \cdot 10^{-0.4(\sigma_V + AB_V + 5)}$$
$$= 2.5 \times 10^{11} \cdot [0.00571] \cdot 10^{-0.4(23.3 + 3.12 + 5)}$$
$$= 0.00039$$

For the sharpness function we will use "pixel corner" values (least optimistic choice) from Table 6.5. Using read noise and dark current from Table 6.6, and Equation 6.6 for point source SNR:

$$SNR = \frac{R_{object} \cdot t}{\sqrt{R_{object} \cdot t + \frac{readnoise^2 + P_{dark} \cdot (t + 46) + P_{sky} \cdot t + P_{background} \cdot t}{sharpness}}}$$
$$= \frac{0.23 \cdot 2400}{\sqrt{0.23 \cdot 2400 + \frac{(5.3)^2 + 0.004 \cdot (2400 + 46) + (0.00039 \cdot 2400) + (0.00080 \cdot 2400)}{0.103}}}$$
$$= \frac{552}{\sqrt{552 + 395}}$$
$$= 17.9$$

for this single exposure. The SNR for multiple 40 min. exposures would be simply $17.9(N^{1/2})$, where N is the number of exposures.

Star Superposed on Galaxy, On-Line Calculator

The above calculation could also be performed with the on-line WFPC2 Exposure Time Calculator. One would select the "Point source + stellar

background" form, and complete it as in Figure 6.5, and then click on "calculate." Figure 6.6 shows some of the results.

Figure 6.5: Point Source + Stellar Background Fill-out Form for WFPC2 On-Line Exposure Time Calculator. SNR is calculated for B=25 star (class B0) superposed on an elliptical galaxy (gE) with σ_V=22. WFC is used with F300W.

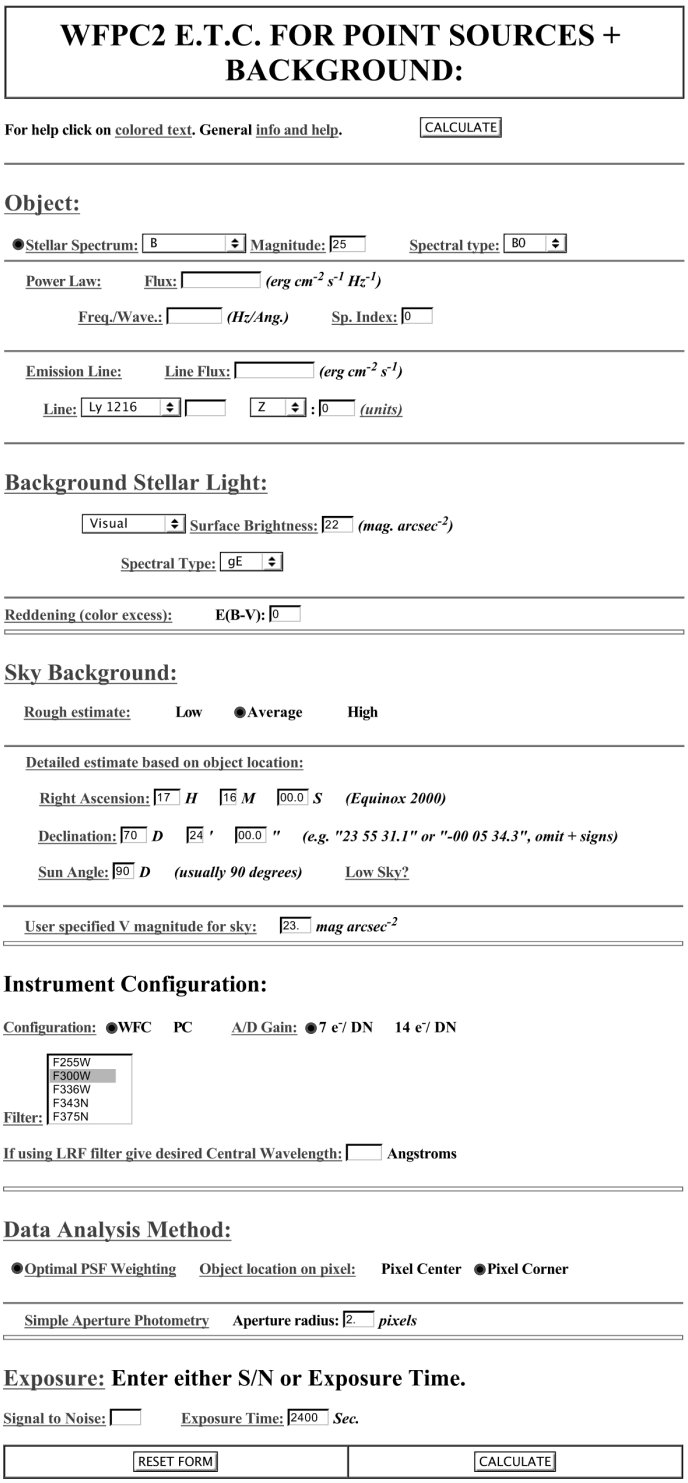

Figure 6.6: Sample Output from WFPC2 On-Line Exposure Time Calculator.

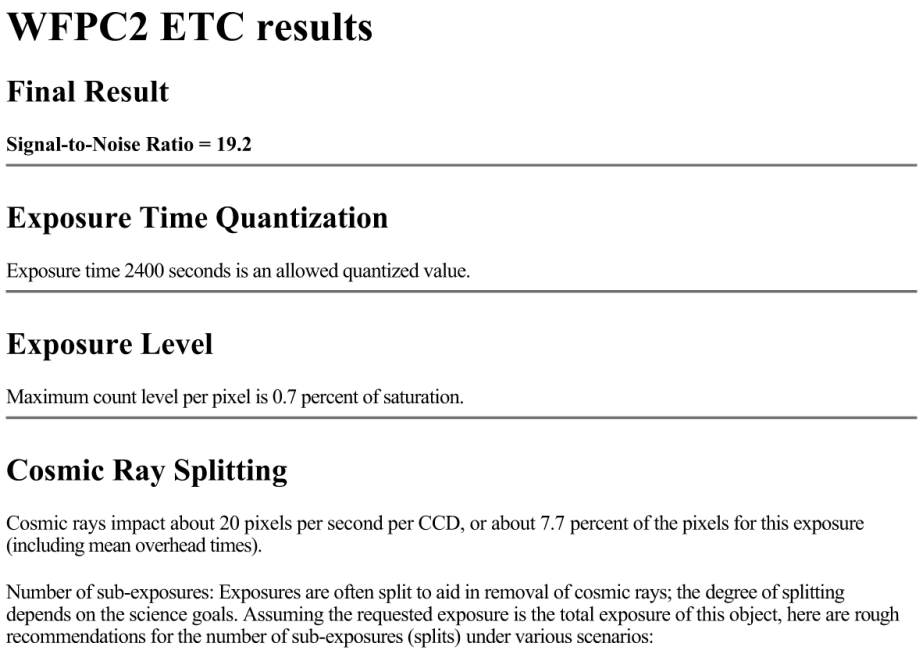

WFPC2 ETC results

Final Result

Signal-to-Noise Ratio = 19.2

Exposure Time Quantization

Exposure time 2400 seconds is an allowed quantized value.

Exposure Level

Maximum count level per pixel is 0.7 percent of saturation.

Cosmic Ray Splitting

Cosmic rays impact about 20 pixels per second per CCD, or about 7.7 percent of the pixels for this exposure (including mean overhead times).

Number of sub-exposures: Exposures are often split to aid in removal of cosmic rays; the degree of splitting depends on the science goals. Assuming the requested exposure is the total exposure of this object, here are rough recommendations for the number of sub-exposures (splits) under various scenarios:

6.7.2 Extended Sources

In general, the signal-to-noise level for extended sources can be computed by comparing the expected signal, S, in each pixel, determined from Equations 6.8 through 6.13, to the noise $N=(S+B)^{1/2}$, where B is the equivalent background, determined in a manner similar to that for point sources. Unlike for point sources, the calculation does not, in a first approximation, involve the sharpness of the point spread function. For example, let us consider the observation of a source with a V surface brightness of 24 mag arcsec^{-2}, assuming the F569W filter, WFC camera, and sky background V=23.3 mag arcsec^{-2}. The signal-to-noise estimate goes as follows. The signal in each WFC pixel is 24.0+5.0 = 29.0 magnitude. By Equation 6.11, the total signal collected from the source in a 3000 second integration is S = 44.1 electrons, neglecting the small AB color correction. The sky signal per pixel is 84.1 electrons. The dark current is ~12 electrons. The total equivalent background is thus B = $84.1+5.3^2+12$ = 124.2 electrons, larger than the signal detected, thus the noise is background-dominated. The noise is $N=(S+B)^{1/2}$= 13.0 electrons, and the signal-to-noise *per pixel* expected in this case is 3.4. Similar calculations can be carried out for other filters; for observations in narrow-band filters and in the UV, the sky background signal will usually be unimportant. For very long observations of faint objects, other noise

terms, such as flat field uncertainty, and errors in dark (and possibly bias) subtraction, must be considered more carefully.

If the scale of features in the target is larger than one pixel, the signal-to-noise can sometimes be improved by smoothing the observed image or - if read noise is a significant contributor - by reading the image out in AREA mode (see Section 2.8).

6.7.3 Emission Line Sources

The signal-to-noise ratio calculation for point-like or extended emission-line sources is similar to that for continuum sources. However, the details of the calculation are different, because of the units used for the line flux, and because the flux is in a narrow line. The integrated filter efficiency is not relevant for the signal calculation; what matters is the total system throughput QT at the wavelength of the line, which can be determined from inspection of the figures in Appendix A. For lines near the center of the filter bandpasses the QT_{max} values from Table 6.1 can be used. The total signal expected for a point source of line strength F, expressed in erg s^{-1} cm^{-2}, is S=2.28x10^{12} λ t QT F, where t is the exposure time in seconds, and λ the wavelength of the line in Angstroms. Thus, H_α emission at 6563Å, with flux F=10^{-16} erg s^{-1} cm^{-2}, observed for 1000 seconds through the F656N filter (total system throughput QT=0.11 from the plots of Appendix A.1.10), will produce a total signal of S=165 electrons. The equivalent background per pixel is read-noise dominated: B=1+5.3^2+4=33, for a background noise of ~6 electrons. The total noise is dominated by photon noise from the signal itself, and the signal-to-noise ratio achieved in this observation is ~27.

If the source is extended, the expected signal *per arcsecond* must be multiplied by the effective pixel area: 0.0099 $arcsec^2$ for the WF, 0.0021 for the PC. For a line flux of, say, F = 10^{-15} erg s^{-1} cm^{-2} $arcsec^{-2}$, this corresponds to 16 electrons in 1000 seconds for a WFC pixel. The noise is now dominated by the background, and the single-pixel signal-to-noise ratio is $16/(33 + 16)^{1/2} \sim 2.3$.

Extended Line Emission Source, Manual Calculation

We now consider a detailed example of a planetary nebula observed on the PC with the F502N filter. The nebula has a diameter of 5″ and a total flux F=4x10^{-13} erg s^{-1} cm^{-2} in the [OIII] 5007Å line. We want to estimate the SNR for an 1800s exposure, which will be CR-SPLIT.

First we must estimate the flux per square arcsecond. Using the nebula diameter, the average brightness is I_ν = 2.0x10^{-14} erg s^{-1} cm^{-2} $arcsec^{-2.}$

From the plots in Appendix A, we see that QT=0.058. Using Equation 6.10 for the target count rate per pixel:

$$\begin{aligned} P_{object} &= 4.8 \times 10^9 \cdot (QT) \cdot I_{\nu} \cdot \lambda \\ &= 4.8 \times 10^9 \cdot (0.058) \cdot 2.0 \times 10^{-14} \cdot 5007 \\ &= 0.028 \end{aligned}$$

Next we estimate the SNR for each 900s sub-exposure using Equation 6.14 and Table 6.9. For this narrow filter the sky background can be ignored. We presume there is no background light from astrophysical sources:

$$\begin{aligned} SNR &= \frac{P_{object} \cdot t}{\sqrt{P_{object} \cdot t + (readnoise^2 + P_{dark} \cdot (t + 46) + P_{sky} \cdot t + P_{background} \cdot t)}} \\ &= \frac{0.028 \cdot 900}{\sqrt{0.028 \cdot 900 + (5.3^2 + 0.004 \cdot (900 + 46) + 0 \cdot 900 + 0 \cdot 900)}} \\ &= 3.3 \end{aligned}$$

Hence SNR=3.1 per pixel for each 900s sub-exposure. The SNR per pixel for the total 1800s is

$$\begin{aligned} SNR_{total} &= SNR\sqrt{N} \\ &= 3.3 \cdot \sqrt{2} \\ &= 4.7 \end{aligned}$$

The SNR for the entire nebula is this SNR per pixel times the square root of the number of pixels in the image, or ~460. In actuality, uncertainties in the photometric calibration and flat fields, would limit the SNR to ~100.

Extended Line Emission Source, On-Line Calculator

The above example could be calculated with the "Extended Source" form of the ETC program. The fill-out form would be completed as shown in Figure 6.7.

Figure 6.7: Extended Source Form for WFPC2 On-Line Exposure Time Calculator. Here the target is a galactic [OIII] 5007 line emission source and is observed on PC with filter F502N. SNR is computed for 1800s exposure.

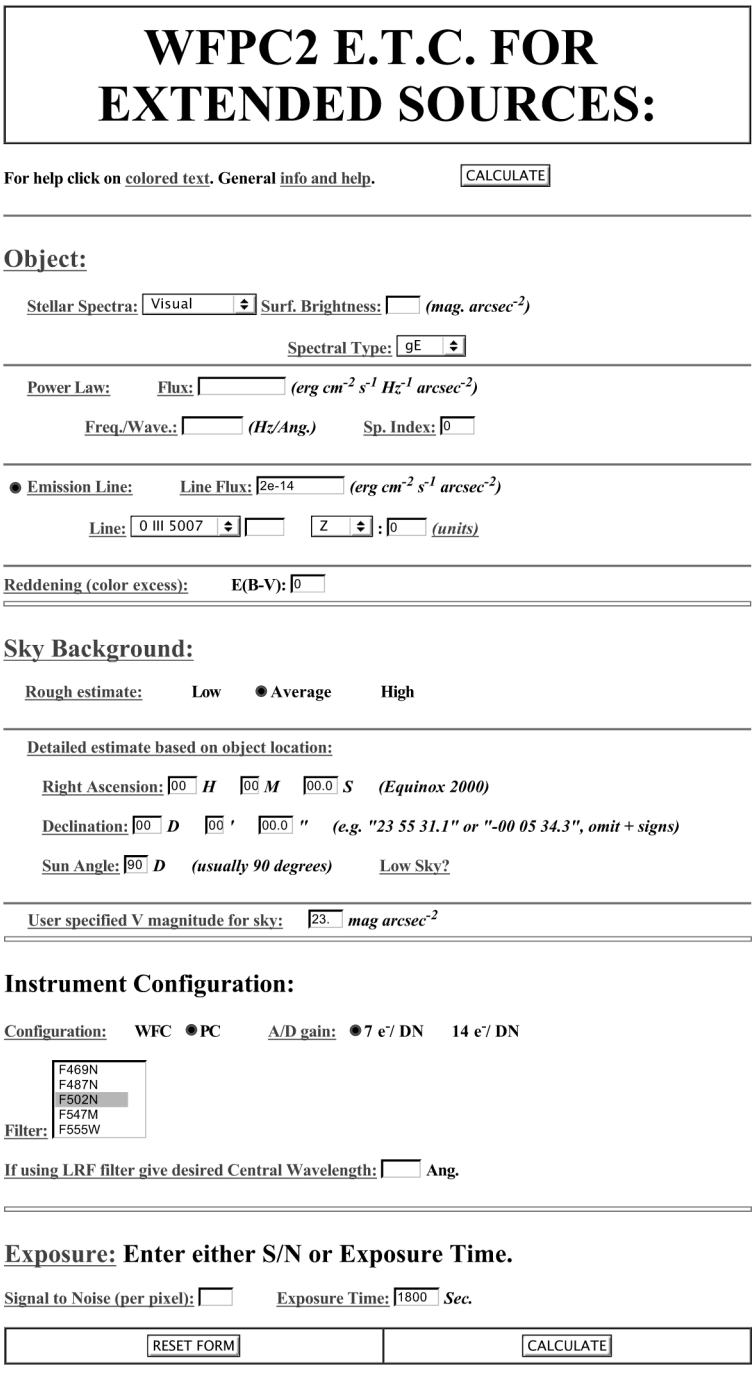

We have selected “[OIII] 5007” on the emission line menu, and have left the redshift (z) set to zero. The PC and F502N filter are selected. Note we have entered the exposure time as 1800s. Scrolling down through the

output page we find a table of SNR for various CR-SPLITings of the exposure (see Figure 6.8). “No. Sub-Exposures = 2” gives the answer we want, SNR=4.6 per pixel.

Figure 6.8: Sample Results on CR-SPLITing from WFPC2 On-Line Exposure Time Calculator Results Page.

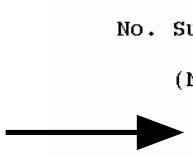

No. Sub-Exposures	Total SNR	Pixels Lost
(No Split)	5.3	5.856250%
2	4.6	0.085739%
3	4.1	0.000744%
4	3.8	0.000005%
6	3.3	0.000000%
8	3.0	0.000000%
12	2.5	0.000000%
16	2.2	0.000000%
32	1.6	0.000000%

Line Emission Point Source w/ LRF, Manual Calculation

In this example we consider an unresolved source of H_α emission in a galaxy at redshift z=0.22 with flux F=1.5x10^{-16} erg s^{-1} cm^{-2}. We want the SNR for a 2400s exposure without CR-SPLITing.

Since the redshift is significant, we cannot observe with the F656N filter. Instead we will use the Linear Ramp Filter (LRF). The observed wavelength will be 8007Å. From Table 3.7 we see that this will be observed using the FR868N filter on CCD WF3. Combining the LRF transmission from Figure 3.3 and the “WFPC2 + OTA System Throughput” from Figure 2.4 we estimate QT=0.054. We compute the count rate using Equation 6.4.

$$\begin{aligned} R_{object} &= 2.3 \times 10^{12} \cdot (QT) \cdot F \cdot \lambda \\ &= 2.3 \times 10^{12} \cdot (0.054) \cdot (1.5 \times 10^{-16}) \cdot 8007 \\ &= 0.15 \end{aligned}$$

To estimate the SNR we use Equation 6.6, which assumes that PSF fitting will be used to analyze the image. Since the filter is narrow, we will ignore the sky emission. We use Table 6.6 for the WFC sharpness and also the read noise.

$$
\begin{aligned}
SNR &= \frac{R_{object} \cdot t}{\sqrt{R_{object} \cdot t + \frac{readnoise^2 + P_{dark} \cdot (t + 46) + P_{sky} \cdot t + P_{background} \cdot t}{sharpness}}} \\
&= \frac{0.15 \cdot 2400}{\sqrt{0.15 \cdot 2400 + \frac{5.3^2 + 0.004(2400 + 46) + 0 \cdot 2400 + 0 \cdot 2400}{0.11}}} \\
&= \frac{360}{\sqrt{360 + 344}} \\
&= 14
\end{aligned}
$$

which is for an un-split 2400s exposure. The Poisson noise and background noises contribute nearly equally. For three such exposures over three orbits

$$
\begin{aligned}
SNR_{total} &= SNR\sqrt{N} \\
&= 14\sqrt{3} \\
&= 23.
\end{aligned}
$$

Line Emission Point Source w/ LRF, On-Line Calculator

The above calculation can be performed using the ETC program. The "Point Source" form is used. "Emission Line" source and the "H 6563" line are selected; the redshift is set to 0.22. The program will automatically choose between PC and WFC, depending on the LRF setting. The least optimistic case of placing the object on a "pixel corner" is selected. The filter "LRF" is selected from the filter menu, and 8007Å is given for the central wavelength. The exposure time is specified as 2400s. See Figure 6.9 for an example of the completed form.

Figure 6.9: Point Source Form for WFPC2 On-Line Exposure Time Calculator. The target is an unresolved galaxy (z=0.22) nucleus with Hα line emission which is observed with LRF. SNR is computed for 2400s exposure.

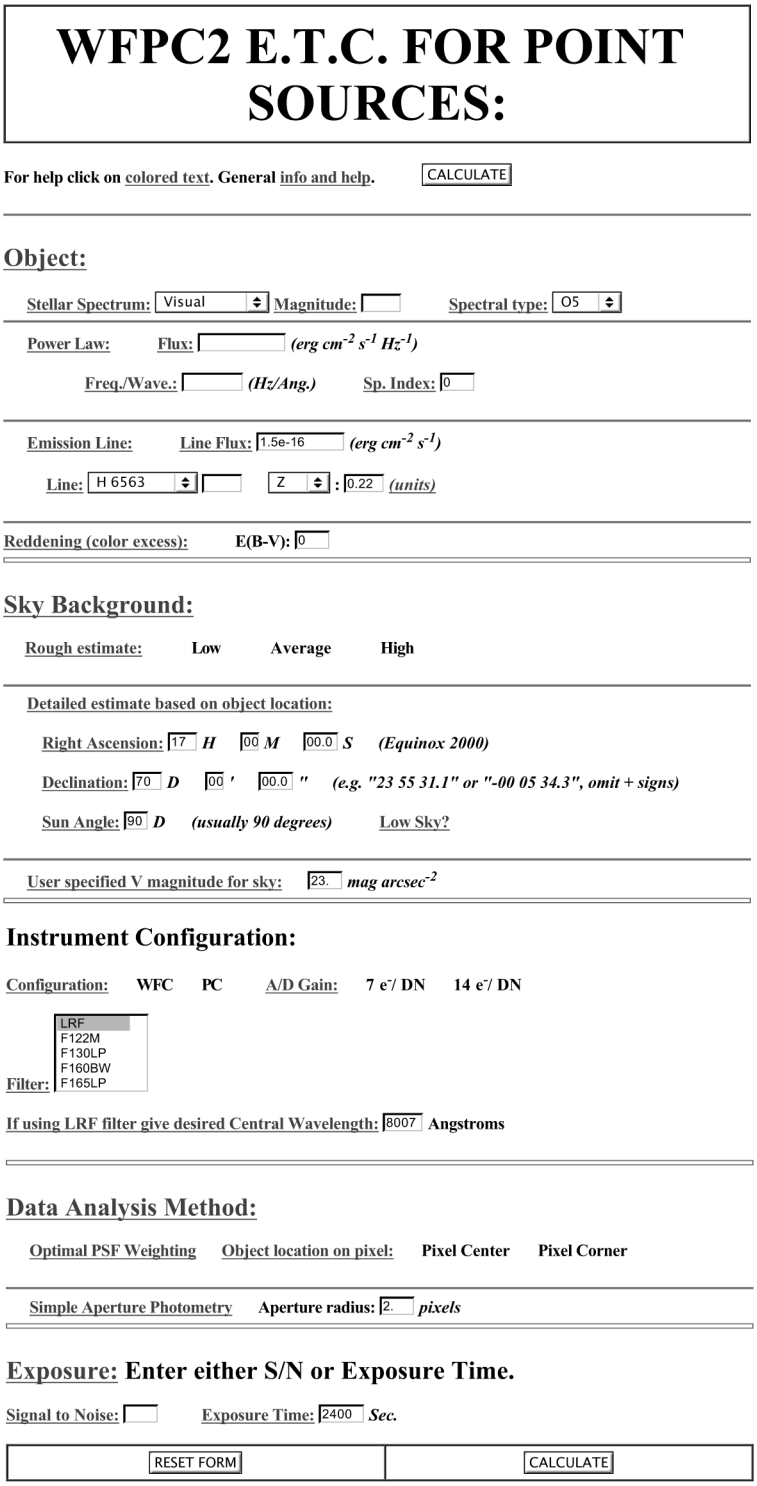

WFPC2 E.T.C. FOR POINT SOURCES:

For help click on colored text. General info and help. CALCULATE

Object:

Stellar Spectrum: Visual **Magnitude:** **Spectral type:** O5

Power Law: **Flux:** *(erg cm^{-2} s^{-1} Hz^{-1})*

Freq./Wave.: *(Hz/Ang.)* **Sp. Index:** 0

Emission Line: **Line Flux:** 1.5e-16 *(erg cm^{-2} s^{-1})*

Line: H 6563 Z : 0.22 *(units)*

Reddening (color excess): **E(B-V):** 0

Sky Background:

Rough estimate: **Low** **Average** **High**

Detailed estimate based on object location:

Right Ascension: 17 *H* 00 *M* 00.0 *S* *(Equinox 2000)*

Declination: 70 *D* 00 ′ 00.0 ″ *(e.g. "23 55 31.1" or "-00 05 34.3", omit + signs)*

Sun Angle: 90 *D* *(usually 90 degrees)* **Low Sky?**

User specified V magnitude for sky: 23. *mag arcsec^{-2}*

Instrument Configuration:

Configuration: **WFC** **PC** **A/D Gain:** **7 e$^-$/ DN** **14 e$^-$/ DN**

Filter: LRF / F122M / F130LP / F160BW / F165LP

If using LRF filter give desired Central Wavelength: 8007 **Angstroms**

Data Analysis Method:

Optimal PSF Weighting **Object location on pixel:** **Pixel Center** **Pixel Corner**

Simple Aperture Photometry **Aperture radius:** 2. *pixels*

Exposure: Enter either S/N or Exposure Time.

Signal to Noise: **Exposure Time:** 2400 *Sec.*

RESET FORM | CALCULATE

The result is SNR=13.1 for the un-split 2400s exposure (Figure 6.10), which is comparable to the manual calculation of SNR=14.

Figure 6.10: Sample Output for WFPC2 On-Line Exposure Time Calculator.

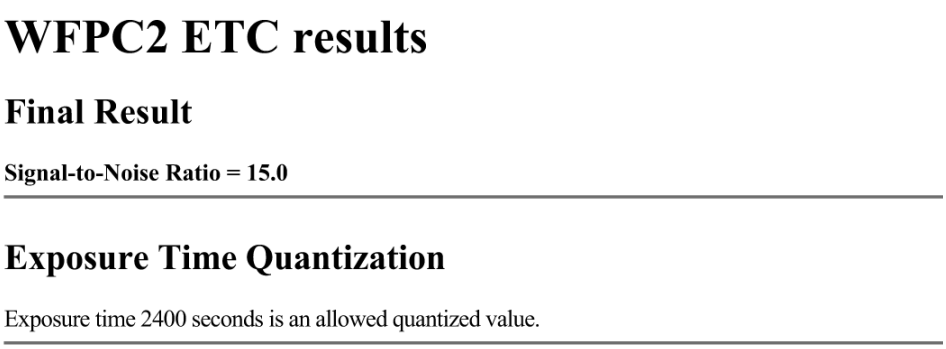

WFPC2 ETC results

Final Result

Signal-to-Noise Ratio = 15.0

Exposure Time Quantization

Exposure time 2400 seconds is an allowed quantized value.

6.8 Photometric Anomalies

There are two photometric anomalies resulting from nonlinearities of the WFPC2 detectors. The first is due to the imperfect charge transfer efficiency (CTE) of the detectors, which causes sources at high row and column numbers to appear fainter because the charge is transferred over a bigger fraction of the chip. This anomaly is increasing with time, especially for faint sources, presumably as a consequence of on-orbit radiation damage. We have developed correction formulae which appear to reduce the impact of this anomaly to about 1-3% for faint sources. The second, called “long vs. short”, causes sources to have a lower count rate - and thus appear fainter - in short exposures than in longer exposures, and appears independent of the position on the chip. The most likely explanation is that this effect is due to an overestimate of the sky measurement in the short exposure due to the presence of scattered light around bright stars. For further discussion, see Section 4.12.

We also note the F1042M filter has an anomalous PSF which can impact aperture photometry; see Section 5.8.

6.9 Red Leaks in UV Filters

The presence of significant red leaks in the UV filters, together with the much greater sensitivity and wavelength coverage in the red part of the spectrum, can make UV observation and calibration difficult. Observers must sometimes be prepared to take additional frames at red wavelengths, in order to estimate the contribution of red leak to the UV counts. The counts contributed by red leak can be a significant noise source, and must also be taken into account during SNR and exposure time estimation. See section 3.8 for detailed information. Note that the SYNPHOT synthetic photometry package can be used to estimate counts due to red leak for particular filter / target combinations.

6.10 Long-term Photometric Stability

The long-term photometric stability of WFPC2 has been evaluated by examining the photometric monitoring data collected over the lifetime of the instrument. Our primary standard, GRW+70D5824, has been observed roughly every four weeks, before and after decontamination procedures, both in the far UV and in the standard photometric filters. Early observations were taken monthly in both the PC and WF3. Later observations (since Cycle 6) were on a rotating schedule, where observations are taken in a different chip each month. Overall, a baseline of over ten years is available for the PC and WF3, and about eight years in WF2 and WF4. The data have been analyzed and reported by Baggett and Gonzaga (1998); here we summarize their main conclusions.

Overall, the WFPC2 photometric throughput, as measured via our primary standard, has remained remarkably stable throughout. Its long-term behavior in filters longward of F336W is characterized by small fluctuations (2% peak-to-peak) which appear to have no specific pattern, and there is no significant overall sensitivity trend. Aside from contamination corrections, which are only significant shortward of F555W, the same photometric zeropoints can be applied to non-UV data throughout the life of WFPC2.

In contrast, the UV photometric throughput of WFPC2 has changed measurably over the years. In most cases, the throughput has increased slowly, perhaps as a result of continuing evaporation of low-level contaminants. In F170W, the best-characterized UV filter on WFPC2, the clean throughput (immediately after a decontamination) has *increased* in the PC by about 12% from 1994 to 1998. Not all UV filter / detector combinations show this behavior; some combinations show a modest *decline* in throughput (e.g. 3% in F255W). Baggett and Gonzaga (1998)

report the details of the secular throughput changes for the filters we monitor.

Finally, the contamination rates - the rate at which the camera throughput declines after a decontamination, due to the gradual buildup of contaminants on the cold CCD windows - have generally decreased since installation of WFPC2, possibly also because the environment has become cleaner with time. (This excludes brief periods of increased contamination just after servicing missions.) For example, the contamination rate in F170W in the PC has decreased from ~0.56%/day to ~0.45%/day. See section 6.11 for additional discussion of the UV response variations.

Baggett and Gonzaga (1998) suggest a number of ways users can correct long-term changes in WFPC2 photometry. While these changes are generally small, users wishing to achieve high-precision photometry, especially in the UV, should follow their recommendations.

A comprehensive re-analysis of the entire WFPC2 throughput history is being carried out during 2008, and the results will be documented in a future WFPC2 ISR. Preliminary results of this analysis are generally consistent with previous trends. There is also considerable evidence for a long-term throughput decrease in the F255W filter, and filters adjacent in wavelength, affecting all four CCDs. Please consult the WFPC2 web site for future results.

6.11 Short-term Time Dependence of UV Response

The UV throughput of the WFPC2 degrades in a predictable way after each monthly decontamination. The photometric calibration given in Section 6.1 is applicable at the start of each cycle, and measurements taken at other times must be corrected to account for the change in sensitivity since the last decontamination. In addition, a long-term change in sensitivity is present for the F160BW and F170W filter observations on the PC, and may be present to a lesser degree at other wavelengths.

Figure 6.11 shows the photometric monitoring data for the standard star GRW+70D5824 (a white dwarf classified DA3; B-V = -0.09) in the WF3 and PC1 for the set of filters which are routinely monitored. Only data after April 24, 1994, when the CCD operating temperatures were lowered from -76˚C to -88˚C, are shown. Figure 6.11 also shows that the effect of contamination on the F675W and F814W filter observations is essentially negligible. However, at UV wavelengths contamination effects are readily apparent; the upper envelope of points indicate measurements made shortly *after* a decontamination, while the lower envelope are data taken shortly *prior* to a decontamination. Contamination effects are largest for the F160BW filter where they cause a 30% - 40% modulation in throughput. Table 6.10 shows the monthly decline in throughput based on this data. The

values in parentheses are based on similar observations of the globular cluster ω Cen (NGC 5139; mean B-V ~ 0.7 mag). In general, the values derived from the ω Cen data are in good agreement with the values derived from GRW+70D5824 data.

Table 6.10: Change in WFPC2 Throughput Over 30 Days[a].

Filter	PC1	WF2	WF3	WF4
F160BW	-0.263 ± 0.030		-0.393 ± 0.051	
F170W	-0.160 ± 0.011	-0.284 ± 0.005	-0.285 ± 0.006	-0.232 ± 0.006
F218W	-0.138 ± 0.009		-0.255 ± 0.010	
F255W	-0.070 ± 0.007		-0.143 ± 0.009	
F336W	-0.016 ± 0.008		-0.057 ± 0.011	
	(-0.038 ± 0.018)	(-0.043 ± 0.010)	(-0.046 ± 0.008)	(-0.047 ± 0.007)
F439W	-0.002 ± 0.007		-0.021 ± 0.010	
	(0.002 ± 0.014)	(-0.022 ± 0.007)	(-0.023 ± 0.009)	(-0.023 ± 0.007)
F555W	-0.014 ± 0.006		-0.016 ± 0.008	
	(0.007 ± 0.013)	(-0.007 ± 0.007)	(-0.009 ± 0.009)	(-0.008 ± 0.008)
F675W	-0.001 ± 0.006		-0.001 ± 0.006	
	(-0.020 ± 0.020)	(0.001 ± 0.011)	(0.002 ± 0.011)	(0.004 ± 0.011)
F814W	0.007 ± 0.007		0.003 ± 0.008	
	(0.013 ± 0.019)	(-0.002 ± 0.009)	(-0.000 ± 0.009)	(-0.002 ± 0.010)

a. Values in parentheses are from the ω Cen observations.

A slight difference between the throughput declines for GRW+70D5824 and ω Cen might be expected due to differences in spectral shape, especially for filters like F336W which have a substantial red leak. However, even in the case of F336W the effect should be less than 0.01 mag based on SYNPHOT simulations.

Figure 6.12 and Figure 6.13 show the throughput decline for the F170W filter in all four chips as a function of days since the last decontamination. The contamination rate is remarkably constant during each decontamination cycle, and can be accurately modeled by a simple linear decline following the decontaminations, which appear to return the throughput to roughly the nominal value each month. While the contamination rates are similar for the three WF chips, the values for the PC are significantly lower.

In addition to the monthly changes in throughput there is evidence for a long-term variation in the F170W data on the PC, where the throughput has *increased* at the rate of approximately 3.3% ± 0.2% per year. This is

evident in Figure 6.11, but is much clearer in the top panel of Figure 6.12 where lines are fitted separately to the epoch ~1994 (dotted line) and ~1998 data (solid line). The effect is most evident in Figure 6.14 where only data taken 4 days or less after a decontamination are shown. The F160BW filter shows an even stronger trend but with larger uncertainties (i.e., an increase of 9.0% ± 1.7% per year). The WF chips do *not* show this effect, nor do the observations on the PC at longer wavelengths. One possible explanation of the throughput increase is that WFPC2 was flown with some initial contaminant on the PC1 optics which is slowly evaporating on-orbit. The pre-launch thermal vacuum test gave evidence of elevated contamination in PC1, which is consistent with this hypothesis.

A second long-term effect is also apparent in Figure 6.12 and Figure 6.13. In all four CCDs the line fitted to the later data show a shallower slope, which indicates a slower throughput decline. The decline rate is reduced by 19% (PC) to 30% (WF4) over the four-year interval between the dotted and solid lines in each panel. This is likely caused by contamination slowly escaping the camera.

ISRs WFPC2 96-04 and WFPC2 98-03 describe detailed results of this monitoring (available from the WFPC2 web site). A comprehensive re-analysis of the entire WFPC2 throughput history, including contamination affects, is being carried out during 2008. The results will be documented in a future WFPC2 ISR. Users are asked to consult the STScI WFPC2 web page for the latest information at the following address:

http://www.stsci.edu/hst/wfpc2

Figure 6.11: Photometric Monitoring Data for WFPC2.

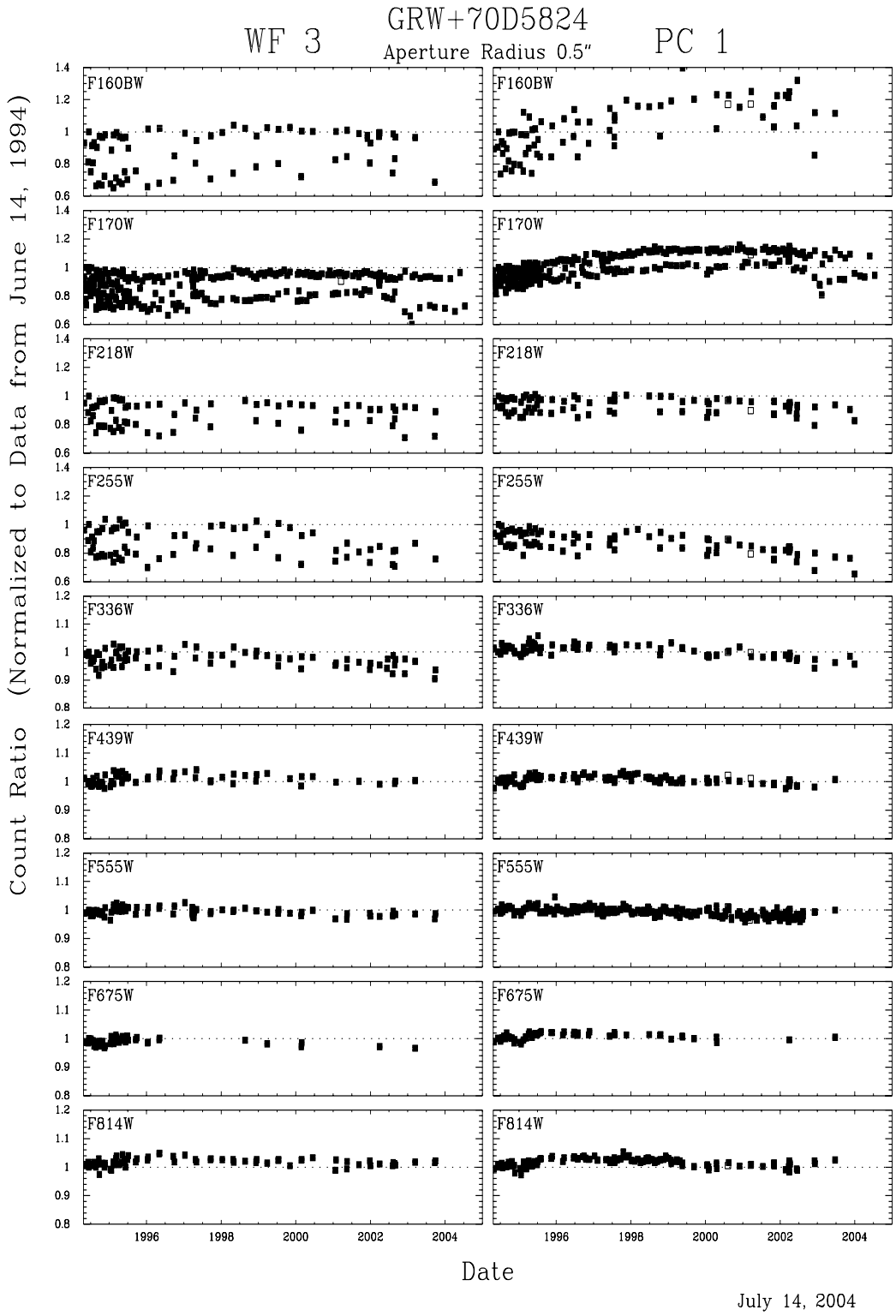

Figure 6.12: Post-decontamination Throughput for F170W Filter in PC and WF2.

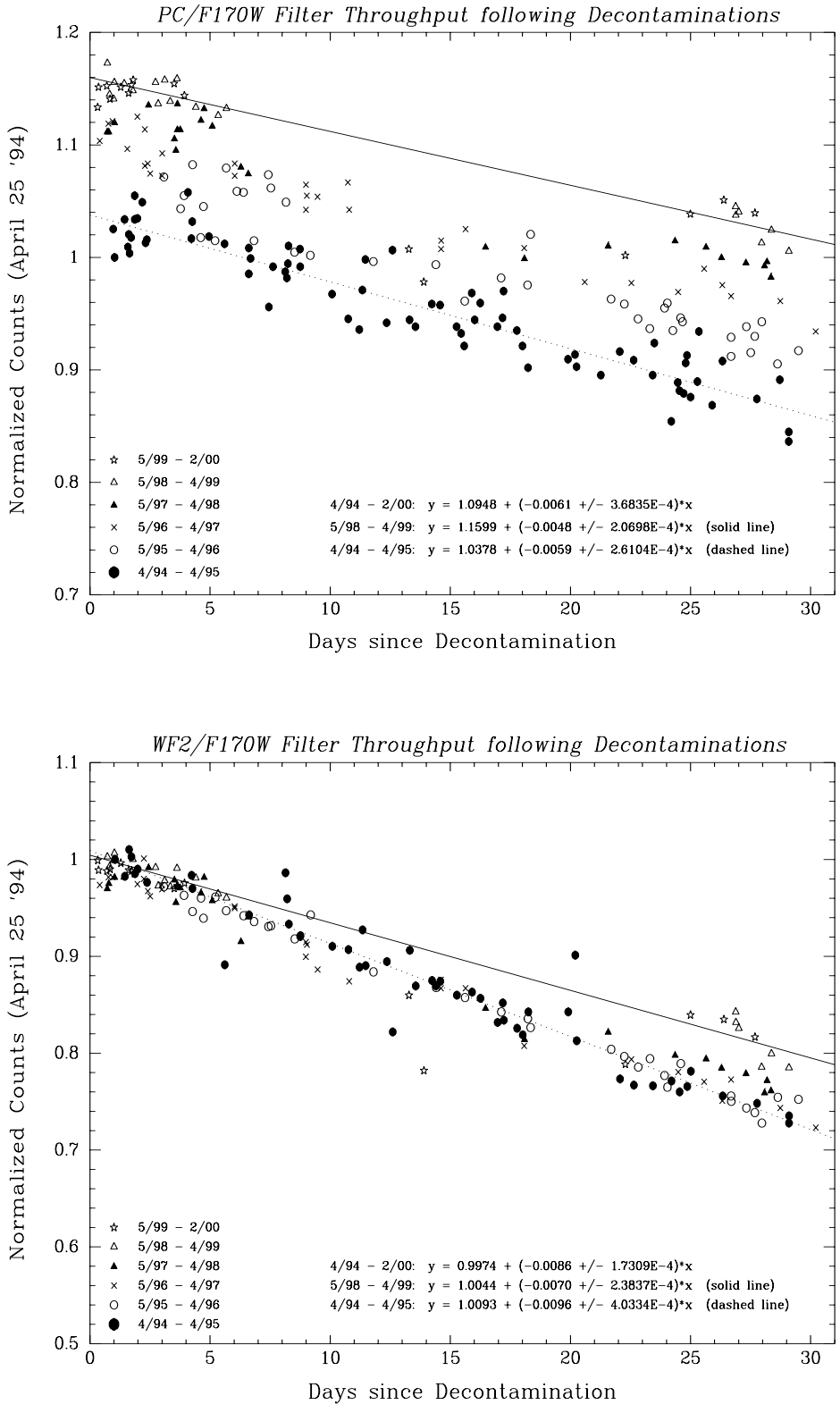

Figure 6.13: Post-decontamination Throughput for F170W Filter in WF3 & WF4.

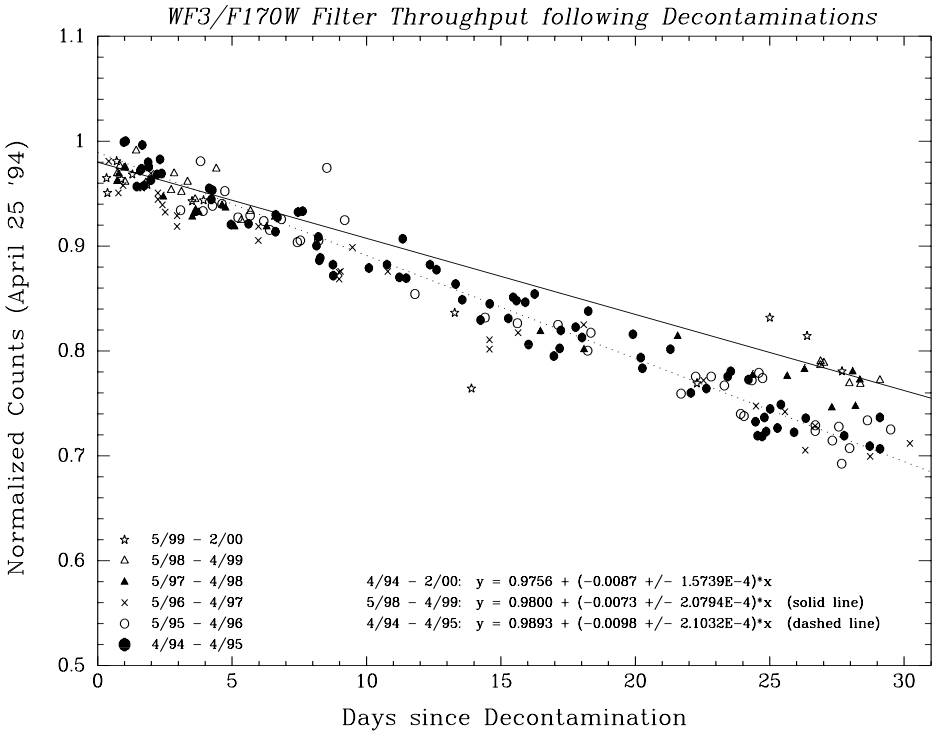

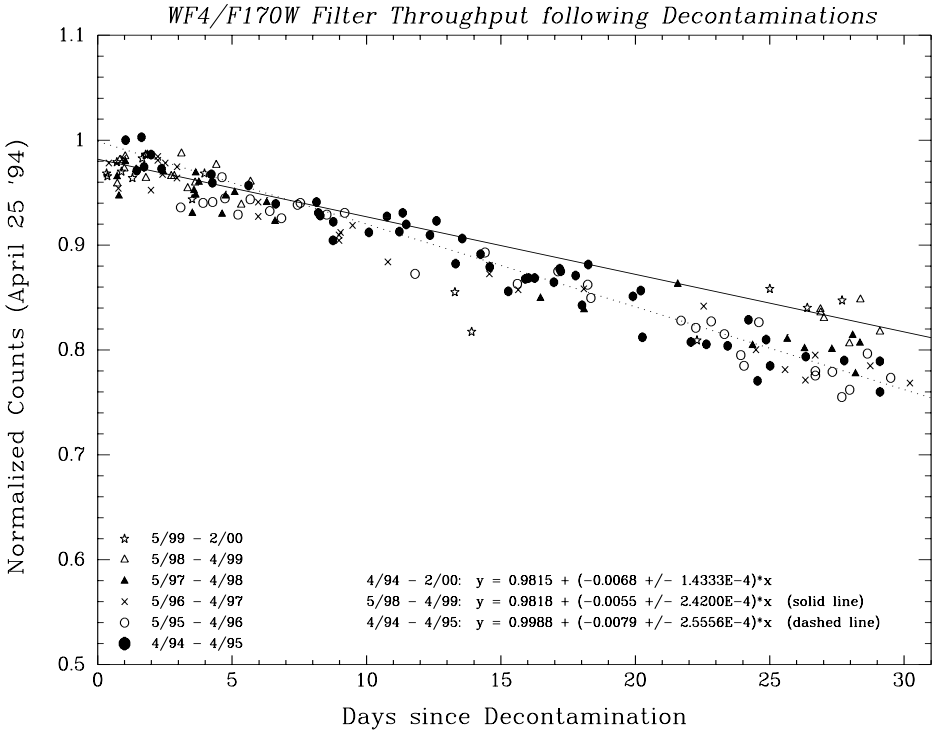

Figure 6.14: Change in Throughput vs. Time.[1]

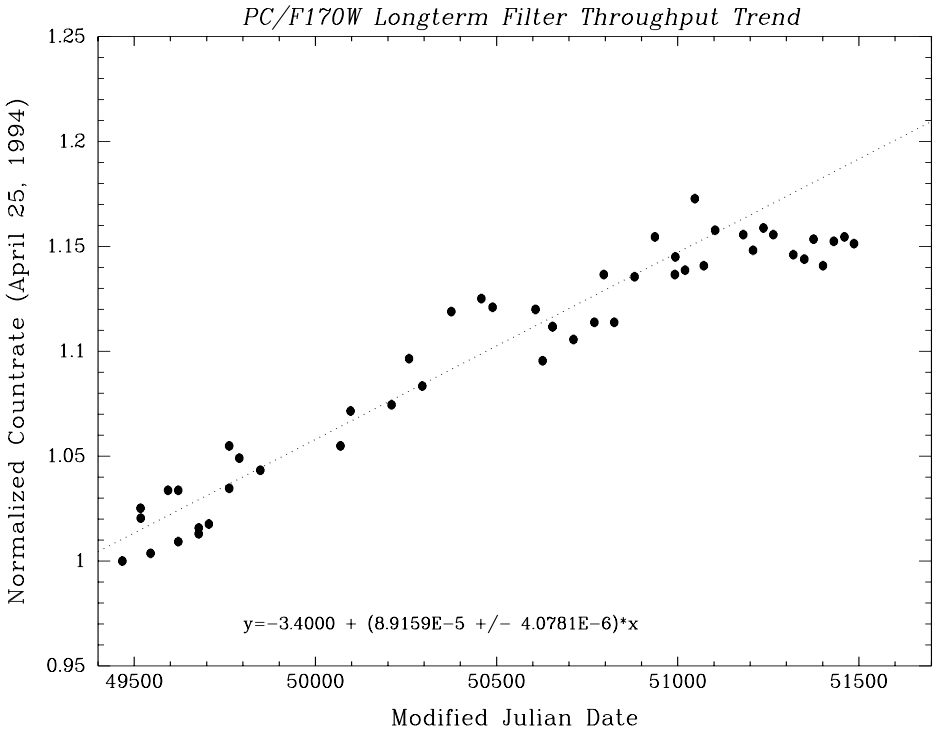

1. Only data taken 4 days or less after a decontamination are shown. Data taken 0 to 60 days after service missions are also excluded. The fit is to data prior to MJD 51100.

CHAPTER 7:

Observation Strategies

In this chapter. . .

7.1 Observing Faint Targets

For broad band filters the sky background limited the detection of faint targets. For example, an 8-orbit observation in F555W gave a ~5σ detection limit at Johnson V=28.6 for an average sky level of 23 mag arcsec^{-2} in V. Note that the sky background is a strong function of position, especially for targets near the ecliptic; the sky level can vary from V=23.3 mag arcsec^{-2} at the ecliptic pole to about V=20.9 mag arcsec^{-2} on the ecliptic near the solar avoidance limit. (See Table 6.3 for sky level as function of ecliptic coordinates.)

If these higher sky levels would severely impact the science data, observers should have considered specifying the special requirement LOW-SKY on the Phase II proposal. This parameter forces the observation to be made when the sky background is within 30% of the minimum value for the target. Note, however, that this also reduced the number of HST calendar windows available to the observation, and so might have resulted

in scheduling delays or may even have made the observation infeasible if there were other constraints such as ORIENTs. A minor decrease in the per-orbit visibility period also resulted from LOW-SKY, but for background limited programs this was a minor price to pay for the guarantee of a much lower background. Note that CVZ targets could not have also been LOW-SKY since that would have implied mutually exclusive pointing constraints.

Scattering of bright Earth light in the OTA can produce non-uniformities in the background which may hamper analysis of faint target images. Most often these take the form of diagonal bars of suppressed background light in several of the CCDs. These effects tend to occur for broad band filters when the OTA axis is about 25˚ from the bright Earth. This effect is most often seen in observations of targets in the CVZ (continuous viewing zone), since the Earth limb is never very far from the OTA axis when observing in the CVZ. Figure 7.1 shows a typical case. LOW-SKY eliminated this effect for non-CVZ targets, as it placed the OTA axis more than 40˚ from the bright Earth. Alternatively, one could have placed the target away from the CCD center to avoid these artifacts.

Another option for reducing the sky brightness, was the special requirement SHADOW, which forced the observation to be made when HST was in the Earth's shadow. This usually had a large negative impact on the observing efficiency, and was recommended only when observing far-UV emission lines (e.g. Ly α and OI 1304Å). Its primary goal was only to reduce geocoronal emission lines. Moreover, it did not attempt to minimize zodiacal emission, which dominates at visible wavelengths.

Figure 7.1: Example of Scattered Earth Light. Scattered light contributes ~100 e^- of background throughout this image. The camera spiders block some of this scattered light along CCD diagonals, hence forming "X" patterns and bars where the background is reduced by ~40% in this image.

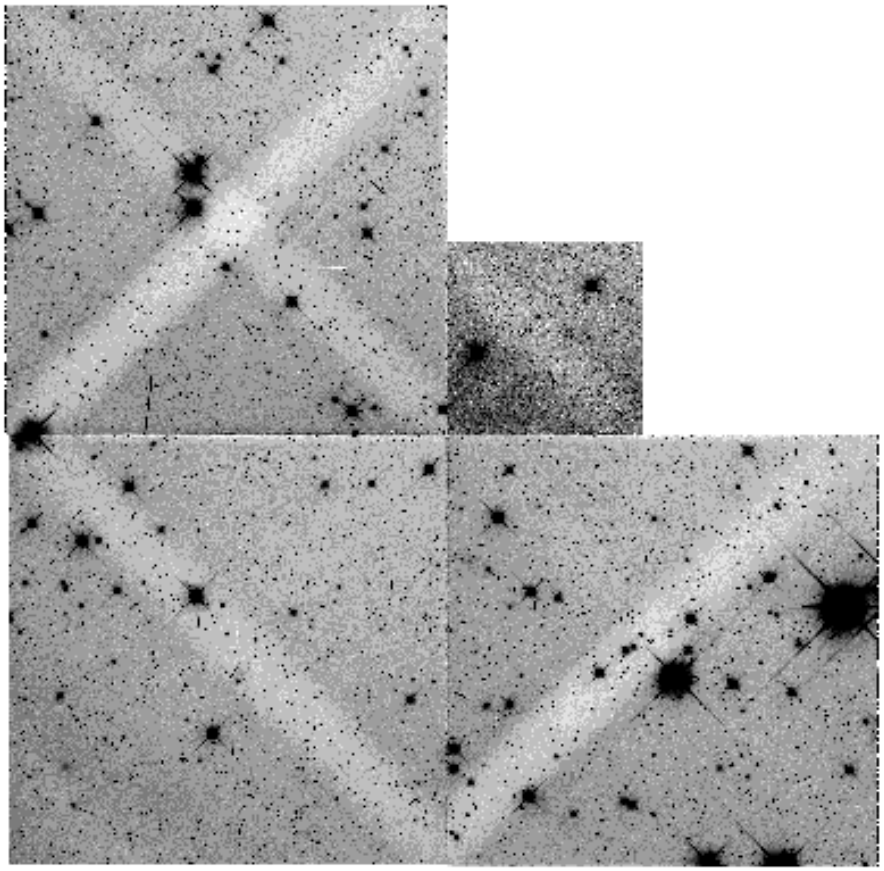

7.2 Observing Bright Targets

Saturation was the primary concern when observing bright targets. The analog-to-digital converter ran out of bit codes at ~28,000 e^- $pixel^{-1}$ in the ATD-GAIN=7 (default) setting, and at ~53,000 e^- $pixel^{-1}$ in the ATD-GAIN=15 setting. Count levels above these are merely reported as 4095 DN in the raw (uncalibrated) data. Hence ATD-GAIN=15 was recommended for targets approaching 28,000 e^- $pixel^{-1}$. The disadvantage of this setting is that the read noise is poorly sampled by this coarse digitization, and hence the read noise is slightly increased.

At count levels above ~90,000 e^- $pixel^{-1}$ charge will overflow the potential well of each pixel, and begin to bloom up and down the CCD columns. For example, this occurs in the F555W filter at about V=13.5 for a 10s exposure on the WFC, and at about V=13.0 on the PC1.

At very high count levels, above ~10^8 e^- per CCD column, the charge bloom will reach the top and bottom of the CCD and flow into the serial registers. CLOCKS=YES disposed of this charge as it reached the ends of the CCD, and thus prevented it from leaking back into adjacent CCD columns. This exposure level corresponds roughly to a 10s exposure of a V=7 star in F555W. Note that CLOCKS=YES offered no benefit unless the bloom reached the ends of the CCD, and that it may have slightly compromised the bias and dark calibration. Moreover, CLOCKS=YES resulted in anomalous exposure times; exposure times are rounded to the nearest integral second, minus a delay time of up to 0.25s for the shutter to open. (See section 2.6 for further discussions about the use of CLOCKS=YES.)

Besides setting ATD-GAIN=15, the PC CCD could have been used to reduce saturation effects for stellar objects. The peak of the PSF spreads over more pixels on the PC (vs. WFC), so stars can be exposed about 50% longer on the PC before saturation set in.

Note that the narrow band filters could have been used when observing very bright targets. For example, stars as bright as V~4.4 could be observed without saturation in F502N using the PC at ATD-GAIN=15 with a 0.11s exposure time.

7.3 Observing Faint Targets Near Bright Objects

The concerns here are similar to those for observing bright targets; saturation and blooming of the bright companion PSF must not impact the faint target. Also, one may need to consider subtracting the PSF of the bright object, and effects which limit the accuracy of that subtraction.

If the bright companion saturated and bloomed, it may have been necessary to rotate the CCD so that blooming along the CCD columns did not obliterate the faint target. See figure 7.10 for an illustration of the bloom directions. It may also have been useful to orient the field so that the OTA diffraction spikes from the bright companion (along diagonal lines on the CCDs) avoided the faint target. Table 7.1 summarizes ORIENTs which could be used to avoid CCD blooming tracks and OTA diffraction spikes caused by bright objects. For example, if a faint companion was at PA 60° on the sky relative to a bright companion, it was advantageous to observe on PC1 with ORIENT= PA + 45° = 105°. Ideally, some range in ORIENT was specified to ease scheduling, hence “ORIENT=90D TO 120D” might be specified on the Phase II proposal. Note that “ORIENT=270D TO 300D” was also feasible, and would be reflected in the visit level comments.

Table 7.1: ORIENTs for Avoiding Bloom Tracks and Diffraction Spikes. "PA" is the position angle of the faint target relative to the bright object. Note that ORIENT should be between 0D and 360D, so subtract 360˚, if necessary. In the proposal these are specified as, e.g., "ORIENT=231D TO 261D".

CCD	ORIENT
PC1	PA+30˚ to PA+60˚, PA+210˚ to PA+240˚
WF2	PA+120˚ to PA+150˚, PA+300˚ to PA+330˚
WF3	PA+30˚ to PA+60˚, PA+210˚ to PA+240˚
WF4	PA+120˚ to PA+150˚, PA+300˚ to PA+330˚

If instead of observing a known companion, one was *searching* for companions, it is advisable to observe at several ORIENTs so that the CCD bloom track and OTA diffraction spikes did not hide possible companions. For example, three ORIENTs, each separated by 60˚, gave good data at all possible companion position angles.

If PSF subtraction will be needed during data analysis, then data from the PC CCD may have some advantage, since it provides better sampling of fine undulations in the PSF. It may also be helpful to use observations of a second bright star for PSF calibration, though these may be of limited utility since thermal effects and OTA "breathing" can modify the telescope focus, and hence the PSF, on time scales of less than one hour. Any such PSF star should be similar in color to the target, and should have been observed at the same CCD position (within 1″) and with the same filter. Sub-pixel dithering may also be useful, so as to improve sampling of the PSF (see Section 7.6).

Figure 7.2 illustrates the effect of OTA breathing, and periodic focus adjustments, on PSF subtraction. It shows the difference between an "in focus" PSF and one where the OTA secondary mirror has been moved by 5μm. This amount of focus change is comparable to the range of OTA "breathing" effects (time scale <1 hour), and the periodic (semi-annual) focus adjustments of the OTA. Each panel shows a different contrast setting; the percentages indicate the energy per pixel which is plotted as white, expressed as a fraction of the total (un-subtracted) PSF energy. For example, features which are just white in the "0.003%" panel contain 0.003% of the total PSF energy in each pixel. In other words, the feature labeled "a" is, in effect, ~10 magnitudes fainter than the PSF of the bright object, so that it may be very difficult to detect a "real" companion object ~10 magnitudes fainter than the bright object, at this distance from the bright object. In a real PSF subtraction situation, other effects including PSF sampling, noise, and pointing instability would further degrade the subtraction. (The elongated appearance of the residuals in the PSF core is due to astigmatism in PC1).

Figure 7.2: Impact of OTA Focus Shift on PSF Subtraction. Each image shows the difference between an “in focus” and a 5 micron defocused PSF at different contrast settings. Numbers indicate the energy per pixel which is plotted as white, as a percentage of total energy in the un-subtracted PSF. Based on TinyTIM models for PC1 in F555W filter.

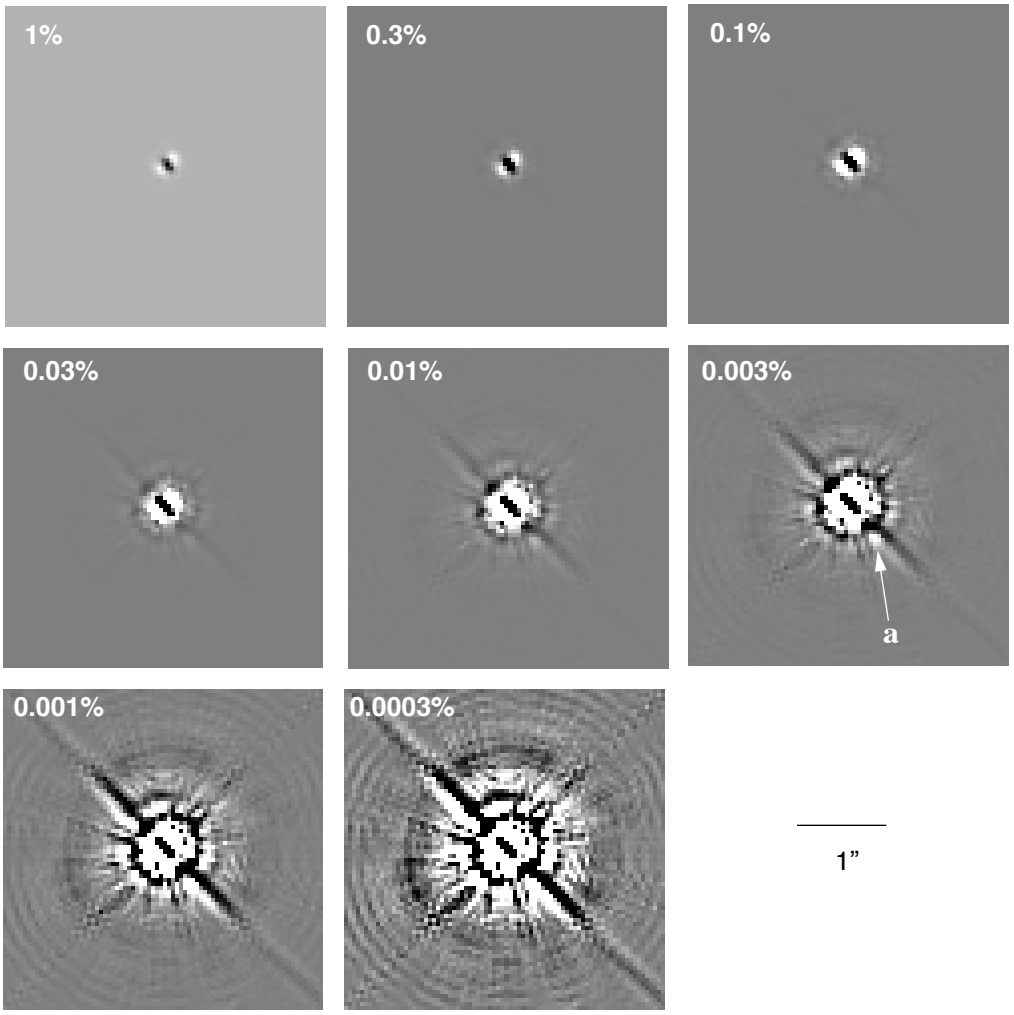

Table 7.2 gives some quantitative indication of the performance expected for PSF subtractions in the high signal-to-noise limit. It gives the magnitude of “star-like” artifacts remaining in the subtracted image, as a function of distance from the bright object, and magnitude m_{bright} for the bright object. The right-most column gives an effective magnitude limit imposed by artifacts from the PSF subtraction. These results are derived for the 5μm focus shift described above, and are for PC1 and filter F555W. It may be possible to do somewhat better than these limits by subtracting accurate model PSFs, or by finding an observed PSF with matching focus.

Table 7.2: Approx. PSF Subtraction Artifact Magnitudes and Magnitude Limits.

Distance from Bright Object	Effective Magnitude of Subtraction Artifacts	Effective Faint Object Detection Limit (3σ)
0.1″	m_{bright}+4.7	m_{bright}+3.5
0.3″	m_{bright}+8.6	m_{bright}+7.4
1″	m_{bright}+11.4	m_{bright}+10.2
3″	m_{bright}+13.2	m_{bright}+12.0

Results indicate that PSF subtraction and detection of faint objects very close to bright objects can be improved by using a composite PSF from real data, especially dithered data. Table 7.3 indicates limits that may be obtained for well-exposed sources (nominal S/N > 10 for the faint object) where a dithered PSF image has been obtained.

Table 7.3: Limiting Magnitudes for PSF Subtraction Near Bright Objects.

Separation in arcsec (on PC)	Limiting Δm (without PSF subtraction)	Limiting Δm (with PSF subtraction)
0.15	2.5	5.0
0.25	4.5	6.4
0.4	6.5	7.3
1.0	8.9	10.7
3.0	10.7	12.9

A technique that has been used with some success to search for nearby neighbors of bright stars was to image the source at two different roll angles, and use one observation as the model PSF for the other. In the difference image, the secondary source appears as a positive residual at one position and a negative residual at a position separated by the change in roll angles. PSF artifacts generally do not depend on roll angle, but rather are fixed with respect to the telescope. Thus, small changes in the PSF between observations will not display the positive or negative signature of a true astrophysical object. Again, it was recommended that the observations at each roll angle be dithered.

Large angle scattering may also impact identification of very faint objects near very bright ones. This scattering appears to occur primarily in the camera relay optics, or in the CCD. Hence, if a faint target is more than ~10″ from a bright object (i.e. very highly saturated object), it would have been advisable to place the bright object on a different CCD, so as to minimize large angle scattering in the camera containing the faint target.

For more information on large angle scattering, please see Section 5.9. Note also that highly saturated PSFs exist for PC1 in filters F439W, F555W, F675W, and F814W, and for F606W on WF3; these may be useful when attempting to subtract the large-angle scattered light. TinyTIM does not accurately model the large angle scattering, and should be used with caution when analyzing highly saturated images. To obtain available PSFs please visit the WFPC2 PSF page at:

`http://www.stsci.edu/hst/wfpc2/analysis/wfpc2_psf_page.html`

It was generally unwise to place bright companions or other bright objects just outside the area imaged by the CCDs. The region of the focal plane just outside the CCDs (within about 6″ of the CCDs) contains a number of surfaces which can reflect light back onto the CCDs, hence placing bright targets there could have undesired results. Also, the un-imaged "L" shaped region surrounding PC1 should have been avoided, since incomplete baffling of the relay optics allowed out-of-focus images of objects in this region to fall on the CCDs. Figure 7.3 illustrates various bright object avoidance regions near the WFPC2 field-of-view; the indicated avoidance magnitudes that produced 0.0016 e^{-} s^{-1} $pixel^{-1}$ in the stray light pattern for F555W. Figure 7.4 and Figure 7.5 show examples of artifacts which resulted from bright stars near the PC1 CCD. The report "A Field Guide to WFPC2 Image Anomalies" (ISR WFPC2 95-06, available on the WFPC2 web pages and from (`help@stsci.edu`) gives more detailed discussions of artifacts associated with bright objects, and their avoidance.

Figure 7.3: Bright Object Avoidance Regions Near WFPC2 FOV.

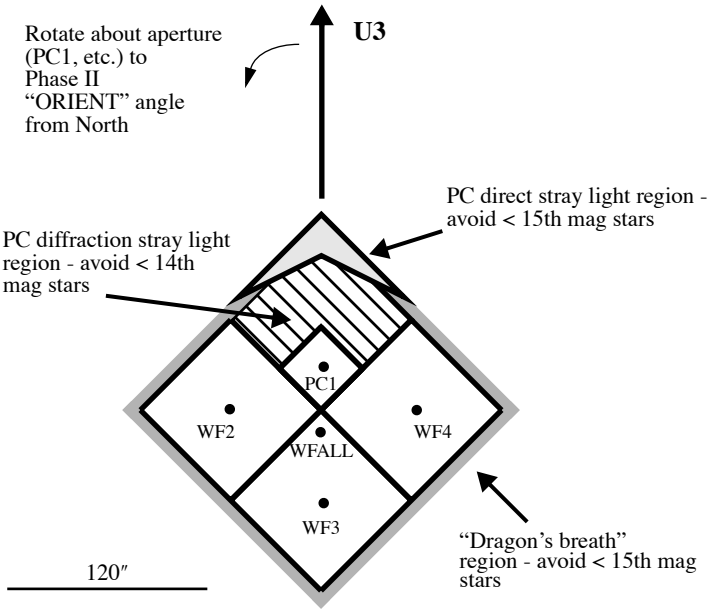

Figure 7.4: Example of PC1 “Direct” Stray Light Ghost.

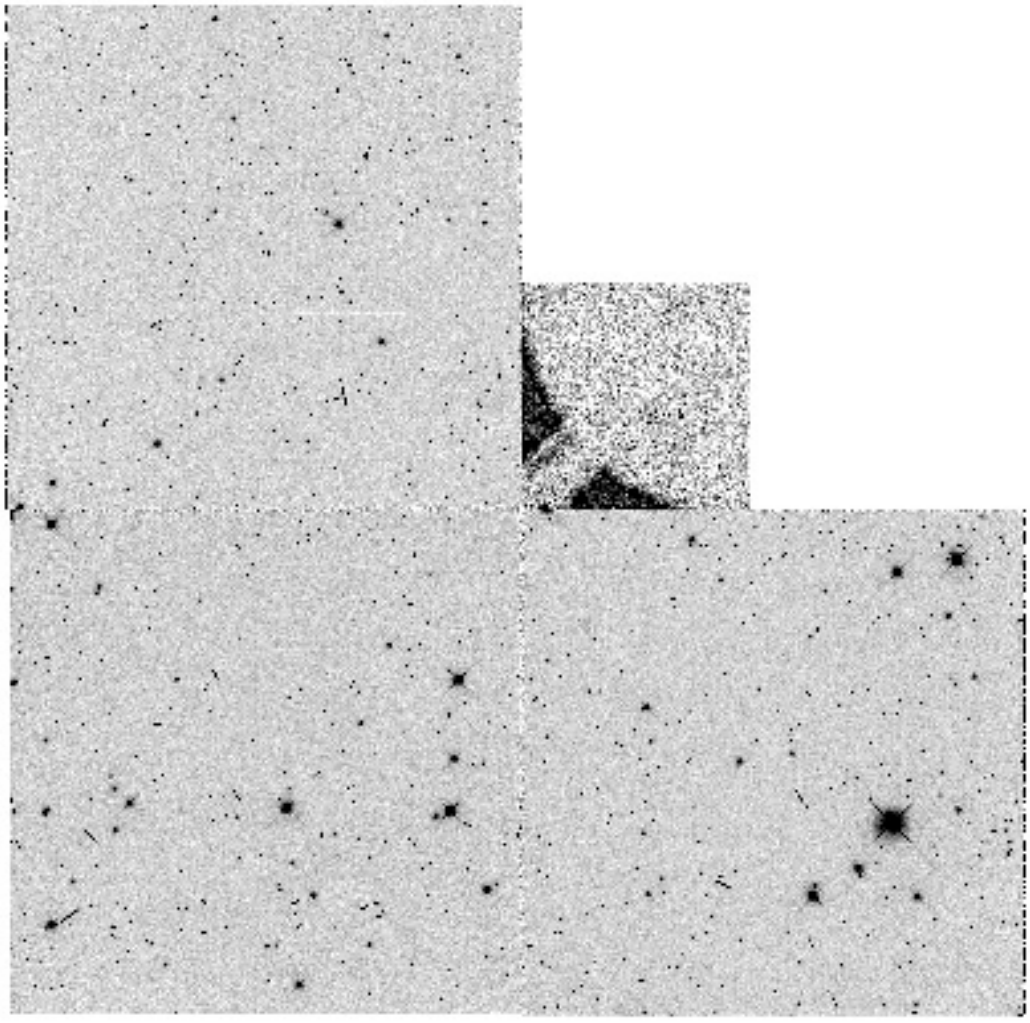

Figure 7.5: Example of PC1 “Diffraction” Stray Light Ghost.

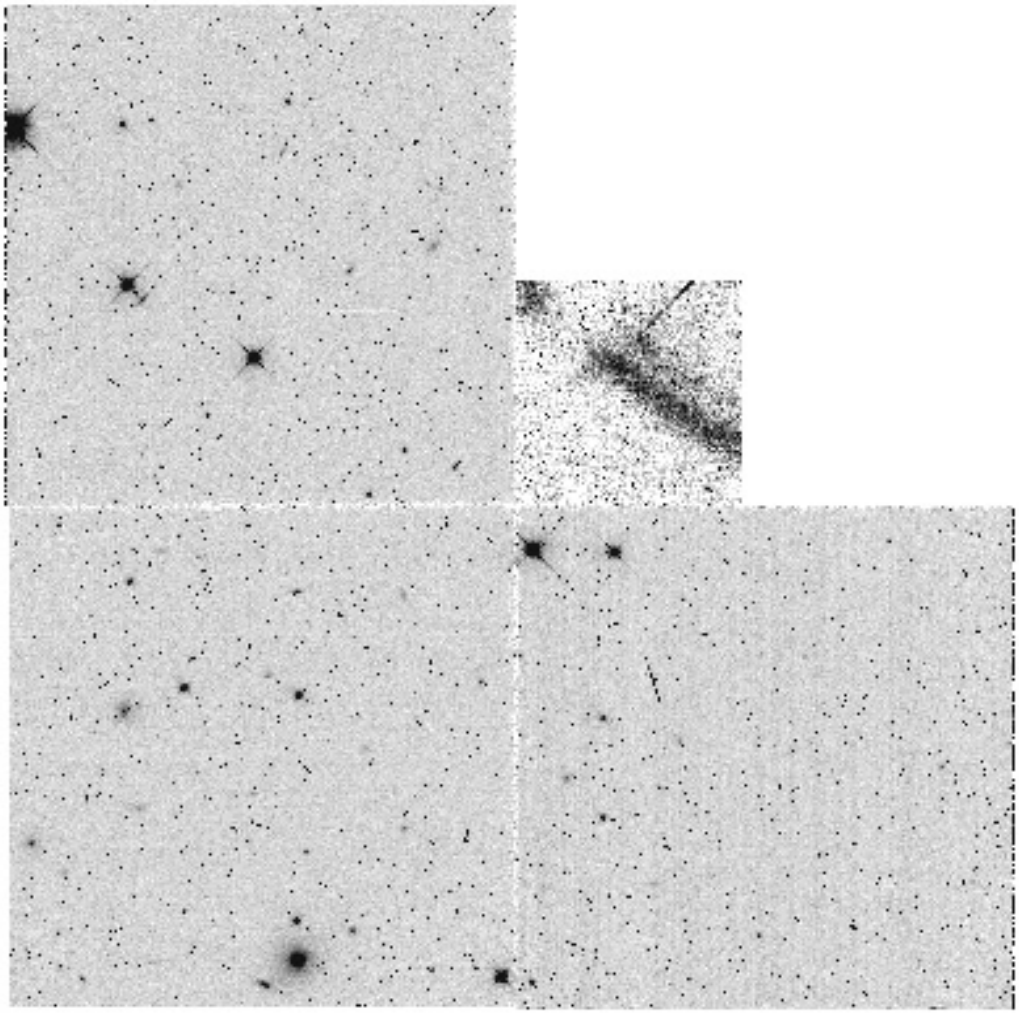

7.4 Cosmic Rays

Cosmic rays contaminated ~20 pixels per second per CCD. It was imperative that two or more images be obtained at each pointing position, if these artifacts are to be removed from the data. The default action by the Phase II proposal processing software was to split exposures longer than 600s into two nearly equal parts, so as to allow removal of the cosmic ray tracks. The CR-SPLIT and CR-TOLERANCE optional parameters on the Phase II proposal allowed observers to adjust this behavior. CR-SPLIT could be set to either DEF (default), NO, or a numeric value (0.0 to 1.0) giving the fraction of the total exposure allotted to the first sub-exposure of the pair. CR-TOLERANCE indicates the spread allowed in dividing the

exposure, as a fraction of the total exposure time. For example, the default CR-TOLERANCE=0.2 allowed the first sub-exposure to range from 0.3 to 0.7 of the total exposure. Setting CR-TOLERANCE=0 forced equal-length sub-exposures, assuming CR-SPLIT was set to 'DEFAULT' or 0.5.

The required degree of cosmic-ray avoidance will depend on the science goals of the proposal; observations of a single small target usually suffered much less impact from cosmic rays than programs needing very "clean" data over a large area. Table 7.4 gives very rough recommendations for the number of sub-exposures for a given total exposure time. Note that splitting into *many* sub-exposures introduced additional overhead time and increased the noise for "read noise" limited exposures (usually exposures in UV or narrow band filters), and hence more sub-exposures than are truly required by the science goals should not have been used.

Table 7.4: Recommended Exposure Splittings.

Total Exposure Time (s)	Rough Recommended Number of Sub-exposures	
	Programs with Single Small Target	Wide-area Search Programs
<300	1	3
300 - 600	1 or 2	4
600 - 1600	2 or 3	4
1600 - 5000	3	5
5000 - 10000	4	6
>10000	One exposure per orbit (2400s each)	

7.5 Choice of Exposure Times

The choice of exposure time generally depended on the signal-to-noise ratio required to meet the science goals. This could be assessed using information in Chapter 6 or plots in Appendix B, or by using the on-line WFPC2 Exposure Time Calculator tool at:

http://www.stsci.edu/hst/wfpc2/software/wfpc2-etc.html

However, when packing orbits, compromises were often needed to decide which exposures to lengthen or shorten. Table 7.5 provided relevant information. It shows the total time required to execute a single CR-SPLIT=NO exposure, *excluding* any time needed to change filters.

Note that the most efficient exposure times were those whose length approaches or equals, but does not exceed, an integral number of minutes *plus* 40s. Figure 7.6 illustrates event timings during a typical 60s WFPC2

exposure, similarly, Figure 7.7 illustrates events during a (more efficient) 100s exposure. (See section 2.7 for more information about exposure timings).

Figure 7.6: Event Timings During a 60s WFPC2 Exposure. All events, except shutter opening, start on 1 minute spacecraft clock pulses. Both the CCD clear and readout of each CCD require 13.6s. This 60s exposure, including the filter change, requires 4 minutes.)

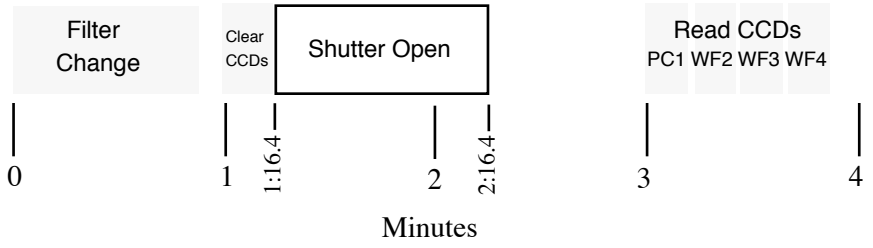

Figure 7.7: Event Timings During a 100s WFPC2 Exposure. This exposure, including the filter change, requires 4 minutes.

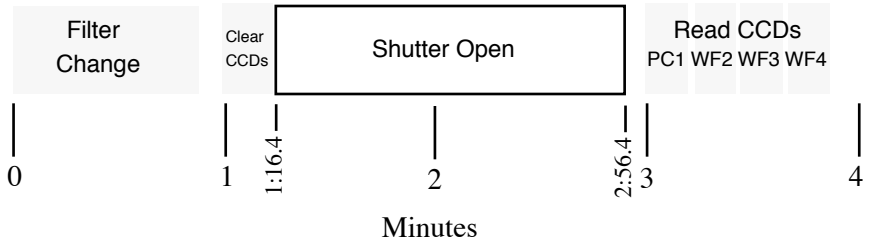

Due to the various overheads, shortening or lengthening an exposure could have unexpected effects on the orbit packing. For example, shortening an exposure from 400s to 350s had no effect on orbit packing; they both require 9 minutes to execute (CLOCKS=NO, the default setting). On the other hand, shortening an exposure from 180s to 160s trims the execution time by 2 minutes (again CLOCKS=NO, the default setting).

CLOCKS=YES may have had some advantage in a long series of exposures whose lengths were 180s or somewhat greater. Each savings of 1 minute can add up to a few more exposures per orbit. The down side is that most calibrations were derived for exposures with CLOCKS=NO, so the calibration may be slightly compromised. The largest calibration error is expected to occur in the dark current, where there may be a slight increase near the top and bottom of each CCD. In many situations this error may be acceptable, such as a small target near a CCD center, or broad band filter images where the sky completely dominates the dark current. CLOCKS=YES will have had more impact on calibration of narrow filters, or situations requiring an extremely flat background. (Also, see Section 2.6 for discussion of exposure time anomalies associated with CLOCKS=YES, though these are most important for exposures <30s.)

An exposure with CR-SPLIT=YES required the total time for each sub-exposure as given by Table 7.5, again, plus any time needed to change filter before the first exposure. However, the default CR-SPLITting allowed schedulers some latitude in dividing the exposures (CR-TOLERANCE=0.2 is the default) so the exact overheads were unpredictable. For example, a 700s exposure with CR-SPLIT=0.5 (the default) could be split into a pair of 350s exposures totaling 18 minutes, or a 300s and 400s exposure totaling 17 minutes.

Table 7.5: Basic Time to Execute Single Non-CR-SPLIT Exposure. This includes time to prep the CCD, execute the exposure, and read out the CCDs. Times needed to change filter (1 minute), or insert a second filter (1 minute), are *excluded*. See Section 2.7 for more discussion and other overheads.

Exposure Time (s)	Total Execution Time (min.)	
	CLOCKS=NO (default)	CLOCKS=YES
0.11 to 30	2	(not recommended)
35, 40	2	2
50,60,70,80,100	3	3
120,140,160	4	4
180,200	6	5
230,260	7	6
300	8	7
350,400	9	8
500	11	10
600	13	12
700	14	13
800	16	15
900	18	17
1000	19	18
1100	21	20
1200	23	22

7.6 Dithering with WFPC2

Dithering is the technique of displacing the telescope between observations either on integral pixel scales (to assist in removing chip blemishes such as hot pixels) or on sub-pixel scales (to improve sampling and thus produce a higher-quality final image). Here we briefly discuss observation and data analysis for dithered data.

7.6.1 Dither Strategies

There was no single observing strategy that was entirely satisfactory in all circumstances for WFPC2. One needed to consider cosmic rays, hot pixels (i.e. pixels with high, time variable dark count), spatial undersampling of the image, and large-scale irregularities such as the few arcsecond wide region where the CCDs adjoin. One strategy that was used to minimize the effects of undersampling and to reduce the effects of hot pixels and imperfect flat fields was to dither, that is, to offset the telescope by either integer-pixel or sub-pixel steps. The best choice for the number and size of the dithers depended on the amount of time available and the goals of the project. In the following we will address a few issues related to dithering:

1. **Undersampling:** Individual images taken with ***sub-pixel*** offsets can be combined to form an image with higher spatial resolution than that of the original images. A single dither from the original pixel position -- call it (0,0) -- to one offset by half a pixel in both x and y, (0.5,0.5) will produce a substantial gain in spatial information. On the other hand, very little extra information is gained from obtaining more than four positions if the standard four point dither was used, and if the telescope successfully executed the dither. Therefore the recommended number of sub-pixel dither positions was between 2 and 4.
2. **Hot Pixels:** There are three ways in which hot pixels could be dealt with: correct them by using "dark frames" that bracketed the observation, dither by an ***integer*** amount of pixels, or use a task such as "**WARMPIX**" within STSDAS to filter out the known hot pixels. Note that the integer dither strategy would have ideally used six images, i.e. two CR-SPLIT images at each of three different dither positions. This was because in addition to hot pixels, low or "cold" pixels[1] could be present and simple strategies where the minimum of two pixel values was selected could fail. However, even four images (two each at two dither positions) greatly aided in eliminating hot pixel artifacts.

1. Cold pixels usually result from hot pixels in the dark calibration file which do not actually appear in the science data.

3. **Cosmic Rays:** Although dithering naturally provided many images of the same field, it was better to take several images at each single pointing in order to remove cosmic rays. The dither package (see further below) was developed to allow cosmic ray removal from dithered data. This, for example, allowed single images at each pointing, which was important if observing time was limited (e.g. less than one orbit). This capability was tested and worked fairly well. For effective cosmic ray removal it was generally recommended to obtain a minimum of three to four images, and preferably more if practical. For very long integrations it was convenient to split the exposure into *more than two separate images*. As an example, for two 1500s exposures, about 1500 pixels per chip were hit with cosmic rays in both images and would have therefore been unrecoverable. However, dividing the same observation into 3x1000s resulted in only about 20 pixels on each chip that were hit by cosmic rays in all three exposures. Moreover, since CR events typically affected 7 pixels per event, these pixels would not have been independently placed, but rather were frequently adjacent to other unrecoverable pixels.

4. **Accuracy of dithering**: The telescope pointing accuracy is typically better than 10 mas, but on occasion can deviate by much more, depending on the quality of the guide stars. For example, during the Hubble Deep Field, nearly all dithers were placed to within 10 mas (during ±1.3″ offsets and returns separated by multiple days), although in a few cases the dither was off by more than 25 mas, and on one occasion (out of 107 reacquisitions) the telescope locked on a secondary FGS peak causing the pointing to be off by approximately 1″ as well as a field rotation of about 8 arcminutes. The STSDAS "drizzle" software (initially developed by Fruchter and Hook for the Hubble Deep Field, and now used generally for many other programs) is able to reconstruct images even for these non-optimal dithers, still gaining in resolution over non-dithered data.

The recommended way dithers were scheduled was to specify dither patterns WFPC2-LINE (e.g. for two-point diagonal dithers) or WFPC2-BOX (for four-point dithers). An alternative approach was to use POS TARGs. Note that when the WF3 was specified as an aperture, the POS TARG axes ran exactly along the WF3 rows and columns. For the other chips, they only ran approximately along the rows and columns due to the small amount of rotation between CCDs. For small dithers (less than a few pixels) these rotations were unimportant.

Some specific offsets allowed one to shift both the PC and the WFC chips by convenient amounts. For instance, an offset of 0.5″ is equivalent to 5 WFC pixels and 11 PC pixels. Likewise, the default WFPC2-LINE spacing of 0.3535″ along the diagonal is equivalent to shifts of (2.5,2.5) pixels for the WFC and (5.5,5.5) pixels for the PC.

Dithers larger than a few pixels incurred errors due to the camera geometric distortion which increases toward the CCD corners and alters the image scale by about 2% at the corners. Hence a 1.993″ offset is 20.3 WF pixels at the field center, but suffers a 0.4 pixel error at the CCD corners. Large dithers also occasionally required a different set of guide stars for each pointing, thus the expected pointing accuracy was greatly reduced (accuracy only ~1″ due to guide star catalogue).

Below are examples of dither patterns that have been used in WFPC2 observations. These small-scale dither patterns were designed to improve the rejection of detector artifacts and/or create sub-sampled data. The patterns given in Table 7.6 are projected onto the detector pixel space in Figure 7.8 below.

The "line" dither patterns shown in Table 7.6 were one-dimensional and derived from a template which could be modified with the following defaults: there could be from 2 to 10 points and the point spacing could be from 0.01 to 3.0 arc seconds.

The default line pattern (Figure 7.8, red line, pattern 10) produced a shift of 2.5 x 2.5 pixels on the WF chips and 5.5 x 5.5 pixels on the PC chip. The two integral pixel shift patterns, patterns 11 (orange) and 12 (light green), produced shifts of 5 x 5 and 10 x 10 pixels, respectively, on the WF chips. The values were suggested because they would also produce integral-pixel shifts of 11 x 11 and 22 x 22 pixels, respectively, on the PC chip.

The two seam dither patterns produced shifts of 20 x 20 pixels and 5 x 40 pixels, respectively, on the WF chips; they also produced shifts of 44 x 44 and 11 x 88 pixels on the PC. They were designed to help reject the chip edge effects that produce noticeable "seams" between the chips. Pattern 13 in Figure 7.8 (pink line) shifts in both dimensions for all the chip seams, whereas pattern 14 (the purple line which extends outside the figure) shifts mostly across the WF2-WF3 boundary, if only those two chips were being used.

The default WFPC2 box pattern (brown 'box', pattern 15), has pixel coordinates, relative to the pixel location of the aperture, of (0, 0), (5.0, 2.5), (7.5, 7.5), (2.5, 5.0) on the WF chips, and (0, 0), (11.0, 5.5), (16.5, 16.5), (5.5, 11.0) on the PC. It was a parallelogram pattern designed for half-pixel sampling on all chips in both x and y. The overall dimensions were large enough to help reject typical detector artifacts such as bad columns and hot pixels.

The intermediate box (pattern 16, dark green box), has relative pixel coordinates (0, 0), (10.0, 7.5), (17.5, 17.5), (7.5, 10.0) on the WF chips and (0, 0), (22.0, 16.5), (38.5, 38.5), (16.5, 22.0) on the PC. It was a parallelogram pattern which was designed for half-pixel sampling in both x and y. Its larger overall dimensions helped to reject any atypically large detector artifacts.

The large dither box (pattern 17, light blue box), has relative coordinates (0, 0), (20.0, 12.5), (27.5, 27.5), (12.5, 20.0) on the WFs, and (0, 0), (44.0,

27.5), (60.5, 60.5), (27.5, 44.0) on the PC. It too was a parallelogram pattern designed for half-pixel sampling in both x and y on all chips. Its overall dimensions were large enough to help reject atypical detector artifacts and remove the "seams" between the detectors. Note that the large shifts reduced the overall field of view.

Figure 7.8: Small-scale WFPC2 dither patterns (relative to WF chip pixels)

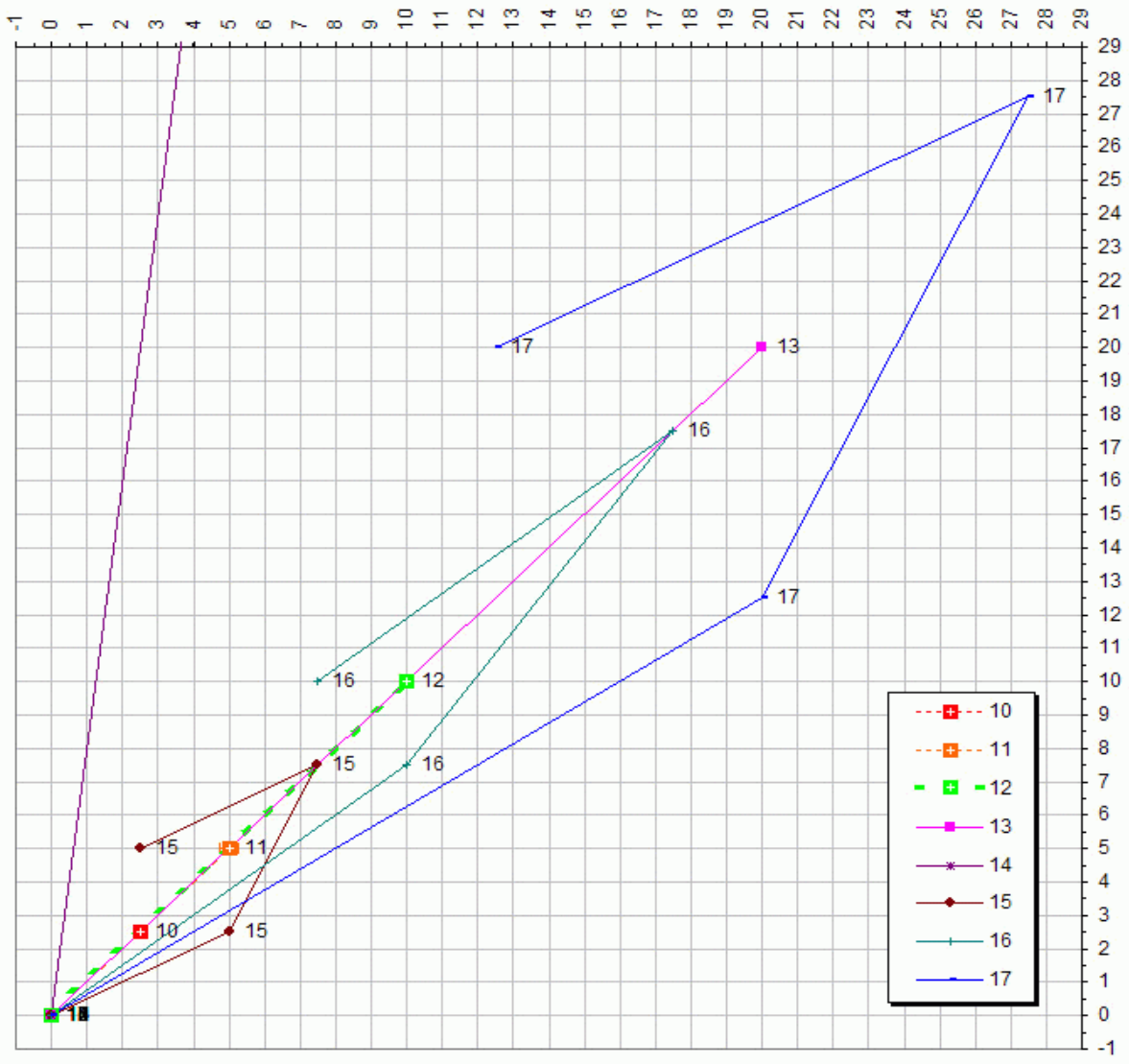

Table 7.6: Common WFPC2 Small Scale Dither Patterns

Name	Points	Point Spacing[a]	Line Spacing[a]	POSTARG (arc sec)[b]	PC Pixel Shift (x,y)[c]	WF Pixel Shift (x,y)[c]
Default Line	2	0.353	---	0.000 , 0.000 0.249 , 0.249	(0, 0) (5.5, 5.5)	(0, 0) (2.5, 2.5)
Integral Pixel Shift 1	2	0.704	---	0.000 , 0.000 0.498 , 0.498	(0, 0) (11, 11)	(0, 0) (5, 5)
Integral Pixle Shift 2	2	1.409	---	0.000 , 0.000 0.996 , 0.996	(0, 0) (22, 22)	(0, 0) (10, 10)
Chip Seam 1	2	2.817	---	0.000 , 0.000 1.992 , 1.992	(0, 0) (44, 44)	(0, 0) (20. 20)
Chip Seam 2	2	4.015	---	0.000 , 0.000 0.498 , 3.984	(0, 0) (11, 88)	(0, 0) (5, 40)
Default Box	4	0.557	0.557	0.000 , 0.000 0.498 , 0.249 0.747 , 0.747 0.249 , 0.498	(0, 0) (11.0, 5.5) (16.5, 16.5) (5.5, 11.0)	(0, 0) (5.0, 2.5) (7.5, 7.5) (2.5, 5.0)
Intermediate Box	4	1.245	1.245	0.000 , 0.000 0.996 , 0.747 1.743 , 1.743 0.747 , 0.996	(0, 0) (22.0, 16.5) (38.5, 38.5) (16.5, 22.0)	(0, 0) (10.0, 7.5) (17.5, 17.5) (7.5, 10.0)
Large Box	4	2.349	2.349	0.000 , 0.000 1.992 , 1.245 2.739 , 2.739 1.245 , 1.992	(0, 0) (44.0, 27.5) (60.5, 60.5) (27.5, 44.0)	(0, 0) (20.0, 12.5) (27.5, 27.5) (12.5, 20.0)

a. Distance, in arc seconds, between the two endpoints of a line or the length of a line segment for box dithers
b. Distance, in arc seconds, from the aperture center (PC1-FIX, WF2-FIX, WFALL, etc.)
c. Distance from the pixel center of an aperture (e.g. (420,424.5) for PC1-FIX)

7.6.2 Analysis of Dithered Data

The software we recommend for combining dithered data is known as "MultiDrizzle" (Koekemoer, et al. 2002), which is based on the "drizzle" program (Fruchter and Hook 2002). This method has been incorporated into the IRAF/STSDAS **dither** package, and allows effective cosmic ray removal from dithered data.

In order to help users reduce dithered images, several examples have been prepared and are located on the WFPC2 Web pages:

http://www.stsci.edu/hst/wfpc2/analysis/WFPC2_drizzle.html

These examples cover a range of characteristics which a user might encounter in their analysis of dithered images; links to sample data sets are also provided.

Despite all the improvements in the combination of dithered images, users should be mindful of the following cautionary notes:

- Processing singly dithered images can require substantially more work (and more CPU cycles) than processing data with a number of images per pointing.
- Removing cosmic rays from singly dithered WFPC2 data requires good sub-pixel sampling; therefore one should probably not consider attempting this method with WFPC2 using fewer than four images and preferably no fewer than six to eight if the exposures are longer than a few minutes and thus subject to significant cosmic ray flux.
- It is particularly difficult to correct stellar images for cosmic rays, due to the undersampling of the WFPC2 (particularly in the WF chips). Therefore, in cases where stellar photometry better than a few percent is required, CR-split images should have been taken, or, alternatively, only use the combined image to find sources, and then extract the photometry from the individual images, rejecting entire stars where cosmic ray contamination has occurred.

Figure 7.9: On the left, a single 2400s F814W WF2 image taken from the HST archive. On the right, the drizzled combination of twelve such images, each taken at a different dither position.

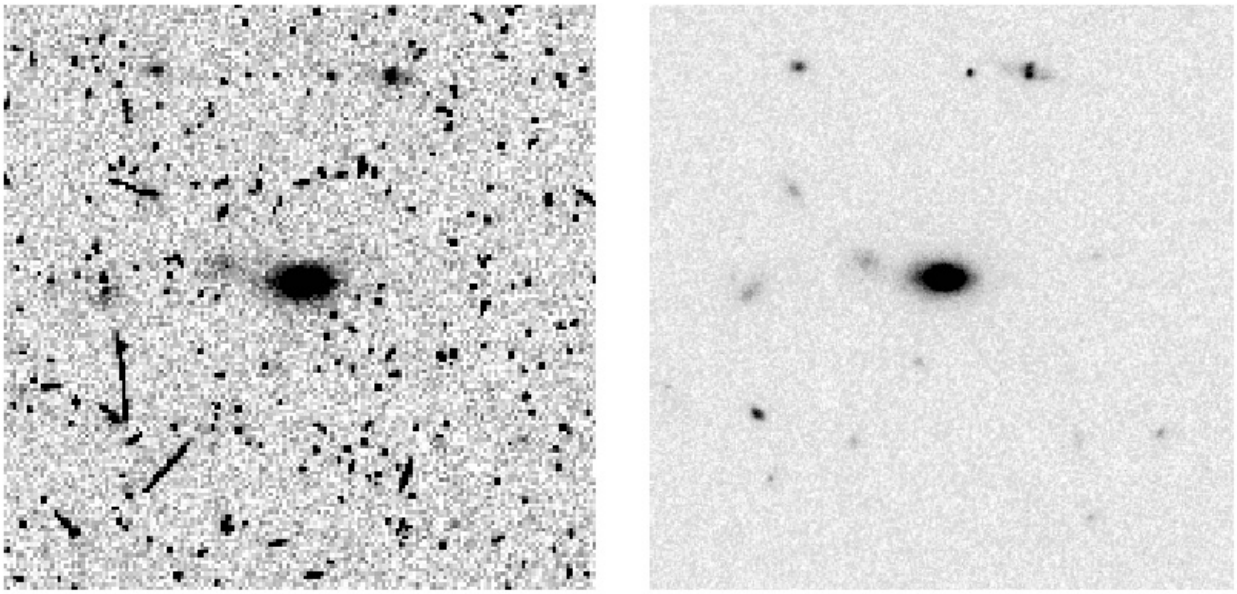

- Offsets between dithered images must be accurately determined. The jitter files, which contain guiding information, cannot always be relied upon to provide accurate shifts. Therefore, the images should

be deep enough for the offsets to be measured directly from the images themselves (typically via cross-correlation). In many cases, an observer should have taken at least two images per dither position to allow a first-pass removal of cosmic rays for position determination.

- Finally, dithered images provide little additional spatial information unless the objects under investigation had a signal-to-noise per pixel of at least a few at each dither position. In cases where the signal-to-noise of the image was low, the observer only needed to dither enough to remove detector defects.

7.7 Pointing Accuracy

Some WFPC2 programs had critical target positioning constraints (i.e. the target must be as close as possible to a specified aperture). A sure way to meet such requirements was to include an interactive acquisition. However, INT ACQs were costly in terms of allotted orbits. A variation of the Reuse Target Offset (RTO) capability could be used to acquire and position a target in the WFPC2 FOV. The user would have requested an additional orbit for the acquisition. The first orbit was used for the acquisition and the second orbit for the science observations. Only very rarely did WFPC2 observations make use of these approaches.

7.7.1 Absolute Pointing Accuracy

We have looked carefully at a sequence of images to assess the absolute pointing performance that HST delivers to WFPC2. The apertures used in the observations studied were either PC1, PC1-FIX, or WF2. The observed positions of stars on WFPC2 images were measured and compared with the proposed coordinates and apertures. Where necessary, coordinate and proper motion errors were accounted for (with the assumption that SAO catalog coordinates are exact - they form the astrometric basis for the guide star coordinate system). The typical residual pointing error is 0.86″, with 1.84″ being the largest error seen. This study did bring out several easy-to-make target coordinate errors (which we corrected in the analysis, but which frequently dominated the pointing error), so we discuss these first.

In a number of cases studied, the proposal coordinates were from the printed version of the Yale Bright Star Catalog. One problem is that the equinox 2000 positions in the BSC are given in the FK4 (Besselian) reference system. The proposal system assumes that equinox 2000 and later coordinates are in the FK5 (Julian) reference frame, and that earlier

ones are in the FK4 frame. This could have been overridden by specifying B2000 instead of J2000 for the equinox in the proposal. The latest digital version of the BSC (BSC5) is in J2000. The 1950 edition of the SAO catalog is in B1950 (FK4), and a digital version is available for J2000 (FK5). An error of up to 1.5″ can result from assuming BSC positions are J2000 instead of B2000 in the proposal.

Another common problem with target coordinates is that they lack precision. For example, in the BSC, RA is given to the nearest 0.1^s and DEC to the nearest arcsecond. This can cause an error of up to 0.75″ in RA and 0.5″ in DEC. The SAO coordinates have higher precision, 0.001^s in RA and 0.01″ in DEC, and should be used when possible.

A common error source is not specifying proper motion or specifying it in the wrong units. It was critical to follow the current version of the proposal instructions on this. Even small proper motions are significant at the resolution of HST images.

Residual pointing errors (after coordinate errors and aperture location changes) range from 0.26″ to 1.84″. The average is 0.93″ and the median is 0.86″. There are no obvious trends in any coordinate system. These are errors which cannot be accounted for by a proposer, being due to guide star position errors, FGS alignment uncertainties, and residual aperture location errors.

In summary, a target with good coordinates (and proper motion) referenced to the SAO catalog was typically placed within 0.9″ of a specified aperture. However, errors of around 1.5″ occasionally happened.

7.7.2 Updates to Aperture / Coordinate Systems

Definitions of apertures and coordinate systems have changed a few times over the long lifetime of WFPC2. Proper coordinates will exist in the headers for data retrieved from the On The Fly Reprocessing System (OTFR) after May 16, 2001, or for the uniformly reprocessed WFPC2 data expected to be phased in during the latter half of 2008. Only if you wish to understand the provenance of coordinate details for data retrieved before May 16, 2001 would the remainder of this sub-section be relevant.

On 11 April, 1994, an update was made to the spacecraft database which tells HST where to place targets relative to the FGSs. This update affected both the location of targets in the WFPC2 field-of-view, and the position reference frame in the image headers. The nominal (or intended) pixel locations of the apertures in the WFPC2 focal plane did not change. Only the (V2,V3) coordinates of the apertures changed, as their locations relative to the FGSs became better known. For example, PC1 and PC1-FIX are designated to be at pixel (420,424.5). Before April 1994, this aperture was thought to be at (V2,V3) =(4.95″,-30.77″), which, using the most current information, was actually located at pixel (X,Y) = (459.8,377.3). Since April 1994, the aperture in the spacecraft's database has been at (V2,V3) =

(1.87″,-30.96″) or, assuming the current best estimate is exactly correct, at (X,Y) = (414.9,428.1). Thus, for the same coordinates and aperture, the pixel position of a target in an image taken before April 1994, could be nearly 3″ different from its position in later images, due to aperture updates. Similar corrections apply to all WFPC2 data taken before this date.

This update also affects the position information placed in the image headers, which maps sky coordinates onto each individual CCD. Observations taken before April 11, 1994, have preliminary plate scales, rotations, and reference pixel locations in their image headers. Thus, the sky coordinates associated with a given pixel will be different for otherwise identical images taken before and after April 11, 1994, due to improvements in the aperture locations. The change is primarily an approximate 3″ shift, as well as a small rotation. There is a 0.8° rotation for WF2, and smaller rotations for the other chips (0.28° in PC1, 0.46° in WF3, and 0.06° in WF4). We note that the On-The-Fly Calibration System initiated in 2000 does not correct for these offsets, since the pointing information is set upstream of the pipeline calibration; the On-The-Fly Reprocessing System installed in May 2001 does, however, correct the pointing offsets.

The STSDAS tasks **METRIC/INVMETRIC** and **WMOSAIC** use this header information; hence, images taken before April 11, 1994, required header updates in order for these tasks to produce optimum results. In this situation, observers were advised to run the STSDAS task **UCHCOORD**, to update the headers, prior to running **METRIC/INVMETRIC** and/or **WMOSAIC**.

The On-The-Fly Calibration System (OTFC), in place from Dec. 1999 to May 2001, did not correct for these offsets. Observers submitting requests to the archive prior to May 16, 2001 received data processed through OTFC; this data would benefit from running **UCHCOORD**.

As of May 16, 2001, however, the On-The-Fly Reprocessing System (OTFR) is in place and OTFR data does contain the most up-to-date header information. The IRAF/STSDAS task, **UCHCOORD**, should not be run on OTFR data. OTFR data can be identified by the presence of the keyword `PROCTIME` in the header. Please see Section 8.7 for more details on OTFC, OTFR, and the use of UCHCOORD.

We also note, that in April and May 1996, two updates were made to the (V2,V3) coordinate system. This update should not affect observers. The purpose was to remove a slow drift in the position of WFPC2 in the HST focal plane; the largest change was 0.6″. (See table 3.15 for details.) An additional update of 0.2″ was made on December 1, 1997. All the apertures are now thought to be correct to within 0.3″, and future updates should be small. Also see section 7.8.1. Anyone wishing more history, may refer to:

`http://www.stsci.edu/hst/observatory/apertures/siaf.html`

The date column gives the date after which the information in the rest of the row applies.

7.7.3 Pointing Repeatability

The Hubble Deep Field (HDF) afforded an opportunity to study the repeatability of pointing over many images and acquisitions of the same field. The pointing appears to have been stable to better than 5 mas accuracy while taking many images of the same field without interruption over several orbits. The accuracy for full-up acquisition of the same field after slewing to other targets appeared to be ~10 mas typically, with occasional 20 mas errors seen. However, a few large errors were seen; in about 1 in 100 acquisitions the FGSs locked-up incorrectly resulting in a ~1″ error.

Other programs report similar 3 mas pointing accuracy if simple re-acquisitions are done between orbits. Approximately once per day a "full-up" acquisition is usually required (for engineering reasons) where the dominant FGS is fixed in position, but the sub-dominant FGS performs a spiral search for the guidestar and tracks wherever the star is found. On rare occasion these full-up acquisitions produce position errors of several hundred mas, and field rotations of up to ~0.1°, relative to previous images of the same field. This may have impacted long sequences of exposures requiring half a day or more to execute.

7.7.4 Tracking Modes

Two guiding modes were available: Gyro Hold, and Fine Lock. Fine Lock (PCS MODE FINE) was used by default, since use of Coarse Track may be harmful to the Fine Guidance Sensors. Use of Gyro Hold (PCS MODE GYRO) was not generally recommended, even for snapshot (SNAP) observations, since the pointing accuracy was only 14″. Also the drift rate was 0.0014″ s^{-1} so exposures >100s could result in smeared images. However, if the reduced pointing accuracy could be tolerated, and the exposures were only a few seconds or less, Gyro Hold could give a significant savings in the target acquisition overhead time.

7.8 CCD Position and Orientation on Sky

During observation the target was placed at the aperture (PC1, WF2, WFALL, etc.) specified on the Phase II proposal. Locations of the principal apertures are shown in Figure 7.10 (Table 3.14 gives a complete list of apertures; the (V2,V3) system here is post 1996 day 127).

The POS TARG special requirement was used when a position offset was needed. The target was positioned with offset "POS TARG x,y", measured in arcseconds, from the specified aperture. The approximate directions (within 1°) of the POS TARG offsets are shown in Figure 7.10. The exact directions of the offsets are parallel to the rows and columns of the CCD on which the aperture is specified. There are small rotations (few tenths of a degree) between the CCDs.

It was often useful to explicitly specify the desired rotation of the WFPC2 field-of-view on the sky. This was specified in the Phase II proposal using the ORIENT special requirement. It is defined as the PA (measured from North through East) of the +U3 axis on the sky. Figure 7.10 shows the CCD orientation and aperture locations relative to the U3 axis.

Figure 7.10: ORIENT Definition, Aperture Positions, and CCD Alignments. "FIX" apertures are in same locations, unless otherwise indicated. Dashed lines show vignetted regions along CCD boundaries. Short lines and "X"s in outer CCD corners indicate directions of bloom and OTA diffraction spikes, respectively. Origin of the (V2, V3) system is at the origin of the plot axes, with V2 and V3 exactly along diagonal lines as marked. POS TARGs are offsets measured from the aperture specified on the proposal (PC1, WF2, WFALL, etc.); their directions are as indicated. CCDs have pixel (1,1) where the four CCDs overlap.

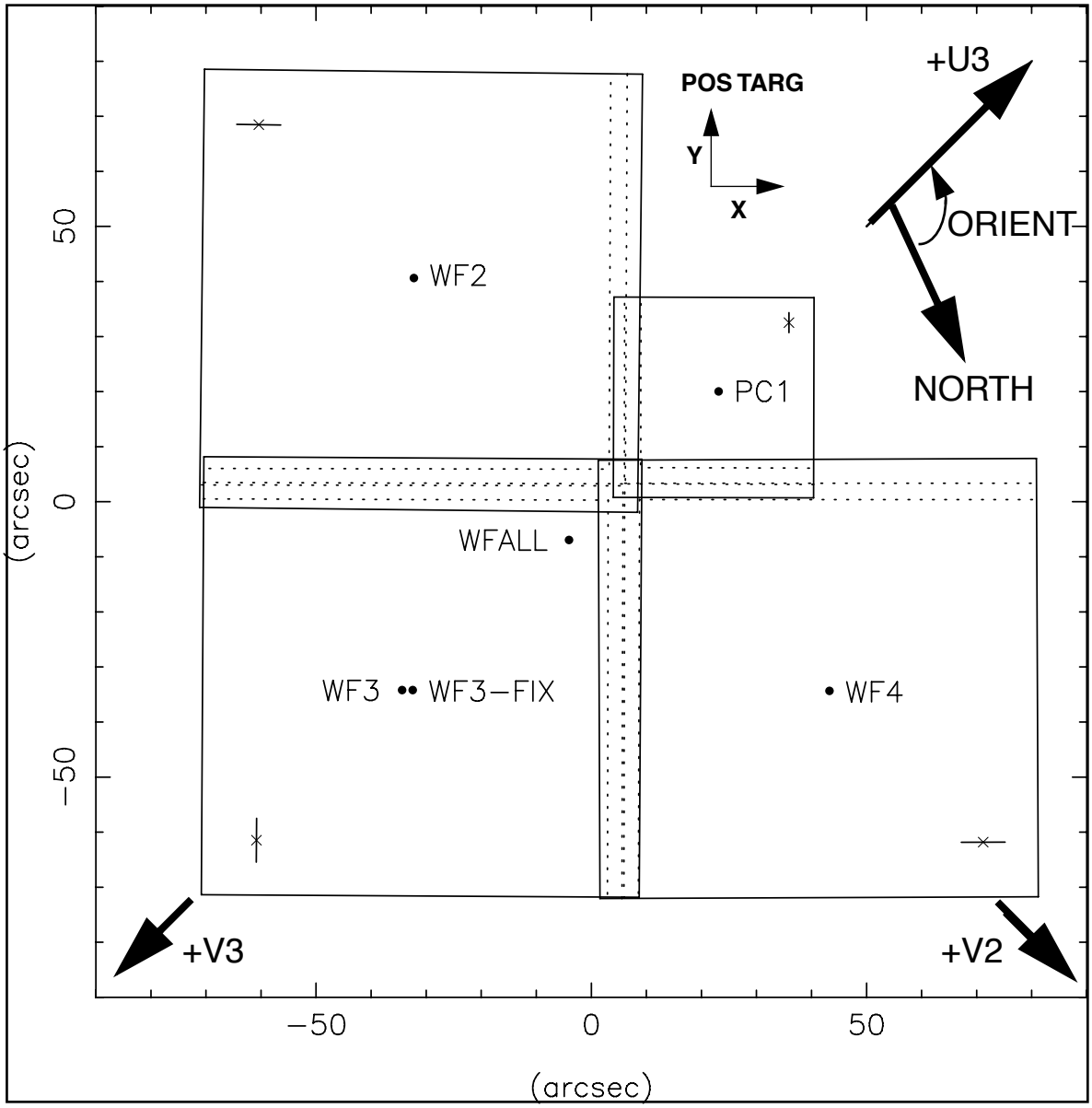

ORIENT is defined as the Position Angle of the +U3 Axis on the Sky.

In effect, the sequence of events is to first move the target to the desired aperture, then offset by any specified POS TARG from the aperture, and finally to rotate the target "in place" on the CCDs to the desired ORIENT.

In order to increase the efficiency of the telescope, observers were encouraged, wherever possible, to give the schedulers maximal freedom in setting the ORIENTs for the observations. Often, the science objectives did not require an exact ORIENT, so a range of values would be specified in the proposal. Moreover, an observation could often attain the same science goals with an ORIENT that was 90˚ or 180˚ different from the original value. For this reason, proposals typically allowed multiple ORIENTs or multiple ranges of ORIENTs.

The ORIENT for any observation can be computed as follows:

1. Obtain the Position Angle (PA) of the source axis on the sky, measured in the standard way, North through East.
2. Look at Figure 7.10 and decide what angle you want, measured clockwise, from the +U3 axis to the source axis.
3. Sum the angles in steps 1 and 2.
4. ORIENT must be between 0˚ and 360˚, so subtract 360˚, if necessary. The result is the ORIENT that would have been on the proposal.

Another way to select the ORIENT, was to place Figure 7.10 on an image of the target, shift and rotate to get the desired alignment, and then simply measure the position angle of the +U3 axis relative to North.

Note that the +V3 axis is quite different from the +U3 axis. They are exactly parallel, but oppositely directed. The +U3 axis is used for specifying orientation (ORIENT) in the proposal, while the +V3 axis is used in the data headers to indicate field orientation. Data header keyword `PA_V3` gives the position angle of the +V3 axis on the sky.

We now give two examples of how the POS TARG and ORIENT special requirements might have been used. The first example (Figure 7.11) shows placement of a 100″ long jet along the CCD diagonals in PC1 and WF3 (i.e. along the -U3 direction). The coordinates of the nucleus were given on the proposal. Aperture PC1 together with POS TARG +10, +10 were used to place the nucleus near the outer corner of PC1. It was desired to rotate the WFPC2 field-of-view about the nucleus so the jet was diagonal on PC1 and WF3. The desired orientation was computed as:

```
ORIENT = (source PA on sky)
+ (desired source angle in field-of-view measured CW from
+U3 axis)
= 290° + 180° = 470° - 360° = 110°
```

On the Phase II proposal, in order to allow some range in the angle (to ease scheduling), "ORIENT 105D TO 115D" might have been specified.

Figure 7.11: Example of ORIENT and POS TARG Selection. (A) A jet at PA=290° is observed using PC1 and WF3; the position of the nucleus is used for the target position. (B) The aperture is specified as “PC1” and the nucleus is placed near the outer corner of PC1 using “POS TARG +10,+10.” To place the jet across PC1 and WF3 “ORIENT 105D TO 115D” is specified.

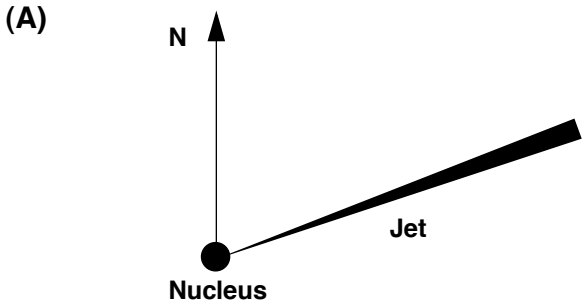

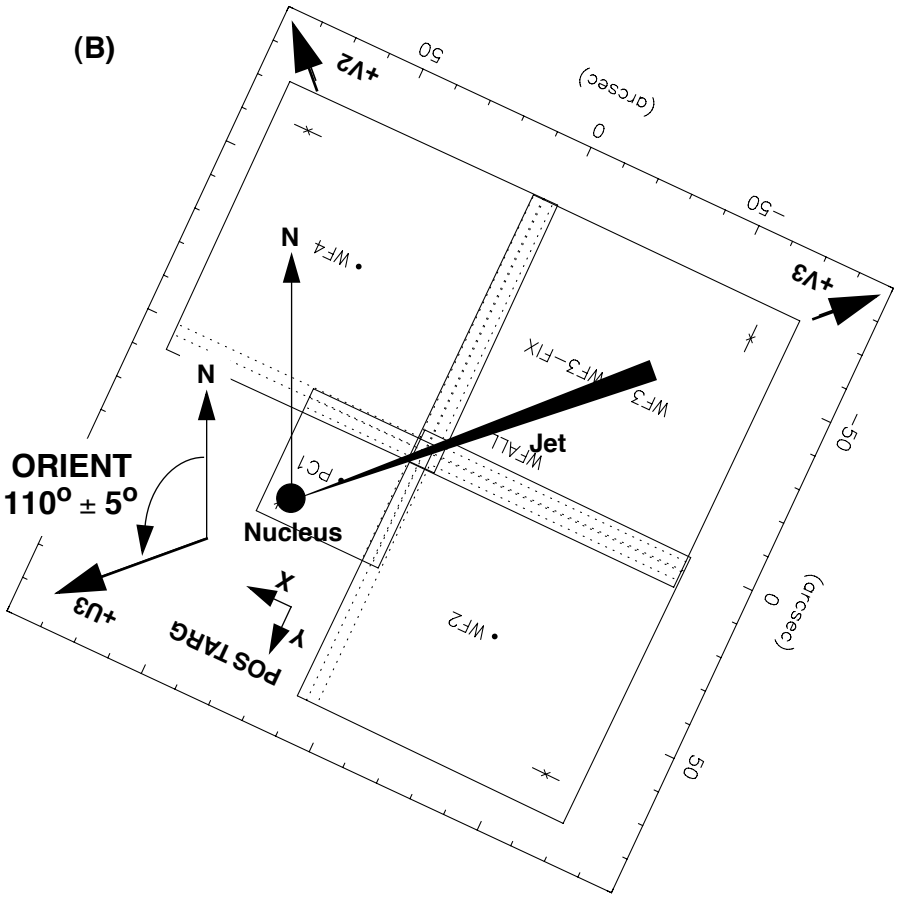

The second example (Figure 7.12) shows placement of a galaxy across WF2 and WF3, with the nucleus on WF3 safely away from the vignetted region. Aperture WF3 together with POS TARG +20, 0 was used to place the nucleus near the outer edge of WF3. The WFPC2 field-of-view was rotated about the nucleus so the galaxy's major axis was across WF2 and WF3. The desired orientation was thus computed as

```
ORIENT = (source PA on sky)
+ (desired source angle in field-of-view measured CW from +U3 axis)
= 60° + 315° = 375° - 360° = 15°
```

On the Phase II proposal, some range in the angle would again have been allowed (to ease scheduling), hence "ORIENT 5D TO 25D" would have been specified. Note that "ORIENT 185D TO 205D" was also feasible, and could be indicated in the visit level comments. Note also, that WF3 and WF4 could be used with either "ORIENT 95D TO 115D" or "ORIENT 275D TO 295D".

7.8.1 ORIENT Anomaly

A minor anomaly was discovered in the data header values pertaining to image orientation (i.e. rotation about the target aperture) for data taken prior to September 15, 1997. Specifically, the header keywords `PA_V3` and `ORIENTAT` were affected. During long visits, their values were incremented by up to 0.05 degree per hour whenever the telescope pointing was changed, when in fact these header values should have remained fixed. Observers requiring highly accurate image orientations should check values in the jitter files (*jit.fits and *jif.fits), which were not affected by the bug. For data extracted from the HST archive after mid-2001, this problem has been corrected.

Figure 7.12: Example of ORIENT and POS TARG Selection. (A) A galaxy with major axis at PA=60° was to be placed across WF2 and WF3. (B) The aperture was specified as "WF3" and the nucleus was placed near the outer edge of WF3 using "POS TARG +20,0." To place the major axis across WF2 and WF3, "ORIENT 5D TO 25D" was specified. Note that "ORIENT 185D TO 205D" was also feasible.

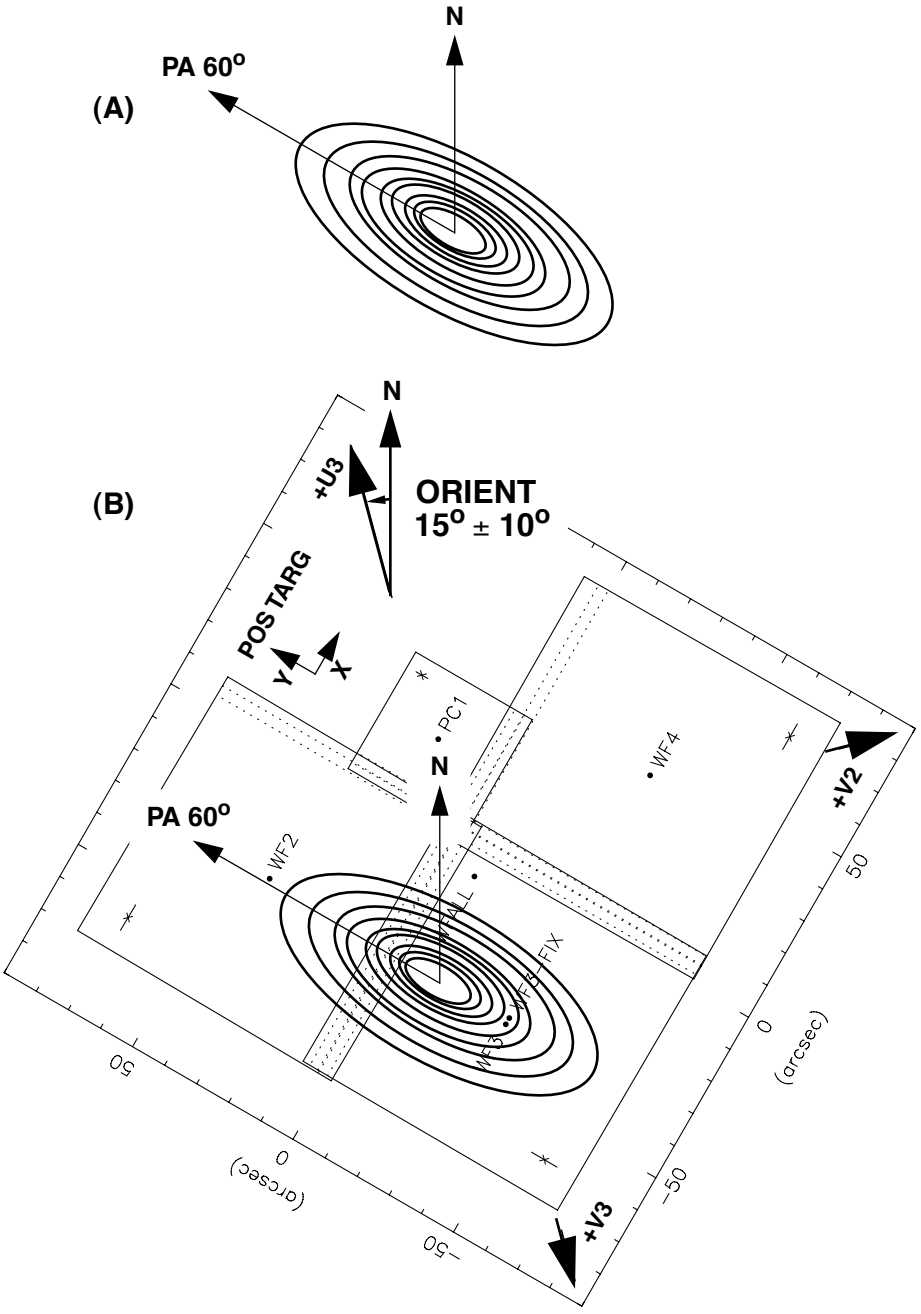

7.9 Polarization Observations

Polarization observations required three or more images with the polarizing filter spanning a large range of position angles on the sky. For WFPC2, this could be achieved by using different quads of the polarizing filter (each quad being oriented 45° to the others), by rotating the spacecraft though different angles, or by a combination of these methods. Rotating the spacecraft through use of ORIENTs provided the simplest calibration, as a single polaroid could be used for all images. However, in practice, it was the most difficult method to schedule. For further information see Biretta and Sparks (1995, ISR WFPC2 95-01).

Note that WFPC2 had significant instrumental polarizations which made measurements on targets with less than 3% polarization difficult. The pick-off mirror introduced about 6% instrumental polarization. Furthermore, the pair of mirrors in the calibration channel, which was used to generate the polarizer flat fields, introduced ~12% polarization. In principle, these effects can be calibrated out, but this has yet to be demonstrated.

The polarizers were most effective in the range from 3000Å to 6500Å; this corresponds roughly to filters in the range F255W to F675W. At shorter wavelengths the transmission decreased sharply, and at longer wavelengths they ceased to polarize the incoming light.

7.10 Observing with Linear Ramp Filters

The Linear Ramp Filters (LRFs) provided a narrow band ($\Delta\lambda/\lambda = 0.013$) imaging capability which was continuously tunable from 3710Å to 9762Å. These were essentially a collection of narrow band interference filters whose central wavelength varied with position on the filter glass. The filter and aperture were specified as LRF on the Phase II proposal, and the desired central wavelength was also specified. The HST scheduling software then selected the target position so as to provide the desired wavelength.

Note that it was not possible to choose between PC1 and WFC for the LRFs; whatever CCD was automatically assigned by the scheduling software was the one used.

It was possible to use POS-TARGs with LRF observations; the offsets were made from the default pointing for the specified wavelength. The unvignetted field-of-view had a maximum size of ~10″ in diameter, so that only small POS-TARGs (<4″) should have been used.

While it was recommended that observers assume a 10″ diameter field-of-view when using the LRFs, larger elongated (e.g. 15″ x 10″) targets

could sometimes be accommodated by placing the target's major axis along the direction of the wavelength variation on the filter. This resulted in a small reduction in throughput (i.e. small central wavelength offset) at the outer edges of the target. However, placing targets outside the central 10″ of each ramp was strongly discouraged. Outside the central 10" width, perpendicular to the wavelength direction, the light would pass through more than one ramp segment, which had the effect of mixing light from different wavelengths, and consequently making the data very difficult to calibrate. (See section 3.3 for further details on the LRFs.)

A common situation was one in which observers desired to make observations through an LRF filter, and then repeat the observation in a standard broad or narrow band filter at the same position on the CCD. The LRF Calculator Tool, available on the WFPC2 WWW pages (http://www.stsci.edu/hst/wfpc2/software/wfpc2_lrfcalc.html), would tell observers the aperture (PC1-FIX, WF2-FIX, etc.) and POS-TARG for any wavelength setting of the LRFs. Observers merely needed to use this same aperture and POS-TARG for the exposure through the other filter. If it was necessary to calculate the POS-TARG manually, this could be done using the information in Table 3.7, Table 3.8, Table 3.14, and Figure 7.10. For example an LRF observation at 5034Å would be made on WF2 at pixel (673.4, 235.7) (from interpolation by wavelength between X1 and X2, and between Y1 and Y2 in Table 3.7). These offsets referred to the WF2-FIX aperture which is located (Table 3.14) at pixel (423.5,414). From Figure 7.10, we can deduce that the pixel X direction is parallel to POS-TARG "+Y" on WF2, and that the pixel Y direction runs in the POS-TARG "-X" direction. Using the pixel scale we have:

POS-TARG "X" = -0.09961 (235.7-414) = 17.76″, and

POS-TARG "Y" = 0.09961 (673.4-423.5) = 24.89″,

hence POS-TARG=+17.76,+24.89 would have been requested for the non-LRF exposure.

Note that analysis of FR533N VISFLAT images has revealed an apparently randomly occurring offset in the filter position (Gonzaga et al. 2001, WFPC2 ISR 01-04). This anomalous offset corresponds to one step in the filter wheel rotation, or about 0.5 degrees. No significant impact on point-source observations is expected; any photometric effect is less than 1%. But caution needs to be exercised for extended sources greater than about 5 arcseconds. (A cursory check of several other filters on other filter wheels shows no similar problems.) Figure 7.13 shows throughput plotted against CCD pixels in the direction of the anomalous offset/rotation. The two curves in each plot show the throughput effect of the filter offset. Several points in the wavelength mapping (from actual GRW+70D5824 observations in proposals 6939, 8054, and 8454) are indicated for illustrative purposes. At this time, the source of this anomaly, whether it is mechanical or due to a software error, is not known. This anomaly was investigated further as part of the WFPC2 Cycle 10 Calibration Plan.

Figure 7.13: Linear Ramp Filter Anomaly.

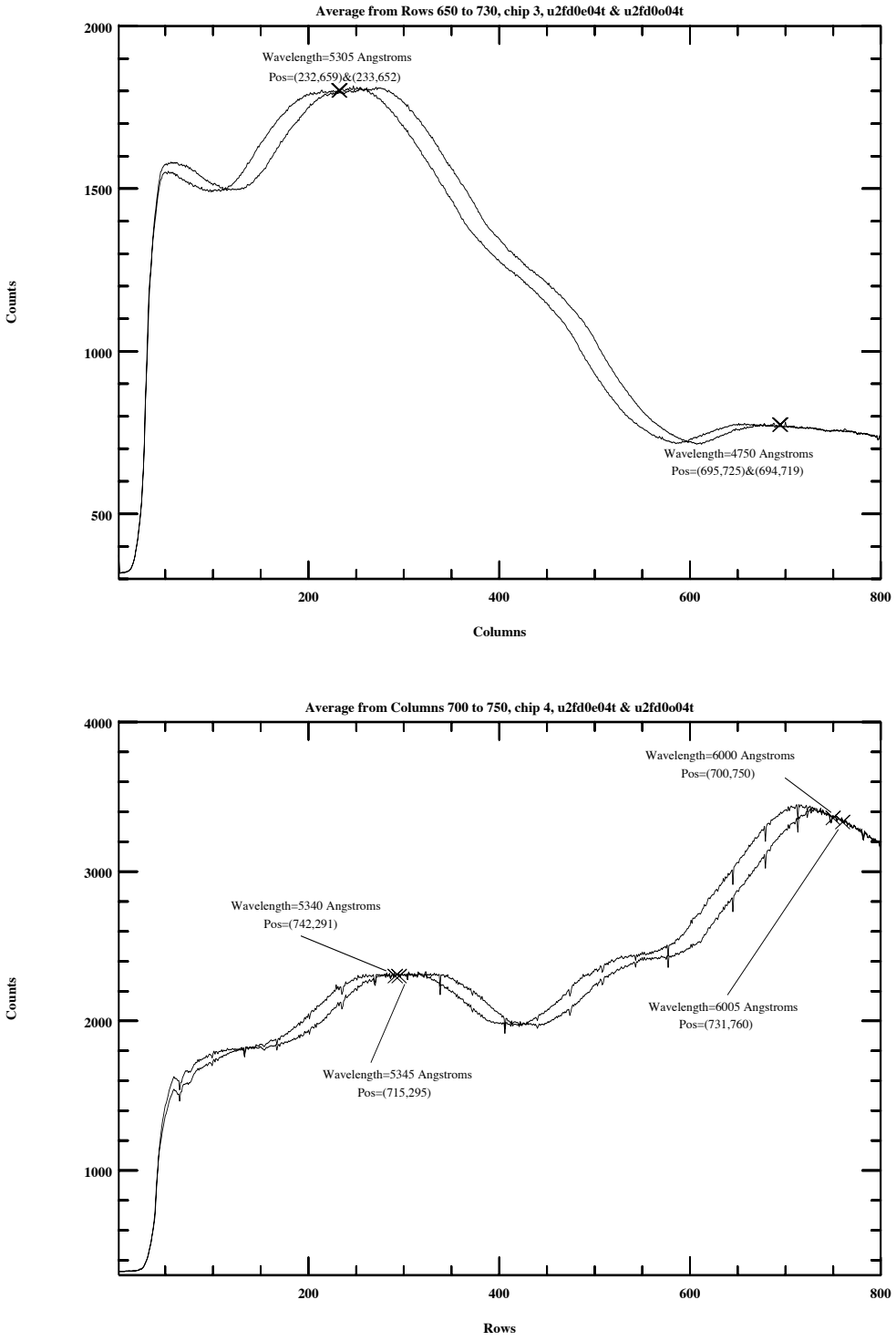

7.11 Emission Line Observations of Galaxy Nuclei

Saturation was a common problem for narrow band filter images of galaxy nuclei. Sometimes, the surface brightness of the emission line was estimated from ground based images with 1″ resolution; other times, line fluxes were quoted for apertures several arcseconds in radius. However, at HST resolution, much of this flux may have occurred in a single unresolved spot at the galaxy nucleus, thus leading to saturated images.

CHAPTER 8:

Calibration and Data Reduction

In this chapter . . .

8.1 Calibration Observations and Reference Data

Standard calibration observations are obtained and maintained in the HST archive at the STScI, and can be retrieved by external users using StarView. This includes those flat field, dark, and bias reference files needed to operate the Post Observation Data Processing System (PODPS; now called OPUS, and usually just called the "pipeline"), photometric calibration derived from standard star observations and the measured filter profiles, and derived determinations of the plate scale, distortion, and so on. The first set of these calibrations was provided to the STScI by the WFPC2 IDT from the Servicing Mission Observatory Verification (SMOV) and System Level Thermal Vacuum (SLTV) testing periods, and has been

maintained and updated thereafter by the STScI with assistance from the IDT as part of the long term calibration program. For measurements requiring more precise calibrations, special calibration observations may have been needed as part of the observing proposal.

A database of laboratory characterizations of optical components, CCD sensors, filters, and the flat field channel has been collected to support the instrument calibration. On-orbit pointed calibrations require large HST resources, taking time that could otherwise be used for direct scientific observations. They can also be unsatisfactory due to the limitations of the available astronomical reference sources. For WFPC2, the inherent stability and uniformity of the CCD sensors, the well-calibrated filters, the internal flat field calibration system, and an archive populated with flat field images obtained in SLTV prior to launch improve the scientific data analysis and productivity. Hence the need for on-orbit calibrations has been minimized.

8.2 Flat Fields

The process of correcting for the effect of the variation in the sensitivity of the WFPC2 with field position is known as flat-fielding, or flattening. For ground based observations, usually a "flat field" (an exposure of a spatially uniform source) is observed through the telescope with the desired filter. Unfortunately, there is no uniformly illuminated target available on-orbit. Instead, several assets are available to estimate the flat field and monitor any changes -- these include pre-launch SLTV optical stimulus flats, Earth flats, calibration channel flats (VISFLATS), and internal flats (INTFLATS).

During SLTV (System Level Thermal Vacuum) ground tests of WFPC2, flat fields were obtained using both the calibration channel and the WFPC2 optical stimulus (HST simulator). The later provided a close approximation to a uniform target as viewed through HST, and are a prime ingredient for the final calibration flats.

The Earth is an imperfect flat field target because it is too bright for the WFPC2 in the broad-band green and red filters. In addition, the rapid motion of the HST creates streaks across the flat field images, though the streaks can be removed by combining multiple Earth observations with the streaks at different angles on the CCDs. An extensive discussion of the generation of Earth flat fields is available in Chapter 6 of the WF/PC-1 IDT OV/SV Report, as well as in the History records of the flat field reference files themselves.

While imperfect, Earth flats are an important part of the flat field calibration; they provide corrections to the SLTV flats for any differences between the SLTV optical stimulus illumination, and the OTA illumination

pattern. Flat fields in narrow bandpass filters are obtained using the sunlit Earth (Target = EARTH-CALIB) as part of routine calibration. These are used primarily to remove the low spatial frequency effects in the calibration flats.

Flat field calibration files have been generated for all filters by combining information from the SLTV test flats (which are good for all but the lowest spatial frequencies), and on-orbit Earth flats obtained for a small subset of narrow band filters (F375N, F502N and F953N). These Earth flats are used to correct low spatial frequency errors in the ground based SLTV flats, which result from imperfect simulation of the HST OTA illumination pattern. These Earth flats taken regularly during available occultation time periods (i.e., no impact to science observations).

There are also two types of on-board flats available in WFPC2, which can be used to monitor changes in the flat field. The calibration channel (VISFLAT system) produces a reasonably flat illumination pattern down to about 1800Å. It works by imaging an illuminated diffuser plate onto the WFPC2 exit pupil (relay secondary) by means of an MgF_2 lens. Two lamps provide optical and FUV illumination, yielding a flat field which resembles the input beam from the OTA between 1600Å and 10000Å. The system is mounted outside, but adjacent to, WFPC2, and light is directed into WFPC2 via a mechanically actuated flip mirror. A second system is much cruder, but provides a measure of redundancy: the internal flat system (INTFLAT system) consists of small lamps which, when commanded on, illuminate the back side of the shutter blade. The INTFLAT illumination pattern is not very uniform, but provides a robust backup capability.

The calibration channel data (VISFLATS) are used to monitor time dependent changes in the flat fields; only small changes have been seen to date in the visible filters. INTFLATS are also taken on a routine basis, and provide a redundant monitor capability. As of this writing (June 2001), both types on internal flats have been used only as monitors, with no corrections being made to the actual calibration files.

A major update of the flat field reference files for all standard filters redward of 300nm (F300W) was completed, using on-orbit data from Earthflat exposures covering the period from September 1995 to May 2001 (Koekemoer, Biretta & Mack 2002). The flat fields have been divided into epochs depending on the appearance of new dust spots, as well as long-term changes in existing features. The new correction flats are accurate for pixel-to-pixel variations down to an intrinsic level of approximately 0.3% for the PC and 0.1% for the WF chips, and they result in an improved rms noise of many of the flats by a factor of two or more. Since early 2002, the new flat fields are automatically applied to any WFPC2 data in relevant filters when the data are retrieved from the archive.

Note that the flat fields presently used in the pipeline are based on gain 14 data. The gain ratios are not constant from chip to chip, and therefore a small correction to photometric results derived from gain 7 data should be applied (see Table 4.2). (See Biretta 1995 for further discussion of WFPC2 flat fields; also see the *HST Data Handbook*.)

8.3 Dark Frames

Dark frames are long exposures that are taken with no light incident on the CCDs. They are used to detect CCD counts (the dark current) caused by thermal processes at the interfaces between the silicon and oxide layers, as well as charged particle and secondary radiation events. Estimated dark current and cosmic ray event rates are given in Section 4.8 and Section 4.9, respectively. Observers are cautioned that the calibration provided by the pipeline may not use the most up-to-date dark frames until several weeks after the observation is taken. The time delay is the time it takes for coeval dark frames to be taken, archived, and processed into dark reference files, and delivered for use in the pipeline and OTFC. Use of optimal darks can be important due to the new hot pixels continually being generated. Each week of observations typically has one applicable (optimum) dark reference file.

8.4 Bias Frames

The WFPC2 bias correction is performed in the pipeline in two steps: a pedestal level is removed and a bias image subtracted. The pedestal level is determined from the overscan columns in each science image; the specific values subtracted are documented in the bias-even / bias-odd science image header keywords. However, the value of the pedestal can also vary with position across the chip. Therefore, after the pedestal correction is performed, the pipeline removes any position-dependent bias pattern by subtracting a bias reference file. This reference file is typically generated from a stack of 120 bias frames (CCD readouts without an exposure); new bias reference files are usually installed in the pipeline about once a year.

8.5 Data Products and Data Reduction

The routine processing of WFPC2 science data consists of the pipeline functions described below. The resulting images will be available in FITS format on magnetic tape or via FTP transfer, and as grey scale images in PDF format. The reformatted raw data will also be available, along with the relevant calibration data. The *HST Data Handbook* or *STSDAS Calibration Guide* should be consulted for a more complete description than the summary presented here.

The following data are supplied to observers on FITS tapes:

- Edited Image and DQF (uncalibrated): `.d0h`,`.q0h`

- Standard Header Packet: .shh
- Extracted Engineering Data and DQF: .x0h,.q1h
- Trailer File (ASCII file): .trl
- Calibrated Image and DQF: .c0h,.c1h

In addition, a histogram file used for monitoring of the signal chain (.c2h file), and a calibration table containing the throughput curve (.c3t file) used in populating the photometric keywords are included.

Further data reduction and analysis can be performed under the STScI's science data analysis software system (STSDAS). Standard routines are available, operating under IRAF, for the analysis of data for image photometry, spectral analysis, astrometry, and the generation of the calibration data files.

8.6 Pipeline Processing

The pipeline processing of WFPC2 data sets reformats the telemetry received from HST into group FITS format images, generates headers containing a large number of keywords taken from both the HST and WFPC2 telemetry streams, in addition to various STScI ground system databases, and applies the corrections described below. This calibration is done with a software module known as "CALWP2" which is written in the IRAF SPP language and is available, in identical form, to users of the STSDAS system. Therefore, off-line recalibration of observations is fairly easy, and will use the same program as the OPUS system. Documentation is available in the *HST Data Handbook*, and the *STSDAS User's Guide*.

CALWP2 performs the following operations if required by the observation:

- A-to-D correction (depending on ATODGAIN)
- Bias pedestal level removal
- Bias image subtraction (depending on the gain and mode [FULL or AREA])
- Dark image scaling and subtraction (depending on gain, serials, and mode)
- Shutter shading correction (depending on exposure time and shutter in place at the beginning of the observation)
- Flat field image correction (depending on filters and mode used)
- Population of various photometric calibration keywords

In addition, the following conditions are flagged in the Data Quality File (DQF):

- Transmission failures and other possible failures
- Known bad pixels (e.g. blocked columns)
- Pixels at or above the maximum A/D converter level (i.e. saturated)
- Bad pixels in calibration reference files

During 2008, additional steps are being added to the CALWP2 software. These will include corrections for the WF4 anomaly (CCD gain), placement of CTE information in the headers, improved astrometric information, etc. Please see the *HST Data Handbook* and WFPC2 web pages for the latest information.

8.7 On-The-Fly and Static Archive Systems

The On-The-Fly Calibration (OTFC) system, publicly released in Dec. 1999, calibrated data at the time a user requested data from the archive. The advantages to using OTFC included the automatic application of improved calibration files and switches, use of most recent calibration software (allowing for rapid access to improved algorithms, new capabilities, and software fixes), and correction of header keywords if needed. An additional benefit is that only the uncalibrated data needs to be stored in the archive.

The On-The-Fly Reprocessing (OTFR) system replaced OTFC on May 16, 2001. *The change is transparent to most HST archive users*. Requests for data are submitted as usual via StarView or WWW; raw and freshly-calibrated data will be delivered. There is no need to explicitly ask for OTFR: all requests for WFPC2 data are handled by the OTFR system.

The primary difference between the two systems is that OTFR begins earlier in the data path. It uses the original telemetry files ("POD" files) received from Goddard Space Flight Center and performs all pipeline processing steps; OTFC performed only the last pipeline processing step (calibration), on raw files retrieved from the archive. An overview of the data flow for both systems is summarized in the table below. The benefits of the OTFR system encompass the benefits in the OTFC system; in addition, OTFR data needs fewer header corrections (most problems are fixed as part of the pre-calibration pipeline processing) and the system as a whole requires significantly less maintenance effort than OTFC.

It is anticipated that during 2008 or 2009 the WFPC2 data archive will be transitioned from the current on-the-fly system to a static archive. Once "final" calibrations for WFPC2 data are determined, there will no longer be an advantage to calibrating data each time an archive request is made. Instead, the plan is to process all WFPC2 data through the OTFR system

one final time, and then archive the calibrated products into a static archive. Future archive requests will then be fulfilled from this static archive. Ultimately, software maintenance efforts, as well as the computational load on the archive, should be reduced.

UCHCOORD and OTFR

Improved knowledge of the detector plate scales and chip rotations, as well as changes in reference pixel locations, have resulted in periodic changes to the pointing parameters, especially early in the instrument's lifetime. These header parameters, which define the mapping between the pixel and world coordinate systems, can be updated using the STSDAS task, **UCHCOORD**. The keywords affected include the reference pixel locations (`CRPIX*`), the values of the world coordinate system at the reference location (`CRVAL*`), the partial derivatives of the world coordinate system with respect to the pixel coordinates (`CD*`), and the orientation of the chip (`ORIENTAT`).

Prior to OTFR (released to the public on May 16, 2001), observers requiring the most up-to-date pointing information in their science image headers ran **UCHCOORD** on their calibrated images. Since the implementation of OTFR in May 2001, all WFPC2 data retrieved from the archive, regardless of its observation date, has had these corrections applied automatically before being delivered, thus we have discouraged running the **UCHCOORD** task on OTFR data since it is no longer needed (as described in WFPC2 STAN 45, March 2001 by Baggett, Hsu & Gonzaga). In fact, running **UCHCOORD** (versions prior to September 2003) on OTFR data would apply unnecessary corrections and corrupt the astrometry (for example, Section 4.3.3 in WFPC2 Data Handbook, Version 4.0, 2002, S. Baggett et al.).

The new version of **UCHCOORD** in the September 2003 STSDAS release will correctly check whether or not the images have been processed through OTFR, and will no longer modify the header astrometric keywords in such cases. We remind users that it is no longer necessary to run the **UCHCOORD** on any WFPC2 data that is retrieved via OTFR, and we recommend that any old WFPC2 data should rather be re-retrieved via OTFR since many other calibrations are also improved.

Table 8.1: Comparison of Dataflow in On-The-Fly Systems.

OTFC	OTFR
Request for data is submitted to the archive via StarView or WWW interface; archive responds with acknowledgement email.	Same as OTFC.
Raw files are retrieved from the HST archive and passed to the OTFC system. For WFPC2, the raw files include d0, q0, q1, x0, and trl files.	POD file (original telemetry file) is retrieved from HST archive and passed to OTFR system. For WFPC2, there is typically 1 POD file for each image. Pre-calibration OPUS processing is performed: data partitioning, data editing, and generic conversion; these steps generate the raw files (d0, q0, q1, x0, and trl files).
Any problems in the header keywords are fixed by special lookup table.	*Same as OTFC* although the OPUS pre-calibration processing will have fixed the majority of keyword problems automatically (i.e., significantly fewer header corrections required in OTFR).
The best calibration files & switches are determined by separate standalone task, and header keywords updated accordingly.	*Not needed*. The best calibration files & switches are set by the pre-calibration OPUS code (generic conversion).
Images are calibrated by STSDAS calxxx module and sent back to the archive system.	Same as OTFC.
Archive delivers raw + calibrated data and emails completion notification to the requestor.	Same as OTFC.

8.8 Fluxes and Standard Magnitudes

The pipeline calibrated data are not flux calibrated and the data are in units of Data Numbers (DN). However, a flux calibration is supplied in the header keywords. To obtain the flux density, multiply DN by the value of the keyword PHOTFLAM in the calibrated (`.c0h`) science header file, and divide by the value of the keyword EXPTIME.

The magnitude of an object can be determined using the photometric zero-point keyword PHOTZPT as:

$$m = -2.5\log_{10}\left(PHOTFLAM \times \frac{DN}{EXPTIME}\right) + PHOTZPT$$

where m is in the STMAG system which is based on a spectrum with constant flux per unit wavelength set to roughly match the Johnson system at V. The more conventional systems are based on Vega's spectrum. Table 8.2 was generated using SYNPHOT to provide rough conversions from STMAG to the Johnson UBVRI and Cousins RI systems. Typical uncertainties are 5%, and probably much worse for the U filter. The

correction depends on the spectrum of the object, hence the table was generated using a wide range of Bruzual models.

For example, to convert to the Cousins I band for an object on WF4, get PHOTZPT=-21.1 and PHOTFLAM=2.6044 x 10^{-18} from the header. Then convert from WFPC2 counts to magnitudes in Cousins I using:

$$I_c = -2.5\log_{10}\left(2.6044 \times 10^{-18}\frac{DN}{EXPTIME}\right) - 21.2 - 1.21$$

Note that the Cousins I filter is much closer to the F814W filter than Johnson I, as shown by the nearly constant correction as a function of spectral type (i.e. color term).

Table 8.2: Conversion from STMAG to Johnson UBVRI and Cousins RI.

	U-F336W	B-F439W	V-F555W	R_J-F675W	I_J-F814W	R_C-F675W	I_C-F814W
O5V	0.53	0.67	0.05	-0.67	-1.11	-0.71	-1.22
B0V	0.46	0.66	0.05	-0.67	-1.13	-0.70	-1.22
A0V	-0.08	0.67	0.02	-0.68	-1.22	-0.67	-1.21
F2V	-0.03	0.62	-0.00	-0.69	-1.28	-0.63	-1.22
G0V	-0.02	0.58	-0.01	-0.70	-1.31	-0.60	-1.23
K0V	-0.10	0.53	-0.01	-0.69	-1.32	-0.58	-1.23
M0V	-0.04	0.43	-0.00	-0.78	-1.48	-0.54	-1.22
M6V	0.05	0.29	-0.03	-1.05	-1.67	-0.56	-1.21

This procedure will provide typical accuracies of about 0.05 mag, worse in the UV. More accurate photometry will require a variety of corrections (e.g., CTE effect, contamination and red leaks for the UV filters, variable gains on different chips, color terms, geometric distortions) which are discussed in detail in Holtzman et al. (P.A.S.P., 1995b) and in the HST Data Handbook.

8.9 Color Transformations of Primary Filters

The WFPC2 UBVRI system is fairly close as regards effective wavelengths to the Johnson UBVRI system, but cross-calibration is necessary to convert to Johnson magnitudes. See the IDT OV/SV Report and Harris, et al., A.J. 101, 677 (1991) for examples in the case of WF/PC-1. Figure 8.1 through Figure 8.5 show the results of regression fits between these two systems on the main sequence stars in the Bruzual,

Persson, Gunn, Stryker atlas that is installed in the calibration database system (CDBS). This atlas, and others, are available directly via:

http://www.stsci.edu/hst/observatory/cdbs/astronomical_catalogs.html

Figure 8.1: F336W-F439W against Johnson U-B for the BPGS atlas of MS dwarf spectra. The change in slope in the transformation for U-B greater than about 0.1 is due to red leak in the F336W filter. For hotter stars, the transformation is quite linear.

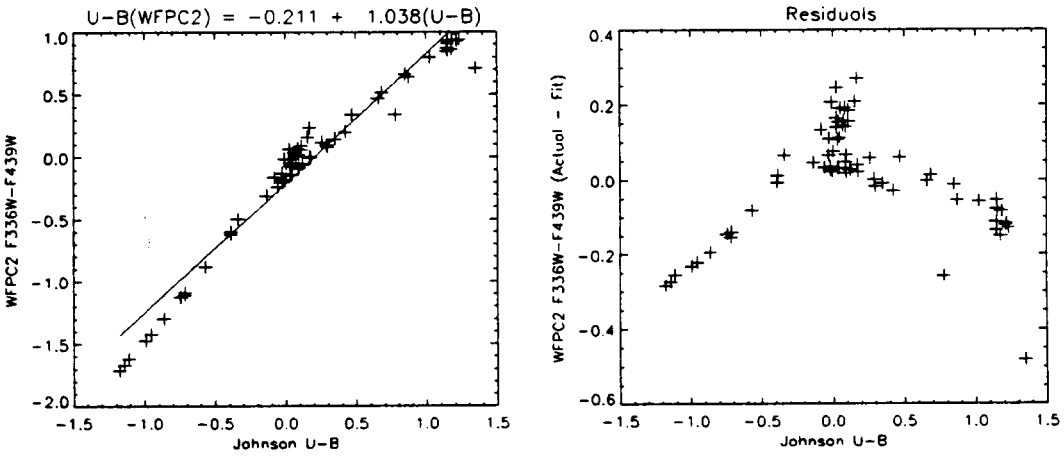

Figure 8.2: F439W-F555W against Johnson B-V. The residuals from the best linear fit are quite similar to those that apply if F569W (instead of the preferred F555W) is chosen for a WFPC2 passband.

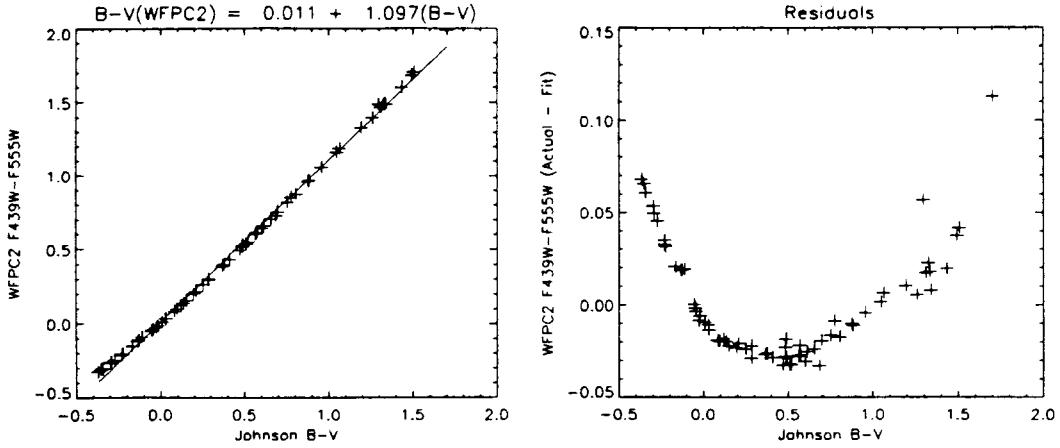

Figure 8.3: F555W-F814W against Johnson V-I_C. The residuals from the best linear fit are generally very small. This particular color combination is widely used.

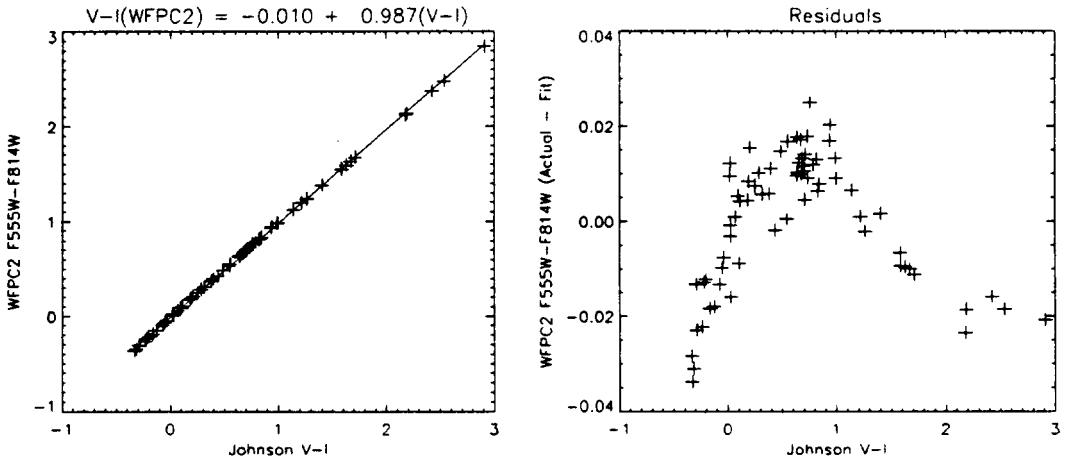

Figure 8.4: F555W-F675W against Johnson V-R_C. The residuals from the best linear fit are somewhat larger for blue stars than those that apply if F569W is chosen.

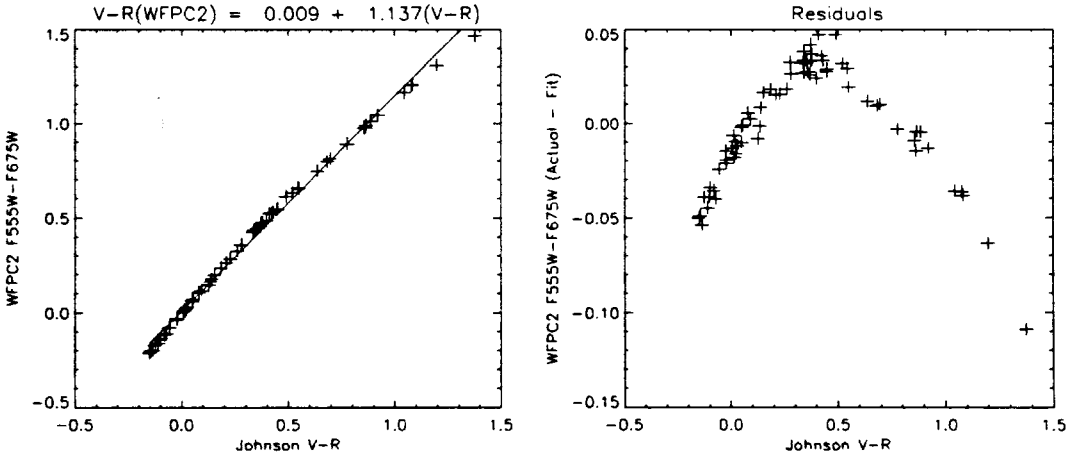

These fits should be used with caution for quantitative work. The zero-points in all cases are defined so that Vega's spectrum integrated over the bandpass is exactly magnitude zero (VEGAMAG in XCAL). The zero-points of the canonical Johnson-Cousins system differ from this by up to 0.02 magnitudes. The zero-points thus defined for the HST filters do not coincide with the STMAG definition used in the previous section. In addition, the ground based filter curves used, which are taken from Bessel (P.A.S.P. 102, 1181), give a good approximation to the standard Johnson-Cousins system, but are not as accurate as taking Landolt's curves and applying his color corrections to transform to the standard system. The latter procedure was used to derive the transformations given in Holtzman et al. (P.A.S.P., 1995b), which also discusses the changes in the

transformations that result from source spectrum variations (such as metallicity and gravity effects).

Figure 8.5: F675W-F814W against Cousins R_C-I_C. The residuals from the best linear fit are similar to those that apply if F791W is chosen for a WFPC2 I passband. For spectral type M8V and later (not shown) the transformation will not work as well.

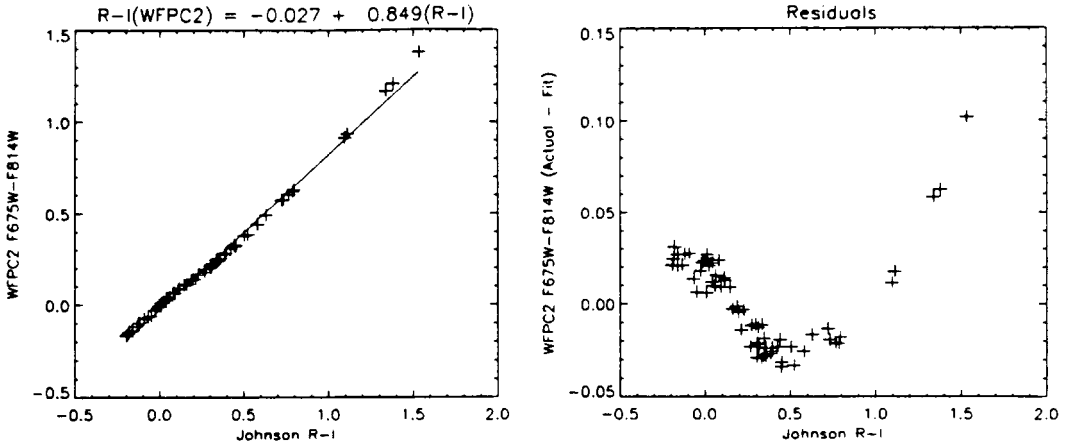

8.10 Calibration Plan Summary

Table 8.3 summarizes the nominal proposal cycle boundaries. The dates are intended as a rough guideline only, since in reality, of course, there are no sharp cycle boundaries. Some GO proposals are identified as candidates for early execution while other proposals take longer to complete due to various scheduling constraints. Additional observatory restrictions factor in as well, for example, the acceleration of the NICMOS observations in Cycle 7 (due to the limited lifetime of the NICMOS cryogen) caused many WFPC2 and other programs to be delayed.

Table 8.3: Nominal Proposal Cycle Boundaries.

cycle	start date	end date
4	May 28, 1994	July 1, 1995
5	July 1, 1995	July 1, 1996
6	July 1, 1996	July 1, 1997
7	July 1, 1997	July 1, 1999
8	July 1, 1999	July 1, 2000
9	July 1, 2000	July 1, 2001
10	July 1, 2001	July 1, 2002
11	July 1, 2002	October 1, 2003
12	October 1, 2003	October 1, 2004
13	October 1, 2004	October 1, 2005
14	October 1, 2005	July 1, 2006
15	July 1, 2006	July 1, 2007
16	July 1, 2007	SM4[a]

a. Servicing Mission 4 - Fall 2008

The following tables give an overview of the WFPC2 calibration programs that occurred during Cycle 4 through Cycle 16. The full proposals are available through STScI's proposal information web page:

http://www.stsci.edu/hst/scheduling/program_information

For more information on these programs, please see the WFPC2 Calibration Plan Summary document, located at:

http://www.stsci.edu/hst/wfpc2/

or see the WFPC2 Calibration Plan or Closure Report ISRs at:

http://www.stsci.edu/hst/wfpc2/documents/isrs

Table 8.4: Summary of Cycle 4 Calibration Plan

ID	Title	Frequency	notes
Internals			
5568	Decontaminations	1 x month	internals plus decon itself
5560	Internal Monitor 1.	2 x week	intflats, biases, kspots
5561 5655	Internal Monitor 2. - Flats	~2 x month	darks, visflats. UVflats suspended after June 12; one set of uvflats run as a test (Oct. 1994)
5562	Internal Monitor 3. - Darks	5 per week	serials=ON taken in 5561/5655
5569 5764	Internal Flats	once	intflats & visflats, in variety of filters
6140	Ramps: Internals & Earthcals	once	internals to aid in LRF calibration
Photometry			
5563	Photometric Monitor - UV Std.	2 x month	GRW+70D5824, std.filters. Clocks OFF except Dec. 1994, 1994 (ON).
5565 5663	Photometric Monitor - Fields	2 x month	Usually NGC5139. Clocks OFF except Dec. 1994 (ON).
5629	Photometric Monitor - Four Chip Std.	1 x week	GRW+70D5824; 4 CCDs, F170W
5572	Photometric Filter Calibration	run twice during Cycle 4	GRW+70D5824 in all filters used by GO/GTOs during Cycle 4; NGC5139 done in subset of broadbands.
5646	CTE Dither Test	run once	Omega Cen, nine 40 sec images in F555W, offset in 15” steps
5659	CTE Dither Test - Part 2	run once	same as 5646 but in F439W, F814W
5564	Photometric Calibration: 4-CCD	to be run once	GRW+70D5824, in 4 CCDs, standard broadband filters
Earth Flats			
5570	Earth flats - Large Set	~ 40 per week	200 Earthflats in each of four filters: F375N, F502N, F656N and F953N
5571	Earth flats - Small Set	~14-20 per week	20 Earthflats in each of ~20 filters
Other			
5643	Partially Rotated Filters	done once	GRW+70D5824 & visflats, FQUVN, FQCH4N and partial rotations
5632	Preflash Test	done twice	Omega Cen in broadband filters; includes preflash done with intflat; replaced 5565 during Apr. 1994
5778	Lyman Alpha Throughput Check	do twice	target: BD+75D325
5573	Ramp Calibration		
5574	Polarization Calibration	done once	G191B2B, BD+64D106, RMon, NGC 4147, and visflats

Table 8.4: Summary of Cycle 4 Calibration Plan

ID	Title	Frequency	notes
Placeholders/Contingency (no plans to execute, may not be run at all)			
5627	Photometric Monitor 1a: Std. in UV		Not needed.
5628	Photometric Monitor 1b: Std. in Vis.		Not needed.
5645	Optimum Preflash Test		Not needed.
5648	Charge Transfer Test		Withdrawn.
5566 5567	UV Campaign Photometry UV Campaign Flats		Not needed; no UV campaigns run
5575	Dither Test		Not needed.

Table 8.5: Summary of Cycle 5 Calibration Plans.

ID	Proposal Title	Schedule	Results	Accuracy	External Time (orbits)	Notes
6179	Photomet. Zero.	Late 95	CDBS	1%	8	1ABE, 2AB
6182	Photomet. Trans.	9/95, 3/96	CDBS	2%	6	2ABE
6183	Decontamination	1x per 4 wks.	ISR	N/A	0	F
6184	Photometric Mon.	2x per 4 weeks	ISR	1%	24	3E
6186	UV Throughput	Early in Cyc. 5	CDBS	10%	6	1AB, 3C
6187	Earth Flats	Continuous	CDBS	1%	0	4ABE
6188	Darks	Weekly	CDBS	6%	0	5ABC
6189	Visflat Monitor	2x per 4 weeks	ISR	0.6%	0	4E
6190	Internal Flats	Early Cyc. 5	CDBS	0.6%	0	4F,7E
6191	UV flats	2x in Cyc. 5	ISR	2%	0	4ABE
6192	CTE Calibration	Early Cyc. 5	TIPS	<1%	4	4ABD
6193	PSF	CTE+2m	TIM	10%	5	8ABD
6194	Polarizers+Ramps	TBD	CDBS	3%+2%	8	9DE, 1AB
6195	Flat field Check	Late 95	CDBS	1%	2	4B
6250	Internal Monitor	2x per week	ISR	N/A	0	5,6,10F
	TOTALS				63	

A. Improved the existing calibration - in particular towards the goal of 1% absolute photometric accuracy.
B. Assessed the accuracy of the existing and new calibrations.
C. Recalibrated important known time variable features of the instrument.
D. Calibrated some important instrumental effects that are not well understood.
E. Monitored the instrument and telescope to ensure that no new problems or variability in their performance are missed.
F. Maintained the instrument in a healthy state and ensured that in the event of partial

instrumental failures, the calibration can be maintained when possible.
1. Photometric zero-point: converting count rates to flux units.
2. Photometric transformations: converting DN values to magnitudes in standard systems. Two separate photometric calibrations can be used for this, a direct approach and a synthetic approach.
3. Photometric temporal variations: particularly important in the UV where significant variability is seen.
4. Photometric spatial variation: flat fields and charge transfer efficiencies.
5. Dark current: including its time variability and hot pixels.
6. Bias.
7. Analog-to-Digital converter errors.
8. PSF: crucial for PSF fitting photometry, PSF subtraction, PSF modeling, and deconvolution efforts. Because PSF subtraction of very saturated sources is specialized to a few very diverse programs, PSF calibration in the image halo (beyond about 0.5 arcsecond) is not supported and must be requested with the program as a special calibration.
9. Polarization and Linear Ramp Filter calibrations.
10. Geometric calibration.

Table 8.6: Summary of Cycle 6 Calibration Plan.

ID	Proposal Title	Schedule	Results	Accuracy	External Time (orbits)	Notes
			Routine Monitoring Programs			
6902	Photometric Monitor	2x per 4 weeks	SYNPHOT	2%	26	
6903	Decontamination	1x per 4 weeks	CDBS	n/a	0	(darks, internals)
6904	Darks	Weekly	CDBS	1 e/hr	0	WWW hot pixel lists
6905	Internal Monitor	Weekly	CDBS	0.8 e	0	
6906	Visflat Monitor	2x per 4 weeks	ISR	0.3%	0	(monitor lamp health)
6907	Intflat Monitor	1x per 4 weeks	ISR	0.3%	0	
6908	UV Flat Field Monitor	2x in Cyc. 6	ISR	2-8%	0	
6909	Earth Flats	Continuous	CDBS	0.3%	0	
			Special Calibration Programs			
6934	Photometric Zeropoint	1x in Cyc. 6	SYNPHOT	2%	6	Add 2 new standards
6935	Photometric Trans.	2x in Cyc. 6	ISR	2-5%	9	Three targets
6936	UV Throughput & Ly α	2x in Cyc. 6	SYNPHOT	3-10%	12	Include BD+75D325
6937	CTE Calibration	1x in Cyc. 6	ISR	1%	2	
6938	PSF Characterization	1x in Cyc. 6	CDBS	10%	7	
6939	Linear Ramp Filters	1x in Cyc. 6	CDBS	3%	4	
6940	Polarizers	1x in Cyc. 6	CDBS	3%	4	
6941	Astrometry Verification	1x in Cyc. 6	STSDAS	0.01″	4	
6942	Camera Elect. Verification	1x in Cyc. 6	ISR	0.5%	1	
6943	Narrow Band Throughput	SNAP	SYNPHOT	3%	8	SNAP
	TOTALS				83	

Table 8.7: WFPC2 Cycle 7 Calibration Plan.

ID	Proposal Title	Frequency	Estimated Time (orbits) "External"	Estimated Time (orbits) "Internal"	Products	Accuracy	Notes
			Routine Monitoring Programs				
7618	Photometric Monitor	1–2/4 weeks	36		SYNPHOT	1–2%	Also focus monitor
7619	Decontamination	1/4 weeks		288	CDBS	n/a	Used together with darks, internals
7620	Standard Darks	weekly		360	CDBS, WWW	1 e/hr	Also hot pixel lists on WWW
7621, 7712, 7713	Supplemental Darks	weekly		2016		n/a	No analysis provided
7622	Internal Monitor	2/4 weeks		72	CDBS, TIR	0.8 e/pixel	New superbias (with 7619)
7623	Internal Flats	1/4 weeks		75	TIR	0.3%	Mostly INTFLATs
7624	UV Flat Field Monitor	2/cycle	4	8		2-8%	Before and after decon
7625	Earth Flats	continuous		155	CDBS	0.3%	Also LRF, Methane quads
7626	UV Throughput	2/cycle	4		SYNPHOT	3–10%	
7627	Astrometric Monitor	2/cycle	2	2	TIPS, TIR	0.″05	Also K-spots
			Special Calibration Programs				
7628	Photometric Characterization	1	10		ISR	2–5%	Also test zeropoint differences between chips, UV vignetting, astrometry
7629	PSF Characterization	1	5		WWW	10%	Covers widely used, high-throughput filters
7630	CTE Characterization	1	14		ISR	0.01 mag	Extensive coverage of preflash levels and exposure times in F555W, spot checks in F555W, F300W, hysteresis, CTE ramp
7929	CTE Monitor	4	4		ISR	0.02 mag	Measure changes in CTE ramp
8053	Supplemental Earth Flats	1		155	CDBS	0.3%	Repeat Earth Flats towards end of cycle
8054	LRF Calibration	1	10		ISR	3–5%	Complete LRF calibration, test stability
	TOTAL TIME (including all executions)		89	3131			

Table 8.8: WFPC2 Cycle 8 Calibration Plan.

ID	Proposal Title	Frequency	Estimated Time (orbits)		Scheduling Required	Products	Accuracy Required	Notes
			"External"	"Internal"				
Routine Monitoring Programs								
8441 8459	WFPC2 Decons & Associated Observations	1-2/4 weeks	32	72	every 28 days	Synphot, CDBS	1-2%	Includes decons, photometric monitor, focus monitor, internals, UV throughput.
8442	Standard Darks	weekly		324	every 7 days	CDBS	1 e/hr	Also hot pixel lists on WWW.
8443	Supplemental Darks (8460, 8461)	0-3/day		1308	anytime		n/a	For archive only, no analysis provided.
8444	Internal Monitor	3/4 weeks		45	every 7days	CDBS	0.8e/pixel	New superbiases, not run on decon weeks.
8445	Earth Flats	continuous		442	mid-cycle	CDBS	0.3%	Also LRF, Methane quads.
8446	Astrometric Monitor	2/cycle	2		early & late	ISR	0.05"	Also K-spots & plate scale check in red.
8447	CTE Monitor	2/cycle	4		mid- & late	ISR	0.01 mag	
8448	Intflat and Visflat Sweeps	1/cycle		43	mid-cycle	TIR	0.3%	Mostly intflats.
8449	UV Flats Internal Monitor	1/cycle	2		mid-cycle	TIR	2-8%	Uses UV cal channel lamp.
Special Calibration Programs								
8451	Photometric Characterization	1	2		mid-cycle	ISR	2.5%	Subset of Cycle 7 proposal, as check.
8452	PSF Characterization	1	2		late in cycle	CDBS	10%	Subset of standard broadband filters.
8453	Polarization	1	6	10	early in cycle	CDBS	3-5%	Subset of Cycle 6, as check.
8454	Linear Ramp Filters	1	4		late in cycle	CDBS	3%	Placeholder, pending results from Cycle 7.
8450	Noiseless Preflash	1	5		early in cycle	TIR	0.01 mag	Test scheme to reduce CTE problem.
8455	Photometry of Very Red Stars	1	2		mid-cycle	ISR	2-5%	Outsourcing candidate.
8456	CTE for Extended Sources (2-3")	1	4		mid-cycle	ISR	0.01 mag	Outsourcing candidate.
8457	UV Earth Flats	continuous		720	early in cycle	CDBS	10%	Outsourcing candidate.
8458	Plate Scale Verification	1	1		mid-cycle	ISR	0.05%	Outsourcing candidate.
	~10% reserve for unexpected items		7					Placeholder.
TOTAL TIME (including all executions)			73	2964				

Table 8.9: WFPC2 Cycle 9 Calibration Plan.

ID	Proposal Title	Frequency	Estimated Time (orbits)		Scheduling Required	Products	Accuracy Required	Notes
			"External"	"Internal"				
			Routine Monitoring Programs					
8822-8825	WFPC2 Decons & Associated Observations	1-2/4 wks	30	82	every 28 d	Synphot, CDBS	1-2%	Decons, phot. & focus monitor, internals, UV throughput, VIS-FLATs, and UV FLATs
8811	Standard Darks	weekly		366	every 7 d	CDBS	1 e^-/hr	Also hot pixel lists on WWW.
8826-8828	Supplemental Darks (8460, 8461)	0-3/day		1282	anytime		n/a	For archive only, no analysis provided
8812	Internal Monitor	weekly		76	every 7d	CDBS	0.8e/pixel	Includes INTFLAT monitor, for possible future preflashed observations.
8815	Earth Flats	continuous		210	mid-cycle	CDBS	0.3%	
8816	UV Earth Flats	continuous		400	mid-cycle	CDBS	3-10%	Outsourcing candidate.
8813	Astrometric Monitor	2/cycle	2		early & late	ISR	0.05"	Omega Cen as well as K-spots.
8817	Intflat Sweep and Linearity Test	1/cycle		21	mid-cycle	TIR	0.3%	
			Special Calibration Programs					
8818	Photometric Characterization	1	2		mid-cycle	ISR	2-3%	GRW+70D5824; nonstandard filters.
8819	PSF Characterization	1	6		late in cycle	CDBS	10%	Omega Cen; standard broadband filters.
8814	Read Leak Check	1	2		mid-cycle	Synphot, CDBS	2%	Solar analogs used to measure UV filter read leaks.
8821	CTE - Monitor and Absolute Calibration	1	15		mid/late	ISR	0.01 mag	Includes monitor as well as follow up to ground based observations. Outsourcing candidate.
8820	Wavelength Stability of Narrow-band and Linear Ramp Filters	1	4	15	mid/late	CDBS, ISR	2Å	Check of wavelength/aperture mapping and test for changes in LRFs.
	~10% reserve		6					Placeholder.
	TOTAL TIME (including all executions)		**67**	**2452**				

Table 8.10: WFPC2 Cycle 10 Calibration Plan.

ID	Proposal Title	Frequency	Estimated Time (orbits)		Scheduling Required	Products	Accuracy Required	Notes
			"External"	"Internal"				
			Routine Monitoring Programs					
8932-8934	WFPC2 Decons & Associated Observations	1-2/4 wks	19 photmon 2 UV thru.put 2 UV flats	82	every 28 d	CDBS, IHB, Synphot, WWW reports	1-2%	Decons, phot. & focus monitor, internals, UV throughput, vis-flats and uvflats.
8935	Standard Darks	weekly		318	every 7 d	CDBS	1 e/hr	Also for WWW hot pixel lists.
8836-8838	Supplemental Darks	0-3/day		1095	every day		n/a	For archive only, no analysis.
8839	Internal Monitor	weekly		76	every 7 d	CDBS	$0.8e^-$/pix	Incl. intflats for preflash.
8840	Earth Flats	continuous		210	mid to late	CDBS	0.3%	
8841	UV Earth Flats	continuous		400	early to mid	CDBS	3-10%	Outsourcing candidate.
8842	Intflat & Visflat Sweeps	1/cycle		61	mid-cycle	TIR	0.3%	Incl. filter rotation offset check.
			Special Calibration Programs - Continuations					
9253	Astrometric Monitor	2/cycle	2	2	early & late	ISR, STSDAS	0.05"	ω Cen as well as K-spots.
9254	CTE Photometric Monitor	2 x 3 orbits	6		mid & late	ISR	0.01 mag	Continuation of monitors.
9251	Photometric Characterization	1	4		mid-cycle	ISR, Synphot	2-3%	All four chips.
			Special Calibration Programs - New					
9255	Astrometric Effects of CTE	1	12		late	ISR	1-2 mas	Target kept on 1 chip.
9257	Super-PSF	1	6		mid-cycle	CDBS, STS-DAS, ISR	10%	PSF wing characterization.
9252	Clocks ON Verification	1	1	50	early	ISR, Synphot	2-3%	Closure calibration.
9256	Methane Quad Filter Check	1	1		mid-cycle	Synphot, ISR	5%	Test of transmission curve across aperture (GO suggestion). Outsourcing candidate.
	~10% reserve		6					Placeholder for unexpected items.
	TOTAL TIME (including all executions)		**61**	**2294**				

Table 8.11: WFPC2 Cycle 11 Calibration Plan.

ID	Proposal Title	Frequency	Estimated Time (orbits)		Scheduling Required	Products	Accuracy Required	Notes
			"External"	"Internal"				
Routine Monitoring Programs								
9589	WFPC2 Decons & Associated Observations	Decons every 49d (from 28d)	20 (13 photmon, 5 UV thruput, 2 UV flats)	124	every 49d, UV thruput early	CDBS, Inst Hbk, Synphot, WWW reports	1-2%	Decons, phot.monitor, internals, UV throughput, VISFLATS and UVFLATS.
9592	Standard Darks	weekly, except decon week		294	every 7 days, except decon wk.	CDBS	1 e-/hr	Also for WWW hot pixel lists.
9593, 9594, 9595	Supplemental Darks	0-3/day		1182	every day		n/a	For archive only, no analysis.
9596	Internal Monitor	weekly, except decon week		53	every 7 days, except decon week	CDBS	0.8e-/pix	
9598	Earth Flats	continuous		150	mid-to-late	CDBS	0.3%	
9599	UV Earth Flats	continuous		200	early-to-mid	CDBS	3-10%	
9597	Intflat & Visflat Sweeps, Filter Anomaly Check	1/cycle		166	mid-cycle	TIR	0.3%	
Special Calibration Programs								
9600	Astrometric Monitor	1/cycle	1	1	mid-cycle	ISR, STSDAS	0.05''	ω Cen as well as K-spots.
9591	CTE Characterization	1/cycle	5		early, late	ISR	0.03 mag	Continuation of monitors, new tests (2x2 binning & long vs. short).
9590	Photometric Characterization	1/cycle	3		early	ISR, Synphot	1%	Std. star in all 4 chips. Non-monitor broadband filters, not UV.
9601	WFPC2-ACS Photometric Cross-Calibration	1/cycle	8		early	ISR, Synphot	1%	Cross-calibration with ACS, using NGC2419, 47 Tuc, ACS calib star, & Sloane Calibration Field.
	~10% reserve		3					Placeholder for unexpected items.
TOTAL TIME (including all executions)			**40**	**2171**				

Table 8.12: WFPC2 Cycle 12 Calibration Plan.

ID	Proposal Title	Frequency	Estimated Time (orbits)		Scheduling Required	Products	Accuracy Required	Notes
			"External"	"Internal"				
Routine Monitoring Programs								
10067	WFPC2 Decons & Associated Observations	Decons every 49d	8	124	every 49d	CDBS, IHB, Synphot, WWW reports	1-2%	Decons, phot.monitor, internals, UV throughput, VISFLATS and UVFLATS.
10068	Standard Darks	weekly, exc. decon wk		264	every 7 days, exc.decon wk	CDBS	1 e-/hr	CDBS updates and weekly WWW hot pixel lists.
10069, 10070, 10071	Supplemental Darks	0-3/day		1195	every day		n/a	For archive only, no analysis. Schedule at a low priority. Useful for calibrating WFPC2 parallels.
10072	Internal Monitor	weekly, exc. decon wk		44	every 7 days, exc.decon wk	CDBS	0.8e-/pix	BIAS, INTFLATS in F555W for gain and throughput stability measurements
10073	Visible Earth Flats	continuous		50	mid-to-late	CDBS	0.3%	Reduce to 1 filter (time dep. only)
10074	UV Earth Flats	continuous		20	mid-to-late	CDBS	0.3%	
10075	Intflat & Visflat Sweeps, Filter Anomaly Check	1/cycle		80	mid-cycle	TIR	0.3%	Flats in all the filters used in Cycle 12, both gain settings/shutters.
10076	CTE Monitor	1/cycle	2		mid-to-late	ISR	0.03 mag	Continue CTE monitor.
10077	Photometric Monitor	1/cycle	2		mid-cycle	ISR, Synphot	1%	GRW+70D5824 in filter/chip combos used for science in Cycle 12.
Close-Out Calibration Programs								
10078	Photometric Cross-Calibration	once	6		mid-cycle	ISR, Synphot	1%	Several standard stars in a range of WFPC2 filters, for ACS & WFC3 cross-calibration.
10079	UV Astrometric Characterization	once	3	1	mid-cycle	ISR, Synphot	0.05"	Determine astrometric solution in new UV filters (not done before), and K-spots.
10080	Narrow-Band/LRF Characterization	once	2	3	mid-to-late	ISR, Synphot	1-2%	Check filter wavelength stability: observe emission-line source in narrow-band filters, and crossed with LRFs
	~10% reserve		2					Placeholder for unexpected items.
TOTAL TIME (including all executions)			**25**	**1601**				

Table 8.13: WFPC2 Cycle 13 Calibration Plan.

ID	Proposal Title	Frequency	Estimated Time (orbits)		Scheduling Required	Products	Accuracy Required	Notes
			"External"	"Internal"				
				Routine Monitoring Programs				
10356	WFPC2 Decons & Associated Observations	Decons every 49d	8	124	every 49d	CDBS, IHB, Synphot, WWW reports	1-2%	Decons, phot.monitor, internals, UV throughput, VISFLATS and UVFLATS.
10359	Standard Darks	weekly, exc. decon wk		264	every 7 days, exc.decon wk	CDBS	1 e-/hr	CDBS updates and weekly WWW hot pixel lists.
10360	Internal Monitor	weekly, exc. decon wk		44	every 7 days, exc.decon wk	CDBS	0.8e-/pix	BIAS, INTFLATS in F555W for gain and throughput stability measurements
10361	Visible Earth Flats	continuous		50	mid-to-late	CDBS	0.3%	F502N only (time dependence only)
10362	UV Earth Flats	continuous		20	mid-to-late	CDBS	0.3%	F255W only
10363	Intflat & Visflat Sweeps, Filter Anomaly Check	1/cycle		80	mid-cycle	TIR	0.3%	Flats in all the filters used in Cycle 12, both gain settings/shutters.
10364	CTE Monitor	1/cycle	2		mid-to-late	ISR	0.03 mag	Continue CTE monitor.
10365	Photometric Monitor	1/cycle	3		mid-cycle	ISR, Synphot	1%	GRW+70D5824 in filter/chip combos used for science in Cycle 13.
				Close-Out Calibration Programs				
10366	Photometric Cross-Calibration	once	2		mid-cycle	ISR, Synphot	1%	T-dwarf star in a range of WFPC2 filters, for ACS & WFC3 cross-calibr.
	~10% reserve		2					Placeholder for unexpected items.
TOTAL TIME (including all executions)			**17**	**582**				

Table 8.14: WFPC2 Cycle 14 Calibration Plan.

ID	Proposal Title	Frequency	Estimated Time (orbits)		Scheduling Required	Products	Accuracy Required	Notes
			"External"	"Internal"				
10744	WFPC2 Decons & Associated Observations	Decons every 50-60d	6	94	every 50-60d	CDBS, IHB, Synphot, WWW reports	1-2%	Decons, phot.monitor, internals, UV throughput, VISFLATS and UVFLATS, darks.
10748	Standard Darks	weekly, exc. decon wk		264	every 7 days, exc.decon wk	CDBS	1 e-/hr	CDBS updates and weekly WWW hot pixel lists.
10745	Internal Monitor	weekly, exc. decon wk		44	every 7 days, exc.decon wk	CDBS	0.8e-/pix	BIAS, INTFLATS in F555W for gain and throughput stability measurements
10749	Visible Earth Flats	continuous		50	mid-to-late	CDBS	0.3%	F502N only (time dependence only)
10750	UV Earth Flats	continuous		20	mid-to-late	CDBS	0.3%	F300W only
10751	Intflat & Visflat Sweeps, Filter Anomaly Check	1/cycle		80	mid-cycle	TIR	0.3%	Flats in all the filters used in Cycle 14, both gain settings/shutters.
10746	CTE Monitor	1/cycle	4		mid-to-late	ISR	0.03 mag	Continue CTE monitor. Test for chip dependence.
10747	Photometric Monitor	1/cycle	7		mid-cycle	ISR, Synphot	1%	GRW+70D5824 in filter/chip combos used for science in Cycle 14.
	~10% reserve		2					Placeholder for unexpected items.
TOTAL TIME (including all executions)			**19**	**552**				

Table 8.15: WFPC2 Cycle 15 + 16 Calibration Plan

ID	Proposal Title	Frequency	Estimated Time (orbits)[a]		Scheduling Required	Products	Accuracy Required	Notes
			"External"	"Internal"				
11022, 11796	WFPC2 Decons & Associated Observations	Decons every 40-60d	15	236	every 40-60d	CDBS, IHB, Synphot, WWW reports	1-2%	Decons, phot.monitor, internals, UV throughput, VISFLATS and UVFLATS, darks.
11023, 11070, 11302	Standard Darks	weekly, exc. decon wk		660	every 7 days, exc.decon wk	CDBS	1 e-/hr	CDBS updates and weekly WWW hot pixel lists.
11024, 11793	Internal Monitor	weekly, exc. decon wk		110	every 7 days, exc.decon wk	CDBS	0.8e-/pix	BIAS, INTFLATS in F555W for gain and throughput stability measurements
11025	CTE Monitor	1/cycle	5		mid-to-late	ISR	0.03 mag	Continue CTE monitor. Test for chip dependence.
11026, 11805	Photometric Monitor	1/cycle	3		mid-cycle	ISR, Synphot	1%	GRW+70D5824 in filter/chip combos used for science in Cycle 15 & 16.
11027, 11794	Visible Earth Flats	continuous		125	mid-to-late	CDBS	0.3%	F502N only (time dependence only)
11028, 11795	UV Earth Flats	continuous		50	mid-to-late	CDBS	0.3%	F300W only
11029	Intflat & Visflat Sweeps, Filter Anomaly Check	1/year		160	mid-cycle	TIR	0.3%	Flats in all the filters used in Cycle 15 & 16, both gain settings/shutters.
	~10% reserve		2					Placeholder for unexpected items.
TOTAL TIME (including all executions)			**25**	**1341**				

a. As of May 2008

Table 8.16: WFPC2 Closeout Calibration Plan

ID	Proposal Title	Frequency	Estimated Time (orbits)[a]		Scheduling Required	Products	Accuracy Required	Notes
			"External"	"Internal"				
11030	WF4 Anomaly	as needed	5	81	as needed	CDBS, IHB, WWW reports	1-2%	Two additional WFPC2 temperature adjustments to keep WF4 CCD functioning, if needed.
11031	CTE & Background Dependence	once	16		mid-to-late	ISR, IHB	0.03 mag	Evaluate CTE corrections near mission end.
11032	CTE Extended Targets	once	34		mid-to-late	ISR, IHB	0.03 mag	Evaluate extended target CTE near mission end.
11033	Full Moon Earth Flats	continuous	12	(200)	mid-to-late	CDBS, ISR	0.3%	Test / improve broadband flats.
11034	Photometric Closeout	once	4		mid-to-late	CDBS, ISR	1%	Filters not calibrated recently.
11035	Photometric Zero Points	once	8		mid-to-late	CDBS, ISR	1%	Final cross-calibration vs. ACS
11036, 11327	Red Leaks	once	22		mid-to-late	CDBS, ISR, Synphot	1%	Improve calibration.
11037	Red Filters	once	6		mid-to-late	CDBS, ISR, Synphot	1%	Cross-calibrate WF3 CCD vs ACS.
11038	Narrow-Band and Ramp Filters	once	10	20	mid-to-late	CDBS, ISR, Synphot	1%	Check for long-term changes in bandpasses.
11039, 11326	Polarizers	once	10	2	mid-to-late	CDBS, ISR, Synphot	3%	Check for changes in polarizer performance.
11040	Geometric Distortion	once	8		mid-to-late	CDBS, ISR	0.05"	Better astrometry in red and blue; skew terms.
11804	Standard Star CTE	once	8		late	ISR	0.02 mag	CTE for star GRW+70D5824
TOTAL TIME (including all executions)			**143**	**103 (303)**				

a. As of May 2008

8.11 Outsourced Calibration Programs

Besides the standard calibrations carried out by the WFPC2 team and summarized in the previous section, observers were also encouraged to submit Calibration Proposals as a special class of program solicited in the Call for Proposals. These programs were sometimes called "Outsourced Calibration Programs". This was a recognition that there were areas of calibration where greater expertise resided outside the WFPC2 team, and provided a means to facilitate calibration work by the external community. Table 8.17 summarizes the outsourced calibration programs.

Table 8.17: Outsourced WFPC2 Calibration Programs

ID	Proposal Title	PI	# of Observations	Result References
(00108)	WFPC2 Flatfields with Reduced Noise	Karkoschka	Archive Proposal	ISR WFPC2 01-07
9526	Characterization of Spatial Variations in the Transmission of WFPC2 Filter FQCH4N-D	Karkoschka	Archive Proposal	
9898	Calibration of the ACS Emission Line Filters	O'Dell	16 ACS, 16 WFPC2	
9918	CTE Corrections for WFPC2 and ACS	Dolphin	Archive Proposal	CTE Corrections
11231	Calibration of the WFPC2 HeII and [SII] Filters	O'Dell	9 Exposures	
11244	WFPC2 CTE and Photometric Zero Points	Dolphin	Archive Proposal	CTE corrections and Zero Points[a]
11274	A Final Calibration of the Primary WFPC2 Emission-Line Filters Using the Orion Nebula	O'Dell	Archive Proposal	

a. http://purcell.as.arizona.edu/wfpc2_calib

8.12 Calibration Accuracy

Table 8.18 summarizes the accuracy to be expected from WFPC2 observations in several areas. The numbers in the table should be used with care, and only after reading the relevant sections of this handbook and the documents referenced therein; they are presented in tabular form here for easy reference.

Table 8.18: Accuracy Expected in WFPC2 Observations.

Procedure	Estimated Accuracy	Notes
Calibration (flatfielding, bias subtraction, dark correction)		
Bias subtraction	0.1 DN rms	Unless bias jump is present
Dark subtraction	0.1 DN/hr rms	Error larger for warm pixels; absolute error uncertain because of dark glow
Flatfielding	<1% rms large scale	Visible, near UV
	0.3% rms small scale	
	~10%	F160BW; however, significant noise reduction achieved with use of correction flats
Relative photometry		
Residuals in CTE correction	< 3% for the majority (~90%) of cases	
	up to 10% for extreme cases (e.g., very low backgrounds)	
Long vs. short anomaly (uncorrected)	< 5%	Magnitude errors <1% for well-exposed stars but may be larger for fainter stars. Some studies have failed to confirm the effect
Aperture correction	4% rms focus dependence (1 pixel aperture)	Can (should) be determined from data
	<1% focus dependence (> 5 pixel)	
	1-2% field dependence (1 pixel aperture)	
Contamination correction	3% rms max (28 days after decon) (F160BW)	
	1% rms max (28 days after decon) (filters bluer than F555W)	
Background determination	0.1 DN/pixel (background > 10 DN/pixel)	May be difficult to exceed, regardless of image S/N
Pixel centering	< 1%	
Absolute photometry		
Sensitivity	< 2% rms for standard photometric filters	Red leaks are uncertain by ~10%
	2% rms for broad and intermediate filters in visible	
	< 5% rms for narrow-band filters in visible	
	2-8% rms for UV filters	
Astrometry		
Relative	0.005" rms (after geometric and 34th-row corrections)	Same chip
	0.1" (estimated)	Across chips
Absolute	1" rms (estimated)	

References

In this chapter . . .

References

- Anderson, J, and King, I. R. 1999, *Astrometric and Photometric Corrections for the 34th Row Error in HST's WFPC2 Camera*, PASP 111, 1095.
- Anderson, J., King, I. 2003, PASP, 115, 113.
- Baggett, S., et al. 1998, *WFPC2 Dark Current Evolution*, TIR WFPC2 98-03.
- Baggett, S., Gonzaga, S. 1998, *WFPC2 Long-Term Photometric Stability*, ISR WFPC2 98-03.
- Baggett, S., Gonzaga, S., Biretta, J. 2000, *CTE Effects on Aperture Photometry of Extended Sources*, (private communication).
- Baggett, S., Biretta, J., Hsu, J. C., 2000, *Update on Charge Trapping and CTE Residual Images in WFPC2,* ISR WFPC2 00-03.
- Baggett, S., McMaster, M., et al. 2002, in HST WFPC2 Data Handbook, V.4.0, ed. B. Mobaster, Baltimore, STScI
- Bessell, M. S. 1990, *UBVRI Passbands*, PASP 102, 1181.
- Biretta, J. A, and Sparks, W. B. 1995, *WFPC2 Polarization Observations: Strategies, Apertures, and Calibration Plans*, WFPC2 ISR 95-01.

- Biretta, J. A. 1995, “WFPC2 Flat Field Calibration,” in *Calibrating Hubble Space Telescope: Post Servicing Mission*, eds. A. Koratkar and C. Leitherer, p. 257.
- Biretta, J., Baggett, S., 1998, *Proposed Modification to the WFPC2 SAA Avoidance Contour,* TIR WFPC2 98-04 (plus update).
- Biretta, J., McMaster, M. 1997, *WFPC2 Polarization Calibration*, ISR WFPC2 97-11.
- Biretta, J., Mutchler, M. 1998, *Charge Trapping and CTE Residual Images in the WFPC2 CCDs*, ISR WFPC2 97-05.
- Biretta, J., Kozhurina-Platais, V. 2005, *Hot Pixels as a Probe of WFPC2 CTE Effects,* ISR WFPC2 05-01.
- Blouke, D. P. 1991, eds. Janesick, J. and Elliot, T., PASP, 8, 153.
- Burrows, C. et al. 1991, *The Imaging Performance of the Hubble Space Telescope*, ApJL 369, L21.
- Casertano, S., Mutchler, M 1998, *The Long vs. Short Anomaly in WFPC2 Images*, ISR WFPC2 98-02.
- Casertano, S., et al., editors, *The 1997 HST Calibration Workshop Proceedings*, STScI, 1998.[1]
- Casertano, S., Wiggs, M. 2001, WFPC2 ISR 01-10, Baltimore, STScI.
- Clarke, J.T. and the WFPC2 IDT 1992, *White Paper for WFPC2 Far-Ultraviolet Science*.[2]
- *Dithering: Relationship Between POS TARG’s and CCD Rows/Columns*.[1]
- Dolphin, A., 2000, PASP 112, 1397.
- Dolphin, A., 2002, *Proceedings of the 2002 HST Calibration Workshop*, STScI, 2003.
- Evans, R. E. 1992, JPL Memorandum, DFM #2031.
- Fruchter, A. S., Hook, R. N. 1997, "A Novel Image Reconstruction Method Applied to Deep Hubble Space Telescope Images", in *Applications of Digital Image Processing XX*, Proc. SPIE, Vol. 3164, A. Tescher, editor, p.120.
- Fruchter, A.S., Hook, R.N. 2002, “Drizzle: A Method for the Linear Reconstruction of Undersampled Images”, PASP 114, 144.
- Gilliland, R. L. 1994, ApJ 435, L63.

1. Available at http://www.stsci.edu/stsci/meetings/cal97/proceedings.html

2. These documents may be requested by e-mail from help@stsci.edu.

- Gilmozi, R., et al. 1995, WFPC2 ISR 95-02, Baltimore, STScI
- Gonzaga, S., et al. 1998, *The Drizzling Cookbook*, ISR WFPC2 98-04.
- Gonzaga, S., et al. 1999, *WFPC2 Aperture Photometry Corrections as a Function of Chip Position*, TIR WFPC2 99-01.
- Gonzaga, S., Baggett, S., Biretta, J. 2001, *Preliminary Assessment of the FR533N Filter Anomaly*, ISR WFPC2 01-04.
- Gonzaga, S., Baggett, S., Biretta, J. 2002, *An Analysis of WFPC2 Filter Positional Anomalies*, ISR WFPC2 02-04.
- Gonzaga, S., Biretta, J. 2002, *Predicting Photometry Errors due to Linear Ramp Filters*, TIR WFPC2 02-06.
- Groth, E. and Shaya, E. 1991, in *Wide Field/Planetary Camera Final Orbital/Science Verification Report*, S., M., Faber, Ed.
- Griffiths, R. Ewald, S. and MacKenty, J. W. 1989, in *CCDs in Astronomy*, PASP 8, 231, ed. G. Jacoby.
- Gunn, J. E., and Oke, J. B. 1983, ApJ 266, 713.
- Harris, H. C., et al. 1991, *Photometric Calibration of the HST WF/PC-1 Camera: I. Ground Based Observations of Standard Stars*, AJ 101, 677.
- Harris, H. C., et al. 1993, AJ 105, 1196.
- Hasan, H. and Bely, P. 1993, *Restoration of HST Images and Spectra II,* p.157.
- Hasan, H. and Burrows, C. J. 1993, “Calibrations of the Hubble Space Telescope Optical Telescope Assembly” in *Calibrating Hubble Space Telescope,* eds. C. Blades and S. Osmer, p. 395.
- Hill, R. J., et al. 1998, ApJ, 496, 648.
- Holtzman, J., et al. 1995a, “The Performance and Calibration of WFPC2 on the Hubble Space Telescope,” PASP, 107, 156.
- Holtzman, J., et al. 1995b, “The Photometric Performance and Calibration of WFPC,” PASP, 107, 1065.
- *HST Data Handbook*, C. Leitherer, ed., (Version 2.0, December 1995).[1]
- *HST Phase II Proposal Instruction*, (Version 8.0, 15 December 1995).[1]
- Interface Control Document (ICD) 19, "PODPS to STSDAS".
- Interface Control Document (ICD) 47, "PODPS to CDBS".

- Janesick, J., Elliot, T., Bredthauer, R., Cover, J., Schaefer, R. and Varian, R. 1989, in *Optical Sensors and Electronic Photography*, SPIE Proc. 1071.
- Janesick, J., Elliot, T., Blouke, M. and Corrie, B. 1989b, in *Optical Sensors and Electronic Photography*, SPIE Proc. 1071, 115, ed. B. Pophal.
- Janesick, J. R. 2001, in *Scientific Charge-Coupled Devices* (Bellingham: SPIE), pp 387-487.
- Jones, M. R. 2000, *ACS WFC CCD Radiation Test: The Rdiation Envrionment,* ISR ACS 00-09.
- Jordan, Deltorn, and Oates 1993, *Greenwich Observatory Newsletter*, Sept. 1993.
- Kelson, D. D., et al. 1996, ApJ, 463, 26.
- Koekemoer, A. M., et al. 2002, *HST Dither Handbook* (Version 2.0)
- Koekemoer, A. M., Fruchter, A.S., Hook, R.N., Hack, W. 2002, "MultiDrizzle: An Intergrated Script for Registering, Cleaning and Combining Images", *2002 HST Calibration Workshop,* eds. S. Arribas and A.M. Koekemoer and B. Whitmore, p. 339.
- Koekemoer, A.M., Biretta, J., Mack, J. 2002, *Updated WFPC2 Flatfield Reference Files for 1995 - 2001*, ISR WFPC2 02-02.
- Koornneef, J. et al. 1983, "Synthetic Photometry and the Calibration of the Hubble Space Telescope," in *Highlights of Astronomy*, 7, 833, ed. J.-P. Swings.
- Kozhurina-Platais, V., Anderson J., Koekemoer, A. 2003, WFPC2 ISR 03-02, Baltimore, STScI
- Krist, J., Burrows, C. 1995, *Applied Optics* 34, 4951.
- Krist, J. E. 1995, "WFPC2 Ghosts, Scatter, and PSF Field Dependence," in *Calibrating Hubble Space Telescope: Post Servicing Mission*, eds. A. Koratkar and C. Leitherer, p. 311.
- Lauer, T. 1989, *The Reduction of WF/PC Camera Images*, P.A.S.P. 101, 445.
- Lauer, T. 1991, in *Wide Field/Planetary Camera Final Orbital/Science Verification Report*, ed. S. M. Faber.
- Oke, J.B. and Gunn, J. 1983, ApJ 266, 713.
- Riess, A. 2000, *How CTE Affects Extended Sources*, ISR WFPC2 00-04.
- Riess, A., Biretta, J., Casertano, S. 1999, *Time Dependence of CTE from Cosmic Ray Trails*, ISR WFPC2 99-04.

- Saha, A., et al. 1996, ApJ, 466, 55.
- Saha, A., Labjardt, L., and Prosser, C. 2000, PASP, 112, 163.
- Stetson, P. B. 1998, PASP, 110, 1448.
- *STSDAS Calibration Guide* (November 1991).[1]
- STDAS Users' Guide.
- Schneider, D. P., Gunn, J. E., and Hoessel, J. G. 1983, ApJ 264, 337.
- Schultz, A., Heyer, I., Biretta, J. 2001, *Noiseless Preflashing of the WFPC2 CCDs,* ISR WFPC2 01-02.
- Schultz, A., Baggett, S., Biretta, J. 2002, *WFPC2 Clocks-ON Close Out*, ISR WFPC2 02-01.
- Suchkov, A., Casertano, S. 1997, *Impact of Focus Drift on Aperture Photometry*, ISR WFPC2 97-01.
- Trauger, J. T. 1989, in *CCDs in Astronomy*, PASP 8, 217, ed. G. Jacoby.
- Trauger, J. T., ed. 1993, *The WFPC2 Science Calibration Report*, Pre-launch Version 1.2. [IDT calibration report]
- Trauger, J. T., Vaughan, A.H., Evans, R.W., Moody, D.C. 1995, "Geometry of the WFPC2 Focal Plane" *Calibrating Hubble Space Telescope: Post Servicing Mission*, eds. A. Koratkar and C. Leitherer, p. 379.
- Voit, M., ed., *HST Data Handbook*, (Version 3.0, October 1997).[3]
- WF/PC-1 IDT OV/SV Report (No Longer Available)
- Westphal, J., et al. 1982, *The Wide Field/Planetary Camera in The Space Telescope Observatory*, IAU 18th General Assembly, Patras, NASA CP-2244.
- Whitmore, B. 1998, "Time Dependence of the Charge Transfer Efficiency on the WFPC2."[4] WFPC2 TIR 98-01
- Whitmore, B., Heyer, I. 1997, *New Results on Charge Transfer Efficiency and Constraints on Flat-Field Accuracy*, ISR WFPC2 97-08 (updated in 1998).
- Whitmore, B., Heyer, I., Casertano, S. 1999, PASP 111, 1559.
- Whitmore, B., Heyer I. 2002, *Charge Transfer Efficiency for Very Faint Objects and a Reexamination of the Long-vs-Short Problem for the WFPC2*, ISR WFPC2 02-03.
- Woodgate, B. E. 1989, in *CCDs in Astronomy*, PASP 8, 237, ed. G. Jacoby.

3. Available at: http://www.stsci.edu/instruments/wfpc2/Wfpc2_dhb/WFPC2_longdhbcover.html

4. Available at: http://www.stsci.edu/hst/wfpc2/documents/tir/tir9801.html

Instrument Science Reports

These documents may be requested by e-mail from help@stsci.edu or online at:

http://www.stsci.edu/hst/wfpc2/documents/isrs.

- ISR WFPC2 08-02: *Evolution of WFPC2 Superbiases,* Thatte, D. and Biretta, J.
- ISR WFPC2 08-01: *Flat Fields from the Moonlit Earth,* Bohlin, R. C., Mack, J., and Biretta, J.
- ISR WFPC2 07-01: *Temperature Reductions to Mitigate the WF4 Anomaly,* Dixon, V., Biretta, J., Gonzaga, S., and McMaster, M.
- ISR WFPC2 05-02: *Early Assessment of the WF4 Anomaly,* Biretta, J. and Gonzaga, S.
- ISR WFPC2 05-01: *Hot Pixels as a Probe of WFPC2 CTE Effects,* Biretta, J. and Kozhurina-Platais, V.
- ISR WFPC2 04-01: *The Accuracy of WFPC2 Photometric Zeropoints,* Heyer, I., Richardson, M., Whitmore, B., Lubin, L.
- ISR WFPC2 03-03: *WFPC2 Cycle 12 Calibration Plan*, Koekemoer, A. M., Heyer, I., Brammer, G., Kozhurina-Platais, V., Rhoads, J., Whitmore, B.
- ISR WFPC2 03-02: *Toward a Multi-Wavelength Geometric Distortion Solution for WFPC2*, Kozhurina-Platais, V., Anderson, J., Koekemoer, A. M.
- ISR WFPC2 03-01: *WFPC2 Cycle 9 Closure Report*, Koekemoer, A. M., Baggett, S., Casertano, S., Gonzaga, S., Heyer, I., and the WFPC2 Group.
- ISR WFPC2 02-07: *Updated Contamination Rates for WFPC2 UV Filters*, McMaster, M., Whitmore, B.
- ISR WFPC2 02-06: *Results of the Observatory Verification for WFPC2 after Servicing Mission 3B*, Koekemoer, A. M., and the WFPC2 Group.
- ISR WFPC2 02-05: *WFPC2 Cycle 11 Calibration Plan*, Gonzaga, S., and the WFPC2 Group.
- ISR WFPC2 02-04: *An Analysis of WFPC2 Filter Positional Anomalies*, Gonzaga, S., Baggett S., Biretta, J.
- ISR WFPC2 02-03: *Charge Transfer Efficiency for Very Faint Objects and a Reexamination of the Long-vs-Short Problem for the WFPC2*, Whitmore, B., Heyer I.

- ISR WFPC2 02-02: *Updated WFPC2 Flatfield Reference Files for 1995 - 2001*, Koekemoer, A.M., Biretta, J., Mack, J.
- ISR WFPC2 02-01: *WFPC2 Clocks-ON Close Out*, Schultz, A., Baggett, S., Biretta, J.
- ISR WFPC2 01-11: *Summary of WFPC2 SM3B Plans,* A. M. Koekemoer, S. Gonzaga, I. Heyer, L. M. Lubin, and V. Kozhurina-Platais.
- ISR WFPC2 01-10: *An Improved Geometric Solution for WFPC2,* S. Casertano and M. Wiggs
- ISR WFPC2 01-09: *The WFPC2 Photometric CTE Monitor*, I. Heyer.
- ISR WFPC2 01-08: *Creating WFPC2 Dark Reference Files: Addendum*, J. Mack, S. Baggett, and J. Biretta.
- ISR WFPC2 01-07: *WFPC2 Flatfields with Reduced Noise*, E. Karkoschka and J. Biretta.
- ISR WFPC2 01-06: W*FPC2 Cycle 8 Closure Report,* S. Baggett, S. Gonzaga, J. Biretta, S. Casertano, I. Heyer, A. M. Koekemoer, J. Mack, M. McMaster, A. Riess, A. Schultz, and M. S. Wiggs.
- ISR WFPC2 01-05: *WFPC2 Dark Current vs. Time,* Mack, J., Biretta, J., Baggett, S., Proffitt, C.
- ISR WFPC2 01-04: *Preliminary Assessment of the FR533N Filter Anomaly,* Gonzaga, S., Baggett, S., Biretta, J.
- ISR WFPC2 01-03: *WFPC2 Cycle 10 Calibration Plan,* Baggett, S., et al.
- ISR WFPC2 01-02: *Noiseless Preflashing of the WFPC2 CCDs,* Schultz, et al.
- ISR WFPC2 01-01: *Creating WFPC2 Dark Reference Files,* Mack and Wiggs.
- ISR WFPC2 00-04: *How CTE Affects Extended Sources,* Riess.
- ISR WFPC2 00-03: *Update on Charge Trapping and CTE Residual Images in WFPC2,* Baggett, et al.
- ISR WFPC2 00-02: *Results of the WFPC2 Observatory Verification after SM3a,* Casertano, et al.
- ISR WFPC2 00-01: *WFPC2 Cycle 9 Calibration Plan,* Baggett, et al.
- ISR WFPC2 99-05: *WFPC2 Cycle 7 Closure Report*, Baggett, et al.
- ISR WFPC2 99-04: *Time Dependence of CTE from Cosmic Ray Trails*, Riess, et al.

- ISR WFPC2 99-03: *Summary of WFPC2 SM3a Plans*, Casertano, et al., (revised: December 20, 1999).
- ISR WFPC2 99-02: *WFPC2 Cycle 8 Calibration Plan*, Baggett, et al.
- ISR WFPC2 99-01: *Internal Flat Field Monitoring II. Stability of the Lamps, Flat Fields, and Gain Ratios*, O'Dea, Mutchler, Wiggs.
- ISR WFPC2 98-04: *The Drizzling Cookbook*, Gonzaga, et al.
- ISR WFPC2 98-03: *WFPC2 Long-Term Photometric Stability*, Baggett and Gonzaga.
- ISR WFPC2 98-02: *The Long vs. Short Anomaly in WFPC2 Images*, Casertano and Mutchler.
- ISR WFPC2 98-01: *WFPC2 Cycle 6 Calibration Closure Report*, Baggett, et al.
- ISR WFPC2 97-11: *WFPC2 Polarization Calibration*, Biretta and McMaster.
- ISR WFPC2 97-10: *WFPC2 SYNPHOT Update*, Baggett, et al.
- ISR WFPC2 97-09: *Results of the WFPC2 Post-Servicing Mission-2 Calibration Program*, Biretta, et al.
- ISR WFPC2 97-08: *New Results on Charge Transfer Efficiency and Constraints on Flat-Field Accuracy*, Whitmore and Heyer.
- ISR WFPC2 97-07: *WFPC2 Electronics Verification*, Stiavelli and Mutchler.
- ISR WFPC2 97-06: *WFPC2 Cycle 7 Calibration Plan*, Casertano, et al.
- ISR WFPC2 97-05: *Charge Trapping and CTE Residual Images in the WFPC2 CCDs*, Biretta and Mutchler.
- ISR WFPC2 97-04: *Properties of WFPC2 Bias Frames*, O'Dea, et al.
- ISR WFPC2 97-03: *Summary of WFPC2 SM97 Plans*, Biretta, et al.
- ISR WFPC2 97-02: *WFPC2 Cycle 5 Calibration Closure Report,* Casertano and Baggett.
- ISR WFPC2 97-01: *Impact of Focus Drift on Aperture Photometry*, Suchkov and Casertano.
- ISR WFPC2 96-02: *Contamination Correction in SYNPHOT for WFPC2 and WF/PC-1,* Baggett, et al.
- ISR WFPC2 96-01: *Internal Flat Field Monitoring,* Stiavelli and Baggett.
- ISR WFPC2 95-07: *WFPC2 Cycle 4 Calibration Summary,* Baggett, Casertano, and Biretta.

- ISR WFPC2 95-06: *A Field Guide to WFPC2 Image Anomalies,* Biretta, Ritchie, and Rudloff.
- ISR WFPC2 95-05: *Wavelength / Aperture Calibration of the WFPC2 Linear Ramp Filters,* Biretta, Ritchie, Baggett, MacKenty.
- ISR WFPC2 95-04: *Demonstration Analysis Script for Performing Aperture Photometry*, Whitmore and Heyer.
- ISR WFPC2 95-03: *Charge Transfer Traps in the WFPC2*, Whitmore and Wiggs.
- ISR WFPC2 95-02: *The Geometric Distortion of the WFPC2 Cameras*, Gilmozzi, R. et al.
- ISR WFPC2 95-01: *WFPC2 Polarization Observations: Strategies, Apertures, and Calibration Plans,* Biretta and Sparks.
- ISR WFPC2 94-03: *WFPC2 Pipeline Calibration*, Burrows, C.
- ISR WFPC2 94-01: *Large Angle Scattering in WFPC2 and Horizontal "Smearing" Correction*, Krist, J. and Burrows, C.
- ISR WFPC2 93-01: *Polarizer Quad Nomenclature*, Clampin, M.
- ISR WFPC2 92-06: *WFPC2 CCDs,* Clampin, M.
- ISR WFPC2 92-05: *WFPC2 AFM and POMM Actuation Algorithm,* Burrows, C.
- ISR WFPC2 92-04: *Science with the Second Wide Field and Planetary Camera*, Trauger, J.T. et al.
- ISR WFPC2 92-03: *WFPC2 Science Observation and Engineering Modes*, Trauger, J.T. and Brown, D.I.
- ISR WFPC2 92-02: *System Level Contamination Issues for WFPC2 and COSTAR*, Clampin, M.

Technical Instrument Reports

Internal memos, available by request to help@stsci.edu.

- TIR WFPC2 08-02: *Updated Procedures for Creating a WFPC2 Yearly Superdark,* Thatte, D. and Biretta, J.
- TIR WFPC2 08-01: *PSF Characterization for the HST One-Gyro Mode Test,* Sirianni, M. and McMaster, M.
- TIR WFPC2 05-04: *Creating a WFPC2 Yearly Superdark,* Richardson, M. and Biretta, J.

- TIR WFPC2 05-03: *Creating a WFPC2 Yearly Superbias,* Richardson, M.
- TIR WFPC2 05-02: *Delivering WFPC2 Weekly Dark Reference Files to the Archive,* Richardson, M.
- TIR WFPC2 05-01: *Creating WFPC2 Weekly Dark Reference Files & Hot and Warm Pixel Tables,* Richardson, M.
- TIR WFPC2 02-06: *Predicting Photometry Errors due to Linear Ramp Filters*, Gonzaga, S., Biretta, J.
- TIR WFPC2 02-05: *SMOV3B WFPC2 Lyman-Alpha Throughput Check*, L.M. Lubin, B. Whitmore, A.M. Koekemoer, I. Heyer.
- TIR WFPC2 02-04: *SMOV3B WFPC2 Photometry Check*, B. Whitmore, I. Heyer.
- TIR WFPC2 02-03: *SMOV3B WFPC2 UV Contamination Monitoring and Throughput Check*, A. M. Koekemoer, S. Gonzaga, L. Lubin, B. Whitmore, I. Heyer.
- TIR WFPC2 02-02: *SMOV3B Flat Field Verification,* A. M. Koekemoer and I. Heyer.
- TIR WFPC2 02-01: *SMOV3b Check of the WFPC2 Point-Spread-Function*, V. Kozhurina-Platais, L.M. Lubin, and A.M. Koekemoer.
- TIR WFPC2 01-02: *Testing the On-The-Fly-Reprocessing System with WFPC2 Data,* S. Gonzaga, S. Baggett, J. Biretta.
- TIR WFPC2 01-01: *Shutter Jitter History Measured from INTFLATs*, Riess, A., Casertano, S., and Biretta, J.
- TIR WFPC2 00-05: *Testing the On-The-Fly-Calibration System with WFPC2 Data*, Wiggs, M.S., and Baggett, S.
- TIR WFPC2 00-04: *WFPC2 Internal Monitoring*, O'Dea C., Heyer I., and Baggett, S.
- TIR WFPC2 00-03: *SM3a SMOV WFPC2 Photometry Check*, Schultz, A., Gonzaga, S., Casertano, S.
- TIR WFPC2 00-02: *Results of the WFPC2 SM3a Lyman-Alpha Throughput Check*, Baggett, S., Heyer, I.
- TIR WFPC2 00-01: *SMOV3a Flat Field Stability Check*, Koekemoer, A., Biretta, J., Wiggs, M.S.
- TIR WFPC2 99-02: *Preliminary Results of the Noiseless Preflash Test*, Schultz, A., Heyer, I., Biretta, J.
- TIR WFPC2 99-01: *WFPC2 Aperture Photometry Corrections as a Function of Chip Position*, Gonzaga, S., O'Dea, C., Whitmore, B.

- TIR WFPC2 98-04A: *Addendum to TIR WFPC2 98-04*, Biretta, J., Baggett, S.
- TIR WFPC2 98-04: *Proposed Modification to the WFPC2 SAA Avoidance Contour*, Biretta, J., Baggett, S.
- TIR WFPC2 98-03: *WFPC2 Dark Current Evolution*, Baggett, S., Casertano, S., Wiggs, M.S.
- TIR WFPC2 98-02: *Analysis of the Excess Charge in WFPC2 Overscans*, Mutchler, M., O'Dea, C., Biretta, J.
- TIR WFPC2 98-01: *Time Dependence of the CTE on the WFPC2*, Whitmore, B.
- TIR WFPC2 97-11: *Long-Term Study of Bias Jumps*, O'Dea, C., McMaster, M., Heyer, I.
- TIR WFPC2 97-10: *WFPC2 Photometry from Subtraction of Observed PSFs*, Surdej, J., Baggett, S., Remy, M., Wiggs, M.S.
- TIR WFPC2 97-09: *The WFPC2 PSF Library*, Wiggs, M.S., Baggett, S., Surdej, J., Tullos, C.
- TIR WFPC2 97-08: *SMOV Flat Field Check*, Biretta, J., Wiggs, M.S.
- TIR WFPC2 97-07: *WFPC2 Internal Monitoring for SM97*, Mutchler, M., Stiavelli, M.
- TIR WFPC2 97-06: *SMOV Check of WFPC2 PSF Stability*, Fruchter, A., McMaster, M.
- TIR WFPC2 97-05: *Results of the WFPC2 SM-2 Lyman-Alpha Throughput Check*, O'Dea, C., Baggett, S., Gonzaga, S.
- TIR WFPC2 97-04: *VISFLAT Channel Monitoring*, Stiavelli, M.
- TIR WFPC2 97-03: *OTA Focus during SMOV*, Casertano, S., Lallo, M., Suchkov, A., Krist, J.
- TIR WFPC2 97-02: *SM-2 UV Monitoring and Cooldown Procedure*, Stiavelli, M., Biretta, J., Baggett, S., Gonzaga, S., Mutchler, M.
- TIR WFPC2 97-01: *Results of the WFPC2 SMOV Relative Photometry Check*, Whitmore, B., Gonzaga, S., Heyer, I.

Other Selected Documents and Web Pages

Available online at:

http://www.stsci.edu/hst/wfpc2/documents

- *The WFPC2 Instrument Handbook*, Version 10.0
- *The HST Data Handbook*, Version 4.0
- *HST Dither Handbook*, Version 2.0
- *The WFPC2 Tutorial*, a step-by-step guide to reducing WFPC2 data
- *The Space Telescope Analysis Newsletter (*STAN)

http://www.stsci.edu/hst/wfpc2/analysis/wfpc2_history.html

- *The WFPC2 History* memo, containing chronological information on decontaminations, darks, focus changes, and miscellaneous items

http://www.stsci.edu/hst/wfpc2/analysis/lrf_calibration.html

- How to calibrate WFPC2 Linear Ramp Filter data.

http://www.stsci.edu/hst/wfpc2/analysis/cte

- Charge Transfer Efficiency (CTE) Resources.

http://www.stsci.edu/hst/observatory/cdbs/SIfileInfo/WFPC2/reftablequeryindex_wfpc2

- The WFPC2 Reference Files, a complete list of all reference files available for recalibrating WFPC2 data.

http://www.stsci.edu/hst/wfpc2/analysis/photometry

- Photometry and SYNPHOT Resources.

The WFPC2 Data Analysis Library

The WFPC2 Data Analysis Library (formerly the WFPC2 Clearinghouse) is a web-based tool designed to provide users with a searchable listing of all known journal articles, STScI documentation and

reports, as well as user-submitted documents which report on all aspects of the performance, calibration, and scientific use of WFPC2. The Data Analysis Library can be found at:

http://www.stsci.edu/hst/wfpc2/software/wfpc2_clrhs.html

The primary goal of the Data Analysis Library is to make it easier for WFPC2 users to take advantage of the fact that there are hundreds of researchers reducing and analyzing WFPC2 data, and of their results.

We have searched through the astronomical literature and selected all articles that contain any reference or description of the calibration, reduction, and scientific analysis of WFPC2 data. Due to the extremely large volume of material, the on-line database is only complete through 1997. After 1997, we have only continued to update the Data Analysis Library with STScI documentation and reports, including Instrument Science Reports and Technical Instrument Reports. Each article that is included in our database had an estimate of its importance in up to 50 calibration topics. The entry for each article has the following format:

```
Author: Holtzman,Mould, Gallagher, et al.
Title: Stellar Populations in the Large Magellanic Cloud: Evidence
for..
Year: 1997
Reference: AJ 113, 656
Science Keyword: IMF,LMC
Calibration Keyword(3): psf_fitting_photometry(3)
Calibration Keyword(2): bias(2)
Calibration Keyword(1): photometric_zeropoint(1)
Comment: Comparison of aperture and PSF fitting photometry,
```

where the category number following each keyword stands for the following:

- (3)= One of the fundamental references on this topic.
- (2)= Some new information on this topic.
- (1)= General information on the subject.

The user can select from a large list of WFPC2 calibration related topics (see below). The results from a Data Analysis Library search will list, alphabetically by author, all articles containing references to the selected topic. For journal articles, each reference is linked to that article's entry in the ADS Abstract Database, so that users can quickly determine if that particular article is relevant to their individual needs.

The following topics are available:

Aperture Corrections	Object Identification
Aperture Photometry	Observation Planning
Astrometry	Photometric Transformations
Bias Frames	Photometric Zeropoint
Bias Jumps	Pipeline Calibration
Calibration Observations	Polarization
CCD Characteristics	PSF Characterization
Charge Transfer Traps	PSF Fitting Photometry
Chip-to-Chip Normalization	PSF Subtraction
Completeness Corrections	Quad Filters
Cosmic Rays	Recalibration
CTE Losses	Red Leaks
Darks	Residual Images
Data Quality	Saturated Data
Deconvolution	Scattered Light
Dithering	Serial Clocks
Drizzle	Size Measurements
Field Distortion	Software
Flats	Surface Photometry
Focus	SYNPHOT
Hot Pixels	T=77 Observations
Image Anomalies	UV Throughput
Linear Ramp Filters	Vignetting
Long vs. Short Exposures	Woods Filters
Narrow Band Photometry	1997 Servicing Mission

APPENDIX A:

Passband Plots

In this appendix . . .

A.1 Filter Passbands, with and w/out Total System

In this Appendix we give two plots for each filter -- one for the filter in isolation (left panel), and for the filter together with all other system elements (HST and WFPC2 optics and WF3 CCD; right panel). Quantities labeled on the plots are defined in "System Throughput" on page 161.

Note that $\overline{\lambda}$ deviates from λ_p and $<\lambda>$ by progressively larger amounts for the wider filters, which is simply a consequence of the way in which $\overline{\lambda}$ is defined.

A.1.1 F122M, F130LP, F160BW

F122M (Wheel:1 Pos:4)

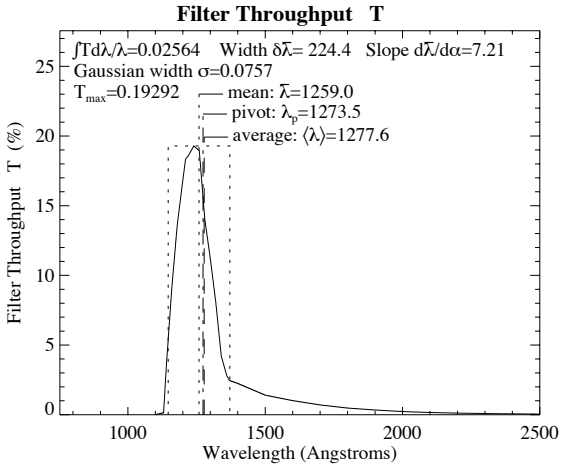

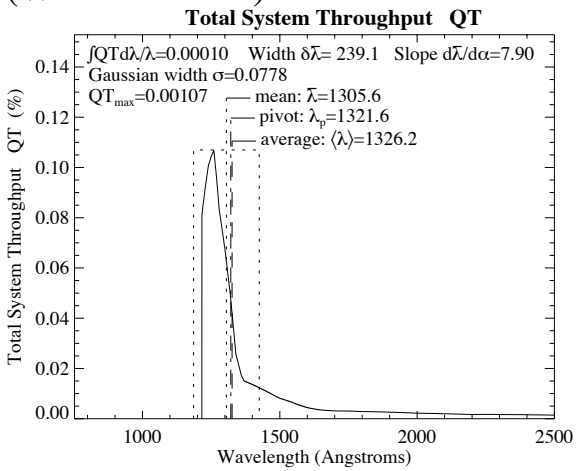

F130LP (Wheel:2 Pos:1)

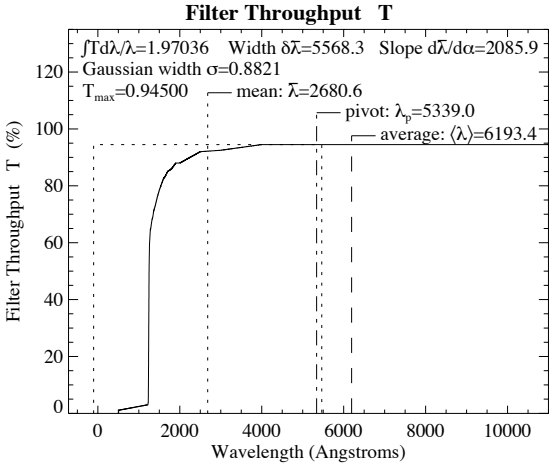

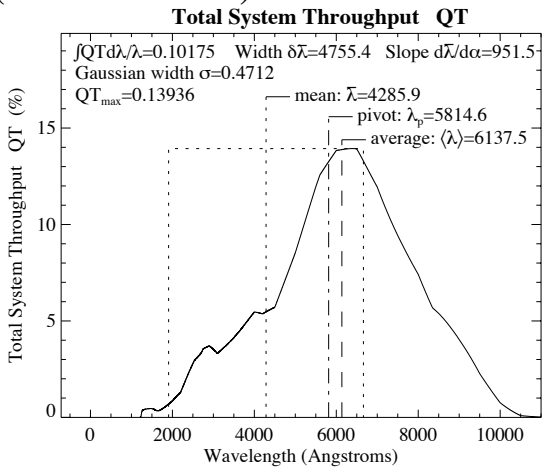

F160BW (Wheel:1 Pos:2)

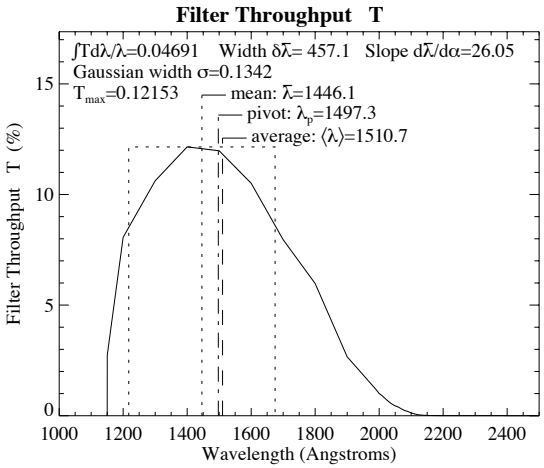

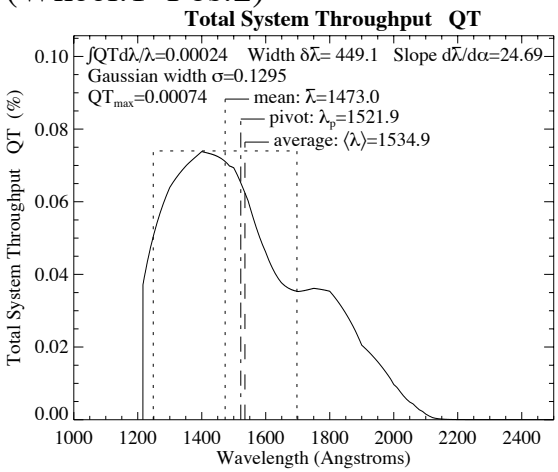

A.1.2 F165LP, F170W, F185W

F165LP (Wheel:2 Pos:2)

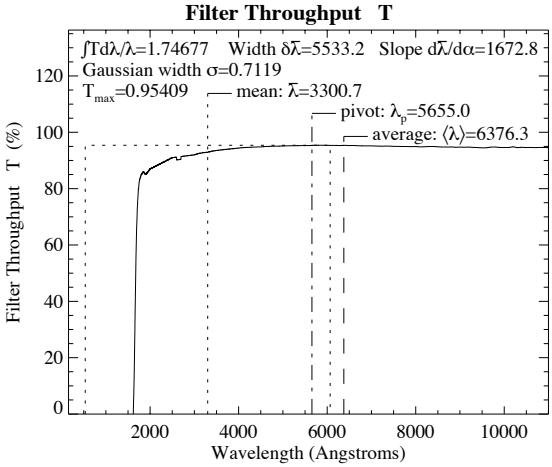

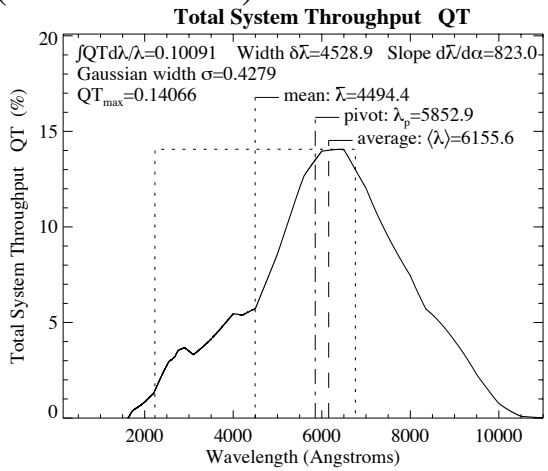

F170W (Wheel:8 Pos:1)

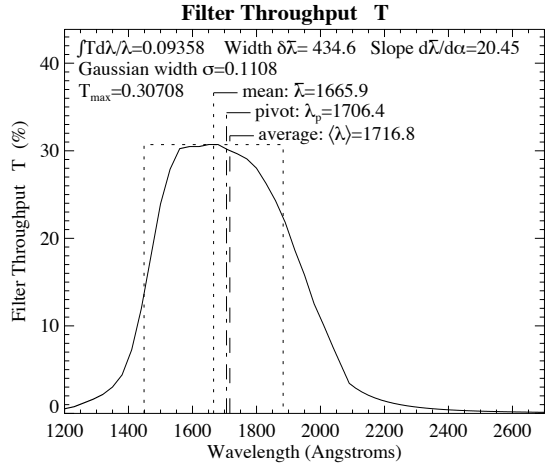

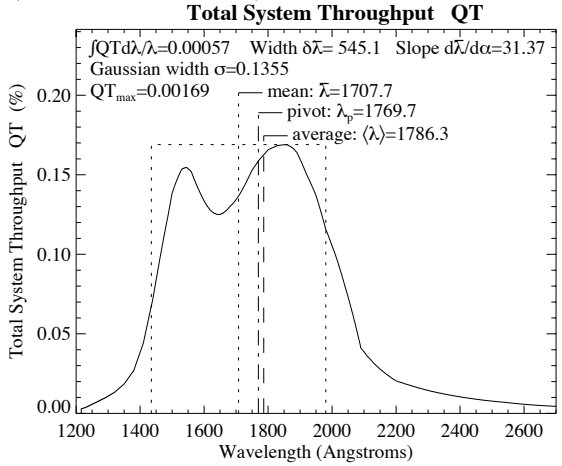

F185W (Wheel:8 Pos:2)

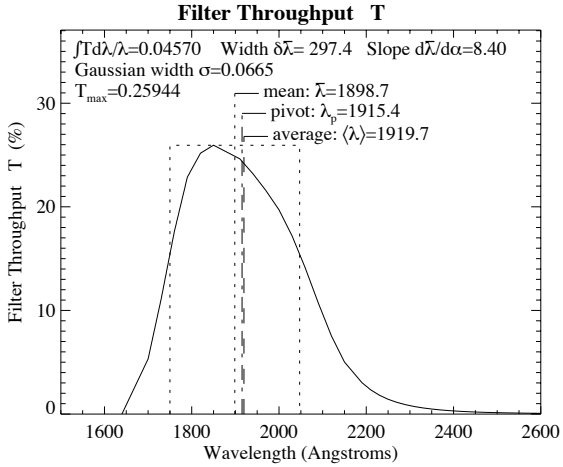

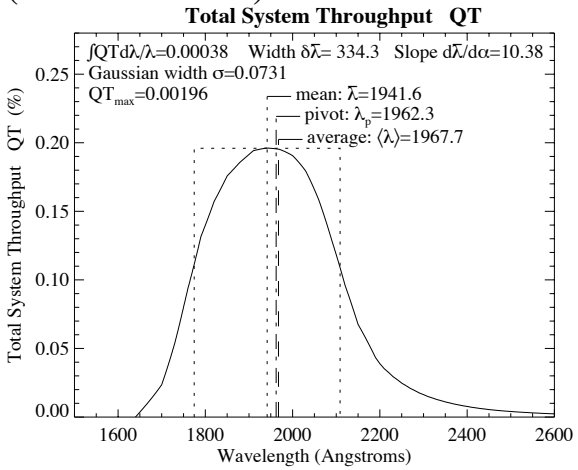

A.1.3 F218W, F255W, F300W

F218W (Wheel:8 Pos:3)

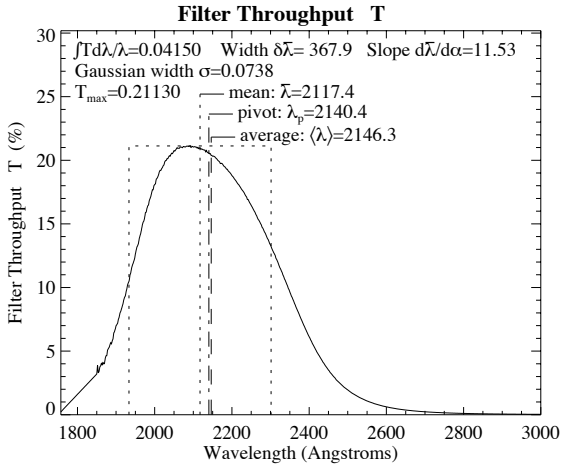

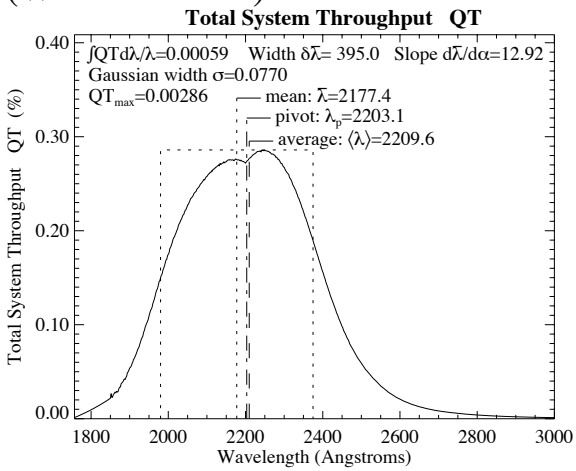

F255W (Wheel:8 Pos:4)

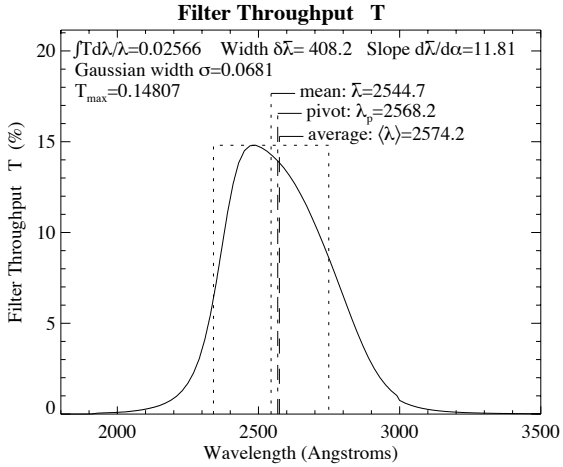

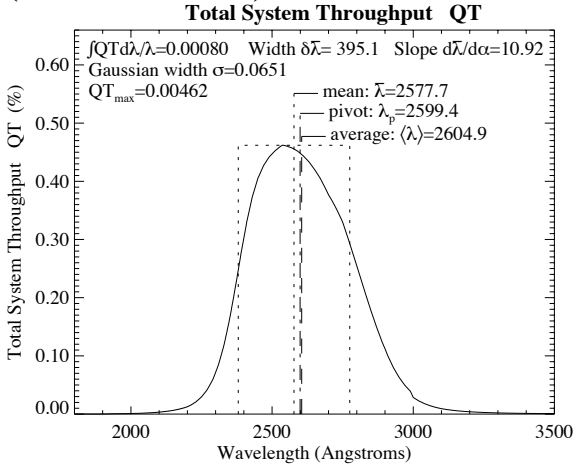

F300W (Wheel:9 Pos:4)

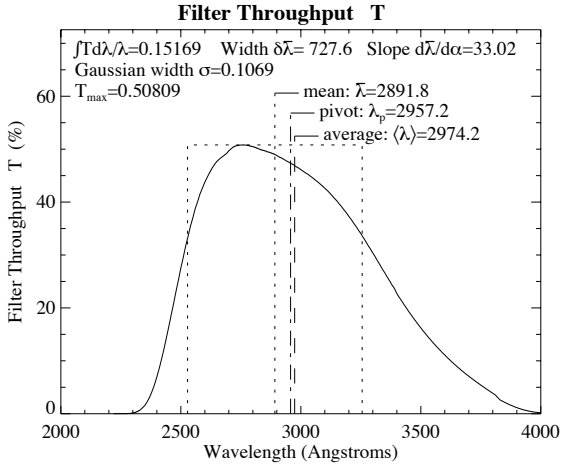

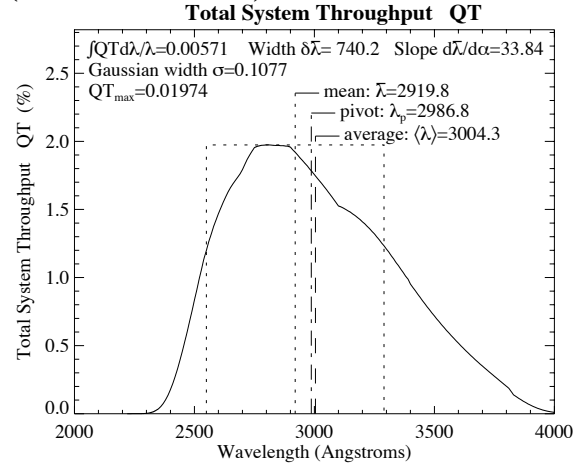

A.1.4 F336W, F343N, F375N

F336W (Wheel:3 Pos:1)

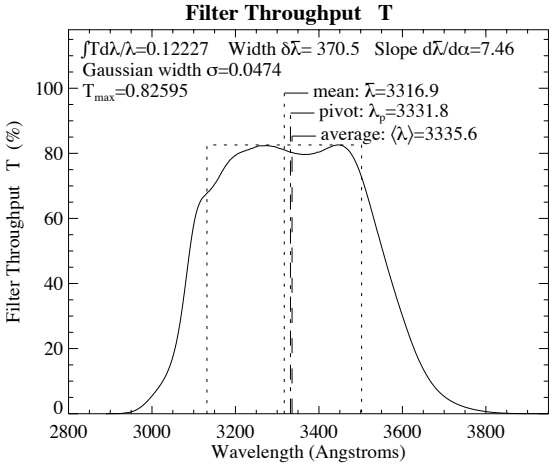

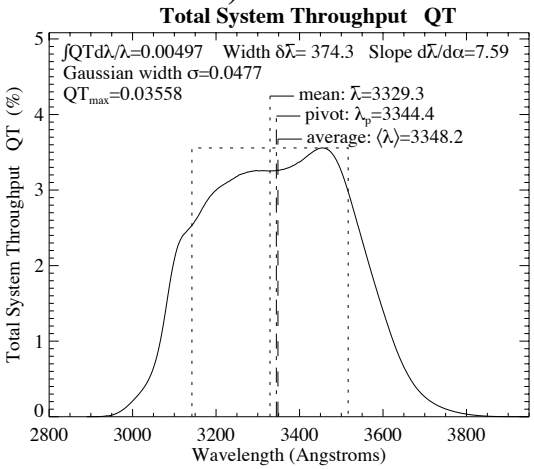

F343N (Wheel:5 Pos:1)

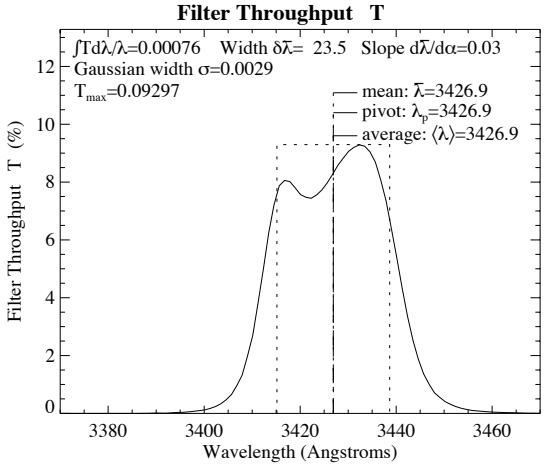

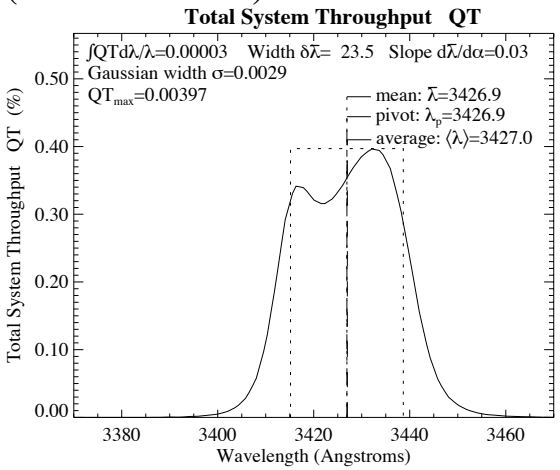

F375N (Wheel:5 Pos:2)

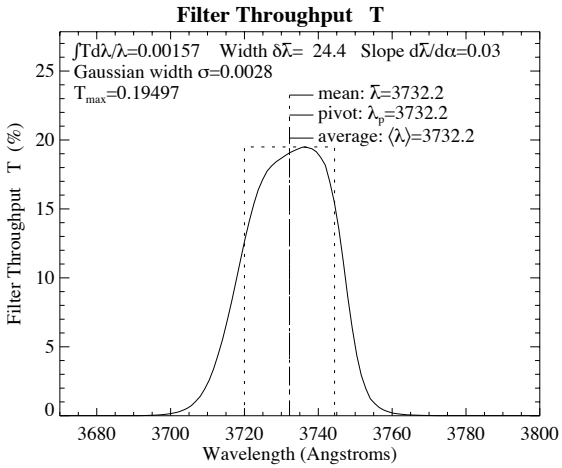

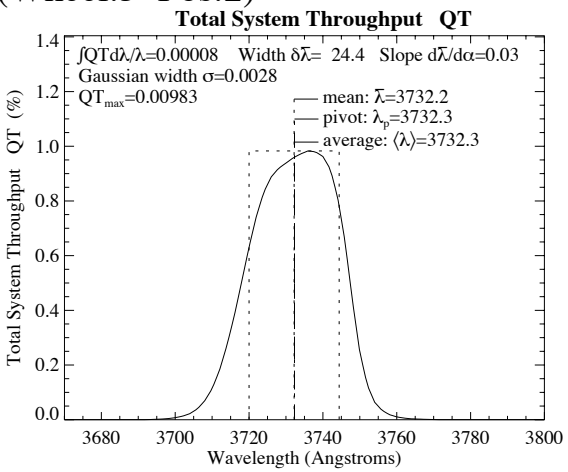

A.1.5 F380W, F390N, F410M

F380W (Wheel:9 Pos:1)

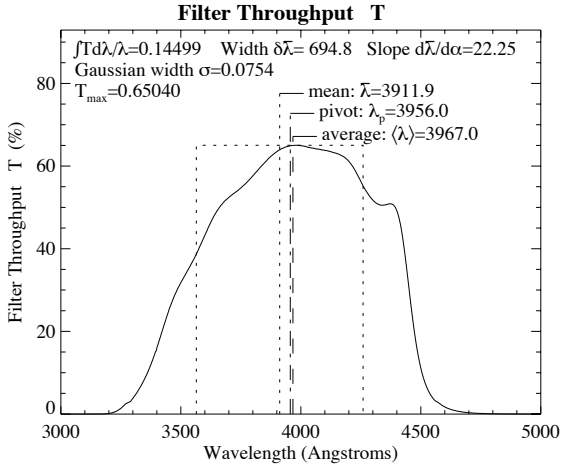

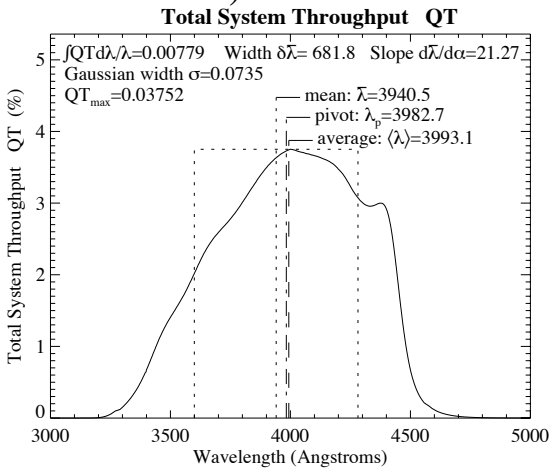

F390N (Wheel:5 Pos:3)

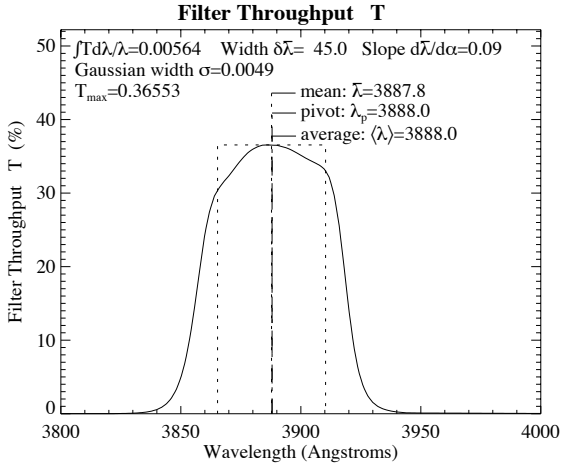

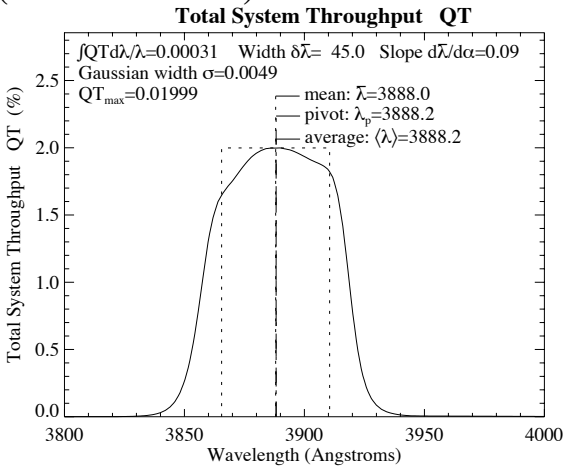

F410M (Wheel:3 Pos:2)

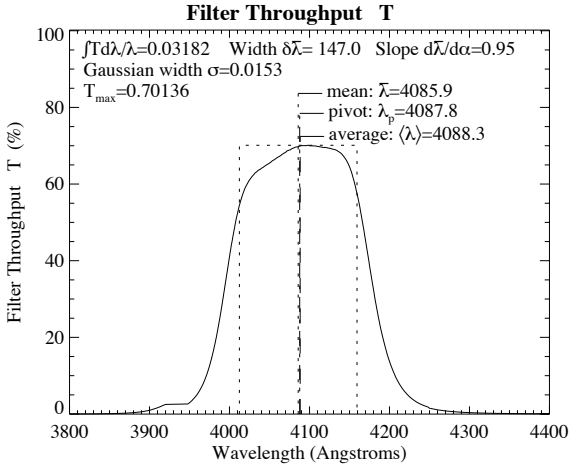

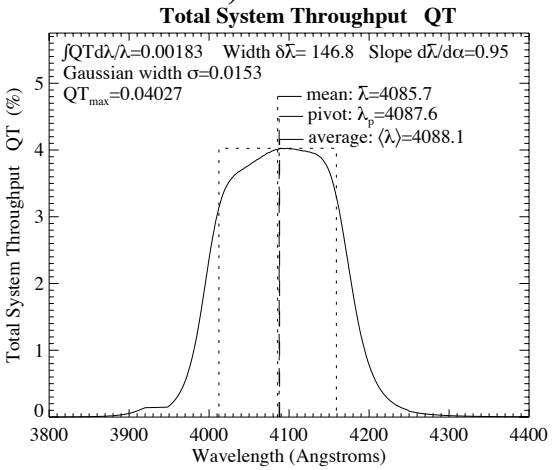

A.1.6 F437N, F439W, F450W

F437N (Wheel:5 Pos:4)

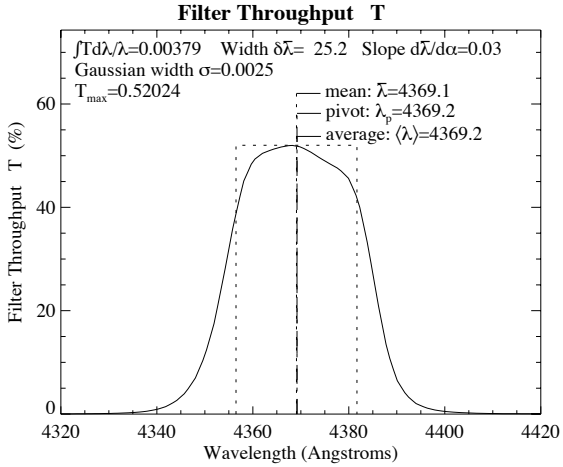

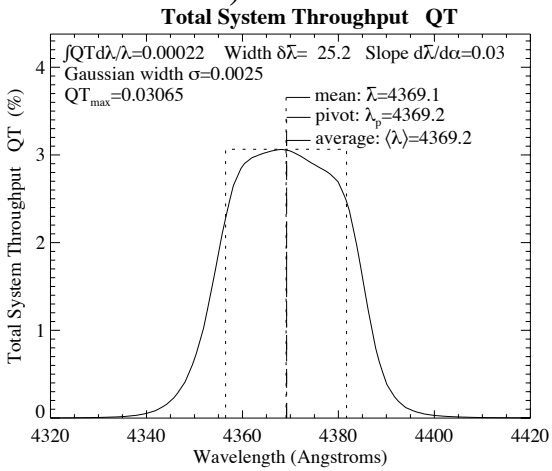

F439W (Wheel:4 Pos:4)

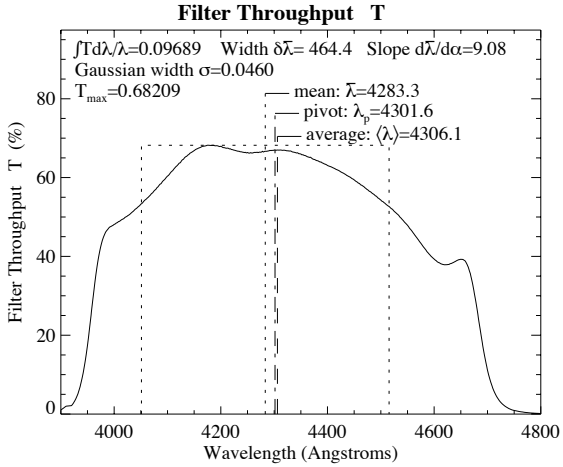

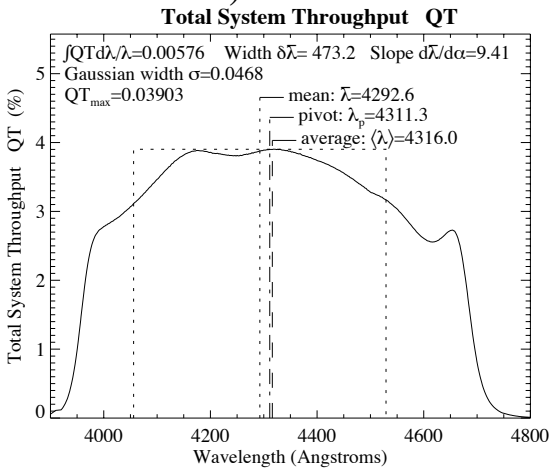

F450W (Wheel:10 Pos:4)

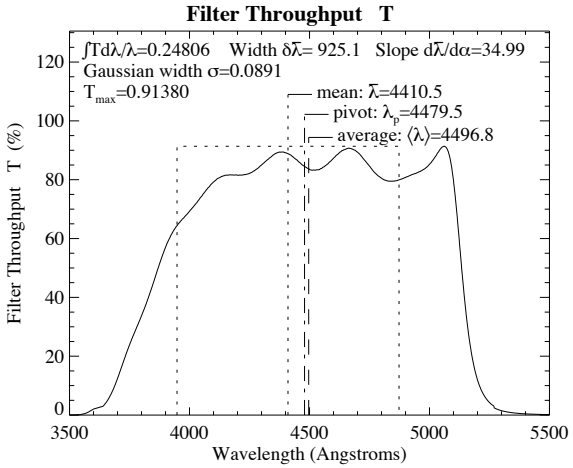

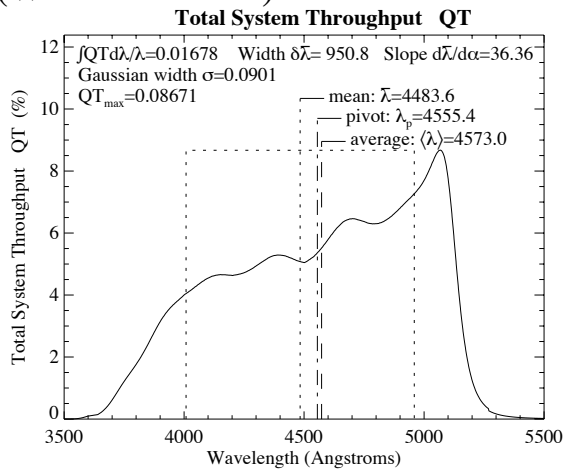

A.1.7 F467M, F469N, F487N

F467M (Wheel:3 Pos:3)

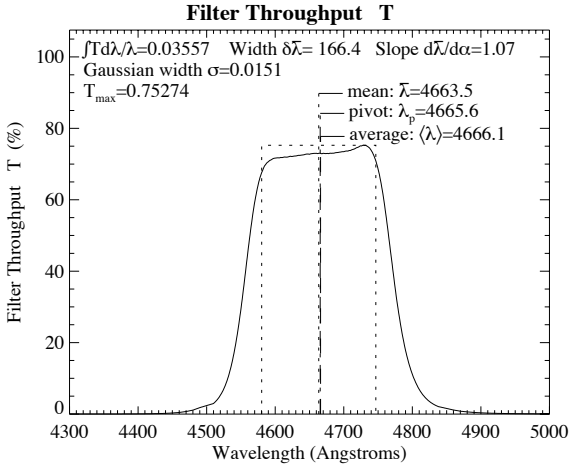

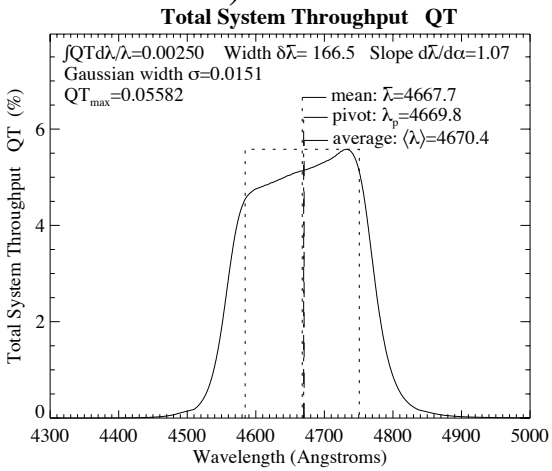

F469N (Wheel:6 Pos:1)

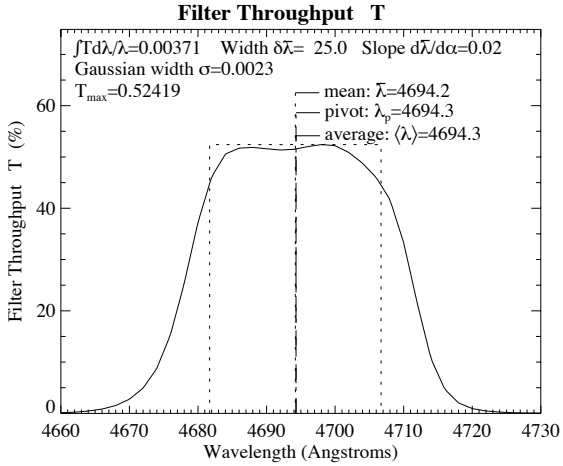

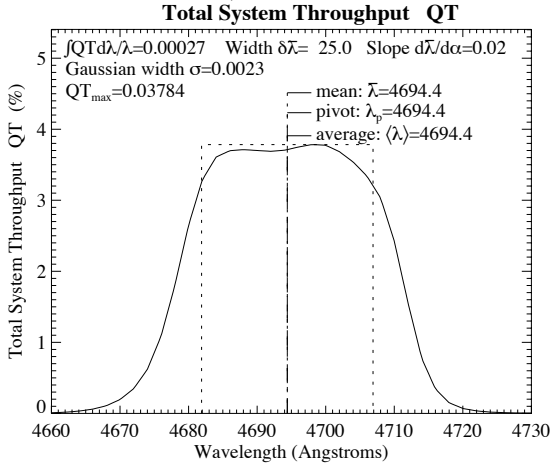

F487N (Wheel:6 Pos:2)

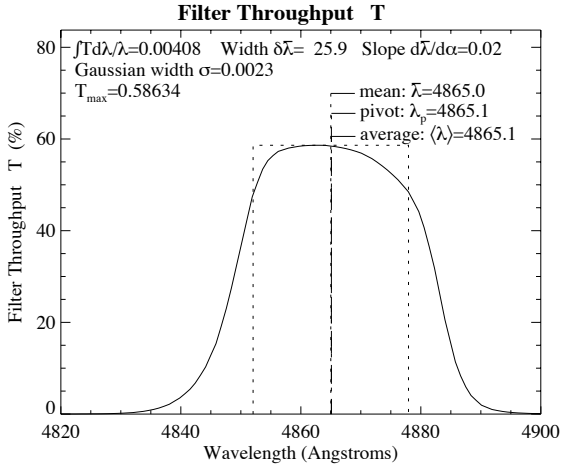

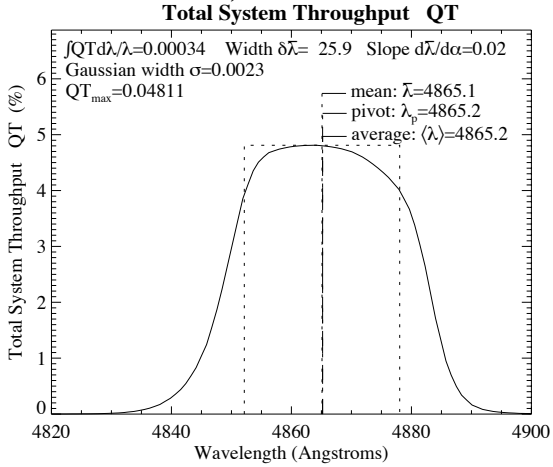

A.1.8 F502N, F547M, F555W

F502N (Wheel:6 Pos:3)

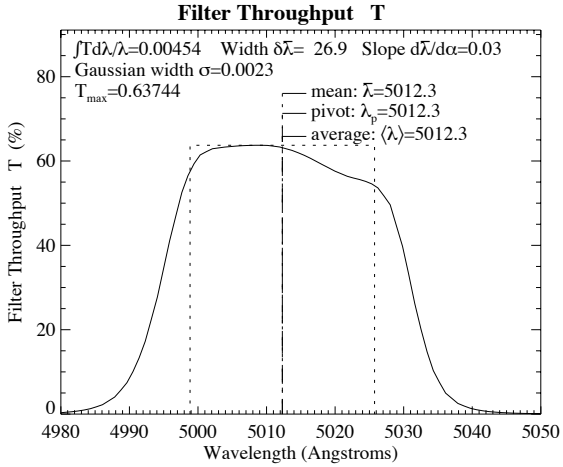

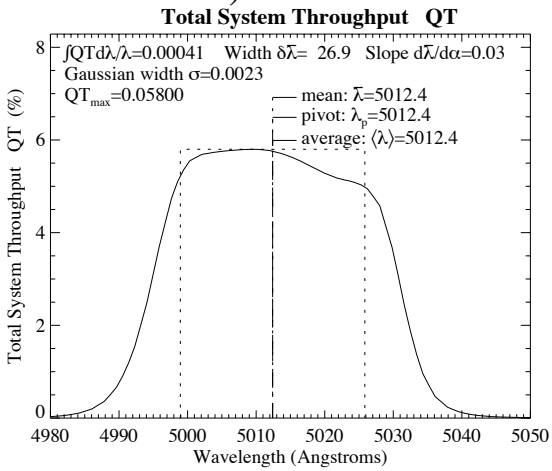

F547M (Wheel:3 Pos:4)

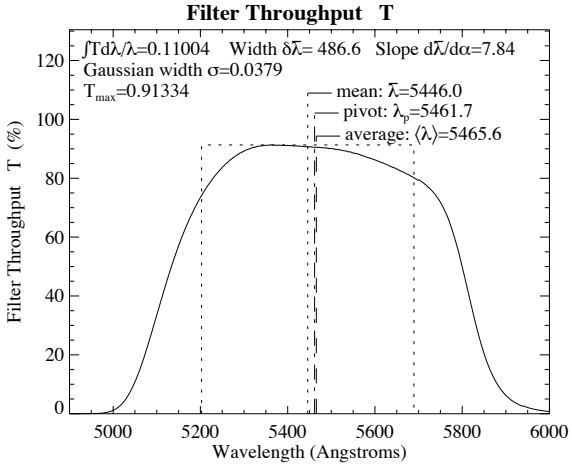

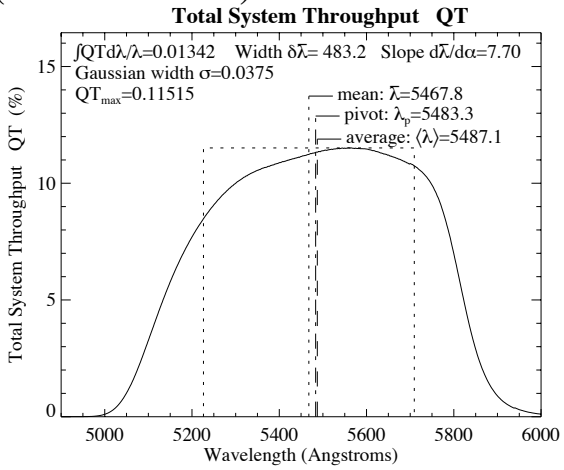

F555W (Wheel:9 Pos:2)

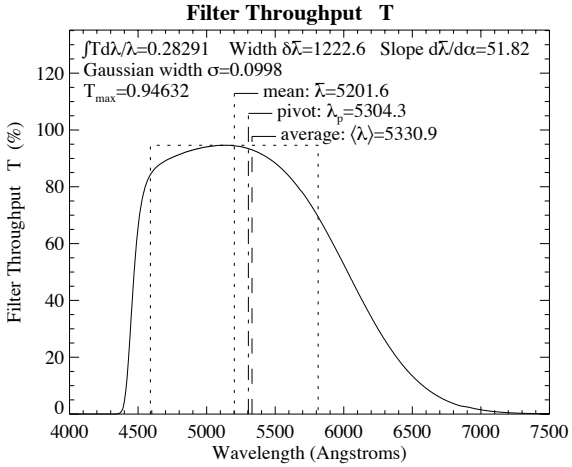

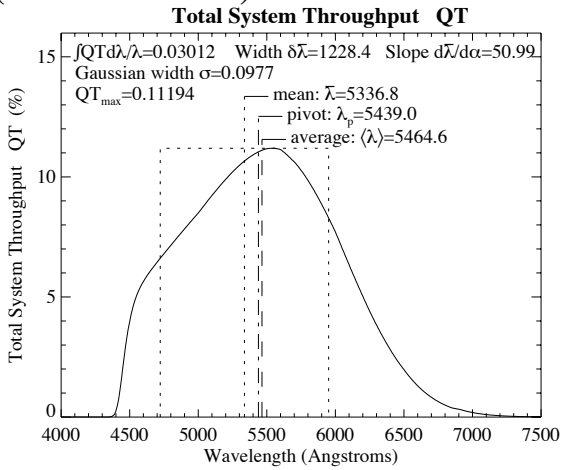

A.1.9 F569W, F588N, F606W

F569W (Wheel:4 Pos:2)

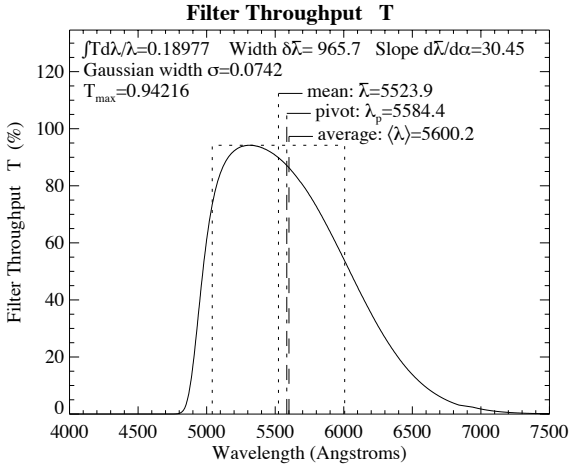

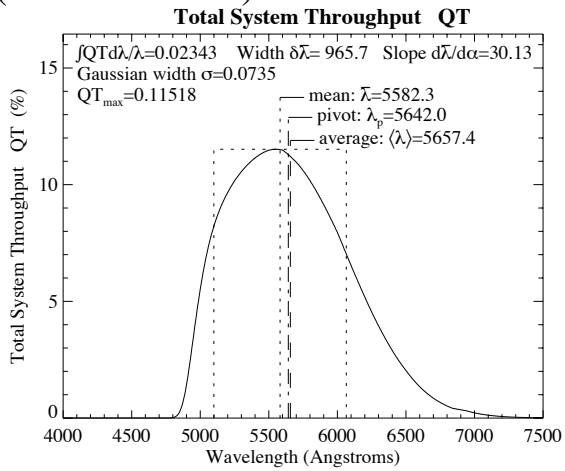

F588N (Wheel:6 Pos:4)

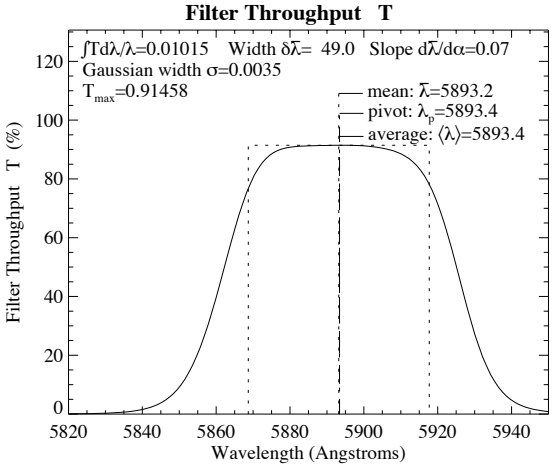

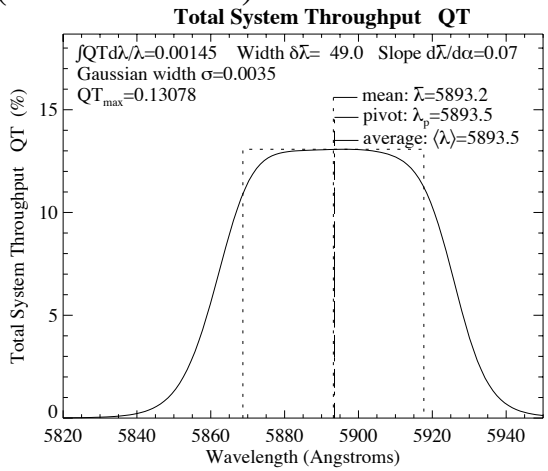

F606W (Wheel:10 Pos:2)

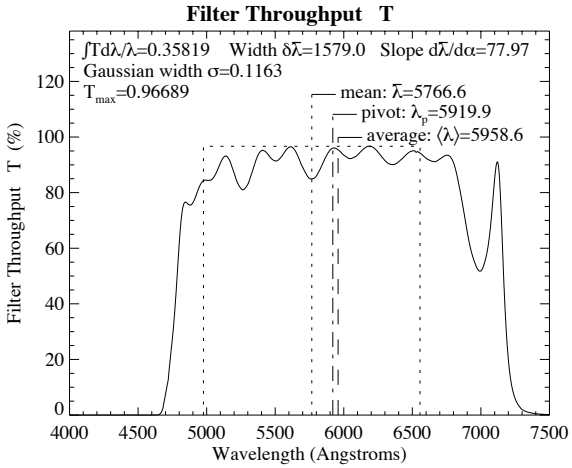

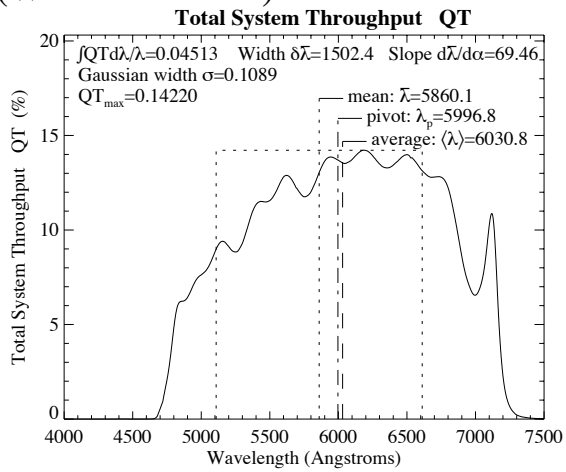

A.1.10 F622W, F631N, F656N

F622W (Wheel:9 Pos:3)

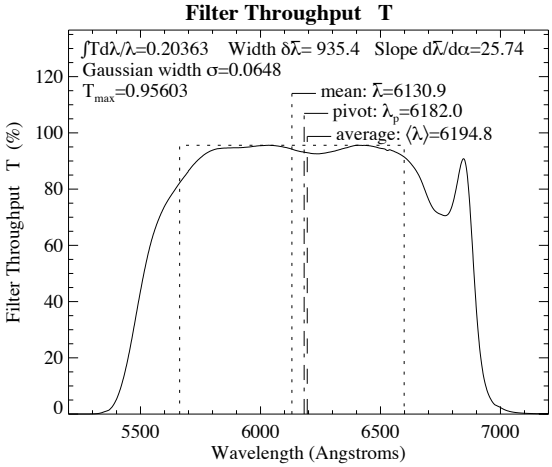

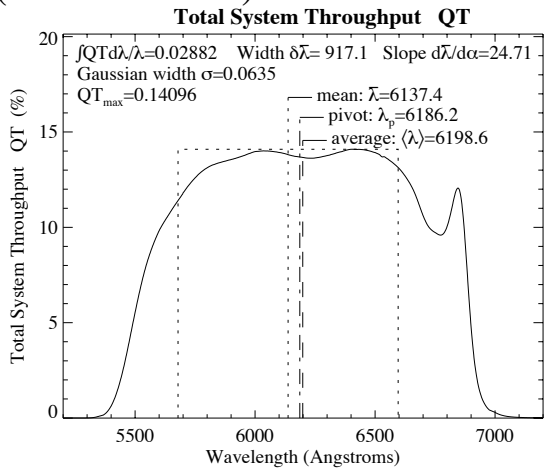

F631N (Wheel:7 Pos:1)

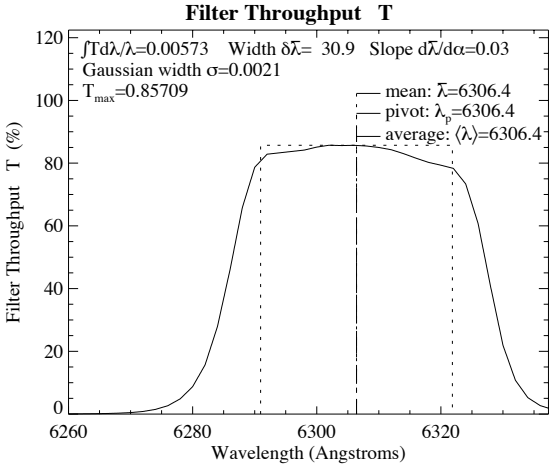

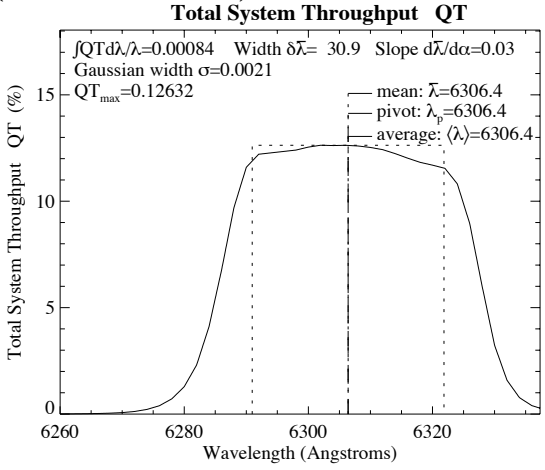

F656N (Wheel:7 Pos:2)

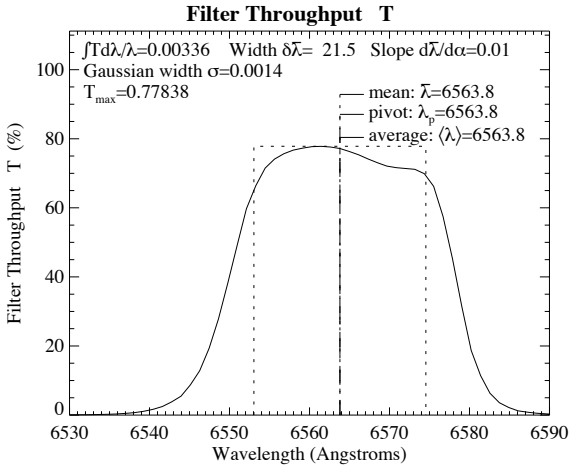

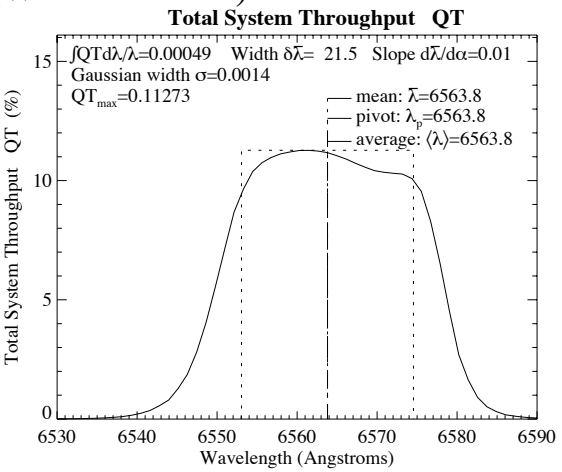

A.1.11 F658N, F673N, F675W

F658N (Wheel:7 Pos:3)

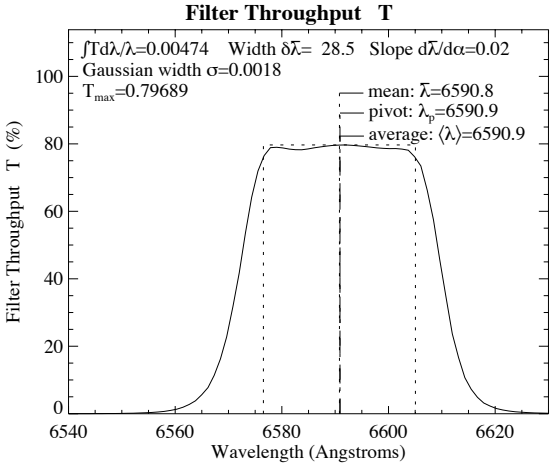

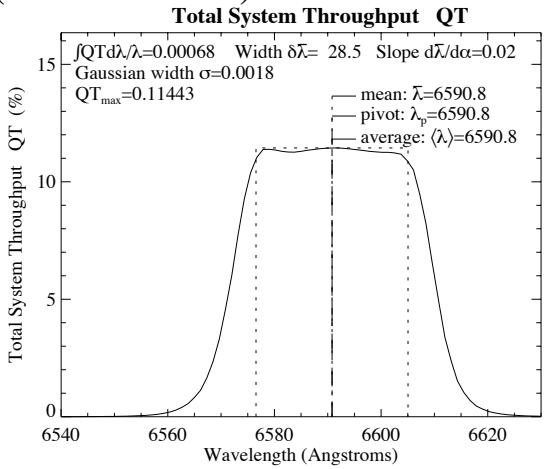

F673N (Wheel:7 Pos:4)

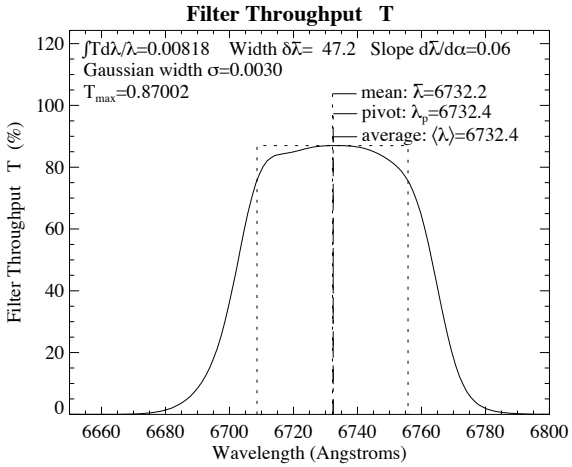

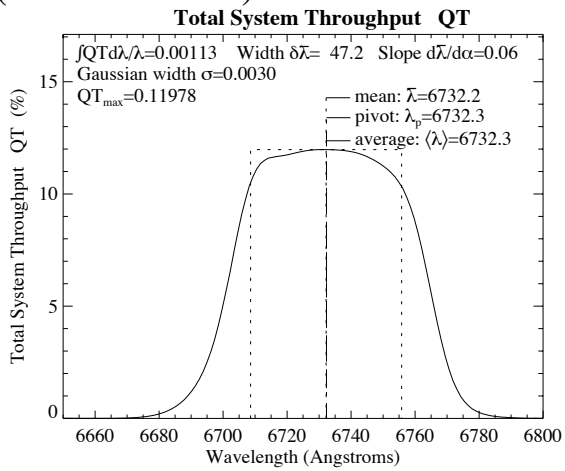

F675W (Wheel:4 Pos:3)

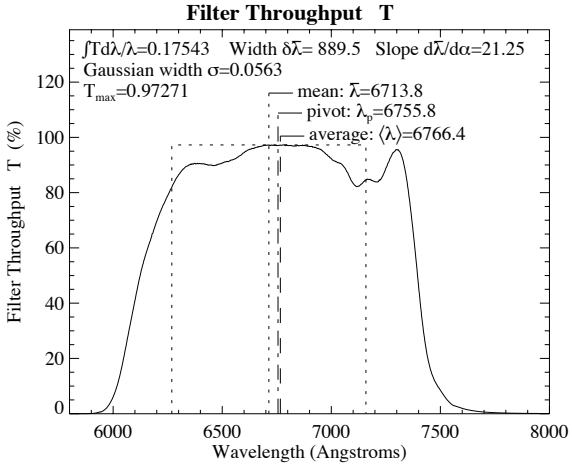

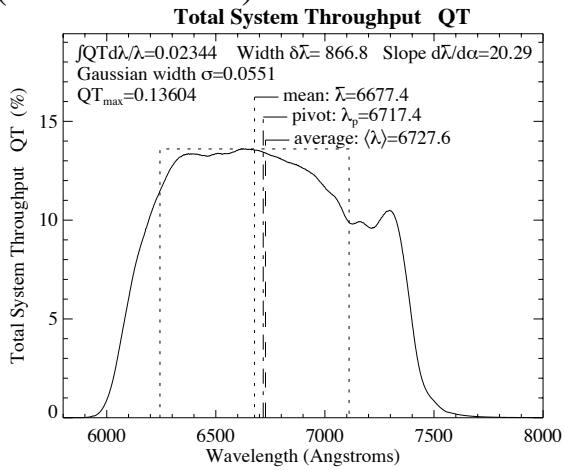

A.1.12 F702W, F785LP, F791W

F702W (Wheel:10 Pos:3)

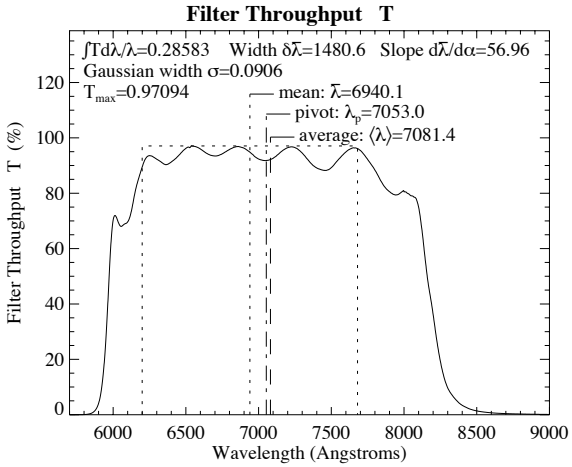

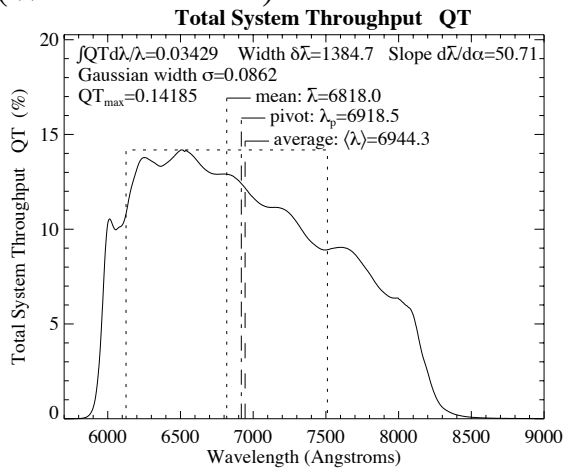

F785LP (Wheel:2 Pos:3)

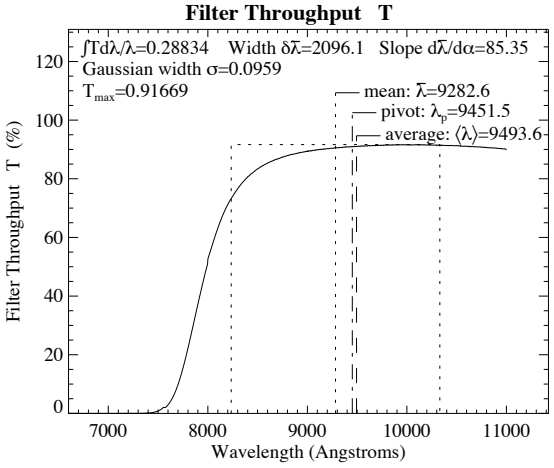

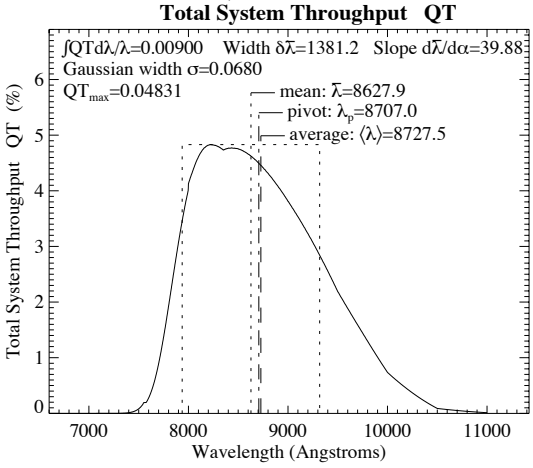

F791W (Wheel:4 Pos:1)

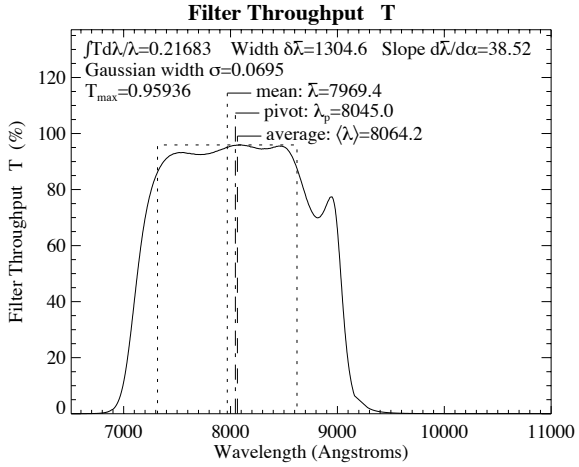

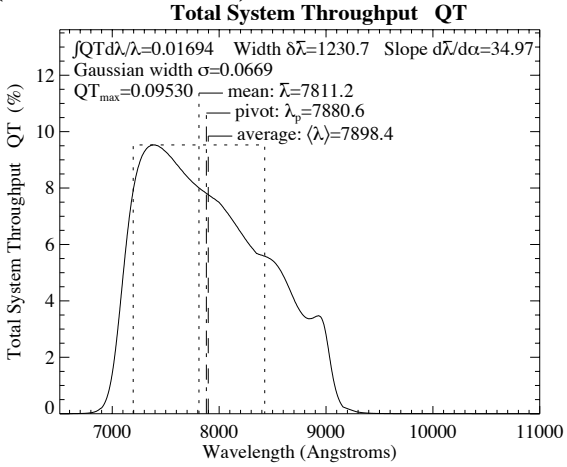

A.1.13 F814W, F850LP, F953N

F814W (Wheel:10 Pos:1)

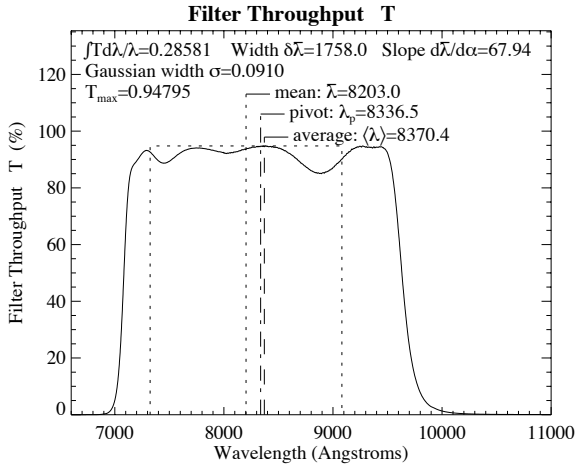

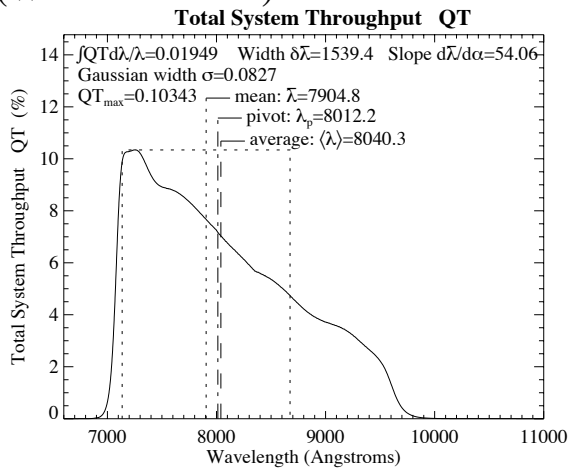

F850LP (Wheel:2 Pos:4)

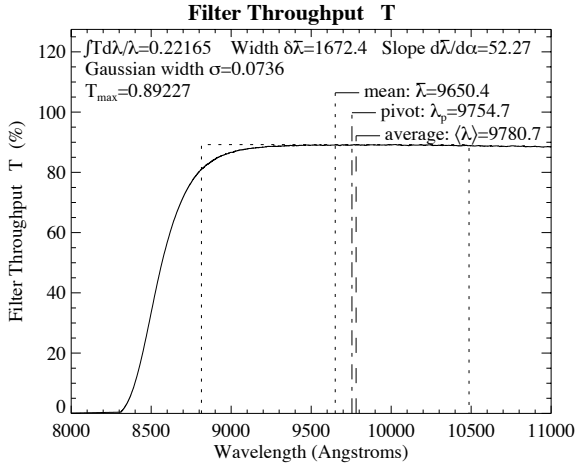

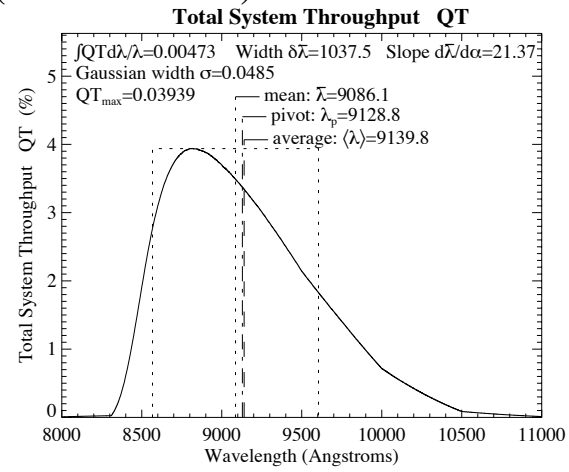

F953N (Wheel:1 Pos:1)

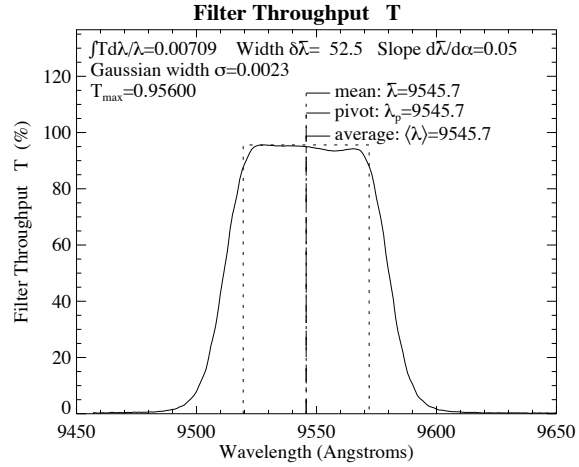

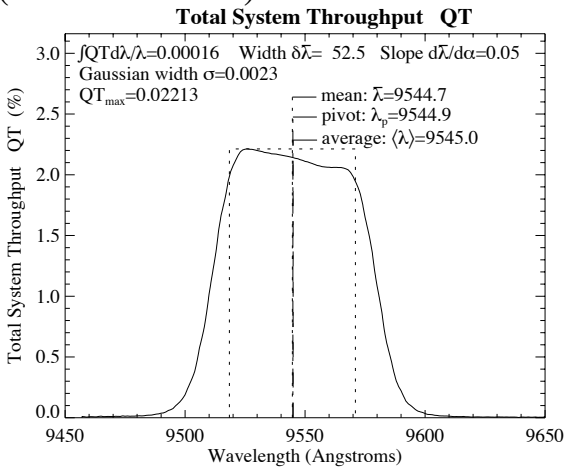

A.1.14 F1042M, FQUVN-A, FQUVN-B

F1042M (Wheel:11 Pos:2)

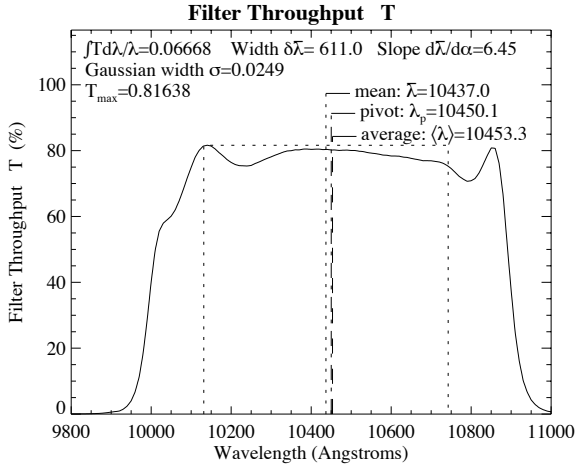

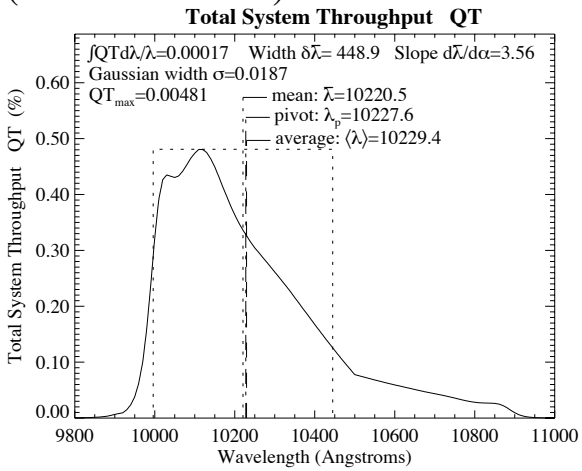

FQUVN-A (Wheel:11 Pos:3)

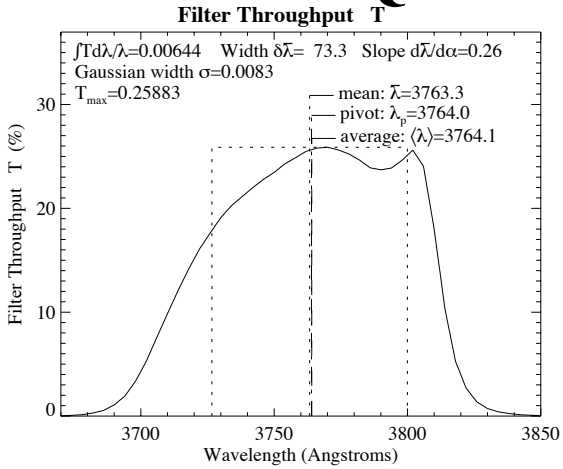

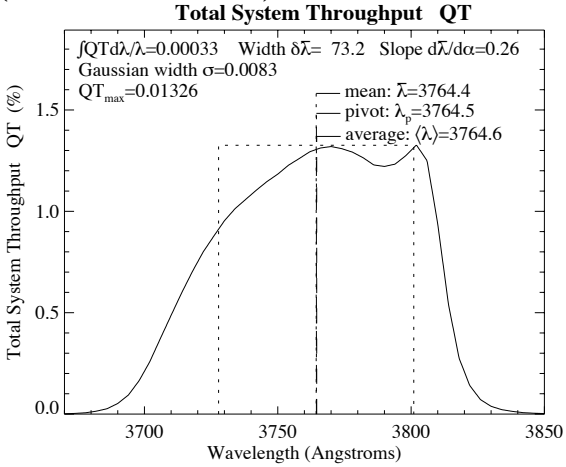

FQUVN-B (Wheel:11 Pos:3)

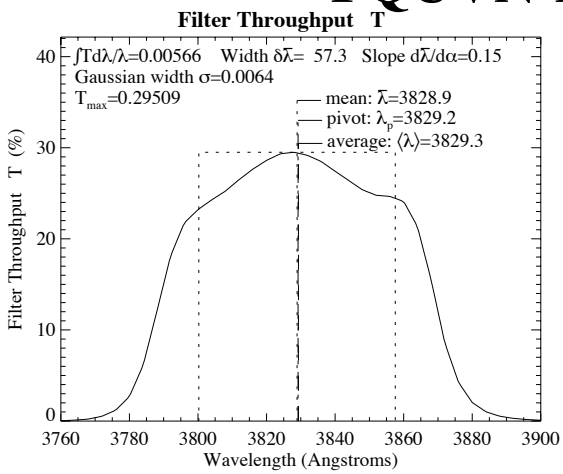

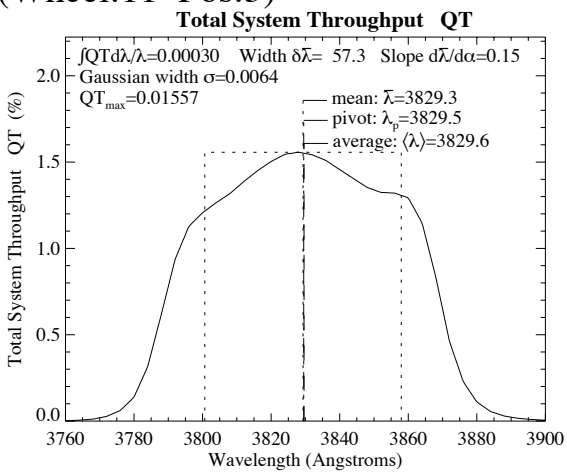

A.1.15 FQUVN-C, FQUVN-D, FQCH4N-A

FQUVN-C (Wheel:11 Pos:3)

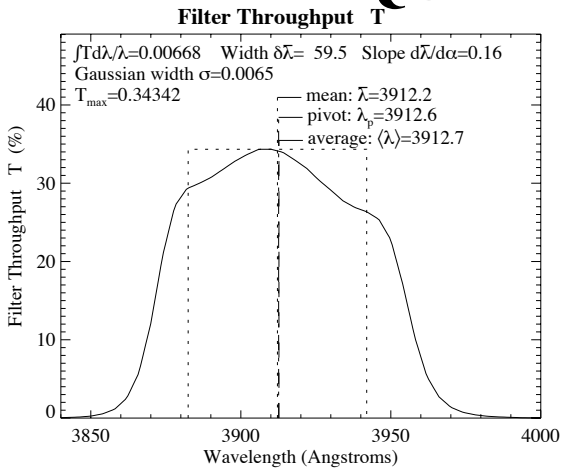

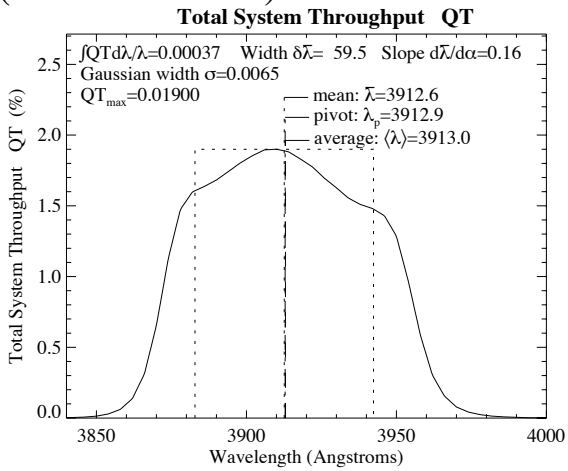

FQUVN-D (Wheel:11 Pos:3)

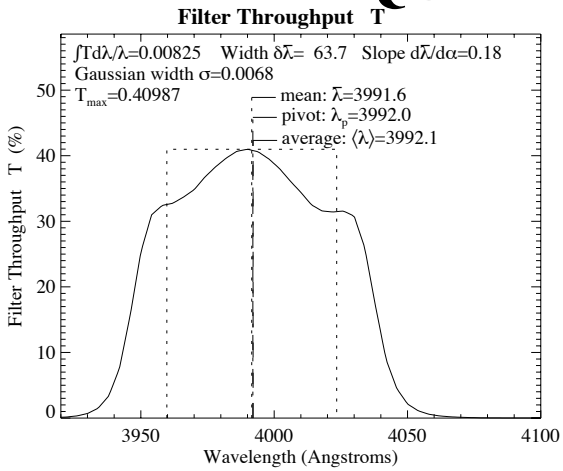

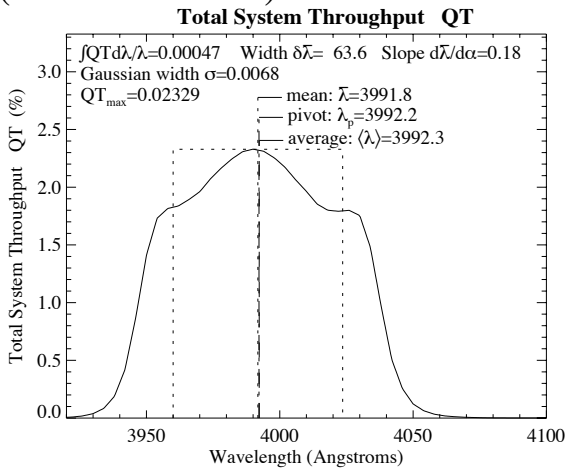

FQCH4N-A (Wheel:11 Pos:4)

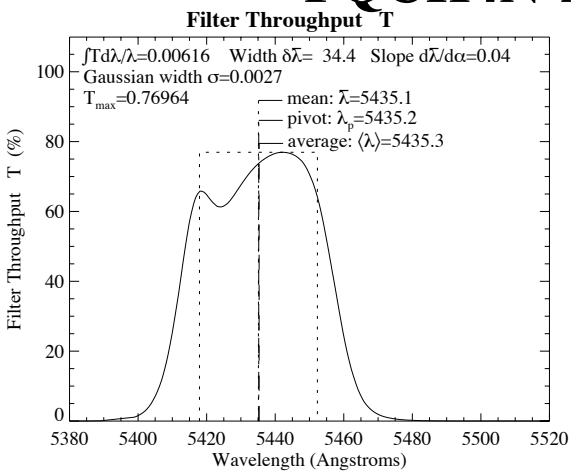

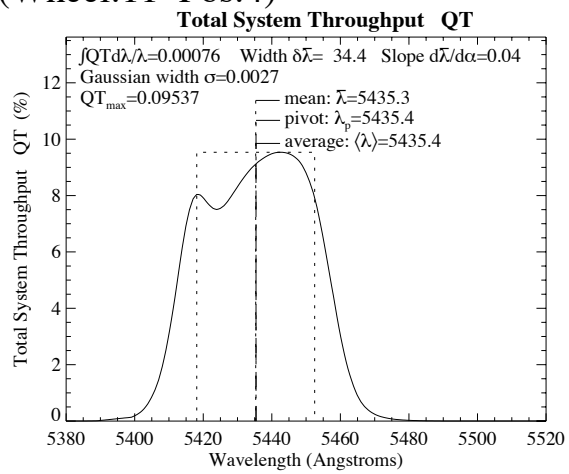

A.1.16 FQCH4N15-B, FQCH4N33-B, FQCH4N-C

FQCH4N15-B (Wheel:11 Pos:4)

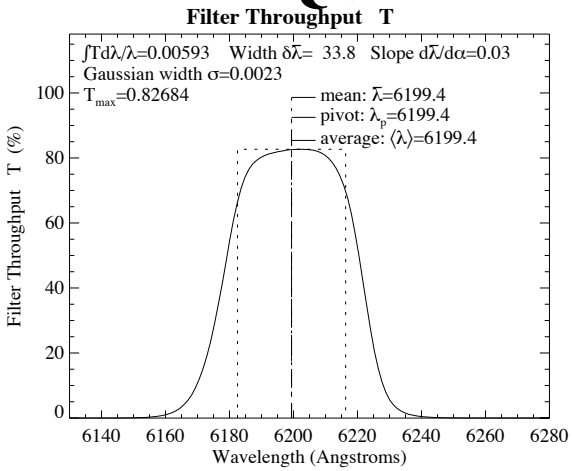

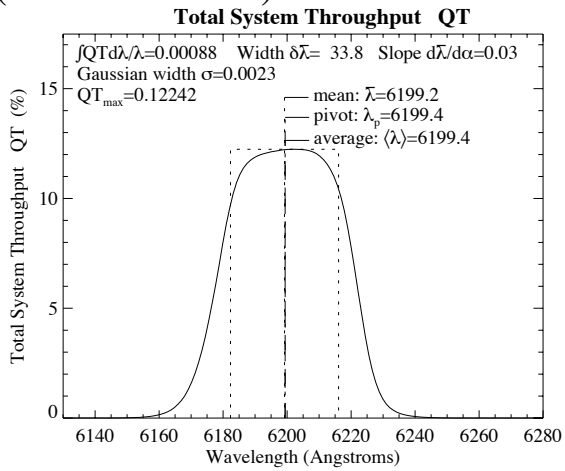

FQCH4N33-B (Wheel:11 Pos:4)

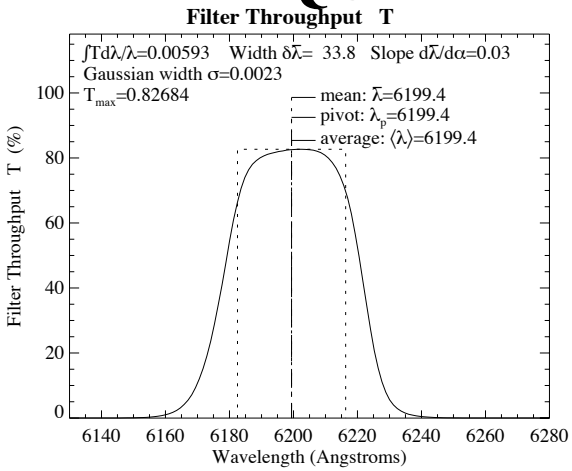

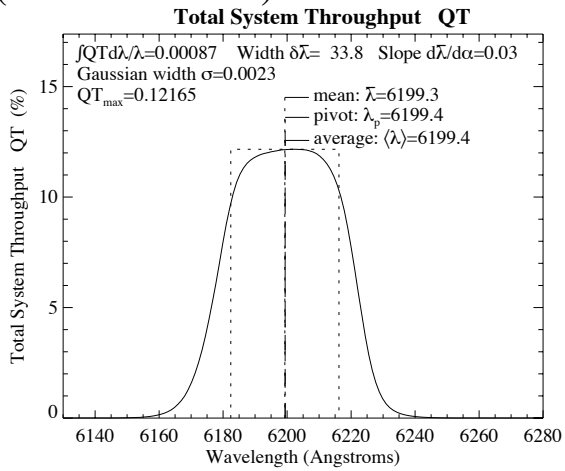

FQCH4N-C (Wheel:11 Pos:4)

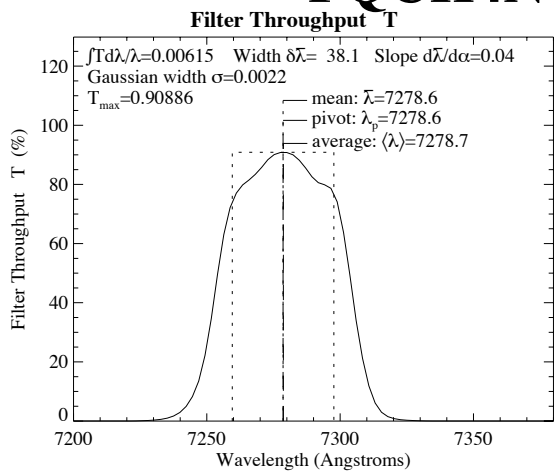

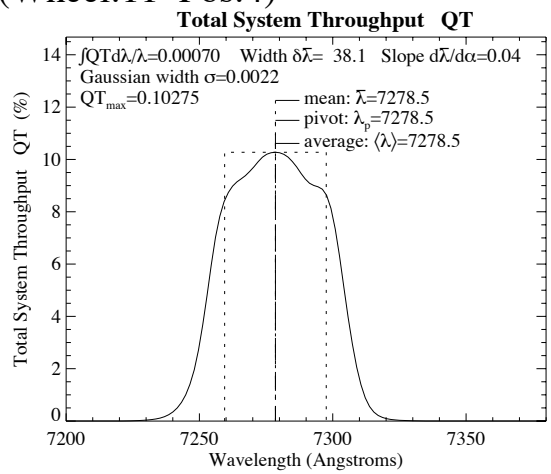

A.1.17 FQCH4N-D, Parallel and Perpendicular Polarizers

FQCH4N-D (Wheel:11 Pos:4)

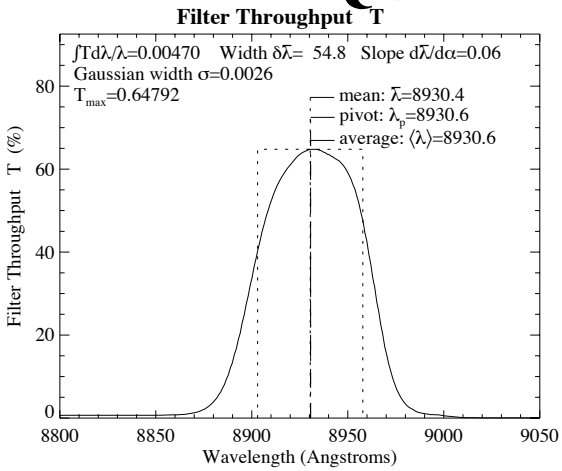

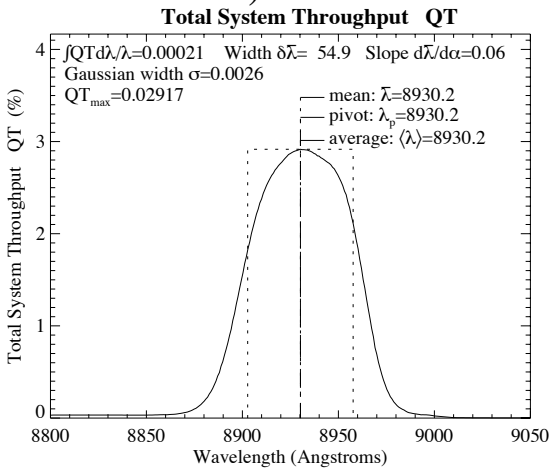

POLQ_par (Wheel:11 Pos:1)

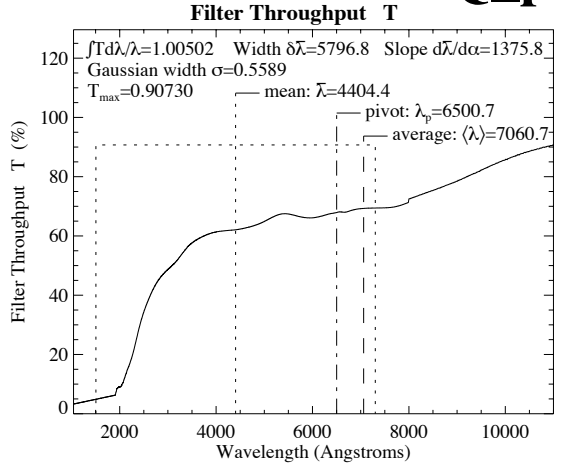

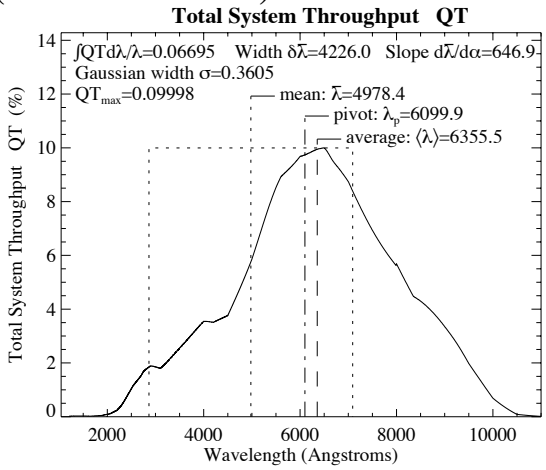

POLQ_per (Wheel:11 Pos:1)

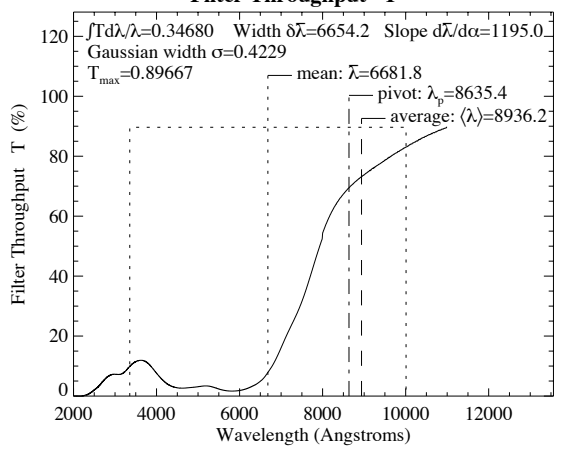

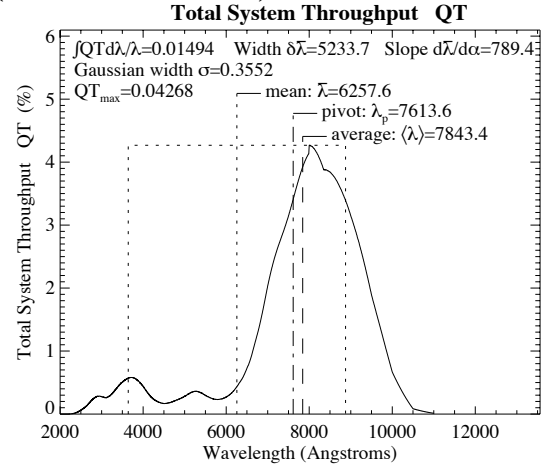

A.2 Normalized Passbands including System Response

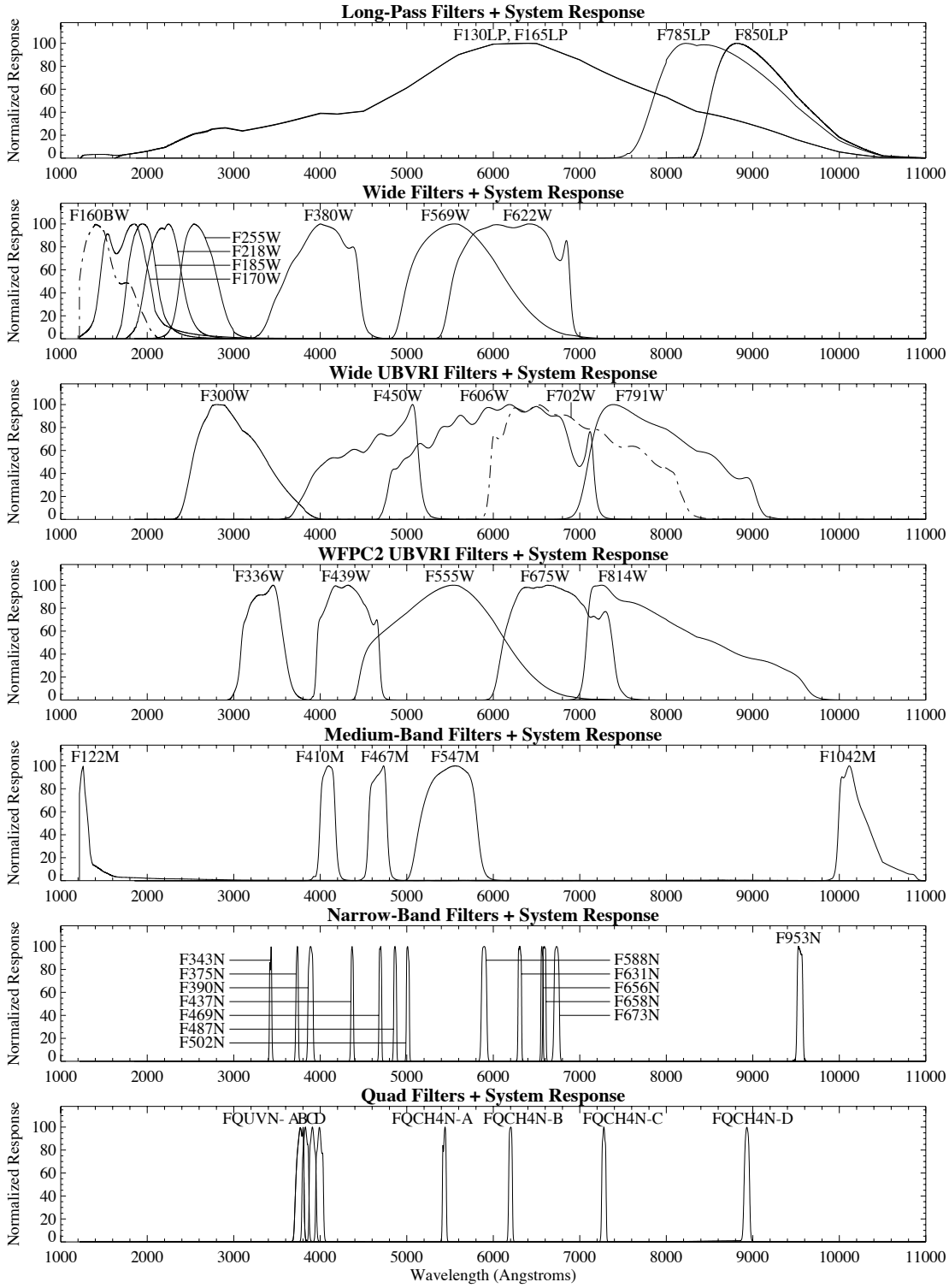

APPENDIX B:

Point Source SNR Plots

In this section we present plots which may be used to rapidly estimate signal-to-noise ratio (SNR) for point sources with stellar spectra observed through popular WFPC2 filters. Plots are given for filters F160BW, F218W, F255W, F300W, F336W, F410M, F439W, F502N, F547M, F555W, F606W, F675W, F702W, and F814W. These plots assume that the data will be analyzed by PSF fitting, which optimizes the SNR in the background noise limited case. They also assume an average sky background of V=22.9 mag arcsec^{-2}. These plots do not explicitly include SNR reduction due to CR-SPLITing when the read noise dominates, but this effect is easily included as described below.

In situations requiring more detailed calculations (non-stellar spectra, extended sources, other sky background levels, don't know target V magnitude, etc.), the WFPC2 Exposure Time Calculator tool, located on the WFPC2 WWW pages, should be used instead.

One uses these plots as follows:

1. Examine Table B.1 and find the spectral type and wavelength of the desired filter (e.g. F555W ≈5500Å). Interpolate in the table to get AB_V.
2. Sum the V magnitude of the target and AB_V derived from the table.
3. Find the appropriate plot for the filter in question, and locate $V+AB_V$ on the horizontal axis. Then read off the SNR for the desired exposure time, or vice-versa.
4. To get accurate values for CR-SPLIT exposures, one should use the sub-exposure time when consulting the plot, and then multiply the resulting SNR by $\sqrt{N}$, where N is the number of sub-exposures to be averaged.

There are separate lines for PC1 (light lines) and the WFC (heavy lines), as well as for ATD-GAIN=7 (default, solid lines), and ATD-GAIN=15 (dashed lines).

Dotted lines across the top of each plot indicate the onset of saturation. There are lines for saturation of the ATD-GAIN=7 setting (G=7), saturation of the ATD-GAIN=15 setting (G=15), and finally a line where blooming starts (top-most line for given camera).

We now give a sample SNR calculation using these plots. Consider a V=20 star of spectral class G0, for which we want to derive the SNR for 1200s CR-SPLIT exposure in F555W on PC1. We look up the G0 spectral class and F555W filter (5500Å) in Table B.1, and obtain AB_V=0.02. We thus have V+AB_V=20.02. We look at Figure B.10 and find this value on the horizontal axis. We locate exposure time 600s (one-half of the total 1200s CR-SPLIT exposure), and find SNR~200. For the total 1200s exposure the SNR would be $200\sqrt{2} = 280$. This exposure is well below the saturation lines in the plot, so saturation is not a concern. If instead, the star had V=19, we would be approaching the "Saturate G=7 PC" line indicating A-to-D converter saturation at gain 7, and so would want to specify ATD-GAIN=15.

Table B.1: AB_ν as a Function of Wavelength. AB_ν is defined as a color-dependent correction from V magnitude to AB magnitude at frequency ν. Wavelength (Å) runs along the top; spectral classes run down the left most column. The second column contains B-V. See Section 6.3.

	B-V	1500	2000	2500	3000	3500	4000	4500	5000	6000	7000	8000	9000	10000
sky	1.10	2.45	5.46	5.46	3.12	2.00	1.03	0.55	0.18	-0.11	-0.33	-0.55	-0.65	-0.75
B0	-0.31	-1.60	-1.50	-1.20	-0.78	-0.62	-0.46	-0.36	-0.22	0.16	0.46	0.76	0.96	1.17
A0	0.00	2.22	1.35	1.11	1.21	1.00	-0.23	-0.16	-0.09	0.11	0.22	0.33	0.36	0.4
F0	0.27	7.22	4.10	3.11	1.99	1.38	0.29	0.06	0.03	0.03	0.05	0.08	0.09	0.1
G0	0.58	8.9	6.35	4.61	2.46	1.63	0.67	0.26	0.08	-0.04	-0.12	-0.21	-0.23	-0.25
K0III	1.07	13	10.3	8.11	5.46	2.13	1.16	0.46	0.2	-0.24	-0.42	-0.61	-0.66	-0.72
M0III	1.60	15	12.3	9.36	6.21	4.63	2.26	0.96	0.51	-0.46	-0.76	-1.06	-1.12	-1.19
gE	1.00	6.82	6.41	5.43	3.63	2.49	1.40	0.55	0.21	-0.19	-0.52	-0.81	-1.07	-1.29
Sa	0.80	5.40	4.80	4.10	3.00	2.01	1.12	0.44	0.19	-0.17	-0.44	-0.7	-0.95	-1.16
Sbc	0.60	4.03	3.18	2.86	2.46	1.54	0.84	0.34	0.17	-0.14	-0.37	-0.6	-0.84	-1.04
Scd	0.45	2.67	2.29	2.15	1.76	1.35	0.65	0.28	0.13	-0.11	-0.26	-0.39	-0.47	-0.58
Ir I	0.30	1.77	1.40	1.36	1.24	0.94	0.43	0.34	0.17	0.13	-0.04	-0.21	-0.33	-0.45

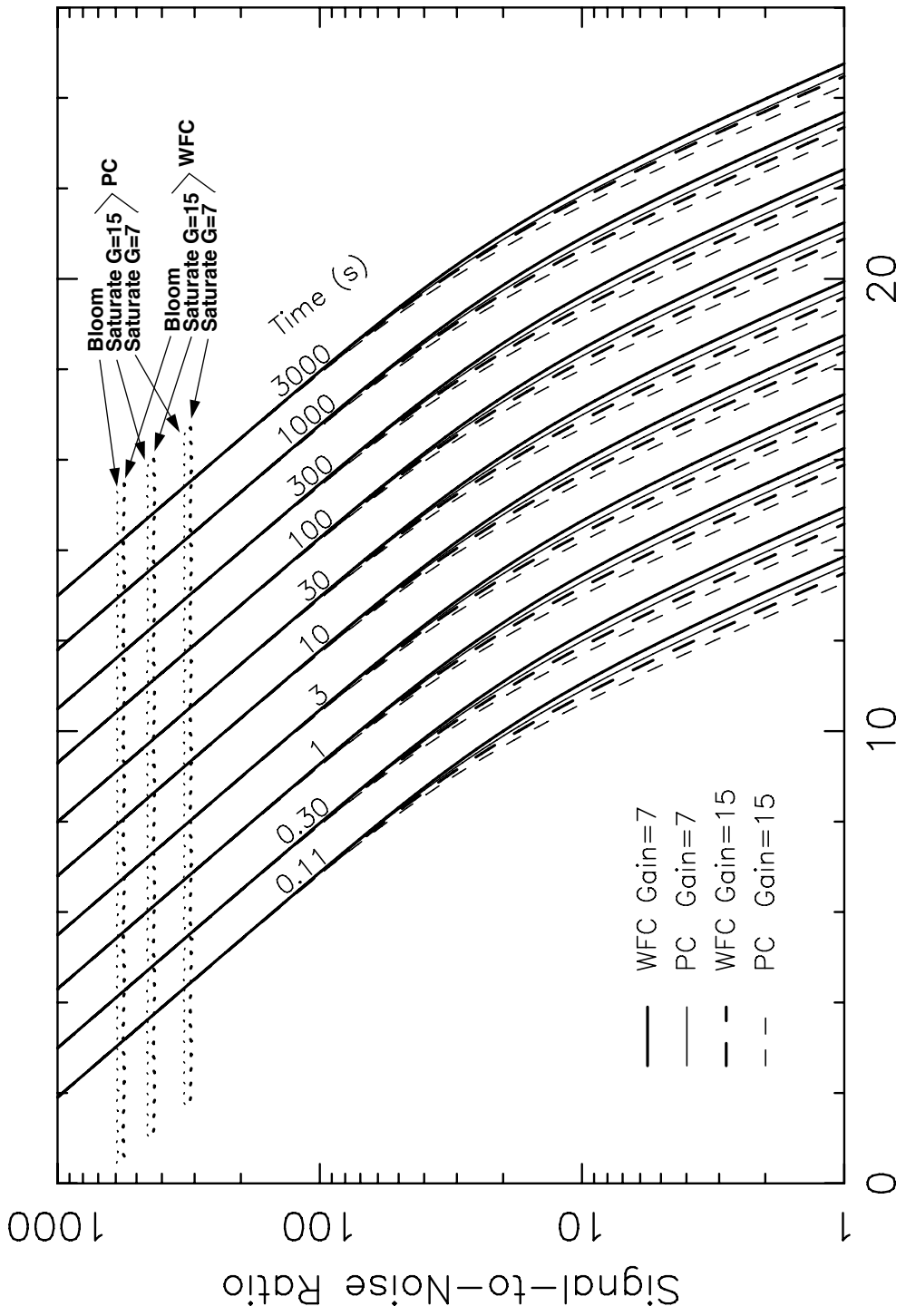

Figure B.1: Point Source SNR vs. V+AB$_V$ for F160BW Filter.

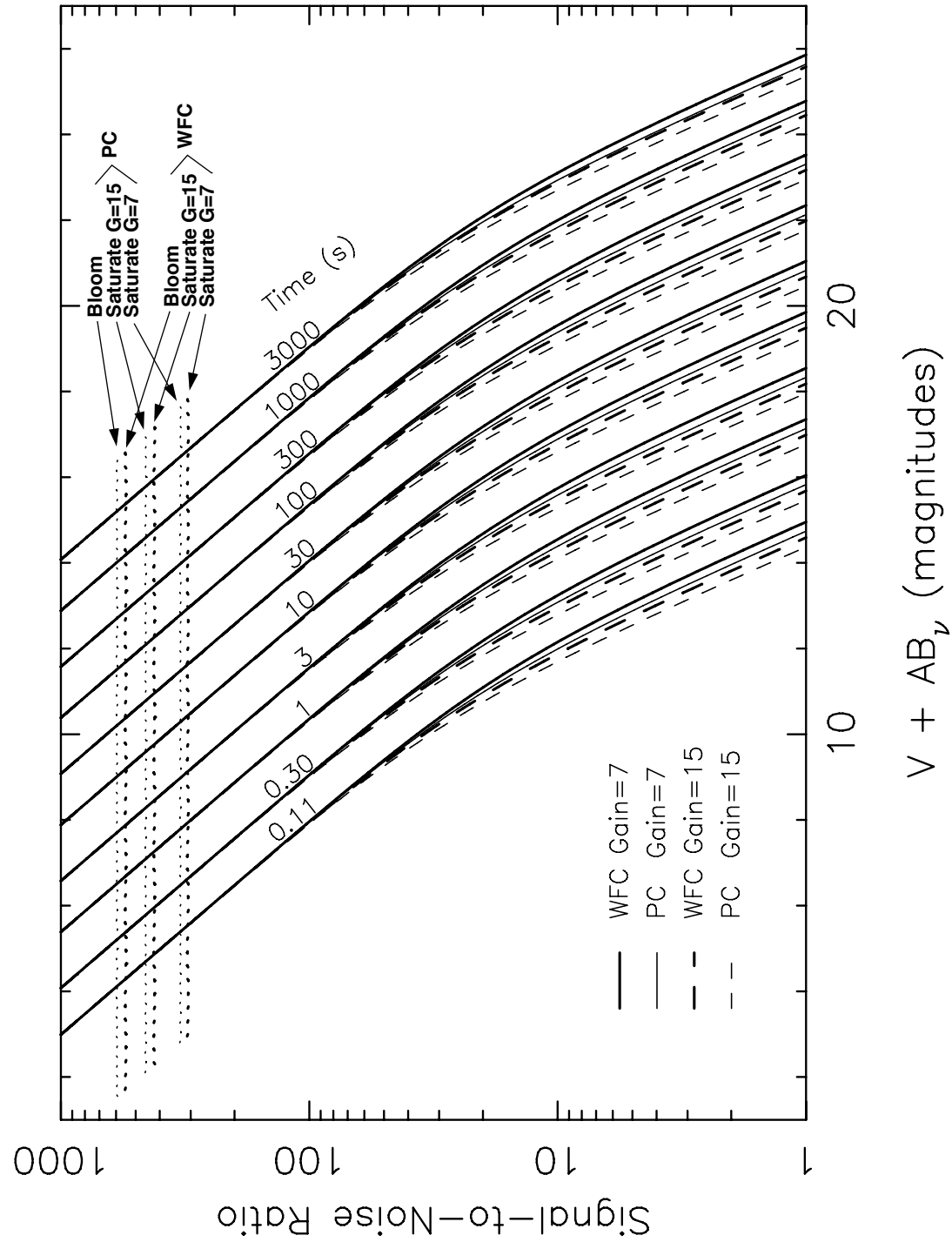

Figure B.2: Point Source SNR vs. V+AB$_V$ for F218W Filter.

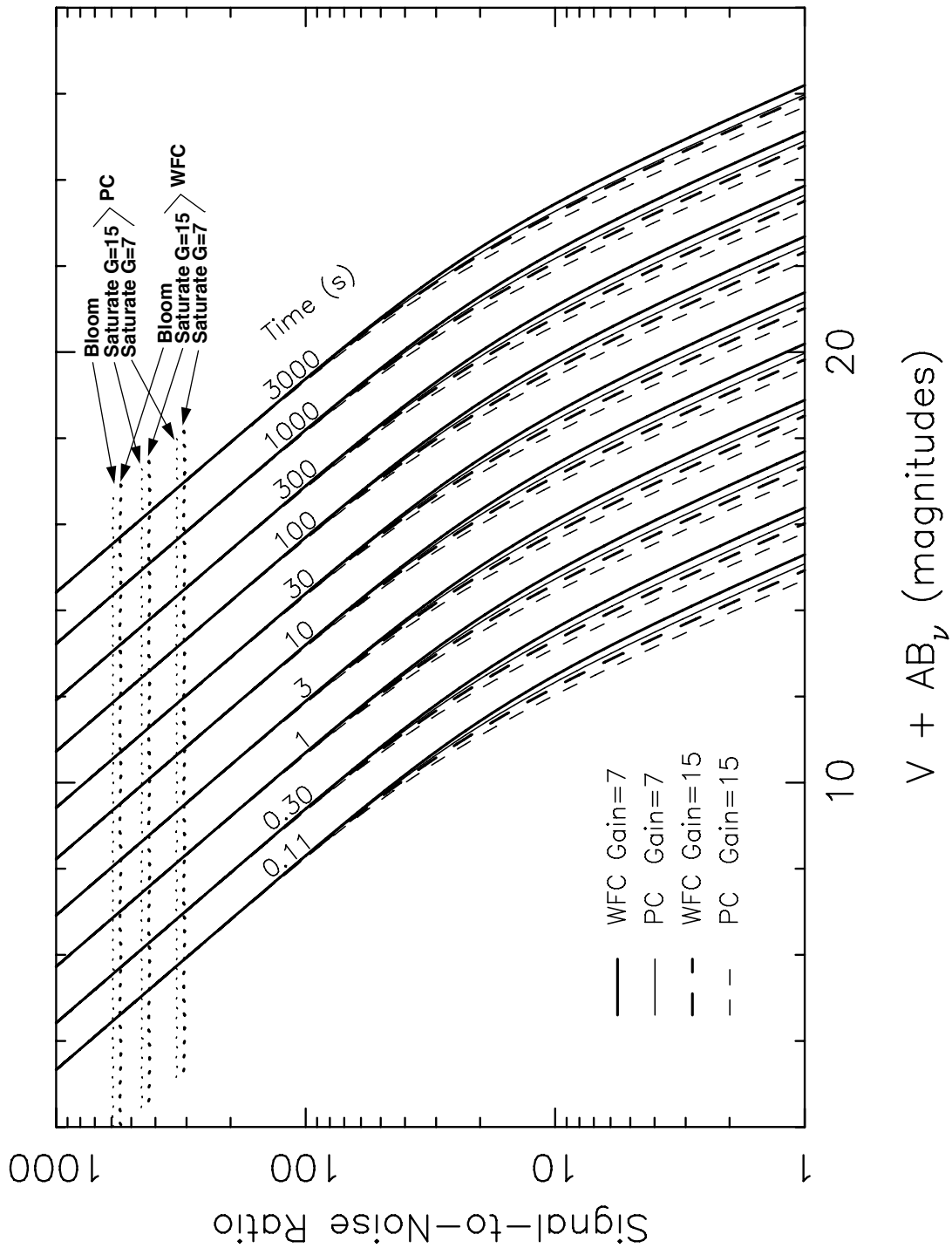

Figure B.3: Point Source SNR vs. V+AB$_V$ for F255W Filter.

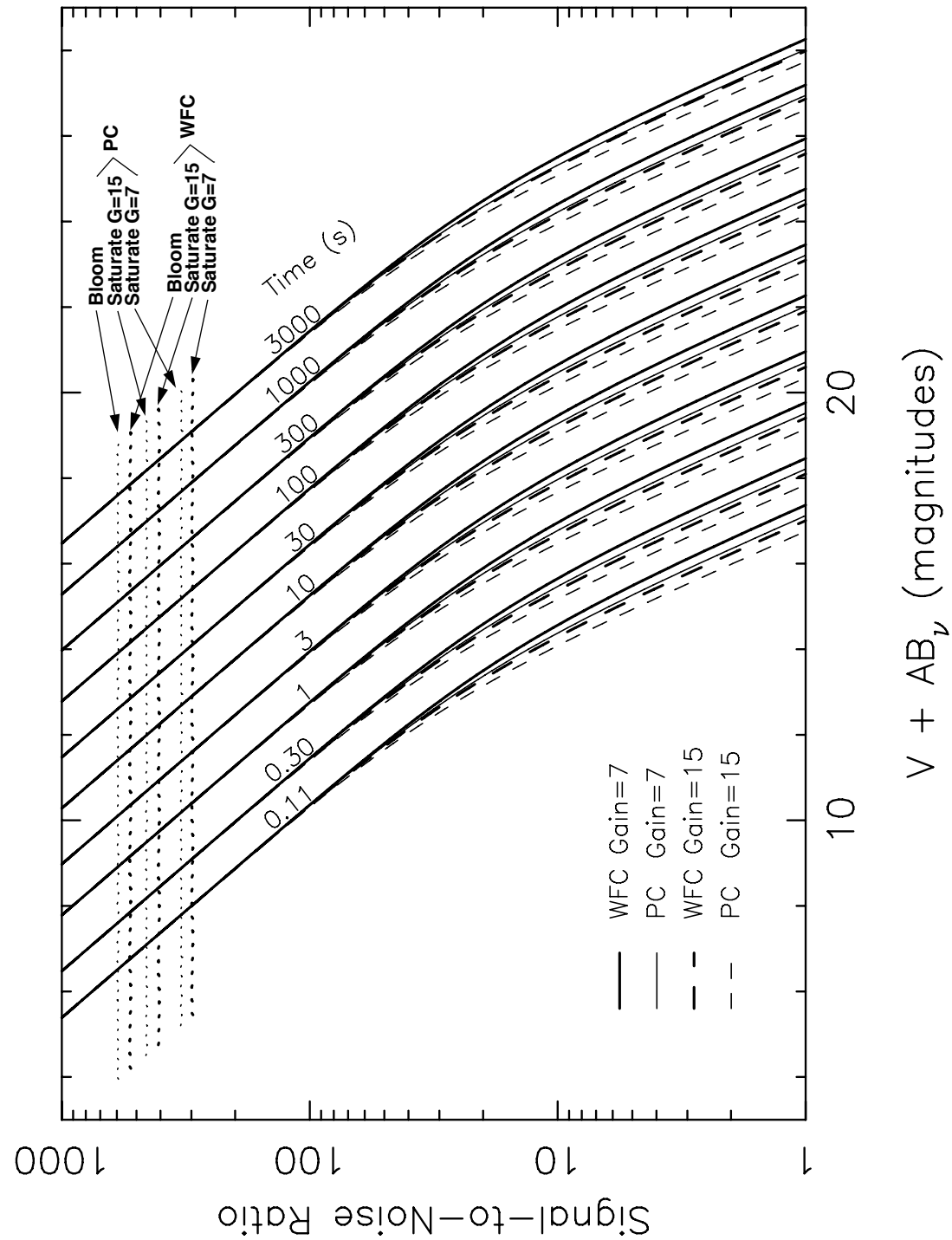

Figure B.4: Point Source SNR vs. V+AB$_\nu$ for F300W Filter.

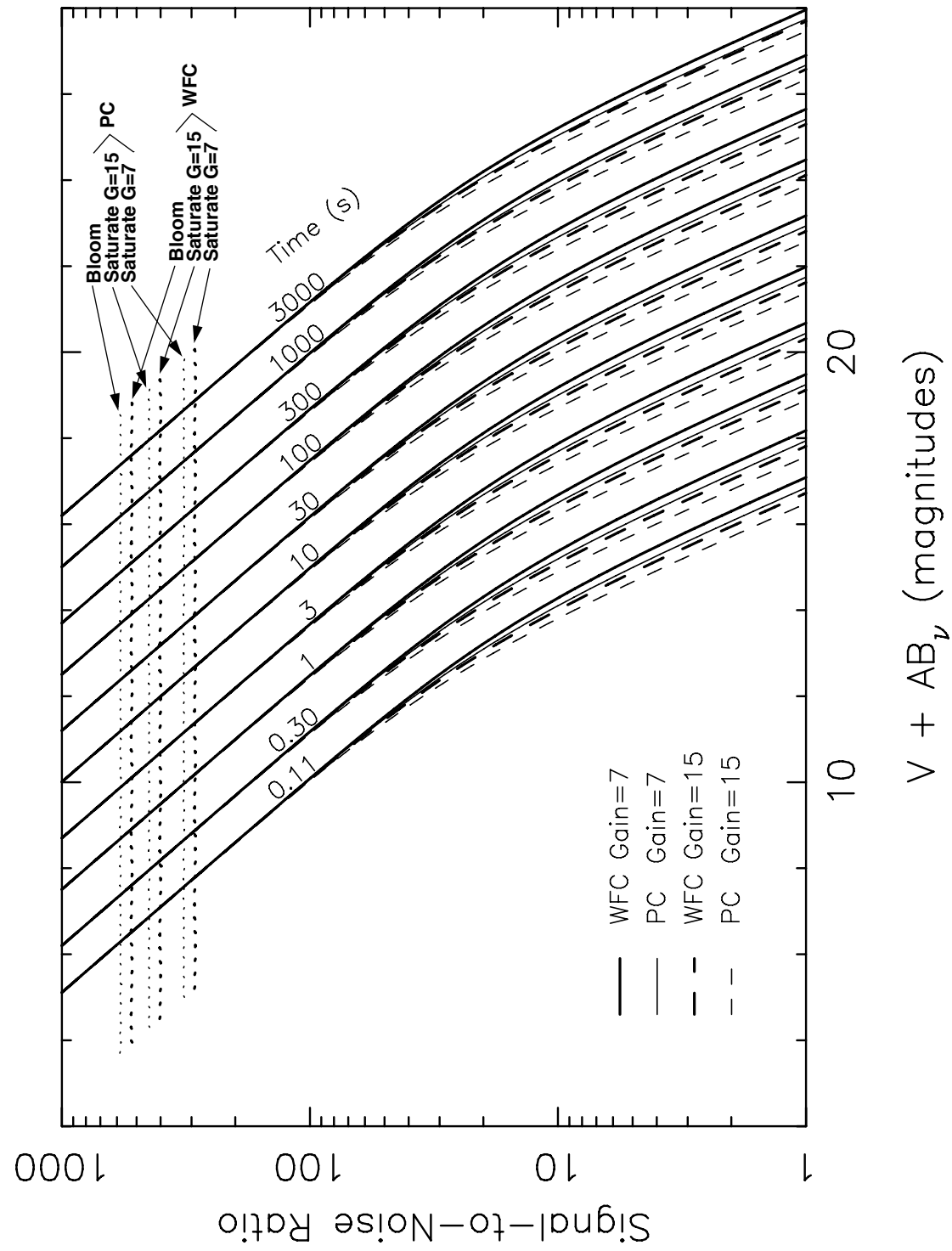

Figure B.5: Point Source SNR vs. V+AB$_V$ for F336W Filter.

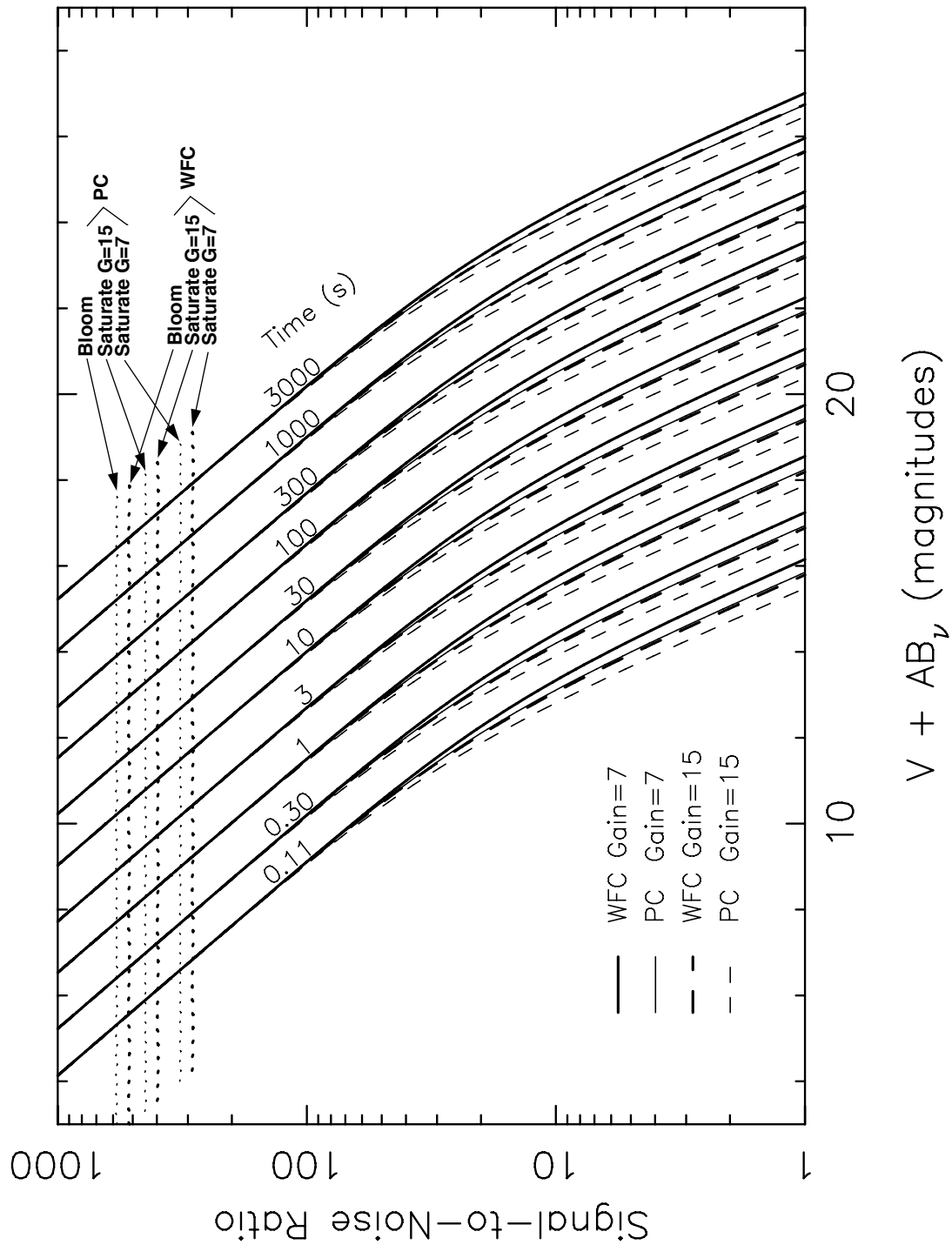

Figure B.6: Point Source SNR vs. V+AB$_V$ for F410M Filter.

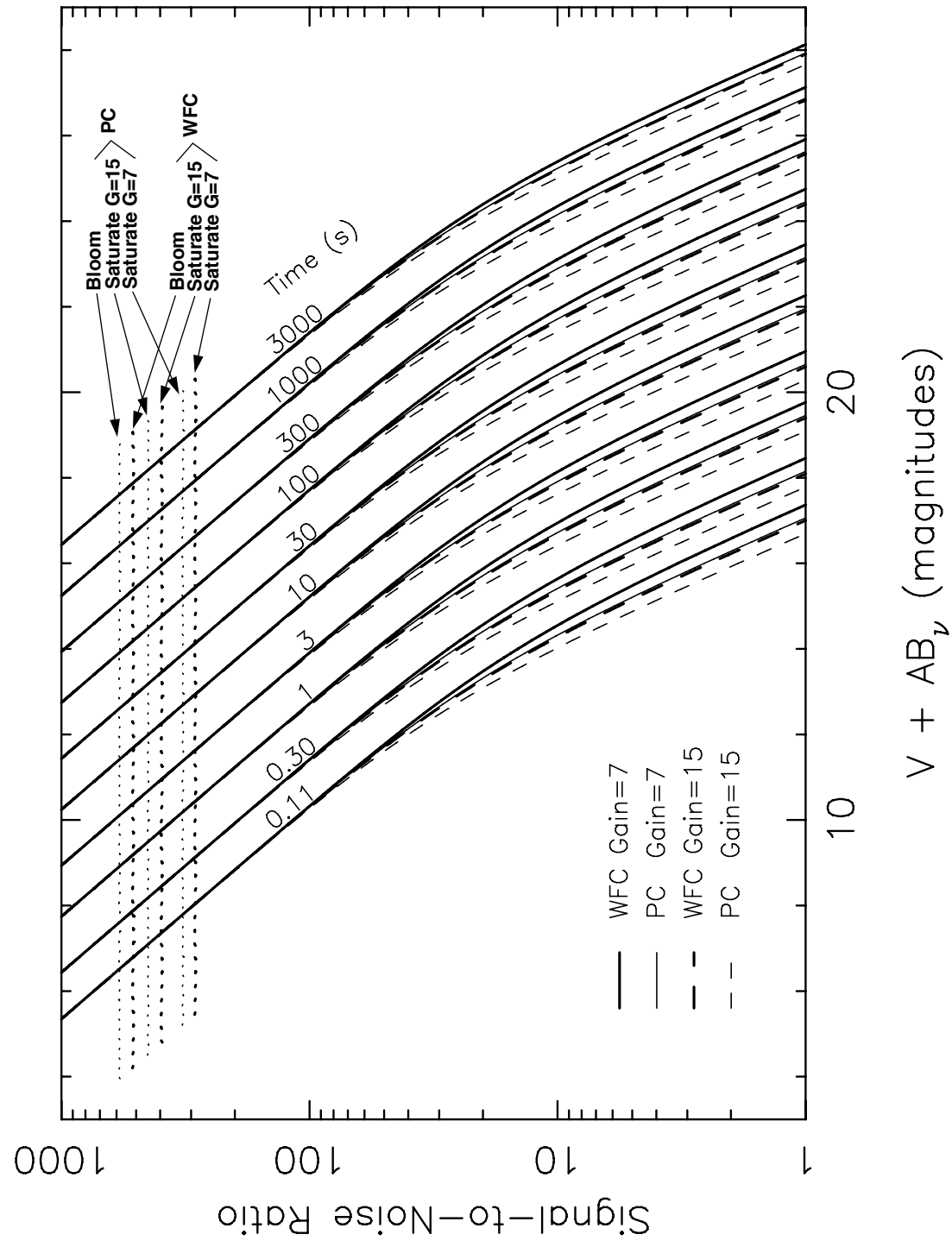

Figure B.7: Point Source SNR vs. V+AB$_V$ for F439W Filter.

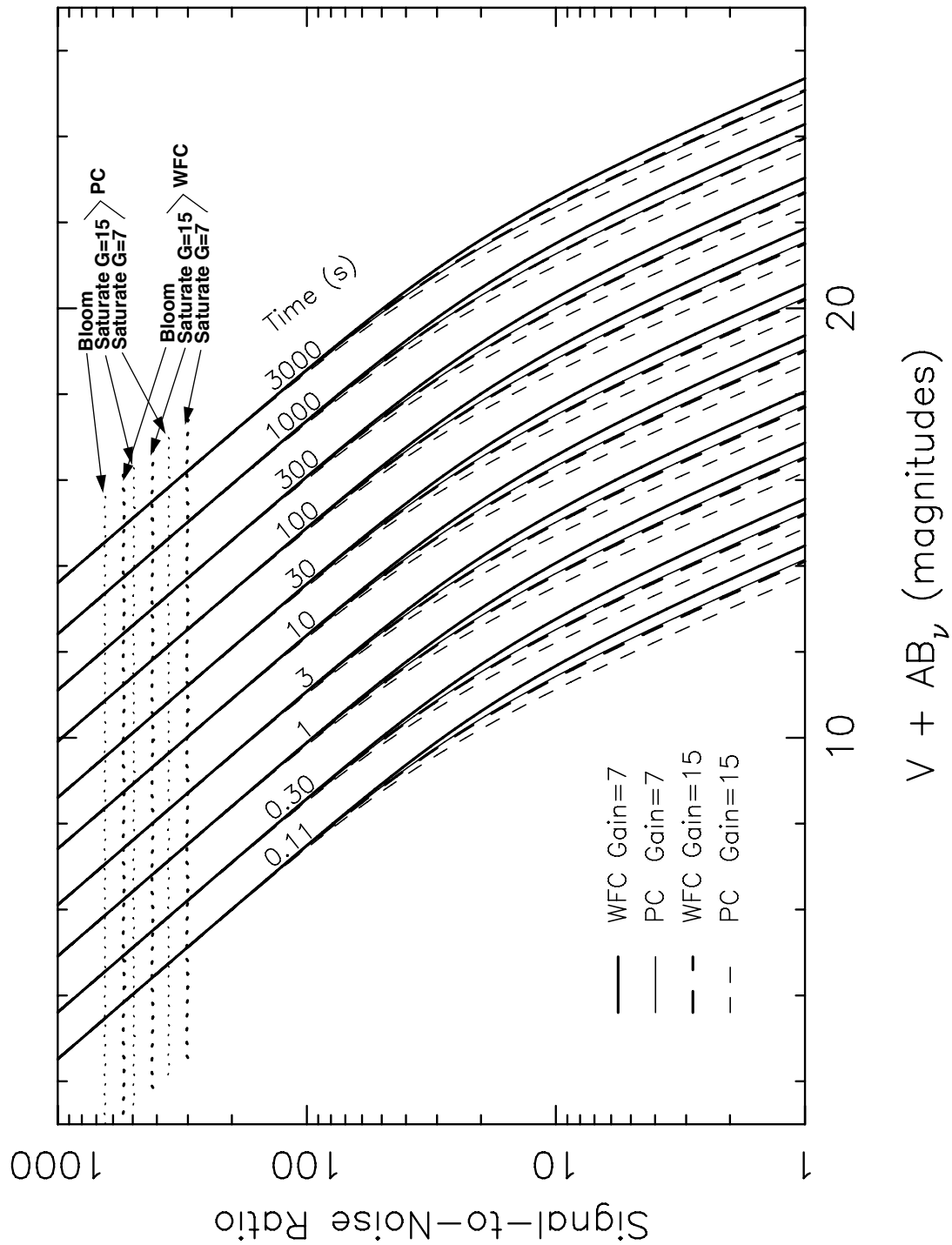

Figure B.8: Point Source SNR vs. V+AB$_V$ for F502N Filter.

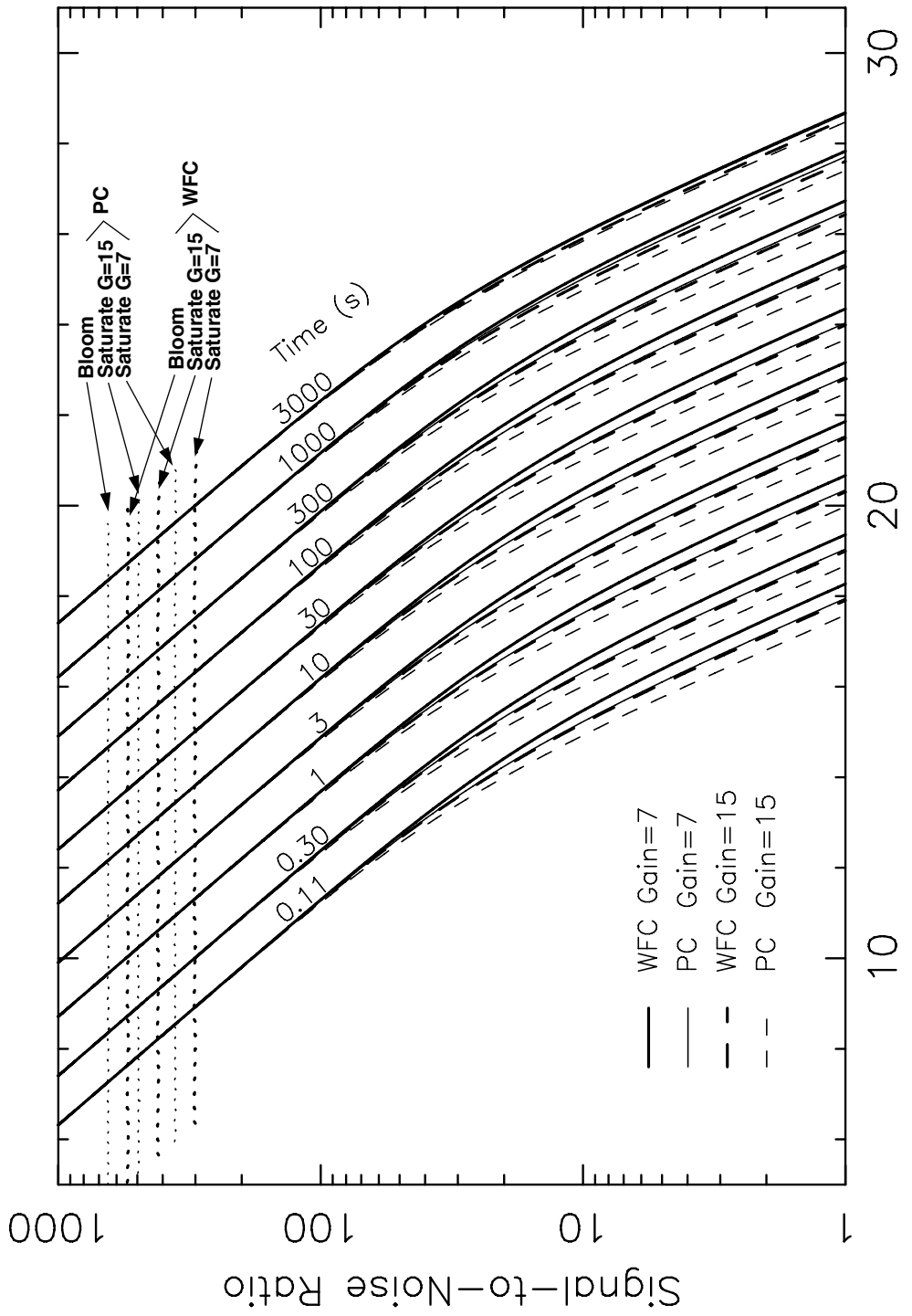

Figure B.9: Point Source SNR vs. V+AB$_\nu$ for F547M Filter.

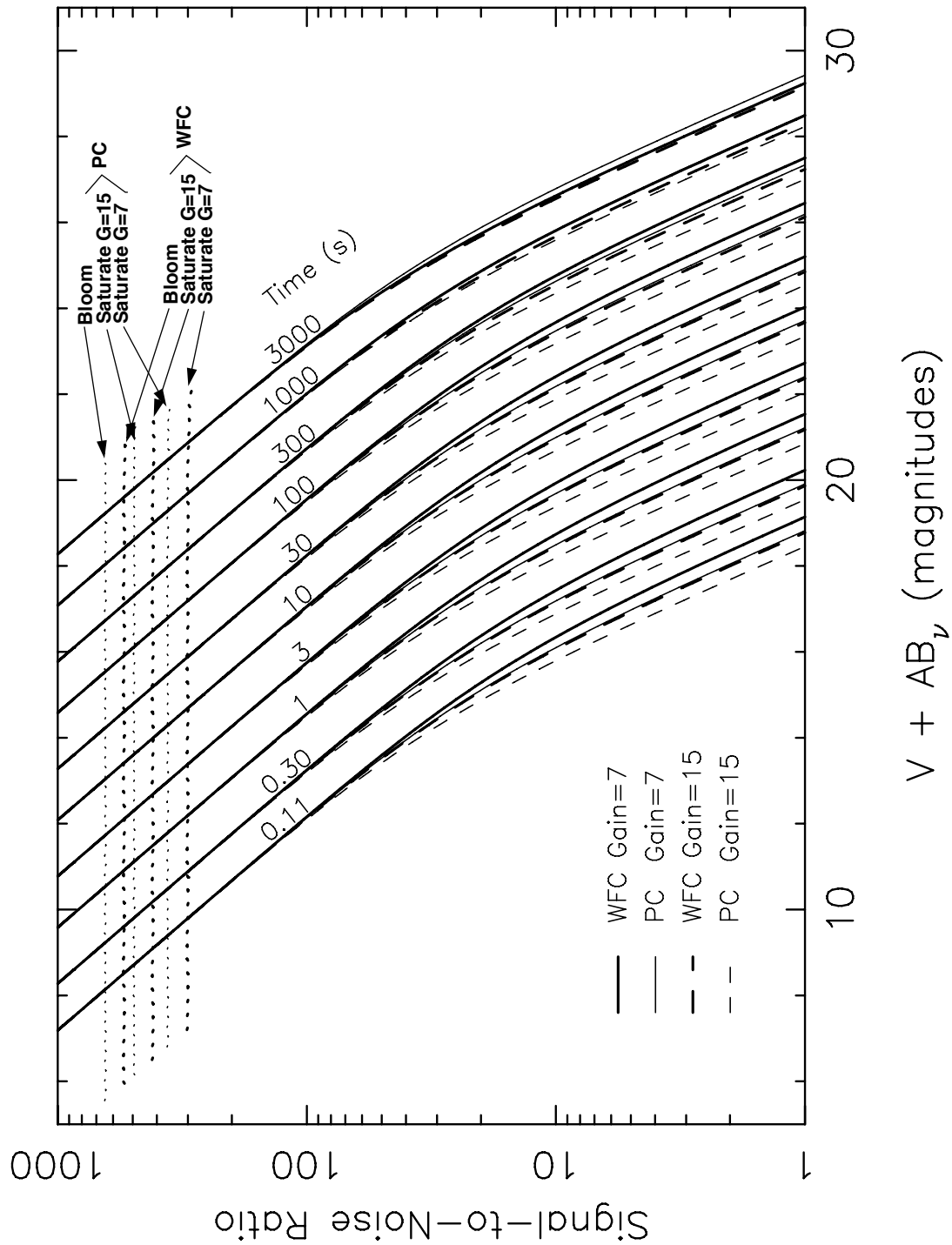

Figure B.10: Point Source SNR vs. V+AB$_V$ for F555W Filter.

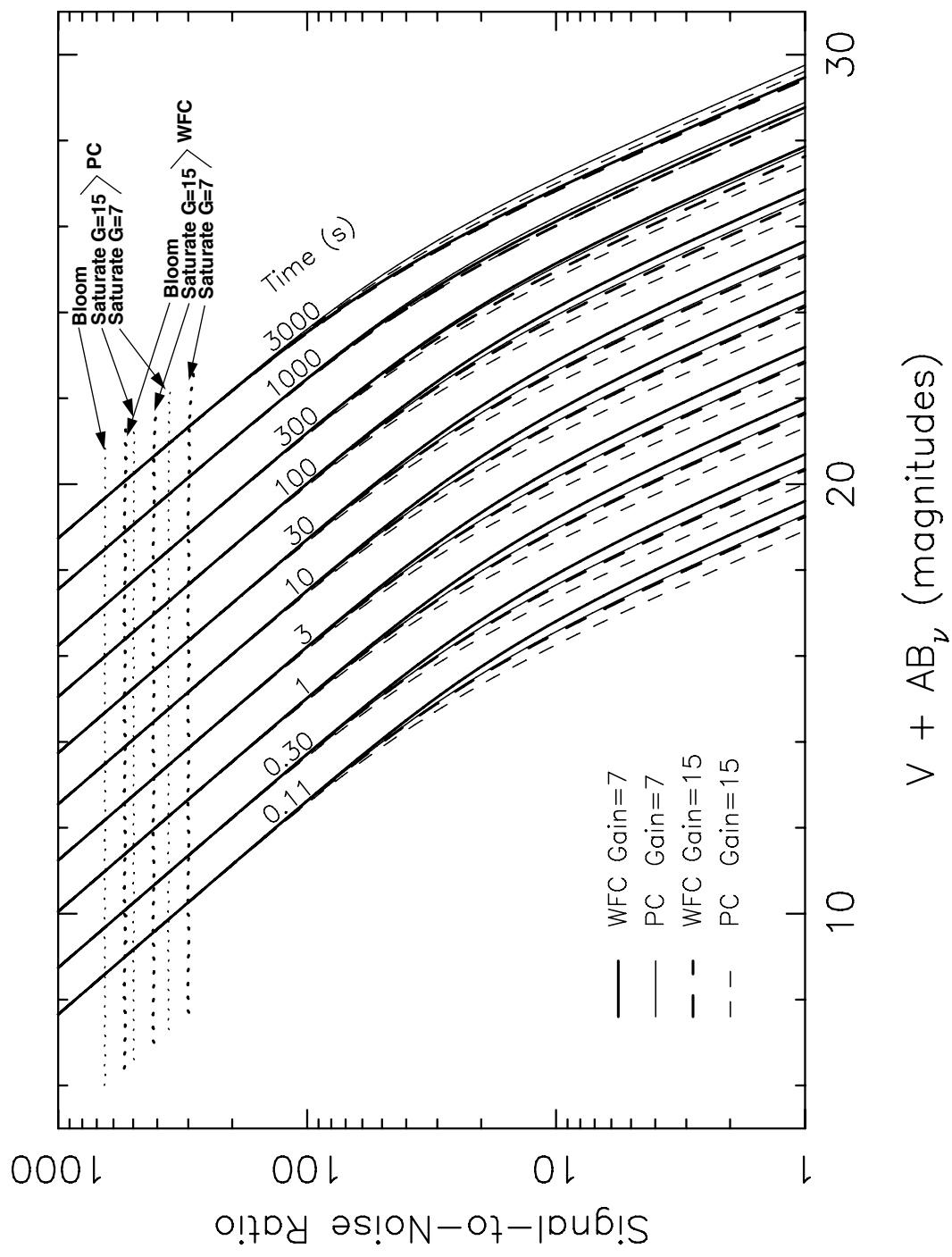

Figure B.11: Point Source SNR vs. V+AB$_v$ for F606W Filter.

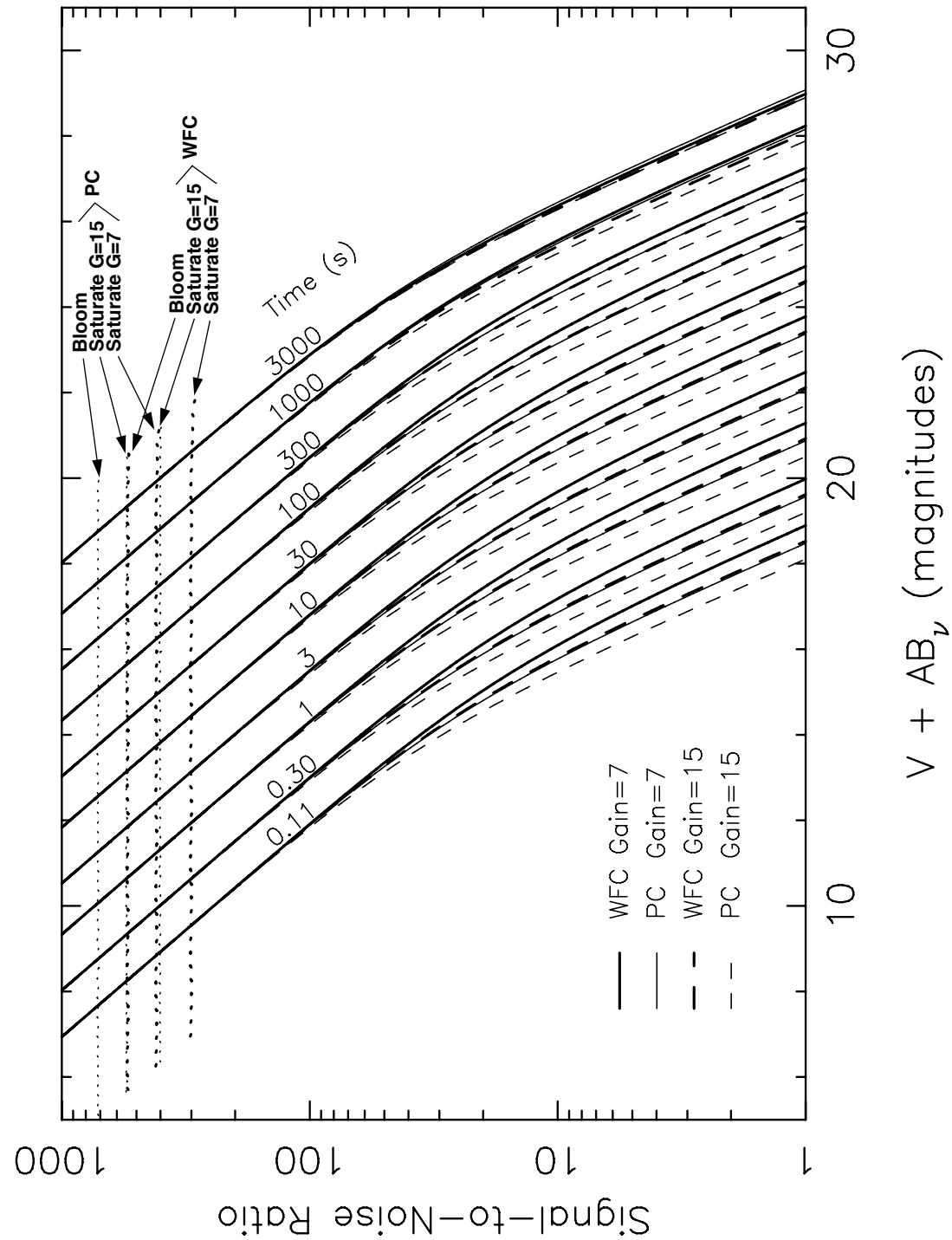

Figure B.12: Point Source SNR vs. V+AB$_V$ for F675W Filter.

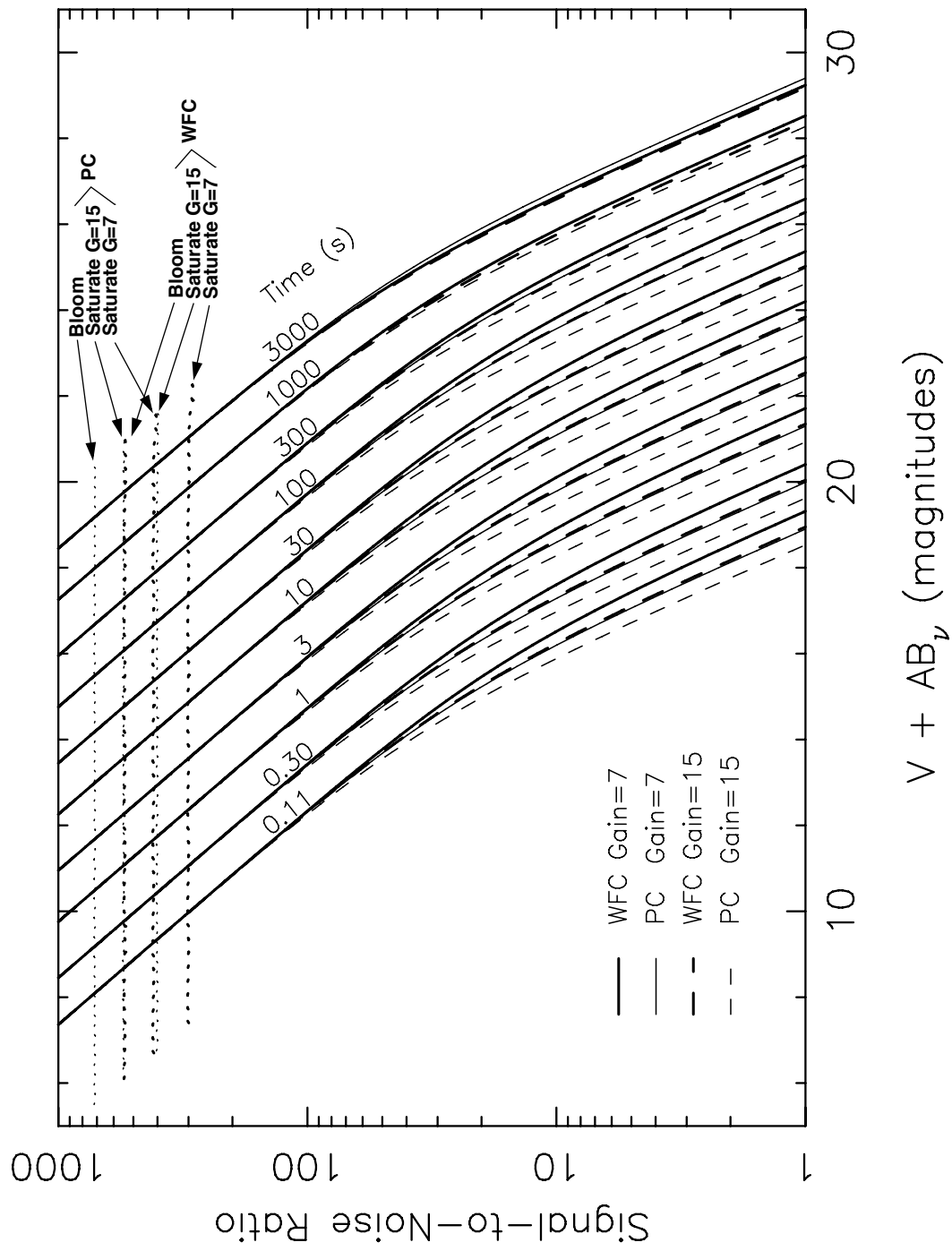

Figure B.13: Point Source SNR vs. V+AB$_v$ for F702W Filter.

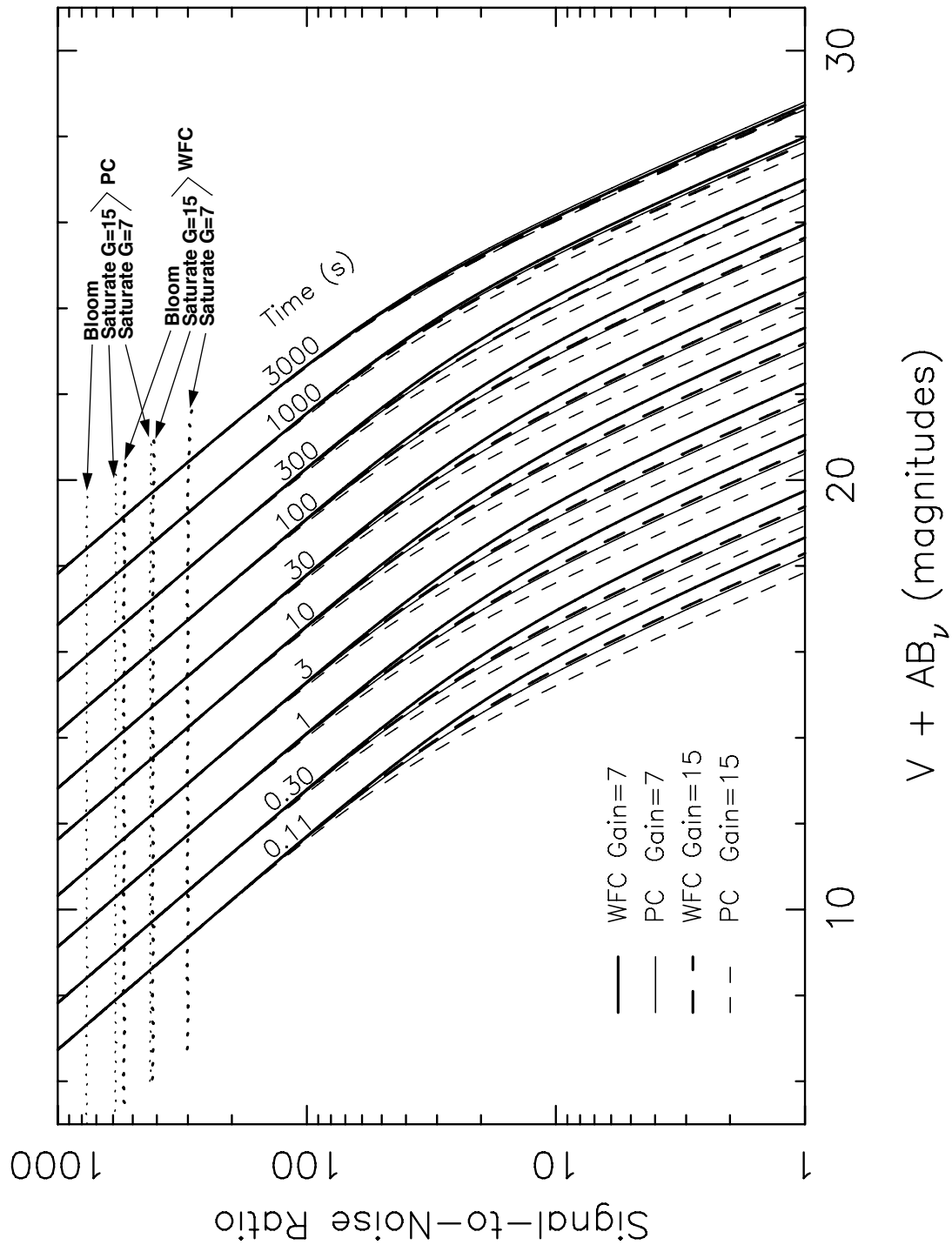

Figure B.14: Point Source SNR vs. V+AB$_V$ for F814W Filter.

Acronyms

ACS	Advanced Camera for Surveys
ADC	Analog-to-Digital Conversion
ADU	Analog-to-Digital Units (see DN)
CCD	Charge-Coupled Device
CDBS	Calibration DataBase System
CEIS	Contract End Item Specification
CVZ	Continous Viewing Zone
DQE	Detector Quantum Efficiency
DN	Data Number (output of A-to-D converter)
EE	Encircled Energy
FITS	Flexible Image Transport System
FOC	Faint Object Camera
FOV	Field of View
GEIS	Generic Edited Information Set
GO	General Observer
GSFC	Goddard Space Flight Center
GTO	Guaranteed-Time Observer
HDF	Hubble Deep Field
HST	Hubble Space Telescope
ICD	Interface Control Document
IDT	Instrument Definition Team
IR	Infrared
ISR	Instrument Science Report
JPL	Jet Propulsion Laboratory
LEO	Low Earth Orbit
mas	milliarcsecond
MPP	Multi-Pinned Phase

MTF	Modulation Transfer Function
NICMOS	Near-IR Camera and Multi-Object Spectrograph
OTA	Optical Telescope Assembly
PC	Planetary Camera
PI	Principal Investigator
PODPS	Post Observation Data Processing System
PSF	Point Spread Function
QEH	Quantum Efficiency Hysteresis
RBI	Residual Bulk Image
RMS	Root Mean Square
RTO	Reuse Target Offset
SAA	South Atlantic Anomaly
SLTV	System Level Thermal Vacuum Test
SMOV	Servicing Mission Orbital Verification
SNR	Signal-to-Noise Ratio
STAN	Space Telescope [Data] Analysis Newsletter
STEIS	Space Telescope Electronic Information Service
STIS	Space Telescope Imaging Spectrograph
STScI	Space Telescope Science Institute
STSDAS	Space Telescope Science Data Analysis System
TIPS	Telescope and Instruments Performance Summary
TIR	Technical Instrument Report
UV	Ultraviolet
WF/PC-1	Wide Field and Planetary Camera
WFC	Wide Field Camera
WFPC2	Wide Field and Planetary Camera 2
WWW	World Wide Web

Index

D

E

F

G

H

I

P

Q

R

S

T

U

V

W

X

Y

Z